REVIEW OF THE VKI DOCTORAL RESEARCH

2012 - 2013



von Karman Institute for Fluid Dynamics

Covert art : *Design of heavy-liquid metal pump of the MYRRHA research reactor by Lasse Müller who has been attributed the best presentation award during the symposium.*

©2013 by the von Karman Institute for Fluid Dynamics

Waterloosesteenweg 72, B-1640 Sint-Genesius-Rode
To order: https://www.vki.ac.be

ISBN 978-2-87516-060-7

D/2013/0238/625, T. Magin, Editor-in-Chief

The contents of this book are the property of the von Karman Institute for Fluid Dynamics. No part of this book may be reproduced or distributed in any form of by any means, or stored in a database or retrieval system, without the prior written permission from the Publisher.

PREFACE

The fourth symposium on the doctoral research of the von Karman Institute for Fluid Dynamics took place during the period March 4 to 6, 2013. The doctoral students have presented the progress of their research work carried out in the three departments: Aeronautics and Aerospace, Environmental and Applied Fluid Dynamics, Turbomachinery and Propulsion. The first year students have presented a poster on their research plans and some preliminary results, while the most advanced students have proposed a twenty minute presentation followed by a session of questions.

This event was attended by the faculty of the von Karman Institute as well as by some colleagues from universities and industrial partners. The Symposium was open to external attendees free of charge. In addition to the presentations of the PhD candidates, we had the pleasure to welcome prominent keynote lecturers who have opened each day the Symposium:

- Marc Schyns, ANS Deputy Director and MYRRHA Project R&D Program Manager, "***MYRRHA - Multipurpose hYbrid Research Reactor for High-tech Applications - Contributing to the 3rd Pillar of the European Strategy for Partitioning &Transmutation – Project status end 2012***".
- Thomas Doerr, Chief of Combustion Aero-Thermals, Rolls-Royce Deutschland Ltd & Co KG, ***"Challenges and current researches in Combustion".***
- Kurt Sermeus, EADS, Cassidian Air Systems, ***"CFD in applied aerodynamics - examples from the aircraft industry".***

This year, the best presentation award has been attributed to Lasse Müller for his research on ***Design of heavy-liquid metal pump of the MYRRHA research reactor***. We would like to congratulate him on his achievement. The illustrated cover art of these proceedings is based on his research results.

This proceedings volume contains 31 papers which are divided into the following topics: "Noise and aeroacoustics," "Multiphase flow," "Aero-thermal investigations in turbomachinery," "Optimization in turbomachinery," "Numerical modeling of aerothermodynamics during re-entry," "In-flight experiments," "Hypersonic flows in ground facility," "Development of Advanced CFD".

We would like to emphasize that this publication serves as a tool for communication and aims to enhance exchange between the doctoral candidates, and the faculty and external attendees. The annual publication of their results in proceedings is of crucial importance to the VKI research providing a thorough review of the different activities within the three departments.

As such, the doctoral candidate students of the VKI play a key role in strengthening the expertise in experimental and numerical/physical modeling of the Institute. In addition to basic research, works carried out at the Institute often leads to implementation of real life industrial applications critical to the fluid dynamics community.

This edition contains a new who's who section. The present proceedings are registered under an ISBN number and may be referred to in any further publication.

Clara Garcia Sánchez
Jérôme Sans
Phd Representatives and
Symposium co-Chairs

Patrick Rambaud
Associate Professor
Symposium Chair

Jean Muylaert
VKI Director

The contribution of all VKI members who helped with this event is deeply acknowledged in particular the faculty, library and printing office.

TABLE OF CONTENTS

Editorial notes i

Table of contents iii

Noise and aeroacoustics

Filip Ballien (first year doctoral summary) 3
Hybrid numerical simulation of aeroacoustics of detached flows with residual distribution method

Leandro Dantas de Santana 5
A calibration procedure for wall pressure measurements by electret-microphones and determination of wake-airfoil interaction noise parameters

Ugur Karban (first year doctoral summary) 15
Scale-resolved and stochastic approaches for the prediction of the noise produced by ducted singularities in HVAC systems

Multiphase flow

Bart Janssens 19
Development and validation of a finite element solver for dispersed two-phase flows

Clara Garcia Sanchez (first year doctoral summary) 27
Realistic statistical input model for microscale atmospheric boundary layer simulations

Imre Horvath 29
Validation of the multi wavelength light extinction technique on a sub-micron KCl aerosol by scanning mobility particle sizing measurements

Jorge Pinho 41
Experimental study of two-phase flow induced by cavitation through a safety relief valve at inlet subcooling conditions

Alessia Simonini (first year doctoral summary) 53
Study of cryogenic sloshing and moving contact line in microgravity conditions

Chiara Spaccapaniccia 55
Experimental study of a buoyant plume and thermal stratification in a liquid metal nuclear reactor

Aero-thermal investigations in turbomachinery

Francesco Baldani 69
Heat transfer in high subsonic velocity environments behind the fan of a gas turbine

Cis De Maesschalck (first year doctoral summary) 81
Design, analysis, optimization and control of rotor tip flows

Fabrizio Fontaneto 83
Detailed aero-thermal analysis of a film-cooled turbine vane: methodology of the experimental campaign

Jérôme Sans 95
The effect of solidity on compressor performance and stability

Sebastian Scholl 107
Development of a conjugate heat transfer solver in COOLFluid 3

Stefano Vagnoli (first year doctoral summary) 117
Towards full annulus coupled simulations on gas turbines

Optimization in turbomachinery

Christopher Chahine (first year doctoral summary) 121
Robust multidisciplinary optimisation of composite fan blades

Michael Joly 123
Evolutionary optimization for multidisciplinary design of transonic turbomachinery components

Lasse Müller 131
Design of heavy-liquid metal pump of the MYRRHA research reactor

Numerical modeling of aerothermodynamics during re-entry

Alessandro Munafo 145
Multiscale models and computational methods for aerothermodynamics

Pierre-Louis Schrooyen 155
Development of a numerical simulation tool for the aerothermal flow through an ablative Thermal Protection System for atmospheric entry

James B. Scoggins 165
The development of the MUlticomponent Thermodynamics And Transport properties for IONized gases in C++ library: MUTATION++

Gennaro Serino 177
Development of advanced hypersonic models for transition to turbulence: uncertainty quantification of transition prediction

Erik Torres 189
Physico-chemical models for rarefied gas-kinetic simulations with application to atmospheric entry flows

Alan Viladegut (first year doctoral summary) 203
Validation of gas-surface interaction modeling for lifting body re-entry flight design

In-flight experiments

Gilles Bailet 207
Radiative and ablative studies for in-flight validation on reentry platforms

Işıl Şakraker 217
In-flight experiment design and ground testing of a re-entry Cubesat

Thorsten Scholz 227
Mission analysis for a network of atmospheric science and in-orbit demonstration CubeSats

Hypersonic flows in ground facility

Bernd Helber 239
Material response characterization of low density carbon-phenolic ablators in high-enthalpy plasma flows

Guillaume Grossir 251
Design of boundary layer transition experiments at large hypersonic Mach numbers focusing on the determination of free-stream conditions

Bart Van Hove 263
Density reconstruction in hypersonic entry using flush air data systems

Development of Advanced CFD

Martin Vymazal 277
High–order RDS and p-multigrid Solution Algorithms for Compressible Flow

Who's who? 285

NOISE AND AEROACOUSTICS

Hybrid Numerical Simulation of Aeroacoustics of Detached flows with Residual Distribution Method

Filip Baillien

Environmental and Applied Fluid Dynamics Department, von Karman Institute for Fluid Dynamics, Belgium, filip.baillien@vki.ac.be

Supervisor: Christophe Schram

Associate Professor, Environmental and Applied Fluid Dynamics Department, von Karman Institute for Fluid Dynamics, Belgium, christophe.schram@vki.ac.be

Abstract

The aim of the current Ph.D. is to improve the Residual Distribution solver of the in-house code COOLFluiD for aeroacoustic problems. The turbulent source regions will be computed using the Large Eddy Simulation turbulence model which will then, for computational efficiency, be coupled with a Linearized Euler Equation solver in the far-field. This project is part of the ANADE project (Advances in Numerical and Analytical tools for DEtached flow prediction), ran inside the Marie Curie program.

Keywords: Computational Aeroacoustics, Residual Distribution Method (RDM), Large Eddy Simulation, Linearized Euler Equations, ANADE

1. Introduction

Two main classes of aeroacoustic simulations can be distinguished: the direct and the hybrid approach. The direct approach computes the whole computational domain, which for aeroacoustics is very large, using a single solver. For LES simulations the mesh requirements are stringent and have to be applied across the whole domain, massively increasing the computational and storage costs associated with a simulation. Moreover, all aeroacoustics computations are unsteady, further increasing the costs.

A solution to this problem is found in the hybrid approach: the computational domain is divided in two zones, a source region and a propagation region. The source part of the domain, where the noise generation occurs, is computed using an LES solver. This is because the source region is a highly turbulent, non–linear region where time dependency and viscosity are important parts of the solution. The propagation region on the other hand, is computed with an LEE solver because noise propagation is linear and non–viscous. Time dependency remains an important factor in this region as well. This combination of the two methods allows to accurately resolve noise generation through the LES region, while taking advantage of the coarser grid requirements of the LEE solver and its simpler set of equations. In flight coupling between the two models is planned and should bring improvements in computational time as well as in memory requirements.

Due to aeroacoustics' high accuracy requirements, new techniques like high order methods or the Residual Distribution method are important as they can further reduce the costs and provide the necessary accuracy.

The RD method is a solution reconstruction method which presents interesting advantages over currently used methods: it is far less impacted by the quality of the mesh than Finite Volume methods and it is capable of maintaining high accuracy, even with a low order reconstruction [1]. The method can be described as an hybrid between Finite Element and Finite Volume [2] where the difference between the continuous solution and the discretized solution is the residual. The residual is computed for every cell and then distributed to its nodes according to the scheme in use. (e.g. in a central scheme the residual will be evenly distributed on all the nodes while in an upwind scheme it will proportionally be distributed to the downstream nodes).

Using pseudo timesteps the solution is then iterated to minimize the residuals until convergence is reached. For unsteady simulations, several approaches, such as the mass matrix method and the space time method, are possible. In this project the space time method will be used where time is analyzed as an additional dimension, providing therefore the same order of accuracy both in space and time [3].

2. Objectives

This project will focus on:

- further improve the coupling between the LES and LEE solver,
- application of the unsteady RDM on quad-cell based meshes,
- analysis of the RD method in aeroacoustics,
- comparison of the RD method with other high order schemes through the ANADE framework.

The following test cases are planned and should be carried out during the first year of the project:

- Two corotating vortices.
- Tandem cylinder configuration.

The two corotating vortices test case, shown in Fig. 2 is a basic test case in aeroacoustics where two vortices, initially separated, interact with each other generating noise while gradually merging. The tandem cylinder configuration, a well know aeroacoustic test case from Lockard [4] is set up as shown in Fig. 1. Since it is difficult to computationally analyze, this is also an international benchmark. In it, two streamwise aligned cylinders generate noise with the interaction of their wakes.

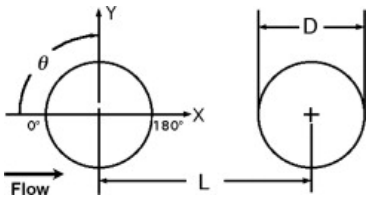

Figure 1: Tandem Cylinder configuration [5]

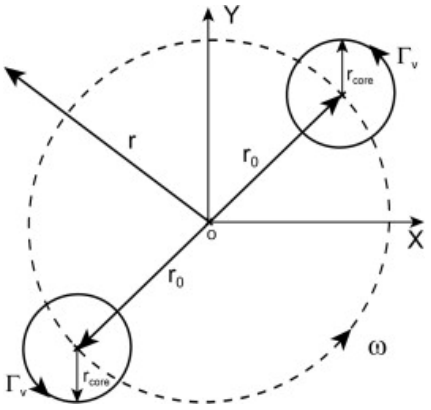

Figure 2: Corotating Vortices configuration [6]

Acknowledgments

The research leading to these results has received founding from the European Community's Seventh Framework Programme (FP7, 2007-2013), PEO-PLE programme, under the grant agreement No. FP7-289428 isc(ANADE project).

References

[1] G. Rossiello, High order accurate Residual Distribution methods for unsteady compressible flows, Ph.D. thesis, Politecnico di Bari (2004).

[2] L. Koloszár, Numerical prediction of noise production and propagation, Ph.D. thesis, Universite Libre de Bruxelles (2012).

[3] Jir Dobesa, Mario Ricchiuto, Herman Deconinck, Implicit space–time residual distribution method for unsteady laminar viscous flow, Computer and Fluids 34 (4-5) (May-June 2005) 593–615.

[4] Lockard, D., Khorrami, M., Choudhari, M., Hutcheson, F., Brooks, T., and Stead,D, Tandem cylinder noise predictions, AIAA 2009-3275.

[5] Ali Uzun and M. Yousuff Hussaini, An application of delayed detached eddy simulation to tandem cylinder flow field prediction, Computers and Fluids 60 (3) (2012) 71–85.

[6] G. Linka, M. Kaltenbacherb, M. Breuerc, M. Dllinger, A 2D finite–element scheme for fluid–solid–acoustic interactions and its application to human phonation, Computer Methods in Applied Mechanics and Engineering 198 (41-44) (2009) 3321–3334.

A Calibration Procedure for Wall Pressure Measurements by Electret Microphones and Determination of Wake-Airfoil Interaction Noise Parameters

Leandro D. Santana

Aeronautics and Aerospace Department, von Karman Institute for Fluid Dynamics, Belgium, leandro.santana@vki.ac.be

Supervisor: Christophe Schram

Associate Professor, Aeronautics and Aerospace Department, von Karman Institute for Fluid Dynamics, Belgium, christophe.schram@vki.ac.be

University Supervisor: Wim Desmet

Full Professor, KULeuven, Department of Mechanical Engineering, Belgium, wim.desmet@mech.kuleuven.be

Abstract

The unsteady wall pressure measurement on wind-tunnel models is a concern for many applications where the experimental calculation of time fluctuating loads, on a localized part of the sample, is aimed. This sort of measurements on wind-tunnel models are particularly challenging due to limitations of space and transducer cost. The use of electret microphones has been shown, given proper calibration, as an interesting alternative to overcome these limitations. The present paper proposes a two-steps calibration procedure for electret microphones and applies this development on an array of flush-mounted electret microphones over the surface of an airfoil subjected to incoming rotating wakes. The chord-wise distribution of pressure and its correlation with the airfoil noise is calculated. Results demonstrate the potential of the proposed experimental approach on accurately compute hydrodynamic fluctuation on an airfoil surface.

Keywords: electret microphone, wall pressure measurements, rotor-airfoil noise

1. Introduction

The accurate wall-pressure measurements is an important problem to several disciplines related with wind-tunnel testing [1; 2; 3; 4; 5]. The efficient and accurate wall-pressure measurement on a wide frequency spectrum and a high dynamic range normally conflicts with issues related to the transducer cost, simplicity and volume [4; 6; 7]. The present works intends to explore the use of electret microphones in order to overcome these difficulties and introduce an experimental procedure, shown as practicable, to the use of this kind of devices.

The present paper presents a portable calibrator device specially developed to calibrate the electret microphones *in-situ*. This calibrator was developed in such way that allows directly considers installation effects that affects the microphone calibration and small amplification differences and phase delays that the electronic amplification circuit may present. The calibration procedure is detailed and sample calibration results are presented. This calibration procedure is afterward applied to an airfoil instrumented with a microphone array on both sides and subject to a rotating wake downstream flow. Its results are first compared with analytical theory results and then related with the far-field noise, from where the main airfoil noise source location can be correlated with the measured far-field noise. The present paper results are in good agreement with the respective theories, proving the success of the calibration procedure.

2. Experimental set-up

2.1. The calibration device

The concept for the calibration is based on a two-step approach, where, on a first step, the transfer func-

tion between two reference Bruel and Kjaer microphones, calibrated against laboratory standards, is obtained and, on a second step, this transfer function is used for obtaining the calibration curve of the desired electret microphone.

The calibrator device presented on Figure 1 is designed to be portable and allow *in-situ* calibrations. This calibrator driven by 20 Watts speaker linked to a Plexiglas tube of 30 mm of diameter and 95 mm length, equipped with a Bruel and Kjaer 4191 microphone on its side. For these dimensions, it is expected acoustic plane wave propagation on frequencies up to 2800 Hz and the first longitudinal mode is expected to be present at 1780 Hz.

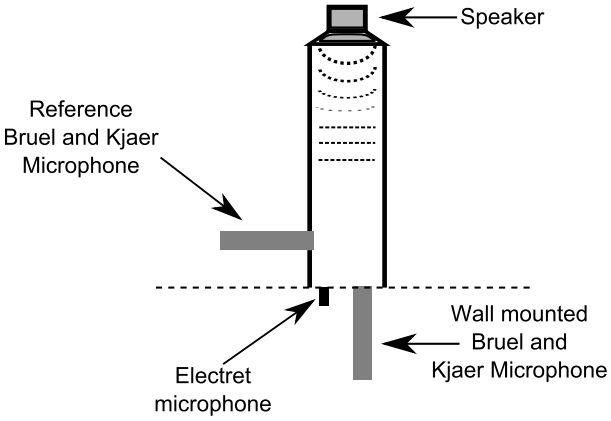

Figure 1: Schematic representation of the calibrator device.

During the calibration procedure, on a first step, the transfer function between two Bruel and Kjaer microphones are established, the reference microphone, indicated on Figure 1, is firmly kept on its position and the calibrator is moved to the test facility in order to calibrate the desired electret microphones, which are located on the wall-mounted position of the calibrator.

2.2. The rotor-airfoil testing facility

The rig is assembled in the fan aeroacoustic facility of the von Karman Institute for Fluid Dynamics, permitting the measurement of acoustic levels simultaneously with the aerodynamic characterization of low-speed fans running at a controlled operating point. Besides the air flow entrained by the fan under consideration, flow can be also supplied through the test rooms by an external blower. This permits to run the rotor at any pressure-flow rate operating point [8]. The rotor blades shape is based on a well-documented airfoil, the Valeo-CD profile [9]. The acoustic pressure can be measured with a Bruel and Kjaer half-in microphone

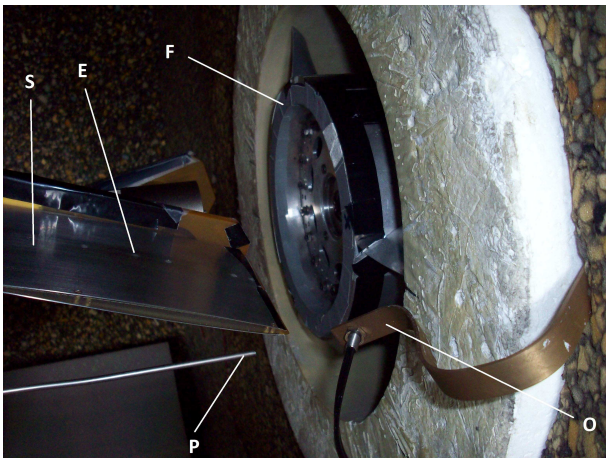

Figure 2: Airfoil subjected to the incoming rotating wakes. The flush-mounted electret microphones. F: fan. O: photodiode. P: Pitot probe. E: electret microphone. S: static pressure

at a distance of 0.6 m above the stator vanes. The reference configuration discussed below is a 3-bladed rotor, rotating at 2000 rpm, inducing a bulk velocity of 17 m/s on the downstream stator. The motivation for using such a low solidity rotor is to obtain reduced frequencies in the same range as for a typical CROR configuration. The baseline axial separation between the rotor trailing edges and the stator vanes leading edges is equal to one rotor chord (0.055 m). Using such large separation is meant to minimize the potential interaction effects from the downstream stator to the upstream rotor. The stator stagger angle is about 15°, which was found to roughly correspond to a 0° angle of attack over the region of interaction between the wakes and stator, as shown by flow visualization studies using tufts.

The external blower was used in order to have the 3-bladed rotor running at a suitable operating point (without flow separation) and generating realistic wakes. As a preliminary test, measurements of the background noise of the facility were conducted with everything switched off, with the rotor motor running without any blade and with/without the externally-driven flow, and finally with the 3-bladed rotor.

2.3. Data acquisition parameters

For the data acquisition the National Instruments compact DAQ 9215 and the National Instruments PXI 6143 acquisition cards were conveniently used. Both acquisition cards have a dynamic range of 16 bits and are able to sample all its channels with a maximum sampling frequency of 100 kHz. An analogical filter with high-pass frequency of 0.3 Hz and low-pass

frequency of 22 kHz was also used to avoid, respectively, low-frequency components and alias effects on the measurements. The following parameters were used for all data acquisition: sampling frequency is of 51200 Hz, the Discrete Fourier Transform (DFT) block size 65536 (2^{16}) samples, these values lead to a narrow-band resolution of 0.7813 Hz, and the hanning window was applied to each block to avoid leakage effects due to the finite sampling. The chosen sampling time was of 60s and the DFT block overlap of 50%, which results a total of 94 averages of the computed spectrum. For the calibrator transfer function determination and electret calibration curve determination the loudspeaker was driven by white noise.

3. Calibration approach

The calibration is executed on a two-step approach: on a first step a Bruel and Kjaer microphone is placed on the wall mounted position and a complex reference transfer function between this microphone and the reference Bruel and Kjaer microphones is computed; on a second step, the free termination of the portable calibrator device is placed on the position of the wall-mounted electret microphone to be calibrated, and a second complex transfer function, between the reference Bruel and Kjaer and the electret microphone is calculated. Finally, from these two transfer functions it is possible to obtain the complex calibration curve that should be used to correct the phase and amplitude of the electret microphone measured signal.

Since the Bruel and Kjaer microphones are calibrated against a laboratory reference, it is straight forward to obtain its signal in pressure level units (Pa), by turn, the electrets microphones have unknown calibration, consequently its signal should be given in units of electric tension (V). Calling the acoustic pressure measured by Bruel and Kjaer microphone, localized on the reference position, as P_{REF} and the Bruel and Kjaer microphone, localized at the wall-mounted position - used on the first step of the calibration procedure, as P_{WALL}, the reference transfer function obtained between the two Bruel and Kjaer microphones is given by the relation:

$$TF_{REF}(f) = \frac{P_{WALL}(f)}{P_{REF}(f)} \tag{1}$$

where P_{TEST} is $E(p'(f))$, expectation of the time domain pressure measured by the Bruel & Kjaer microphone at the wall-mounted position. In addition, P_{REF} is $E(p'(f))$, the expectation for the Bruel & Kjaer microphone at the reference position. TF_{REF} is a non-dimensional quantity. Denominating the wall-mounted electret measured voltage as V_{WALL}, the transfer function between the electret and the reference microphone, which should be obtained on the second step of the calibration procedure is given by the relation:

$$TF_{ELECT}(f) = \frac{P_{REF}(f)}{V_{WALL}(f)} \tag{2}$$

where V_{WALL} is $E(V'(f))$, the expectation of the electret measured voltage. The TF_{ELECT} has dimensions of $Pa \cdot V^{-1}$. After the obtaining these two transfer functions it is possible to establish a complex calibration function for the electret microphone, which allows the computation of the complex measured signal pressure level (P_{ELECT}), in pressure units (e.g. Pascal), as a function of the electret complex measured voltage signal (V_{ELEC}), by the equation:

$$P_{ELECT}(f) = TF_{REF}(f) \times TF_{ELECT}(f) \times V_{ELEC}(f). \tag{3}$$

4. Calibration results

4.1. Calibrator transfer function

In order to validate the previously presented methodology the calibrator transfer function was computed. The Figure 3 shows the amplitude and phase of the obtained transfer function. In order to verify the repeatability of the experiment, this transfer function computation procedure was executed on different days, by different operators and the standard deviation of 10 independent experiments is showed by the area on Figure 3.

From Figure 3 it is seen that the calibrator transfer function presents a high standard deviation for frequencies below 20 Hz, while this deviation dramatically decays for higher frequencies, showing the good repeatability of this calibration. The transfer function amplitude is plane on the frequency range between 20 Hz and 800 Hz and the transfer function phase changes steadily with the frequency on this frequency rage. Based on this result a first frequency limitation to the present calibration procedure was set for the frequency range from 20 Hz to 800 Hz.

4.2. Electret calibration

On the present experiment the electret microphones are flush-mounted over the airfoil surface at both pressure suction sides, facing each other to permit comparisons at identical chord-wise positions x/c =0.046,

0.097, 0.31, 0.41, 0.56 and 0.70. To illustrate the calibration curves obtained the Figure 4 and Figure 5 shows the calibration curve for the microphones located at the suction side at the positions $x/c = 0.046$ and $x/c = 0.31$, respectively.

On Figure 4 and Figure 5 the calibration curve, showed in black, and standard deviation, showed in gray, was obtained by 10 independent experiments realized by distinct operators at different time along one week. From these figures it is seen that the electret calibration curve is not flat along the frequency range analyzed. From the variance error bar it is seen that the calibration has an important uncertainty for lower frequencies, while this uncertainty decays significantly for higher frequencies, showing the great repeatability of this experiment on higher frequencies. Another important conclusion from these results is that the electret calibration is relatively stable along one week period. The evaluation of the standard deviation shows that the calibration presents a low standard deviation on the frequency range varying from 60 Hz to 800 Hz. This result gives the final frequency range where the present methodology is valid. In this way, all the results presented on the following sections of the present paper will be considered on the frequency range of 60 Hz to 800 Hz.

During the development of the present work it was noticed that the electret microphones present a very wide calibration variation even for electret of a same lot. In order to illustrate the necessity to calibrate individually each microphone the Figure 6 presents the mean calibration and the standard deviation on the calibration curve of 18 electret microphones from a same lot.

5. Wake-airfoil interaction verification

In order to verify the present calibration procedure the aerodynamic response of the airfoil to the wakes shed by the upstream rotor is studied. On this first study the pressure jump associated with the blade passing frequency is compared with the expected results given by linearized airfoil theory [10]. This theory says that the normalized chord-wise pressure jump is given on according to the equation:

$$g(\overline{x}, k_x, 0) = \frac{1}{\pi}\sqrt{\frac{1-\overline{x}}{1+\overline{x}}}\,S(k_x) \qquad (4)$$

where $\overline{x}$ is the chord-wise coordinate normalized by the half-chord with origin at the mid-chord (ranging from -1 to 1), k_x is the wavenumber of the incoming parallel gust and S is the Sears' function, which modulates the pressure jump as a function of the perturbation wave-number.

On the present work the pressure jump was obtained as the complex difference between the computed Discrete Fourier Transform from upper and lower electret microphone calibrated signal. All the data is normalized by the airfoil chord and dynamic pressure. Figure 7 and Figure 8 show the comparison between the experimentally obtained results and the measured ones. From Figure 7 and Figure 8 it is possible to notice that the best agreement between the linearized airfoil theory and the experimental data happens for the angle of attack of 2°. This best agreement can be explained by the fact that, first, the linearized airfoil theory is idealized for small angles of attack, and, second, as this airfoil has an small camber it is expected that the angle of attack for zero lift be different of zero, possibly around 2°. For this angle of attack, the agreement is still good for the three first harmonics of the rotor blade passing frequency. The agreement is deteriorated steadily with the variation of the angle of attack from the position of zero lift.

On the present work, the coherence measurements are made between the corrected electret signal, localized on the airfoil surface, and the far-field microphone, which measures the airfoil noise. The coherence between the surface microphone and the far-field microphone is a metric that indicates if the pressure fluctuation present on the airfoil surface is responsible to the far-field measured noise. The Figure 9 and Figure 10 shows the measured coherence results.

Observing first the coherence results for all measured angle of attack it is possible to conclude, as general rule, that the first harmonic of the blade passing frequency is the main responsible for the rotor-airfoil interaction noise generation. For the first blade passing frequency all the airfoil is practically equally efficient on the noise generation, with exception to the point of maximum airfoil's thickness, on this point the maximum flow deceleration and possible present of aerodynamic bubble reduces the noise generation efficiency. For the second and third harmonic of the blade passing frequency it is noticed that most of the noise generation is concentrated on the first quarter of the chord, while the noise generation decays dramatically as the measurement position advances to the trailing edge. For the second and third harmonic of the blade passing frequency it is also seen that the point of maximum thickness is less efficient for noise generation, reinforcing the hypothesis of aerodynamic bubble formation.

6. Conclusions

An experimental procedure has been proposed, based on the use of low-cost electret microphones, for the characterization of the wall pressure fluctuation and verified by the application of a thin airfoil subjected to incoming rotating wakes. By means of a careful calibration procedure, it is shown that the chord-wise variation of the unsteady pressure response to the incoming gusts can be quantified in terms of amplitude and phase. Results are promising in terms of applicability of the technique and accuracy of the calibration procedure. The chord-wise variation of the amplitude of the induced pressure jump has been compared with the incompressible linearized airfoil theory, and a satisfactory agreement has been found for the first three harmonics of the blade passage frequency. Coherence measurements between the surface electret microphones and the far-field microphone shows that the first blade passing frequency is the most efficient on noise generation and, for this harmonic, the noise generation is practically equally efficient along all the airfoil's chord. The coherence measurement also shows that, for the second and third harmonic of the blade passing frequency, the first quarter of the airfoil chord is the most efficient region for noise generation. Results illustrated in this paper demonstrate the applicability of low-cost electret microphones for the determination of aerodynamic wake-airfoil interaction noise, for the complete range of pressure fluctuations and range of frequency of interest encountered on this study.

7. Acknowledgments

Leandro D. Santana acknowledges the Brazilian Coordination for Improvement of Higher Education Personnel - CAPES - process number BEX-0520-10-1.

References

[1] P. A. Ravetta, R. A. Burdisso, W. F. Ng, Wind tunnel aeroacoustic measurements of a 26% scale 777 main landing gear model, in: 10th AIAA/CEAS Aeroacoustics Conference & Exhibit, no. AIAA-2004-2885, 2004.

[2] M. C. Jacob, J. Boudet, D. Casalino, M. Michard, A rod-airfoil experiment as a benchmark for broadband noise modeling, Theoretical and Computational Fluid Dynamics 19 (2005) 171–196, 10.1007/s00162-004-0108-6.
URL http://dx.doi.org/10.1007/s00162-004-0108-6

[3] P. F. Mish, W. J. Devenport, An experimental investigation of unsteady surface pressure on an airfoil in turbulence part 2: Sources and prediction of mean loading effects, Journal of Sound and Vibration 296 (3) (2006) 447 – 460. doi:10.1016/j.jsv.2005.08.009.

[4] S. A. Glegg, W. Devenport, Unsteady loading on an airfoil of arbitrary thickness, Journal of Sound and Vibration 319 (3-5) (2009) 1252 – 1270. doi:10.1016/j.jsv.2008.06.053.

[5] S. Moreau, M. Roger, Back-scattering correction and further extensions of amiet's trailing-edge noise model. part ii: Application, Journal of Sound and Vibration 323 (1-2) (2009) 397 – 425. doi:DOI: 10.1016/j.jsv.2008.11.051.

[6] P. F. Mish, An experimental investigation of unsteady surface pressure on an airfoil in turbulence, Ph.D. thesis, Virginia Tech (2003).

[7] P. F. Mish, W. J. Devenport, An experimental investigation of unsteady surface pressure on an airfoil in turbulence part 1: Effects of mean loading, Journal of Sound and Vibration 296 (3) (2006) 417 – 446. doi:10.1016/j.jsv.2005.08.008.

[8] M. Bilka, J. Anthoine, C. Schram, Design and evaluation of an aeroacoustic wind tunnel for measurement of axial flow fans, Journal Acoustical Society of America 130 (6) (2011) 3788–3796.

[9] S. Moreau, Aerodynamic Noise From Wall-bounded Flows, von Karman Institute For Fluid Dynamics, 2009, Ch. Airfoil noise: experimental database and hybrid approaches, pp. 1–50.

[10] T. von Karman, W. Sears, Airfoil theory for non-uniform motion, Journal of the Aeronautical Sciences 5 (10) (1938) 379–390.

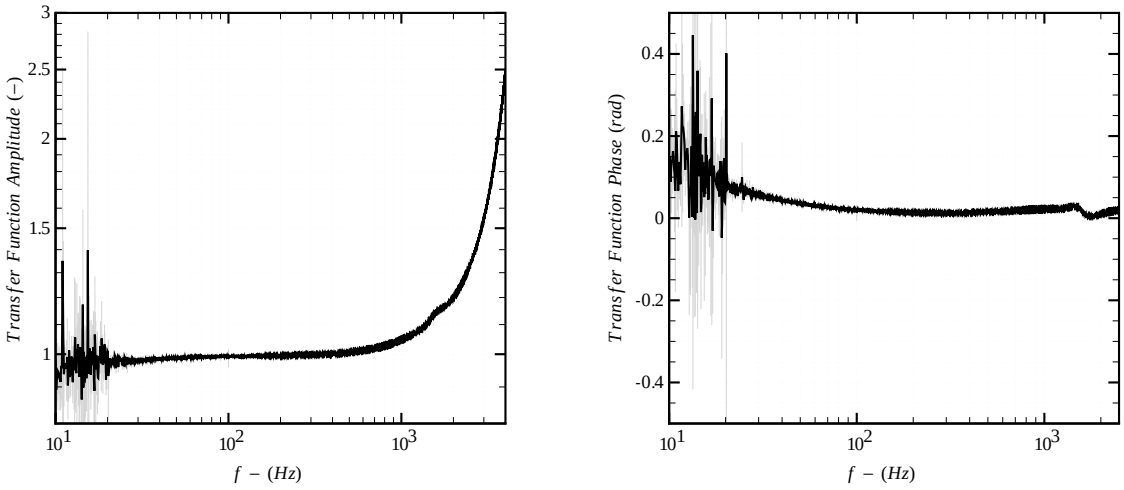

(a) Amplitude (b) Phase

Figure 3: Calibrator transfer function.

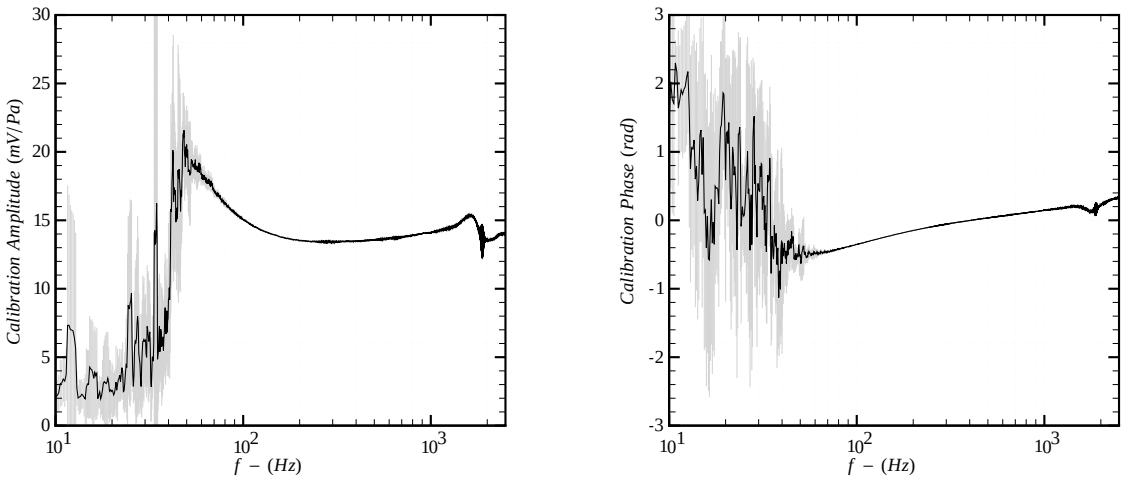

(a) Amplitude (b) Phase

Figure 4: Electret C1 calibration.

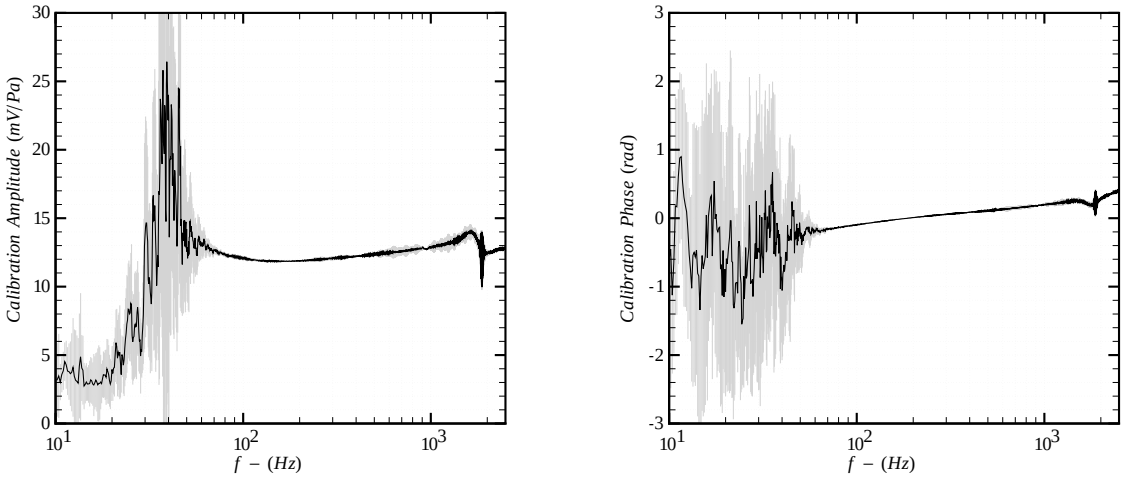

(a) Amplitude (b) Phase

Figure 5: Electret C3 calibration.

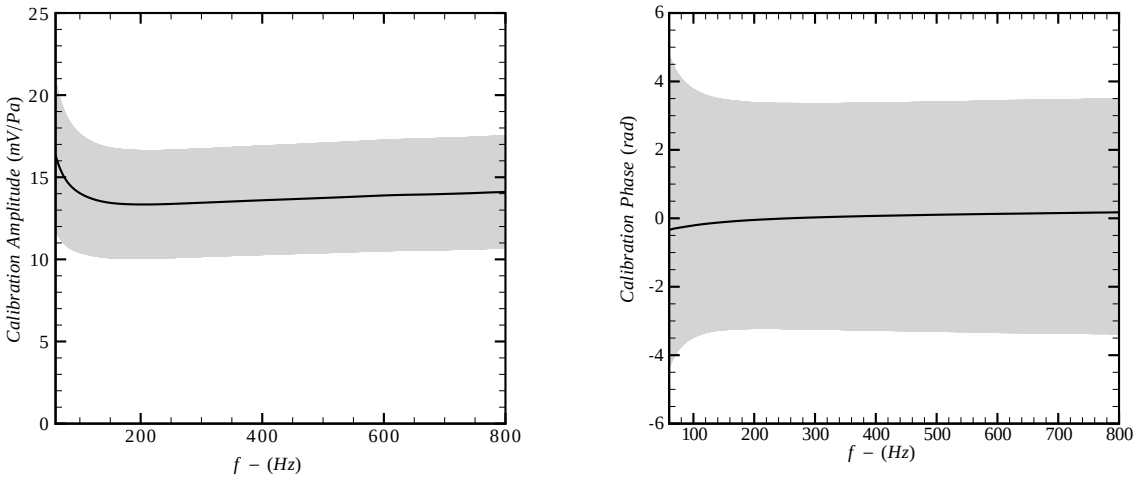

(a) Amplitude (b) Phase

Figure 6: Average calibration of 18 microphones.

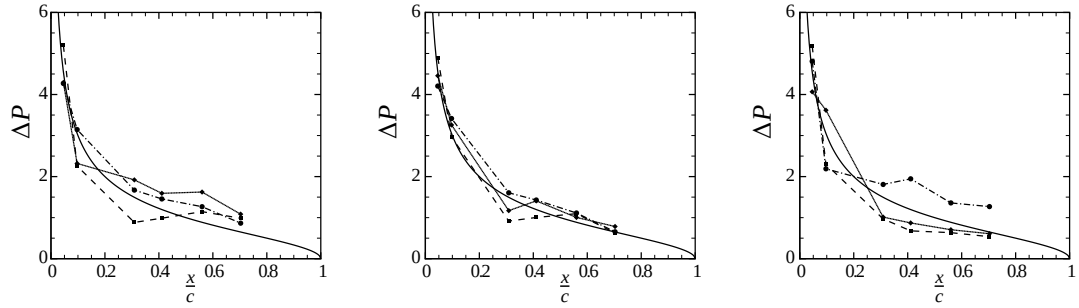

(a) AOA = 0° (b) AOA = 2° (c) AOA = 4°

Figure 7: Pressure jump given by the linearized airfoil theory compared with experimental values. Results given for angles of attack varying from 0° to 4°. Linearized airfoil theory: (———) ; 1st*BPF*: (– – –■– – –■); 2nd*BPF*: (– · – · –●– · – · –●); 3rd BPF: (·····♦·····♦).

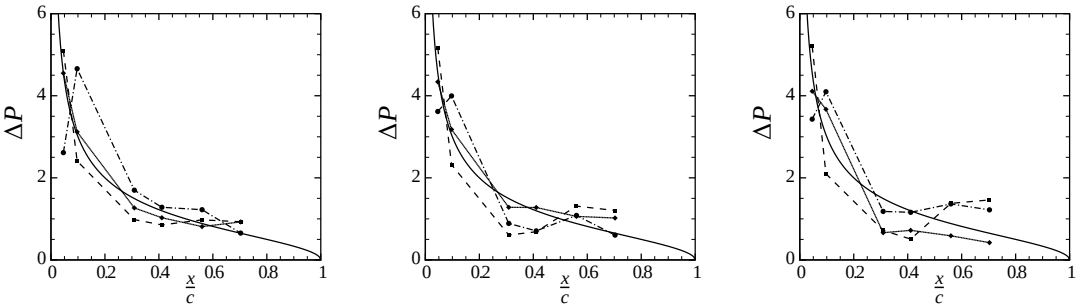

(a) AOA = 6° (b) AOA = 8° (c) AOA = 10°

Figure 8: Pressure jump given by the linearized airfoil theory compared with experimental values. Results given for angles of attack varying from 6° to 10°. Linearized airfoil theory: (———) ; 1st*BPF*: (– – –■– – –■); 2nd*BPF*: (– · – · –●– · – · –●); 3rd BPF: (·····♦·····♦).

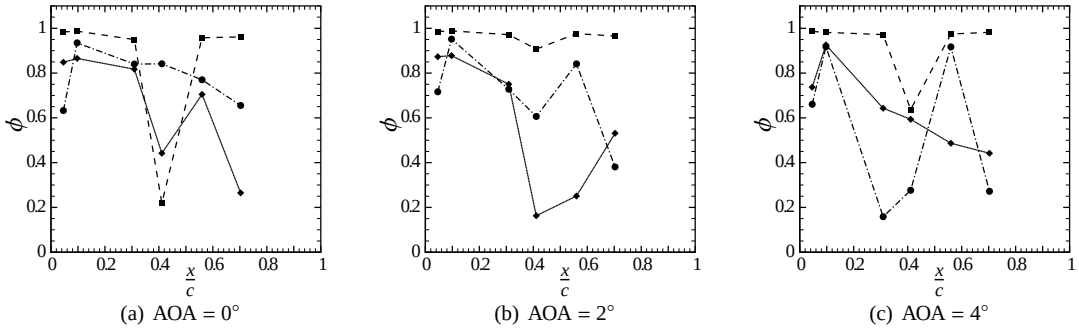

(a) AOA = 0° (b) AOA = 2° (c) AOA = 4°

Figure 9: Coherence between the surface electret microphone and the far-field microphone. Results given for angles of attack varying from 0° to 4°. 1st*BPF*: (– – –■– – –■); 2nd*BPF*: (– · – · –●– · – · –●); 3rd BPF: (·····♦·····♦).

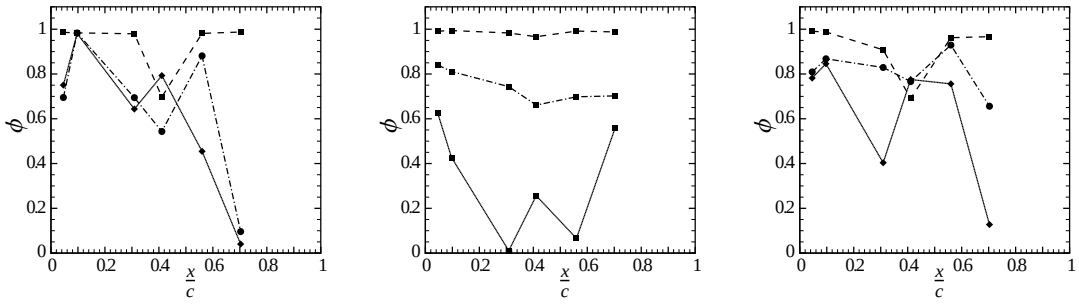

(a) AOA = 6° (b) AOA = 8° (c) AOA = 10°

Figure 10: Coherence between the surface electret microphone and the far-field microphone. Results given for angles of attack varying from 6° to 10°. (— — —■— — —■); 2nd *BPF*: (— · — · —●— · — · —●); 3rd BPF: (·····♦·····♦).

Scale-resolved and Stochastic Approaches for the Prediction of the Noise Produced by Ducted Singularities in HVAC Systems

Ugur Karban

Environmental and Applied Fluid Dynamics Department, von Karman Institute for Fluid Dynamics, Belgium, ugur.karban@vki.ac.be

Supervisor: Christophe Schram

Associate Professor, Environmental and Applied Fluid Dynamics Department, von Karman Institute for Fluid Dynamics, Belgium, christophe.schram@vki.ac.be

Abstract

This study is being conducted within the content of FLOWAIRS project and mainly focused on understanding the acoustic behavior of a ducted turbulent flow generated by a fan operating upstream a diaphragm. The overall process can be analyzed in two parts; estimation of the noise sources and the radiation of the generated sound. Regarding the first part, an extension of the Random Particle Mesh (RPM) method for ducted flows is aimed to be developed in order to estimate the broadband noise generated by the fan and the diaphragm. The method is simply based on application of a digital filter on a random data in order to obtain turbulent velocity fluctuations in the flow field. The filter is designed using a prescribed turbulent integral length scale and kinetic energy distribution which are obtained from a Reynolds Averaged Navier Stokes (RANS) solution. The integral length scale and the turbulent kinetic energy are used to scale the correlation functions and the amplitude of the correlation function, respectively. This makes the resulting synthetic velocity field completely solenoidal, furthermore it reserves all the two-point statistical properties of the turbulent flow.

After obtaining the velocity field, it is possible to calculate the acoustic sources and radiation of the sound through existing analogies. In this case, with the existence of stationary boundaries i.e. the duct and the diaphragm it is convenient to use Curles analogy in order to estimate acoustic field. The results are intended to be compared with both Large Eddy Simulation (LES) solutions and measurements performed in the anechoic chamber. Once it is validated, the method is intended to be applied on various diaphragm designs under different inflow conditions. The presented method is expected to be quite effcient in terms of computational costs so that it will give the flexibility to investigate numerous cases easily. Afterwards, integrating the method with optimization algorithms can be set as a future goal in this respect.

Keywords: Aeroacoustics, RPM method, Stochastic Noise Generation-Radiation (SNGR) method

MULTIPHASE FLOW

Development and Validation of a Finite Element Solver for Dispersed Two-Phase Flows

Bart Janssens

Department of Mechanical Engineering, Royal Military Academy, Belgium, bart.janssens@rma.ac.be
Turbomachinery and Propulsion Department, von Karman Institute for Fluid Dynamics, Belgium

Supervisor: Tony Arts

Professor, Turbomachinery and Propulsion Department, von Karman Institute for Fluid Dynamics, arts@vki.ac.be.

University Supervisor: Walter Bosschaerts

Professor, Department of Mechanical Engineering, Royal Military Academy, walter.bosschaerts@rma.ac.be

University Supervisor: Karim Limam

Professor, Laboratoire d'Étude des Phénomènes de Transfert et de l'Instantanéité, La Rochelle University, France , klimam01@univ-lr.fr

Abstract

We present our method for developing a finite element model for multiphase flow. The implementation makes use of modern C++ techniques to promote code reuse and to present an easy to use interface for the development of additional models. In the present paper, we focus on the model for the carrier phase, which makes use of the PSPG/SUPG finite element formulation. We also employ a segregated semi-implicit scheme, which is more suitable for large meshes. We validated the code using the Taylor-Green test case. Finally, some experimental measurements are shown that will later be used as validation for the multiphase flow.

Keywords: Multiphase flow, Disperse flow, coagulation, nanoparticles

Nomenclature

Δt	Time step
Ω	The volume of the computational domain. When used with an index: the volume of a single element.
ω	Weighting function
ρ	Density
τ	Stabilization coefficient. Index indicates type of stabilization.
θ	Parameter for the theta-scheme
$\mathbf{a}$	Acceleration
$\mathbf{N}$	Element shape function vector
$\mathbf{u}$	Velocity vector
$\mathbf{x}$	Vector of unknowns
A	Stiffness matrix
e	Used as index to indicate element vector or matrix
p	Pressure
T	Mass matrix

1. Introduction

The purpose of the current work is to develop a model for particle-laden flow in the context of air pollution problems. Potential health risks are discussed in i.e. [1] and [2]. We seek to model the behavior of ultra fine particles, as well as inter-particle collision and coagulation.

In order to build a reusable and extensible code, much time was spent on the development of a generic framework for the development of finite element models. This resulted in the creation of a Domain Specific Embedded Language, which was presented at ICCAM 2012 in Gent. The system can be compared to FEniCS [3] and Life [4]. OpenFOAM also has a similar language to express finite volume problems [5]. So far, we have used this system to implement the PSPG/-SUPG method for the fluid phase [6].

In the remainder of this paper, we first present the SUPG/PSPG formulation as it is implemented. We also show how the fully implicit formulation can be transformed into a segregated semi-implicit formulation that should be more scalable. Finally, the model is validated using the Taylor-Green test case.

In the final part of the paper, we present some PIV measurements that will serve as further validation for 3D test cases, as well as some challenges that we currently face regarding the setup of an experiment that can be used to validate the particle model.

2. Fluid model

We present an overview of the implicit SUPG method as detailed in [6]. This implicit method is then reformulated in a semi-implicit way in an attempt to improve scalability for large 3D problems.

2.1. Implicit formulation

The conservation equations for incompressible flow are:

$$\nabla \cdot \mathbf{u} = 0 \tag{1}$$

$$\frac{\partial \mathbf{u}}{\partial t} + (\mathbf{u} \cdot \nabla)\,\mathbf{u} + \frac{\nabla p}{\rho} - \nu \nabla^2 \mathbf{u} = \mathbf{0} \tag{2}$$

The equations are transformed to the weak formulation and PSPG, SUPG and bulk stabilization terms are applied, weighted by the respective coefficients τ. For the time discretization, a forward Euler method is used here for clarity. We also use the skew symmetric formulation for the advection term. This yields the following weak formulation:

$$\int_\Omega \omega \nabla \cdot \mathbf{u}^{n+1} \mathrm{d}\Omega + \int_\Omega \tau_{\text{PSPG}} \nabla\omega \cdot \left(\frac{\mathbf{u}^{n+1} - \mathbf{u}^n}{\Delta t} + \left[(\mathbf{u} \cdot \nabla)\,\mathbf{u} + \frac{\mathbf{u}\nabla \cdot \mathbf{u}}{2} + \frac{\nabla p}{\rho} \right]^{n+1} \right) \mathrm{d}\Omega = 0 \tag{3}$$

$$\int_\Omega \left(\omega + \tau_{\text{SUPG}} \nabla\omega \cdot \mathbf{u}^{n+1} \right) \left(\frac{\mathbf{u}^{n+1} - \mathbf{u}^n}{\Delta t} + \left[(\mathbf{u} \cdot \nabla)\,\mathbf{u} + \frac{\mathbf{u}\nabla \cdot \mathbf{u}}{2} + \frac{\nabla p}{\rho} - \nu \nabla^2 \mathbf{u} \right]^{n+1} \right) \mathrm{d}\Omega + \int_\Omega \tau_{\text{BULK}} \nabla\omega \left(\nabla \cdot \mathbf{u}^{n+1} \right) \mathrm{d}\Omega = \mathbf{0} \tag{4}$$

The superscripts n and $n+1$ indicate the solution at two subsequent time steps, ω represents the weight function and Ω is the problem domain.

We now divide the domain into elements Ω_k over which we define shape functions $\mathbf{N}$ that are used as weight functions and to interpolate the unknowns. This allows us to write the per-element system of equations as:

$$\frac{1}{\Delta t} T_e \left(\mathbf{x}_e^{n+1} - \mathbf{x}_e^n \right) + A_e \mathbf{x}_e^{n+1} = \mathbf{0} \tag{5}$$

The elemental vector of unknowns $\mathbf{x_e}$ is arranged as follows:

$$\mathbf{x_e}^n = \left[p_0^n \quad \dots \quad p_m^n \quad \left(u_0^n\right)_0 \quad \dots \quad \left(u_0^n\right)_m \quad \left(u_1^n\right)_0 \quad \dots \quad \left(u_1^n\right)_m \quad \left(u_2^n\right)_0 \quad \dots \quad \left(u_2^n\right)_m \right]^\mathsf{T} \tag{6}$$

Here, m is the number of nodes for an element. The structuring of the vector of unknowns also allows us to subdivide the element matrices T_e and A_e as follows (showing only A_e and considering three velocity components):

$$A_e = \begin{bmatrix} A_{pp} & A_{pu_0} & A_{pu_1} & A_{pu_2} \\ A_{u_0 p} & A_{u_0 u_0} & A_{u_0 u_1} & A_{u_0 u_2} \\ A_{u_1 p} & A_{u_1 u_0} & A_{u_1 u_1} & A_{u_1 u_2} \\ A_{u_2 p} & A_{u_2 u_0} & A_{u_2 u_1} & A_{u_2 u_2} \end{bmatrix} \tag{7}$$

Each element of this matrix is an $m \times m$ sub matrix for which the rows correspond to the equations at each element node for the variable in the first subscript and the columns represent the nodal contributions for the variable in the second subscript. Comparing this structure with the weak forms (3) and (4) allows us to define each matrix, after applying the interpolation procedure:

$$A_{pu_i} = \int_{\Omega_k} \left((\mathbf{N} + \frac{\tau_{\text{PSPG}} \mathbf{u}_{\text{adv}} \cdot \nabla \mathbf{N}}{2})^\mathsf{T} (\nabla \mathbf{N})_i + \tau_{\text{PSPG}} (\nabla \mathbf{N})_i^\mathsf{T} \mathbf{u}_{\text{adv}} \nabla \mathbf{N} \right) \mathrm{d}\Omega_k \tag{8}$$

$$A_{pp} = \int_{\Omega_k} \tau_{\text{PSPG}} \frac{1}{\rho} \nabla \mathbf{N}^\mathsf{T} \nabla \mathbf{N} \mathrm{d}\Omega_k \tag{9}$$

$$A_{u_i u_i} = \int_{\Omega_k} \Big(\nu \nabla \mathbf{N}^\intercal \nabla \mathbf{N} + (\mathbf{N} + \tau_{\text{SUPG}} \mathbf{u}_{\text{adv}} \nabla \mathbf{N})^\intercal \, \mathbf{u}_{\text{adv}} \nabla \mathbf{N} \Big) \mathrm{d}\Omega_k \tag{10}$$

$$A_{u_i u_j} = \int_{\Omega_k} \Big(\tau_{\text{BULK}} \, (\nabla \mathbf{N})_i \tag{11}$$

$$+ \frac{1}{2} \mathbf{u}_{\text{adv}\,i} \, (\mathbf{N} + \tau_{\text{SUPG}} \mathbf{u} \nabla \mathbf{N}) \Big)^\intercal \nabla \mathbf{N}_j \mathrm{d}\Omega_k \tag{12}$$

$$A_{u_i p} = \int_{\Omega_k} \frac{1}{\rho} \, (\mathbf{N} + \tau_{\text{SUPG}} \mathbf{u}_{\text{adv}} \nabla \mathbf{N})^\intercal \, (\nabla \mathbf{N})_i \, \mathrm{d}\Omega_k \tag{13}$$

$$T_{p u_i} = \int_{\Omega_k} \tau_{\text{PSPG}} \, (\nabla \mathbf{N})_i^\intercal \, \mathbf{N} \mathrm{d}\Omega_k \tag{14}$$

$$T_{u_i u_i} = \int_{\Omega_k} (\mathbf{N} + \tau_{\text{SUPG}} \mathbf{u}_{\text{adv}} \nabla \mathbf{N})^\intercal \, \mathbf{N} \mathrm{d}\Omega_k \tag{15}$$

In these equations, the indices i and j refer to the i-th or j-th row of the gradient matrices of the shape functions and thus take values 0, 1 and 2 for three-dimensional problems. We note that the advective and SUPG terms contain an advection velocity $\mathbf{u}_{\text{adv}}$, which is introduced to obtain a linear system. The value of $\mathbf{u}_{\text{adv}}$ is obtained through a series expansion as detailed by [6].

In order to obtain the final discrete system, equation (5) is transformed, introducing a θ-method for the time discretization and solving for the difference $\Delta \mathbf{x}_e = \mathbf{x}_e^{n+1} - \mathbf{x}_e^n$ between two subsequent time steps:

$$\left(\frac{1}{\Delta t} T_e + \theta A_e \right) \Delta \mathbf{x}_e = -A_e \mathbf{x}_e^n \tag{16}$$

Setting $\theta = 1$ yields a backward Euler method, while setting $\theta = 0.5$ results in the second order accurate Crank-Nicolson scheme. For the continuity equation, we keep $\theta = 1$ at all times to prevent oscillations in the solution.

Finally, the element contributions need to be summed over the domain, resulting in a global linear system. Because the shape functions $\mathbf{N}$ are defined locally, the system is sparse and can be solved using iterative techniques such as GMRES.

The time stepping results in a series of Oseen problems. The Crank-Nicolson approach allows us to employ time steps bounded by the physical process, rather than numerical constraints.

The price for this is that the coupled linear system can be difficult to solve, and storing the sparse system matrix requires a lot of memory. To accelerate the solution, different types of preconditioners could be applied, see i.e. [7; 8]. The considerable memory requirements are easily illustrated: in three dimensions, each node holds four unknowns and for a structured hexahedral mesh one node has 26 neighbors. For a 10 million node mesh, this matrix would require 50 GB of RAM when using double precision. Since preconditioning usually requires the construction of extra matrices, it only aggravates the memory concerns. One way to solve this would be to use a matrix-free implementation, assembling the linear system on the fly each time it needs to be applied to a vector. Unfortunately, this would complicate the implementation, and it would also be slower than using an assembled matrix.

```
1  elements_expression
2  (
3    AllElementsT(),
4    group
5    (
6      _A = _0, _T = _0,
7      for_generic_elements
8      (
9        compute_tau(u, nu_eff, u_ref, lit(tau_ps),
             lit(tau_su), lit(tau_bulk)),
10       element_quadrature
11       (
12         _A(p     , u[_i]) += transpose(N(p) + tau_ps
               *u_adv*nabla(p)*0.5) * nabla(u)[_i] +
               tau_ps * transpose(nabla(p)[_i]) *
               u_adv*nabla(u),
13         _A(p     , p)     += tau_ps * transpose(
               nabla(p)) * nabla(p) / rho,
14         _A(u[_i], u[_i]) += nu_eff * transpose(
               nabla(u)) * nabla(u) + transpose(N(u)
               + tau_su*u_adv*nabla(u)) * u_adv*nabla
               (u),
15         _A(u[_i], p)     += transpose(N(u) + tau_su
               *u_adv*nabla(u)) * nabla(p)[_i] / rho,
16         _A(u[_i], u[_j]) += transpose((tau_bulk +
               0.33333333333333*nu_eff)*nabla(u)[_i]
17                                 + 0.5*u_adv[_i]*(N(u) +
                                       tau_su*u_adv*
                                   nabla(u))) * nabla
                                   (u)[_j],
18         _T(p     , u[_i]) += tau_ps * transpose(
               nabla(p)[_i]) * N(u),
19         _T(u[_i], u[_i]) += transpose(N(u) + tau_su
               *u_adv*nabla(u)) * N(u)
20       )
21     ),
22     for_specialized_elements(supg_specialized(p, u,
           u_adv, nu_eff, u_ref, rho, _A, _T)),
23     system_rhs += -_A * _x,
24     _A(p) = _A(p) / theta,
25     system_matrix += invdt() * _T + theta * _A
26   )
27 )
```

Listing 1: Matrix assembly

As illustration, listing 1 shows the complete matrix assembly, implemented using our DSEL.

2.2. *Segregated formulation*

In the context of the current application, our goal is to use Large Eddy Simulation in order to obtain detailed velocity data as input for the particle model. We will make use of a segregated approach to solve

the linear system, allowing to break down the problem into smaller linear systems -one for the velocity and one for the pressure. To accelerate the iterative solution of the velocity system, we will treat the advective terms explicitly, resulting in what we call a semi-implicit scheme. This imposes a time step restriction, but in the framework of LES this is not too problematic since fairly small time steps are imposed by the physics anyway. We follow the scheme proposed by Brooks et al. [9].

In our matrix notation, the discrete momentum equation reads, introducing the acceleration $\mathbf{a} = \Delta\mathbf{u}/\Delta t$:

$$\left(T_{uu} + \theta\Delta t A_{uu}\right)\mathbf{a} + \theta A_{up}\Delta\mathbf{p} = -A_{uu}\mathbf{u}^n - A_{up}\mathbf{p}^n \quad (17)$$

We now rewrite this to solve for an acceleration difference between two iterations $\Delta\mathbf{a} = \mathbf{a}^{m+1} - \mathbf{a}^m$ and we eliminate the pressure by defining $\Delta\mathbf{a}^* = \Delta\mathbf{a} + \left(T_{uu} + \theta\Delta t A_{uu}\right)^{-1}\theta A_{up}\Delta\mathbf{p}$ to obtain:

$$\left(T_{uu} + \theta\Delta t A_{uu}\right)\Delta\mathbf{a}^* = -A_{uu}\mathbf{u}^m - A_{up}\mathbf{p}^m - \left(T_{uu} + \theta\Delta t A_{uu}\right)\mathbf{a}^m \quad (18)$$

Note that on the right hand side we now use the pressure and velocity from the previous iteration inside the time step, denoted by the superscript m.

Similarly, the continuity equation is:

$$\left(\frac{T_{pu}}{\Delta t} + A_{pu}\right)\Delta\mathbf{u} + A_{pp}\Delta\mathbf{p} = -A_{pu}\mathbf{u}^m - A_{pp}\mathbf{p}^m \quad (19)$$

The velocity increment can be written as: $\Delta\mathbf{u} = \Delta t\Delta\mathbf{a} = \Delta t\left(\Delta\mathbf{a}^* - \left(T_{uu} + \theta\Delta t A_{uu}\right)^{-1}\theta A_{up}\Delta\mathbf{p}\right)$. We introduce this into the continuity equation to obtain an equation for the pressure difference:

$$\left(\left(T_{pu} + \Delta t A_{pu}\right)\left(T_{uu} + \theta\Delta t A_{uu}\right)^{-1}\theta A_{up} - A_{pp}\right)\Delta\mathbf{p} = T_{pu}\Delta\mathbf{a}^* + A_{pu}\left(\mathbf{u}^m + \Delta t\Delta\mathbf{a}^*\right) + A_{pp}\mathbf{p}^m \quad (20)$$

We now have all the ingredients needed to present the iterative predictor-corrector scheme that leads to the solution for the evolution between two time levels n and $n+1$:

1: $\mathbf{u}^0 = \mathbf{u}^n$
2: $\mathbf{p}^0 = \mathbf{p}^n$
3: $\mathbf{a}^0 = \mathbf{0}$
4: **for** $m = 0$ to M **do**
5: Solve linear system (18) for $\Delta\mathbf{a}^*$
6: Solve linear system (20) for $\Delta\mathbf{p}$
7: Compute $\Delta\mathbf{a} = \Delta\mathbf{a}^* - \left(T_{uu} + \theta\Delta t A_{uu}\right)^{-1}\theta A_{up}\Delta\mathbf{p}$
8: Update $\mathbf{u}^{m+1} = \mathbf{u}^i + \Delta t\Delta\mathbf{a}$
9: Update $\mathbf{p}^{m+1} = \mathbf{p}^i + \Delta\mathbf{p}$
10: **end for**

Note that statement 7 requires again a solution of the velocity linear system, so for one step of the algorithm we have to solve the velocity system twice and the pressure system once. We will show later that one of the velocity calculations can be eliminated, however.

Let us now examine this algorithm as it is written above, i.e. without simplifications. This corresponds to a solution of the original system using substitution of variables to solve a separate system for $\mathbf{u}$ and $\mathbf{p}$, so it should be equivalent to the original solution after only one step through the algorithm. This means that when filling in the values of the first iteration, the right hand side of both linear systems should be zero, so the solution doesn't change anymore. When we do this exercise, we notice that some terms are missing from the equations. There are two causes for this: (1) we replaced the previous time step values $\mathbf{u}^n$ and $\mathbf{p}^n$ with the previous iteration values $\mathbf{u}^i$ and $\mathbf{p}^i$; and (2) the velocity system is solved for $\Delta\mathbf{a}^*$, but $\mathbf{a}$ on the right hand side is updated using $\Delta\mathbf{a}$, thus introducing extra Δp contributions. We calculated the missing terms by filling in the result after one iteration into systems (18) and (20) and then requiring that the right hand side be zero, yielding the final formulation of the velocity and pressure systems:

$$\left(T_{uu} + \theta\Delta t A_{uu}\right)\Delta\mathbf{a}^* = -A_{uu}\mathbf{u}^m - A_{up}\mathbf{p}^m - \left(T_{uu} + \theta\Delta t A_{uu}\right)\mathbf{a}^m + (1-\theta)A_{up}\sum_{j=0}^{m}\Delta\mathbf{p}^j + \Delta t A_{uu}\mathbf{a}^i \quad (21)$$

$$\left(\left(T_{pu} + \Delta t A_{pu}\right)\left(T_{uu} + \theta\Delta t A_{uu}\right)^{-1}\theta A_{up} - A_{pp}\right)\Delta\mathbf{p} = T_{pu}\Delta\mathbf{a}^* + A_{pu}\left(\mathbf{u}^m + \Delta t\Delta\mathbf{a}^*\right) + A_{pp}\mathbf{p}^m + T_{pu}\mathbf{a} \quad (22)$$

The new terms are on the last lines of systems (21) and (22). These unsimplified systems can now be used as a basis to develop the iterative method, by making terms explicit as needed and introducing lumping. For the velocity system matrix (named K_{uu}), we only keep

the viscous terms and the mass matrix:

$$K_{u_i u_i} = \theta \Delta t \int_{\Omega_k} \Big((\nu + \tau_{\text{BULK}}) \nabla \mathbf{N}^\intercal \nabla \mathbf{N} \mathrm{d}\Omega_k + \int_{\Omega_k} (\mathbf{N} + \tau_{\text{SUPG}} \mathbf{u}_{\text{adv}} \nabla \mathbf{N})^\intercal \mathbf{N} \mathrm{d}\Omega_k \tag{23}$$

$$K_{u_i u_j} = \theta \Delta t \int_{\Omega_k} \tau_{\text{BULK}} \left(\nabla \mathbf{N}\right)_i^\intercal \nabla \mathbf{N}_j \mathrm{d}\Omega_k \qquad (i \neq j) \tag{24}$$

We keep the SUPG stabilization in the mass matrix contribution, because tests with the Taylor-Green reference case pointed out that removing this term deteriorates the convergence rate of the iterative procedure, i.e. two passes through the algorithm would no longer suffice to maintain the accuracy of the fully implicit solution method. The consequence of keeping this term is that the velocity system matrix now depends on the velocity and that it becomes non-symmetric. In practice, the matrix appears to stay well conditioned, and standard ILU preconditioning can be applied for quick convergence of the GMRES method.

For the pressure system, we first approximate $(T_{uu} + \theta \Delta t A_{uu})$ with the lumped velocity mass matrix M_L, reducing the expression of the pressure matrix to:

$$K_{pp} = \left(T_{pu} + \Delta t A_{pu}\right) M_L^{-1} \theta A_{up} - A_{pp} \tag{25}$$

We observe that $A_{up} = -A_{pu}^\intercal$ when we ignore the stabilization terms and apply integration by parts to the pressure term in the momentum equation. What we obtain is a Poisson equation for the pressure, which can be written in simplified form as:

$$K_{pp} = -\theta \left(\tau_{\text{PSPG}} + \Delta t\right) \int_{\Omega_k} \nabla \mathbf{N}^\intercal \nabla \mathbf{N} \mathrm{d}\Omega_k \tag{26}$$

The scaling factor accounts for the presence of stabilization due to the τ_{PSPG} term. Including this term improves the convergence rate, based on test runs using the Taylor-Green case. The final form of the pressure matrix is independent of the velocity, so for a constant mesh it only needs to be constructed once. For small problems, it is feasible to decompose this matrix once and then reuse the factorization during the entire simulation. For larger problems, the Poisson equation can be solved efficiently using algebraic multigrid preconditioning. The simplified K_{pp} matrix is also easy to construct using an assembly loop over elements and no longer requires large sparse matrix products. In the current method this only reduces the peak memory usage, but for a possible future extension to deforming meshes fast construction of the matrix is an important consideration.

The simplification of the pressure system was based on lumping the velocity mass matrix. When applying the algorithm, computation of the adjusted $\Delta \mathbf{a}$ also requires a solution of the velocity system, so one might ask if using the lumped mass matrix here would be acceptable. Numerical tests show that the effect on convergence and accuracy is minimal, so we can indeed use the lumped M_L^{-1} for the inverse in line 7 of the algorithm.

2.3. Taylor-Green test case

2.3.1. Implicit formulation

We apply the fully implicit formulation to the 2D periodic Taylor-Green vortices, advected with a uniform velocity $(0.3m/s, 0.2m/s)$. Figure 1 shows the difference between the analytical and numerical solution on a 128x128 grid for different element types. Here, the TriagP1 specialized element indicates that a hand-written code is used instead of Gauss quadrature, i.e. the integrals for the element matrices have been worked out analytically using a cell average for the advection velocity. The non-specialized code includes the advection velocity in the integrals, which explains the slightly better accuracy.

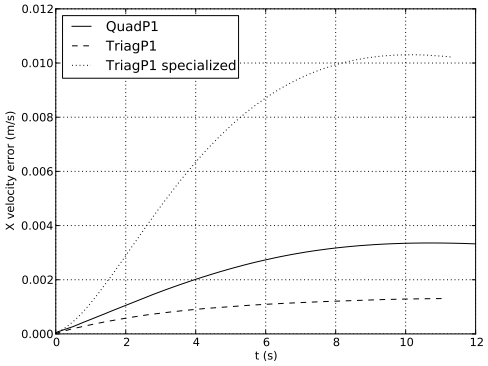

Figure 1: Difference between simulation result and theoretical solution for different element types.

Figure 2 shows the evolution of the error as the grid resolution is increased. All element types follow the expected second order accuracy scaling.

2.3.2. Semi-implicit formulation

We use the Taylor-Green test case to answer two questions about the semi-implicit method: can it retain the same accuracy as the fully implicit case; and

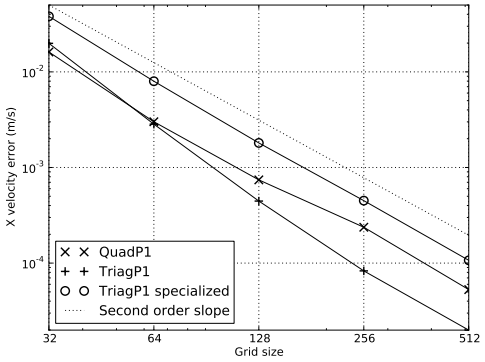

Figure 2: Evolution of the error with grid size: Element type comparison for a time step of 0.001s

how many inner iterations are needed to achieve this accuracy? For the verification of the accuracy, we ran a test using two iterations per time step, as recommended by Brooks et al. [9]. Figure 3 compares the error between the theory and the numerical solution for the implicit and semi-implicit cases, using a time step of 0.0005s. This test was run in parallel, with set-

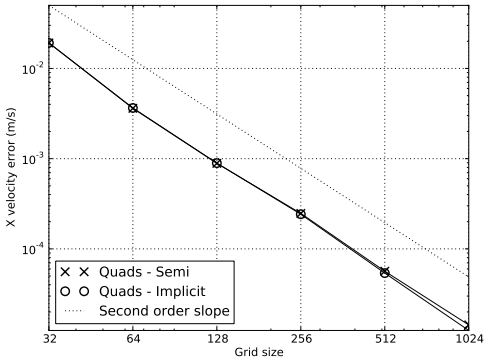

Figure 3: Evolution of the error with grid size: Comparison between implicit and semi-implicit methods for a time step of 0.0005s

tings that would typically be used in a large-scale simulation: for the implicit solution algebraic multigrid preconditioned GMRES was used with a relative convergence tolerance of 10^{-5}; for the semi-implicit solution ILU preconditioned GMRES with a tolerance of 10^{-6} was used for the velocity and an algebraic multigrid preconditioned Conjugate-Gradient method with a tolerance of 10^{-4} was used for the pressure system. The second order accuracy of the semi-implicit formulation is confirmed, showing excellent agreement with the implicit method.

We present the influence of the number of iterations in figure 4. As suggested by Brooks et al. [9], using 2 iterations yields excellent results and in fact the jump from one to two iterations is the only significant improvement that can be observed in the graph. Indeed, when we restrict the algorithm to just one inner iteration, we see that the error from the segregated solution becomes twice as large as the error from the fully coupled solution. Increasing the number of inner iterations to two is enough to eliminate this discrepancy. When we increase the number of iterations further to 64 or 128, both methods recover the same solution up to machine precision, leading us to believe that the segregated solver is indeed implemented correctly.

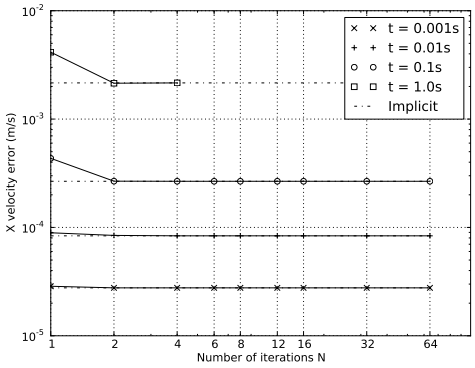

Figure 4: Convergence of the semi-implicit scheme, with the implicit result as reference.

3. Experimental work

A first experiment that is being developed is designed to measure concentration variations and the effect of particle coagulation in a flow field that should be reproducible using numerical simulation. The goal is to produce data that can be used for the validation of the particle model that we will develop. Flow enters a cubic chamber through a narrow slot near the bottom, and exits near the top of the opposite wall (see Fig. 5). For the particle coagulation, a short burst of particles will be injected near the center of the circulation zone.

The inlet conditions are controlled using a device similar to the inlet section of a subsonic wind tunnel, as shown in Fig. 6. The air is supplied by a fan, not shown in this figure.

3.1. First measurement results

In order to validate the future simulations of the flow field, PIV measurements were performed on the

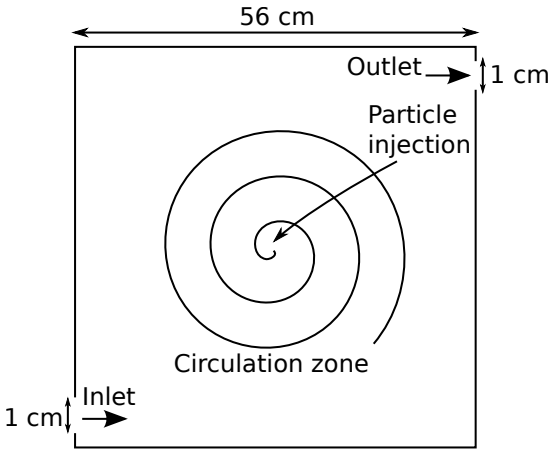

Figure 5: Schematic of the experimental test chamber.

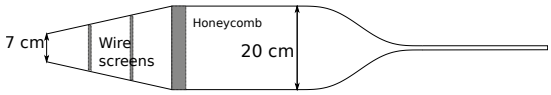

Figure 6: Conditioning of the test chamber inlet.

center plane of the box using a composition of 12 different views. We also took some detailed measurements to characterize the inlet velocity profiles for the purpose of setting up the boundary conditions. Figure 7 shows the velocity magnitude and stream lines, confirming the existence of a circulation zone.

To get an idea of the possibility to spot particle coagulation, we also took some PDA measurements at the exit of the box. First, we injected particles from the Laskin tube into the box until it visually appeared to be completely saturated. We then stopped the particle injection, and took PDA measurements at the exit for a duration of 400s. The sampled particles from these measurements were then grouped into chronological bins of 15000 particles, and their size distribution was calculated. Figure 8 shows the result, where the distribution seems to shift to the right in time. This could indicate particle coagulation, but it needs to be confirmed with experiments on more monodisperse injections.

4. Conclusion and future work

The objective of the current work is to provide a meaningful contribution to the numerical modeling of dispersed phase flow. The inclusion of nanoparticles and coagulation effects constitute new challenges, and should extend the applicability of the method.

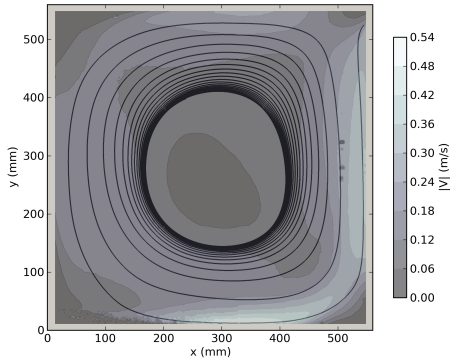

Figure 7: Contours of velocity magnitude and streamlines, for a Reynolds nummber of 648 based on the centerline inlet velocity and the inlet height.

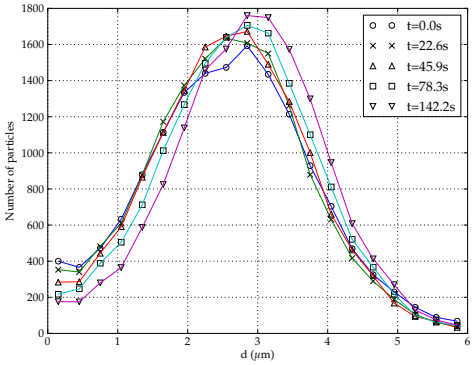

Figure 8: Evolution in time of the particle size distribution

We presented a semi-implicit scheme for the solution of the linear system arising from the finite element discretization, demonstrating the accuracy and convergence rate using the Taylor-Green test case.

Numerical work will be continued by extending the current flow solver with a particle model following [10]. This continuum modeling approach lends itself perfectly for implementation using our reusable finite element framework.

On the experimental side, the main challenge is to find a suitable candidate for particle injection. Indeed, we need particles with a monodisperse size distribution in the size range of PDA and that can be injected in sufficient concentrations to provoke coagulation.

Acknowledgments

The current implementation of the Navier-Stokes solver was realized thanks to the valuable assistance and comments of Tamás Bányai. For the PIV setup, the assistance from Elmar Recker was greatly appreciated.

References

[1] C. A. Pope, D. W. Dockery, Health Effects of Fine Particulate Air Pollution: Lines that Connect, J. Air & Waste Manage. Assoc. 56 (2006) 709–742.

[2] G. Oberdörster, E. Oberdörster, J. Oberdörster, Nanotoxicology: An Emerging Discipline Evolving from Studies of Ultrafine Particles, Environ Health Perspect 113 (2005) 823–839. doi:10.1289/ehp.7339.

[3] M. S. Alnæs, K.-A. Mardal, On the efficiency of symbolic computations combined with code generation for finite element methods, ACM Transactions on Mathematical Software 37 (1) (2010) 1.

[4] C. Prud'homme, Life: Overview of a Unified C++ Implementation of the Finite and Spectral Element Methods in 1D, 2D and 3D 4699 (2007) 712.

[5] H. G. Weller, A tensorial approach to computational continuum mechanics using object-oriented techniques, Computers in Physics 12 (6) (1998) 620. doi:10.1063/1.168744.

[6] T. Bányai, D. Vanden Abeele, H. Deconinck, A fast fully-coupled solution algorithm for the unsteady incompressible Navier-Stokes equations, in: Conference on Modelling Fluid Flow (CMFF'06), Budapest, Hungary, 2006.

[7] H. Elman, V. Howle, J. Shadid, R. Shuttleworth, R. Tuminaro, A taxonomy and comparison of parallel block multi-level preconditioners for the incompressible Navier–Stokes equations*, Journal of Computational Physics 227 (3) (2008) 1790. doi:10.1016/j.jcp.2007.09.026.

[8] T. Heister, G. Rapin, Efficient augmented lagrangian-type preconditioning for the oseen problem using grad-div stabilization, International Journal for Numerical Methods in Fluids 71 (1) (2013) 118–134.

[9] A. N. Brooks, T. J. Hughes, Streamline upwind/petrov-galerkin formulations for convection dominated flows with particular emphasis on the incompressible navier-stokes equations, Computer methods in applied mechanics and engineering 32 (1) (1982) 199–259.

[10] O. Simonin, Statistical and continuum modelling of turbulent reactive particulate flows Part I: Theoretical derivation of dispersed phase eulerian modelling from probability density function kinetic equation, Lecture series - von Karman Institute for fluid dynamics 6 (2000) D1–D42.

Realistic Statistical Input Model for Microscale Atmospheric Boundary Layer simulations

Clara García Sánchez

Environmental and Applied Fluid Dynamics Department, von Karman Institute for Fluid Dynamics, Belgium, clara.garciasanchez@vki.ac.be

Supervisor: Jeroen van Beeck

Professor, Environmental and Applied Fluid Dynamics Department, von Karman Institute for Fluid Dynamics, Belgium, vanbeeck@vki.ac.be

University Supervisor: Alessandro Parente

Assistant Professor , Aero-Thermo-Mechanics Department, Université Libre de Bruxelles, Belgium, Alessandro.Parente@ulb.ac.be

Abstract

Several motivations for the growing interest on studies dedicated to the physical understanding of complex fluid dynamics in urban environments can be found. Some examples can be the forecast of wind fields to benefit from the wind energy resources, or the prediction of pollutant concentrations to protect inhabitants health.

The overarching goal of this project is to predict air quality levels inside cities using computational fluid dynamics (CFD), which resolves the Navier Stokes equations.In the past, most of the simulations in urban environments have been performed using the steady Reynolds-Averaged Navier Stokes (RANS) technique, which permits to obtain the mean variables and to estimate the fluctuations. Recently, despite the computational limitations, some numerical studies have been carried out using the Large Eddy Simulation (LES) method, which explicitly resolves the big scales motion and models the dissipating scales. This technique is more accurate and reliable than RANS. Within this research, both numerical approaches will be used with different scopes.

Since the air quality problem is governed by a large variability in the atmospheric conditions, which determines the boundary conditions for the numerical simulations, a stochastic approach to account for this variability will be developed. The specific focus of the project is the development of a methodology to define a realistic statistical model for the boundary conditions used in microscale simulations of the Atmospheric Boundary Layer (ABL). Considering the paramount importance of the boundary conditions, already remarked in the past, this project targets the following goals:

- Development of a method to define a statistical representation of inflow conditions for Reynolds-averaged Navier Stokes (RANS) simulations, using a Numerical Weather Prediction (NWP) code. The test case considered will be Oklahoma City to validate the methodology with the Joint Urban 2003 (JU2003) [1] field measurement campaign.
- Perform an Uncertainty Quantification (UQ) study using the inflow representation obtained at the first step, and compare the results to the field measurement data from the JU2003 campaign.
- Run a small number of large eddy simulations (LES), and compare the LES and RANS results to determine the magnitude of the discrepancies between both techniques. The purpose is to investigate the relative importance of the RANS model errors as compared to the influence of the boundary conditions.
- Apply the method to the city of Bruxelles to show its feasibility to predict the effect of changes in emissions on the air quality on short and long-term. Furthermore, providing urban planners a reliable decision-making tool for pollution control.

Eventually, this methodology will provide the capability to obtain pollutant concentration estimates with risk assessment ranges, minimizing the computational cost. The flexibility of the proposed approach will allow its application to other different cities.

Keywords: Dispersion, urban physics, RANS, uncertainty quantification, mesoscale, boundary conditions, OpenFOAM, WRF.

Validation of the Multi Wavelength Light Extinction Technique on a Sub-Micron KCl Aerosol by Scanning Mobility Particle Sizing Measurements

Imre T. Horváth

Environmental and Applied Fluid Dynamics Department, von Karman institute for Fluid Dynamics, Belgium, imre.horvath@vki.ac.be

Supervisor: Rosaria Vetrano

Assistant Professor, Environmental and Applied Fluid Dynamics Department, von Karman institute for Fluid Dynamics, Belgium, vetrano@vki.ac.be

University Supervisor: Pierre Colinet

Professor, Transfers Interfaces and Processes Department of the Université Libre de Bruxelles, pcolinet@ulb.ac.be

Abstract

The present paper describes the ongoing work about the development of the Multi Wavelength Light Extinction (MWLE) technique for the characterisation of nano particles. The MWLE technique reconstructs the particle size distribution function from the Ultraviolet Near-Infrared light transmittance spectrum of a particle cloud. The reconstruction is done by the inversion of a mathematical model of light extinction. First, an inversion algorithm is introduced, which allows the robust solution of the arising ill-conditioned Fredholm integral equation of the first kind. The inversion algorithm is based on the Philips-Twomey regularisation and it is optimised by the L-curve method. Simulation results are presented, which show that the algorithm is applicable to the inversion of experimental data. Afterwards, the experimental validation of the MWLE technique is presented in which, solid KCl particles are characterised. The measurement results were compared to Scanning Mobility Particle Sizing (SMPS) measurements. The comparison resulted in a good quantitative agreement of the measured particle size distribution functions.

Keywords: particle sizing, nano particle, optical technique, light extinction, inverse problem, ill-conditioned, validation

1. Introduction

The characterisation of sub-micron sized particles became an important subject of research during the past decades. Such particles are used at numerous fields of science and industry e.g. food and pharmaceutical industry, material science, biotechnology. The online and non-intrusive characterisation of particles of such small size still represents a challenge.

The MWLE technique is a non-intrusive optical measurement technique, which is capable to carry out simultaneous size and concentration measurements of small particles. The technique has numerous advantages, such as the minimal required optical access, the possibly large stand-off distance, the simple optical setup, the short measurement time and the immediate retrieval of the particle size statistics. These advantages could make it widely applicable for both industrial and scientific problems. Its operation relies on the measurement of the transmittance of a UV-Near Infrared (NIR) light beam traveling through a medium containing particles. Fundamentally, the particle size distribution (PSD) function can be retrieved from the inversion of a suitable light extinction model. The detailed description of the MWLE technique can be found in Section 2.

The data inversion leads to the solution of a Fredholm integral equation of the first kind, which turns out to be a severely ill-conditioned problem. [1], [2] and [3] highlighted the difficulties of the data inversion process and investigated their effect on the accuracy of the technique. Section 3 de-

scribes an inversion algorithm, that makes use of the optimised Philips-Twomey algorithm and the Non-Negative Least Squares (NNLS) method. The inversion method ensures robust PSD retrieval.

The evaluation of the mentioned algorithm has been performed by simulating the extinction of the light by hypothetical particle ensembles with lognormal size distribution functions (Section 4). In order to make the simulated extinction spectra more realistic, noise was added to them. The noisy spectra were analysed by the inversion algorithm and the results were compared to the hypothetical PSDs. This simulation study concludes the optimal parameters and limitations of the implemented inversion method and the MWLE technique. The results show, that the MWLE technique together with the developed inversion method can be used as a precise technique for particle characterisation when the governing parameters are chosen adequately.

Section 5 describes the typical MWLE setup and a test facility, which has been developed for the characterisation of different liquid and solid particle aerosols. The test facility involves a commercial Scanning Mobility Particle Sizer (SMPS) instrument, which has been used as a reference for the validation of the MWLE measurements. The main part of this section reports a series of validation measurements in which a KCl (Potassium Chloride) solid particle aerosol has been characterised by simultaneous MWLE and SMPS measurements. The description of the validation methodology, the test conditions and the measurement results themselves can be found in this section.

At the end of the paper (Section 6) a summary of the most important findings is presented.

2. The Multi Wavelength Light Extinction technique

The MWLE technique uses the measured spectrum of transmittance ($Tr(\lambda) = I/I_0$) for the reconstruction of the particle properties. In the definition of $Tr(\lambda)$, I_0 refers to the light intensity incident to the investigated particle cloud and I to the attenuated intensity at the detector side of the particle cloud. The intensities should be measured in a wide spectral range (from UV to Near-Infrared). The MWLE technique attempts to find the best fit to a measured transmittance spectrum by means of a modelled one. The fixed parameters of the model depend on the particle shape, complex refractive index of the particles and the size parameter x ($x = D\pi/\lambda$, where D is the particle diameter and λ is the wavelength of the illuminating light). The variable parameters of the model are the sought particle properties (PSD, concentration). Assuming the shape and morphology of the particles, the fixed parameters of the model can be a priori calculated from an adequately chosen light scattering theory. When the proper assumptions are used for the calculation of the fixed parameters and a satisfactory fit of the measured and simulated transmittance curves is obtained, the variables of the model should correspond to the underlying particle properties.

According to the Lambert-Beer law [4],

$$Tr(\lambda) = e^{-\tau L}, \tag{1}$$

with τ being the optical density of the investigated medium and L the path length that the light travels through the particle cloud. The optical density of a particle cloud is a function of the wavelength (λ) of the illuminating light and the complex refractive index (m) of the particles. It can be expressed in the following form:

$$\tau(\lambda, m) = \int_0^\infty Q_{ext}(D, \lambda, m) \cdot \frac{D^2\pi}{4} \cdot N(D) dD. \tag{2}$$

$Q_{ext}(D, \lambda, m)$ is called the extinction efficiency factor, which is the function of particle size (D), wavelength (λ) and complex refractive index (m). Assuming spherical and homogeneous particles, Q_{ext} can be calculated using the Mie theory [4]. $N(D)$ is the number of particles contained in the dD interval centred around D. Here, the integral is taken over all diameters but it is sufficient to integrate from the smallest to the largest particle being present in the measurement volume. Combining Eq. 1 and Eq. 2 the following relation is obtained:

$$-ln(Tr(\lambda)) = C_n L \cdot \int_{D_{min}}^{D_{max}} Q_{ext}(D, \lambda, m) \cdot \frac{D^2\pi}{4} \cdot f(D)\, dD, \tag{3}$$

where C_n is the number concentration and $f(D)$ is the probability density function (PDF) of the particle size. If the calculations are carried out using Eq. 3, the MWLE technique will retrieve the number concentration distribution function. Another possibility is to express the PSD in volumetric dimensions as $V(D) = C_n \cdot (D^3\pi/6) \cdot f(D)$. Then Eq. 3 can be written as

$$-ln(Tr(\lambda)) \cdot \frac{2}{3L} = \int_{D_{min}}^{D_{max}} Q_{ext}(D, \lambda, m) \cdot \frac{V(D)}{D} dD. \tag{4}$$

In the present work the latter formulation is preferred for numerical reasons, namely to avoid the bad scaling of matrix **S** arising from the integral Eq. 3. In order to obtain the discretized form of Eq. 4 the method proposed in [5] and [6] was implemented. After discretization by linear quadratures for λ and D, the right hand side gets the following form:

$$\sum_{j=1}^{M} S_{i,j} V_j \tag{5}$$

where vector V (the unknown) is the discretized form of V(D) (volumetric particle size distribution function) and $S_{i,j}$ (extinction matrix) can be calculated according to the following equation:

$$S_{i,j} = \int_{D_{j-1}}^{D_j} \frac{Q_{ext}(D, \lambda_i, m)}{D} dD \tag{6}$$

If $i = 1 \ldots N$ and $j = 1 \ldots M$, N divisions are used for the discretization of the wavelength interval and M divisions for the particle size interval. Introducing vector T as the discretized form of the left side part of Eq. 4, the following linear algebraic equation is obtained:

$$T = \mathbf{S} \cdot V \tag{7}$$

In order to retrieve the volumetric PSD function $V(D)$, Eq. 7 should be inverted. Unfortunately, due to the smoothing effect of matrix **S** the above system is ill-conditioned and numerically unstable. For its solution a specific regularized inversion technique is necessary.

3. Inversion technique

The expression *ill-conditioned* refers to the very large condition number of the coefficient (or kernel) matrix **S** (Eq. 7). A large condition number indicates, that some of the equations of the system are linearly nearly dependent, indicating redundant information in the system. Such a coefficient matrix has a smoothing effect when a mapping is performed from the space of PSDs to the space of transmittance functions (Eq. 7). In the presence of small perturbations in vector T (measurement errors) the result of the inverse mapping (V) can easily be such a PSD function, which is not contained in the space of realistic PSD functions. Before solving an ill-conditioned system, it requires numerical treatment. In the present work numerical treatment means the incorporation of a priori assumptions about the solution. Such assumptions may help to avoid mapping outside the space of realistic PSD functions but inevitably causes the modification of the original system. The intrusivity of the numerical treatment should be minimised in order to maintain the correct representation of the modelled physical phenomena.

One of the most widely used methods for overcoming the above-stated problem is called the Philips-Twomey regularisation method. Its detailed description can be found in [7], [8] and [9]. In general form, the regularised solution can be obtained by means of a minimisation problem:

$$V_{reg} = min\left\{\|\mathbf{S} \cdot V - T\|_2^2 + \gamma^2 \|\mathbf{L} \cdot V\|_2^2\right\} \tag{8}$$

if the original ill-posed problem was given in the form of Eq. 7, with V being the unknown vector. The quantity γ is called the regularization parameter, which controls the weight given to the minimisation of the norm of the side constraint ($\|\mathbf{L} \cdot V\|_2^2$) relative to the minimization of the residual norm ($\|\mathbf{S} \cdot V - T\|_2^2$). The choice of the regularization parameter is essential for a successful regularization. In the present method the regularization parameter is optimised in every inversion using the L-curve optimisation, which is described in the book of Hansen [7] and the paper of Hansen dedicated to [8].

In Eq. 8 matrix **L** is the regularization matrix, which formulates a criteria to be minimized, thus representing the a priori knowledge about the nature of the solution. In [10] the role of the regularization matrix is extensively explained, while examples are also given. In the present study the 0th order and 2nd order discrete derivative operators were used to stabilize the solution. Consequently, the side constraint was the minimization of the 0th and 2nd order derivative of the solution. The minimization of the solution itself (using the 0th order operator) is justified by the fact that particle size distribution functions take very small values everywhere outside a certain interval. The use of the 2nd order operator represents another approach, which attempts to find smooth solution functions with minimal 2nd derivative. The main difference of the effects of the two side constraints will be pointed out in Section 4.4.

Because of the non-negativity of a particle size distribution function it is advantageous to complement the Philips-Twomey regularization with a non-negativity constraint. Using the formulation proposed in [7] and [5], the solution can be obtained by the Non-Negative Least Squares (NNLS) algorithm:

$$min_{x>0} \left\| \left(\mathbf{S}^T\mathbf{S} + \gamma^2 \cdot \mathbf{L}^T\mathbf{L}\right) V - \mathbf{S}^T T \right\|_{2-LSQ}^2 \tag{9}$$

Summarizing, the Philips-Twomey method does not seek the solution with the smallest residual norm, but allows small deviation from that, in order to find a solution with smaller overall norm, which satisfies the side constraints, too.

4. Parametric study

The purpose of this parametric study was to evaluate the range of applicability of the MWLE technique and to check its sensitivity to the governing parameters. The present section gives the optimal values for parameters such as the size of the extinction matrix $\mathbf{S}_{i,j}$ (number of measurement wavelengths and particle size classes), the measurement wavelength range and the recoverable particle size range. Furthermore, it reports the investigation of the effects of the parameters (modal value, standard deviation) of the retrievable distribution functions. The numerical tests were conducted by the help of forward modelling. The light transmittance spectrum of a hypothetical PSD function was modelled by Mie's theory. In order to simulate measurement errors, the modelled transmittance spectra were contaminated by normally distributed random noise. The error of the inversion was evaluated by comparing the original and the retrieved distribution functions. Each test was performed 50 times, with different added random errors. The magnitude of the imposed error varied between 1% and 10%.

4.1. Optimal extinction matrix size

The goal of this investigation is to determine the appropriate extinction matrix size i.e. the number of measurement wavelengths and particle size classes for the reconstruction of the PSD. Since an equidistant division was used both on the size and wavelength intervals, the number of divisions controls the quality of discretization of the PSD function and the corresponding transmittance spectrum. There should be sufficiently large number of size divisions for ensuring the smooth integration of Eq. 4 thus the convergence of the transmittance spectrum. It was found, that satisfactory convergence is reached and all the features of realistic, smooth distribution functions are captured by using a resolution of 25 $1/\mu m$. The resolution of the particle size interval was fixed to this value. On the other hand, the number of wavelengths controls the sampling of the measured transmittance spectra and the amount of information available for the PSD reconstruction. [1] and [9] states, that there are maximum 7-8 independent pieces of information available in the UV-NIR wavelength range, ensuring PSD retrieval with maximum accuracy from 7-8 appropriately chosen wavelength channels. Contrary to this, more recent authors such as [11] use much more measurements, e. g. at 289 wavelengths. While selecting the necessary number of divisions, a trade-off has to be found between the accuracy and the computational requirements of the inversion process.

On Fig. 1 the differences between the generated and retrieved distributions are plotted as a function of the number of wavelength divisions in the case of the two different regularization methods.

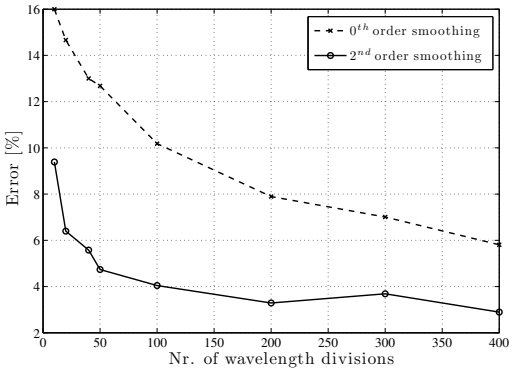

Figure 1: Variation of the inversion accuracy with changing the number of wavelength divisions (the size resolution is fixed to 25 $1/\mu m$, the imposed error is 5%)

The plot displays superior accuracy resulting from the use of the 2nd order difference regularization matrix. The figure also shows, that the accuracy of the inversion indeed improves with increasing the number of wavelength divisions. Since the computational demands have to be kept in mind, 200 divisions were chosen as a good tradeoff. It corresponds to a wavelength resolution of 0.25 $1/nm$ if the wavelength range is $200nm \ldots 1000nm$. Consequently, the employed spectrometer should have the same or higher resolution. One inversion takes 0.05s with the 0th order regularisation and 0.08s with the 2nd order regularisation on a dual core 1.8 GHz computer.

The wavelength and size resolutions concluded from this section are respected throughout the study.

4.2. Optimal size parameter range

The goal of this investigation is to find the wavelength interval that results in the best inversion of a certain PSD. Since the extinction problem scales with the size parameter x, this parameter has been chosen as the variable of this investigation. In other words,

the purpose of this simulation study is the identification of the optimal particle size to wavelength ratio for extinction measurements.

Several different test problems were generated with varying particle modal radii between 25nm and 500nm. The modelled problems were contaminated by 5% error and inverted using systematically varied wavelength intervals. The wavelength intervals providing the best accuracy were chosen and the minimum and maximum values of size parameter were calculated based on the limits of the PSD functions. The limits of the particle size interval were considered as the $+2\sigma/-2\sigma$ interval around the modal value. The formulae for calculating the size parameter limits are written in Eq. 10 and Eq. 11.

$$x_{min} = \frac{2 \cdot \pi \cdot r_{modal-2\sigma}}{\lambda_{max}} \tag{10}$$

$$x_{max} = \frac{2 \cdot \pi \cdot r_{modal+2\sigma}}{\lambda_{min}} \tag{11}$$

The results of the investigation are summarised in Tab. 1, where the minimum and maximum of the obtained optimal size parameter intervals are displayed. The last row of the table contains the mean of the obtained values.

Table 1: Optimal size parameter ranges obtained for inverting distributions with different modal radii

	0th order		2nd order	
r_{modal} [nm]	x_{min}	x_{max}	x_{min}	x_{max}
25	0.345	17.27	0.316	23.43
75	1.08	37.94	0.84	17.13
125	0.99	20.65	1.71	26.63
175	1.23	15.91	2.16	33.39
225	2.19	17.83	2.52	32.2
275	2.47	20.23	2.39	22.49
325	2.25	28.5	2.14	23.19
375	2.47	31.5	2.67	29.66
425	2.89	31.26	2.85	24.52
475	3.25	24.37	2.89	20.67
500	3.54	32.76	3.04	22.29
Mean	2.06	25.29	2.14	25.1

The examination of the values shown in Table 1 shows, that the optimal maximum limit does not vary monotonically with the modal radius of the PSD, thus the mean value can be considered. It can be observed, that the minimum limits of size parameter slightly increase with the modal radius. The limitation of the investigated wavelength range between 10nm and 1010nm could explain this conclusion. Supposing, that the size parameter values were equally biased both for very small and very large modal radii, the calculation of their mean still gives a useful value. Summarising, the results allow to conclude, that an optimal size parameter range could be defined based on the limits of the expected PSD function as $x = 2 \ldots 25$. This result can be qualitatively justified by the fact, that this is the particle size to wavelength ratio for whom the extinction efficiency factors are the highest.

The latter result is illustrated by a realistic example. A test case characterized by $r_m = 125nm$ was inverted with two different wavelength ranges. The first inversion was performed using the general visible-NIR range ($400nm \ldots 900nm$), which is easy to obtain in experiments. The second inversion was performed according to the findings of this section ($20nm \ldots 265nm$). The obtained results are shown only for the NNLS 0th order inversion; in Fig. 2 (non-optimal case) and Fig. 3 (optimal case), where the multiple sets of points correspond to the 50 different random error cases.

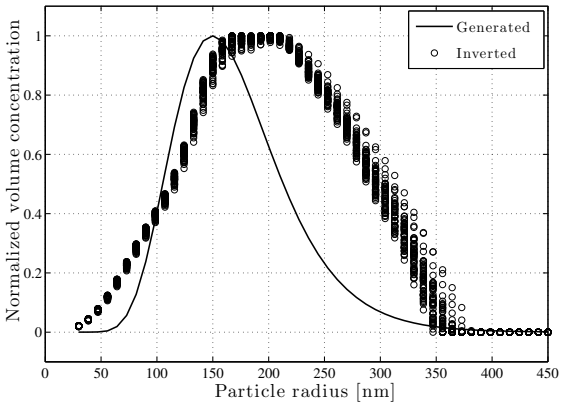

Figure 2: Comparison of the generated and recovered distribution functions obtained with the non-optimal wavelength range

In the non-optimal case, large inversion errors occurred. On Fig. 2 the relatively small scattering of the results comes together with a bias in the modal value. Both of these features are the consequences of the too large regularisation term (Eq. 8). Due to the insufficient information contained in the measurement data, the solution loses its sensitivity to the input data.

The above mentioned problems disappear, when an optimal wavelength range is chosen. Fig. 3 indicates that the obtained distributions are free of significant bias. The scattering of the data is reasonable, since in

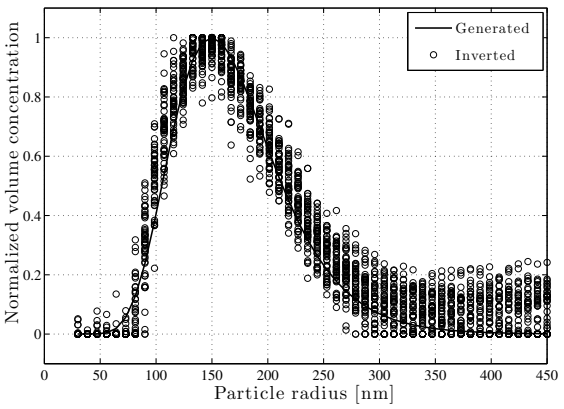

Figure 3: Comparison of the generated and recovered distribution functions obtained with the optimal wavelength range

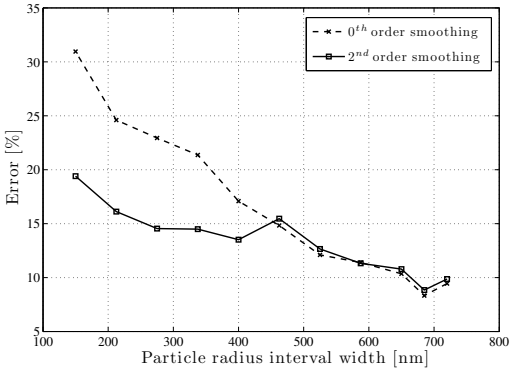

Figure 4: Variation of the error of the inversion as function of the particle radius range

this test 10% error was introduced.

The latter result points out the particular importance of UV light components for the measurement of nanoparticles.

4.3. Particle size interval

In order to apply the present technique, a priori knowledge of the size of the particles is necessary for the generation of the extinction matrix. Ideally, an interval should be chosen, which completely involves that part of the PSD, which is responsible for the main characteristics of the transmittance function. This means that particle sizes with low extinction efficiencies can even be excluded, the PSD can be cut up to a certain extent. A key question concerning the practical applicability of the MWLE technique could be formulated as 'How accurate a priori knowledge of the particle size distribution is necessary for a satisfactory data inversion?'. To answer this question multiple cases were analysed with different particle size intervals that all confined the model PSD with modal radius of 200nm. The number of particle size divisions ensured a constant resolution determined in Section 4.1. Fig. 4 displays the error of the inversion as a function of the particle size interval width.

Significant differences can be observed between the two inversion methods. The NNLS 0th order method is more sensitive to the choice of the size interval width. The larger is the interval, the better is the accuracy of the inversion with both methods. Choosing large intervals results in errors not exceeding 10%, which is the same magnitude wherewith the present test case was contaminated artificially. Fig. 4 shows, that an accurate a priori knowledge of the PSD function is not necessary. It is sufficient to choose a large range of particle size, which certainly involves the whole distribution function, whatever inversion method is used. This is an important conclusion regarding the practical applicability of the MWLE technique.

4.4. Particle size distribution characteristics

In this section the investigation of the influence of the particle size distribution characteristics (modal value (r_m) and standard deviation (σ)) of lognormal distribution is presented. 5% error was added in all the test cases. The obtained results are summarized by Fig. 5 (0th order smoothing) and Fig. 6 (2nd order smoothing).

It is noted, that the displayed values of standard deviation (multiplied by 100) express the dispersion of the particle sizes as a percentage of the modal value. Consequently, the geometric standard deviation always changes with the modal radius, even if σ is kept constant.

The NNLS 0th order method performs best, when both the modal radius and standard deviation are very small. In this case the distribution function has a shape of a sharp peak and the incorporated side constraint (minimization of the 0th order derivative of the solution) can be satisfied very well. Increasing the modal radius leads to slightly increasing errors. For small modal radii and standard deviations the NNLS 2nd order method shows its worst performance, indicating that the 2nd order smoothness is inappropriate in these cases (Fig. 6). The further analysis of Fig. 6 shows, that for standard deviations larger than 0.1 and modal radii larger than 125nm the NNLS 2nd order method performs better.

It can be concluded that different regularization methods should be chosen depending on the charac-

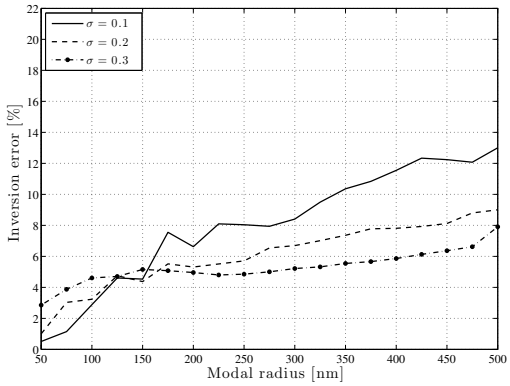

Figure 5: Variation of the inversion error as a function of r_m and σ for the NNLS 0th order method

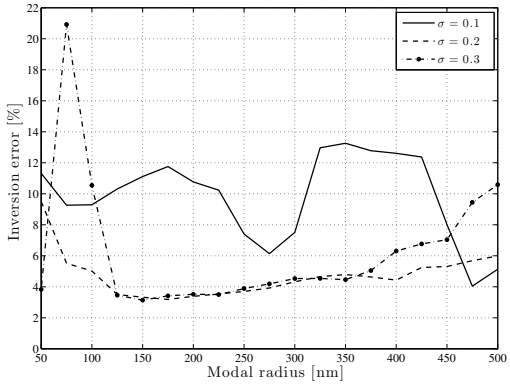

Figure 6: Variation of the inversion error as a function of r_m and σ for the NNLS 2nd order method

teristics of the retrievable PSD function. When the right choice is made, the inversion will not amplify the measurement errors.

4.5. Multimodal PSDs

The main advantage of the regularized inversion algorithm is that it does not require any a priori information about the shape of the underlying distribution. An example is shown below (Fig. 7), in which a bimodal PSD function was reconstructed. The function was generated as a combination of two different lognormal distributions. 5% of noise was introduced to test the robustness of the retrieval.

The initial distribution curve was well reconstructed by both methods, although the NNLS 0th order method underestimated the height of the second mode. Both inversion methods seem to support well the retrieval of multimodal distribution curves.

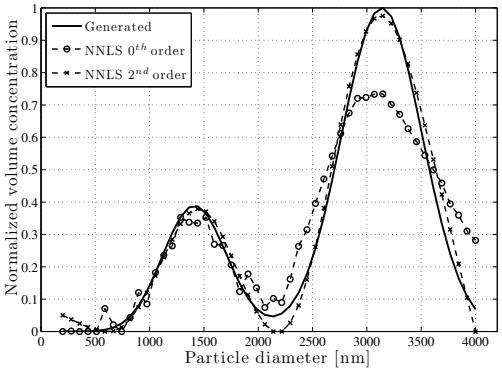

Figure 7: The generated and retrieved bimodal particle size distribution functions in the presence of 5% noise

5. Validation measurements

The goal of the validation measurements is to assess the accuracy of the MWLE technique through comparing the measurement results with Scanning Mobility Particle Sizer (SMPS) measurements carried out with a commercial instrument. The SMPS instrument consists of two main units. The first unit is called Differential Mobility Analyser (DMA). It classifies the investigated particles into narrow size ranges from 10nm to 1000nm, according to their electrical mobility. First the particles pass through a radioactive charger, which establishes a defined charge distribution in the particles. The limitation for particles larger than 1000nm is realised by an impactor plate, which traps the particles that exceed this size limit. The charged particles enter a narrow channel between two concentric electrodes, where an electric field is maintained. The negatively charged particles are displaced towards the inner electrode as they advance through the channel. Depending on the electrical mobility (which is related to the size) of the particles they may or may not enter a narrow slit, which can be found on the central electrode. Once a certain voltage is applied to the two electrodes, only particles corresponding to a narrow size range can enter the slit. These particles proceed to the second unit, which is called Condensation Particle Counter (CPC). In this unit the particles are enlarged to approx. $10\mu m$ by condensing butanol on their surface. The enlarged particles are then counted by an optical method. The SMPS instrument performs the measurement of the different size channels one after the other. The total concentration of the particles below 1000nm can be obtained by integrating the obtained PSD function. The scanning of the complete size range takes approx. 5 minutes. The

instrument can be used without the DMA unit, too. In this case the total concentration of the particles can be effectively determined, also including particles larger than 1000nm.

5.1. Experimental setup

The experimental setup used for validating the MWLE technique by means of SMPS measurements comprises an aerosol generator, suitable test sections for both of the instruments and the instruments themselves. Fig. 8 represents the sketch of the experimental setup. Number 1. indicates the aerosol generation subsystem. A pneumatic atomiser is fed with pressurised air, whose flow rate and pressure are measured by a rotameter and a manometer respectively. A valve controls the latter parameters. The KCl aerosol is produced of 0.1…10 wt% aqueous solutions of KCl. After the atomisation of the liquid, the droplets pass through a diffusion dryer, which is filled with silica gel. After removing the liquid content of the aerosol, the solid KCl particles enter the test section, which is a plexiglas reservoir with circular cross-section. The MWLE measurements are performed inside this reservoir (number 2.). The particles enter at one end of the reservoir from 4 inlets equally distributed around the perimeter. The extraction is performed similarly at the other end of the reservoir. A collimated, white light beam passes through the test chamber along its longitudinal axis. After passing through the particle cloud, the light is received and analysed by a spectrometer and a personal computer. The knowledge of the dimensions of the test chamber provides the path length (L) travelled by the light beam inside the particle cloud. In order to avoid the sedimentation of the particles inside the reservoir, a continuous flow is maintained by an ejector (indicated as Dilution & Exhaust on Fig. 8), which is installed downstream the test chamber. The pressure and flow rate of the ejector feed air are measured with a manometer and a rotameter, respectively. Since the ejector mixes the primary flow (with particles) with a large flow rate of secondary air flow (clean), it also serves as an aerosol dilutor, satisfying the concentration requirements of the SMPS measurements. The measurement of its feed air flow rate allows the calculation of the dilution ratios, which are generally between 100 and 300. The sampling tube of the SMPS instrument is connected downstream the ejector, providing the sampling of the diluted aerosol. The SMPS system and the corresponding aerosol dilutor are indicated by number 3.

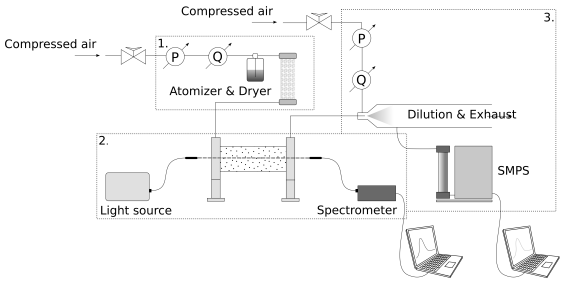

Figure 8: The sketch of the experimental setup

5.2. Experimental conditions

The transmittance of a particle cloud is obtained after the measurement of a dark spectrum (light source switched off), a reference spectrum (light source switched on, no particles) and the sample spectrum (in the presence of particles). Following this procedure, the transmittance is calculated by Eq. 12.

$$Tr(\lambda) = \frac{sample(\lambda) - dark(\lambda)}{reference(\lambda) - dark(\lambda)} \tag{12}$$

A typical transmittance spectrum can be seen on Fig. 9.

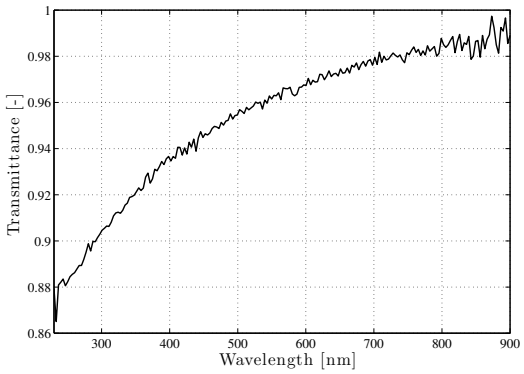

Figure 9: Typical experimental transmittance

Because of the low intensity of the light source outside the range 230…1000nm, the measurements were confined to this interval. According to the results of Section 4.1, the spectrum was sampled at 200 equidistantly spaced points.

The inversion of the data was performed on 4 different particle size ranges. The lower limit was fixed to 10nm, while the upper limit was varied ($1\mu m$, $2\mu m$, $3\mu m$, $4\mu m$). The purpose of testing different ranges was to assess the dependency of the results on this parameter. The 0th order regularization matrix has been used for the inversions.

For the calculation of the extinction efficiency factors, the measured particles were assumed to be spherical. The importance of the accurate knowledge of the complex refractive index of the scattering medium is emphasised in [11]. Since KCl is frequently used as the material for optical components, there is a large number of available data about its complex refractive index. In the present work the values of [12] were used.

Four sets of measurements were performed, varying the concentration of the initial KCl solutions. The experimental parameters are presented in Table 2.

Table 2: Test parameters

KCl solution	p_{atom} [bar]	Dilution ratio
10wt%	1	157.5
1wt%	2.2	205.8
0.5wt%	2.2	194
0.1wt%	2.2	97.2

5.3. Experimental results

The outcome of the MWLE measurements is the volumetric PSD function, while the SMPS instrument measures the number concentration distribution function. The SMPS results are transformed to volumetric PSDs for the sake of comparison. The undiluted SMPS PSDs are obtained after multiplying the results by the measured dilution ratios. First, the effect of choosing different particle size ranges in the MWLE data inversion was evaluated. The result is shown on Fig. 10. The diagram displays the MWLE analysis of the aerosol obtained from 1wt% KCl solution under 2.2 bar atomiser pressure.

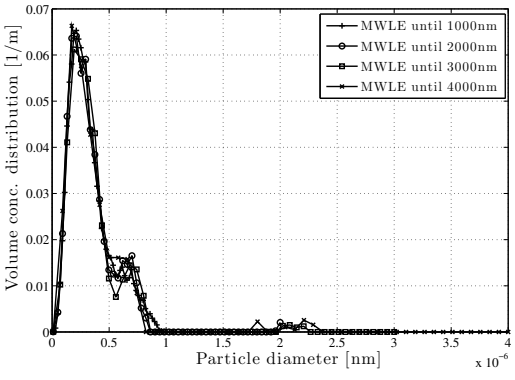

Figure 10: PSDs obtained from MWLE measurements using different upper particle size limits (1wt% KCl solution atomised at 2.2bar)

Fig. 10 shows, that the inversion result is nearly independent of the upper diameter limits. In the followings the MWLE results are only displayed up to the particle diameter, where the particle concentration diminishes. However, the measurements can be compared only up to 1000nm because of the limitations of the SMPS instrument. One way to validate the measurements above this limit is the comparison of the MWLE total concentration values with the ones obtained with the SMPS instrument without using the classifier unit. However, this task will only be fulfilled in the future.

The purpose of the following study was the comparison of the MWLE and SMPS results in case of varying particle parameters. The comparison is performed for 4 different initial KCl solution concentrations. The comparison of the PSD functions is shown in Fig. 15.

Fig. 15 displays a generally good agreement. Both of the techniques displays decreasing standard deviations and total concentrations when the concentration of the initial KCl solution is decreased from 10$wt\%$ to 0.1$wt\%$. Assuming that the size of the atomised droplets is independent of the KCl concentration, the resulting solid particle size should decrease with decreasing proportion of solute in the droplets. The same trend is valid for the total volume concentration due to the same reason. Fig. 11 displays the largest difference between the MWLE and SMPS measurement result. The maximum volume concentration is found for particles with 300nm diameter by both measurement techniques. However, the standard deviation of the MWLE result is much larger than that of the SMPS instrument. The upper particle size limit of the SMPS instrument is set by an impactor plate, which traps all the particles larger than 1094nm. It is possible that such a lowpass filter has a smooth characteristic, which may result in the removal of somewhat smaller particles, too. Fig. 12 displays a much better agreement. The distribution curves agree in terms of mean value and standard deviation, too. It is noted, that a small secondary mode centred at 700nm is equally identified by both techniques. Further decreasing the KCl concentration in the initial solution (Fig. 13) leads ti the disappearance of the secondary mode. In this case only few particles are found above 600nm. The agreement of the two different techniques is still satisfactory, however a small difference of the maximum volume concentration and the mean value is identified. The same phenomenon is recognised on Fig. 14 in a more relevant way. One possible explanation of the discrepancy is the low level of extinction signal experienced in the two latter cases. The trans-

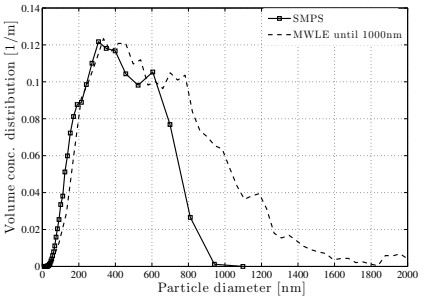

1

Figure 11: C_{KCl} = 10*wt%*

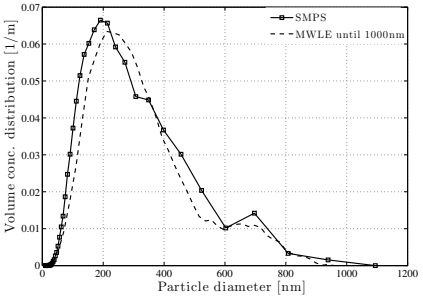

1

Figure 12: C_{KCl} = 1*wt%*

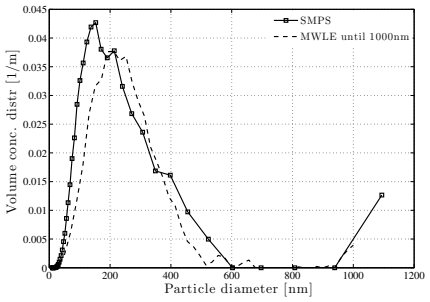

1

Figure 13: C_{KCl} = 0.5*wt%*

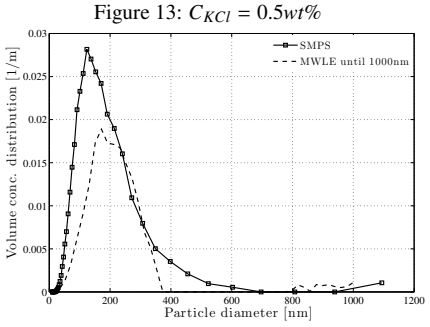

1

Figure 14: C_{KCl} = 0.1*wt%*

Figure 15: Comparison of PSDs of aerosols produced from solutions with varying KCl concentration

mittance spectrum corresponding to Fig. 14 is shown on Fig. 16.

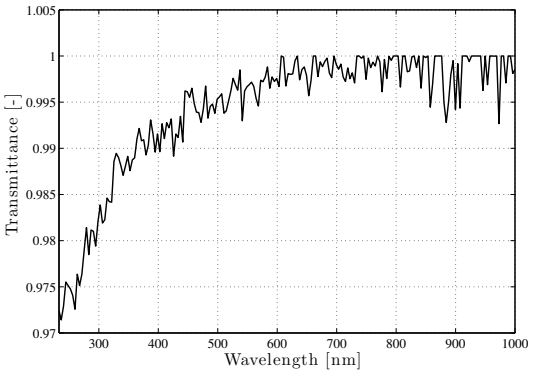

Figure 16: Measured transmittance spectrum of the aerosol obtained from 0.1wt% KCl solution

It is well visible that the low signal level (minimum transmittance of 97%) results in a noisy spectrum. Furthermore, above 600nm the measured spectrum had values larger than 1. These points - being unphysical - were artificially set to 1. The mentioned facts may cause difficulties to the inversion algorithm, leading to decreasing accuracy of the MWLE measurements. The latter hypothesis could be verified by characterising the same aerosol with much larger particle concentration (or optical path length), which could give rise to a higher extinction signal level. The retrieved particle size distribution functions (Fig. 13 and 14) still contain some useful information.

The comparison of the measured volumetric mean diameters can be found in Table 3. Apart from the case of 10wt% KCl solution, the obtained values agree well. The two techniques perfectly match in case of the 1wt% KCl solution. The larger difference encountered in the 0.5wt% case is caused by the secondary peak around 1000nm observed by the SMPS instrument.

The comparison of the measured total volume concentration values can be found in Table 4. When the size of the investigated particles falls within the measurement limits of the SMPS instrument and the particle concentration is suitable for the MWLE measurements (cases of 1wt% and 0.5wt% KCl concentration) the measured concentrations show a satisfactory agreement.

6. Conclusions

After the description of the MWLE technique and the related data inversion algorithm, different tests were reported for the evaluation of the sensitivity, robustness and limitations of the algorithm.

Table 3: Comparison of obtained volumetric mean diameters

KCl solution	p_{atom} [bar]	SMPS $D_{4,3}$ [nm]	MWLE $D_{4,3}$ [nm]
10wt%	1	447.6	657.2
1wt%	2.2	333.5	333.5
0.5wt%	2.2	318.1	264.2
0.1wt%	2.2	216.8	231.9

Table 4: Comparison of obtained total number concentrations

KCl solution	p_{atom} [bar]	SMPS vol. conc. [−]	MWLE vol. conc. [−]
10wt%	1	$6.71 \cdot 10^{-8}$	$1.12 \cdot 10^{-7}$
1wt%	2.2	$2.42 \cdot 10^{-8}$	$2.22 \cdot 10^{-8}$
0.5wt%	2.2	$1.22 \cdot 10^{-8}$	$9.65 \cdot 10^{-9}$
0.1wt%	2.2	$5.64 \cdot 10^{-9}$	$3.62 \cdot 10^{-9}$

First, the optimal size of the extinction matrix was determined. It was found, that a size resolution of 25 $1/\mu m$ is necessary for capturing the important features of real, smooth particle size distribution functions. It was shown, that the use of more wavelength divisions improves the accuracy. A number of 200 wavelength divisions on the UV - near infrared range was found to be a good compromise.

Afterwards the optimal particle size-to-wavelength ratio was investigated. A criterion was given in terms of the size parameter: the optimal range should span the interval $2 \ldots 25$. When the optimal size parameter interval is not possible to ensure, the NNLS 0th order method should be used due to its higher robustness.

The investigation of the effects of the particle size range led to the conclusion, that it is advantageous to apply always a large size interval. Consequently, there is no need for an accurate a priori knowledge about the PSD for successful data inversions.

Afterwards the experimental setup was presented, which can be used for the validation of the MWLE technique.

The reported validation measurements were performed on aerosols consisting of solid KCl particles. Good quantitative agreement was found between the MWLE technique and the commercial SMPS reference technique, both in terms of concentration and particle size distribution function. The observed discrepancies have been explained by the differing measurement ranges of the instruments in terms of particle size and concentration. Some advantages of the MWLE technique compared to the SMPS instrument were identified such as the larger measurement range, applicability for the on-line, real time non-intrusive monitoring of particles.

It can be concluded that the MWLE technique together with the described inversion algorithm can be successfully applied as an accurate sub-micron particle characterisation technique.

In the next step the MWLE technique will be applied to SiC (absorbing) nanoparticles obtained from the atomisation of a SiC nanoparticle dispersion. The aggregation of the particles will be investigated and the non-sphericity of the particles will be taken into consideration.

Acknowledgments

The financial support of the presented work was provided by Fonds de la Recherche Scientifique (FNRS), FRIA fellowship and the Walloon Region under the NANOTECH convention C6405.

References

[1] G. Viera, M. A. Box, Information content analysis of aerosol remote-sensing experiments using an analytic eigenfunction theory: anomalous diffraction approximation, Applied Optics 24 (24) (1985) 4525–4533.

[2] T. Kourti, J. F. Macgregor, A. E. Hamielec, Turbidimetric Techniques Capability To Provide the Full Particle Size Distribution, in: T. Provder (Ed.), Particle Size Distribution II, American Chemical Society, 1991, pp. 2–19.

[3] C. Dellago, H. Horvath, On the accuracy of the size distribution information obtained from light extinction and scattering measurements - I. Basic considerations and models, Journal of Aerosol Science 24 (2) (1993) 129–141.

[4] H. C. van de Hulst, Light scattering by small particles, Dover publications, 1981.

[5] F. Onofri, S. Barbosa, M. Wozniak, O. Toure, J. Mroczka, Optical characterization of nanoparticles and aggregates: light extinction spectrometry, in: 15th Int Symp on Applications of Laser Techniques to Fluid Mechanics, Lisbon, 2010, pp. 1–11.

[6] G. Crawley, M. Cournil, D. Di Benedetto, Size analysis of fine particle suspensions by spectral turbidimetry: potential and limits, Powder Technology 91 (1997) 197–208.

[7] P. C. Hansen, Rank-Deficient and Discrete Ill-Posed Problems, SIAM, 1998.
[8] P. C. Hansen, REGULARIZATION TOOLS: A Matlab package for analysis and solution of discrete ill-posed problems, Numerical Algorithms 6 (1994) 1–35.
[9] S. Twomey, Introduction to the Mathematics of Inversion in Remote Sensing and Indirect Measurements, Dover publications, Mineola, New York, 1996.
[10] W. H. Press, S. A. Teukolsky, W. T. Vetterling, B. P. Flannery, Numerical recipes, 3rd Edition, Cambridge, 2007.
[11] Y. Liu, W. P. Arnott, J. Hallett, Particle size distribution retrieval from multispectral optical depth: Influences of particle nonsphericity and refractive index, Journal of Geophysical Research 104 (D24) (1999) 31753–31762. doi:10.1029/1998JD200122.
[12] H. H. Li, Refractive Index of Alkali Halides and Its Wavelength and Temperature Derivatives, Journal of Physical Chemistry Reference Data 5 (2) (1976) 329–526.

Experimental Study of Two-Phase Flow Induced by Cavitation through a Safety Relief Valve at Inlet Subcooled conditions

Jorge Pinho

Environmental and Applied Fluid Dynamics Department, von Karman Institute for Fluid Dynamics, Belgium, jorge.pinho@vki.ac.be

Supervisor: Patrick Rambaud

Associate Professor, Environmental and Applied Fluid Dynamics Department, von Karman Institute for Fluid Dynamics, Belgium, rambaud@vki.ac.be

Co-Supervisor: Jean-Marie Buchlin

Head of Department, Environmental and Applied Fluid Dynamics Department, von Karman Institute for Fluid Dynamics, Belgium, buchlin@vki.ac.be

Industrial Supervisor: Saïd Chabane

CETIM, Centre Technique des Industries Mécaniques, France

Abstract

The behaviour of a safety relief valve in presence of a vapor/water two-phase flow induced by cavitation is investigated. Two distinct safety relief valves are tested: a transparent model based on API 1 1/2G3 and an original API 2J3 type. The design of both valves is modified to allow the adjustment of the disk at different lifts. Results show a significant limitation on the mass flux through the valve due to the cavitation phenomenon. The liquid recovery factor F_L, which is normally used to identify a choked flow condition in a control valve, is determined experimentally. The existence of a local minimum located at a height position L/D=0.14 indicates in this position, a change on the flow characteristics of both valves. In case of the 2J3 safety valve, it is remarked that the blow down ring adjustment has significant influence on the location of the minimum cross section of the flow and consequently, on the shape of the F_L curve. Hydrodynamic forces acting on the valve disk are measured for the API 2J3 SRV. A change on the forces characteristics is identified just after the inception of cavitation. Finally, unsteady pressure measurements are performed upstream and downstream the transparent model based on API 1 1/2G3. Results suggest that in a choked flow condition, pressure fluctuations caused by the valve, no longer travel upstream since locally, the speed of sound and the flow velocity are the same.

Keywords: safety relief valve, two-phase flow, cavitation, choked flow, speed of sound

NOMENCLATURE

A Discharge section [mm^2]
A_{vc} Section in the vena contracta [mm^2]
C Flow coefficient through an ideal nozzle [-]
C_{Pset} Specific liquid heat capacity at inlet conditions [J/(kg K)]
D Valve discharge diameter [mm]
F_L Liquid pressure recovery factor[-]
F_F Liquid critical pressure ratio factor[-]
h_{vl} Latent heat of vaporization [J/kg]
K_D Discharge coefficient [-]
K_V Flow coefficient [m^3/h]
L Valve lift [mm]
L_p Sound Pressure Level [dB]
$\dot{m}_{SRV}$ Experimental mass flow rate through SRV [kg/s]
$\dot{m}_{nozzle}$ Mass flow rate through an ideal nozzle [kg/s]
N Boiling delay factor [-]
P'_{123} Unsteady pressure upstream and downstream the SRV [bar]

P_b Back pressure [bar]
P_c Thermodynamic critical pressure [bar]
P_{set} Set pressure [bar]
P_v Saturation pressure at inlet temperature conditions [bar]
P_{vc} Pressure in the vena contracta [bar]
Q Volume flow rate [m^3/h]
Q_{max} Maximum flow rate [m^3/h]
SRV Safety Relief Valve
T_{set} Temperature at inlet conditions [K]
v_{vl} Difference between the vapor and liquid specific volumes at P_v [m^3/kg]
x_{FZ} Coefficient of inception cavitation [-]
ΔP Pressure differential [bar]
η Pressure ratio P/P_{set} [-]
η_s Ratio of the saturation pressure to the inlet pressure P/P_v [-]
η_{st} Transition Pressure ratio criterion [-]
ω Compressibility factor [-]
ρ Fluid Density [kg/m^3]
ρ_{set} Fluid Density at inlet conditions [kg/m^3]

1. Introduction

Two-phase flows are present in daily-life and in numerous technical and industrial processes such as nuclear, chemical or mechanical engineering where different gas-liquid reactors, boilers, condensers, evaporators and/or combustion systems can be found. In nuclear and thermal engineering systems the use of SRV is mandatory since it protects them against any over pressure, representing the ultimate protection before an accident occurs. The complete understanding of the multi-physics taking place in the flow through a SRV is therefore important for the security of the protected process. In single phase flow such as liquid or gas discharge, reliable and well established methods are available for the SRV design. On the other hand, when the static pressure of an initially subcooled liquid falls below the saturation pressure, vapor bubbles will form which tend to locally reduce the medium speed of sound. Similarly to a compressible flow, this decrease of the speed of sound will be linked to a limitation on the mass flow evacuated and therefore, the single phase flow methodology becomes inadequate. There are some calculation methods available in the literature, that attempt to predict the critical flow onset in SRV for two-phase systems knowing the inlet flow conditions and the outlet pressure; however none of them is acknowledged as being fully reliable in the entire domain of two-phase flow.

2. Literature Review

Different methodologies exist in the literature providing useful and general guidelines to the sizing of SRV. The most widely known are the Homogeneous Equilibrium Models (HEM) and more recently the HNE-DS model, integrating the thermodynamic and mechanical non-equilibrium in the two-phase flow formulation. It is accepted from different authors[1][2][3], that the HNE-DS method proposed by Diener and Schmidt[4][5] is the most accurate and reliable method for two-phase flow through safety relief valves. On the other hand, international standards IEC 60534-2-3[6], ISO 4126-10[3], API 520 (2000)[7] used in industry for control and safety relief valves recognize the problematic of the two-phase flow and employ models that generally overestimate the mass flux through the mechanical device. This can induce flattering and/or chattering of the valve. Although all the standards basically aim to predict the flow rate through a valve, some differences are raised from the formulation point of view. IEC 60534-2-3[6] develops a set of equations for two phase flows based on a liquid recovery factor F_L of the control valve in case of cavitation, while remaining standards are more focused on the application of the equations to SRV; and take into account the two-phase mixture compressibility, the ω-parameter. It is evident from these differences, that a study of a SRV according to IEC 60534-2-3[6] could give new information on this topic, since the physical phenomenon inside any kind of valve should be modeled and predicted in similar way, despite of what standard is being used.

Several experimental investigations have been performed in the last decades in order to study the two-phase flow in singularities such as valves, orifices, venturi and convergent jet nozzles. The similarity between a complex geometry SRV and a simple venturi or nozzle relies on the fact that both cases produce a sudden restriction on the flow which can therefore be studied in a similar way. The majority of two-phase flow models used to predict the flow in a SRV make use of this similarity.

2.1. IEC 60534-2-3

The international standard IEC 60534-2-3[6] includes test procedures for determining the functional variables used in sizing equations for predicting the flow of compressible and incompressible fluids through control valves. Although the fundamental equations remain the same as in ISO 4126-10[3] and API 520 (2000)[7], its application in sizing valves is

slightly different since this standard attempts to predict the flow rate for each opening position of the valve. According to the International Standard for Automation, the flow coefficient K_V is the fluid volumetric flow rate, expressed in m^3/h, through a valve for a certain opening position in the following conditions: a) The pressure drop through the valve is 1.0 bar. b) The fluid is water at a temperature between 5 C and 40 C. The basic equation for K_V is given by Eq. (1). For water at temperature between 5 C and 40 C, one gets $\rho/\rho_o = 1$.

$$K_V = Q\sqrt{\frac{\rho/\rho_0}{\Delta P}} \tag{1}$$

The flow rate of an incompressible fluid through a valve is normally defined as a function of $\sqrt{\Delta P}$ for a constant upstream pressure, as it is shown in Fig. 1. This function can be divided into three distinct regions:

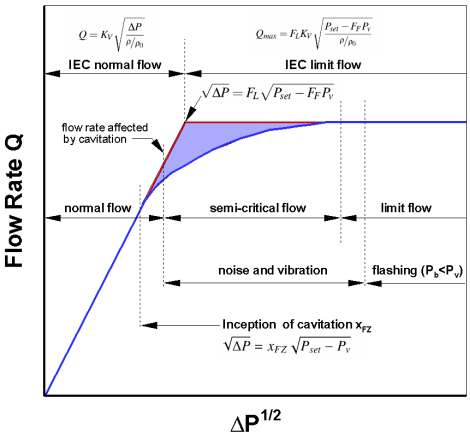

Figure 1: Flow rate diagram of an incompressible fluid through a valve according to IEC 60534-2-3[6].

Normal flow: the flow rate is proportional to $\sqrt{\Delta P}$. This region is established while there is no limitation on the flow rate due to the cavitation.

Semi-critical flow: the flow rate increases with the increment of $\sqrt{\Delta P}$ but not linearly. In this region, the valve capacity in converting pressure loss into flow rate is reduced, due to the liquid vaporization and consequently cavitation. Although cavitation starts in the normal flow region, defined with the coefficient of inception cavitation x_{FZ}, the bubble nucleation only becomes permanent at the beginning of the semi-critical flow in which the flow rate becomes limited.

Limit flow or choked flow: the flow rate is constant despites an increment of $\sqrt{\Delta P}$. In the case the downstream pressure is still inferior to the saturation pressure, vaporization and flashing phenomenon occurs.

Sizing equations recommended by IEC 60534 take into account the shadow area of Fig. 1, since they neglect the semi-critical flow region. This approximation is justified by the simplification it represents to the calculus and thus, it results in only two regions of the flow: normal flow and critical flow. The parameter that defines the beginning of the critical flow region is the liquid pressure recovery factor F_L, originally proposed by Baumann[8], and that depends on the valve body geometry. Its value represents the capacity of the valve in transforming the fluid kinetic energy in pressure, in the vena contracta region. It is defined by:

$$F_L = \sqrt{\frac{P_{set} - P_b}{P_{set} - P_{vc}}} \tag{2}$$

The smaller is the value of F_L, the greater is the capacity of the valve in transforming kinetic energy into pressure (high recovery valve). On the other hand, the higher is the value of F_L, the smaller is the valve capacity (low recovery valve), in which great part of the energy is dissipated by friction forces. Due to the difficulties of measuring the pressure in the vena contracta P_{vc} with high accuracy, this factor is normally determined in critical flow conditions, being only dependent on the maximum flow rate Q_{max} for a given upstream pressure P_{set}. With fixed inlet conditions, choked flow is evidenced by the failure of increasing pressure differentials to produce further increases in the flow rate and therefore, Eq. (2) is replaced by:

$$F_L = \frac{Q_{max}}{K_V}\sqrt{\frac{\rho/\rho_0}{P_{set} - F_F P_v}} \tag{3}$$

The liquid critical pressure ratio factor F_F introduced in Eq. (3) is the ratio between the pressure in the vena contracta and the saturation pressure in a choked flow regime. In experiments performed by Stiles[9], the author has remarked that vaporization of the liquid starts below the saturation pressure of the fluid. The following relation was proposed:

$$F_F = 0.96 - 0.28\sqrt{\frac{P_v}{P_c}} \tag{4}$$

For the case of water at ambient temperature, this factor reduces to F_F=0.96.

2.2. ISO 4126-10

The European normative ISO 4126-10[3] specifies the general prescriptions of SRV with a cross section diameter equal or greater than 6mm which are used for opening pressures above 0.1bar. In case of a two-phase flow, the same standard recommends the HNE-DS method proposed by Diener and Schmidt[4][5], which is an extension of the original ω-method published by Leung[10]. In the formulation of the ω-parameter, which represents the compressibility of a two-phase flow, the HNE-DS method includes a boiling delay factor N, that takes into account the mechanical and thermal non-equilibrium between both phases. In this methodology, the mass flux discharged through a SRV, is determined based on the discharge coefficient K_D, and the theoretical mass flux through an ideal nozzle, which in its turn, is dependent on the flow coefficient C, the discharge section A, the pressure and density at inlet conditions:

$$K_D = \frac{\dot{m}_{SRV}}{\dot{m}_{nozzle}} = \frac{\dot{m}_{SRV}}{CA\sqrt{2P_{set}\rho_{set}}} \tag{5}$$

In case of depressurization of an initially subcooled liquid, vaporization of the liquid may occur upstream or downstream the SRV throat, depending on which region the flow falls in:

$P_v > \eta_{st} P_{set} \Rightarrow$ low subcooling region (vaporization occurs upstream the throat).

$P_v < \eta_{st} P_{set} \Rightarrow$ high subcooling region (vaporization occurs at the throat).

In the above relations, the transition criterion η_{st} defined by Leung[10], is given by the two-phase compressibility factor ω:

$$\eta_{st} = \frac{2\omega - 1}{2\omega} \tag{6}$$

$$\omega = \rho_{set} C_{Pset} T_{set} P_v \left(\frac{v_{vl}}{h_{vl}}\right)^2 \tag{7}$$

In case the above relation from Eq. (6) falls in a low subcooling region, the flow coefficient C from Eq. (5) will be given by Eq. (8), while in the high subcooling region ($\omega = 1$), it reduces to the well known Bernoulli relation from Eq. (9).

$$C = \frac{\sqrt{(1-\eta_s) + \left(\omega\eta_s ln\left(\frac{\eta_s}{\eta}\right) - (\omega - 1)(\eta_s - \eta)\right)}}{\omega\left(\frac{\eta_s}{\eta} - 1\right) + 1} \tag{8}$$

$$C = \sqrt{1-\eta} \tag{9}$$

Typically, the low subcooled region is limited to very high saturation pressure ratios η_s, in the range of 0.9 to 1, [1], which is extremely difficult to obtain experimentally, using water at ambient temperature. For the case of high subcooling region, the present norm predicts a choked flow condition if the back pressure is below the saturation pressure ($P_b < P_v$). In this situation, Eq. (9) becomes:

$$C = \sqrt{1-\eta_s} \tag{10}$$

For the case of sub-critical flow, the back pressure should be used instead, in Eq. (9) ($\eta = \eta_b$).

3. Working principle of SRV

The basic elements of a conventional safety relief valve are illustrated in Figure 2. The nozzle is mounted on the pressure containing system and therefore, is the only part which is exposed to the process fluid during normal operation. The disk is normally held to the seat by the spring, which is housed in a bonnet mounted on top of the body. When the inlet static pressure rises above the set pressure of the SRV, the pressure forces become high compared to the elastic forces of the spring and the SRV opens. As lift begins and the fluid enters the chamber, a larger area of the disk is exposed to the fluid pressure and therefore, the increase in opening force overcompensates the increase in spring force, causing a rapid opening.

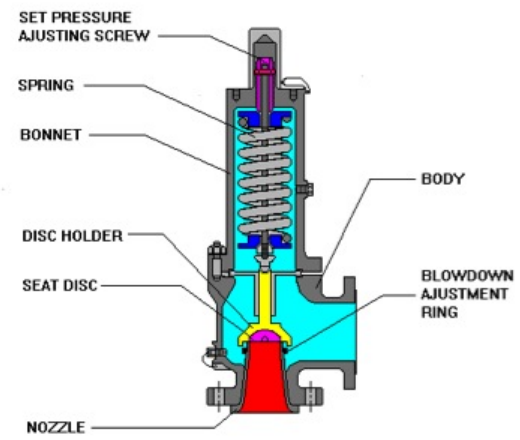

Figure 2: Conventional SRV schematic.

In order to achieve full opening from a small overpressure, the discs of SRV are usually surrounded by

a disk holder. The volume within the disk holder is known as huddling chamber. The blowdown adjustment ring placed around the nozzle is normally used to make fine adjustments to the overpressure and blowdown values of the valves, by changing the volume of the huddling chamber. These adjustments are normally done by counting the number of notches when rotating the ring, taking as the reference, its top position (0 notches).

In this study, two distinct SRV were tested: an API 2J3 type and a transparent model (made of PMMA) based on an API 1 1/2G3 type. Instead of using a spring, the design of both valves allows the adjustment of the disk at any fixed desired lift. Hence, the static flow behavior of the valves is investigated. The main differences between both valves are shown in Figure 3. Apart from the inlet size which is not the same (DN 50 for API 2J3 and DN 40 for API 1 1/2G3), also the actual discharge area of both valves is different (965 mm^2 for API 2J3 and 380 mm^2 for API 1 1/2G3). The convergent nozzle of the valve is much longer in the transparent model than in the API 2J3 SRV, 10D and 5D respectively. Additionally, the internal surface of the body in the API 1 1/2G3 was simplified in order to facilitate the manufacturing of the PMMA transparent model. Finally, the valve disk although having the same cross section in both cases, it is supported by a simpler cylindrical shape compared to the API 2J3 SRV. The transparent model of API 1 1/2G3 allows full optical access to perform flow visualization of cavitation in a SRV.

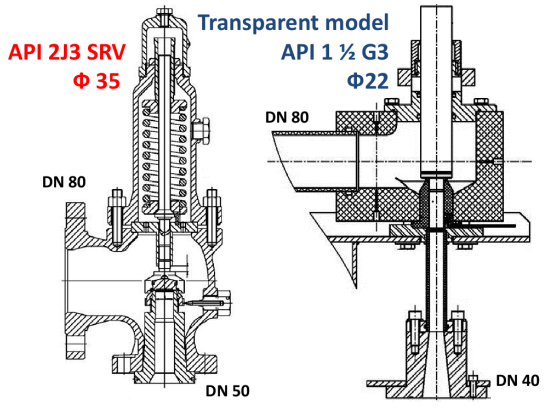

Figure 3: API 2J3 SRV and transparent model API 1 1/2G3 SRV.

4. Experimental facilities

Two different installations were built for each valve being tested: API 2J3 SRV and transparent model based on API 1 1/2G3 SRV. Operative conditions of both facilities are listed in Table 1, while a schematic of each one is presented in Figure 4.

	API 2J3 SRV	API 1 1/2G3 SRV
P_{set}	Up to 12 barg	Up to 4.0 barg
Q	140 m^3/h	35 m^3/h
P_b	-0.1 barg	-0.8 barg → Vacuum
T_{set}	Ambient	Up to 60 C

Table 1: Operative conditions of facilities.

Both installations operate in a similar way but at different magnitude scales. For the case of API 2J3 SRV(Figure 4(a)), a calming reservoir is connected to a high pressure pump (up to 250 m^3/h and 78 bar) which discharges water to the SRV tested. The back pressure can be adjusted with a control valve DN 150. Finally, the water is plunged in a large pool at minimum pressure of -0.1barg. In the second facility (Figure 4(b)), the amount of water is limited by the 750 L reservoir which feeds the system in a closed loop. Maximum operating pressure is defined to 4.0 bar to prevent any damage to the transparent model of the valve made in PMMA. The back pressure is adjusted either by the control valve DN 100, or by the vacuum pump which is located on the top of the reservoir. In this last configuration, a minimum back pressure of -0.8barg can be reached.

In both facilities, the flow rate and operating pressure is controlled with a variable speed motor connected to the pump. The flow rate is measured with electromagnetic flow meters placed upstream the tested SRVs, to guarantee that only liquid is present. Temperature of water is recorded in the calming reservoirs. Finally, pressure transducers are used to measure the static pressure upstream and downstream the SRVs (P_{set} and P_b respectively). For the case of API 1 1/2G3 SRV, unsteady pressure measurements are registered upstream and downstream the SRV (P'_1, P'_2 and P'_3).

The experiments were performed according to IEC 60534-2-3[6] recommendations. Keeping a constant upstream pressure, with the variable speed motor connected to the pump, several measurements were performed at different lifts and at different back pressures. The following test matrix was accomplished.

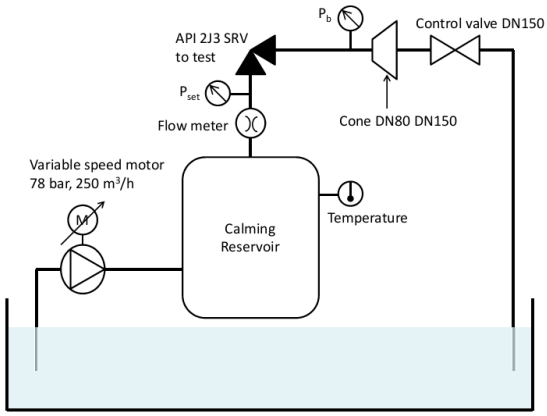

(a) API 2J3 SRV.

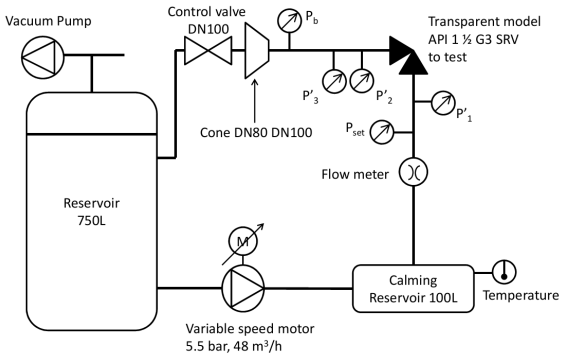

(b) Transparent model API 1 1/2G3 SRV.

Figure 4: Experimental facilities.

5. Results and Discussion

In this section, the experimental results obtained for both valves are discussed. Starting from the flow rate and forces vs. pressure drop diagrams, the characterization of both valves according to the international standards IEC 60534-2-3[6] and ISO 4126-10[3] is presented, as well the influence of the blow down ring adjustment for the case of the API 2J3 SRV. The most important functional parameters determined experimentally were K_V, F_L and K_D at different openings of the valves.

The API 2J3 SRV allows the blow down ring adjustment which does not exist in the transparent model based on API 1 1/2G3. To minimize the influence of the ring adjustment located around the nozzle (API 2J3 SRV), it was decided to perform measurements at a low position for the sake of comparison between both valves. These results are presented in subsection 5.2. Then, the blowdown ring of API 2J3 SRV was adjusted at different levels (see Table 2), to investigate its influence on the valve performance - subsection 5.3. Finally, unsteady pressure measurements performed in API 1 1/2G3 are shown and discussed in subsection 5.4.

	API 2J3 SRV	API 1 1/2G3 SRV
P_{set}	[6.0...10.0] barg	3.5 barg
P_b	[-0.1...7.5] barg	[-0.8...1.2] barg
L	[0.5...16] mm	[0.5...9] mm
Notches	5, 10, 20, 30	NA

Table 2: Test matrix.

5.1. Flow rate and Forces vs. Pressure Drop diagram

Experimental results in Fig. 5 relate the flow rate discharged through the valve with the corresponding squared pressure drop $\sqrt{\Delta P}$ for the API 2J3 and 1 1/2G3 valves, respectively. These experiments were conducted at different openings of both valves and keeping a constant upstream pressure - 10.0 bar for 2J3 and 3.5 bar for 1 1/2G3.

The existence of two distinct regions for each opening of the valve is noticed from these results. In the first region, the flow rate is proportional to the square root of the pressure drop. This is valid for any incompressible fluid according to the well know Bernoulli equation, meaning that in this region the fluid is entirely in the liquid phase. As the pressure drop through the valve increases, there is the appearance of a second region in which the flow rate is no longer proportional to the square root of the pressure drop. The limitation on the flow rate is caused by the formation of tiny vapor bubbles in the critical section which locally reduce the fluid density and also the medium speed of sound. This is evident at openings of 3.4 mm and 5.0 mm for the case of API 2J3 SRV, and 2.0 mm, 3.0 mm and 4.0 mm for the case of the transparent model of API 1 1/2G3 SRV. In these cases, as the pressure drop through the valve increases, the flow rate tends to be constant since locally the fluid velocity equals the speed of sound, and therefore the flow becomes choked, similar to a compressible flow.

Hydrodynamic forces acting on the valve disk were measured for the case of API 2J3 SRV using a balance transducer, and are shown in Fig. 6 for a fixed lift of 5.0 mm, in which the upstream pressure was set to 6.0, 8.0 and 9.5 bar at each experiment. Both the flow rate and the forces are plotted in Fig. 6(a).

From the Q vs. $\sqrt{\Delta P}$ curve, the influence of the upstream pressure is evidenced for the case of a choked

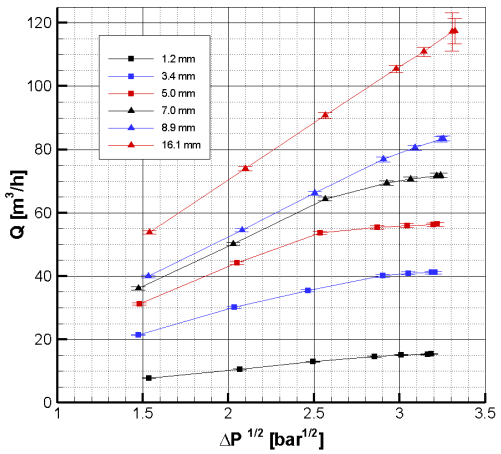

(a) API 2J3 SRV - Upstream Pressure 10.0 bar.

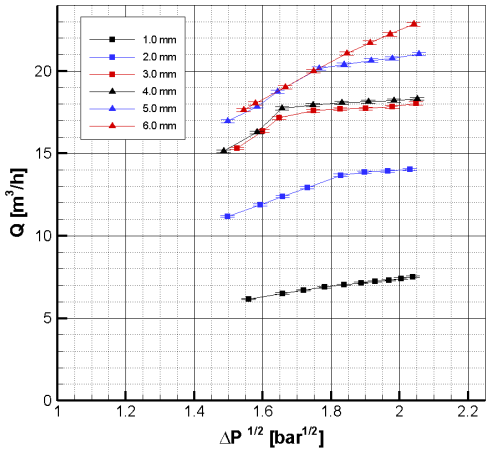

(b) Transparent API 1 1/2G3 SRV - Upstream Pressure 3.5 bar.

Figure 5: Flow rate vs. Pressure drop $\sqrt{\Delta P}$ curves.

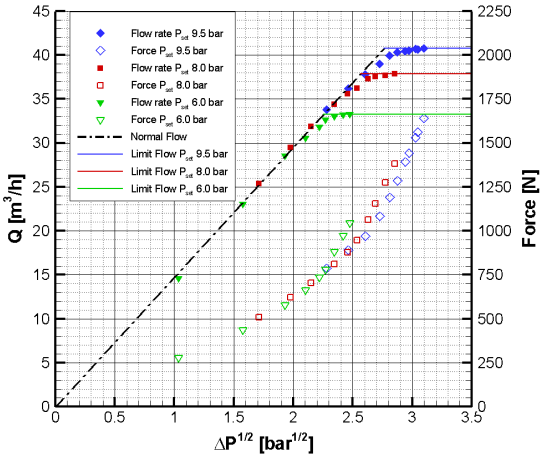

(a) Flow rate and force vs. $\sqrt{\Delta P}$ curves.

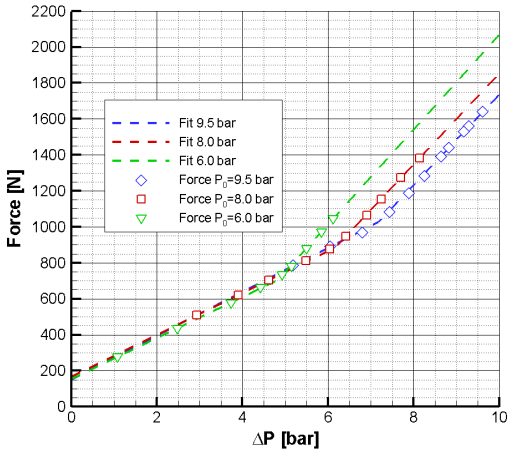

(b) Force vs. ΔP curves.

Figure 6: Hydrodynamic forces acting on the valve disk API 2J3 SRV for a fixed lift L=5.0 mm.

flow condition. Taking into account Eq. 3, this behaviour is expected since the maximum flow rate is proportional to $\sqrt{P_{set} - F_F P_v}$. On the other hand, in the normal flow region, the flow rate is dependent on the pressure drop $\sqrt{\Delta P}$ according to Eq. 1 and therefore, both curves are coincident in this region.

Regarding the F vs. $\sqrt{\Delta P}$ curve, it is noticed that forces are not proportional to $\sqrt{\Delta P}$ as in the case of the flow rate. In fact, it is remarked that forces are proportional to ΔP instead, as evidenced in Fig. 6(b). This relation comes from the fact that forces acting on the valve disk have an important contribution of dynamic pressure, i.e., proportional to Q^2 which in its turn, is proportional to the pressure drop ΔP. In the same curve, a point is noticed at which the slope of the fitted curves is changing. This point indicates a transition on the flow characteristics caused by the influence of cavitation in the forces acting against the valve disk.

5.2. *Characterization of SRV*

The flow coefficient K_V and the liquid recovery factor F_L were determined experimentally for each opening of both valves. For K_V, at least three measurement points were taken from the linear part of the flow rate vs. pressure drop curve - single-phase liquid flow - according to the recommendations of IEC 60534-2-3[6]. Then, both the opening of the valve, and the flow coefficient variables were adimensionalized for the sake of

comparison, with respect to the inlet diameter and the flow coefficient at L/D=0.4, respectively. Regarding the liquid recovery factor F_L, the maximum flow rate achieved at each opening was recorded and Eq. (3) was applied. Results are presented in Fig. 7.

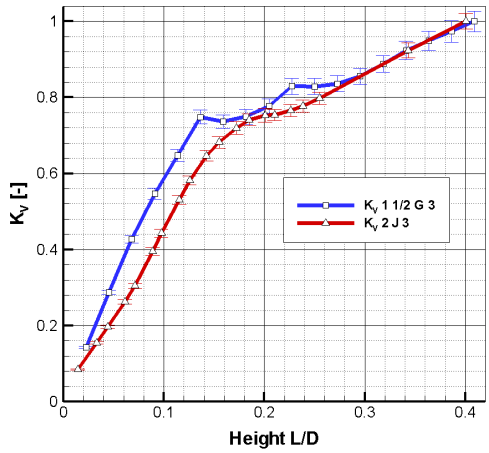

(a) Flow coefficient K_V.

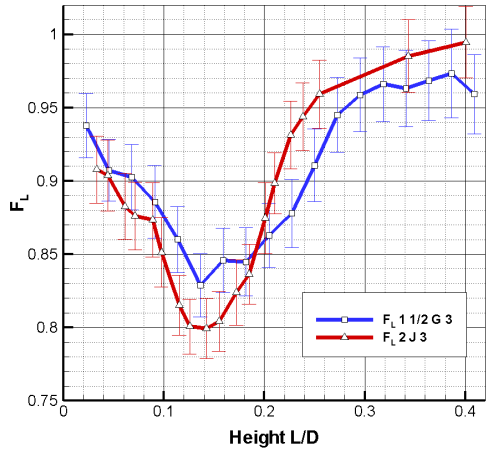

(b) Liquid recovery factor F_L.

Figure 7: API 2J3 and API 1 1/2G3 characteristics curves according to IEC 60534-2-3[6].

Taking into account the flow coefficient experimental results, both valves present a fast opening characteristic. This is perfectly reasonable since a device such a SRV is designed to release as much flow as possible in case of an emergency blow down. Therefore, for small openings (L/D=0.2) of both valves, a significant increase on the flow rate is already experienced (K_V=0.75[-]), while at larger openings this increase is less evidenced. It is noticed a very good agreement on the flow coefficient between both valves namely for larger openings. For smaller openings, the transparent model 1 1/2G3 presents a higher non-dimensional flow coefficient with respect to API 2J3 SRV. This may be explained by the fact that both orifices G and J are different and therefore, the local pressure loss due to the influence of the disk is not identical for both valves. On the other hand, the good agreement for larger openings indicate in this region, a lower influence of the valve disk on the flow coefficient.

Regarding the liquid recovery factor, an excellent agreement is remarked from the experimental results of both valves, within a confidence level of 95%. For small openings (L/D<0.14), the value of F_L is decreasing till it reaches a local minimum; and for larger openings (L/D>0.14), it increases and tends to 1. The existence of a F_L<1, specially for small openings of the valve, demonstrate that in these regions a significant limitation of the flow discharge may occur, even if the working fluid is a high subcooled liquid.

In the methodology proposed by the international standard ISO 4126-10[3], the discharge coefficient K_D does not take into account the liquid recovery factor. More precisely, for the case of an initially high subcooled liquid, the proposed sizing equations of the mass flux through a SRV, simply consider the well known Bernoulli equation for an incompressible fluid. Applying Eq. (5) and Eq. (9) for the determination of the discharge coefficient, results presented in Fig. 8 were obtained where triangle markers correspond to single phase flow measurements, while square markers were obtained in case of a two-phase flow induced by cavitation.

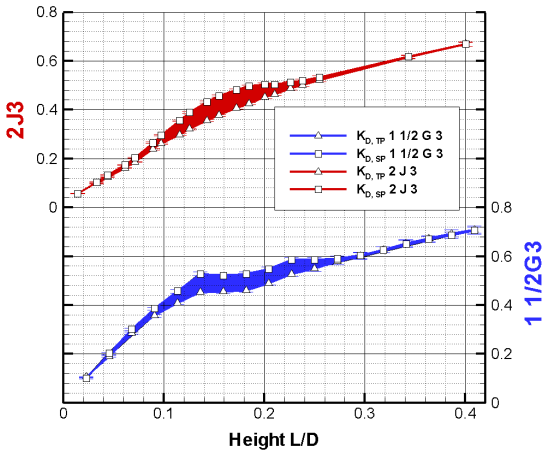

Figure 8: Discharge Coefficient K_D.

For both the valves studied, the discharge coefficient obtained for a single phase flow is higher than the one of two-phase flow, as it is evidenced by the shadowed region on Fig. 8. This difference is more significant around L/D=0.14, whereas it disappears at larger openings (L/D=0.4). This same conclusion was made from the liquid recovery factor presented in Figure 7(b). In fact, there is a direct relation between the liquid recovery factor and the difference obtained from the determination of the discharge coefficient for a single and two-phase flow. According to ISO 4126-10[3], a situation of critical flow for a initially high subcooled liquid is only possible in case the pressure downstream the valve reaches the liquid saturation pressure. On the other hand, it has been demonstrated that due to the recovery pressure downstream the valve, the flow can become choked at a higher back pressure before reaching the saturation level.

5.3. Blow down ring adjustment

The blow down ring located around the nozzle of a SRV, is normally used to adjust precisely the overpressure and blowdown values of a SRV for a specific application in real operation, i.e., in case the spring is placed on the top of the valve disk. In this study, this behaviour is investigated for a fixed lift in which the spring was removed. Results presented in Figure 9, show the influence of the blow down ring adjustment on the flow coefficient K_V, and in the liquid recovery factor F_L, for the case of a API 2J3 SRV.

When the flow is purely in the liquid state, i.e., there is a linear relation between the flow rate and the square root of the pressure drop, the influence of the ring adjustment is evidenced in different regions. For openings L/D<0.2, the flow coefficient increases as the number of notches increases. On the other hand, as illustrated in Figure 9(a), this behaviour is inverted at 0.2<L/D<0.3 and thus, the flow coefficient decreases with the number of notches. These results at L/D=0.25, support the experimental evidence that by adjusting the ring to its top position (less number of notches), the overpressure value will be lower. When the ring is at lower positions (high number of notches), there is a minimal restriction in the huddling chamber and a greater overpressure will be required before the valve is fully opened. Finally, for larger openings L/D>0.3, the influence becomes inexistent as the flow coefficient is constant independently on the ring adjustment.

Regarding the liquid recovery factor, the influence of the ring adjustment is much more complex as one may see from Figure 9(b). It is remarked the existence

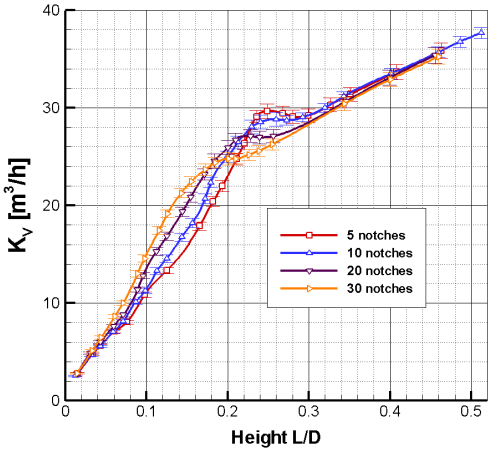

(a) Flow Coefficient K_V.

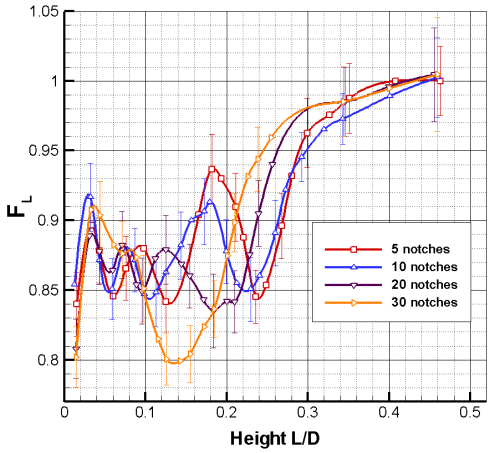

(b) Liquid Recovery Factor F_L.

Figure 9: Influence of the blow down ring adjustment on the characteristic curves of API 2J3 SRV.

of 3 local minimums of F_L for the case of 5, 10 and 20 notches. These local minimums tend to move to the left (lower openings), as the number of notches increase. Finally, for the case of 30 notches adjustment, it is noticed the existence of only 1 local minimum for the curve of F_L.

The existence of a local minimum or maximum on the liquid recovery factor is only possible if the vena contracta location is changing place at different openings of the valve. Recovering the definition of F_L from equation (2), the only variable which does not remain constant at different openings is the vena contracta pressure, p_{vc}. In case the vena contracta location would remain the same at different openings of the

valve, its pressure p_{vc}, would increase at larger openings, according to Bernoulli equation applied from the inlet to the vena contracta:

$$P_{vc} = P_{set} - \frac{1}{2}\rho {v_{vc}}^2 = P_{set} - \frac{1}{2}\rho\left(\frac{Q}{A_{vc}}\right)^2 \qquad (11)$$

Furthermore, considering that p_{vc} increases at larger openings, it would naturally result in a monotonically increasing function of F_L, according to equation (2):

$$\frac{dP_{vc}}{dL} > 0 \Rightarrow F_L \uparrow \qquad (12)$$

As illustrated in Figure 9(b), this hypothetical situation does not apply to a SRV, simply because the vena contracta location is changing place at different openings of the valve and therefore, it results in the existence of local minimums on the F_L curve.

This complex flow pattern on a SRV has been previously reported by Beune[11] and Chabane *et al.*[12], for the case of a purely compressible flow. Three different locations of the minimum cross section of the flow during the SRV blow down operation are identified, as presented in Figure (10).

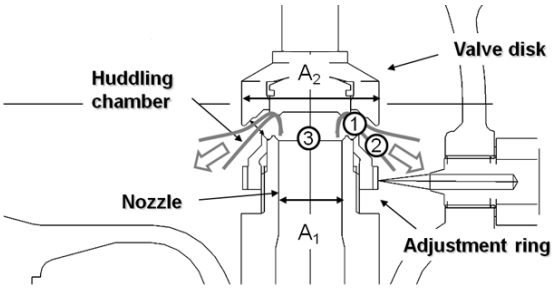

Figure 10: Location of the minimum cross section of a SRV.

For small openings, the critical section is located between the valve seat and the disk (marker 1). As the lift increases, the location changes to the huddling chamber in which the adjustment ring has major influence (marker 2). Finally, at larger openings the critical section moves to the nozzle section (marker 3), passing again through the region between the valve seat and the disk (marker 1). This flow pattern may be identified from the F_L curve obtained in Figure 9(b). For the sake of clarity, the curve is detailed in Figure 11 and markers were inserted to identify the location of the minimum cross sections at each opening of the valve.

For the cases of 5, 10 and 20 notches arrangement, the shape of the F_L curve is very similar. Starting with the minimum section located between the

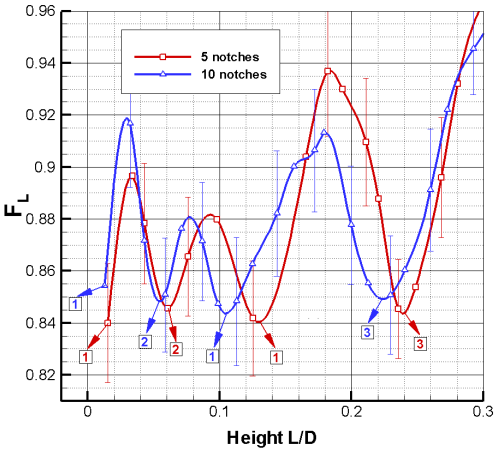

(a) API 2J3 SRV, 5 and 10 notches adjustment.

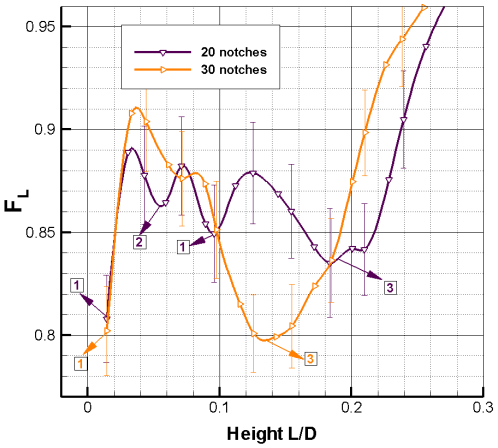

(b) API 2J3 SRV, 20 and 30 notches adjustment.

Figure 11: Influence of the Blow Down ring adjustment on the liquid recovery factor F_L.

valve seat and the disk (1), the F_L is increasing till a point in which the critical section starts to move towards the huddling chamber and therefore F_L decreases. When it reaches the huddling chamber (2), F_L increases again as the location of the critical section is temporarily fixed. Increasing further the lift of the valve, a point will be reached in which the minimum section starts to move in the opposite direction towards the valve seat. When it passes again through the initial position (1), the location of the critical section becomes fixed as the F_L starts to increase. At larger openings of the valve, the minimum section will move again towards the valve nozzle (3), where it finally stabilizes since F_L becomes a monotonically increasing function. For the case of 30 notches arrange-

ment, there is a considerable change on the flow pattern. In this configuration, the blow down ring is located so far from the nozzle that its influence may be neglected. In fact, both the local minimums present in the previous arrangements (markers 2, 1 and 3) are merged in a single point located in the valve seat (3). Without the influence of the blow down ring, the minimum section will be located in only two different places: between the valve seat and the disk (1), and nozzle section (3). This explanation also supports and justifies the curve of F_L obtained for the transparent model of API 1 1/2G3 and presented in Figure 7(b).

5.4. Unsteady Pressure measurements

During the experimental campaign performed for the characterization of the transparent model based on API 1 1/2G3 SRV, unsteady measurements were carried out using three absolute pressure transducers Kulite XTL-190 placed upstream and downstream the SRV (see Figure 4(b) - P'_1, P'_2, P'_3). These transducers provide high natural frequency (240 KHz) and are suitable for cavitating applications. Figure 12 reports the unsteady pressure measurements performed at a sampling frequency of 25 KHz for a lift of 2.0 mm and an upstream pressure P_{set} of 3.5 barg. Each plot is marked from 1 to 8 identifying the experiment in which the back pressure was varied. It is important to notice that upstream the SRV, both the unsteady (P'_1) and static (P_{set}) transducers were placed at different pipe diameters (22 mm and 40 mm respectively), being the reason why the pressure measurements plotted in Figure 12(a) are not centered at 3.5 barg. Moreover, Kulite transducers provide absolute pressure measurements so the difference (P'_1-P_{set}) is due to the atmospheric pressure and dynamic pressure correction. For the transducers placed downstream the SRV, the correction of dynamic pressure is null since the pipe section remains constant (73 mm). The difference (P'_2-P'_3) corresponds to the pressure drop along the downstream pipe since both transducers were distanced of 180 mm.

Cavitation inception can be identified on the experiment 4 due to a sudden increase of the pressure fluctuations in all the transducers. As the pressure drop is increased further, the level of noise remains high for the case of the downstream transducers (P'_2 and P'_3 in Figure 12(b)), but it reduces significantly for the upstream transducer (P'_1 in Figure 12(a)). One possible explanation for this sudden decrease on the noise level upstream the SRV is that the flow has reached choked flow conditions and therefore, pressure waves can no longer travel upstream as the flow velocity equals the

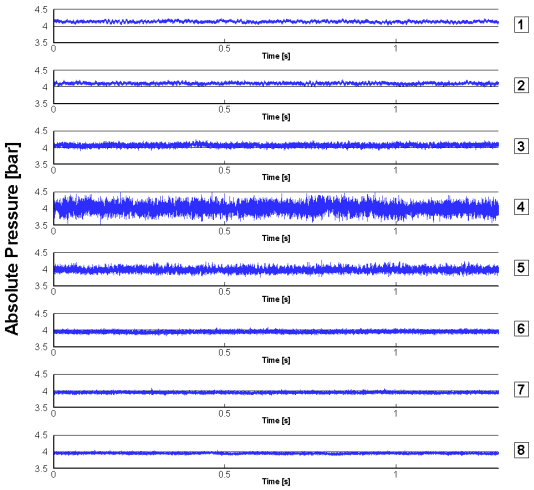

(a) Pressure transducer upstream SRV - P'_1.

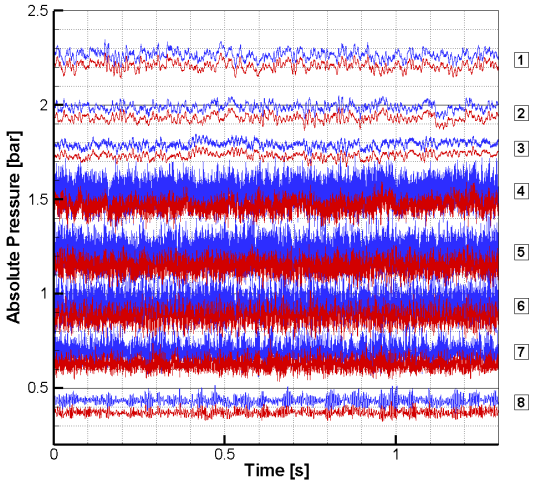

(b) Pressure transducers downstream SRV - P'_2 and P'_3.

Figure 12: Unsteady pressure measurements API 1 1/2G3 SRV.

medium sound velocity. On the other hand, the noise level remains high downstream the SRV since in this case pressure waves propagate in the same direction as the flow and therefore they are not blocked by its velocity. Raw data from Figure 12 was post-processed to retrieve the sound pressure level L_p, defined from the pressure root-mean-square P_{rms} according to the following equation ($P_{ref} = 2 \times 10^{-10}$ bar).

$$L_p = 20log_{10}\left(\frac{P_{rms}}{P_{ref}}\right) \tag{13}$$

Finally, results presented in Figure 13 relate the flow rate vs. pressure drop $\sqrt{\Delta P}$ curve with the sound pressure level.

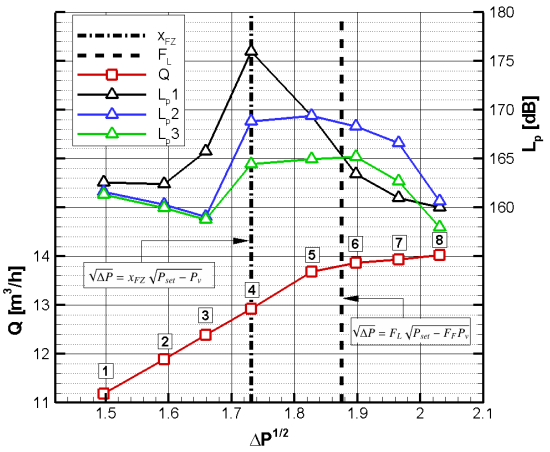

Figure 13: Sound pressure level and flow rate vs. pressure drop $\sqrt{\Delta P}$ for API 1 1/2G3 SRV. Upstream pressure 3.5 bar.

On the cavitation inception defined by x_{FZ}, the flow rate is still not being limited due to the liquid vaporization. This influence is only perceptible at higher pressure drops as it is evidenced by the F_L curve. Between these limits, although cavitation is present as demonstrated by the sound pressure level, the flow rate can be still predicted as an incompressible flow.

6. Conclusions

The experimental characterization of an API 2J3 SRV and a transparent model based on API 1 1/2G3 SRV is performed at different opening positions, according to the recommendations of IEC 60534-2-3[6] and ISO 4126-10[3], for control valves and safety relief valves, respectively. Experimental results show that a reduction on the flow rate occurs due to the liquid vaporization in the valve throat, at initially upstream high subcooling conditions and atmospheric back pressure. Such behavior is not well predicted by ISO 4126-10[3], which defines a critical flow in case the back pressure is lower than the saturation pressure. Moreover, the discharge coefficient K_D determined for a single phase flow is higher than the one of two-phase flow, in agreement with the formulation of the liquid recovery factor F_L defined in IEC 60534-2-3[6].

It is concluded that hydrodynamic forces acting on the valve disk are proportional to the pressure drop ΔP and change their characteristics just after the cavitation inception.

An excellent agreement is found on the F_L of both valves despite of the differences between both orifices. The existence of a local minimum (F_L=0.82) located at L/D=0.14, indicates that a significant limitation of the flow discharge may occur in this region, even at initially high subcooling conditions and back pressures higher than the saturation level.

The blow down ring adjustment influence is investigated for the case of API 2J3 SRV. At valve openings L/D=0.25, results support the experimental evidence that by adjusting the ring to its top position, the overpressure will be lower since a higher flow coefficient is achieved at this opening. Furthermore, it is remarked that the blow down ring adjustment has a significant influence on the location of the minimum cross sections of the flow, as evidenced by the shape of the F_L curve.

Finally, unsteady pressure measurements confirm that the limitation on the flow rate occurs at a higher pressure drop than the cavitation inception.

Acknowledgments

The financial support of the French company CETIM (Centre Technique des Industries Mécaniques) situated in Nantes, France is gratefully acknowledged.

References

[1] J. Schmidt, Sizing of nozzles, venturis, orifices, control and safety valves for initially sub-cooled gas/liquid two-phase flow - the HNE-DS method, Forsch Ingenieurwes 71 (2007) 47–58.

[2] V. Kourakos, Experimental study and modeling of single and two-phase flow in singular geometries and safety relief valves, Ph.D. thesis, Universit Libre de Bruxelles (2011).

[3] ISO 4126-10, Safety devices for protection against excessive pressure – Part 10: Sizing of safety valves and connected inlet and outlet lines for gas/liquid two-phase flow (2006).

[4] R. Diener, J. Schmidt, Sizing of throttling device for gas-liquid two-phase flow part1: Safety valves, Process Safety Progress Vol. 23, No.4 (2004) 335–344.

[5] R. Diener, J. Schmidt, Sizing of throttling device for gas-liquid two-phase flow part 2: Control valves, orifices and nozzles, Process Safety Progress Vol. 24, No.1 (2005) 29–37.

[6] IEC 60534-2 3, Control valve capacity test procedures (1997).

[7] API 520, Sizing, selection, and installation of pressure relieving devices in refineries part1 - sizing and selection (2000).

[8] H. D. Baumann, The introduction of a critical flow factor for valve sizing, ISA Transactions Vol. 2 (1963) 107–111.

[9] G. Stiles, Cavitation and flashing considerations, ISA Handbook of Control Valves 2nd Edition by Hutchinson, J.W. (1976) 206–211.

[10] G. Leung, A generalized correlation for flashing choked flow of initially subcooled liquid, AIChE Jornal Vol. 34, No. 4 (1988) 688–691.

[11] A. Beune, Analysis of high-pressure safety valves, Ph.D. thesis, Technische Universiteit Eindhoven (2009).

[12] S. Chabane, F. Corbin, A. Couzinet, D. Pierrat, M. Bayart, Experimental incompressible forces applied in a safety relief valve, in: ASME Pressure Vessels & Piping Conference, PVP2012-78129, 2012.

Study of Cryogenic Sloshing and Moving Contact Line in Microgravity Conditions

Alessia Simonini

Environmental and Applied Fluid Dynamics Department, von Karman Institute for Fluid Dynamics, Belgium, simonini@vki.ac.be

Supervisor: Maria Rosaria Vetrano

Assistant Professor, Environmental and Applied Fluid Dynamics Department, von Karman Institute for Fluid Dynamics, Belgium, vetrano@vki.ac.be

University Supervisor: Pierre Colinet

Professor, TIPs - Fluid Physics, TIPS - ULB CP165/67, Belgium, pcolinet@ulb.ac.be

Abstract

The development of commercial and scientific space activities depends on the possibility for the spacecraft to operate in terms of space mission requirements. The management of conventional and cryogenic propellants on spacecraft is one of the key technologies which influences the normal operating conditions. The main component of this technology is the tank which allows the storage of the propellant, its pressure and thermal control, the propellant acquisition and its transfer. The development of a system which satisfies space mission requirements, needs a deep understanding of the behaviour of the propellant subjected to extreme environmental conditions. Understanding the propellant behaviour means being able to predict its position and topology inside the tank, for given external unsteady and gravitational accelerations.

The knowledge of the sloshing in tank for the different phases of a typical space mission is challenging due to the different responses of propellant in normal and low gravity conditions, and the coupling of fluid dynamics aspects with thermal aspects due to thermal environmental conditions. The same effect of the surface tension compared with the hydrostatic pressure is different in normal and low gravity conditions: in the first case the surface tension is negligible compared to the hydrostatic pressure while in the second case become dominant. The main investigated features of the sloshing phenomena will concern interfacial phenomena, since the propellant can be both in its gaseous and liquid form and is in contact with the solid wall of the tank.

This Ph.D. research project concerns the study of the sloshing phenomenon for water and liquid nitrogen both in normal gravity conditions and in microgravity. The behaviour of the free liquid surface and the movement of the liquid solid contact line will be investigated as function of the excitation amplitudes and frequencies. The apparent contact angle at the contact line will be also investigated since it is important for the general understanding of the interface behaviour. A cryostat with optical accesses will allow the study of liquid nitrogen at very low temperatures. In normal gravity conditions the sloshing movement will be created by a sloshing table which will allow oscillations of the liquid along three linear directions in a controlled way. As far as the tests in microgravity conditions are concerned, these ones will be performed at the Zarm Drop Tower in Bremen in the framework of a collaboration with the von Karman Institute for Fluid Dynamics and the European Space Agency.

The feasibility of several measurement techniques to study the interface behaviour will be investigated. Two non intrusive measurement techniques are initially planned to be applied, the Level Detection and Recording (LeDaR) technique, developed at VKI since 2001 and Particle Image Velocimetry (PIV). The Ledar technique will allow to monitor in real time the shape of both the liquid free surface (liquid/gas interface) as well as the movement of the contact line (liquid/solid/gas interfaces). The PIV will give quantitative information about the velocity of the flow into the fluid (standard PIV) as well as the 3D velocity of the flow at the interface (interfacial PIV).

A collaboration with the department TIPs from ULB (Université Libre de Bruxelles) is already started to apply the Michelson interferometry technique to measure the contact line profile and the contact angle of a liquid meniscus. The goal of this investigation is to understand the potentiality and the limitations of interferometry technique applied to liquids with different volatility and to study the influence of the inclination of the wall on the contact angle behaviour. This technique could be used to detect with more accuracy the contact line profile of liquid nitrogen on the reservoir wall during sloshing.

The challenge of this work concerns the application of these techniques to a cryogenic liquid and the operation at microgravity conditions.

Cryogenic liquids are challenging due to the particular thermal properties while the operation in 0g requires particular constraints for the experiments as a limited time for the acquisitions (5 seconds for a single drop at the Zarm tower), and limited available space for the entire experimental set-up.

Finally the development of a simplified theoretical model for the interface should be done in the general purpose of better understand the sloshing phenomenon and to compare the theory with the experimental results.

Keywords: cryogenic, sloshing, microgravity, contact angle, contact line, liquid nitrogen, PIV, LeDaR

Experimental Study of Natural Convective Internal Flows

Chiara Spaccapaniccia

Environmental and Applied Fluid Dynamics Department, von Karman Institute for Fluid Dynamics, Belgium,
chiara.spaccapaniccia@vki.ac.be

Supervisor: Philippe Planquart

Research Engineer, Environmental and Applied Fluid Dynamics Department, von Karman for Fluid Dynamics, Belgium,
philippe.planquart@vki.ac.be

University Supervisor: Jean-Marie Buchlin

Professor, Environmental and Applied Fluid Dynamics Department, von Karman for Fluid Dynamics, Belgium,
Professor, Faculté des Sciences Appliquées, Université Libre de Bruxelles, Belgium
buchlin@vki.ac.be

Abstract

The developing of new generation liquid metal cooled reactors lead to numerous advantages in the nuclear energy technology, such as a higher power density and improved operating safety. The Belgian nuclear research institute SCK•CEN is developing MYRRHA, a subcritical liquid metal cooled reactor. The reactor is designed to operate in natural convection decay heat removal conditions. The consequent stratification developing in the upper vessel could affect the heat removal efficiency. The factors influencing the temperature profile should be analyzed by experimental and numerical methods considering a scaled facility.

Keywords: Natural Convection, Stratification, Planar Laser Techniques

1. Introduction

Natural circulation occurs often in energy systems: the simplicity of the principle of working of natural recirculation loops (*thermosyphons*) make this kind of systems reliable and very attractive. However this can of heat removal should be assessed when nuclear reactor is concerned. The present study is undertaken in collaboration with the SCK•CEN, that is developing the LMFBR Myrrha. The coolant of the primary loop of Myrrha is LBE. In passive heat removal conditions a LBE mass flow is driven by the difference in hydrostatic pressure of the core and the heat exchangers [1]. A flow rate is established as a consequence of a balance between frictional pressure losses of the hydraulic loop and Archimedes force driven by the heating power [2]. In these conditions a buoyant jet rises in the upper vessel. Since the height of the vessel is limited by the free level surface a thermal stratification may take place [3].A too strong stratification in the upper plenum is undesired because it affects the efficiency of the heat removal [4] and could compromise the integrity of the structure. The object of this analysis is to determine, which are the geometrical features of the upper vessel that affect mostly the thermal pattern. For such an investigation, a simple water model has been designed as described in [5]. The model is a thermosyphon closed loop. As shown in Fig.2 the model is provided with an upper tank in which are indicated the position of the barrel holes and the high of the buffer plate from the free surface level h_b. Number of holes and as a consequence their position, are changing during the study; that originates different flow topologies and temperature profiles with respect to the nominal case. The analysis is performed for different heights of the buffer plate hp, in order to simulate different heat exchangers entrances, different pressure drops, by means of a regulating valve placed in the bottom part of the loop. The measurement techniques selected for the analysis are thermocouples (TC) , Particle Image Velocimetry and Laser Induced Fluorescence. Differently from TCs the LIF technique

delivers mapping of thermal field. The simultaneous acquisition of velocity and temperature map is appealing for validation of numerical models. The coupling of these two planar techniques (PIV-LIF) were tested for the first time in a small setup presented in Section 11.

2. Scaling

If no externally induced flow is provided and flow arises simply due to the effect of a density difference resulting from a temperature or concentration gradient in a body force field (such as the gravitational field) the process is termed as natural convection [4]. In the present case the flow is generated by a difference of density due to the presence of cooling and heating elements. Since the flow evolves stationary in a hydraulic closed loop the pressure drops are equally important and must be considered in the scaling of the hydraulic system. Fig. 1 shows a schematic of the reactor primary loop in which are indicated the main components, such as heat source and heat sink. The highest pressure drops occur in the barrel holes and in the heat exchangers exit.

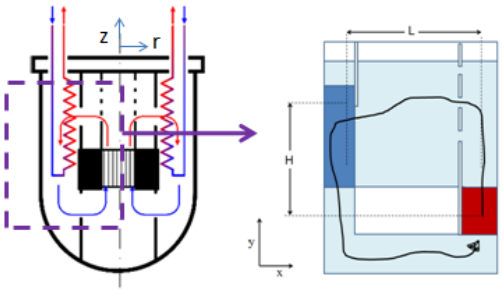

Figure 1: schematic of Myrrha primary loop working in passive heat removal conditions. The red section represents the heater, while the blue section is representing the heat sink.

As depicted in Fig. 1 the fluid motion in the following analysis is approximated as two dimensional. Given that the buoyancy acts only in vertical direction the basic equations of continuity, momentum and energy are, respectively:

$$\frac{\partial u}{\partial x} + \frac{\partial v}{\partial y} = 0 \tag{1}$$

$$u\frac{\partial u}{\partial x} + v\frac{\partial u}{\partial y} = -\frac{1}{\rho}\frac{\partial P_x}{\partial x} + \nu\frac{\partial^2 u}{\partial x^2} + \nu\frac{\partial^2 u}{\partial y^2} \tag{2}$$

$$u\frac{\partial v}{\partial x} + v\frac{\partial v}{\partial y} = -\frac{1}{\rho}\frac{\partial P_y}{\partial y} + \nu\frac{\partial^2 v}{\partial x^2} + \nu\frac{\partial^2 v}{\partial y^2} + g\frac{\rho_0}{\rho} \tag{3}$$

$$u\frac{\partial T}{\partial x} + v\frac{\partial T}{\partial y} = \alpha\frac{\partial^2 T}{\partial x^2} \tag{4}$$

Selecting proper characteristic quantities for length, pressure drops and temperature we can retrieve the following non dimensional variables:

$$X = x/L \quad Y = y/H$$

$$\mathcal{P}_x = P_x/P_{cx} \quad \mathcal{P}_y = P_y/P_{cy} \tag{5}$$

$$\Theta = (T - T_C)/(T_H - T_C)$$

Where H and L are the relative vertical distance and horizontal distance between heat source and heat sink, respectively. P_{cx} and P_{cy} are the pressure drops in horizontal and vertical directions and T_C and T_H are the smallest and the highest temperatures in the flow, respectively. A particular consideration should be given for the selection of a characteristic velocity value V_c . In the present analysis V_c is determined from a balance between buoyant and frictional forces in the loop [1]:

$$f\rho\frac{V_c^2}{2} = gH\Delta\rho \quad \Rightarrow \quad V_c = \sqrt{\frac{2gH\Delta\rho}{f\rho}} \tag{6}$$

From an analysis of order of magnitude applied to the non dimensional continuity equation we get:

$$\frac{\partial U}{\partial X} + \frac{\partial V}{\partial Y} = 0 \quad \Rightarrow \quad U_c = \frac{L}{H}V_c \tag{7}$$

Therefore the non dimensional equations become:

$$U\frac{\partial U}{\partial X} + V\frac{\partial U}{\partial Y} = -f_x\frac{\partial \mathcal{P}_x}{\partial X} + \sqrt{\frac{f}{Gr_H}}\left(A\frac{\partial^2 U}{\partial X^2} + \frac{\partial^2 U}{\partial Y^2}\right) \tag{8}$$

$$U\frac{\partial V}{\partial X} + V\frac{\partial V}{\partial Y} = -f_y\frac{\partial \mathcal{P}_y}{\partial Y} + \sqrt{\frac{f}{Gr_H}}\left(A\frac{\partial^2 V}{\partial X^2} + \frac{\partial^2 V}{\partial Y^2}\right) - f \tag{9}$$

$$U\frac{\partial \Theta}{\partial X} + V\frac{\partial \Theta}{\partial Y} = A^2\frac{1}{Pr}\sqrt{\frac{f}{Gr_H}}\frac{\partial^2 \Theta}{\partial X^2} = A^2\sqrt{\frac{f}{PrRa_H}}\frac{\partial^2 \Theta}{\partial X^2} \tag{10}$$

The dimensionless numbers to be respected for the scaling of the facility are:

$$f = f_x + f_y = \text{The Friction Factor}$$

$$Ra_H = \beta g \Delta T H^3/\nu\alpha = Gr_H Pr = \text{The Rayleigh Number}$$

$$A = H/L = \text{The geometrical Aspect Ratio} \tag{11}$$

3. Aquarium

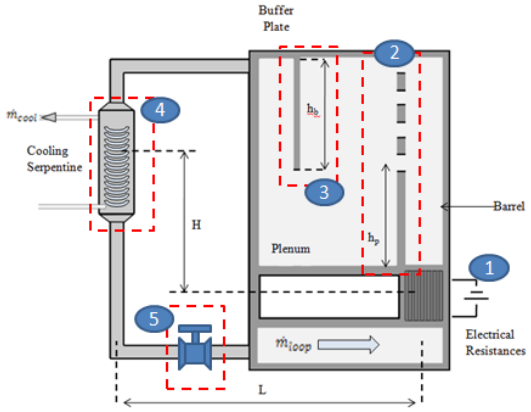

Figure 2: sketch of Aquarium Facility: 1- electrical resistances, 2- barrel plate, 3- buffer plate, 4- heat exchangers, 5- valve.

Fig. 2 shows a sketch of the water model, Aquarium, designed for this study. The main elements of the system are:

1. Core: a series of flat electrical resistances
2. Upper Core Barrel: a inter exchangeable plate provided with holes.
3. Buffer Plate: a plate with adjustable high to simulate the Heat Exchangers entrance level.
4. Heat Exchanger: Helical coil circulating water cooled by an external refrigerating system.
5. Valve: adjustable pressure drops.

The facility has a height of 1 m, width of 0.5 m and a depth of 10 cm. The flow circulates in a clockwise direction The flow circulates in a clockwise direction. Table 1 shows the values of the non dimensional numbers obtained with the Aquarium design and the comparison with the non dimensional number calculated for Myrrha.

The value of the Rayleigh number indicates that the difference with respect to the reactor is of one order of magnitude. However it indicates also that the natural convection in Aquarium, as well as in Myrrha, is turbulent. In the present analysis f is estimated from experimental correlations [6].

Table 1: Non dimensional number values achieved for Aquarium and compared with the values calculated for Myrrha.

N	$N_{Aquarium}$	$N_{Aquarium}/N_{MYRRHA}$
Ra_H	$1.56\ 10^{11}$	1/20
A	0.3	1
f	186	1/1.2

4. Experimental techniques

ΔT_{loop} and mass flow should be measured continuously to qualify the steadiness of the system. Moreover the spreading of the plume in the upper vessel and the consequent stratification of the plenum should be analyzed in detail. For these reasons the techniques applied are:

- Temperature measurements by thermocouples: TC probes were used to measure the minimum and maximum temperature of the loop and the temperature profile in the upper vessel. The thermocouples arrangement is presented In Fig. 3.
- Particle Image Velocimetry: a PIV camera is placed in front of the Plenum to measure the flow topology at the exit of the barrel holes.
- Coupled PIV and Laser Induced Fluorescence: planar velocity and temperature fields were measured at the exit of the barrel holes.

The red window in Fig.3 indicates the region analyzed by means of optical techniques. Section 11 discusses how to realize a coupled PIV and LIF measurement

5. Parametric study

Table 2 gives the range each parameter together with the setting selected as a reference case. The experiments were performed by changing only one of the parameters at once. In the following chapter the results obtained for the reference case are explained in detail. Each test lasts about 49 minutes. Temperature and velocity measurements are gathered for all

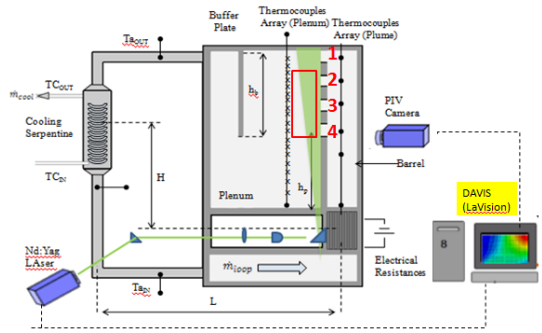

Figure 3: PIV set up for Aquarium (Nd-Yag double pulsed Laser, Camera and Acquisition/synchronization system). The investigation area cover the exit of the last three holes of the barrel plate.

the duration of the test. The start of the experiment coincides with the switching on of the electrical resistances.

Table 2: geometrical details changing during the analysis. The parametric study was performed changing one element at a time.

Variable Geometry	Values	Reference
h_p	20,40,55 cm	40 cm
Holes Number	2,4,6	4
f Number	186,201,240	186

The cooling system is switched on after 8 minutes from the beginning of the experiment to guaranty an established stratified plenum as an initial condition.

6. Reference Case

The characteristic values of Ra_H and f for the benchmark case are indicated in Table 3. Through an energy balance at the heat exchanger it is possible to evaluate the mass flow circulating in the thermosyphon loop at any time using the following relation:

$$\dot{m} = \dot{m}_c \frac{c_{p,cool}\,(T_{c,out} - T_{c,in})}{c_{p,hot}\,(T_{HE,in} - T_{HE,out})} \qquad (12)$$

where $T_{c,out}$ and $T_{c,in}$ are the outlet and inlet temperature, respectively, of the secondary mass flow $\dot{m}_c$ in the heat exchanger whereas $T_{HE,in}$ and $T_{HE,out}$ are the inlet and outlet temperature of Aquarium primary loop. In Fig. 4 is plotted the evolution of the mass flow during the experiment; each point is the result of an average carried out over 3 minutes. Stability in the flow is reached after about 20 minutes. In Fig. 5 is plotted the evolution of the temperature profile measured by the 15 thermocouple rack placed in the upper plenum. In the bottom part of the domain we observe a gradient that is increasing in time while the upper part experiences an almost constant temperature. This temperature increases until the cooling loop is switched on, and then starts to decrease after approximately 15 minutes.

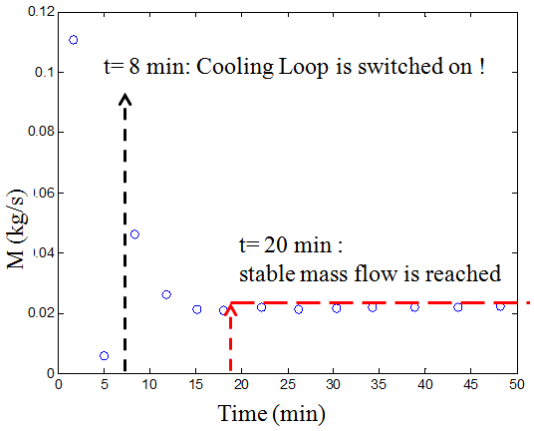

Figure 4: mass flow evolution in time for the benchmark case. Each point of the graph is the result of an average performed on 3 minutes of experiments. The data were acquired at 50 Hz.

The vertical location of the separation between these two regions moves downward with time and it reaches a stability after 30 minutes from the beginning of the experiment.

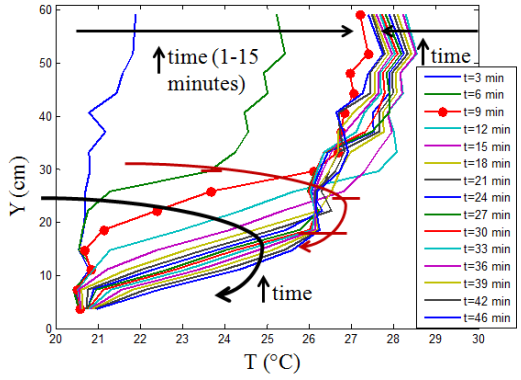

Figure 5: Temperature profile evolution in time for the benchmark case. Each profile is the result of an average performed on 3 minutes of experiments. The data were acquired at 50 Hz.

Fig.6 displays the velocity fields acquired with PIV. The flow topology is reported for different moments.

At the start we observe entrainment of the flow of the plenum through all the holes observed. The stratification is not developed yet and the plume in the barrel is free to rise in the plenum. The second frame corresponds to a time after the starting of the cooling loop, when fluid cooler than the fluid in the upper plenum is rising and exits the first two holes with downward component of velocity. As stated previously temperature stabilizes after 30 minutes; however the velocity field is not totally stable. As a reference for the parametric study we select the flow topology obtained at $t_r \sim 41min$, when steadiness is quasi reached.

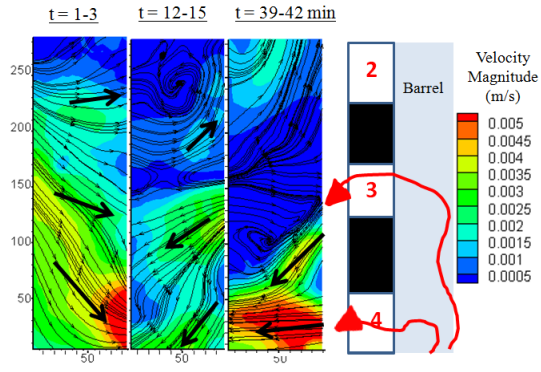

Figure 6: Velocity fields are the result of the average of 600 vector fields, acquired at 3 Hz, with a separation time of 333 ms. The post processing was performed with WIDIM, two step refinement, final window size=16x16 px

Fig.7 compares the temperature profile and the velocity field at t_r. Three different zones can be identified in the upper plenum:

- zone I: stagnation region
- zone II: mixing region
- zone III: diffusion region.

In zone I no fluid motion is detected and the thermal field is uniform. In zone II the temperature is lower with respect to the first zone due to the colder flow outgoing from the first two holes of the barrel. In zone III, the temperature profile results from diffusion.

7. Influence of Buffer Plate position (h_p)

Results obtained with different values of buffer plate height, representing different inlet of the heat exchangers side, are compared to the reference case in terms of temperature profiles and flow topology at t_r.

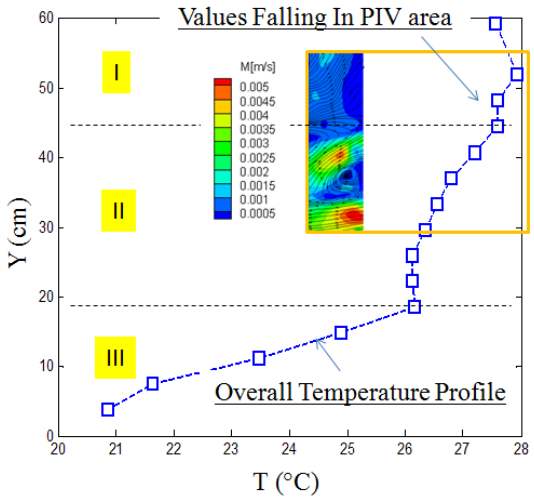

Figure 7: coupling of temperature profile and velocity field. The flow streamlines are fundamental to explain the temperature trend in the upper vessel

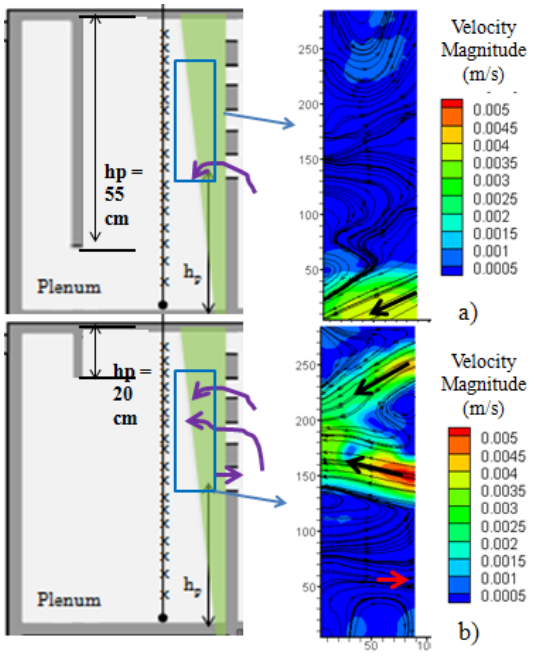

Figure 8: (a) hp=55 cm, (b) hp=20 cm. The streamlines are the results of an average performed on the minutes 39-42 (600 images at 3 Hz) of each experiment.

Fig.8-a shows the streamlines obtained with a reduced buffer plate height h_p: we observe outgoing jets from the second and third hole and a weak entrainment in the lowest hole. The corresponding temperature profile is plotted in Fig.9 the region where the temperature exhibits a uniform trend is extended, as a

sign of a higher degree of mixing with respect to the nominal case (in the part of vessel investigated).

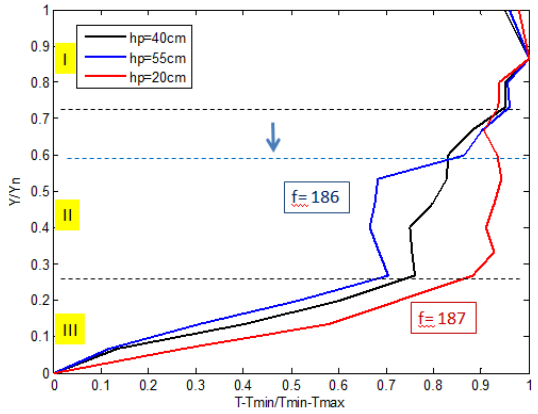

Figure 9: normalized temperature profiles. The profiles changing as a function of hp. Data are the results of an average over 3 minutes of experiment, data were acquired at 50 Hz.

On the contrary the case of Fig.8-b, which corresponds to an incremented buffer plate height h_p, shows a downward jet outgoing from the first hole while the upper region results is almost motionless. Observing the corresponding temperature profile in Fig.9 we can conclude that for the case of the increased h_p the stagnation region results is extended to a lower level of the plenum, reducing the mixing region.

8. Influence of free barrel area (holes N°)

Fig.10 and Fig.11 presents the results obtained for different porosity of the barrel area, expressed in number of holes. In Fig.10-a the streamlines correspond to the case where the number of holes is reduced from 4 to 2. The holes are occupying the higher position of the plate. Two jets are exiting the holes with a positive vertical component of velocity, entraining the surrounding fluid and enhancing the mixing in the region included between the barrel plate and the buffer plate. That leads to an extended mixing region, as confirmed by the temperature profile shown in Fig.11: the size of the diffusion region, characterized by a constant gradient, is reduced to the half.

An extended mixing region is also observed when increasing of the holes number from 4 to 6. The holes are in this case distributed all along the buffer plate.

Observing Fig.10-b, we can conclude that since no jets come out from the top holes the fluid is outgoing from the bottom holes and only a weak component

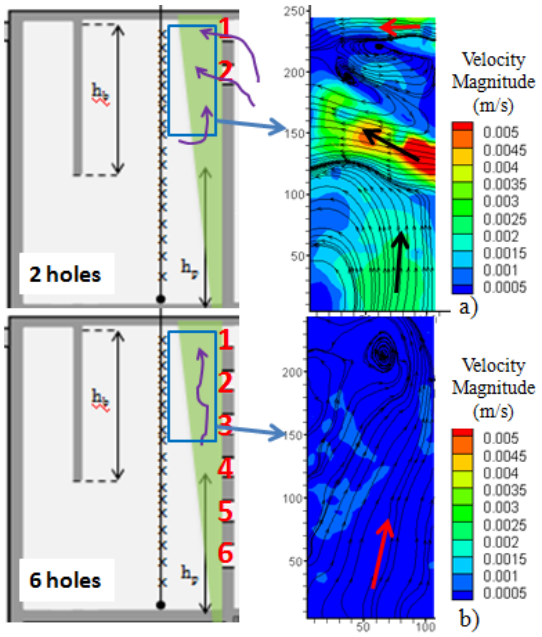

Figure 10: (a) 2 holes, (b) 6 holes. The streamlines are the results of an average performed on the minutes 39-42 (600 images at 3 Hz) of each experiment.

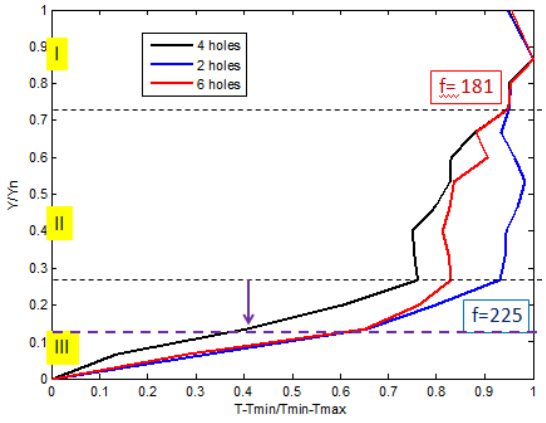

Figure 11: normalized temperature profiles. The profiles changing as a function of the hole number and distribution. Data are the results of an average over 3 minutes of experiment, data were acquired at 50 Hz.

of buoyancy is remaining in the upper barrel. Fig.11 reveals lower temperatures for the case with a greater number of holes when compared to the case of Fig.10-a. This is due to a decreased hydraulic resistance (f number) in the loop that leads to a higher circulating mass flow and, as a consequence, to a drop of the temperature in the flow.

9. Influence of f Number (Pressure Drops)

The increase of the pressure drops (or f number) obtained by adjusting the valve placed in the horizontal branch right after the heat exchangers is illustrated in 12.

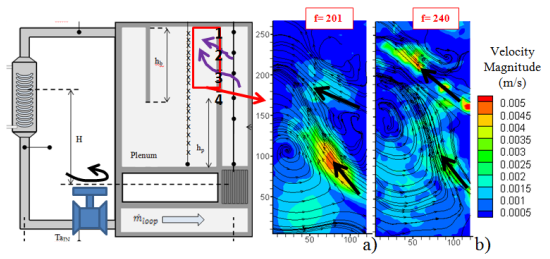

Figure 12: (a) f=201, (b) f=240. The streamlines are the results of an average performed on the minutes 39-42 (600 images at 3 Hz) of each experiment bad quality of flow topology can be due to a missing application of background subtraction as explained in [7].

Fig.12 compares the velocity field obtained with an incremented pressure drop compared to the reference case.

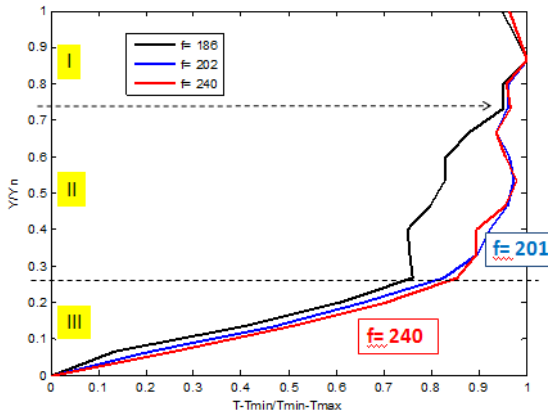

Figure 13: normalized temperature profiles. The profiles changing as a function of hp. Data are the results of an average over 3 minutes of experiment, data were acquired at 50 Hz.

We notice that for both Fig.12-a (f =201) and Fig.12-b (f =240) jets own an upward component due to buoyancy. The effect of increasing the f number is a decrease in the mass flow rate and a subsequent augmentation of the fluid temperature of the fluid leaving the heating core. This increment is apparent in the temperature profiles plotted in Fig. 13. For this case it is however not possible to define a stagnation region, since the flow topologies a and b don't show motionless areas.

10. Conclusion Parametric Study

Changes in the geometry of the vessel and the loop lead to different flow topologies and resulting thermal fields. Velocity and temperatures were measured for all the cases tested, by PIV and thermocouples. Since the study was performed by changing only one variable at a time, it was not possible to keep the hydraulic resistance (f number) constant (it depends on the geometry itself). The objective was to determine which ensures the highest level of mixing. An increase of the pressure drops, even if it eliminates the stagnation region, does not represent a good strategy, since it increases at the same time the temperature in the vessel. Decreasing the buffer plate high h_p leads to a higher uniformity of temperatures in the vessel, and keeps the temperature level low, since the hottest fluid is in direct contact with the heat exchangers. The highest benefits are however achieved by increasing the porosity of the barrel plates, that allows a enlargement of the mixing region and at the same time helps keeping the hydraulic resistance of the loop at a low value. Differently from the velocity the temperature data are measured only along one vertical line We discuss in Section 13 and 13 the issues arising with the application of a fluorescence based technique for temperature measurements.

11. Cavity with differentially heated walls

In order to understand the applicability of the LIF technique a stratification was first measured in a small cavity provided with heat source and heat sink. The cavity was filled with a solution of water and Rhodamine B. The non dimensional analysis proposed for the cavity is similar to the one performed in Section 2. In the case of the cavity however it is possible to neglect the pressure drop term and the a different expression for the characteristic value of velocity V_c should be selected. The typical geometrical lenght quantities are now the high of the cavity H and the boundary layer thickness δ. As Prandtl number is higher than 1 (Pr > 1) the velocity boundary layer is thicker than the thermal boundary layer. The non dimensional variables X and Y are expressed as:

$$X = \frac{x}{\delta} \qquad Y = \frac{x}{\delta} \qquad V = \frac{v}{V_c} \tag{13}$$

Replacing the previous identities in the continuity equation and performing an order of magnitude analysis leads to:

Continuity:

$$\frac{\partial U}{\partial X} + \frac{\partial V}{\partial Y} = 0 \quad \Rightarrow \quad U_c = \frac{\delta}{H} V_c \tag{14}$$

Momentum

$$\left(U\frac{\partial V}{\partial X} + V\frac{\partial V}{\partial Y}\right)\frac{V_c^2}{H} = \nu\frac{V_c}{\delta^2}\left(\frac{\partial^2 V}{\partial X^2} + \frac{\delta^2}{H^2}\frac{\partial^2 V}{\partial Y^2}\right) + g\beta\Delta T\Theta \tag{15}$$

where Θ is defined as seen in Section 2. The left term of the momentum equation represents the inertia; the first term on the right side represents the friction and the last term the buoyancy. For fluids with Pr > 1 the inertia term is negligible and the buoyancy is balanced by friction. As a consequence we can write:

$$\nu\rho\frac{V_c}{\delta^2} \sim g\beta\Delta T \quad \Rightarrow \quad V_c \sim \frac{g\beta\Delta T\delta^2}{\nu} \tag{16}$$

Then, the non dimensional form of the energy equation is:

$$U\frac{\partial\Theta}{\partial X} + V\frac{\partial\Theta}{\partial Y} = \tag{17}$$

$$\frac{\alpha}{\delta^2}\frac{H}{V_c}\frac{\partial^2\Theta}{\partial X^2} = \frac{\alpha\nu}{g\beta\Delta T\delta^2}\frac{H}{\delta^2}\frac{\partial^2\Theta}{\partial X^2} = Ra_H^{-1}\frac{H^4}{\delta^4}$$

Applying an order of magnitude analysis to (17), we obtain:

$$\frac{\delta}{H} \sim (Ra_H)^{-1/4} \tag{18}$$

From which we conclude that the boundary layer thickness-to-cavity height ratio depends only on the Rayleigh number [8] expressed as:

$$Ra_H = \frac{\beta g\Delta T H^3}{\nu\alpha} \tag{19}$$

12. Experimental Set Up

The model is 8.3 cm high, 4 cm large and 8 cm long. The test section is provided with two optical accesses, one for the camera and the other for the Laser sheet. The fluid is water with a proper concentration of Rhodamine B. The tracers for PIV are 32 m of diameter hollow glass spheres. The metal side vertical walls are in contact with Peltier cells, the heat flux of which is adjusted to obtain a stable wall temperature. Fig.14b shows the optical arrangement. A double cavity YAG source produces a Laser beam at 532 nm. The Laser illuminates a section of the cavity, one camera, with a band pass filter centered on 580 nm, detects the fluorescent signal and the other camera, with a band pass filter centered on 532 nm, detects the light scattered by the particles

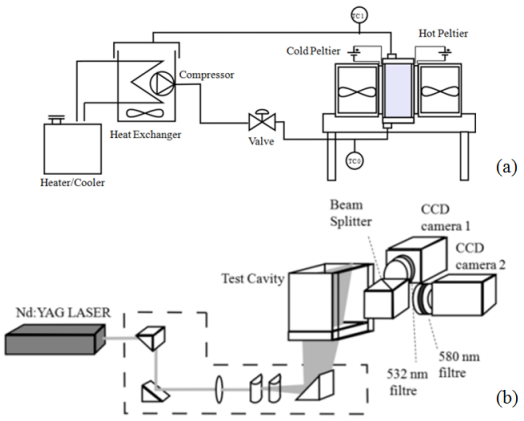

Figure 14: (a)Experimental set up. In the calibration phase the Peltier cells are off, while the flow is circulating through heat exchanger and cavity. (b) The images are obtained by two cameras CCD LaVision, Imager intense, 16bit, with a resolution of 1.4 million of pixels, simultaneously thank to a beam splitter.

13. LIF principle and calibration

The LIF technique is based on the fluorescent emission of an organic dye. The intensity of this re-emitted light is function of the liquid temperature. In the present experiment the molecules of Rhodamine are excited by a 532 wavelength photon flux. The probability of absorption of one photon by a RhB molecule depends on the absorption cross section ε_{RhB} that is only a function of the incident photon wavelength on the range of temperatures [0-100]°C[9].

The excited molecule emits a photon characterized by a lower energy level (fluorescence). The intensity of the emitted photon flux decreases for higher temperatures. For a given temperature and optical set up, the fluorescent signal detected by each pixel of the CCD camera, and as a consequence the resolution of the technique, will depend on:

- The concentration of the fluorescent dye [10]
- The incident Laser light intensity [11]
- The optical magnification factor [12]

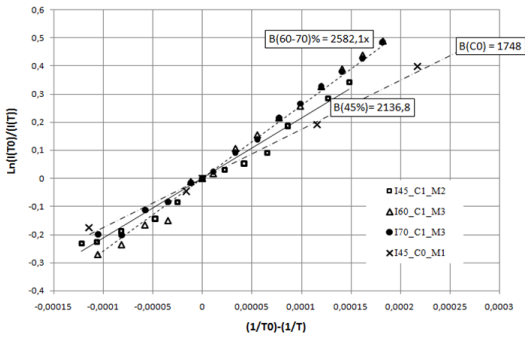

Figure 15: Laser Intensities: I45=45% of total power, I60=60%, I70=70%, Concentrations: C0=10^{-7}mol/l, C1=2.6 10^{-6}mol/l, Magnification factor: M1=0.09 mm/px, M2= 0.03 mm/px, M3= 0.06 mm/px

Typical calibration curves are drawn in Fig.15 for different magnification factors, concentration and Laser intensity. The fitting correlation is [9]:

$$\ln \frac{I(T_0)}{I(T)} = B\left(\frac{1}{T_0} - \frac{1}{T}\right) \tag{20}$$

The resolution of LIF measurements decreases as the slope of the calibration curve, B, lessens.

14. LIF and PIV coupled - Results

Fig.16a shows the domain investigated mapping velocity and temperature. The vertical gradient of temperature is measured in the middle of the cavity (X=L/2) while horizontal profiles of velocity and temperature are drawn for Y=H/2 and Y=H/4 (Fig.16-b)

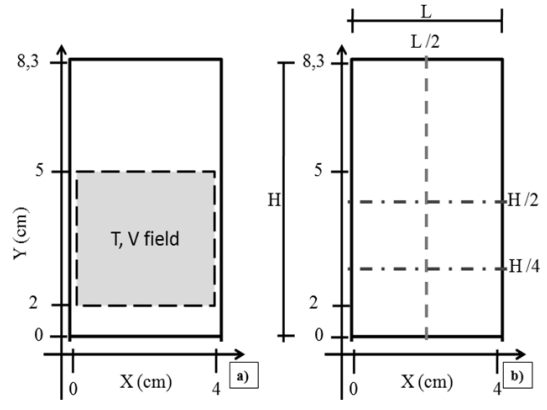

Figure 16: Domain for mapping (a) and lines selected for the extrapolation of velocity and temperature profiles (b)

Tests were carried out for different heat fluxes but in the present paper only results obtained with a power 36 W are presented. Further results are reported [13]. Fig.17 proposes comparisons of LIF and thermocouple measurements. The agreement is rather satisfactory because the difference between the two techniques doesnt exceed 2°C. and because this discrepancy could be explained by the same difference observed on the cold wall temperature between the thermocouple and the LIF tests.

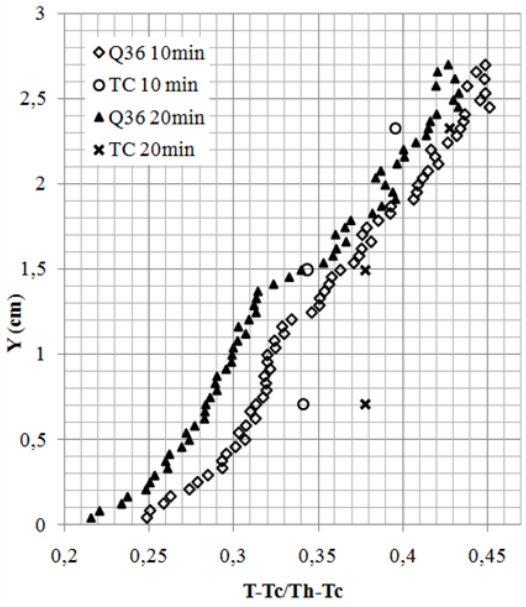

Figure 17: Comparison between thermocouples and LIF measurements, Q36 labels LIF measurements, TC labels thermocouple measurements

The profile of the axial velocity component and temperature are plotted in Fig.18 for Y=H/2 (a) and Y=H/4 (b).

The graphs focus on the region close to the cold wall of the cavity. Table 3 indicates the highest and lowest temperatures measured at the cavity walls by means of thermocouples.

The Ra_H value of the experiments corresponds to a regime characterized by very thin boundary layer. The boundary layers are confined in the wall region and they dont interact [4]. The theoretical value of the boundary layer thickness retrieved with the formulation expressed in Section 11 is 1 mm; that fits reasonably with the one estimated from Fig.18. As the Prandtl number is greater than the unity, the thickness δ_T of the thermal boundary layer is smaller than the thickness δ of the velocity boundary layer. While it is possible to resolve the last one, the spatial resolution is not sufficient to measure the thermal boundary

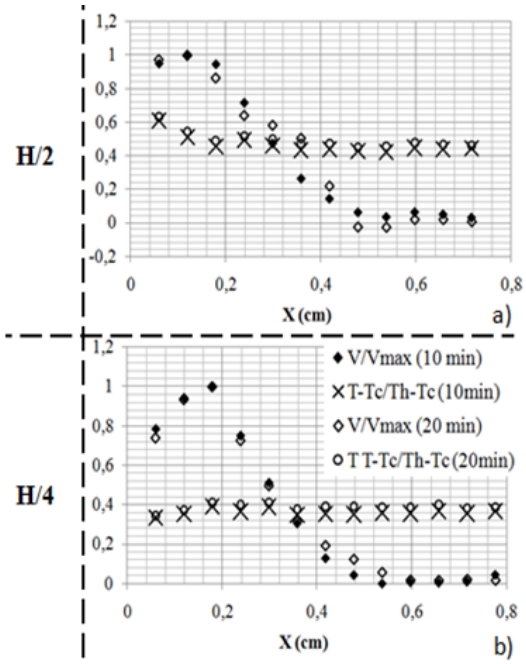

Figure 18: Normalized velocity and temperature values at the cold wall, Q=36W. The profiles are drawn for Y=H/2 (a) and Y=H/4 (b).

layer. Table 3 compares the experimental values of δ and δ_T for Y=H/4. The ratio between the two thickness is in good agreement with the correlation proposed by [8]:

$$\frac{\delta_T}{\delta} < \frac{1}{\sqrt{Pr}} = 0.36 \tag{21}$$

15. CDiscussion

Planar calibration and experiments have been performed in the cavity without changing the optical system or fluorescent dye concentration. An analysis of uncertainty, based on 100 samples revealed 1.25 K of uncertainty in line with recent study which indicates 1.8 K [14]. Beside the relative high uncertainty the main drawback of one color LIF for temperature measurement is the dependency of the fluorescent signal on the input laser light. In the case of a laser light not constant in time, only time averaged temperature mapping is possible. However, the technique is judged suitable to measure temperature gradients higher than 0.2°C/cm, and was as a consequence applied to Aquarium [14].

Table 3: Rayleigh and Prandtl number are calculated thorough an average of water properties performed on the range of temperature observed during the experiment. and T are evaluated for Y=H/4.

T_{cold}	21°C
T_{hot}	37°C
Ra_H	1.8 10^8
Pr	5.8
δ (theory)	~ 1 mm
δ	~ 5.3 mm
δ_T	~ 1.9 mm
δ_T/δ	0.358

16. Future Work

Two set up for experimental natural convection studies were proposed. The scaling of the large scale facility (Aquarium) was performed in order to respect as much as possible the non dimensional numbers values of the nuclear reactor Myrrha. A parametric study was performed in order to understand the influence of the geometry of the upper vessel on the development of temperature profiles. However the flow in Aquarium is characterized by two main components of velocity, vertical and radial, while the tangential component of mixing, that occurs instead in the real case, is not considered. As a consequence the mixing is underestimated in all the cases analyzed and the stratification is overestimated with respect to the real case. For this reason it would be more correct to rely on the data retrieved from a larger scale, three dimensional water model of the reactor. A numerical study on Aquarium is furthermore foreseen in order to extend the range investigated for each geometrical details considered in the previous analysis. Stratification in the small cavity with differentially heated walls was detected and measured by LIF. More experimental work is foreseen in order to measure the thermal boundary layer at the wall the cavity. In particular the spatial resolution in correspondance of the boundary layer region should be increased in order to measure with higher precision thermal and velocity profiles.

References

[1] N. E. Todreas, M. S. Kazimi, Nuclear system II-Elements of Thermal Hydraulic Design, Hemisphere, New York, 1990.

[2] P. K. Vijayan, A. Nayak, D. Saha, M. R. Gartia, Effect of Loop Diameter on the Steady State and Stability Behaviour of Single-Phase and Two-Phase Natural Circulation Loops, Science and Technology of Nuclear Installations 2008.

[3] W. D. Bainest, J. S. Turner, Turbulent buoyant convection from a source in a confined region, Journal of Fluid mechanics 37 (1) (1969) 51–81.

[4] Y. Jaluria, Natural Convection Heat and Mass Transfer, Pergamon Press, HMT- The Science and Application of Heat and Mass Transfer, 1980.
[5] D. S. Martinez Hernandez, C. Spaccapaniccia, P. Planquart, J. M. Buchlin, Experimental and numerical study of natural convection in fuel assembly bundles, Vki internal report, Von Karman Institute for Fluid Dynamics (2012).
[6] I. E. Idelchik, Handbook of Hydraulic Resistance, Jaico Publishing House, New York, 2008.
[7] I. A. Horvat, Simultaneus and Istantaneus Velocity and Concentration Measurements on Model and Real Scale Car Park Fire Scenarios, Ph.D. thesis, Universite Libre de Bruxelles (2012).
[8] A. Bejan, Convection Heat Transfer, Wiley, New York, 2004.
[9] F. Lemoine, Y. Antoine, M. Wolff, M. Lebouche, Simultaneous temperature and 2D velocity measurements in a turbulent heated jet using combined laser-induced fluorescence and LDA, Experiments in Fluids 26 (1999) 315–323.
[10] K. E. Meyer, P. S. Larsen, Temperature and Velocity field in Natural convection by PIV and LIF, no. 11th Int. Symposium on Application of Laser Techniques to Fluid Mechanics, Lisbon, Portugal, 2002.
[11] C. Tropea, A. Yarin, J. Foss, Handbook for Experimental Fluid Mechanics, Springer, New York, 2007.
[12] B. Hiller, R. K. Hanson, Properties of the Iodine Molecule relevant to Laser Induced Fluorescence experiments in gas flows, Experiments in Fluids 10 (1990) 1–11.
[13] C. Spaccapaniccia, Ph. Planquart, M. R. Vetrano, J. M. Buchlin , Simultaneus measurements of temperature and velocity by PIV and LIF techniques in a rectangular cavity with heat fluxes at the walls, no. 13ime Congrs Francophone de Techniques Laser, CFTL , Rouen, France, 2012.
[14] Z. E. Yildirim, C. Spaccapaniccia, P. Planquart, J. M. Buchlin, Study of Stratification in a Natural Convection Loop, Vki internal report, Von Karman Institute for Fluid Dynamics (2013).

AERO-THERMAL INVESTIGATIONS IN TURBOMACHINERY

Heat Transfer in High Subsonic Velocity Environments behind the Fan of a Gas Turbine

Francesco Baldani

Mechanics Department, Belgium Royal Military Academy, francesco.baldani@rma.ac.be

Supervisor: Tony Arts

Professor, Head of the Department, Turbomachinery and Propulsion Department, von Karman Institute for Fluid Dynamics, Belgium, arts@vki.ac.be.

Supervisor: Walter Bosschaerts

Professor, Head of the Department, Mechanics Department, Belgium Royal Military Academy, Walter.Bosschaerts@rma.ac.be

University Supervisor: Souad Harmand

Professor, Head of the Department, University of Lille Nord de France, UVHC, TEMPO, France, Souad.harmand@univ-valenciennes.fr

Abstract

Aim of the project is to propose a methodology to retrieve the heat flux through a finned heat exchanger placed downstream of the fan of a turbine jet engine. The core of the Ph.D. study is the solution of the so called Inverse Heat Conduction Problem (IHCP) through the use of Quantitative Infra Red thermography (QIRT) and proposes a solving methodology for the IHCP as a "ill-posed" problem. To solve the IHCP the surface temperature of a heat conducting body is used as boundary condition after measurement by means of an I.R. camera. The proposed methodology is first tested numerically and, subsequently, experimentally on a heated flat plate in a low subsonic speed wind tunnel. The "ill-posed" nature of the IHCP translates as a high sensibility to measurement errors, possibly leading to non-unique solutions. To reduce this sensibility a ridge regression based regularization methodology is proposed. Results show good agreement between the proposed IHCP solution and reference cases, both for the numerical and the experimental analysis. Moreover, the proposed regularization as applied to the experimental analysis is shown to enhance the accuracy of the obtained solution of the IHCP. Near-wall and free flow boundary conditions are imposed using Constant Temperature Anemometry (CTA).
Besides the experiments performed at low speed to validate the IHCP solving methodology, experimental campaigns have been conducted at high subsonic velocities in order to characterize the flow field of the wind tunnel to be used for the final part of the research. The high subsonic speed are obtained in a blow-down wind tunnel capable to reach Mach numbers of the order of 0.75. The flow field in the blow-down wind tunnel test section is characterized by exploiting the CTA technique. In order to be able to perform multi-point measurements, an 'ad-hoc' hot-wire probes rake has been conceived and manufactured. The work focuses on the analysis of the flow field downstream of the rake itself. The problem has been approached at high speed on the blow down installation using an actual size model of the probes rake and at low speed in an open circuit wind tunnel exploiting a scaled up model of the hot-wire rake. The enlarged scale model is obtained respecting the similarity analogy, i.e. same Reynolds number as in the real case. In the document the results of the two experimental campaigns are summarized. The solution of the IHCP for the high speed case and for more complex geometries is under development and it is not reported in this paper.

Keywords: Inverse Heat Conduction Problem, High Subsonic Speed, Quantitative Infra Red Thermography, Constant Temperature Anemometry, Hot-wire Probes Rake

NOMENCLATURE

Bi Biot number
Re Reynolds number
Pr Prandtl number
k thermal conductivity $\left[W\,m^{-1}K^{-1}\right]$
C_p specific heat capacity $\left[J\,kg^{-1}K^{-1}\right]$
h heat transfer coefficient $\left[W\,m^{-2}K^{-1}\right]$
ρ material density $\left[kg\,m^{-3}\right]$
e electrically injected heat flux density $\left[W\,m^{-2}\right]$
q heat flux density $\left[W\,m^{-2}\right]$
x coordinate in the flow direction $[m]$
y coordinate perpendicular to the flow $[m]$
ξ plate unheated starting length $[m]$
th plate thickness $[m]$
m,M discretization indices x direction
n,N discretization indices y direction
$\alpha_{x,y,z,t}$ case dependent parameters [0, 1]
$\alpha_{0,1,2}$ Tikhonov Regularization parameters
cond() condition number of matrix A

Superscripts

r iteration number
opt optimum
t matrix transpose
p time step

Subscripts

meas measured
comp computed

Acronyms

IHCP Inverse Heat Conduction Problem
CTA Constant Temperature Anemometry
QIRT Quantitative Infra Red Thermography

1. INTRODUCTION

The improvements in the manufacturing techniques as well as in the available materials push the aero-thermal engineers to find better solutions in order to improve engine performance. Indeed, improving turbine engine performance for military and civil purposes has a deep impact on thermal efficiency, fuel consumption, life-time and consequently allows the new environmental, noise and emissions standards to be met.

One of the main challenges in heat transfer study is the accurate determination of the local heat fluxes and convection coefficients, both of which are often indispensable for the design of optimal and efficient heat exchangers but not only. Examples of other applications to benefit from accurate local heat flux knowledge can be found in [15; 19; 14]. The knowledge of local convection coefficients and local heat fluxes gives information on the heat transfer enhancement mechanisms. The work presented is part of a global study aiming to characterize the heat transfer from a hot surface (finned heat exchanger placed just downstream of the fan Figure 1(a), position 16), to a cold flow (main engine flow) under aircraft turbine engine conditions.

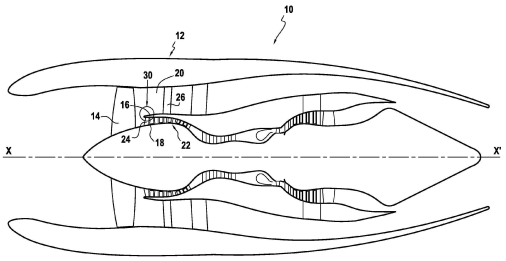

(a) Heat Exchanger Position (16)

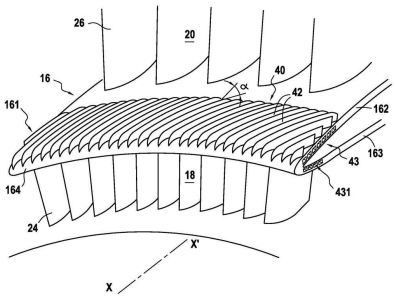

(b) Heat Exchanger Close-up View

Figure 1: Air Cooled Oil Cooler (ACOC)
Techspace Aero Patented Design -
http://www.freepatentsonline.com/EP2075194.pdf

The main difficulty encountered in the study of finned heat exchangers is the determination of the amount of heat transfer through the fin base, necessary for the calculation of fin effectiveness, without disturbing the heat flux distribution significantly. As the introduction of heat flux sensors or thermocouples between the fins and the base would introduce a thermal resistance, the heat fluxes at the fin base have to be determined indirectly by measuring the local heat fluxes through the extended surface and the primary surface [10]. Typical measurement tools are heat flux sensors, local temperature measurements or the solution of the IHCP. Since heat flux sensors introduce rather big disturbances on the heat flux distribution and are

characterized by low accuracy (typically ± 10 % [16]) they are seldom used. Thermocouples are more commonly used as indirect method to determine the heat flux over a surface, and many studies use embedded thermocouples to this purpose, (for instance in [26] a technique to measure heat fluxes with two thermocouples is proposed). However, as it is applicable to one-dimensional conduction only, the method's capability is limited when measuring the heat flux distribution over a surface. Its usefulness is further limited by the number of thermocouples which can be embedded (an increased number of thermocouples interferes more and more with the heat flow, thermocouple's "fin effect" [6]). In recent years, an alternative technique has gained more popularity for identifying local heat fluxes: solve the IHCP [8]. As it already enjoys widespread use to determine heat fluxes at surfaces that are inaccessible for direct measurements [3], the solution of the IHCP was chosen as the most suitable tool for the case under analysis. Since the studied heat conducting body sits in a forced convection regime, the actual flow field is not influenced by the amount of exchanged heat injected into the flow. Therefore, as the flow field is not a priori known, it is measured using the CTA. The installation to be used for the final part of the PhD study is a limited reservoir blow down wind tunnel with a 60 by 70 mm section testing chamber in which it is possible to have velocities ranging from 30 m/s up to 210 m/s and Mach numbers up to ≈ 0.7. When performing experiments with a blow down wind tunnel one of the major issue is to keep perfectly constant the flow conditions. Indeed while performing traverse experiments one should try to let the moving probe facing the same flow field. To overcome this issue a simultaneous multi-point measurements device is designed and manufactured.

2. TRANSIENT INVERSE HEAT CONDUCTION PROBLEM

A description of the IHCP is given in [4], where it is defined as the estimation of the evolution of the surface heat flux using the measured evolution of the temperature at one or more points on a heat conducting body. Already mentioned, the main advantage of this method lies in the fact that it allows indirect measurements where direct measurements might prove infeasible [19] or requiring expensive instruments [21]. To solve an inverse heat conduction problem, the method uses temperature measurements as input. Based on the surface temperatures of the object, the heat fluxes on the surfaces of the object can be estimated, eliminating the need for internal temperature measurements. Additionally the method allows to reconstruct the temperature distribution in the whole object, together with the coupled heat flux distribution. To minimize the disturbance of the surface temperature field and actual heat flux by the used measurement sensor, careful consideration is needed when choosing the used measurement technique. Use of embedded thermocouples will distort the temperature field of the body and may lead to a significant bias in the measurements. The errors of this distortion will propagate into the IHCP results and need to be removed through use of an appropriately detailed correction model accounting for the effect of the thermocouples [25]. However, the main disadvantage of using thermocouples is the poor spatial resolution of the temperature measurement, as only a limited number of thermocouples can be embedded. Use of Liquid Crystal Thermography (LCT) to measure the temperature can be considered [11; 18; 12], but placement of the sensors will disturb the local heat flux (possibly even the local convective boundary layer), which again will need to be compensated for [8]. For this paper, however, the setup of the experiment is prepared so that the use of QIRT was possible, eliminating any disturbance of the temperature field and at the same time allowing for a reasonably high spatial resolution. To validate the proposed method a simple geometry, a heated flat plate, is examined. The plate has length L=0.45 m, width W=0.17m and thickness th= $0.25 \cdot 10^{-5}$ m, and is painted in matt black with a known emissivity of 0.94. The plate is heated via

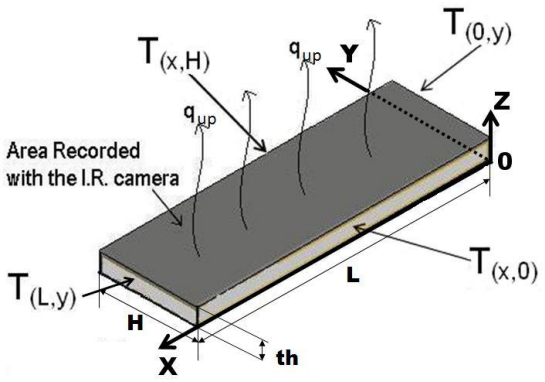

Figure 2: Heat Conducting Plate Sketch

electric power injection and subjected to a forced convection cooling on its upper surface in a wind tunnel. As the plate is mounted in an open wind tunnel, the measured flow field over the flat plate will be used as

boundary condition for the numerical simulation. Using QIRT, the measured surface temperature will be used to calculate the local convective heat transfer coefficients following the numerical IHCP solution approach ([17; 13; 9]). The general expression for the plate temperature field variation is given in eq. 1.

$$\frac{1}{th}\cdot e + k\cdot\left(\alpha_x\frac{\partial^2 T}{\partial x^2}+\alpha_y\frac{\partial^2 T}{\partial y^2}+\alpha_z\frac{\partial^2 T}{\partial z^2}\right)= \frac{1}{th}\left[q_{down}+q_{up}\right]+\alpha_t\cdot\rho\cdot C_p\cdot\frac{\partial T}{\partial t} \quad (1)$$

The plate can be considered as "thermally thin" if $Bi < 0.1$, which is the case (sketch in Figure 2), then the temperature gradient along the z direction can be neglected. The initial and boundary conditions on the plate surfaces are defined as follows:

- Initial Condition: imposed temperature field
- Boundary Conditions:
  - Upper and Side Surfaces: imposed $T_{surface}$
  - Lower Surface: thermally insulated ($q_{down} = 0$)

In the following $q = q_{up}$. The problem reduces to the expression in eq. 2.

$$\frac{1}{th}\cdot e+k\cdot\left(\alpha_x\frac{\partial^2 T}{\partial x^2}+\alpha_y\frac{\partial^2 T}{\partial y^2}\right)=\frac{1}{th}q+\alpha_t\cdot\rho\cdot C_p\cdot\frac{\partial T}{\partial t} \quad (2)$$

Equation 2 can be used to numerically minimize equation 3.

$$F=\sum_x\sum_y\left[T_{comp}(x,y)-T_{meas}(x,y)\right]^2 \quad (3)$$

The stated problem is ill-posed and has therefore a high temperature measurement error sensitivity [4] which almost invariably leads to non-unique or erroneous results. Since the simple minimization of F has no influence on the error amplification of the input data, a regularization is proposed. Also known as ridge regression and first proposed by Tikhonov [23; 24] it can be expressed as in eq. 4.

$$S = F+\alpha_0\cdot S_0+\alpha_1\cdot S_1+\alpha_2\cdot S_2 \quad (4)$$

Applied to the IHCP one obtains:

- F: Minimization Criterion
- S_i: Heat Flux Related Functions
  - $S_0 = \sum_x\sum_y\left[q(x,y)\right]^2$
  - $S_1 = \sum_x\sum_y\left[grad\left(q(x,y)\right)\right]^2$
  - $S_2 = \sum_x\sum_y\left[\Delta q(x,y)\right]^2$
- α_i: Regularization Parameters
  - 0th Order - α_0: limits the values q_{max}
  - 1st Order - α_1: limits q bigger variations
  - 2nd Order - α_2: limits q quick oscillations

The main source of the measurement error in QIRT is the noise on the readout of the thermal camera, resulting in temperature readout fluctuations. As a result, only to the 1st order term will be assigned a weight as it limits these fluctuations, reducing S to eq. 5.

$$S=\sum_x\sum_y\left[T_{comp}(x,y)-T_{meas}(x,y)\right]^2+\alpha_1\cdot\sum_x\sum_y\left[grad\left(q(x,y)\right)\right]^2 \quad (5)$$

To find the heat flux values of next iteration step (q^{r+1}) for the minimization of S in eq. 5, the derivative of eq. 5 with respect to the fluxes of the next time step q^{p+1} needs to be zero. After rearranging the spatial discretization field into a single m by n vector, the derivative of the first part of 5 (defined as F) with respect to q^{p+1} can be expressed in matrix form as in eq. 6:

$$\frac{\partial F}{\partial q^{p+1}} = 2J.\left[T^r_{comp}(q^{p+1})-T_{meas}\right] \quad (6)$$

where J is the temperature sensibility matrix with respect to the variation of each heat flux of the next time step p+1.

$$J=\begin{bmatrix}\frac{\partial T^r_{meas}(1)}{\partial q^{p+1}(1)} & \cdots & \frac{\partial T^r_{meas}[(M-1).(N-1)]}{\partial q^{p+1}(1)}\\ \vdots & \ddots & \vdots\\ \frac{\partial T^r_{meas}(1)}{\partial q^{p+1}[(M-1).(N-1)]} & \cdots & \frac{\partial T^r_{meas}[(M-1).(N-1)]}{\partial q^{p+1}[(M-1).(N-1)]}\end{bmatrix} \quad (7)$$

The value of $T^r_{comp}(q^{p+1})$ remains unknown but it can be calculated through a Taylor expansion of the known $T^r_{comp}(q^p)$. In matrix form it is:

$$T^r_{comp}(q^{p+1}) = T^r_{comp}(q^p)+J^t\Delta q \quad (8)$$

Combining 6 and 8 results in eq. 9:

$$\frac{\partial F}{\partial q^{p+1}} = 2J.\left[T^r_{comp}(q^p)-T_{meas}\right]+2JJ^t\Delta q \quad (9)$$

In a similar way the derivative to q^{p+1} of the first order term S_1 in eq. 5 can be expressed in matrix form as:

$$\frac{\partial S_1}{\partial q^{p+1}} = 2X_1 q^r + 2X_1 \Delta q \tag{10}$$

where X_1 is the regularization matrix obtained deriving the discretized version of S_1 with respect to the heat flux variation. Combining eq. 10 and 9 results in 11 which is set equal to zero in order to calculate the next iteration (r+1) values for heat fluxes q^r:

$$\begin{aligned}\frac{\partial S}{\partial q} =& 2J\left(T^r_{comp}(q^r) - T_{meas}\right) + \\ & 2\alpha_1 X_1 q^r + \left(2JJ^t + 2\alpha_1 X_1\right)\Delta q = 0\end{aligned} \tag{11}$$

Re-arranging eq. 11 to Δq^{r+1} one obtains:

$$\begin{aligned}&\Delta q|_{r\to r+1} = \\ &-\left(JJ^t + \alpha_1 X_1\right)^{-1}\left[J\left(T^r_{comp}(q^i) - T_{meas}\right) + \alpha_1 X_1 q^r\right]\end{aligned} \tag{12}$$

To solve the system in eq. 12 the sensibility coefficients Q^r of matrix J need to be determined. As these coefficients represent the temperature variation caused by the flux variation for each point l they can be estimated using eq. 13

$$Q^r_l = \frac{\partial T^r_{comp}}{\partial q^{p+1}_l} = \frac{T^p_{comp}(q_l - \epsilon \cdot q_l) - T^p_{comp}(q_l)}{\epsilon \cdot q_l} \tag{13}$$

Once the matrix X_1 and the coefficients Q^r are known it is possible to determine the vector of corrections Δq which minimizes S.
The term α_1 is chosen to minimize the condition number of the solution matrix in order to minimize the sensitivity of the used system of linear equations to any errors in the data. Introducing α_1^{opt}:

$$cond\left(JJ^t + \alpha_1^{opt} X_1\right) = min\left[cond\left(JJ^t + \alpha_1 X_1\right)\right] \tag{14}$$

with *cond*() the condition number of the solution matrix. Imposing α_1^{opt} as value for α_1 will result in the best possible conditioning of the posed mathematical problem (see Figure 3).
Switching back to the inverse problem, eq. 12 is solved iteratively using α_1^{opt}.
The iterative computation is stopped when the function S holds constant within an imposed tolerance interval ϵ for two consecutive iterations, and the surface heat flux q(x,y) is found. Since the surface heat flux found is the total heat flux, it can be split into its convective and radiative part:

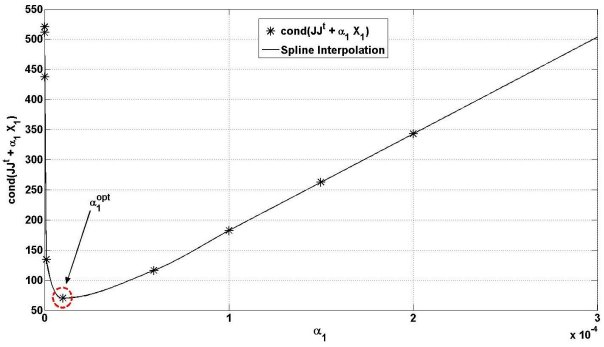

Figure 3: Condition number - α_1^{opt}

$$\begin{aligned}q(x,y) =& q_{conv.}(x,y) + q_{rad.}(x,y) \\ =& h(x,y)\left(T(x,y) - T_{ref.}\right) + \epsilon \cdot \sigma\left(T(x,y)^4 - T^4_{air}\right)\end{aligned} \tag{15}$$

As the emissivity of the paint on the plate surface and T_{air} are both known, the convective flux at the plate surface can be determined. Using a relevant reference temperature, the local convection coefficient at each point on the surface can be computed.

3. IHCP SOLUTION VALIDATION

The numerical validation is performed using commercial CFD software package (*Fluent*©) and can be summarized as:

1. Compute the $h(x)$ profile via the Nusselt correlation for a heated plate with unheated starting length. Equation 16 gives the Nusselt number for a turbulent, isothermal, local flow with $Pr > 0.6$ which holds true for the imposed flow velocity (U_∞) of 9.2 m/s and bulk flow temperature (T_∞) of 18 °C.

$$Nu(x) = \frac{0.0296 \cdot Re(x)^{0.8} \cdot Pr^{1/3}}{\left[1 - \left(\frac{\xi}{x}\right)^{9/10}\right]^{1/9}} \tag{16}$$

   As some of the required fluid properties (particularly viscosity and diffusivity) have a fairly high thermal dependency, there can be some ambiguity as to which temperature should be used to compute the property values. The recommended approach is to use the film temperature, defined as the average of the wall and free-stream temperature, $T_{film} = \frac{T_{surface} + T_{air}}{2}$. After calculation of $Nu(x)$, $h(x)$ can be found directly.

2. Perform a direct simulation imposing the computed $h(x)$ in order to compute the 'hot' reference temperature field $T(x, y, t_1) = T_1$.
3. Perform a second direct simulation to compute the cooling phase and retrieve the surface 'cold' reference temperature field. $T(x, y, t_2) = T_2$.
4. Use T_1 and T_2 as IHCP boundary conditions to compute back $h(x)$

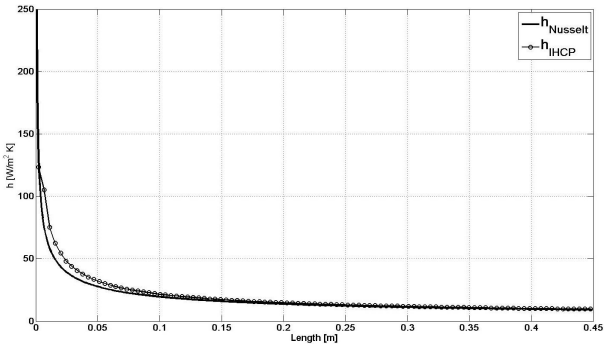

Figure 4: Theory - IHCP solution Comparison

The problem solution reported in Figure 4 shows a very good agreement with the analytical solution except at the very beginning of the plate. In this area the asymptotic nature of the Nusselt correlation used for the theory is difficult to reproduce when using discretized solutions.

3.1. IHCP Solution: Experimental Validation

The choice to exploit a heated flat plate allows an easy comparison between the experimental results and the direct numerical simulations already performed. A copper flat plate heated by an integrated electrical resistance is mounted in the test section of a low speed wind tunnel. The integrated circuit is glued on a bakelite plate placed on a polystyrene support to impose boundary conditions. Figure 5(a) and Figure 5(b) show the experimental setup and a cross section of the plate assembly. The surface temperature is measured using QIRT technique [7; 22; 20] with a *FLUKE - Ti50* I.R. camera. The camera has a 320 x 240 Focal Plane Array (FPA) and uses a vanadium oxide (VOX) uncooled microbolometer. The spectral band ranges from $8\mu m$ to $14\mu m$ with a thermal sensitivity lower than 0.070 °C at 30 °C and an accuracy of ±2 °C or ±2 %. It has a standard 20 mm $f/0.8$ Germanium lens with a 23°horizontal by 17°vertical field of view. The camera has a spatial resolution (IFOV) of 1.3 mrad and a minimum focus of 0.15 m. The refresh rate of the camera is 7.5 Hz. Emissivity correction is provided by user input, and ranges from 0.01 to 1 with a 0.01 step. The I.R. camera is calibrated using a black body as reference source.

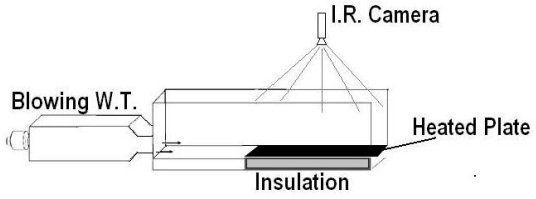

(a) Experimental Set Up Sketch



(b) Heated Plate Close Up View

Figure 5: Experimental Set Up Preparation Overview

The black body used for the camera calibration is the HGH Infrared Systems *ECN 100 blackbody*. It has a radiant surface dimension ranging from 150 mm x 150 mm to 1 m x 1 m for temperatures up to +550 °C, enabling infrared sensor calibration without collimator. The benchmarking of the plate's temperatures measured by the I.R. camera is made against the temperature measurement of a set of four thermocouples attached to the surface, repeated for several imposed temperatures [22]. The wind tunnel is set to have a bulk flow velocity in the test section of 9.2 m/s. To allow direct QIRT measurements of the flat plate, the upper part of the wind tunnel section is left open. As such, the actual flow field inside the wind tunnel has to be measured. To minimize any horizontal velocity gradients, the plate is mounted between two high vertical walls. The far field flow is measured using a *TSI* anemometer "Velocicalc Plus Air Velocity Meter". The anemometer has an uncertainty of ±3% of the reading or 0.015 m/s with a resolution of 0.01 m/s in the range from 0 m/s to 40 m/s. The anemometer also incorporates a temperature sensor, with a resolution of 0.1 °C and uncertainty of ± 0.3 °C from -10 °C to 60 °C. To validate the turbulent boundary layer hypothesis used in eq. 16 the near wall flow is measured with a specific boundary layer hot-wire probe

(Dantec 55P15 probe) connected to a Dantec Streamline 90N10 acquisition box with a 90C10 module for CTA. The boundary layer is measured in a traverse of 77 points by means of a robotized system at different heights starting from 0.025 mm. As the output of I.R. camera temperature recording is incompatible for direct input in the used IHCP solving code, the recorded images need to be adapted using a procedure given as:

1. Take any I.R. image with the color map legend present, which links the colors to the temperature levels.
2. Retrieve a vector capable to translate the R(ed)-G(reen)-B(lue) data contained in the I.R. images into a matrix containing the corresponding temperatures.
3. Translate the image into any standard *Matlab*© exploitable matrix.
4. Crop the image to the area of interest, in particular the flat plate.

Once the I.R. images are converted for the analysis, the right surface dimensions, time step and plate material characteristics should be inserted in the script. As last step to start the proposed IHCP method, the script requires the hot (T_1) and the cold (T_2) surface temperature matrices [2], which are recorded according to the the following procedure:

1. Heat the plate up to the maximum allowed temperature.
2. Start the wind tunnel and set the intended target velocity.
3. Once the velocity and the plate T_{surf} are stabilized acquire a reference surface thermograph (hot reference temperature or T_1).
4. Switch off the heating resistance.
5. After a given amount of time (Δt) record the plate T_{surf} with the I.R. camera (cold reference temperature or T_2)

4. HOT-WIRE RAKE CHARACTERIZATION

The designed hot-wire probes rake is shaped out as a symmetrical 4-digits NACA profile, in which it is possible to insert up to 5 probes and up to 2 thermocouples. The analysis of a 3 probes rake has preceded the conception of the 5 probes support able to grant the velocity profile measurement of the whole test section height at once [1]. The conceived rake is a NACA 0026 profile with a maximum thickness of 12 mm, a chord length of 46.15 mm and a total height of 59 mm. The rake is manufactured with a "CNC" machine and the probe holders are installed at a distance of 12.5 *mm* from each other. Previous investigations showed that the presence of the probes support does not affect the flow upstream of the rake itself [1]. This work deals with the characterization of the flow field reaching the heat exchanger, once the hot-wire probe rake is placed upstream of the finned heat exchanger itself. The experiments are performed at both high and low subsonic velocity. The dynamic similarity concept, i.e. imposing the same Reynolds number, is used to scale up the experimental set up allowing a drastic reduction of the testing velocity and the possibility to work in a continuous open circuit wind tunnel. For both the experimental campaigns the flow characterization is carried out by analyzing the velocity field, the turbulence intensity and the turbulence scales (Integral scale, Taylor's micro-scale and Kolmogorov scale). A frequency content analysis of the recorded signals is performed to assess if coherent structures are present within the investigated flow field.

4.1. High Subsonic Speed Experiments

The experiments consisted in a set of vertical traverses in different horizontal positions at the same longitudinal position, right in front of the place where the heat exchanger is normally installed. For this experimental campaign the finned heat exchanger is not installed during the measurements. A model of the hot-wire rake (with no probes installed) is manufactured with a polyurethane based material. All the experiments are performed with a single wire fiber film probe with thin coating (Dantec 55R01) with straight prongs and the sensor perpendicular to probe axis. In Figure 6 a working diagram of the blow-down installation.

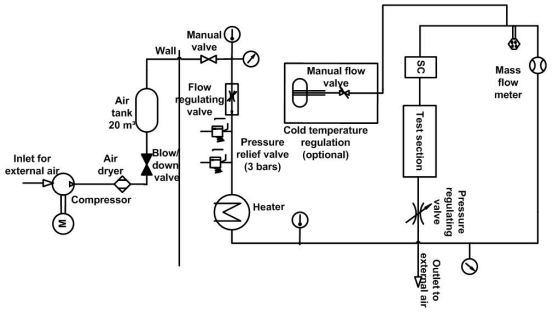

Figure 6: Facility Working Principle Diagram (Courtesy of ULB)

The experimental campaign consisted in hot-wire traverse measurements at three different velocity

regimes: 30 m/s, 120 m/s and 180 m/s. The measurements grid is composed of 35 points subdivided into 7 vertical positions and 5 horizontal positions. The sketches in Figure 7 show the measurement grid with respect to the test chamber inlet and to the rake trailing edge.

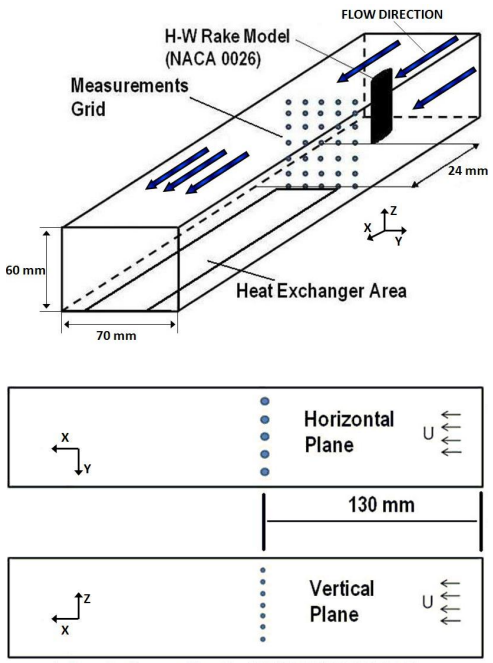

Figure 7: High Speed Experimental Campaign Measurements Grid

4.2. Low Subsonic Speed Experiments

In this case the experimental campaign is performed using a Dantec 55P61 probe, which is a miniature dual wire X-probe with straight prongs. Mounted with the probe axis parallel to the direction of the main flow the predominant flow vector attacks the two wires under 45 °measuring two velocity components. The experimental campaign at low speed is performed in the suction type open circuit wind tunnel available at the RMA characterized by a $0.6 \times 0.6 \times 1.2$ meters test chamber in which the air speed is continuously adjustable from 3.5 to 45 m/s and the turbulence level is lower than 0.5%. To obtain results applicable to the real case, i.e. high subsonic speed, the dynamic analogy is exploited with the actual wind tunnel hydraulic diameter (d_h) as reference parameter. The Reynolds number is therefore computed as in eq. 17:

$$Re = \frac{\rho}{\mu} \cdot U_m \cdot d_h; \tag{17}$$

A velocity that matches with the dynamic analogy requirement and the wind tunnel capability can be found (see eq. 18).

$$V_m = V_a \frac{\rho_a}{\rho_m} \cdot \frac{d_{h_a}}{d_{h_m}} \cdot \frac{\mu_m}{\mu_a}; \tag{18}$$

where the subscript a stands for "actual" and the subscript m stands for "model". The chosen testing velocity is 16.7 m/s to represent the regime at 180 m/s in the actual wind tunnel. According to the scaling factor found, aiming to obtain a blockage ratio very close to the one in the high speed installation and taking into account also for the manufacturing constraints the scaled up rake model is manufactured with a 375.4 mm chord, a 596 mm height and a thickness of 98 mm. Defining the blockage as the ratio between the object frontal area and the wind tunnel cross sectional area one obtains a blockage ratio of 16.85 % for the high speed case and of 16.22 % for the low speed case. After a rough analysis performed all over the test section a smaller area of investigation was chosen (area in the dashed line rectangle in Figure 8).

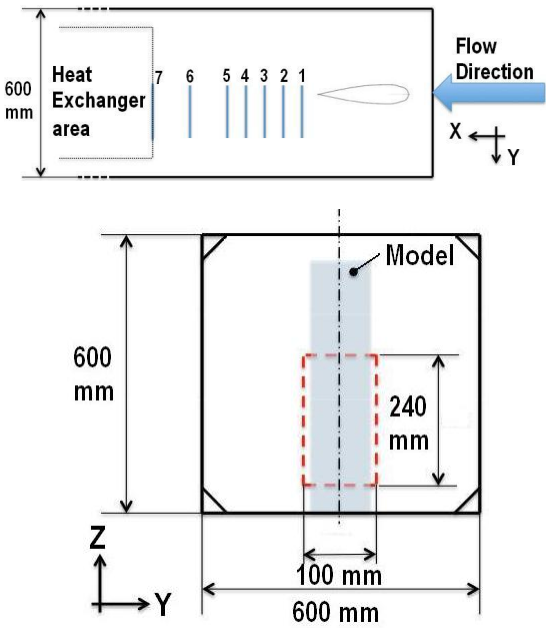

Figure 8: Low Speed Experimental Campaign

The measurements are performed at seven different locations downstream of the scaled up model. The first location is at 25 mm from the rake trailing edge, for locations 1 to 5 the step is 25 mm for locations 5 to 7 the step is 50 mm. At every location a mea-

surement grid of 533 points is performed for a total of 3731 points of measurements, the task is completed by means of a robotized system.

RESULTS: IHCP SOLUTION

Figure 9 shows the velocity and the turbulence intensity profiles at the heated plate leading edge, (position $x = 0\ mm$), for both the boundary layer and the free flow region. The results show that the flow field generated for the experimental campaign meets the requirements of the theoretical reference case, with Figure 9(a) showing the typical figure of a turbulent boundary layer.

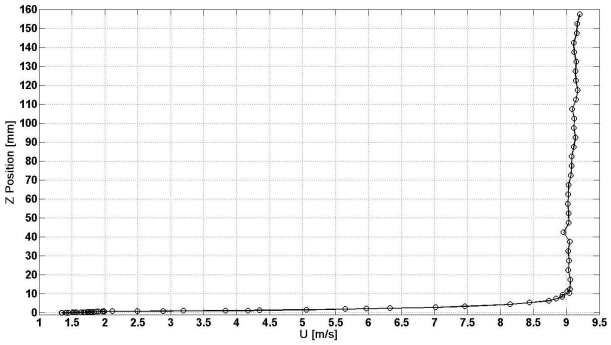

(a) Velocity Profile

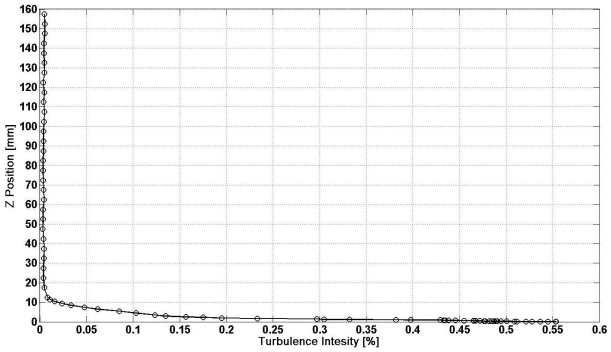

(b) Turbulence Intensity Profile

Figure 9: Boundary Layer Analysis

The effects of the regularization can be seen in Figure 10, where the left figure show the results of the surface temperature using the raw I.R. camera data and the contour plots on the right the resulting temperatures obtained after regularization. To illustrate the effect of the parameter α_1 on the computed surface heat flux, Figure 11 plots the computed heat transfer coefficient as a function of α_1. Additionally, the elimination of the fluctuation dampening ($\alpha_1 = 0$) shows

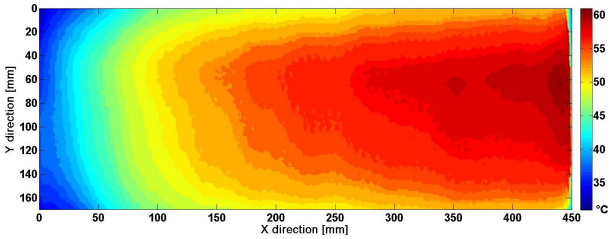

(a) T beginning - Raw data

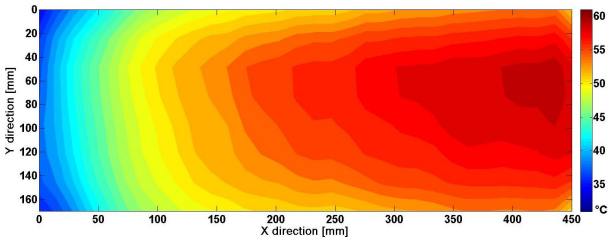

(b) T beginning - Regularization

Figure 10: Regularization Effect on the Measured Surface Temperature

the ill-posed character of the IHCP solution as measurements errors are amplified into large nonphysical oscillations on the calculated heat transfer coefficient profile. Figure 11 shows that the use of α_1^{opt} gives the best estimation for the heat transfer coefficient and that higher values of α_1 will lead to the underestimation of the heat transfer coefficient. A comparison between the theory and the results of the proposed IHCP methodology is given in Figure 12. The experiment was conducted with a time step of 5.41 seconds between two I.R. images. The theory uncertainty bounds come from a 3% of relative uncertainty on U_∞, while the error for $h(x)$ mainly originates from an average 2.8% of relative uncertainty on the measured T_{surf}. The biggest discrepancy can be seen on the leading edge the plate, where the steepness of the h curve becomes problematic due to the discretization of the calculated result. Nonetheless the quality of the obtained results can be controlled by a comparison of the heat flow lost per unit distance between the theoretical and the experimental case. The lost heat flow can be computed by eq. 19 as:

$$Q = \int h \cdot \Delta T_{surf} dS \tag{19}$$

which puts the heat flow at 2.35 W/m for the theory, and 2.5 W/m for the experimental result.Figure 13 plots the heat transfer coefficient $h(x, y)$ for the whole plate.

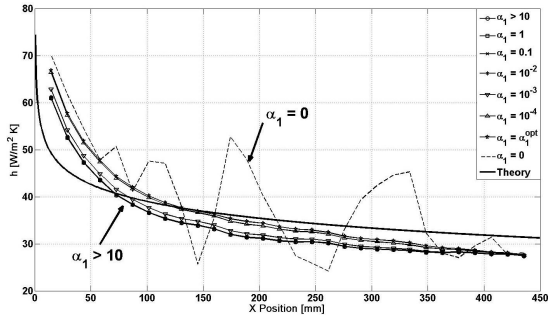

Figure 11: Regularization Effect on the IHCP Solution

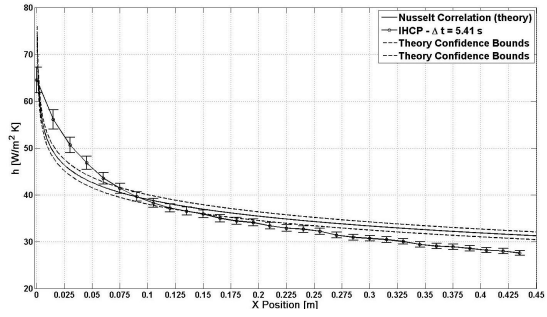

Figure 12: IHCP Solution Result - Comparison with Theory

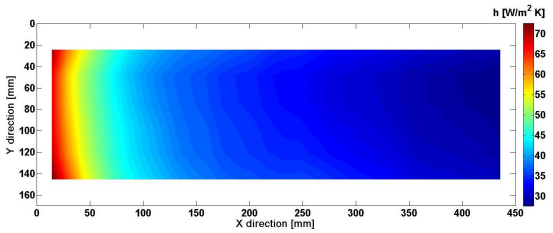

Figure 13: IHCP Solution Result - $h(x, y)$ Map

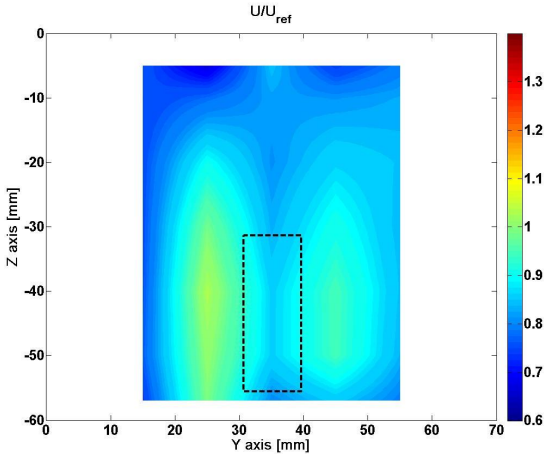

Figure 14: High Velocity Measurement Domain - Area of Interest for the Comparison

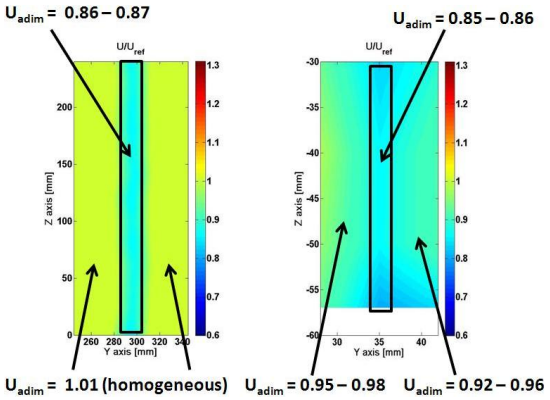

Figure 15: Non-dimensional Velocity Comparison

RESULTS: HOT-WIRE RAKE

For a sake of completeness is to be said that for the presented experimental campaigns a descriptive static statistic analysis is performed, computing averaged values, variance, standard deviation and higher order moments (skewness and flatness) together with a frequency content analysis and a signal correlation analysis exploited to compute the turbulence scales. The turbulence scales (integral scale, Taylor microscale and Kolmogorov scale) are computed according to the Taylor's frozen turbulence hypothesis [5]. The whole set of results for the low and the high speed case are not reported since the scope of the investigation is rather a comparison between the two.

The comparisons are performed between the whole investigation area of the low speed experimental campaign and the lower-central part of the high speed experiments measurements domain, i.e. from the bottom of the test chamber up to 30 mm (mid height) and from 25 mm to 45 mm along the y axis. The portion of measurement domain that can be used for comparison is the area in the dashed rectangle in Figure 14. The comparison of the non-dimensional velocity maps is presented in Figure 15. An agreement between the two plots is visible, especially focusing on the central part where the velocity reduction due to the wake is very similar: it ranges from 13% to 14% for the low speed experiments and from 14% to 15% for the high speed experiments. To conclude a comparison at 1/4 of the probes rake height is performed. In Figure 16 and Figure 17 horizontal cuts of the velocity and turbulence intensity fields are presented for the high and the low speed case.

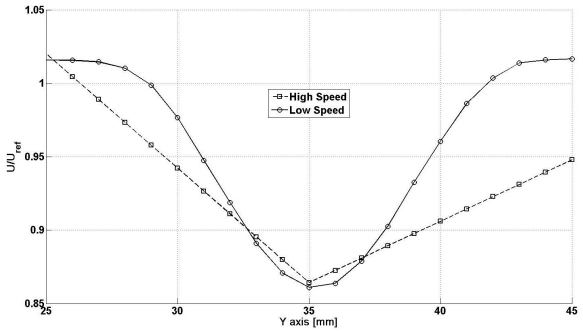

Figure 16: Non-dimensional Velocity Comparison

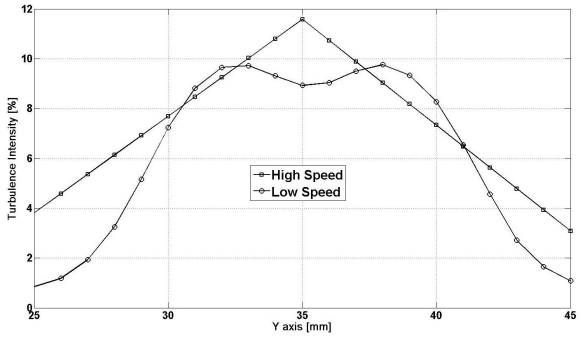

Figure 17: Turbulence Intensity Comparison

CONCLUSIONS

A solving methodology for the transient inverse heat conduction problem is proposed, using infra red thermography to measure the surface temperatures. To reduce the sensibility of the IHCP solution to the measurements noise a regularization method, based on the Tikhonov ridge regression, is applied to the specific case under analysis. The methodology is first validated numerically, using a commercial CFD code to calculate the imposed surface temperatures. A very good match between the calculated values and the theoretical Nusselt correlation results was found. An experimental validation of the proposed methodology followed. The constant temperature anemometry technique was used to characterize the flow field. The results shown a good agreement between theoretical and experimental data and proved the enhancements obtainable by applying the proposed regularization procedure, with the correct choice of parameter α_1 proven to be crucial.
For the hot-wire rake characterization the obtained results let understand the possibility to exploit the low speed experiments to perform a qualitative, and up to a certain extent also quantitative, analysis of the high speed flow field. The advantages of increasing the size of the whole experimental set-up come mainly from the chance to use an open circuit wind tunnel, i.e. long run experiments with respect to the short time experiments that can be performed with the blow down installation. The actual limitation for this kind of approach sits in the fact that one cannot take into account for the compressibility effects.

FUTURE DEVELOPMENTS

A parametric study on the influence of the time interval, Δt, between the two recorded thermographs is underway. An adaptation of the proposed methodology in order to be used within a commercial CFD code is under development. This might reduce the problems encountered when discretizing part of the domain in which sudden variations of the surface heat flux might occur. Moreover the modeling of more complex geometries will be also possible. The starting approach is to propose optimization algorithms to be exploited in a CFD commercial code to subsequently implement the use of recorded surface thermographs as boundary conditions for the thermal problem.
To complete the analysis on the probes rake and validate the proposed dynamic analogy approach an experimental campaign with pressure taps inserted on the rake's surface is planned. CFD simulations are underway and a comparison with the pressure coefficients measured on the rake's surface is foreseen.

References

[1] F. Baldani and W. Bosschaerts. Turbulence measurements in a high subsonic non-isothermal flow field. turbine engines inlet conditions analysis. *Conference Proceedings*, (ISABE 2011 Paper nr. 1815), 2011.

[2] F. Baldani, W. Bosschaerts, and R. Wagemakers. High velocities wind tunnel flow field investigation and heat exchanger infra-red analysis. part 1: Experimental set-up, experiments and first results. *Conference Proceedings*, (ISAIF10-11), 2011.

[3] J.V. Beck, B. Blackwell, and A. Hoji-Sheikh. Comparison of some inverse heat conduction methods using experimental data. *International Journal of Heat Mass Transfer*, (Vol. 39, pp. 3649-3657), 1996.

[4] J.V. Beck, B. Blackwell, and C.R. St. Clair Jr. *INVERSE HEAT CONDUCTION - Ill-posed Problems*. International Text Books in Mechanical Engineering. Wiley Interscience Publication, first edition edition, 1985.

[5] H.H. Bruun. *Hot-wire Anemometry, Principles and Signal Processing*. Oxford University Press Inc., 1995.

[6] TSZENG T. C. and SARAF V. A study of fin effects in the measurement of temperature using surface-mounted thermocouples. *Journal of heat transfer*, 125(5):926–935, 2003.

[7] G. Cardone, T. Astarita, and G.M. Carlomagno. Wall heat transfer in static and rotating 180 degrees turn channels by quantitative infrared thermography. *Rev. Gï¿½ n. Therm.*, (37, 644-652), 1998.

[8] P.R. Childs, J.R. Greenwood, and C.A. Long. Heat flux measurement techniques. *Proceedings of The Institution of Mechanical Engineers Part C-journal of Mechanical Engineering Science*, 213:655–677, 1999.

[9] F. Coletti, A. Armellini, T. Arts, and C. Scholtes. Aerothermal investigation of a rib-roughened trailing edge channel with crossing jets - part ii: Heat transfer analysis. *ASME paper No. GT2008 - 50695*, 2008.

[10] B. Cukurel, T. Arts, and C. Selcan. Conjugate heat transfer characterization in a ribbed cooling channel. *Conference Proceedings*, (ISAIF10 Paper nr.161), 2011.

[11] Cavallero D. and Tanda G. An experimental investigation of forced convection heat transfer in channels with rib turbulators by means of liquid crystal thermography. *Experimental Thermal and Fluid Science*, 26(2):115–121, 2002.

[12] Malay K. Das, A. Tariq, P. K. Panigrahi, and K. Muralidhar. Estimation of convective heat transfer coefficient from transient liquid crystal data using an inverse technique. *Inverse Problems in Science and Engineering*, 13(2):133–155, 2005.

[13] Pr. H Groeber and Dr. S. Erk. *Fundamentals of Heat Transfer*. McGraw-Hill Series in Mechanical Engineering. McGraw-Hill Book Company, INC., third revised edition by dr. u. grigull edition, 1962.

[14] CHEN Han-Taw, SONG Jen-Pin, and WANG Yi-Tong. Prediction of heat transfer coefficient on the fin inside one-tube plate finned-tube heat exchangers. *International journal of heat and mass transfer*, 48(13):2697–2707, 2005.

[15] Cheng-Hung Huang and Hung-Chi Lo. A three-dimensional inverse problem in estimating the internal heat flux of housing for high speed motors. *Applied Thermal Engineering*, 26(14-15):1515–1529, 2006.

[16] Hukseflux and Website. Rc01 radiation convection heat flux sensor. `http://www.hukseflux.com/product/rc01?referrer=/product_group/heat-flux-sensors`.

[17] F. Kreith. *Principles of Heat Transfer*. International Text Books in Mechanical Engineering. International Textbook Company Ltd, 158 Buckingham Palace Road London, second revised edition edition, 1965.

[18] MINGJIE LIN and TING WANG. A transient liquid crystal method using a 3-d inverse transient conduction scheme. *International journal of heat and mass transfer*, 45(17):3491–3501, 2002.

[19] Alifanov O.M. and Nenarokomov A.V. Three-dimensional boundary inverse heat conduction problem for regular coordinate systems. *Inverse Problems in Engineering*, 7(4):335–362, 1999.

[20] J. Pellï¿½ and S. Harmand. Heat transfer measurement in an opened rotor stator system air gap. *Experimental Thermal and Fluid Science*, 2006.

[21] GOLBAHAR HAGHIGHI M. R., EGHTESAD M., MALEKZADEH P., and NECSULESCU D. S. Three-dimensional inverse transient heat transfer analysis of thick functionally graded plates. *Energy conversion and management*, 50(3):450–457, 2009.

[22] S. Rainieri, F. Bozzoli, and G. Pagliarini. Characterization of an uncooled infrared thermographic system suitable for the solution of the 2-d inverse heat conduction problem. *Experimental Thermal and Fluid Science*, (32, pages 1492-1498), 2008.

[23] AN Tikhonov and V.Y. Arsenin. Solutions of ill-posed problems. *WH Winston, Washington, DC*, 1977.

[24] AN Tikhonov and V.Y. Arsenin. Methods for solving ill-posed problems. *Scripta Series in Mathematics (Scripta Mathematics, New York, 1977)*, 1979.

[25] Jonathan W. Woolley and Keith A. Woodbury. Thermocouple data in the inverse heat conduction problem. *Heat Transfer Engineering*, 32(9):811–825, 2011.

[26] T. Wu and K. Vierow. A local heat flux measurement technique for inclined heat exchanger tubes. *Experimental Heat Transfer*, 19(1):1–14, 2006.

Design, Analysis, Optimization and Control of Rotor Tip Flows

Cis De Maesschalck

Turbomachinery and Propulsion Department, von Karman Institute for Fluid Dynamics, Belgium, demaess@vki.ac.be

Supervisor: Guillermo Paniagua

Associate Professor, Turbomachinery and Propulsion Department / Aeronautics and Aerospace Department, von Karman Institute for Fluid Dynamics, Belgium, paniagua@vki.ac.be

Promotor: Chris Lacor

Professor, Vrije Universiteit Brussel, Faculty of Applied Sciences, Department of Mechanical Engineering, Brussels, Belgium, chris.lacor@vub.ac.be

Abstract

Developments in turbomachinery focus on efficiency and reliability enhancements, while reducing the production costs (through weight reduction and the use of standard materials). Aiming for better aero-thermal performances, the high-pressure turbine blades are subjected to strong aero-thermal loads. One of the major challenges for a turbine designer is undoubtedly the tip of the rotor airfoils. The tip region is responsible for about one third of the total turbine losses, due to the flow that propagates above the tip at high speeds, that eventually gives rise to the tip leakage vortex. Besides the aerodynamic impact, the thermal loads play an important role. The stage loading and rotational speeds are steadily increased to achieve higher turbine efficiency, and hence the overtip leakage flow may exceed the transonic regime. However, conventional blade tip geometries are not designed to cope with supersonic tip flow velocities. A great potential lays in the modification and optimization of the blade tip shape as a means to control the tip leakage flow aerodynamics, limit the entropy production in the overtip gap, manage the heat load distribution over the blade tip and improve the turbine efficiency at high stage loading coefficients.
In the frame of the present research investigation, an optimization strategy has been developed to produce a set of blade tip profiles with enhanced aerothermal performance for a number of tip gap flow conditions. The tip clearance flow was numerically simulated through two-dimensional compressible Reynolds-Averaged Navier-Stokes (RANS) calculations that reproduce an idealized overtip flow along streamlines. A multi-objective optimization tool was adopted to obtain optimized 2D tip profiles with reduced aerodynamic losses and heat transfer levels for relevant gap flow conditions. It is demonstrated that tip geometries which perform superior in subsonic conditions are not optimal for supersonic tip gap flows. Subsequently, the 2D prime tip profiles were used to construct fully carved 3D tip profiles for a modern transonic turbine rotor blade (Reynolds number is 5.5 x 10^5, relative exit Mach number is 0.9). The aerodynamic behavior and thermal characteristics were compared to those for conventional blade tip shapes by means of three-dimensional RANS calculations.
The final objective of this PhD research project is the redesign of the rotor tip of a high pressure turbine through the use of both active and passive flow control techniques to improve the aerodynamic performance as well as the thermal loadings. This combined numerical optimization and experimental quantification will lead to a detailed physical characterization of the overtip leakage flow in a transonic regime and will form a base for the use of innovative designs.

Keywords: Tip design, leakage flows, high pressure turbine, aerothermal optimization

Detailed Aero-Thermal Analysis of a Film-Cooled Turbine Vane: Methodology of the Experimental Campaign

Fabrizio Fontaneto

Jacques Chauvin Laboratory

Turbomachinery and Propulsion Department, von Karman Institute for Fluid Dynamics, Belgium, fontaneto@vki.ac.be

Supervisor: Tony Arts

Professor and Head of Department, Turbomachinery and Propulsion Department, von Karman Institute for Fluid Dynamics, Belgium, arts@vki.ac.be

University Supervisor: Giovanna Barigozzi

Associate Professor, Faculty of Industrial Engineering, University of Bergamo (IT), giovanna.barigozzi@unibg.it

Abstract

An extensive measurement campaign was held in the last two years with the intent of creating a solid experimental test case for codes validations. The methodology of the application of three different measurement techniques (hot-wire anemometry, pressure probes and thin-films thermometry) is herein assessed, providing a detailed description of the actions taken to improve their performance and, in the end, an analysis of the uncertainty is carried out.

Keywords: Gas turbines, aero-thermal performance, methodology, hot-wire anemometry, pneumatic pressure probe, thin-films thermometry, calibration, uncertainty, data reduction, dynamic compensation, convective heat-transfer coefficient

1. Introduction

The availability of reliable numerical simulations is a critical issue for the speeding up of the product development and its costs reduction process in the framework of the Turbomachinery industry, characterized by a long design time and a high specific value of the product itself. Therefore, given that Computational Fluid Dynamics (CFD) is a fundamental tool that directly affects the quality of the product since the early design phases, it must show a high degree of robustness normally tested on experimental test cases. In-house and commercial numerical codes have been historically validated and calibrated upon *ad-hoc* experiments, designed to provide high completeness as well as high reliability of results. In the last two years at the von Karman Institute (VKI) a wide measurement campaign was carried out with the intent of producing a solid experimental test case for Turbomachinery (gas turbines) code validation to provide as reliable as possible measurements on the inlet free-stream turbulence, on the downstream pressure wakes and on the blade convective heat-transfer distributions. The present paper directly derives from the latter research activity and it focuses on the used measurement techniques and all the efforts done to reduce as much as possible the sources of spurious and erroneous results: the final target is in fact to be able to provide a reliable evaluation of the measurement uncertainty and not necessarily its reduction. In the following paragraphs Hot-Wire anemometry (HW), pneumatic pressure probe (PP) and thin-film gauges (TF) techniques are analysed. For each one, a quick theoretical overview is provided to better understand the limits of the techniques and the possible improvements. The calibration and data-reduction procedures are then described and, when possible, a benchmark is used to test the quality of the taken actions. An evaluation of the measurement uncertainty is provided in the end.

2. Geometry and Experimental setup

A transonic film-cooled turbine vane was investigated in a five-blade linear cascade configuration. Two rows of staggered film-cooling holes are present on both the suction and the pressure sides and they are fed by two independent settling chambers as shown in fig. 1.

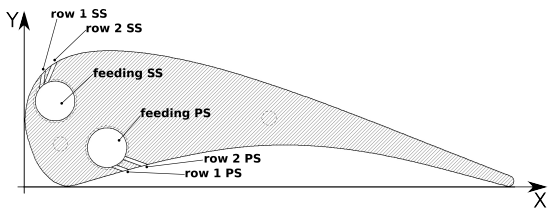

Figure 1: LS-94 film-cooled transonic turbine vane

Tests were performed in the VKI light-weight-piston compression tube tunnel CT-2 (fig. 2). It is composed of a compression cylinder that is separated from the test section by means of a fast opening shutter. By regulating on the timing of the shutter and on the pressure levels that can be set in the compression tube and in the test section, the Mach and the Reynolds numbers can be varied independently, matching real engine flow conditions. The coolant feeding system can be also adjusted to provide engine representative flow-to-coolant temperature ratios.

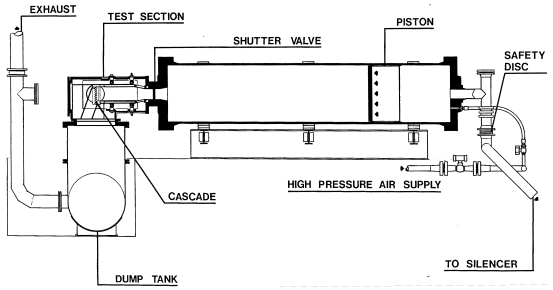

Figure 2: VKI light-weight-piston compression tube tunnel CT-2

3. Hot-Wire Anemometry

Hot wire anemometry is a well known and robust anemometry technique. The name "hot wire" is generally indicating the sensing element, its supports and the circuitry of which the wire itself is a part: the sensing element and the two prongs that are holding it are in fact one of the legs of the measuring circuit, typically a Wheatstone bridge where the current is servo-adjusted to keep constant the resistance of the wire. Thanks to the reduced dimensions to which the sensing element can be built ($5 - 9[\mu m]$), hot-wire anemometers provide a high frequency response that makes them the most used tools for unsteady flow field investigations.

3.1. Hot wire anemometry for heated compressible flows

A measurement by means of Hot-Wire Anemometry is performed by linking the tendency of the wire to change its temperature to the velocity of the flow that is investing it. The physical phenomenon on which this technique is based on is therefore the convective heat transfer that takes place between the wire and the flow itself and that depends of the convective heat-transfer coefficient and on the temperature difference between the wire and the flow, as explained by eq. 1.

$$q = hA(T_w - T_\infty) \tag{1}$$

Thus, HW measurements can be strongly affected by flow-temperature variations and it is common practice to keep the temperature of the wire (T_w) as high as possible, making it therefore insensible (or less sensible) to temperature fluctuations. Kovasznay [1] [2] and Morkovin [3] followed another approach and proposed instead to quantify the sensitivities of the wire with respect to all the affecting parameters in order to decouple the effect of each component and "isolate" a true velocity measurement. For a compressible one-dimensional flow, by performing a sensitivity analysis under the hypothesis of small perturbations, they expressed the fluctuations of the Wheatstone bridge in which the HW is inserted as a function of density, velocity and temperature fluctuations as reported in eq. 2, being E the bridge voltage and S_ρ, S_u and S_T the corresponding sensitivities.

$$\frac{E'}{\overline{E}} = S_\rho \frac{\rho'}{\overline{\rho}} + S_u \frac{u'}{\overline{u}} + S_T \frac{T_0'}{\overline{T_0}} \tag{2}$$

These coefficients can be known, for example, by means of a methodical process where one single independent parameter is changed by keeping all the other constant, making therefore the calibration procedure a highly time-consuming process that necessarily requires a closed loop facility.

3.2. Novel high-speed calibration and data reduction procedure

Recently, Cukurel et al. [4], in order to overcome the evident experimental difficulties of a traditional

sensitivity calibration, developed and tested a novel methodology that provides accurate results against a simple experimental setup and a fast calibration procedure. The convective heat transfer phenomenon over the wire can be made non-dimensional by expressing it in terms of Nusselt number (Nu). In a one-dimensional incompressible flow field with fixed fluid properties and relatively small total temperature variations, the latter becomes a function only of the Reynolds number (Re) if a proper over-heating of the wire is also provided. By rewriting the Nusselt number as in eq. 3 (Nagabushana and Stainback [5]), based on the bridge voltage E, calibration data can be easily made non-dimensional if the flow total and static pressure and total temperature are known. The latter quantities can be easily measured in a standard open-jet nozzle like the one sketched in fig. 3.

$$Nu = \frac{E^2}{k(T_w - \eta T_0)} \left(\frac{R_w}{\pi l (R_t + R_l + R_w)^2} \right) \qquad (3)$$

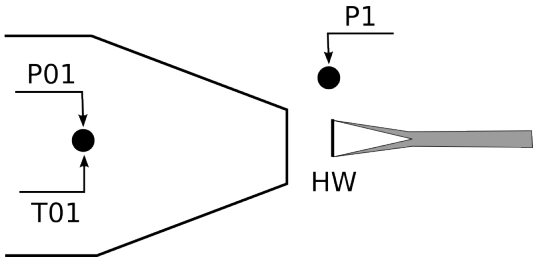

Figure 3: Open-jet calibration facility

In eq. 3, the only unknown is the wire temperature T_w given that the resistances are fixed in constant-temperature anemometry (CTA) and that the recovery factor η can be computed by well established correlations based on the flow total temperature T_0. As suggested by Cukurel, T_w can be iteratively computed by maximizing the R^2 value of a 4th order polynomial fitting on a Nu-Re population that is obtained by varying the calibration jet velocity and total temperature. When T_w is retrieved the data cloud distribution (fig. 4 - (a)) collapses on one single curve (fig. 4 - (b)), providing therefore an unequivocal link between the flow velocity and the bridge voltage for every combination of flow total temperature and velocity.

3.3. Measurements and data reduction

In "measurement "configuration, the HW bridge voltage is first transformed in terms of Nusselt number, requiring the flow total temperature to be measured by an independent probe. Once the non-dimensional calibration polynomial is applied, the flow density and viscosity must be computed to retrieve the velocity value from the calibrated Reynolds number. This can be done by acquiring also the flow total and static pressures that, together with the total temperature measurement, allow to compute the flow static temperature with isentropic flow relations.

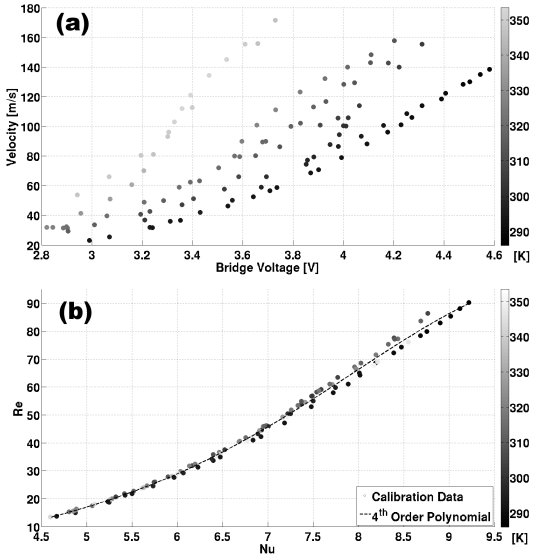

Figure 4: (a) The effect of flow temperature on HW calibration data; (b) The result of the non-dimensional iterative data reduction

3.4. Turbulent spectra measurements

In the present project, HW measurements were performed in order to characterize the inlet free-stream turbulence to the test section described in sec. 2. As shown in fig. 5, a total pressure probe, a static pressure tap and a total temperature probe were placed in the inlet section at the same axial position at which the HW was fixed, while a turbulence generator was moved in four different upstream positions. Fig. 6 reports the evolution of the turbulence spectra with respect to the position of the grid: the longer is the time (or space) given to the decay to act, the smaller is the turbulent energy content of the flow field and therefore the more depressed becomes the spectrum. The typical slopes ("-1 ", "-5/3 ", "-3 "and "-7 ") characterizing the energy cascade in the so called Universal Equilibrium Range can be recognized.

3.5. Uncertainty analysis

The uncertainty analysis, referred to a 95 % confidence interval, was performed by means of

a perturbation method. At the inlet section, the uncertainty on the temperature measurement was set to be equal to $\delta T_{01} = \pm 0.5[K]$ while the error related to pressure measurements was computed from the variance of the slope of several calibration curves and found to be approximately equal to $\pm 10[mbar]$. The derived uncertainties on the computed values of density and static temperature were then found to be respectively equal to $\delta\rho_1 = \pm 0.015[kg/m^3]$ and $\delta T_1 = \pm 3[K]$. Although the latter quantities are all affecting its uncertainty, only T_{01} demonstrated to have a strong effect (on higher order of magnitude) on the Nusselt number that was therefore taken to be dependent only on the flow total temperature and on the noise level of the bridge voltage E. A computed uncertainty of ± 0.02 on Nu implies an error on the fitted Reynolds number of ± 1.4 that, in turns, produces an uncertainty in the velocity values slightly higher than 3% of the mean value.

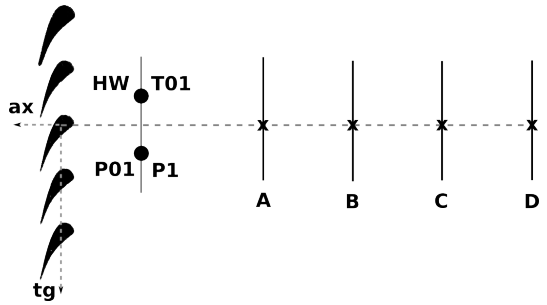

Figure 5: Hot-Wire measurements setup

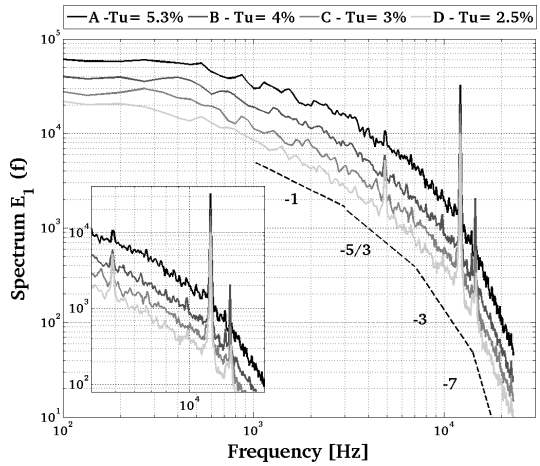

Figure 6: Spectra evolution with respect to the turbulence generator position

4. Pneumatic pressure probe

In the present experimental campaign, a three-hole pneumatic pressure probe was used to measure the downstream total pressure wakes and flow angle distributions. It consists of a thin L-shaped head connected to a 200[*mm*] long stem: all along the length, three independent cavities (0.8[*mm*] in diameter) are obtained, connecting the measuring head of the probe to plugs placed on the opposite side of the stem. Here, plastic tubes are then used to put the probe in communication with the transducers. The two lateral holes on the head tip are inversely slanted with respect to the central one as shown by the detail in fig. 12.

4.1. Dynamic calibration

The natural damping-delaying behaviour of pneumatic systems

A pneumatic pressure probe can be theoretically modelled by means of the so called *simple organ pipe resonance theory*. By neglecting the effect of viscosity and heat conductivity, and by also taking the assumption (not far from reality indeed) that in the tubings the flow velocity keeps smaller than the one of sound, Bergh and Tijdeman [6] computed the response of such a system to a periodic variation of the pressure input and they found out that, in the most idealistic condition, the system produces a great magnification in correspondence of the resonant frequencies while the phase distribution jumps instantaneously of $\pi[rad]$ every time a resonant peak is present (see Fig. 7).

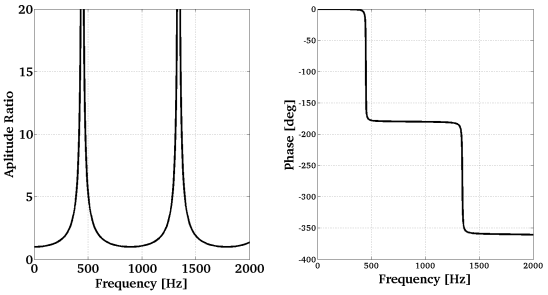

Figure 7: Simple organ pipe theory prediction

This purely theoretical result that is derived from a too crude approximation of the problem, allows anyway to draw an important conclusion: except for the very first frequencies, all the other spectral components of an input signal will be distorted by the piping system, leading therefore to the measurement of a different signal with respect to the real one.

Compensation of a signal: the system transfer function

With the name *transfer function*, one refers to the relation linking the input and the output of a system. It can be evaluated in both, the time and the frequency domain by exploiting the property of convolution of spectra and, in the latter case, it can be directly computed by performing a ratio between the spectral content of the system output with respect to the input one (eq. 4).

$$TF(f) = \frac{OUT(f)}{IN(f)} \tag{4}$$

In this form, it is clearly a complex function that takes into account the information in terms of both, amplification factor and delay between the input and output. In fact, by expanding the terms and expressing them in polar coordinates, it is clarified that its modulus equals the ratio of the two moduli while the phase coincides with the difference between the two phases at each frequency component.

$$\begin{aligned} TF(f) &= \frac{|OUT(f)|e^{-i\phi_{OUT(f)}}}{|IN(f)|e^{-i\phi_{IN(f)}}} = \\ &= \frac{|OUT(f)|}{|IN(f)|}e^{-i(\phi_{OUT(f)}-\phi_{IN(f)})} = \\ &= |TF(f)|e^{-i\phi_{TF(f)}} \end{aligned} \tag{5}$$

This formulation is particularly helpful to understand the mechanism of compensation: let us suppose that the transfer function $\overline{TF(f)}$ of a pneumatic system is known a priori and let us consider a set of data *d(t)* measured by means of the same identical pneumatic system. Because of what was stated previously, it is clear that *d(t)* is not representing the real phenomenon but it is contaminated by distortions introduced by the system itself. If $\overline{TF(f)}$ is known then it can be used to correct *d(t)* in order to retrieve the true excitation signal (eq. 6):

$$D_{comp}(f) = \frac{D(f)}{\overline{TF}} \longrightarrow d_{comp}(t) = IFT\{D_{comp}(f)\} \tag{6}$$

The latter concept is the most critical step of the whole procedure: the quality of the compensation strongly depends on the quality of the computed transfer function. If, for any reason, TF does not represent the real, complete and most generic behaviour of the system, the compensated signal will not correspond to the real input.

Evaluation of the system transfer function: the dynamic calibration

Retrieving experimentally a transfer function, nominally corresponds to a dynamic calibration procedure and it is therefore of crucial importance to select the correct and most generic input to obtain a robust and reliable result. Even though different excitation signals could be selected for this purpose, in the present project a pressure step was used because a step function is able in fact to excite at the same time all the frequencies up to $+\infty$, providing therefore a fast calibration process.

The pressure step was produced by means of the setup shown in Fig. 8: the groove placed on the lateral surface of the cylindrical support allows to block the neck of a balloon in such a way that the probe and a fast reference transducer could be completely enclosed inside the internal volume of the balloon. The latter is then pressurized 100[*mbar*] over the atmospheric pressure and burst. Assuming the signal measured by the fast reference transducer to be representative of the true not-damped-not-delayed pressure input, the transfer function of each hole of the probe can be then computed by means of the procedure outlined in the previous paragraph. The latter calibration methodology, the so called *"balloon test"*, was developed and tested by Paniagua et al. [7] with the intent of performing a dynamic compensation of a pressure system in the time domain (i.e. time domain fitting) that, in the present project, was extended to the more general case of a frequency domain transfer function.

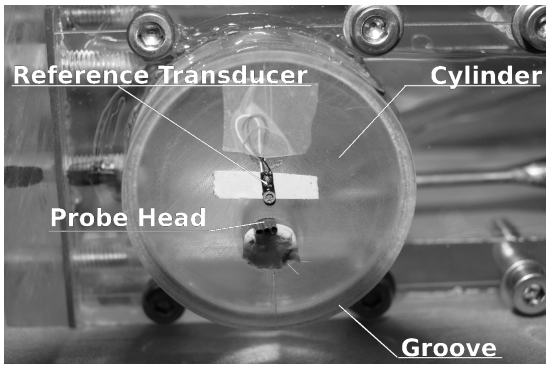

Figure 8: Support for the balloon test

Data processing

As mentioned before, a pressure step excites all the frequencies of the system but with an equal amount of energy. This produces a particularly noisy spectrum that necessarily requires an averaging procedure

over different time records. The data shown afterwards were computed by acquiring and processing 12 different time stories. It has to be remarked then that the phase distribution corresponds to the delay with respect to the first point of the spectrum. In presence of an imperfect trigger, the acquisition starting point could vary from test to test, producing a different phase pattern in the low frequency range. When averaging the different spectra, a mean value among all the signals is computed that leads to the loss therefore of any possible deterministic oscillations of the phase (fig. 9-a). The resulting TF will be therefore necessarily misleading and the reconstructed signal non-physical. To avoid this kind of artefacts, the time series have been shifted with respect to a known unequivocal point (e.g. the half-step point) before applying the Fourier Transform and the effect is well visible in fig. 9-b.

Since the sampling rate could be varied from the one adopted during the dynamic calibration, steps have been acquired at a high frequency ($1[MHz]$ - much higher than the cut-off frequency of the probe itself) in order to allow the re-sampling of the calibration time series to match the last spectrum point in the frequency domain. A low-pass Butterworth filter set to the half of the re-sampling frequency has been always applied to avoid any aliasing artefact. The acquisition time of a record determines the spectral resolution of its Fourier Transform and the best practice would be in fact to guarantee that the data to be compensated are acquired over the same observation time to exactly match the resolution of the spectra. When dealing with the burst of a balloon, this is almost impossible to obtain (because of the short characteristic time of the phenomenon) and therefore a different way has to be followed. In the present work, each time series was elongated by adding blocks of the first portion of the record at the beginning of the time series and blocks of the last data at its end, providing to increase the two sides of the signal with the same quantity of points. This process produces a high resolution TF that can be interpolated locally in the complex domain when the spectral resolution of the compensated signal is not precisely corresponding. Windowing of the signal is mandatory. The high frequency components introduced by the FFT to approximate non-periodicity of the step signal, critically affect the quality of the reconstruction. In the present project a custom window was created as shown by fig. 10: a common Hanning window was split in two symmetric parts and as many unitary values as needed to match the length of the data vector were added among them.

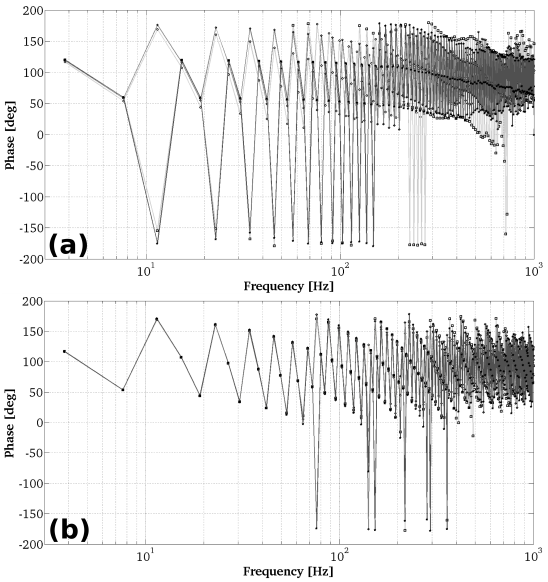

Figure 9: Comparison among 4 different records of the same phenomenon before re-phasing them with respect to the half step point (a) and after the re-phase (b)

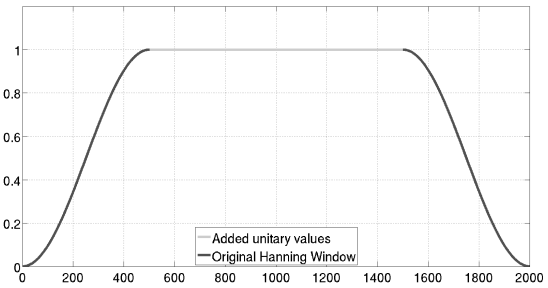

Figure 10: Custom Hanning window

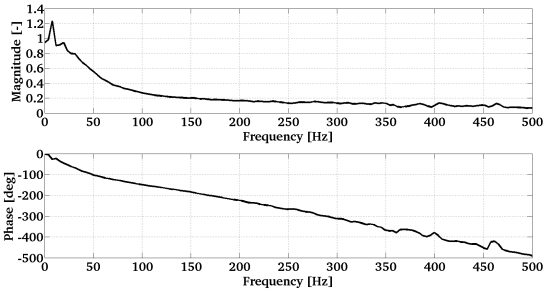

Figure 11: Step-test computed transfer function

Computed transfer function

The computed transfer function is presented in Fig. 11. The magnitude remains almost equal to unity up to about 10[Hz] where a resonant peak is present. It is then followed by a short plateau equal to 0.9 up to 20[Hz] where it starts descending with a typical damped second order behaviour. The phase plot keeps equal to 0 up to 10[Hz]. In correspondence of the plateau commented previously, the phase jumps of 20[deg] and then starts a constant decrease that confirms the conclusion that the system probe-transducers belongs to the second order group.

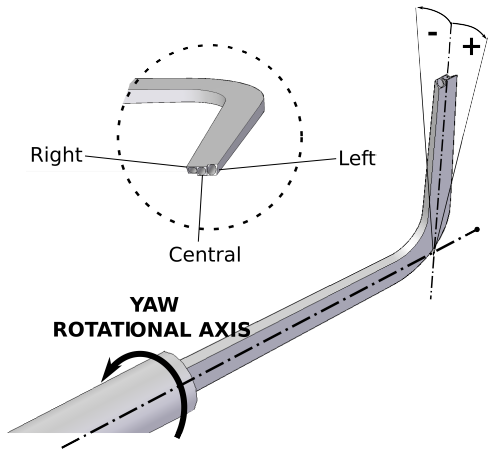

Figure 12: Used conventions for three-holes probe angle measurements

4.2. Angular Calibration

By traversing the probe downstream the cascade, total pressure wakes and pitch-wise flow angle distributions can be retrieved once the link between the flow angle and the pressure read by each hole is known. The probe must undergo therefore an angular calibration procedure where, for each expected Mach number, the probe is rotated inside the core of a controlled jet, providing to sweep the range of variation of the expected flow angles. In the frame of the present project the probe was calibrated between Ma=0.5 and Ma=0.9 with a yaw-angle raging between ±30[deg]. Data are then converted in terms of dimensionless coefficients in order to avoid the dependency on the absolute value of the pressure measurements: in Fig. 13, the resulting calibration maps for C_{Pt} and C_{yaw} are reported while their expression is presented in equations 7.

$$
\begin{aligned}
C_{Pt} &= \frac{P_{central} - P_{ref}}{P_{ref} - P_{av}} \\
C_{yaw} &= \frac{P_{left} - P_{right}}{P_{central} - P_{av}} \\
P_{av} &= \frac{P_{left} + P_{right}}{2}
\end{aligned}
\tag{7}
$$

P_{ref} is the reference pressure that, during experiments, coincides with the inlet total pressure P_{01}. Conventions for $P_{central}$, P_{left} and P_{right} are also reported in fig. 12 together with the conventions adopted for the angle. Once measurements are performed, C_{pt} and C_{yaw} are computed on the acquired data and by means of an iterative procedure, local total pressure P_{02} and flow angle β_2 are retrieved from the calibration maps. The complete calibration and data extrapolation procedure, even though described for a five-holes probe, is clearly reported by Morrison et al. in [8]. By assuming that no transversal pressure gradient is taking place along the span-wise direction, the static local pressure P_2 can be considered equal to the one measured by wall pressure taps distributed all along the traversing path at the same axial position in which the head of the probe is placed. A linear interpolation within pairs of pressure taps is performed to provide a value of the downstream static pressure also when the head of the probe is not found exactly in correspondence of a pressure tap.

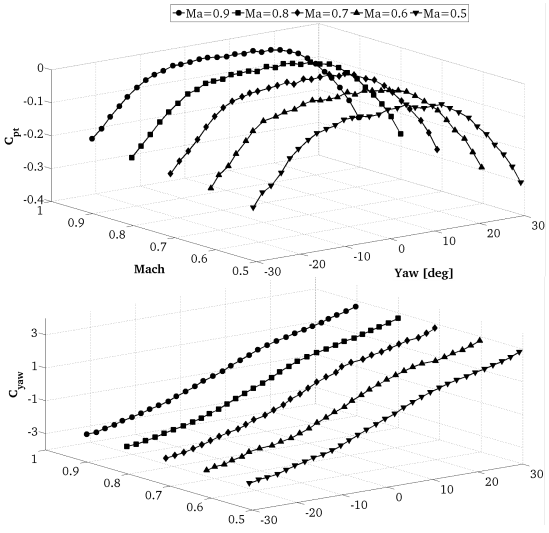

Figure 13: C_{Pt} and C_{yaw} calibration maps

4.3. Shock correction

Any time the head of the probe is facing a supersonic flow-field, a bow-shock detached from the thick nose is created, at a distance proportional to the local Mach number of the flow. When this condition is reached, the pressure input acting on the head is describing a subsonic flow field rather than a supersonic one, leading therefore to spurious measurements. By taking the assumption that the shock is normal in correspondence of the entrance of the measuring holes, a correction can be applied to retrieve the correct total pressure.

$$P_{0up} = \frac{P_{0down}}{\left[\frac{(\gamma+1)Ma_{up}^2}{(\gamma-1)Ma_{up}^2+2}\right]^{\frac{\gamma}{\gamma-1}} \left[\frac{(\gamma+1)Ma_{up}^2}{2\gamma Ma_{up}^2-\gamma+1}\right]^{\frac{1}{\gamma-1}}} \tag{8}$$

$$Ma_{up} = \left\{\left[\frac{2}{\gamma-1}\left(\frac{P_{0up}}{P_{up}}\right)^{\frac{\gamma-1}{\gamma}} - 1\right]\right\}^{0.5} \tag{9}$$

As shown in equations 8 and 9, by knowing the static pressure upstream the shock P_{up}, the true total pressure P_{0up} can be computed from the total pressure P_{0down}, measured downstream the shock. The solution is obtained by iterating on the upstream Mach number Ma_{up}. Fig. 14 presents the distribution in space and time of the difference $P_{2_{traversing}} - P_{2_{notraversing}}$, the downstream static pressure evolution with and without traversing respectively. This allows to draw on top of it the trajectory followed by the probe during its movement in order to highlight any possible effect of its presence on the static pressure distribution. Given that the difference keeps always close to zero and does not show any particular modification of the flow pattern in correspondence of the probe position, then P_2 can be always considered as representative of the undisturbed static pressure upstream the shock and the system of two equations in three unknown can be solved.

4.4. Total pressure wakes and flow angles measurements

When a measurement is performed, a static calibration is applied to transform the acquired data from volts to pressures. The signal is then windowed and Fourier-transformed and the complex transfer function used to compensate the spectrum. By means of the inverse Fourier Transform the compensated pressure signals are brought back to the time domain

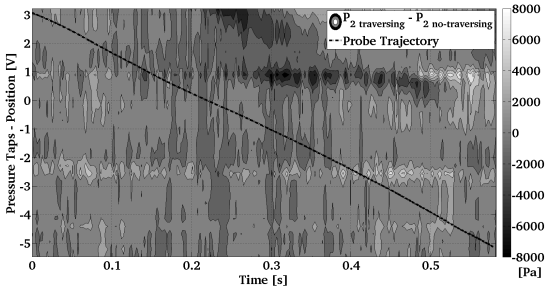

Figure 14: $P_{2_{traversing}} - P_{2_{traversing}}$ versus the probe trajectory for $Ma_{2s} = 1.1$

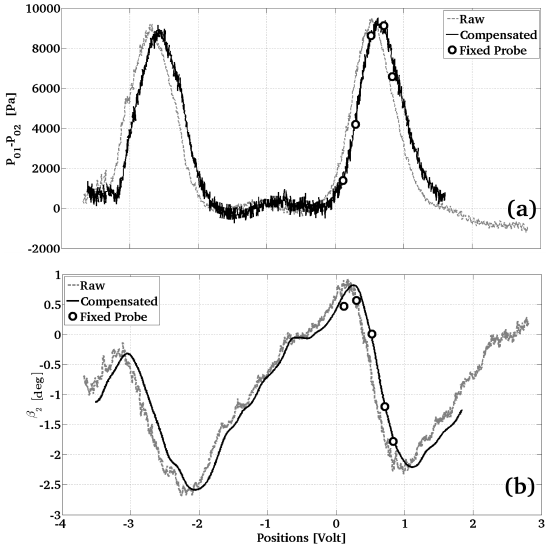

Figure 15: (a) Wakes distributions - (b) Flow Angle distribution in the downstream section

and then used to compute the coefficients of the angular calibration and the total pressure, Mach number and flow angles are retrieved for every position of the probe. In the end, if the ratio between P_2 and P_{02} if found to be smaller than the critical value ($(P_2/P_{02})_{crit} = 0.5283$), the bow-shock correction is automatically applied to compute the true undisturbed Mach number and total pressure. Fig.15-(a) reports an example of a wake measurement used to verify the quality of the dynamic compensation. The raw wakes distribution is plotted against the result of the dynamic compensation and angular calibration. The circles correspond to reference measurements performed by fixing the probe along the traversing path in different positions across the wake. As it can be clearly seen, the agreement between the compensated signal and the reference ones is definitely good: the total pressure profile of the compensated pressure signal is truly

describing the pressure drop across the wake of the blade. In fig.15-(b) the pitch-wise flow angle variation is instead presented: the compensated signal retrieved from the angular calibration is precisely following the reference distribution, demonstrating therefore the effectiveness of the dynamic calibration also for the lateral holes.

4.5. Uncertainty analysis

The uncertainty on the downstream total pressure and flow angle is position and Mach number dependent. In the present analysis the quoted errors correspond to the pitch-wise most frequent value for the worst case (highest Mach number and lowest Reynolds number) and the iterative procedure for the angular calibration is also taken into account in the error-propagation computation. The flow angle uncertainty was found to be equal therefore to $\pm 0.16[deg]$ while $\delta P_{02} = \pm 0.18\%$ of the mass averaged value $\widehat{P_{02}}$.

5. Thin-Film thermometry

Thin-films are widely used sensors for surface temperature measurements. They consist of a thin platinum layer painted on a surface (fig. 16) and connected to a leg of a constant current Wheatstone bridge. If for any reason (i.e. convective heat transfer) the temperature of the surface varies, then the gauge will change its own resistance producing a disequilibrium in the resistive bridge that unequivocally links the temperature variation to the output voltage of the circuitry. Thanks to its small thickness (typically $0.5[\mu m]$), a thin-film shows a frequency response of about $50[kHz]$ while the high resistivity of the material guarantees a sensitivity as high as $10[K/Ohm]$. In the present project, thin-film thermometers are used to map the time wall temperature variation and to quantify the wall heat flux and the convective heat transfer coefficient distributions by means of a transient measurement technique.

5.1. Unsteady heat-conduction through a semi-infinite solid

In absence of heat generation, the unsteady one-dimensional heat conduction phenomenon in a medium is described by eq. 10.

$$\frac{\partial^2 T}{\partial x^2} = \frac{1}{\alpha}\frac{\partial T}{\partial t} \tag{10}$$

It basically states that the temperature distribution in the x-direction within a medium depends on the physical characteristics of the medium itself as well as on the evolution of temperature in time. To solve such a differential equation an initial homogeneous temperature condition ($T_{t=0,x} = T_i$) and two boundary conditions are needed ($T_{t,x=0}$ and $T_{t,x=L}$) and, in the most general case when no assumptions can be taken, this problem can only be solved by means of numerical methods with a coherent discretization of the time and space domains. An analytical solution exists anyway when the medium through which conduction is taking place can be assumed as semi-infinite. The latter condition implies that the medium's extension in the x-direction is so high that, no matter which the characteristic time of the phenomenon is, the temperature at $x = L \to \infty$ will, in principle, not drift from the initial value, thus $T_{t,L} = T_i$ (Incropera et al. [9]). Under this assumption, the unsteady one-dimensional heat conduction equation can be rewritten by Laplace-transforming and by imposing that the Fourier's law at $x = 0$ equals the surface heat transfer rate $\dot{q}_s$ (eq. 11).

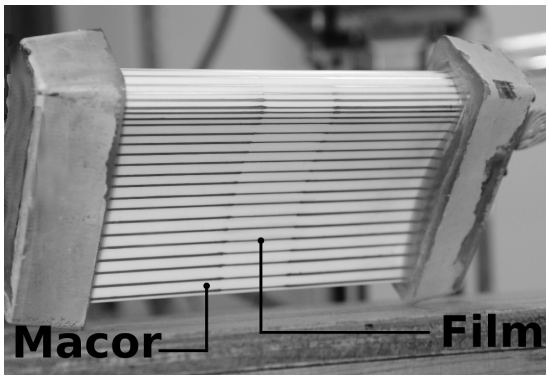

Figure 16: Thin-films instrumented blade

$$-k\left.\frac{\partial T}{\partial x}\right|_{x=0} = \dot{q}_s \tag{11}$$

$$\dot{q}_s = \sqrt{\frac{\rho c k}{\pi}}\left[\frac{T_w(t)}{\sqrt{t}} + \int_0^t \frac{T_w(t) + T_w(\tau)}{(t-\tau)^{1.5}} dt\right] \tag{12}$$

$$\dot{q}_s = h\,(T_0 - T_w) \tag{13}$$

If the surface wall temperature evolution is known *a priori*, then the solution can be expressed in terms of $\dot{q}_s$ following Schultz and Jones [10] study as in equation 12. Once the surface heat transfer rate is known, a third condition can be placed that equals the surface heat flux to the convective one provided by a flow of known temperature T_0 (eq. 13). In the end the convective heat transfer coefficient can be retrieved.

5.2. *Transient measurement technique for heat transfer measurements*

In order to use eq.12 for efficiently quantify the convective heat transfer coefficient distribution, the semi-infinite substrate condition must be checked. This is done by evaluating the penetration depth d (eq.14) that measures how deep a variation in the surface heat flux penetrates into the substrate; it is a function of the characteristics of the material and of the duration of the phenomenon. It is clear therefore that, in order to obtain acceptable values, a low conductivity substrate and a quick application of the heat transfer must be guaranteed.

$$d = 4\sqrt{\alpha t^*} \tag{14}$$

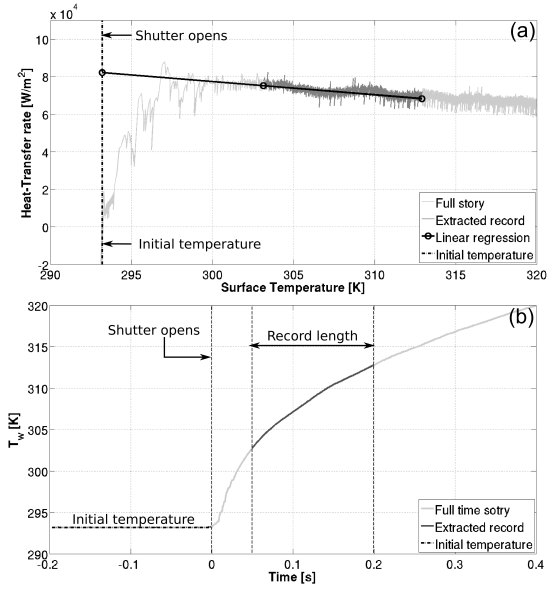

Figure 17: (a) $\dot{q}_s$ against T_w variation - (b) T_w variation in time

In the present application, thin-films have been painted on a blade made of Macor®, a glass-ceramic material that provides good machinable performance and low thermal diffusivity (α) while the characteristic time t^* is taken equal to the test time length that, in CT-2 is about 0.2[s]. This results in a penetration depth of about 1.5[mm] that allows to respect the semi-infinite condition all along the blade surface except for the trailing edge region where in fact data have to be carefully considered. When the shutter opens and the hot-compressed air is injected in the test section, the blade surface is subjected to a steep temperature variation and gradually increases its own temperature. If this step would have been ideal, then the heat transfer rate computed from eq. 12 should be also a perfect step but with a negative slope due the diminishing of the difference $T_0 - T_w$ as the time increases. In these conditions, the value of $\dot{q}_s$ that best respects the semi-infinite assumption is clearly the one computed at the shutter opening as the conduction phenomenon is not yet taking place. In the reality of the experiments, because of the finite time response of the measuring devices, the heat transfer rate increase cannot absolutely be considered as a step function and taking the first point will inevitably lead to wrong evaluations. To avoid this source of spurious results, in the present project $\dot{q}_s$ is evaluated with respect to the relative increase in wall temperature (light grey line in fig. 17-a). A portion of the heat transfer rate evolution is then extracted (dark grey line in fig. 17-a) that corresponds to the surface temperature variation taken 0.05[s] after the shutter opens for a total length of 0.15[s] (fig. 17-b), guaranteeing in fact the main stream to be fully established as well as the semi-infinite condition to be respected everywhere as discussed above. A linear regression is then performed on the extracted record and the heat transfer rate for a surface temperature equal to the initial one (at the shutter opening) is extrapolated. In the end, by means of eq. 13, the convective heat transfer coefficient h is retrieved using $T_{01} - T_{w-initial}$.

5.3. *Convective heat transfer coefficient distribution around a profile with film-cooling*

In fig. 18 the distribution h/h_{ref} with three different pressure side cooling conditions is presented, being h_{ref} the convective heat transfer coefficient for the uncooled case and I the momentum flux ratio (eq. 15). The downstream isentropic Mach and Reynold numbers are nominally equal to 1.1 and $1.5 * 10^6$ respectively while the turbulent intensity was increased by means of a turbulence generator up to 5.3%.

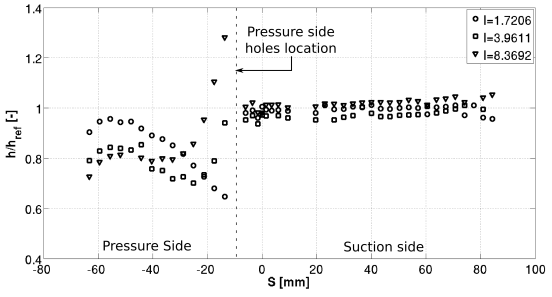

Figure 18: Evolution of h/h_{ref} with respect to the injection rate on the pressure side only

$$I = \frac{\rho_c V_c^2}{\rho_\infty V_\infty^2} \tag{15}$$

Given that only the pressure side holes are fed with coolant, the ratio keeps close to unity all along the suction side and also in the leading edge area before the location of the holes (dotted line in fig. 18). Immediately downstream the holes rows, the distributions drift from one and, for the lowest injection rate, it assumes a values as low as the 65% of the reference, highly increasing the protection of the surface. The distribution then increases slowly as the boundary layer tends to become fully turbulent but keeping always lower than one. By enhancing the injection, the evolution along the PS drastically changes in the proximity of the LE region: most probably the coolant flow momentum becomes high enough to trigger an early boundary layer transition that reduces therefore the protection of the surface. Further downstream, at about $S = 25[mm]$, anyway the trend is inverted and a re-laminarization of the boundary layer is obtained that clearly creates a better protection for the rest of the pressure side. A further increase of the injection rate critically decreases the protection performance immediately downstream the LE area, leading to values higher than unity. In this case the coolant momentum is so high that the holes jets are able to "drill "the boundary layer leading to an ingestion of hot air from the main stream that highly increases the magnitude of h. As soon as the boundary layer is reconstructed, h drops to values close to the intermediate injection condition.

5.4. Uncertainty analysis

The uncertainty on the convective heat transfer coefficient is a function of $\delta\dot{q}_s$, δT_{01} and δT_w. The two latter parameters are taken to be equal to $\pm 0.1[K]$ as they have been statically calibrated against a reference mercury thermometer with such a resolution. $\delta\dot{q}_s$ depends again on δT_w even though the highest contribution comes from the the uncertainty in the estimation of the thermal product $\delta\sqrt{\rho c k} = \pm 3\%$. The present uncertainty analysis takes also into account the fitting errors of the calibrations of both the films and the bridges. Taking conditions representative of the majority of the tests ($T_{01} = 420[K]$ for $T_w = 295[K]$) the uncertainty on the convective heat transfer coefficient was finally estimated by means of a perturbation analysis and found to be equal to $\delta h = \pm 6.8\%$.

6. Conclusions

The present paper describes the experimental methodology applied to the creation of an experimental test-case for numerical codes validation. Given that such a target necessarily requires a high reliability of the measured data, great attention has been paid to the design of each experiment to avoid any spurious sources of artefacts that could lead to wrong evaluation of the uncertainty. For each one of the three techniques previously described (hot-wire anemometry, pneumatic pressure probes and thin-films thermometry), a basic description of the measuring principle is provided, highlighting the limits of the technique and the actions taken to improve its performance. In the end, a typical measurement is presented and described and the uncertainty analysis for each technique is assessed by means of a perturbation method.

References

[1] L.S.G. Kovasznay, Hot-Wire Anemometer in Supersonic Flow, Journal of the Aeronautical Sciences 17 (1950) 565–572,584.

[2] L.S.G. Kovasznay, Turbulence in Supersonic Flow, Journal of the Aeronautical Sciences 20 (1950) 657–677,682.

[3] M.V. Morkovin, Fluctuations and Hot-Wire Anemometry in Compressible Flows, AGARDograph 24, AGARD (1954).

[4] B. Cukurel, S. Acarer , T. Arts, A novel perspective to high-speed cross-hot-wire calibration methodology, Experiments in Fluids 53 (2012) 1073–1085.

[5] KA Nagabushana, PC Stainback, Heat transfer from cylinders in subsonic slip flows, CR 4429, NASA (1992).

[6] H. Bergh, H. Tijdeman, Theoretical and Experimental Results for the Dynamic Response of Pressure Measuring Systems, NLR-TRF 328, Dutch National Aero and Astronautical Research Institute (1965).

[7] Paniagua G. , Denos R., Digital compensation of pressure sensors in the time domain, Experiment in Fluids 32 (2002) 417–424.

[8] G.L. Morrison, M.T. Schobeiri, K.R. Pappu, Five-hole pressure probe analysis technique, Flow Measurement and Instrumentation 9 (1998) 153–158.

[9] F.P. Incropera, D.P. DeWitt, T.L. Bergman, A.S. Lavine, Fundamental of Heat and Mass Transfer, John Wiley and Sons, 2011.

[10] Schultz and Jones, Heat-Transfer Measurements in Short-Duration Hypersonic Facilities, AGARDograph 165, AGARD (1973).

The Effect of Solidity on Compressor Performance and Stability

Jérôme Sans

Turbomachinery and Propulsion Department, von Karman Institute for Fluid Dynamics, Belgium, sans@vki.ac.be

Supervisor: Jean-François Brouckaert

Associate Professor, von Karman Institute of Fluid Dynamics, Turbomachinery and Propulsion Department, Belgium, brouckaert@vki.ac.be

Co-Supervisor: Tony Arts

Professor, von Karman Institute of Fluid Dynamics, Turbomachinery and Propulsion Department, Belgium, arts@vki.ac.be

University Supervisor: Philippe Chatelain

Professor, Université Catholique de Louvain, Institute of Mechanics, Materials and Civil Engineering, Belgium, philippe.chatelain@uclouvain.be

Abstract

The solidity in a compressor is the ratio of the aerodynamic chord over the pitch. The following PhD project aims at investigating numerically and experimentally the effect of the solidity on both compressor performance and stability. A low-pressure compressor stage designed and manufactured by TechSpace Aero and representative of a state-of-the-art booster helps to support the study. Existing compressor correlations are reviewed to extract the influence of solidity on deviation, incidence, losses and blade loading. Then, the effect of solidity is investigated by CFD with FINE/Turbo of NUMECA International. Rotor and stator blade numbers of TechSpace Aero's booster are varied independently to generate different compressor stages. The performance of all the configurations are assessed from choke to stall. The effect of solidity on pressure ratio, efficiency and stall limit is discussed. Finally, based on the same channel contour and design rotor pressure ratio of the DREAM project booster, the rotor solidity distribution is optimized at the level of the meridional calculation. This is achieved with an axial compressor design tool implemented at VKI coupled with the VKI optimization code. The importance of the maximum diffusion factor and the loss correlations along the span is highlighted.

Keywords: Compressor, solidity, pitch, chord, blade number

Nomenclature

Roman symbols

c	[m]	Aerodynamic chord length
s	[m]	Pitch
M	[-]	Mach number
p	[Pa]	Pressure
V	[m/s]	Absolute velocity
DF	[-]	Diffusion factor
D_{eq}	[-]	Equivalent diffusion ratio

Greek symbols

β	[°]	Flow angle
δ	[°]	Deviation angle
ϕ	[°]	Camber angle
θ	[m]	Momentum thickness
σ	[-]	solidity
ω	[-]	Total pressure losses
Ψ	[-]	Zweifel coefficient

Acronyms

DCA	Double circular arc
VKI	von Karman Institute

Subscript

0	Stagnation condition
1	Upstream condition
2	Downstream condition
s	Static condition
θ	Tangential direction

1. Introduction

The solidity is the ratio of the aerodynamic chord over the peripheral distance between two blades also called the pitch. This parameter must be selected early in the design process and the important role played by the solidity in the loading assessment makes its choice a crucial step that should be regarded with great care. Despite some spurious attempts to define an optimum solidity in terms of loading or efficiency, no general rule exists to guide the designer in this choice.

In the last decades, a constant increase of solidity in engine compressors has been noticed (Fig. 1). This reflects the need for the engineer to satisfy more and more severe high loading requirements that can only be achieved with high solidity. As

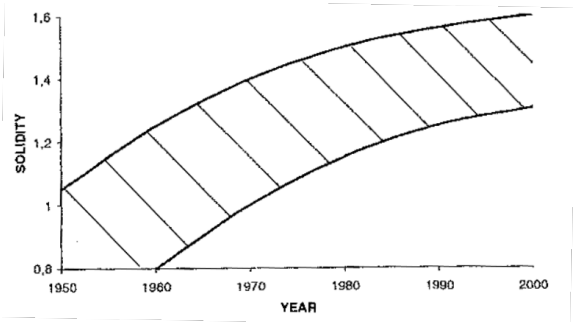

Figure 1: Evolution of the solidity in engine compressors over the last years [1] (Obrecht, 2006).

shown in Fig. 2, the solidity trend observed over the last 50 years is mainly explained by the use of long-chord blades (i.e. low aspect ratio[1]) which brought many experimental evidences of stability enhancements and a better behaviour with respect to secondary flows [2] (Wennerstrom, 1989). However, this chord enlargement is limited by the axial extent of the compressor which is imposed by mechanical requirements. Some improvements might still emerge

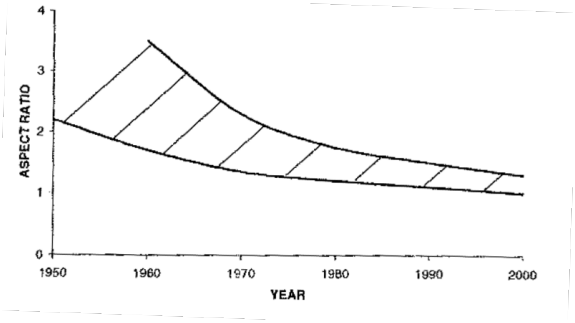

Figure 2: Evolution of the aspect ratio in engine compressors over the last years (Obrecht, 2006).

by looking at the pitch effect that is directly linked to the blade number.

Unfortunately, even though either a chord extension or a blade number increase allows to work at higher loading, both methods present the undeniable disadvantage of increasing the engine weight, meaning a higher fuel consumption and pollutant emissions. It is therefore essential to fully understand the benefits and the drawbacks when adjusting those parameters. In that prospect, the following PhD project aims at investigating numerically and experimentally the effect of the solidity on both compressor performance and stability. As a support to this investigation, the low-pressure compressor stage studied at VKI within the framework of the DREAM project is considered. The stage has been designed and manufactured by TechSpace Aero and is representative of a state-of-the-art booster. Its performance has been assessed both numerically with the CFD software FINE/Turbo^{TM} from Numeca International and experimentally in the VKI R4 facility.

The first part of the work covers all the existing compressor cascade correlations and tries to characterize the influence of solidity on deviation, incidence

[1]The aspect ratio is defined as the ratio of the blade height over the aerodyamic chord.

and losses. The important role played by solidity on the blade loading is also addressed.

After reviewing the literature, the effect of solidity is assessed through CFD. The study is achieved in 3D using the complete geometry and design conditions of the baseline booster of the DREAM project. Different stage configurations are analyzed by changing the blade number of both rotor and stator. The focus is set on the impact on pressure ratio and efficiency as well as the stability margin.

Finally, an axial compressor design tool recently implemented at VKI is used to investigate the issue of the optimum solidity from a designer point of view. The channel contour of the R4 stage is kept the same and only the rotor solidity profile is optimized at the level of the meridional stage.

2. Literature review

Despite the fact that the flow in axial compressors is mainly governed by three-dimensional effects, cascade theory allows to shed some light on the physical phenomena taking place in the three-dimensional machine. Cascade correlations, presented in this section, essentially come from the 1960's. They may have been corrected since then by engine manufacturers but all compressor designers once dealt with those data.

The required geometrical definitions follow the NASA-SP36 conventions ([3], 1965). They are given in Fig. 3. The angles refer to the axial direction and are usually given in degrees.

- β_1 relative inlet flow angle;
- β_2 relative outlet flow angle;
- κ_1 inlet blade metal angle;
- κ_2 outlet blade metal angle;
- ϕ camber angle;
- i incidence angle;
- δ deviation angle;
- γ stagger angle;
- c aerodynamic chord;
- s pitch.

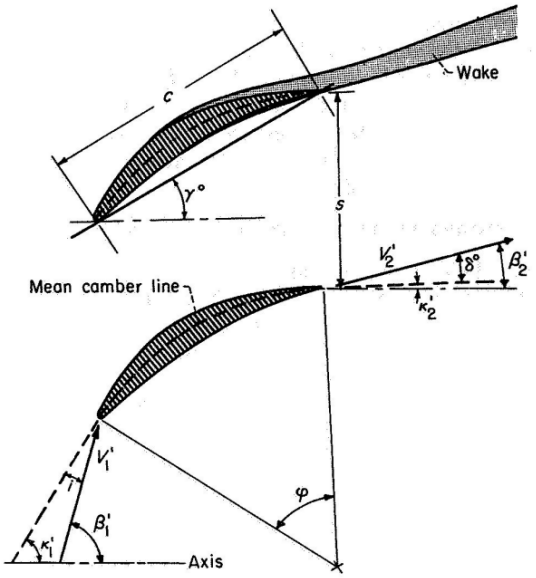

Figure 3: Geometrical configuration and angle definition in a compressor cascade

Three parameters are commonly used to characterize the performance of compressor cascades: the incidence, the deviation and the pressure losses. The angles are defined in Fig. 3 while the losses are given by Eq. 1.

$$\bar{\omega} = \frac{p_{02} - p_{01}}{p_{01} - p_{s1}} \tag{1}$$

The minimum loss incidence is considered as the reference incidence and is illustrated in Fig. 4. Correlations have been established from low-speed (i.e. $M < 0.3$) cascade tests performed on NACA65 and DCA blades of various solidities, thicknesses, camber angles and inlet flow angles. Hence, knowing the type of blade (NACA65 or DCA), the turning, the maximum thickness and the solidity, the designer is able to predict the optimum incidence, the deviation and the total pressure losses.

Regarding the deviation angle, Carter ([4], 1949) highlighted with Eq. 2 the guidance role of the solidity: the higher the solidity, the better the flow follows the blade and the lower is the deviation. The famous Carter's rule directly relates the deviation to the camber and the solidity. The empirical coefficient m of Eq. 2 is tabulated in [4]. Carter's law has been used for decades to design axial compressor bladings but nowadays, NASA's correlation are considered as

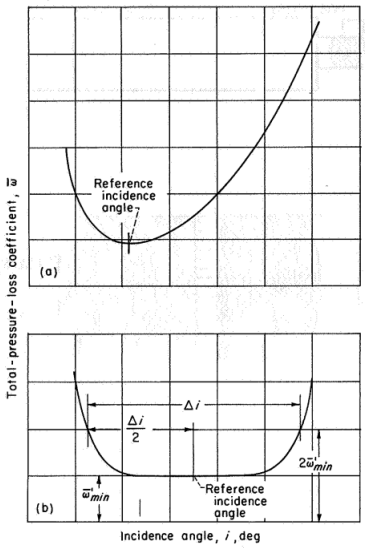

Figure 4: Definition of the reference incidence angle:(a) minimum loss angle clearly defined; (b) minimum loss angle taken as the mean of the incidence angle range defined by the angles where the losses reach twice its minimum value.

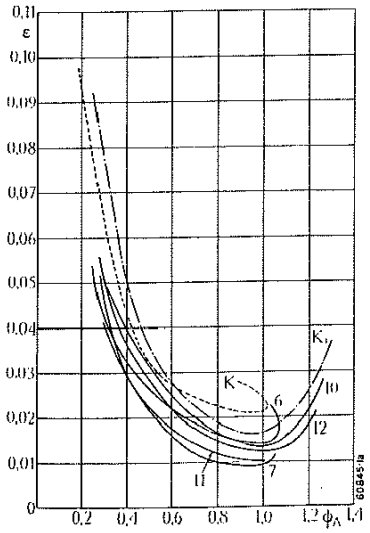

Figure 5: Drag-lift ratio in function the Zweifel loading factor Ψ for different type of blading [5] (Zweifel, 1945).

more reliable, more accurate and more systematic.

$$\delta = m\phi\sqrt{\frac{1}{\sigma}} \tag{2}$$

The solidity also plays an important role in the blade loading. The loading assessment is essential to characterize in which conditions the blade is operating. The first attempt in characterizing the loading comes from Zweifel (1945, [5]) comparing the lift of the blade to a reference lift based on the outlet velocity. After arrangement, the Zweifel coefficient Ψ is given below:

$$\Psi = \frac{\Delta V_\theta (V_1 + V_2)}{\sigma V_2^2} \tag{3}$$

To establish this coefficient, Zweifel relied on different cascade tests from turbines and compressors. Surprisingly, this coefficient has the remarkable property that for many different blades the minimum drag-lift ratio is independent on the inlet and outlet flow angles β_1 and β_2 and always lies between $\Psi = 0.9$ and $\Psi = 1$. This is illustrated in Fig. 5.

This means that, for given β_1 and β_2, an optimum pitch distance can be defined in order to operate at maximum lift-drag ratio. The data used by Zweifel mainly come from turbine cascade tests but his method can be trusted to select an optimum pitch -at least as a first guess- in compressor blade design. Eck ([6], 1973), Wallis ([7], 1983) or Dixon ([8], 1998) refer to Zweifel's optimum pitch distance when designing optimum fan blades. This parameter is also mentioned by Obrecht ([1]) when addressing the loading assessment of compressor blades.

Regarding the loading and the stability limit of cascades, the greatest advancement comes from Lieblein and his diffusion factor in 1953 [9]. It was admitted that the suction side boundary layer, facing an adverse pressure gradient, was responsible for the limiting pressure rise and turning of the flow. Therefore, Lieblein linked the suction side deceleration of the flow to a local diffusion factor:

$$D_{loc} = \frac{V_{max} - V_2}{V_2} \tag{4}$$

where V_{max} is the peak suction side velocity and V_2 the outlet velocity. Under the form of Eq. 4, the calculation of the diffusion factor was very time-consuming and not practical. A simplified diffusion factor was then defined to assess the loading of the blades:

$$DF = (1 - \frac{V_2}{V_1}) + \frac{\Delta V_\theta}{2V_1\sigma} \tag{5}$$

This simplification brings up the outlet-inlet velocity ratio, the tangential velocity difference as well as the solidity. Then, Lieblein put the wake momentum thickness in relation with the diffusion factor for many various types of blading as illustrated in Fig.

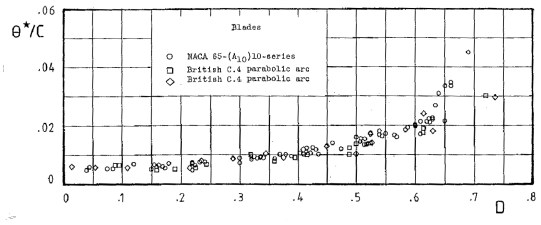

Figure 6: Variation of the wake momentum thickness with diffusion factor [3] (Robbins et al., 1965).

6 from [3]. The wake momentum thickness starts to rise more steeply for diffusion factors above 0.6. Therefore, a diffusion factor of 0.6 has been selected as the inception of blade stall.

Because the measurement of the blade momentum thickness is not always realizable, Lieblein proposed to use loss parameters which would mainly rely on the total pressure losses and flow angles and which would closely approach the wake momentum thickness. Those are given by:

$$\frac{\theta}{c} \approx \frac{\omega \cos(\beta_2)}{2\sigma} \tag{6}$$

$$\frac{\theta}{c} \approx \frac{\omega \cos(\beta_2)}{2\sigma} \left(\frac{\cos(\beta_2)}{\cos(\beta_1)}\right)^2 \tag{7}$$

All Lieblein's results are gathered on Fig. 7 using the loss parameters of Eq. 6 and Eq. 7. Plotted in function of the diffusion factor, the two curves of Fig. 7 offer good approximations of Fig. 6. The loss parameter of Eq. 6 is the most common one (because it is easier to measure) and the most widely quoted in the literature. It remains more or less constant and close to 0.007 until a diffusion level of 0.6. However, the second loss parameter of Eq. 7 looks to be a better indicator of stall.

The work of Lieblein allows to shed light on the role played by the solidity in the appraisal of the loading and the losses. An increase of solidity allows to reduce the diffusion factor but gives more total pressure losses. It also helps to lower the diffusion ratio and, then, to delay the stall emergence. When the solidity decreases, the losses follow until the diffusion ratio approaches its limit. When the solidity is too low, the blade is highly loaded and operates close to separation at very low diffusion factor and high pressure losses. The designer is thus confronted to a trade-off between low losses and high stability.

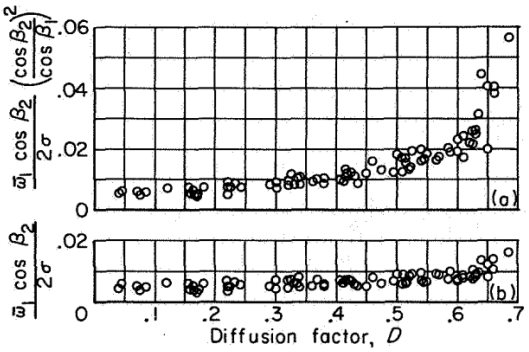

Figure 7: Variation of downstream losses in function of the diffusion factor [3] (Robbins et al., 1965).

Later, Lieblein provided new correlations of momentum thickness (and loss parameter) in terms of an equivalent diffusion ratio [10]. This equivalent diffusion ratio expresses the ratio of the maximum suction side velocity to the inlet velocity. This approach encountered a great support and has been used and adapted by many as Koch and Smith ([11], 1976) or Wright and Miller ([12], 1991). It is widely accepted that Koch and Smith data are the most complete and accurate. In the prospect of this paper, Lieblein's data are more convenient to understand the role played by the solidity in the loading assessment and the loss development.

3. Numerical investigation: preliminary study

3.1. Introduction

Since nowadays computational means are easily available, it appears very appealing to approach the effect of solidity by CFD. The investigation is performed on the DREAM project booster and the effect of both rotor and stator blade number variation is studied. The LP compressor used in the current section has been studied at VKI both numerically with the commercial software FINE/Turbo of NUMECA International and experimentally in the high-speed R4 facility (Sans et al., 2013, [13] and [14]). A 3D view of the stage preceded by inlet guide vanes is available in Fig. 8.

The whole 1.5 stage has been considered and rotor and stator blade numbers have been varied independently. For each different blade number a new mesh has been created. The baseline mesh and its properties are extensively described in [15]. In order to optimize the post-processing the number

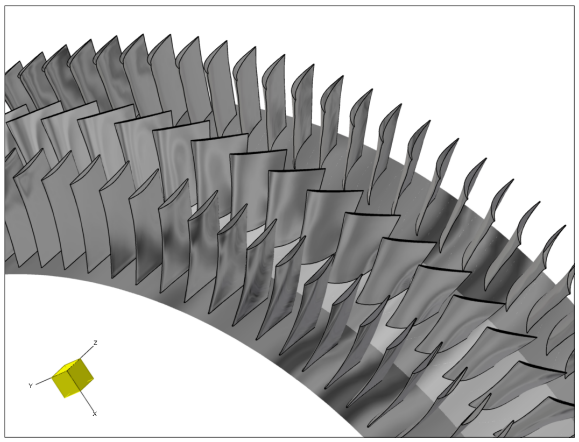

Figure 8: Three-dimensional view of the 1.5 stage (inlet guide vanes, rotor, stator).

of points and configuration of the meshes remain constant and only the blade periodicity is varied from one case to another. The boundary conditions are part of the specifications of TechSpace Aero as well as the turbulence model that is the low Re Yang Shih k-ϵ model. The compressors have been throttled by increasing the static pressure at stator outlet and always ensuring the radial equilibrium. Approaching the stall region the back-pressure has been raised iteratively to find the last stable conditions. This point has been considered as the stall point.

The booster has been designed in a way that the stall starts from the rotor hub (between 20% and 40% of the blade height from the hub). This has been done by recambering the blade locally (between 20% and 40% of the span). Those blade sections operate at higher incidences that tend to promote the stall. Unfortunately, as it will be presented below, such a design choice may compromise the stability analysis of the compressor.

3.2. Influence of rotor blade number

The performance of three different rotors have been assessed from choke to stall. The corresponding blade numbers are indicated in the Table 1. The rotor pressure ratio and efficiency are plotted in Fig. 9 and Fig. 10. Looking at Fig. 9, it appears that the high solidity rotor achieves the highest pressure ratio. This is in agreement with cascade theory or Carter's rule (Eq. 2) which predicts that the deviation is reduced when the solidity increased. As the deviation is lower, the flow turning increases and more pressure rise is achieved. However, the situation is not so obvious at

TESTED ROTOR SOLIDITIES				
	Blade number	σ_{hub}	σ_{tip}	Relative to design (%)
Design	66	1.32	1.09	-15%
	76	1.52	1.26	-
	86	1.72	1.43	+15%

Table 1: Tested rotor blade numbers and solidities

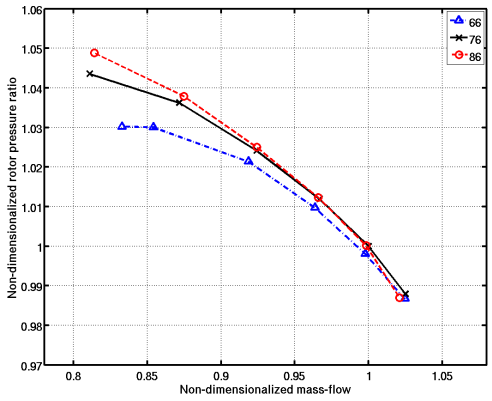

Figure 9: Rotor pressure ratio versus mass-flow for 66, 76 and 86 rotor blades on DREAM compressor.

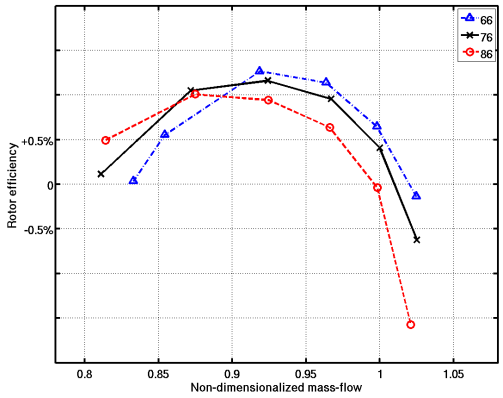

Figure 10: Rotor efficiency versus mass-flow for 66, 76 and 86 rotor blades on DREAM compressor.

choke.

The effect on the maximum efficiency is clear and the lowest solidity shows the best efficiency. This is rather expected as cascade correlations predict less losses for low solidity. Nonetheless, the trend does not remain the same on the whole operating range.

The low solidity rotor is less stable. This is most probably coming from a very high diffusion on the blades. No improvement appears between the mid and the high solidity rotors. It is believed that the expected stability enhancement of the high solidity rotor is injured by the blade recambering between 20% and 40% of the span.

3.3. Influence of stator blade number

The influence of stator solidity has also been studied by changing the number of vanes. The tested stator solidities are available in the Table 2. In

TESTED STATOR SOLIDITIES				
	Blade number	σ_{hub}	σ_{tip}	Relative to design (%)
Design	80	1.47	1.46	-20%
	100	1.83	1.82	-
	120	2.20	2.19	+20%

Table 2: Tested stator blade numbers and solidities

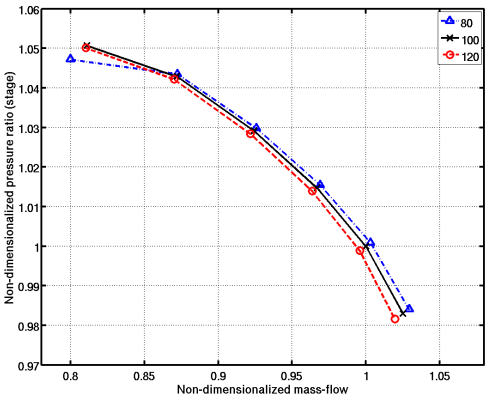

Figure 11: Stage pressure ratio versus mass-flow for 80, 100 and 120 stator blades on DREAM compressor.

terms of efficiency and pressure ratio, the effect of stator solidity is more straighforward than for the rotor. Removing blades improve both pressure ratio (Fig. 11) and efficiency (Fig. 12). When there is no work addition, a blade row only represents a source of friction losses that decreases the total pressure. Then, the same temperature rise is achieved whatever the number of blades while less pressure losses are encountered when less stator vanes are present. It results in a higher pressure ratio and a higher efficiency. The opposite happens with adding

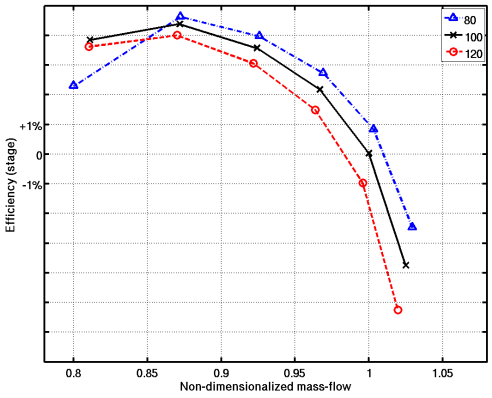

Figure 12: Stage efficiency versus mass-flow for for 80, 100 and 120 stator blades on DREAM compressor.

some blades. These conclusions are in agreement with cascade correlations. Regarding the stability, no difference appears between the 100 and 120 blades stators. This is due to the rotor that has been designed to induce the stall. Increasing the stator loading by lowering its solidity brings the stall to the stator. Comparing the 80 (Fig. 13) and the 120 (Fig. 14) stator blades configuration with total pressure maps reveals a clear total pressure deficit around the tip sections of the low solidity stator.

The latter observation highlights that the off-

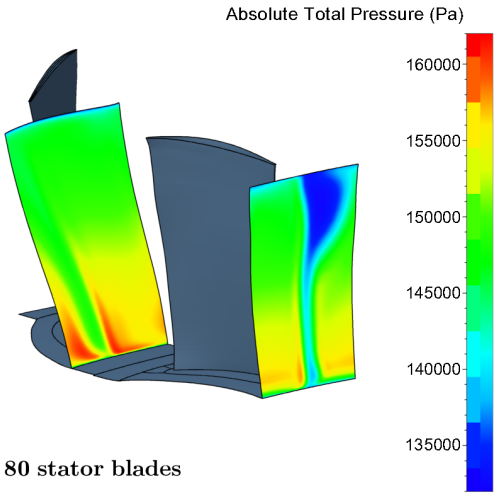

Figure 13: Stator outlet total pressure maps at near stall of the 80 stator blades configuration

design analysis is compromised considering the design and the recambering of the rotor. The solidity

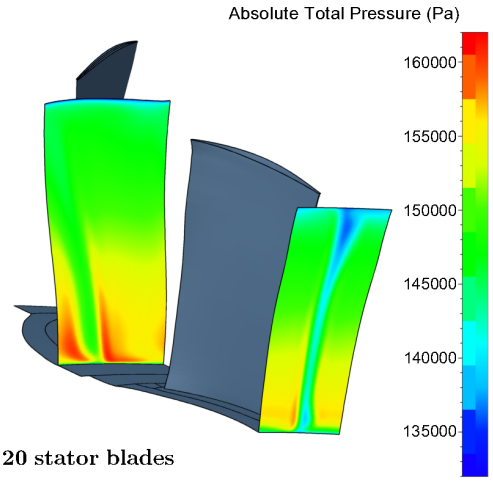

Figure 14: Stator outlet total pressure maps at near stall of the 120 stator blades configuration

is selected early in the design process and the whole meridional design relies on that choice. During the blade-to-blade and/or 3D optimization procedure, the solidity does not change anymore. Changing the solidity afterwards does not offer a fair comparison as the whole design would have been different if a lower or higher solidity had been selected. To really sit at the designer position, the solidity effect must be assessed on compressors designed for the same objectives with different solidity distributions. This approach would yield compressor designs having different blade shapes but, regarding the design target, being fully comparable.

4. Meridional design: optimum solidity

The solidity is chosen at the stage of the meridional design. It consists of solving the NISRE equations iteratively until the desired pressure ratio or efficiency is met. The designer requires an estimation of the losses that comes from experimental correlations such as the ones offered by NASA ([3]). Knowing the blade metal angles along the span, a three-dimensional blade can be drawn. This first guess can finally be optimized through 3D RANS computation. During the optmization process, the solidity does not change anymore. It is therefore important to focus on the optimum solidity as early as possible, i.e. at the level of the meridional design.
In industry, some axial compressor design tools enable off-design predictions at the level of the meridional calculation. Such programs allow to specify a stall margin as a design target. For the present work, a multi-stage axial compressor design program (referred as *ACD* in the rest of the paper) from (1968, [16]) has been implemented at VKI and has been coupled to an optimization algorithm to find the solidity distribution providing the best efficiency for a specified pressure ratio distribution. Currently, the program does not offer yet off-design predictions.

4.1. Input definitions

The channel geometry is imposed and divided into a number of axial stations where the radial equilibrium equations will be solved. The mass flow, the inlet total pressure and temperature, the desired global mass-averaged pressure ratio and the rotating speed of every stage - if different - must be provided. If the flow does not enter the rotor axially, the rotor inlet tangential velocity distribution can be modeled by an IGV. For each stage, the following information is required:

- a normalized rotor pressure ratio distribution;
- stator outlet tangential velocity distribution;
- rotor solidity distribution;
- stator solidity distribution.

During the optimization process, only the rotor solidity distribution has been optimized. Since the pressure ratio is fixed and that only the efficiency must be maximized, the designer is facing a single objective optimization problem.
The R4 compressor stage studied within the DREAM project is used as test-case in this section. The channel geometry and the axial station repartition are available in Fig. 15. Both rotor inlet and stator outlet tangential velocity profiles have been imposed following the original design specifications. The desired normalized rotor pressure ratio distribution is given in Fig. 16. The design mass-averaged rotor pressure ratio has been set to 1.25. The stator solidity of the R4 stage is given and kept constant while the rotor solidity must be optimized in order to maximize the rotor efficiency. Despite the whole stage is calculated, only the rotor performance are considered. Finally, the maximum spanwise diffusion factor DF_{max} is an important constraint that must be provided by the designer. This parameter has a big influence on the result and will be discussed in the next sections.

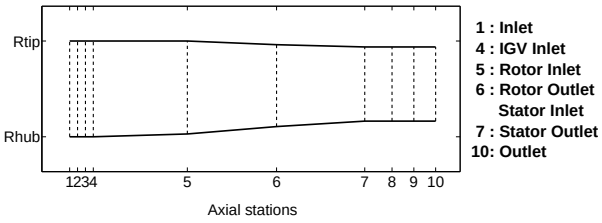

Figure 15: Channel and axial station repartition.

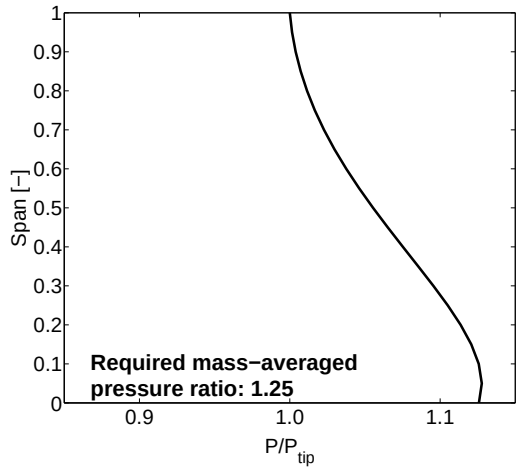

Figure 16: Normalized pressure ratio distribution to achieve a mass-averaged pressure ratio of 1.25.

4.2. Method and constraints

To get the optimum solidity, the VKI optimization code is employed. This code is based on a genetic algorithm and is extensively explained by Pierret (1999, [17]) or Verstraeten (2008, [18]). Firstly, random solidity distributions are generated. This constitutes the first generation of individuals. For each solidity distribution, ACD iterates until it converges to the loading distribution yielding the desired pressure ratio. Only the individuals that have a diffusion factor below DF_{max} are kept and considered as successful. All the others are discarded. Among the successful cases, a new generation is generated according to the genetic algorithm in order to produce new candidates providing better efficiency. For a given DF_{max}, convergence was reached on one single solidity profile after 50 generations of 200 individuals.

4.3. Results

To get a reference, ACD has been run to achieve the required pressure ratio with the current rotor solidity distribution of the R4 stage, releasing any diffusion factor constraint. The maximum diffusion factor along the span reaches 0.38. Optimization studies have then been performed with DF_{max} of 0.38, 0.40, 0.42, 0.45 and 0.50. The optimum solidity distributions are given in Fig. 17. They are distinguished by $\sigma_{0.38}$, $\sigma_{0.40}$, $\sigma_{0.42}$, $\sigma_{0.45}$, $\sigma_{0.50}$ and σ_{R4} respectively for the results with DF_{max} of 0.38, 0.40, 0.42 and 0.45 and with the R4 solidity distribution.

Firstly, it is easy to observe that when higher

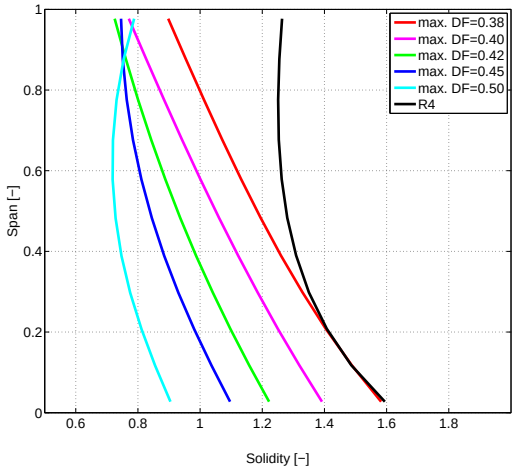

Figure 17: Optimum solidity distributions for various maximum diffusion factors

diffusion factors are allowed, the mean solidity level decreases. Looking at the spanwise profile, it is interesting to see, that, apart from the σ_{R4} distribution, for $DF_{max} \leq 0.42$, the profiles are quite linear. To understand better this behaviour, the diffusion factor spanwise distributions have been plotted in Fig. 18. It can be seen that for $\sigma_{0.38}$, $\sigma_{0.40}$ and $\sigma_{0.42}$, the diffusion factor distributions are uniform. For $\sigma_{0.45}$ and σ_{R4}, the distributions are quite similar but they are not linear anymore. Comparing $\sigma_{0.38}$ and σ_{R4} that have the same maximum diffusion factor along the span, it appears that the hub sections have quasi the same solidities and diffusion factor. Going to the tip radii, the $\sigma_{0.38}$ profile keeps the diffusion factor around 0.38 while the σ_{R4} profile experiences lower loading by slightly raising the solidity in the tip sections.

The rotor efficiency are plotted in Fig. 19. From the hub to 70% of the blade height, the lower the solidity, the higher the efficiency. For the last 30%, the trend is less obvious and the most efficient solidity appears to be $\sigma_{0.42}$. Regarding $\sigma_{0.38}$ and σ_{R4} candidates, results are predictable: the efficiencies are the same close to hub because solidities are the same and, around the

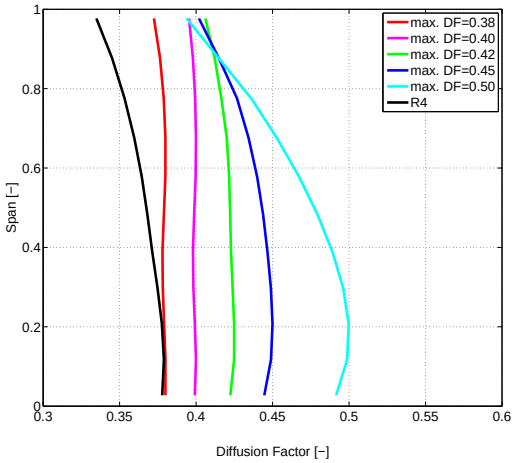

Figure 18: Diffusion factor distributions of the optimum solidity candidates

tip, the $\sigma_{0.38}$ profile has a better efficiency since its solidity is lower.

To fully understand these results, one should look at the loss correlations used in ACD (directly coming from [3]). They vary along the span and have been plotted in Fig. 20. One can now understand that the resulting solidity distributions depend on both the maximum diffusion factor and the loss variation along the span. As displayed in Fig. 20, for a rotor, hub losses are greater than mid span losses but the profile is only translated from the mid-span curve to higher losses. Its dependence regarding the diffusion factor is similar. It means that, if the pressure ratio was uniform, the mid-span optimum solidity would tend to be the same as the hub optimum solidity. However, with the same solidity and working at the same diffusion factor, the efficiency at the hub will be lower than the efficiency at mid-span as the loss mean levels are different. Tip losses start at the same level as the mid-span curve but when the diffusion factor reaches 0.40, the slope rises. It represents the loss increase observed in axial compressor due to the influence of the tip leakage vortex at high loading. Such an evolution in the loss pattern explains why, for $DF_{max} \leq 0.40$, the obtained optimum solidity profiles yield to a uniform loading distribution. Allowing higher maximum diffusion factors changes the loading distribution: the optimum solidity tries to keep the loading as close as possible to 0.40 in the tip region but allows higher loading at the hub sections. This reflects the importance of the loss correlations. Numerical investigation are currently ongoing at VKI by Resmini (2013, [19]) to check and update the low-speed NASA correlations to more representative blades and flow conditions.

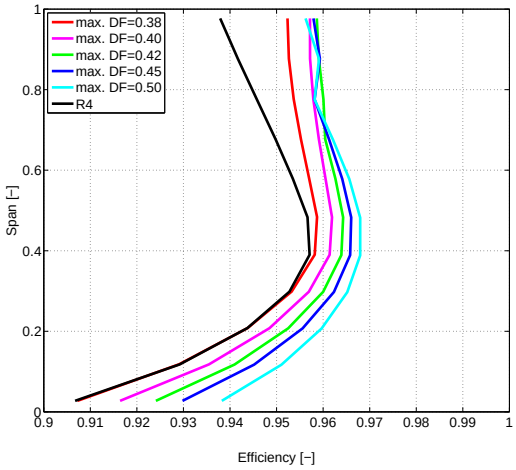

Figure 19: Efficiency distributions of the optimum solidity candidates

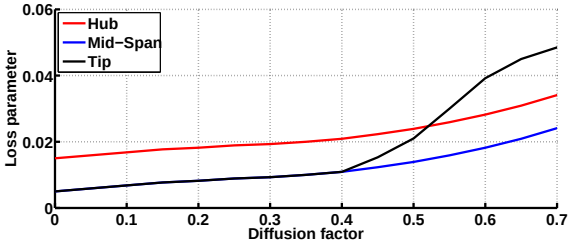

Figure 20: Loss correlations used in ACD

To complete this study the off-design performance should be analyzed. A blade generator has been implemented at VKI and the blades have already been designed for the different solidity distributions. The design and off-design performance will be investigated within FINE/Turbo. Expected trends are that the lower the solidity (i.e. the higher the design diffusion factor), the faster the stall appears.

5. Conclusion

The solidity effect has been reviewed in the literature to highlight the parameters the solidity could influence. A numerical investigation has been performed in order to see some effect on the booster designed and manufactured by Techspace Aero within the framework of the European DREAM project and studied both numerically and experimentally at VKI.

Both rotor and stator blade numbers have been varied independently to analyze their impact on the compressor performance. It appeared that:

- the higher the solidity, the lower the deviation and the better the guidance;
- the higher the solidity, the higher the losses (and the lower the efficiency)

For a rotor, the better guidance results in a higher turning and consequently, to a higher pressure ratio. A stator sees a higher solidity only as a source of higher losses. This is reflected in both lower efficiency and pressure ratio. The design of the rotor compromised the stability analysis. It is essential to perform the same comparison on compressors designed to achieve the same performance in terms of pressure ratio or efficiency.

This has been done by using ACD, an axial compressor design program implemented at VKI. For a given pressure ratio distribution, the solidity has been optimized at the level of the meridional design. This optimum depends on the maximum diffusion factor allowed. Results have been compared in terms of efficiency and loading distribution. They all provide the same pressure ratio but with different solidity profiles due to different maximum diffusion factor limits. The analysis revealed the importance of the loss correlations and, in that prospect, current numerical investigation are ongoing at VKI on a cascade geometry (cf. Fig. 21) (cf. [19]). This work will help to update ACD by using more representative loss correlations. Experimental investigation are also planned in the VKI C3 high-speed cascade facility to support the numerical investigation.

To finalize the study, based on ACD results, three-dimensional DCA blades will be designed and off-design calculations will be performed with FINE/Turbo on the different optimum candidates. This will allow to quantify the predictions of ACD and to assess the performance of the optimum compressors regarding the stall.

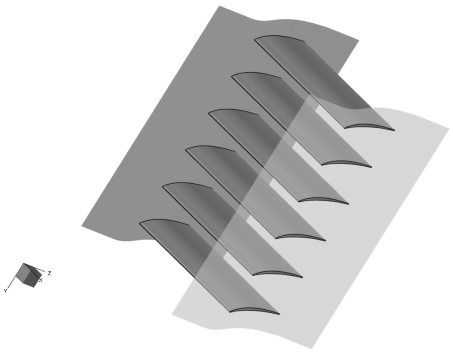

Figure 21: Cascade model used to study the solidity effect [19].

Acknowledgments

This research is supported by TechSpace Aero.

References

[1] Obrecht, T., HP compressor preliminary design, in: Advances in axial compressor aerodynamics, von Karman Institute for Fluid Dynamics Lecture Series, Belgium, 2006.
[2] Wennerstrom, A. J., Low aspect ratio axial flow compressors: why and what it means, Journal of Turbomachinery 111 (4) (1989) 357–365.
[3] Robbins, W. H., Jackson, R. J., and Lieblein, S., Aerodynamic design of axial-flow compressors, NASA SP-36 (1965).
[4] Carter, A. D. S., The low-speed performance of related aerofoils in cascades, A.R.C. Tech. Report, NGTE (September 1949).
[5] Zweifel, O., The spacing of turbo-machine blading, especially with large angular deflection, The Brown Boveri Review.
[6] Eck, B., Fans, Pergamon Press, 1973.
[7] Wallis, R., Axial flow fans and ducts, John Wiley & Sons, Inc., 1983.
[8] Dixon, S., Fluid mechanics, thermodynamics of turbomachinery, 4th Edition, Butterworth-Heinemann, 1998.
[9] Lieblein, S., Diffusion factor for estimating losses and limiting blade loadings in axial-flow compressor blade elements, Tech. rep., NACA, Lewis Flight Propulsion Laboratory, Cleveland, Ohio (June 1953).
[10] Lieblein, S., Loss and stall analysis of compressor cascades, Journal of Basic Engineering 81 (4) (1959) 387–400.
[11] Koch, C. C. and Smith, L. H. J., Loss sources and magnitudes of axial flow compressors, Journal for Engineering for Power.
[12] Wright, P. I. and Miller, D. C., An improved compressor performance prediction model, in: Proceedings of Institution of Mechanical Engineering, 1991.
[13] Sans, J., Desset, J., Dell'Era, G., and Brouckaert, J.-F., Performance Testing of a Low-Pressure Compressor, in: The 10th European Turbomachinery Conference, Lappeenranta, Finland, 2013.
[14] Sans, J., Desset, J., Dell'Era, G., and Brouckaert, J.-F., Time-Resolved Measurements of the Unsteady Flow Field in a Single Stage Low Pressure Axial Compressor, in: Proceedings of ASME Turbo Expo 2013, San Antonio, Texas, USA, 2013, ASME Paper No. GT2013-94264.
[15] Sans, J., Numerical Investigation of a Single Stage Axial Compressor, Master Thesis, von Karman Institute for Fluid Dynamics, Rhodes-Saint-Genese, Belgium, VKI PR 2010-10 (2010).
[16] Creveling, H. F. and Carmody, R. H., Axial Flow Compressor Design Computer Programs Incorporating Full Radial Equilibrium, NASA CR-54531 (1968).

[17] Pierret, S., Designing Turbomachinery Blades by Means of the Function Approximation Concept Based On Artificial Neural Network, Genetic Algorithm and Navier-Stokes Equations, PhD Thesis, von Karman Institute for Fluid Dynamics - Faculté Polytechnique de Mons, Rhodes-Saint-Genese, Belgium (1999).

[18] Verstraeten, T., Multidisciplinary Turbomachinery Component Optimization Considering Performance, Stress and Internal Heat Transfer, PhD Thesis, von Karman Institute for Fluid Dynamics - Universiteit Gent, Rhodes-Saint-Genese, Belgium (2008).

[19] Resmini, M., Numerical Investigation of the effect of solidity on compressor performance and stability, Master Thesis, von Karman Institute for Fluid Dynamics - Politecnico di Milano, Rhodes-Saint-Genese, Belgium, VKI SR 2013 (2013).

Development of a Conjugate Heat Transfer Solver in Coolfluid 3

Sebastian Scholl

Turbomachinery and Propulsion Department, von Karman Institute for Fluid Dynamics, Belgium, sebastian.scholl@vki.ac.be

Supervisor: Tom Verstraete

Assistant Professor, Turbomachinery and Propulsion Department, von Karman Institute for Fluid Dynamics, Belgium, tom.verstraete@vki.ac.be.

Promotor: Wolfgang Schröder

Professor, RWTH Aachen, Aerodynamisches Institut, Germany, office@aia.rwth.de.

Abstract

We developed a conjugate heat transfer solver for computations of conjugate heat transfer in rib roughened cooling channels of turbine blades. This solver is implemented within the collaborative, object oriented environment Coolfluid 3 using the domain specific language for the Finite Element Method provided by the framework. In future work, turbulence will be simulated and modeled via Large Eddy Simulation. The computations will be validated through the comparison with existing experimental data for the cooling channel flow.

Keywords: Conjugate Heat Transfer, Coupling Procedure, Turbine Blade, Cooling Channel, Large Eddy Simulation, Finite Element Method, Domain Specific Language

Nomenclature

Latin

b	solid plate width	$[m]$
Bi	Biot number	
D	Diameter	$[m]$
h	heat transfer coefficient	$[Wm^{-2}K]$
K,B,z	coefficients for analytic solution	
L	characterisitc length scale	$[m]$
p	pressure	$[Nm^{-2}]$
Pe	Peclet number	
Pr	Prandtl number	
q	heat flux	$[Wm^{-2}]$
r	relaxation factor	
Re	Reynolds number	
T	temperature	$[K]$
t	time	$[s]$
u	velocity	$[ms^{-1}]$

Greek

α	diffusion coefficient	
δ	coefficient for analytic solution	
λ^*	conductivity ratio	
λ_f	fluid conductivity	$[Wm^{-1}K^{-1}]$
λ_s	solid conductivity	$[Wm^{-1}K^{-1}]$
μ	dynamic viscosity	$[Pa^1s^1]$
ν	kinematic viscosity	$[m^2s^{-1}]$
ρ	density	$[kg^1m^{-3}]$

Abbreviations

BL	boundary layer
DS(E)L	domain specific (embedded) language
FEM	finite element method
FFTB	flux forward temperature backward
hFFB	heat transfer coefficient forward flux backward
hFTB	heat transfer coefficient forward temperature backward
LES	large eddy simulation
TFFB	temperature forward flux backward
VKI	Von Kármán Institute for Fluid Dynamics

Super- and Subscripts

∞	free stream quantity
b	quantity at the bottom of the solid domain
i	current time step
w	interface quantity from solid to fluid

1. Introduction

Trying to comply with the claims for environmental awareness and the rising use of energy, the turbomachinery industry improves the thermal efficiency of gas turbine engines in several regions, with the major contirbution to increase the turbine inlet temperature. Since the life time of turbine blades is reduced by half with an increased temperature of 30 Kelvin [1], the prediction of local heat transfer coefficients and temperatures is a crucial step towards the design of turbine blades.

In turbulated cooling channels of turbine blades (see figure 1), the complex flow field influences the temperature field at the interface to the solid. The flow field is itself affected by the temperature distribution at the interface. Since the temperature distribution is unknown a priori, we are dealing with a conjugate heat transfer problem.

For accurate calculations it is crucial to take both the heat conduction in the solid, and the fluid convection into account, exchanging boundary conditions from one solver to the other during the computations.

Albeit a significant influence of the conjugate heat transfer has been shown in experiments and numerical simulations, the coupled effect is neglected in most computations. Besides the need of two solvers, the varying time scales of the fluid and the solid make the computations expensive.

With a coupled approach, we aim to do conjugate heat transfer computations using large eddy simulations (LES), to resolve parts of the turbulent spectrum and to obtain an unsteady solution needed for conjugate heat transfer predictions. The cost of the expensive LES is further increased by the coupled calculations.

We implemented four coupling procedures - one of which has recently been developed at VKI - into the collaborative environment for multi-physics COOLFLuiD 3, validated them by comparing the numerical with an existing analytical solution for a flat plate conjugate heat transfer test case to investigate the different procedures considering their stability properties.

Within COOLFLuiD 3 framework, a programming language has recently been developed, using the C++ boost proto library, to ease the implementation of new solvers for the finite element method (FEM). Building upon the FEM solvers for the Navier-Stokes equations and the solid conduction in COOLFluiD 3, we extended the existing solver and integrated the coupling procedures presented in this paper.

2. Literature review and motivation

The cooling channel flow can be turbulated by different objects such as ribs, pin fins, dimpled surfaces or by surface roughness. The channel geometry can be rectilinear or curved and the channel section can be squared or triangular.

We will focus on rectilinear, rib-roughened cooling channels. The following parameters affect the flow field inside the channel: The rib shape, the number of

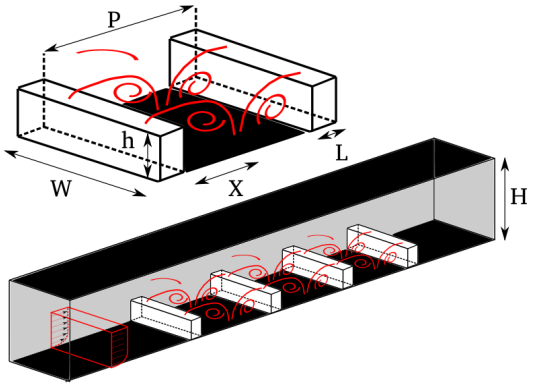

Figure 1: Schematic cooling channel

ribbed walls, the channel aspect ratio W/H with the channel width W and hight H, the rib angle of attack, the blockage factor h/D with the rib hight h, the channel hydraulic diameter D and the pitch to rib height ratio P/h. To fit into the blade, the channel geometry depends also on the blade shape. Moreover, the choice of the parameters is limited due to manufacturing constraints.

Overviews of investigations of the parameter influence on the flow field and the enhancement on the convective heat transfer are given by Lohasz [2], Casarsa [3], Lakshminarayana [4] and Han [1]: An increased blockage ratio h/D increases heat transfer [5] [6]. The pressure drop increases with a higher rate than the heat transfer as shown by Han et al.[7]. The effect of the pitch to rib high ration has also been investigated [7], Taslim[6],[8],[9]). It can be summarized that a ratio of P/h 10 is a good choice in terms of heat transfer enhancement for most geometries. If $P/h << 10$, the flow does not reattach and thus is less turbulated. For $P/h >> 10$, the reattached flow redevelops and thus decreases heat transfer while not decreasing the pressure drop. An increased angle of attack also increases both heat transfer and pressure drop [10]. Angles of 45 were found to give the greatest enhancement [9], dependent on the channel aspect ratio [5]. Further-

more, the studies suggest an angle of $45 - 60°$ for narrow channels and $30 - 45°$ for wide channels. The influence of the rib shape on the flows has also been investigated. V-shaped ribs augment the heat transfer and increase it best with an 45 angle and aligned to the mean flow direction [5] [6]. Moreover, broken configurations perform better than full length objects. The heat transfer can further be augmented by adding obstacles to the upper and lateral walls [11]. For each additional ribbed wall the heat transfer is increased by about 10 %. For the channel aspect ratio, it was found that squared channels perform better than rectangular [12].
Most of both experimental and numerical investigations on conjugate problems treat the problem in an uncoupled manner, not taking both dependencies of the flow field on the temperature, but also the temperature field on the flow filed into account. Recent experimental studies investigated the conjugate problem taking the solid heat transfer into account, as performed by Cukurel [13] or by Coletti et al. [14] [15], have shown significant variations of the temperature distribution in comparison with uncoupled investigations. Numerical studies of conjugate heat transfer combined with LES have been done by Soto [16] and also came to the conclusion that the conjugate effect is important. The study showed the need for improvement for the conjugate heat transfer coupling method, since due to the varying time scales in the solid and the fluid domain, with this coupled approach, the solid domain did not fully converge.

3. Methods

3.1. Governing equations

The fluid (equations 1-3) and solid (equation 4) domains are governed by:

$$\nabla \cdot \mathbf{u} = 0 \tag{1}$$

$$\frac{\partial \mathbf{u}}{\partial t} + (\mathbf{u} \cdot \nabla \mathbf{u}) + \frac{\nabla p}{\rho} - \nu \nabla^2 \mathbf{u} = 0 \tag{2}$$

$$\frac{\partial T}{\partial t} + (\mathbf{u} \cdot \nabla T) - \alpha \nabla^2 T = 0 \tag{3}$$

$$\lambda_s \nabla^2 T = 0, \tag{4}$$

with the velocity vector $\mathbf{u}$, the temperature T, the pressure p, the density ρ, the diffusion coefficient α and the conductivity of the solid λ_s. Note that we apply unsteady fluid and steady solid equations for the conjugate heat transfer solver.

3.2. Solver

The solver is embedded into the framework COOLFLuiD 3, which is based on a component-based architecture made of reusable numerical methods and physical models.
The component that is used in this project is the plugin for the Unsteady Finite Element Method (UFEM), described by Janssens [17] discretizing the incompressible Navier-Stokes equations as described by Banyai [18], where the flow equations are solved by the second order accurate Pressure Stabilized Petrov Galerkin Finite Element method with a Streamline Upwind Petrov Galerkin stabilization. The time is integrated with a backward Euler scheme. The convective terms are linearized in time as described in [18]. The solid conduction is solved with a steady state Finite Element Method.
In the UFEM plugin, user requirements from a developers point of view are transformed into a Domain Specific Embedded Language (DSEL) that facilitates the implementation of equations in the formulation of the Finite Element Method. A Domain Specific Language (DSL) in general can be seen as a programming language that is closer on the demands of a developer, respectively on the modelling equations.
In the case of the UFEM plugin of COOLFLuiD 3 this DSL is embedded into the C++ programming language used for the implementation of the COOLFLuiD 3 kernel. This unique approach uses the boost proto library to define a new programming language for the implementation. The proto library itself is a DSL embedded into C++, and is valid C++ code. The purpose of the proto library is to ease implementations of Domain Specific Embedded Languages without loosing performance.
We extended the existing solver in COOLFluiD 3 using this domain specific embedded language with the scalar-advection equation, the Spalart-Allmaras turbulence model that will be used to obtain a mean velocity profile as inlet condition for the LES (to be superposed with a fluctuating velocity field), and four coupling procedures for conjugate heat transfer described in the following section.

3.3. Coupling Procedures

There are two main approaches to solve conjugate heat transfer problems. The monolithic approach (often also referred to as the conjugate method) uses one solver for both domains. The partitioned approach

(often referred to as the coupled method) uses different solvers for each domain. Further, there are different ways to use and improve both main approaches. For our approach, we use the partitioned method, which has the following advantages: Different solvers for solid and fluid domain can be used, also possibly different non-matching grids for different domains. It is possible to deal with the varying time scales in the solid and the fluid domain by using an unsteady fluid solver and a steady solid solver and solving multiple fluid iterations before passing boundary conditions to the solid. With a partitioned method, the solid does not need to be solved for each fluid iteration and more important, the fluid does not need to be solved for the total amount of time corresponding to the solid characteristic time scale.
Four different methods partitioned methods exist - one of which has been developed at VKI - that have different stability properties as shown by Verstraete [19]. The stability depends on the Biot number:

$$Bi = \frac{hL}{\lambda_s}. \tag{5}$$

The physical meaning of this dimensionless number can be interpreted as the ratio of conductive resistance in the solid L/λ_s, with the solid conduction coefficient λ_s and the convective resistance in the fluid boundary layer 1/h with the heat transfer coefficient h.

3.3.1. The flux forward temperature back method

The flux forward temperature back method (often referred to as the FFTB method, named from the perspective of the fluid domain) imposes a wall temperature distribution to the fluid solver. After the fluid calculation the resulting heat flux distribution is imposed to the solid conduction solver, which returns an updated temperature in turn imposed to the fluid domain. The exchange of boundary conditions is repeated until continuous temperatures and heat fluxes between both domains. The FFTB procedure is stable for $Bi < 1$. With a relaxation factor r simulations for $Bi > 1$ can be done with the drawback of slower convergence. The relaxation is used for the exchange of the boundary conditions as follows [19]:

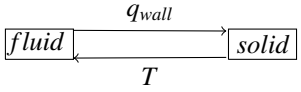

Figure 2: FFTB coupling.

$$T_{wall}^{fluid,i} = r_T \cdot T_{wall}^{fluid,i-1} + (1 - r_T) \cdot T_{wall}^{solid,i-1}, \tag{6}$$

and:

$$q_{wall}^{solid,i} = r_q \cdot q_{wall}^{solid,i-1} + (1 - r_q) \cdot q_{wall}^{fluid,i-1}, \tag{7}$$

with the current iteration step i fluxes q and temperature T. The stability criterion is then: $Bi < \frac{1+r}{1-r}$.

3.3.2. The temperature forward flux back method

The temperature forward flux back method (often referred to as the TFFB method, named from the perspective of the fluid domain) imposes a heat flux distribution as boundary condition to the fluid solver. The resulting temperature is imposed to the solid solver, which returns a new heat flux distribution to the fluid domain. The TFFB method is stable if $Bi > 1$. With a relaxation factor r simulations for $Bi < 1$ are possible; again, with the drawback of slower convergence. The stability criterion is then: $Bi > \frac{1-r}{1+r}$.

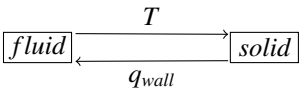

Figure 3: TFFB coupling.

3.3.3. The heat transfer coefficient forward temperature back method

The heat transfer coefficient forward flux back method (referred to as the hFTB method, named from the perspective of the fluid domain) starts with an initial temperature distribution as boundary condition for the fluid computation. It uses Newton's law of convective heat transfer to return a Robin (mixed type) boundary condition to the solid domain:

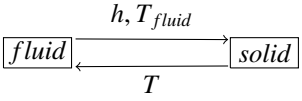

Figure 4: hFTB coupling.

$$q_{wall} = h \cdot (T_{wall} - T_{fluid}), \tag{8}$$

with the heat transfer coefficient h the heat flux q_{wall}, the temperature at the wall T_{wall} and the ambient fluid temperature T_{fluid}. T_{wall} and q_{wall} are passed to the solid solver as Robin condition. Note that h and T_{fluid} have to be computed for this method. This is done with the algorithm proposed in [19] that sets a fixed positive heat transfer coefficient. The advantage of this method is that after the one-dimensional stability criterion, it is stable for $Bi < 1$, but also for $Bi >= 1$, if an appropriate heat transfer coefficient for the method is used: $\hat{h} < 2h$, with the imposed heat transfer coefficient $\hat{h}$ and the actual heat transfer coefficient h.

3.3.4. The heat transfer coefficient forward flux back method

Verstraete [20] proposed a fourth method (referred to as the hFFB method, named from the perspective of the fluid domain), which imposes a heat flux distribution to the fluid domain returning mixed type boundary conditions to the solid solver. Again, for the mixed type boundary condition, Newton's law of convective heat transfer is used:

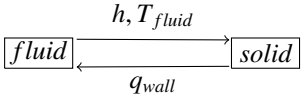

Figure 5: hFFB coupling.

$$q_{wall} = h \cdot (T_{wall} - T_{fluid}). \tag{9}$$

This method is stable for $Bi > 1$ and also for $Bi <= 1$, if an appropriate heat transfer coefficient is used: $\hat{h} > \frac{h}{2}$, with the imposed heat transfer coefficient $\hat{h}$ and the actual heat transfer coefficient h.

4. Results and Discussion

4.1. Validation of the transport equation

To validate the implemented transport equation, we did a test case described as follows. The considered domain is shown by figure 6. The velocity is constant over the whole rectangular domain. On the top and the bottom adiabatic boundary conditions were imposed. On the left and the right two distinct constant temperatures were set, such that the problem reduces to a one dimensional problem. We could compare our numerical simulation with an analytic solution given by:

$$\frac{T - T_0}{T_1 - T_0} = \frac{e^{Pe\frac{x}{L}} - 1}{e^{Pe} - 1}, \tag{10}$$

where ϕ is a scalar, in our case the temperature. The Peclet number is given by:

$$Pe = \frac{\rho u L}{\alpha}, \tag{11}$$

with the velocity u, a characteristic length L, density ρ and the diffusion coefficient α. Figure 7 shows the good agreement of the simulation with the analytic solution, where the discrete points show the numerical results. The lines represent the corresponding analytical solution.

4.2. Conjugate heat transfer of flow over a flat plate

For the validation of the implemented coupling procedures in COOLFluiD 3 we used a flat plate test case for conjugate heat transfer by Luikov [21] as described in[19].

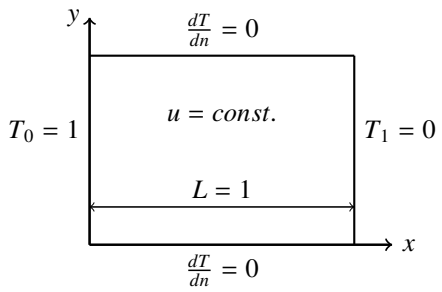

Figure 6: Domain for scalar-advection-diffusion test case

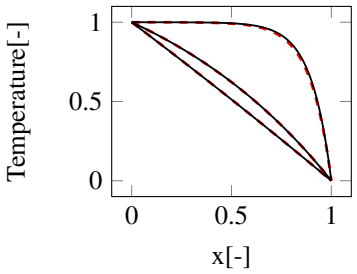

Figure 7: Validation test case for the scalar transport equation. Red dashed lines show the numerical results. The lines represent the corresponding analytical solution.

4.2.1. Problem description and its analytical solution

Luikov [21] provides two different analytical solutions for an incompressible flow over a flat plate with conjugate heat transfer (see figure 8) that we could use for a comparison with the numerical simulation of the different coupling procedures. The temperature at the interface is part of the solution rather than an imposed condition. The boundary conditions used were a constant pressure at the outlet, adiabatic conditions for the temperature and slip velocity conditions on the top and the front of the flat plate. A temperature T_b was imposed at the bottom of the solid part. Temperatures and fluxes exchanged at the interface, where a no slip condition was set for the velocity. The temper-

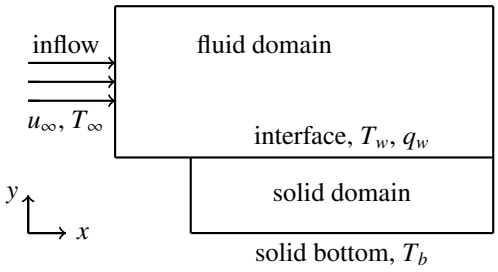

Figure 8: Domain for conjugate heat transfer test case

ature T_∞ and velocity u_∞ was specified at the inlet. The first analytical solutions, Luikov's differential heat transfer equation reads:

$$\begin{aligned}\frac{T_f(x,y)-T_b}{T_\infty-T_b} = \frac{K-\frac{1}{2}B}{K-B} exp[(K^2-BK)+\lambda^*\frac{y}{b}] \\ \cdot erfc\left(K-\frac{1}{2}B+\frac{1}{2}+\frac{1}{2}\lambda^*\frac{y}{Kb}\right)+\frac{1}{2} \\ erfc\left(\frac{1}{2}B-\frac{1}{2}\lambda^*\frac{y}{Kb}\right)-\frac{1}{2}\frac{exp\left[\frac{B}{K}\lambda^*\frac{y}{b}\right]}{1-B/K} \\ \cdot erfc\left(\frac{1}{2}B+\frac{1}{2}\lambda^*\frac{y}{Kb}\right),\end{aligned} \tag{12}$$

with the error function erfc, the Prandtl number Pr, the ratio of solid to fluid conductivity λ^* and the coefficients $K = \lambda^*\frac{x}{b}Pr^{\frac{1}{2}}\overline{Re}_x^{-\frac{1}{2}}$, $B = \frac{\bar{v}_y}{\bar{v}_x}\sqrt{Pr\overline{Re}_x}$, $\bar{v}_x = 0.66v_\infty$, $\bar{v}_y = 0.43v_\infty(\frac{xv_\infty}{\nu})^{-\frac{1}{2}}$, and an averaged local Reynolds number $\overline{Re}_x = \frac{x\bar{v}_x}{\nu}$.
The second analytic solution, derived from the boundary layer equation, lead for the fluid temperature to:

$$\begin{aligned}T_f(x,y) = T_w + \frac{3}{2}\frac{T_\infty - T_w}{\delta_T}\cdot y - \\ \frac{1}{2}\frac{T_\infty - T_w}{\delta_T^3}y^3,\end{aligned} \tag{13}$$

and for the solid temperature:

$$T_s(x,y) = T_w + \frac{T_\infty - T_w}{b}\cdot y. \tag{14}$$

The wall temperature is given by:

$$T_w(x) = T_b + (T_\infty - T_b)\frac{z}{1+z}, \tag{15}$$

with $z = \frac{3}{2}\lambda^*\frac{b}{\delta_T}$, $\delta_T = \delta\cdot\sqrt[3]{\frac{13}{14}}\cdot\sqrt[3]{\frac{1}{Pr}}$ and $\delta = \frac{4.64x}{\sqrt{Re_x}}$. Important for the simulations is the determination of the Biot number, which is described in [19].

4.2.2. Grid

Figure 9 shows the computational grid (for space 8, meaning it is 8 times smaller than the largest grid used for the grid dependence study which consisted of 240x80 grid points in the fluid domain) for the fluid and the solid domain. The first point indicates an extrapolated value for the temperature (using the Richardson extrapolation). Based on the grid dependence study we chose to use a grid with 120 grid points in the x direction and 40 points in the y direction for the fluid. 40 times 40 grid points were used in the solid domain for the shown gird and less grid points for a thin plate accordingly.

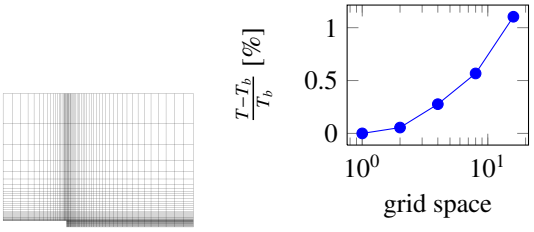

(a) Coarse grid.

(b) Grid study for simulations with $Bi = 1$. $T_b = 10$, $T_\infty = 0$. Figure shows temperature at the end of the flat plate.

Figure 9: Grid dependence study

4.2.3. Computation

Table 1 shows the flow conditions for the comparison with the analytical solution of Luikov as in [19] for the simulations. The Biot number is determined as in [19]: $\overline{Bi} = \frac{\bar{h}\cdot b}{\lambda_s}$, with the average heat transfer coefficient $\bar{h} = \frac{1}{L}0.664\lambda_f\sqrt[3]{Pr}\sqrt{Re}$. The Biot number was changed by varying the conductivity in the solid λ_s. The simulations started with adiabatic boundary conditions for the fluid until convergence (50 fluid iterations, see figure 15(a) and 15(b)). Then, boundary condiions were exchanged, with usually 10 fluid iterations to converge the fluid solution between one coupling iteration (see figure 15(a) and 15(b)). The procedure was repeated until a full convergence of the conjugate heat transfer problem. Figures 11, 10 and 12 show that the flat plate results are in good accordance with the analytical solutions provided by Luikov[21]. Moreover, the computations confirmed the stability criterion derived in [19] for all methods. For the FFTB method, the simulations were stable without a needed relaxation factor for Biot numbers smaller than one, which is in good accordance with the stability criterion. However, by reducing the time step as required for finer grids as for Large Eddy Simulations, the FFTB method destabilizes and needs to be relaxed also for Biot numbers equal unity or smaller than one. In turn, the TFFB method de-stabilizes for larger time steps or a larger amount of fluid solves per iteration. Further, the TFFB method showed wiggles at the leading edge of the flat plate for small Biot number (see figure 11). The heat transfer coefficient methods are advantageous over the latter two methods, since they

parameter	value	SI unit
Bi	varying	
Pr	0.6629	
Re	21418	
T_∞	1000	K
T_b	600	K
L	0.2	m
b	0.05	m
ρ	0.3525	kg/m^3
μ	$3.95 \cdot 10^{-5}$	Ns/m^2
λ_f	0.6808	W/mK

Table 1: Parameters used for the conjugate heat transfer test case.

provide the opportunity to adjust the convergence by adjusting the heat transfer coefficient. The only danger is a possible divergence by choosing a too unphysical heat transfer coefficient. Comparing the hFTB with the hFFB method, figures 17 and 18 show the hFFB method to be more stable and converging faster, not only for large Biot numbers, but also for Biot numbers of order unity.

The hFTB method never explicitly passes the heat flux. Figure 13 shows the continuity between solid and fluid domain for the hFTB method. The hFFB method never explicitly passes the temperature as boundary conditions between both domains. Figure 14 shows the difference of temperature between solid and fluid domain on the interface of the flat plate leading edge .

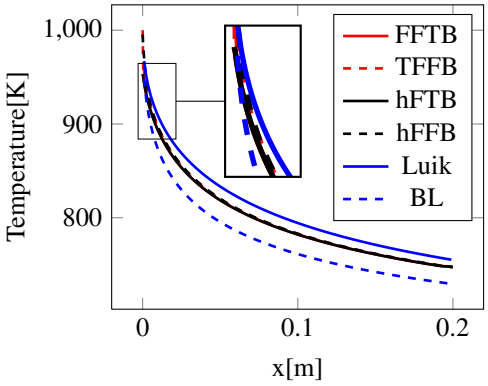

Figure 10: Comparison of the FFTB, TFFB, hFTB and hFFB methods with Luikov's Boundary Layer and differential heat transfer analytical equations showing the temperature distribution at the interface of the flat plate, with $Bi = 1$.

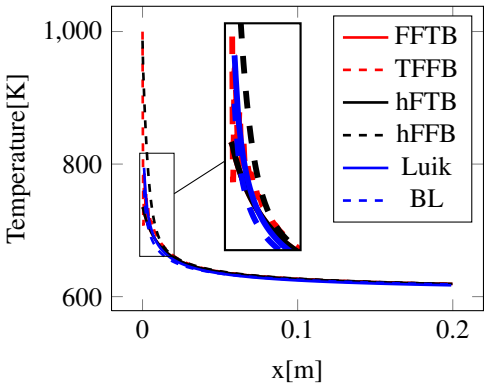

Figure 11: Comparison of the FFTB, TFFB, hFTB and hFFB methods with Luikov's Boundary Layer and differential heat transfer analytical equations showing the temperature distribution at the interface of the flat plate, with $Bi = 0.1$.

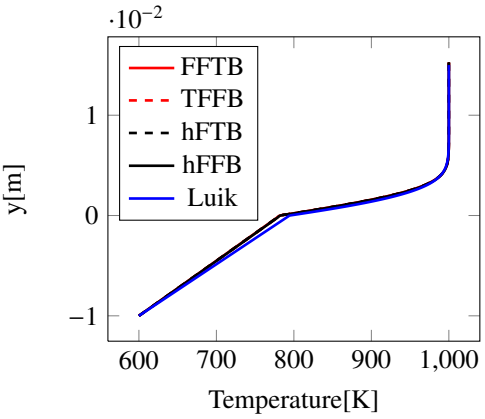

Figure 12: Comparison of the FFTB, TFFB, hFTB and hFFB methods with Luikov's Boundary Layer and differential heat transfer analytical equations at $x = 0$, with $Bi = 1$

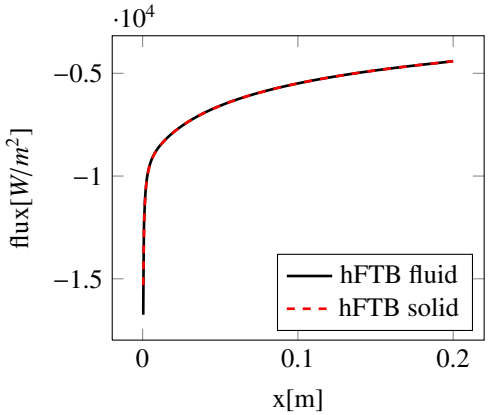

Figure 13: Comparison of the flux at the interface of the solid and fluid domain for the hFTB method, with $Bi = 1$.

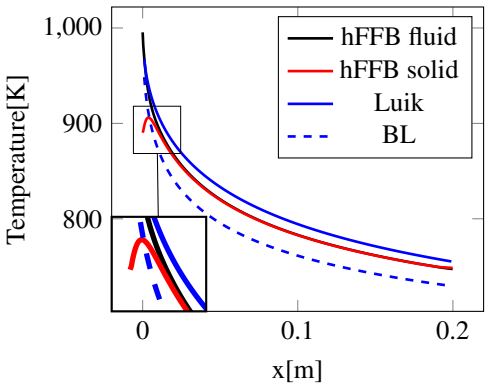

Figure 14: Comparison of the temperature in the solid and fluid domain for the hFFB method compared with Luikov's boundary layer and differential heat transfer analytical solutions showing the temperature distribution at the interface of the plate, with $Bi = 1$.

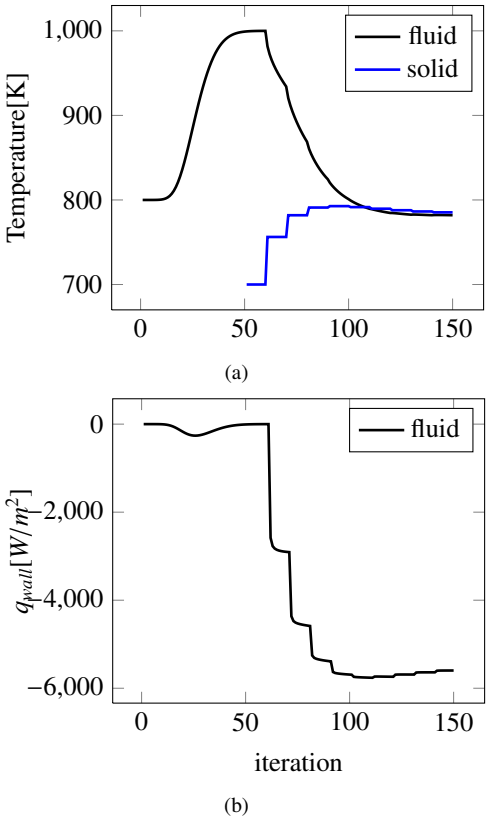

Figure 15: Evolution of temperatures (figure 15(a)) in solid and fluid domains and fluid flux (figure 15(b)) for the hFFB method at x=0.1m and y=0.0001m for $Bi = 1$ and a heat transfer coefficient of $h = 10W/m^2K$.

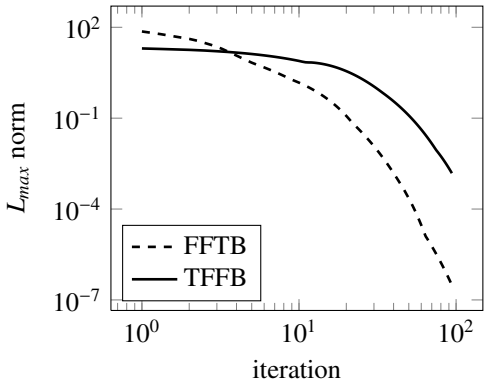

Figure 16: Convergence history for the heat transfer coefficient methods at $Bi = 1$ with an interval of 10 fluid solves per iteration.

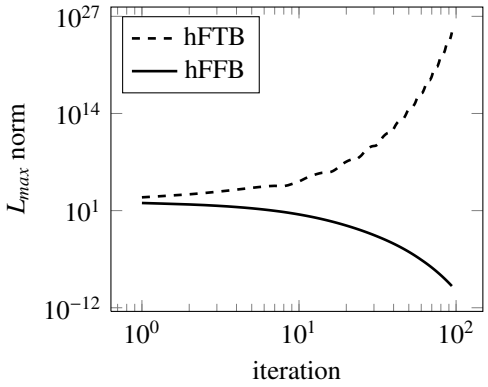

Figure 17: Convergence history for the heat transfer coefficient methods at $Bi = 1$ with an interval of 10 fluid solves per iteration and $h = 10W/m^2K$.

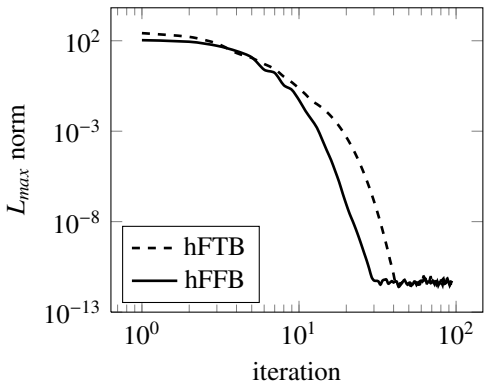

Figure 18: Convergence history for the heat transfer coefficient methods at $Bi = 1$ with an interval of 10 fluid solves per iteration and $h = 100W/m^2K$.

5. Conclusions

Within the unsteady finite element method plugin of COOLFLuiD 3 we coupled the fluid with the solid solver with different coupling strategies and could confirm the stability criterion previously derived by Verstraete [19] with the restriction of a counterintuitive de-stabilization of reducing time steps for the temperature backwards methods.
All methods are in good agreement with the analytical solution for a validation flat plate test case for conjugate heat transfer.
All methods have advantages in certain regimes of Biot numbers, but we found the hFFB method to be superior due to its faster convergence at Biot numbers of order unity in comparison with the other coupling methods. The behavior of all methods in conjunction with unsteady simulations remains to be investigated.
Future steps include the application of the conjugate heat transfer solver on cooling channel flow in conjunction with large eddy simulation.
Further investigations will involve acceleration techniques for the coupling by extrapolating values of the heat transfer coefficient.

Acknowledgments

The author is grateful to his supervisor Professor Tom Verstraete and Promotor Professor Wolfgang Schröder for the support and promotion of this doctoral research.
We would further like to thank Bart Janssens for his valuable help considering implementations in his programming language.
The research leading to these results has received funding from the European Community's Seventh Framework Programme (FP7, 2007-2013), PEOPLE programme, under the grant agreement No.FP7-290042(COPAGT project).

References

[1] J. Han, S. Dutta, S. Ekkad, Gas Turbine Heat Transfer and Cooling Technology, Taylor & Francis, 2000.
[2] M. M. Lohasz, Large eddy simulation of heat transfer in ribbed ducts, Ph.D. thesis, Budapest University of Technology and Economics and Von Karman Instititue for Fluid Dynamics (2008).
[3] L. Casarsa, Aerodynamic performance investigation of a fixed rib-roughened internal cooling passage, Ph.D. thesis, Universita Degli Studi Udine and Von Karman Instititue for Fluid Dynamics (2003).
[4] B. Lakshminarayana, Fluid Dynamics and Heat Transfer of Turbomachinery, John Wiley and Sons, 1995.
[5] J. Han, Heat transfer and friction in channels with two opposite rib-roughened walls, J. of Heat Transfer 110 (1984) 321–328.
[6] M. Taslim, T. Li, D. Kercher, Experimental heat transfer and friction in channels roughened with angled, v-shaped and discrete ribs on two opposite walls, ASME, 94-GT-163.
[7] J. Han, L. Glicksman, W. Rohsenow, An investigation of heat transfer and friction for rib-roughened surfaces., Int. J. of Heat and Fliud Flow 21 (1978) 1143–1153.
[8] K. Ichmiya, M. Yokoyama, R. Shimomura, Effect of several roughness elements for the heat transfer from a smoothed heated wall., Proceeding ASME/JSME Thermal Engineering Joint Conference 1 (1983) 359–364.
[9] M. Cakan, Aero-thermal investigation of fixed rib-roughened cooling passages, Ph.D. thesis, Universite Catholique de Louvain and Von Karman Instititue for Fluid Dynamics (2000).
[10] J. Han, Y. Zhang, C. Lee, Influence of surface heat flux ratio on heat transferaugmentation in square channels with parallel, crossed and v-shaped angled ribs, J. of Turbomachinery 114 (1992) 872–880.
[11] P. Chandra, M. Niland, J. Han, Turbulent flow heat transfer and friction in a rectangular channel with varying number of ribbed walles, J. of Turbomachinery 119 (1997) 374–380.
[12] J. Han, J. Park, Developing heat transfer in rectangular channels with rib turbulators., Int. J. of Heat and Mass Transfer 31 (1988) 183–195.
[13] B. Cukurel, Conjugate heat transfer investigation of a fixed rib roughened cooling passage., Ph.D. thesis, Purdue University and Von Karman Institute for Fluid Dynamics (2012).
[14] F. Coletti, A. Armellini, T. Arts, C. Scholtes, Aerothermal investigation of a rib-roughened trailing edge channel with crossing jets - part 2: Heat transfer analysis, ASME Journal of Turbomachinery 133 (2011) 031024–1 – 031024–8.
[15] F. Coletti, M. Scialanga, T. Arts, Experimental investigation of conjugate heat transfer in a rib-roughened trailing edge channel with crossing jets, ASME Journal of Turbomachinery 134.
[16] F. Garcia Soto, Investigation of interaction of coherent structures on heat transfer in ribbed duct, Master's thesis, VKI (2011).
[17] B. Janssens, T. Banyai, W. Bosschaerts, K. Limam, T. Arts, Discretization of the incompressible navier-stokes equations using a domain specific embedded language, 9th National Congress on Theoretical and Applied Mechanics.
[18] T. Banyai, D. Abeele, H. Deconinck, A fast fully-coupled solution algorithm for the unsteady incompressible navier-stokes equations, in: CMFF, 2006.
[19] T. Verstraete, Multidisciplinary turbomachinery component optimization consifering performance, stress, and internal heat transfer, Ph.D. thesis, Universiteit Gent (2008).
[20] T. Verstraete, Z. Alsalihi, R. A. V. den Braembussche, Numerical study of the heat transfer in micro gas turbines, ASME Journal of Turbomachinery 129 (2007) 835–841.
[21] A. Luikov, Conjugate convective heat transfer problems., International Journal of Heat and Mass Transfer. 17 (1974) 257–265.

Towards Full Annulus Coupled Simulations on Gas Turbines

Stefano Vagnoli

Turbomachinery and Propulsion Department, von Karman Institute for Fluid Dynamics, Belgium, stefano.vagnoli@vki.ac.be

Supervisor: Tom Verstraete

Assistant Professor, Turbomachinery and Propulsion Department, von Karman Institute for Fluid Dynamics, Belgium, tom.verstraete@vki.ac.be.

University Supervisor: Francesco Martelli

Professor, Energy Engineering Department, University of Florence, francesco.martelli@unifi.it

Abstract

In the design and analysis of gas turbines, Computational Fluid Dynamics (CFD) is nowadays widely used to analyze every part of the engine. Because of this, specialized flow solvers have been developed, and every component is thus analyzed separately. When the flow in compressors and turbines is studied, phenomena such as the reproduction of turbulent or transient boundary layer and separation regions are of primary concern. Due to the lower computational costs, RANS approaches are usually employed. On the other hand, when the flow in combustion chamber is analyzed, many different phenomena have to be accurately reproduced, such as mixing between reactive and non-reactive flows, heat release, aeroacoustic oscillations. An LES approach demonstrates to be more accurate to correctly analyze such phenomena.
The idea of this work is to try to couple solvers developed for different parts of the machine to analyze interactions between components. At the end, the objective is to obtain a full annulus coupled analysis of a real engine.
In fact, this would lead to the accurate analysis of many phenomena that cannot be reproduced by traditional approaches: compressor-combustor instabilities, combustor-turbine hot-streak migration and combustion instabilities, as well as nonperiodic phenomena that cannot be reproduced by imposing classical periodic conditions on single blade passages.

Keywords: Coupling, Large Eddy Simulation, gas turbine, full annulus, URANS

1. Introduction

A previous work with the aim to obtain a full annulus simulation of a complete engine has been done by Shluter et al. [1]. The aim of that was to obtain a full coupled simulation of a commercial aeroengine, using an URANS approach for compressor and turbine, and an LES approach for combustor (figure 1).

The treatment of interfaces between different components has been the most challenging part of the work.
An important task is based on how to exchange information between different codes. While first works based on coupling were based on MPI to manage the exchange of information between softwares, modern publications are in the direction to use a separated code, removing part of the workload from the solvers (search, interpolation, and communication routines). The solvers communicate with the coupler software only, and not each other [2]. In the present work, an approach based on an external coupler will be followed as well.
When LES and URANS solvers are coupled, we have to take in account that solvers are working with very different time steps and with a different method to analyze turbulent fluctuations.
At the compressor-combustor interface, the URANS computation passes the averaged velocity value to the LES side.Many methods can be used to obtain veloc-

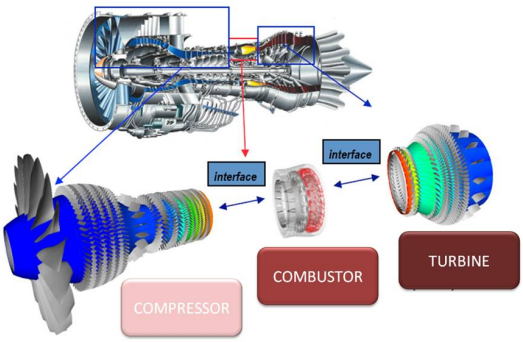

Figure 1: Approach followed by Shluter et al [1] to obtain a full simulation of a aeroengine: an URANS approach has been used for compressor and turbine, an LES approach for combustor, with a reciprocal transfer of boundary conditions between different solvers.

ity fluctuations for the LES inlet. One of the most promising is based on a separated LES analysis of a channel with periodic boundary conditions in the streamwise direction and with a forcing method [3]. This represents a fully developed flow, used to create a database of velocity fluctuations. Based on that database, the inlet condition for velocity for LES can be scaled by using the turbulent kinetic energy of URANS.
At the combustor-turbine interface, a wave transmissive boundary conditions based on the NSCBC approach [4] will be held at the LES outlet, whose averaged pressure value will be established by the downstream RANS analysis. Moreover, averaged values of input quantities will be passed at the interface from LES (upstream) to URANS (downstream). A method shall be investigated at depth to create the correct turbulent RANS parameters from velocity fluctuations.

2. Objectives

The aim of the present work is to obtain a full annulus coupled simulation of a real commercial geometry of aeroengine. An LES approach will be used to simulate the combustor, while compressor and combustor will be analyzed by an unsteady RANS approach.
In parallel, we will point out which are the technical issues that can be properly analyzed with large full annulus and coupled computations: the accuracy of the coupled approach to reproduce interactions between combustor, compressor and turbine will be investigated at depth, as well as the advantage of full annulus computations to correctly analyze spatially non periodic fluid dynamic phenomena inside the annulus.

Acknowledgments

The research has received funding from the European Community's Seventh Framework Programme (FP7, 2007-2013), People programme, under the grant agreement No.FP7-290042 (COPA-GT project).

References

[1] Shluter, Kim, Alonso, and Pitch (2004), Integrated RANS-LES for a realistic compressor-combustor assembly, Stanford annual research brief.
[2] Schluter, Apte, Kalitzin, v.d.Weide, Alonso and Pitsch (2005), Large-scale integrated LES-RANS simulations of a gas turbine engine. Stanford research brief.
[3] Schluter, Pitsch and Moin (2004), Large Eddy Simulation Inflow Conditions for Coupling with Reynolds-Averaged Flow Solvers, AIAA Journal, 42(3):478-484
[4] Poinsot and Lele (1992), Boundary conditions for direct simulations of compressible viscous flows, Journal of Computational Physics (ISSN 0021-9991), vol. 101, no. 1, p. 104-129
[5] Pierce and Moin (1998). Method for generating equilibrium swirling inflow conditions, AIAA journal, 36:13251327

OPTIMIZATION IN TURBOMACHINERY

Robust Multidisciplinary Optimisation of Composite Fan Blades

Christopher Chahine

Turbomachinery and Propulsion Department, von Karman Institute for Fluid Dynamics, Belgium, christopher.chahine@vki.ac.be

Supervisor: Tom Verstraete

Assistant Professor, Turbomachinery and Propulsion Department, von Karman Institute for Fluid Dynamics, Belgium, tom.verstraete@vki.ac.be

Abstract

To achieve higher fuel efficiency, aero engine manufacturers develop turbofans with higher bypass ratio, which can only be achieved with larger (and heavier) fan sections. This makes weight reduction in fan components a major consideration and becomes a key driver for the use of composite materials in future engines. Using fan blades made of composite materials introduces significant weight saving potentials for the fan blades themselves, but also for the surrounding fan casing. One of the central tasks of the fan casing is to prevent that parts of the blade are penetrating the fuselage or the wing in the case that a blade brakes off during operation. Since composite fan blades are lighter and more brittle than titanium fans, they are easier to contain in the case of such a blade failure. Thus, the fan casing can also become lighter, leading to a further weight reduction of the overall engine.

The design of composite blades is a multidisciplinary problem as the fan performance feature described by one discipline affects many other performance aspects; e.g. composite blades tend to become thicker than hollow metallic ones in order to meet the structural performance targets but this affects the aerodynamic performance (efficiency). The goal of this Ph.D. project is to use advanced numerical optimisation techniques to maximise the blades' efficiency and minimise mass subject to a number of constraints, including: maximum stress and strain, flutter margin, pressure ratio at the operating point and other flight conditions, stall range, manufacturing considerations, noise and safety against foreign object impact.

Manufacturing tolerances and changing operation conditions can have an adverse influence on the fans performance. Therefore, these variabilities need to be considered in the design process. This aspect will be addressed in this project by making use of methods for robust optimisation. These methods take into account the uncertainties of design variables and their influence on the performance in order to find high performing designs with a low sensitivity against probable parameter changes.

Keywords: Composite fan design, robust multidisciplinary optimisation, high velocity impact, composite material optimisation

Evolutionary Optimization for Multidisciplinary Design of Transonic Turbomachinery Components

Michael Joly

Turbomachinery and Propulsion Department, von Karman Institute for Fluid Dynamics, Belgium, joly@vki.ac.be

Supervisor: Tom Verstraete

Assistant Professor, Turbomachinery and Propulsion Department, von Karman Institute for Fluid Dynamics, Belgium, tom.verstraete@vki.ac.be

Supervisor: Guillermo Paniagua

Associate Professor, Aeronautics and Aerospace Department, von Karman Institute for Fluid Dynamics, Belgium, paniagua@vki.ac.be

University Supervisor: Paul Cizmas

Professor, Aerospace Engineering, Texas A&M University, USA, cizmas@tamu.edu

Abstract

Recent progress in evolutionary computing made available robust and efficient optimization algorithms, enabling aerospace engineers to address challenging design problems. Emerging high-speed propulsion systems require turbomachinery components that achieve a high load in a compact environment, leading to their operation in the transonic regime with strong shock interactions. Related challenges are inherently multidisciplinary and optimization techniques offer interesting prospects. This paper is a research proposal for doctoral studies in the field of Multidisciplinary Design Optimization (MDO) of innovative transonic turbomachinery components using evolutionary computing. Contra-rotation is a promising design to reduce the number of stages while increasing the load in an axial compressor. A first study investigates multidisciplinary design optimization of contra-rotating fans with the concurrent objectives of high load and compactness, using an Evolutionary Algorithm (EA) to develop an integrated design methodology. Single stage high-pressure turbines experience strong shock interactions and EAs are used in a second study to attenuate the unsteady vane-rotor interaction by means of a soft optimization approach. The trailing edge region of a high-pressure turbine, also called a base region, is further investigated in a third study with Computational Fluid Dynamics (CFD) developments to evaluate the effect of turbulence modeling in supersonic base regions. This paper includes the current research progress and results as of March 2013.

Keywords: Evolutionary Computing, Multidisciplinary Design Optimization (MDO), Turbomachinery, Computational Fluid Dynamics (CFD), Turbulence Modeling, Massively Parallel Computing (MPC)

1. Introduction

Research on high-speed air-breathing propulsion aims at developing aircraft with antipodal range and space access. Among diverse possible engine configurations, an Air Turbo Rocket (ATR) engine provides the necessary thrust from takeoff to scramjet takeover [1]. It combines both turbojet and rocket architectures to boost the thrust-to-weight ratio of the engine [2]. This technology uses a very high expansion ratio turbine and a high compression ratio fan to limit the size of the engine [3]. Light weight turbomachinery is vital to avoid hindering the scramjet operation. The concurrent objectives of high load and compactness augment the complexity of the already challenging problem of turbomachinery design. Because they include 2D and 3D effects, turbomachinery flows are extremely complex, so the use of optimization techniques to improve aerodynamic performances is an

active field of research [4; 5; 6; 7]. Multidisciplinary optimization techniques have also been considered in several studies [8; 9; 10; 11].

Worthwhile progress has been made over the last decades on Multidisciplinary Design Optimization (MDO) techniques. Evolutionary Algorithms (EAs) are particularly suitable for the design optimization of novel complex turbomachinery components. Based on Darwinian evolution, populations of individuals evolve and adapt to the environment through the use of mutation, crossover, and selection. The individuals with a higher fitness are more likely to survive and/or reproduce. Conventional optimization techniques, such as gradient-based methods, are difficult to extend to multi-objective cases; in practice, multi-objective problems have to be reformulated as single objective prior to optimization [12]. EAs, on the other hand, are well suited to multi-objective optimization. They can handle complex problems, involving features such as discontinuities, multi-modality, disjoint feasible spaces and noisy function evaluations. Differential Evolution (DE) is a relatively recent evolutionary method developed by Price and Storn [13]. Compared with Genetic Algorithms (GAs) [14], this algorithm does not require the transformation of continuous variables into binary strings. The method of Madavan [15] allows one to extend the algorithm to multi-objective problems; it uses the non-dominated sorting and ranking selection scheme of Deb et al. [16]

Besides improving the multidisciplinary performances of already existing components, EAs offer promising prospects in finding tradeoffs among unexplored configurations. Conventional gas turbines consist of blade rows spinning in the same direction. Alternatively, contra-rotation introduces two opposite directions of rotations and when applied to two consecutive rotor rows, allows the intermediate stator to be removed. This contributes to further reduce the size and weight of the machine. EAs will be used to smooth the design process of novel configurations with an integrated multi-level, multi-disciplinary methodology, which gives access to an enlarged design space. With the similar objective of limited weight, the two stages of a high-pressure turbine are often concatenated, resulting in a highly loaded single-stage turbine experiencing strong vane-rotor interactions. EAs have the potential to attenuate the unsteady forcing on the rotor with a computationally affordable optimization of the vane. We propose to redesign the vane contraction channel to mitigate the downstream propagation of shock waves. The impact on the unsteady forcing on the rotor will be assessed. A third study suggests extending this subject towards computational fluid dynamics (CFD) development. A multi-block Reynolds Averaged Navier-Stokes solver will be developed with different turbulence models and evaluated on a supersonic backward facing step. In sum, this research proposal investigates Multidisciplinary Design Optimization (MDO) methodologies based on evolutionary algorithms (EAs) to generate innovative transonic turbomachinery components with particular focus on Computational Fluid Dynamics (CFD) analysis. It consists of three distinctive parts:

- Multidisciplinary design optimization of contra-rotating fans with the concurrent objectives of high load and compactness
- Attenuation of the unsteady shock interaction in a high-pressure turbine using a soft computing optimization methodology
- Numerical evaluation of turbulence modeling effect in the base region behind the trailing edge of a high-pressure turbine

2. Multidisciplinary design optimization of highly-loaded contra-rotating fans

2.1. Problematic

Conventional design strategies for single-stage highly-loaded compressors are lengthy, iterative and capable to explore only a confined design space. The aerodynamic design usually consists in three steps [17]. A parametric study is first performed with empiric models, such as a through-flow, to define a preliminary design. Subsequently, one designs and optimizes several blade-to-blade two-dimensional profiles to generate a three-dimensional geometry. A three-dimensional optimization is ultimately applied to improve the performances, introducing sweep and lean laws to the geometry. Once a first aerodynamic design is achieved, the mechanical response of the rotor is computed to verify its structural integrity. Typically several iterations between different departments are usually necessary to finalize the geometry, making the design process lengthy and enables one to explore only few possible candidates.

Contra-rotation offers the prospect to reduce the weight of multi-stage machines by suppressing the intermediate stator rows. It is actively investigated for propellers, axial turbines [18] and open rotors [8]. Research on high-pressure ratio contra-rotating axial compressors is however scarce in the open liter-

ature. Studies that achieved designs with low pressure ratio are however available [19; 20]. Some experiments of high pressure ratio contra-rotating axial compressors had been performed in the 50's, but limited information about the used geometry was available [21; 22; 23]. More recently, Minato et al. proposed a CFD-based design that achieved a 2.8 pressure ratio [24]. Parker et al. investigated a geometry with an aspiration device and measured a maximum pressure ratio of 3.02 [25].

2.2. *Proposed approach*

It is proposed to revise the whole design process of axial flow compressor with a multi-level multidisciplinary methodology that is capable to conceive highly-loaded, compact contra-rotating fans. First, the aerodynamic design of the highly-loaded rotor is enhanced. The through-flow based parametric study is replaced by an optimization, enlarging considerably the explored design space during the preliminary design phase. A novel parameterization is used to smooth the handover between the preliminary design and the three-dimensional geometry definition. The design strategy consists then in only two successive steps, a through-flow optimization and a three-dimensional optimization. This suppresses the two-dimensional step, which was ignoring important effects such as end-wall geometry and secondary flows during the profile design phase. Secondly recent work showed that the inter-disciplinary iterations can be superseded by the simultaneous consideration of all involved disciplines, turning the design process into a multidisciplinary optimization [8; 9; 10; 11]. A similar strategy is applied to compute Computational Fluid Dynamics (CFD) and Computational Structural Mechanics (CSM) performances during the three-dimensional optimization. The final result is a rapid and smooth design process with a large design space where performances from different disciplines are evaluated concurrently. Applied to two-stage contra-rotating machines, it eventually allows the two rotors to be designed simultaneously.

2.3. *Current research progress*

The present research has been published in four conference papers [52; 51; 53; 54]. One journal article was submitted [46] and a second one is under preparation [47].

The design of the flow path with a through-flow solver shows that optimization enables one to investigate a large set of candidates, while considering the three conflicting objectives of high-load, low losses and compactness. The results are a set of non-dominated optima distributed along a Pareto front.

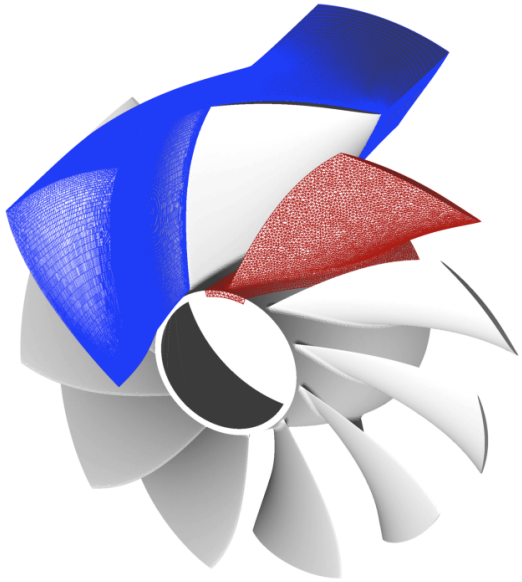

Figure 1: CFD and CSM grids on a compressor blade row [46]

The three dimensional optimization is initialized based on the selected optimal flow path. A novel parametrization is developed to ease the transition between the through-flow and the geometry generation. It consists of span-wise distributions that provide smooth variations along the span; it also provides a convenient way to convert through-flow data into parameters of the detailed rotor geometry.

The final result shows that through-flow models can be employed for the design of supersonic compressors. Comparable level of entropy generation are observed between the CFD-based optimized geometry and the through-flow predictions. The span-wise distributions of relative flow turning also appear similar with smooth evolutions along the span thanks to the parametrization. Both rotors encounter shock waves, whose behavior shows agreement with theoretical investigations of supersonic compressor profiles. Eventually, a high pressure ratio of 3.07 is achieved with an adiabatic efficiency of 72.4%.

From the structural point of view, both rotors provide a safety margin of 20% with regards to the yielding strength of titanium. The stress is distributed along the whole span with limited peaks. The maximal stress appears close to the hub, where the fillet is observed to compensate the extra load generated by the aerodynamic pressure.

This proposed accelerated methodology requires a

total computational time of 3 weeks on 40 processors. The novel parametrization developed with spanwise distributions enables one to reduce the time-to-market cost compared to conventional methodologies and to produce innovative configurations such as highly-loaded and compact contra-rotating fans. It made possible the use of a strategy with only two successive optimizations, one with a through-flow and one with a three-dimensional multidisciplinary evaluation. This 1D-3D approach is promising and can be generalized to the design of other turbomachinery components.

3. Attenuation of shock interaction in high-pressure turbines

3.1. Problematic

In the development of any modern aeroengine, the most expensive component is the high pressure turbine due to the harsh environment (high temperatures downstream of the combustor and mechanical solicitations). Higher loading per row allows to reduce the number of stages, limiting the weight of the machine. It contributes therefore to lower the fuel consumption of commercial aircrafts. However, an increase of load implies that the flow across the turbine passages is transonic, resulting in shockwave interactions [26]. Denton et al. [27] describes the aerodynamics of the trailing-edge shock system within transonic turbine vanes. The vane shocks waves travel downstream, impacting periodically on the rotor blades (See Fig. 2). Giles [28] identified the sweeping of the direct shock from the crown of the rotor blade towards the leading edge, causing variations in the rotor lift of 40% of the mean level. The downstream rotor is therefore prone to suffer from high cycle mechanical and thermal fatigue.

Attempts to mitigate the unsteady vane-rotor shock interaction could be classified into improved designs through a better physical understanding [30; 31; 32; 29], active control systems [33], and numerical optimizations with neural networks [34; 35]. Unsteady turbine stage computations with high-fidelity Navier-Stokes solvers (such as URANS, LES, DES) remain extremely expensive with modern computers and their implementation together with optimization algorithms is limited to 2D profiles. The unsteady optimization of real 3D geometries is unpractical even with the assistance of surrogate models.

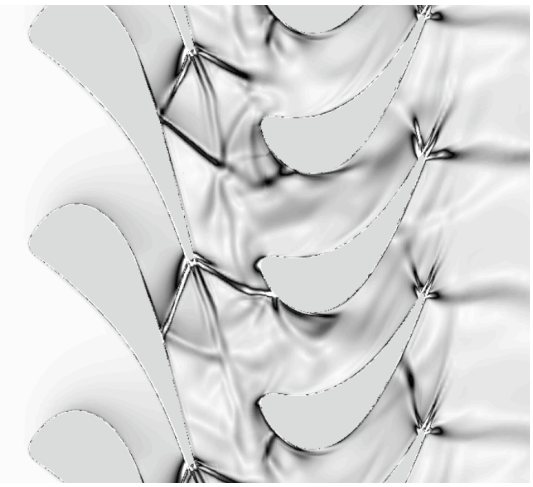

Figure 2: Vane/Rotor shock interaction [29]

3.2. Proposed approach

The present research proposes alternatively a soft computing methodology based on evolutionary optimization, and considers robust, accurate, and computationally affordable evaluations to redesign the vane for attenuated downstream pressure distortion, with the ultimate goal to limit the unsteady vane-rotor shock interaction.

3.3. Current research progress

Results have been published in two conference papers [49; 50] and one accepted journal article [48].

The optimization process is shown to be effective with 43.2% and 56.1% reductions of the pitch-wise static pressure distortion, for the 2D and 3D cases respectively. The parameterization allows to explore widely the design space and offers an original optimized vane passage. The optimal vane 2D section presents a convergent-divergent contraction channel, leading to an over-acceleration of the flow within the channel. The trailing edge shock system is modified and the resulting shock waves that propagate to the following blade row exhibit lower intensity. 3D optimization with lean and section adaption enables further improvements in downstream distortion with no alteration on stage efficiency compared to the baseline.

Subsequently to the vane optimization, the unsteady forcing on the rotor downstream of the optimal vane is computed with a non-linear harmonic method to evaluate the impact on the vane-rotor interaction. Attenuations up to 61% are observed and confirms the reduction in rotor high-cycle fatigue risk.

Evolutionary optimization with robust, accurate simulations with low computational cost is therefore shown to reduce the unsteady vane-rotor shock interaction in high-pressure turbines. This approach is suitable to any turbomachinery application where strong pressure distortions are dictated by the upstream blade row. In those cases, we could rely on optimizing the single row using high fidelity simulations, without the need of running high computing simulations for the whole stage.

4. Numerical evaluation of the turbulent flow in base regions

4.1. Problematic

The emergence of shock waves downstream of the vane trailing edge affects the performance of high-pressure turbines. In this so-called base region, boundary layers from both sides of the blade profile merge generating expansion fans and shock waves [27]. A similar flow pattern exists in the vicinity of a supersonic backward facing step (See Fig. 3).

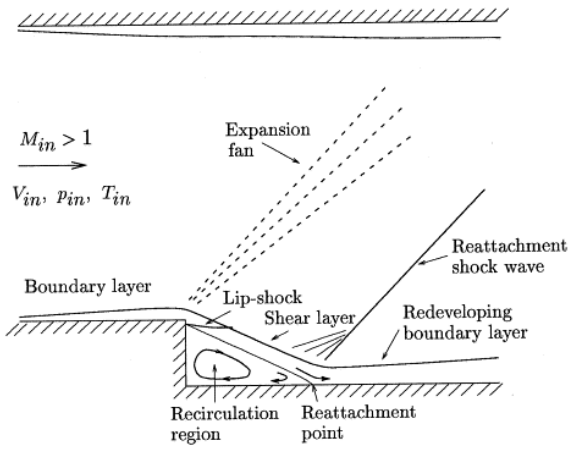

Figure 3: Supersonic flow over backward facing step [36]

Turbomachinery high-speed stages operate at high Reynolds number, where the assumption of completely turbulent boundary layers is reasonable in numerical computations. The complex nature of turbulence flows makes the approximation of boundary layers by mathematical models very challenging. An ideal turbulence model should introduce the minimum amount of complexity while capturing the essence of the relevant physics [37]. Turbulence models can be classified as follows with increasing degree of complexity: algebraic (zero-equation), one-equation, two-equation, second-order closure models. Whereas the later has found few applications, the three first ones compete with each other and are suitable to different applications depending on the desired tradeoff between accuracy and complexity.

Massively parallel algorithms are also actively investigated, especially with the recent process on Graphics Processing Units (GPUs), and are capable to speed up CFD computations. A GPU is a processor that exhibits a higher level of parallelism (higher rate of floating-point operations per second) compared to conventional Central Processing Units (CPUs). Applications to aerospace computing showed potential acceleration from 10 to 20 times [38; 39]. Extensive parallelism requires significant changes to the implementation of the underlying code. NVIDIA provides in this concern an extension to the C programming language called CUDA [40]. The idea is to identify within the code repetitive sequences of computation that apply on a large set of data. A kernel can then be defined to express the required calculation, and the GPU will process the data with the execution of many parallel threads. Particular attention needs to be addressed on memory allocation to maximize the benefit of the implementation.

4.2. Proposed approach

The present research proposes to investigate the effect of turbulence modeling on supersonic base regions flows, comparing the one-equation Spalart-Allmaras [41] and the two-equation SST k-omega model [42]. A more recent four-equation model is also considered [43]. Two codes are available for this study: a self-made solver (multi-block RANS laminar solver) that needs to be extended with turbulence models and the UNS3D code of the Aerospace Numerical Simulation Laboratory of Texas A&M University. Implementation on GPUs is an option to accelerate the computations.

4.3. Current research progress

The current status is the implementation of a multi-block RANS laminar solver. It uses a structured finite volume spatial discretization. The convective fluxes are computed using the flux-difference splitting scheme of Roe [44]. The first derivates of the velocity components and of temperature are calculated using the Green's theorem for the discretization of the viscous fluxes [45]. A Runge-Kutta explicit time-stepping scheme is employed to obtain a steady-state solution. Local time-stepping is implemented as an acceleration technique.

5. Conclusion

The outcome of the present research contributes to the development of simulation-based design methodologies for aerospace applications. The prospects for innovative aircraft engine configurations are promising. Further progress is possible with continuous investigations in the fields of Multidisciplinary Design Optimization (MDO), Computational Fluid Dynamics (CFD) and Massively Parallel Computing (MPC).

Acknowledgments

This work was performed within the Long-Term Advanced Propulsion Concepts and Technologies II project investigating high-speed air-breathing propulsion. LAPCAT II, coordinated by ESA-ESTEC, is supported by the EU within the 7th Framework Programme Theme 7 Transport, Contract no.:ACP7-GA-2008-211485.

This work was performed while being a recipient of a Fellowship of the Belgian American Educational Foundation.

References

[1] W. H. Heiser, D. T. Pratt, Hypersonic Airbreathing Propulsion, AIAA Education Series, Washington D.C.: American Institute of Aeronautics and Astronautics, 1994.

[2] J. Kerrebrock, Aircraft engines and gas turbines, 1992.

[3] M. I. Rodriguez, V. V. Fernandez, G. Paniagua, Modeling, analysis and optimization of the air turbo rocket expander engine, Proceedings of 8th AIAA International Space Planes and Hypersonic Systems and Technologies Conference.

[4] T. Verstraete, Multidisciplinary turbomachinery component optimization considering performance, stress and internal heat transfer, Universiteit Gent, Belgium.

[5] S. Pierret, R. Van den Braembussche, Turbomachinery blade design using a navier-stokes solver and artificial neural network, in: RTO Meeting proceedings, 1999, pp. 30–1.

[6] N. Madavan, Turbomachinery airfoil design optimization using differential evolution, in: 2 nd International Conference on Computational Fluid Dynamics, Sydney, Australia, Vol. 15, 2002.

[7] A. Arias-Montano, C. Coello Coello, E. Mezura-Montes, Multi-objective evolutionary algorithms in aeronautical and aerospace engineering.

[8] I. Lepot, M. Leborgne1, R. Schnell2, J. Yin, G. Delattre, F. Falissard, J. Talbotec, Aero-mechanical optimization of a contra-rotating open rotor and assessment of its aerodynamic and acoustic characteristics, Journal of Power and Energy 225 (2011) 850–863.

[9] T. Verstraete, Z. Alsalihi, R. A. V. den Braembussche, Multidisciplinary optimization of a radial compressor for micro-gas turbine applications, ASME Journal of Turbomachinery 132 (3).

[10] S. Pierret, C. Filomeno, H. Kato, Multidisciplinary and multiple operating points shape optimization of three-dimensional compressor blades, Journal of Structural and Multidisciplinary Optimization 33 (2007) 61–70.

[11] Y. Lian, M. Liou, Aerostructural optimization of a transonic compressor rotor, Journal of Propulsion and Power 22 (4) (2006) 880–888.

[12] C. M. Fonseca, R. J. Fleming, An overview of evolutionary algorithms in multiobjective optimization, Journal of EvolutionaryComputation 3 (1) (1995) 1–16.

[13] R. Storn, K. Price, Differential evolution a simple and efficient heuristic for global optimization over continuous spaces, Journal of Global Optimization 11 (1997) 341–359.

[14] D. Goldberg, Genetic algorithms in search, optimization and machine learning, Addison-Wesley.

[15] N. Madavan, Multiobjective optimization using a pareto differential evolution approach, In the proceedings of the Congress on Evolutionary Computation.

[16] K. Deb, S. Agrawal, A. Pratap, T. Meyarivan, A fast elitist non-dominatedsorting genetic algorithm for multi-objective optimization:nsga-ii, In the proceedings of the Parallel Problem Solving from Nature VI Conference.

[17] W. J. Calvert, R. B. Ginder, Transonic fan and compressor design, Journal of Mechanical Engineering Science 213 (5) (1999) 419–436.

[18] R. Varvill, G. Paniagua, H. Kato, M. Thatcher, Design and testing of the contra-rotating turbine for the scimitar precooled mach5 cruise engine, Journal of the British Interplanetary Society 62 (225).

[19] H. Nouri, F. Ravelet, F. Bakir, C. Sarraf, Design and experimental validation of a ducted counter-rotating axial-flow fans system, Journal of Fluids Engineering 134.

[20] P. Schimming, Counter rotating fans - an aircraft propulsion for the future?, Journal of Thermal Sciences 12 (2).

[21] W. W. Wilcox, An analysis of the potentialities of a two-stage counterrotation supersonic compressor, Tech. Rep. RM E52E01, NACA (1952).

[22] W. W. Wilcox, L. C. Wright, Investigation of two-stage counterrotating compressor iii - design of second-stage rotor and preliminary over-all performance, Research Memorandum RM E56G30a, NACA (1956).

[23] W. W. Wilcox, W. Stevans, Investigation of two-stage counterrotating compressor iv - over-all performance of compressor with modified second-stage rotor, Research Memorandum RM E58A27, NACA (1958).

[24] R. Minato, D. Kato, K. Higashino, N. Tanatsugu, Development study on counter rotating fan jet engine for supersonic flight, Proceedings of International Society for Air Breathing Engines (1233).

[25] D. V. Parker, Design and operation of a counter-rotating aspirated compressor blowdown test facility, Massachusetts Institute of Technology Thesis.

[26] I. Jennions, J. Adamczyk, Evaluation of the interaction losses in a transonic turbine hp rotor/lp vane configuration, Journal of turbomachinery 119 (1) (1997) 68–76.

[27] J. Denton, L. Xu, The trailing edge loss of transonic turbine blades, Journal of turbomachinery 112 (2) (1990) 277–285.

[28] M. Giles, Stator/rotor interaction in a transonic turbine, Journal of Propulsion and Power 6 (5) (1990) 621–627.

[29] G. Paniagua, T. Yasa, A. de la Loma, T. Coton, Unsteady strong shock interactions in a transonic turbine: experimental and numerical analysis, Journal of propulsion and power 24 (4) (2008) 722–731.

[30] C. Sieverding, M. Stanislas, J. Snoeck, The base pressure problem in transonic turbine cascades, Journal of Engineer-

ing for Power 102 (1980) 711–718.
[31] D. Ashworth, K. Grindrod, J. La Graff, D. Schultz, Unsteady aerodynamic and heat transfer processes in a transonic turbine stage, J. Eng. Gas Turbines Power 107 (4).
[32] G. Guennette, A. Epstein, M. Giles, R. Haimes, R. Norton, Fully scaled transonic turbine rotor heat transfer measurement, Journal of turbomachinery 111 (1989) 1–7.
[33] B. Saracoglu, G. Paniagua, S. Salvadori, F. Tomasoni, S. Duni, T. Yasa, A. Miranda, Trailing edge shock modulation by pulsating coolant ejection, Applied Thermal Engineering.
[34] N. Madavan, M. Rai, F. Huber, Neural net-based redesign of transonic turbines for improved unsteady aerodynamic performance, NASA (19990008889).
[35] M. Rai, N. Madavan, F. Huber, Improving the insteady aerodynamic performance of transonic turbines using neural networks, NASA (1999208791).
[36] Y. Halupovich, B. Natan, J. Rom, Numerical solution of the turbulent supersonic flow over a backward facing step, Fluid Dynamics Research 24 (5) (1999) 251 – 273.
[37] D. Wilcox, Turbulence modeling for CFD, Vol. 3, DCW industries La Cañada, CA, 2006.
[38] E. Elsen, P. LeGresley, E. Darve, Large calculation of the flow over a hypersonic vehicle using a gpu, Journal of Computational Physics 227 (24) (2008) 10148–10161.
[39] T. Brandvik, G. Pullan, An accelerated 3d navier-stokes solver for flows in turbomachines, Journal of Turbomachinery 133 (2) (2011) 21025.
[40] C. Nvidia, Nvidia cuda programming guide (2011).
[41] P. SPALART, S. ALLMARAS, A one-equation turbulence model for aerodynamic flows, in: AIAA, Aerospace Sciences Meeting and Exhibit, 30 th, Reno, NV, 1992, p. 1992.
[42] F. Menter, Zonal two equation kappa-omega turbulence models for aerodynamic flows.
[43] B. Basara, S. Krajnovic, S. Girimaji, Z. Pavlovic, Near-wall formulation of the partially averaged navier-stokes turbulence model, AIAA journal 49 (12) (2011) 2627–2636.
[44] P. Roe, Approximate riemann solvers, parameter vectors, and difference schemes, Journal of computational physics 43 (2) (1981) 357–372.
[45] J. Blazek, Computational fluid dynamics: principles and applications, Elsevier Science, 2001.

Journal articles as of March 2013

[46] M. Joly and T. Verstraete and G. Paniagua, Multidisciplinary design optimization of a compact highly-loaded fan, (**submitted**).
[47] M. Joly and T. Verstraete and G. Paniagua, Integrated multilevel, multi-disciplinary evolutionary optimization for the design of contra-rotating compressors, (**in preparation**).
[48] M. Joly and T. Verstraete and G. Paniagua, Differential evolution based soft optimization to attenuate vane-rotor shock interaction in high-pressure turbine, Journal of Applied Soft Computing (**acccepted, in press**).

Conference proceedings as of March 2013

[49] M. Joly and T. Verstaete and G. Paniagua, Attenuation of Vane Distortion in a Transonic Turbine using Optimization Strategies, Part I - Methodology, no. ASME GT2010-22370, in the proceedings of ASME Turbo Expo 2010, 2010.
[50] M. Joly and G. Paniagua and T. Verstaete, Attenuation of Vane Distortion in a Transonic Turbine using Optimization Strategies, Part II - Optimization, no. ASME GT2010-22371, in the proceedings of ASME Turbo Expo 2010, 2010.
[51] M. Joly and R. Mafulli and V. Villace and G. Paniagua, Air Turbo Rocket Turbomachinery Design and Evaluation, no. ISABE-2011-1333, in the proceedings of the 20th International Society for Air Breathing Engines, 2011.
[52] M. Joly and T. Verstaete and G. Paniagua, Design-Optimization for Compactness of Highly-Loaded Fan Rotor, no. ISAIF10-110, in the proceedings of the 10th International Symposium on Experimental Computational Aerothermodynamics of Internal Flows, 2011.
[53] M. Joly and T. Verstaete and G. Paniagua, Full Design of a Highly Loaded Fan by Multi-Disciplinary Optimization of Through-Flow and High-Fidelity Aero-Mechanical Performances, no. ASME GT2012-69686, in the proceedings of ASME Turbo Expo 2012, 2012.
[54] M. Joly and T. Verstaete and G. Paniagua, Full Design of a Highly Loaded and Compact Contra-Rotating Fan Using Multidisciplinary Evolutionary Optimization, no. ASME GT2013-94433, in the proceedings of ASME Turbo Expo 2013, 2013.

Design of the Heavy-Liquid Metal Pump of the MYRRHA Research Reactor

Lasse Mueller

Turbomachinery and Propulsion Department, von Karman Institute for Fluid Dynamics, Belgium, lasse.mueller@vki.ac.be

Supervisor: Tom Verstraete

Assistant Professor, Turbomachinery and Propulsion Department, von Karman Institute for Fluid Dynamics, Belgium, tom.verstaete@vki.ac.be

Abstract

This paper presents the design of a liquid-metal pump for the primary cooling system of the advanced nuclear reactor MYRRHA conceived by the Belgian research center (SCK·CEN). The focus of this report is on the rotor design of the pump, as the most crucial component of the entire machine especially regarding erosion.

The single stage axial-flow pump has been designed with the optimization algorithm developed at the von Karman Institute for Fluid Dynamics (VKI) based on evolutionary methods. Two sequential optimization cycles have been applied to meet the required total head rise at design flow rate, while limiting the maximum velocity in the rotor tip section due to erosion.

In the preliminary design phase, the meridional flow path and rotational speed have been assessed by a 1D-model in the hub, mid, and tip section of the rotor. The outcome of this rather simple but very fast approach is a moderate specific speed, high hub-to-tip ratio rotor of $N_s = 70$ and $R_{hub}/R_{tip} = 0.88$, respectively. In the second design step, accurate 3D-Navier-Stokes computations have been performed to design and automatically optimize the entire pump comprising the inlet section, the rotor and stator blade rows, and the diffuser. The high fidelity CFD analysis has been assisted by an Artificial Neural Network (ANN) to accelerate the optimization and to reduce the computational cost.

Keywords: MYRRHA, Primary Pump, Design Optimization

1. Introduction

The MYRRHA project initiated by the Belgian nuclear research center (SCK·CEN) is aimed at constructing and operating a flexible fast spectrum experimental facility. It is conceived as an accelerator driven system (ADS), able to operate in sub-critical and critical modes [1] and will allow the demonstration and performance assessment of the transmutation concept and associated technologies starting in 2023.

The primary system of the MYRRHA research reactor is a pool-type design, as illustrated in Fig. 1. All components of the primary loop, i.e. the pumps, heat exchangers, fuel handling tools, experimental rigs, etc., are inserted from the top and immerged in the reactor vessel, which is filled with lead-bismuth eutectic (LBE) as primary coolant. The relatively high boiling temperature of LBE of 1670°C leads to a passively safe design regarding a loss of coolant accident (LOCA), as it allows the operation without pressurizing the reactor even at high temperatures. However, the high density of LBE of 10,000 kg/m^3 adds additional restrictions to the primary pump. To avoid excessive erosion inside the pump, especially in the rotor tip section, the maximum relative velocity is limited to rather low values, e.g. pumps OKBM [2] has developed for reactors using LBE operate at maximum velocities of W_{max} = 25 - 30 m/s.

Reducing the maximum velocity to limit erosion is an essential objective within the design task of the pump. This will be accomplished using advanced evolutionary optimization methods.

2. Design Procedure

The choice of the machine type (axial flow, mixed flow, or radial flow) is related to the design requirements of the pump, i.e. to the flow rate Q and the

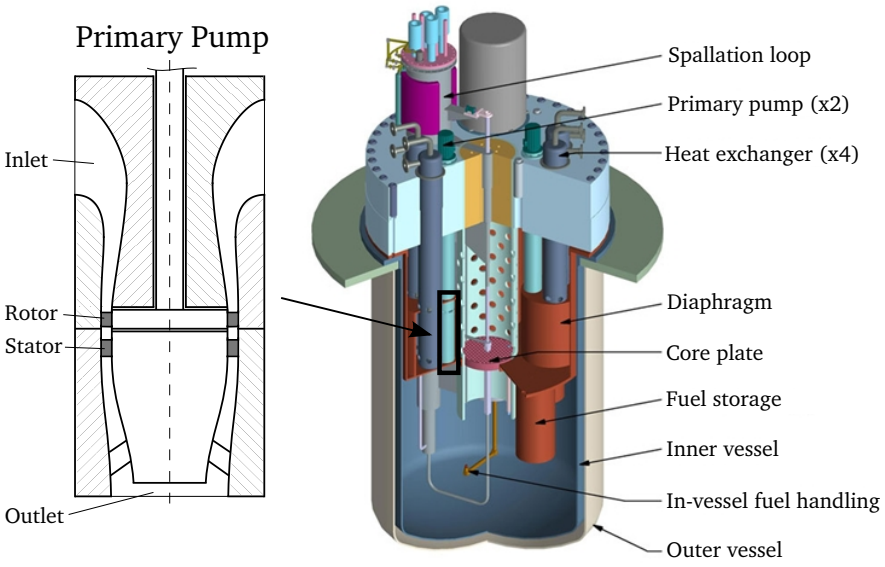

Figure 1: **Schematic Assembly of the MYRRHA Reactor [1] with a Close Up on the Primary Pump (Dimensions Not to Scale)**

total head ΔH. A classical parameter in the selection of hydraulic machinery is the specific speed

$$N_s = \frac{RPM\sqrt{Q}}{\Delta H^{3/4}}. \quad (1)$$

Based on the design requirements of the MYRRHA pump provided by SCK·CEN the specific speed is in the range of mixed to axial-flow pumps $N_s \approx 156$ (see Fig. 2). Although towards lower RPM a mixed-flow configuration might provide higher efficiency, an axial-flow pump is regarded as the best trade-off solution due its lower mechanical complexity and simplified manufacturing.

The use of preliminary design tools in the design process is recommended as it allows evaluating rapidly various design choices. Especially with regard to the erosion induced requirement of low relative velocity, it was decided to analyze various design options in this preliminary design phase. For that reason a simple one-dimensional model has been applied in

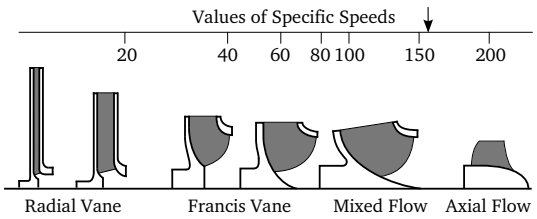

Figure 2: **Specific Speed Chart**

the hub, mid, and tip section of the rotor to assess the meridional flow path and its rotational speed (Fig. 3, left). This rather simple model based on velocity triangles up- and downstream of the rotor blade allows a rapid screening of several design parameters, such as blade angles, rotational speed (RPM), and hub and tip radii, R_{hub} and R_{tip}, respectively. Although it does not include complex flow features, e.g. flow deviation or even flow separation, it provides a good estimation of the initial rotor design as an input for the following 3D-optimization.

Input parameters to the 3D-optimization are the hub and tip radii (R_{hub} and R_{tip}) and the RPM of the rotor as illustrated in Fig. 3, (right). These parameters were unchanged in the subsequent high fidelity 3D-optimization, in which the three dimensional design of the pump comprising the inlet section, the rotor and stator rows, and the diffuser has been performed.

3. 1D Optimization

3.1. Computational Model

The 1D computational model is illustrated in Fig. 4. Input parameters are the hub and tip radii, R_{hub} and R_{tip}, and the RPM, next to the pump requirements (ΔH and Q). The axial velocity V_x is derived from the hub and tip radius for the specified flow rate Q. It is assumed at this stage that the axial velocity upstream of the rotor is constant from hub to tip although the pump will have a radial inlet bend (see Fig.1).

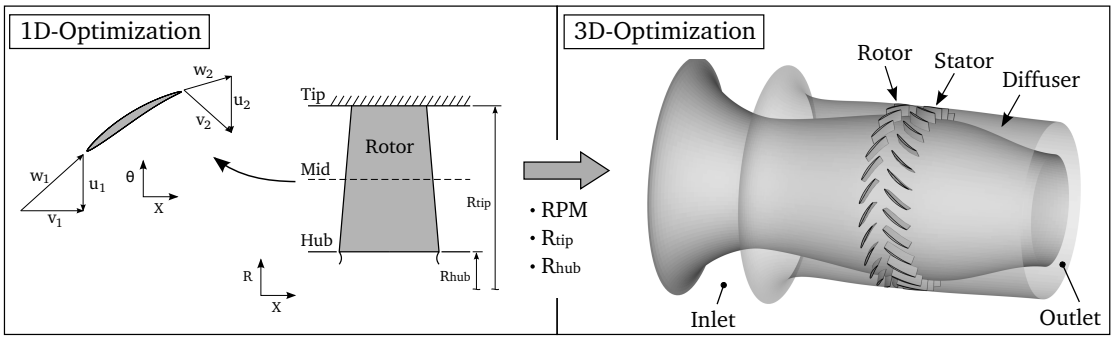

Figure 3: **Design Procedure**

The peripheral speed U is computed at three sections (hub, mid and tip) from the rotational speed and the respective radii. The mid section is positioned in the middle of the hub and tip radius: $R_{mid} = 0.5 \cdot (R_{hub} + R_{tip})$.

The inlet absolute velocity V_1 is assumed to be axial (no pre-rotation), which allows to compute the relative velocity W_1 and the relative flow angle β_1.

The quantities downstream of the rotor (index 2) are computed based on the required total head ΔH and assuming no losses ($\eta_{hyd} = 1.0$) using the Euler-equation for pure axial inlet flow ($V_{1\theta} = 0$)

$$\frac{g \cdot \Delta H}{\eta_{hyd}} = U_2 V_{2\theta} - U_1 V_{1\theta} = U_2 V_{2\theta} \,. \tag{2}$$

and assuming the axial velocity V_x to maintain constant through the rotor (i.e. free vortex design). The absolute velocity downstream of the rotor V_2, the absolute flow angle α_2, therelative velocity W_2, and the relative flow angle β_2 are computed as illustrated in Fig. 4.

3.2. Objectives and Constraints

Three design parameters (hub radius R_{hub}, tip radius R_{tip}, and RPM) can be chosen to obtain the required total head ΔH and flow rate Q. However, additional requirements need to be imposed:

- The turning of the flow in the rotor (β_2 - β_1) needs to be limited to reduce the losses, not accounted for in this preliminary design phase. According to [3] the turning is limited to 30° to 25°.
- The diffusion in the rotor (W_2/W_1) needs to remain feasible. A limit of 0.72 is often used, known as the de Haller number [4].
- The maximum relative velocity in the rotor W_{max} needs to remain at low values (10 - 20 m/s) to limit erosion.
- The absolute exit flow angle (α_2) needs to be small (from axial direction) to perform a feasible diffusion in the subsequent stator [3].

Choice of R_{tip} and R_{hub}

$$V_x = \frac{Q}{\pi \, (R_{tip}^2 - R_{hub}^2)}$$

Choice of RPM

$$\omega = \frac{RPM \cdot 2\pi}{60}$$

$$U_{mid} = R_{mid} \cdot \omega$$

Determination of W_1, β_1

$$W_1 = \sqrt{V_x^2 + U_1^2}$$

$$\beta_1 = \operatorname{atan}\left(\frac{U_1}{V_x}\right)$$

Determination of V_2, α_2, W_2, β_2

$$\Delta h_{tot} = g \cdot \Delta H$$

$$V_{2\theta} = \frac{\Delta h_{tot}}{U_2}$$

$$V_2 = \sqrt{V_x^2 + V_{2\theta}^2}$$

$$\alpha_2 = \operatorname{atan}\left(\frac{V_{2\theta}}{V_x}\right)$$

$$W_2 = \sqrt{(U_2 - V_{2\theta})^2 + V_x^2}$$

$$\beta_2 = \operatorname{atan}\left(\frac{U_2 - V_{2\theta}}{V_x}\right)$$

Figure 4: **1D Computational Model**

The corresponding optimization problem is formulated as:

Minimize:

$$Obj_1 = W_1^{tip} \quad (3)$$

$$Obj_2 = -W_2^{hub}/W_1^{hub} \quad (4)$$

Subject to:

$$Constr_1 = abs(\beta_2^{hub} - \beta_1^{hub}) \leq \Delta\beta_{max} \quad (5)$$

$$Constr_2 = V_x \leq V_{x,max} \quad (6)$$

The first objective Obj_1 (Eqn. 3) reduces the maximum relative velocity in the rotor, which is in the tip section at the inlet. A value in the range of W_1^{tip} = 10 to 20 m/s is considered as feasible, although lower values are preferred, as they would increase the lifetime with respect to erosion. The second objective Obj_2 (Eqn. 4) maximizes the diffusion ratio near the hub to prevent an excessive diffusion. For a free vortex design the highest diffusion occurs in the hub section. The first constraint Eqn. 5 restricts the turning at the hub, where the largest relative flow turning will take place, while the second constraint (Eqn. 6) puts an additional limitation on the axial velocity to limit the erosion risk in the meridional passage.

3.3. Methodology

Three different design variables are allowed to be changed during the preliminary design phase, i.e. the hub and tip radii (R_{hub} and R_{tip}) and the rotational speed RPM. Each design variable is allowed to change within a specified range. For each choice of the hub radius R_{hub}, tip radius R_{tip}, and RPM, the velocity triangles can be computed by the 1D model and the requirements can be evaluated. In order to find the three design parameters that give a suitable compromise for the diffusion W_2/W_1, turning $\Delta\beta$, and maximum velocity W_{max} requirements, a Differential Evolutionary (DE) algorithm [5] has been used. Figure 5 illustrates schematically the optimization flowchart.

3.4. Results

The results of the 1D optimization are illustrated in Fig. 6, showing both the diffusion in the hub section W_2^{hub}/W_1^{hub} (top) and the flow turning β_2^{hub} - β_2^{hub} (bottom) with respect to the relative velocity in the rotor tip section W_1^{tip}. A Pareto front is found instead of one single optimal design, which is typical of multi-objective optimization. This is a set of so called

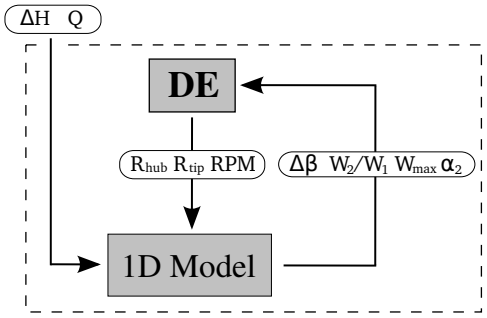

Figure 5: **1D Optimization Flowchart**

non-dominated designs, in which one objective cannot be improved without worsening the other. In Fig. 6, (top), a clear Pareto front (towards the upper left hand corner) is visible indicating that a lower maximum ve-

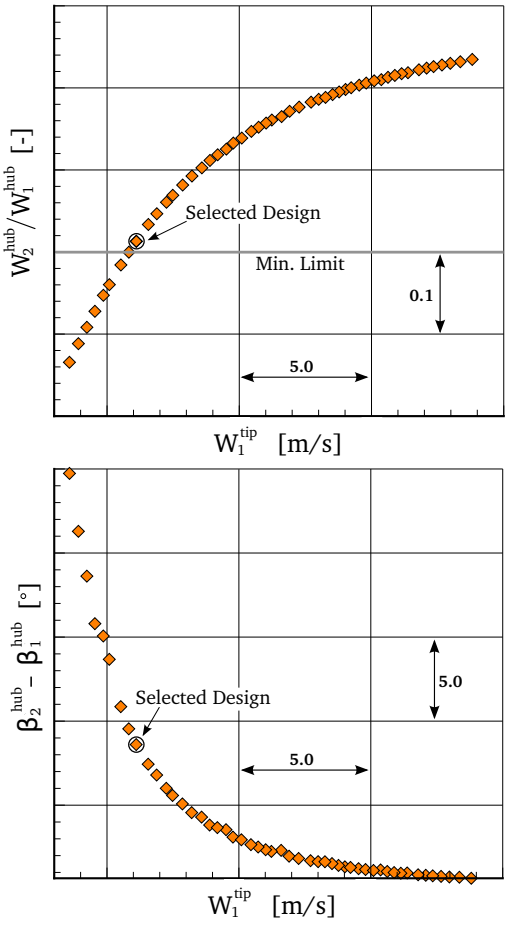

Figure 6: **Diffusion in the Hub vs. Relative Velocity in the Tip Section (top), Turning in the Hub Section vs. Relative Velocity in the Tip Section (bottom)**

locity W_1^{tip} comes at the expense of a larger diffusion near the hub (lower W_2^{hub}/W_1^{hub}). This evidently results also in a higher flow turning near the hub, as can be seen in Fig. 6, (bottom). The resulting Pareto front allows the designer to select designs depending on the weight given to each objective. In the present case, it was decided to select the design with a hub diffusion ratio (W_2^{hub}/W_1^{hub}) close to the minimum limit as indicated in Fig. 6, (top). This design has a specific speed of $N_s \approx 70$ with a high hub-to-tip ratio of $\nu = R_{hub}/R_{tip} = 0.88$, which is larger than commonly used for axial (propeller-like) pumps in the range of $\nu = 0.3$ - 0.7 [3].

However, this is due to the very low velocity requirement (i.e. low V_x and W_1^{tip}) and high diffusion (i.e. low W_2^{hub}/W_1^{hub}) for a single stage pump. Similar conclusions were drawn within a design study of axial pump rotors for liquid rocket application [6; 7; 8]. Several rotors (see Fig. 7) were designed and tested with hub-to-tip ratios between $\nu = 0.4$ - 0.9 for a specified diffusion, which confirms the results obtained from this preliminary design optimization.

4. 3D Optimization

4.1. Methodology

The 3D design of the primary pump has been performed with the optimization algorithm developed at the von Karman Institute (VKI) with special focus on turbomachinery applications. The system (Fig. 8) makes use of a Differential Evolution algorithm (DE), a metamodel based on an Artificial Neural Network (ANN), a database, and high fidelity simulation tools for the flow analysis (CFD). The basic approach of this method is that the Artificial Neural Network substitutes the computational expensive tools for the CFD in the *Generation Loop* (see Fig. 8) and provides less accurate but very fast performance predictions to evaluate the large number of geometries necessary by the DE during its search for the optimum. However, the metamodel requires a validation which is then performed in the *Iteration Loop* according to Fig. 8. After a specified number of generations, the optimum geometries according to the ANN predictions are analyzed by the more accurate but much more computationally expensive CFD calculations to verify the accuracy of the metamodel. The results of the accurate performance analysis are added to the database and a new *Generation Loop* is started after a new training of the metamodel on the enlarged database. In this way the whole system is self-learning, resulting in a more accurate ANN.

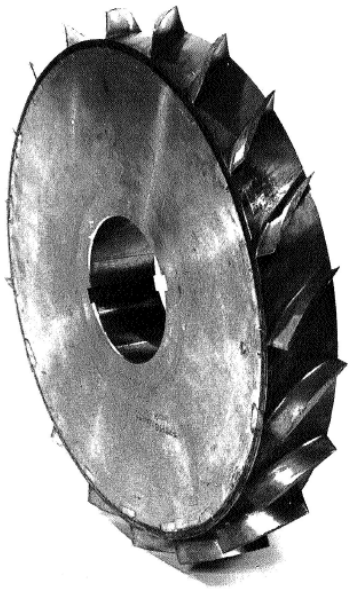

Figure 7: **NASA Axial Pump Rotor for Liquid Rocket Application (hub-to-tip ratio $\nu = 0.9$) [8]**

The Differential Evolution algorithm used was developed by [5]. In present optimization, 1000 generations are created with a constant population size of 40 individuals. To validate the ANN predictions in each *Iteration Loop* eight individuals were selected and reassessed by the high fidelity tools.

The initial sampling of the database was performed by means of a Design of Experiments (DOE) [9]. The DOE is based on statistical methods and considers, that k design variables can take two values fixed at a specified position in the design space (here: 20% and

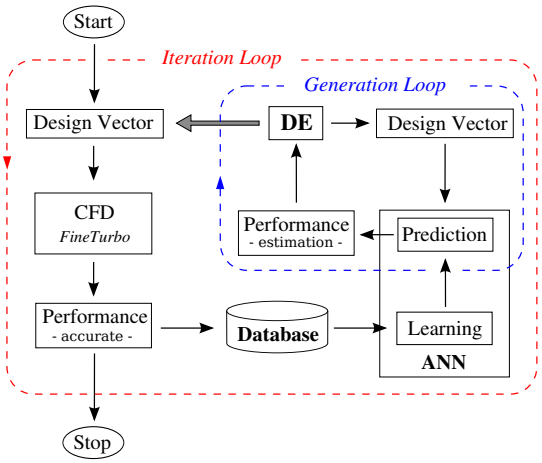

Figure 8: **VKI Optimization Algorithm**

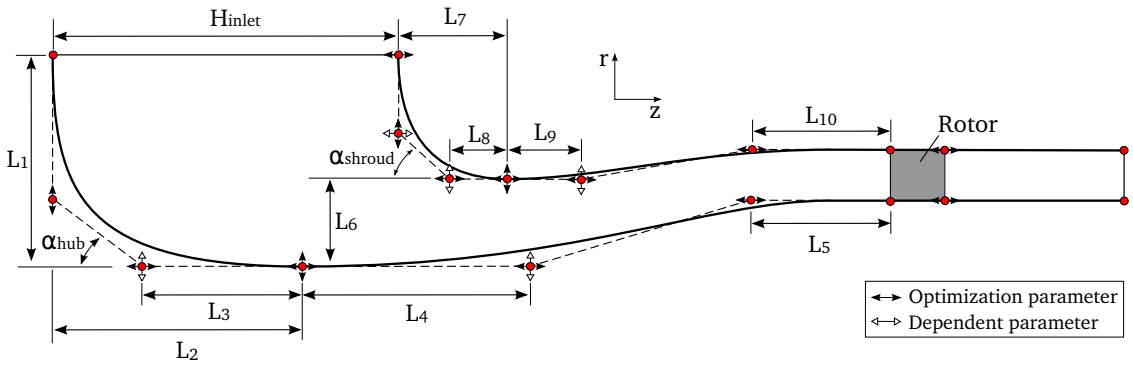

Figure 9: **Meridional Parameterization of the Inlet Section and the Rotor**

80% plus one central case = 50%). Further, to reduce the number of required evaluations, the fractional factorial design approach [10] is used: $2^{(k-p)}$ with $(k-p)$ = 6, thus resulting in 64 experiments plus the central case, which are the initial sampling of the database.

4.2. Parameterization

The 3D model of the rotor of the pump (cf. Fig. 1) is based on Bézier and B-spline curves and surfaces and is defined by:

1. the meridional contour,
2. the blade camber line at hub and tip,
3. the thickness distribution, which is added normal to the camber line at hub and tip, and
4. the number of blades.

The definition of the meridional contour is shown in Fig. 9. The meridional flow path is subdivided into different patches: an inlet patch (90°-bend and swan neck), a blade patch, and an outlet patch. The blade patch corresponds to where the rotor blade is located in the meridional plane. The coordinates of the control points are the geometrical parameters which can be modified by the optimization program and the possible variation in axial and radial direction is indicated by arrows. In order to have a good control about the geometry and to avoid undesirable shapes, lengths and angles are used (e.g. L_1 to L_{10}, H_{inlet}, α_{hub} and α_{shroud}). In total 15 parameters define the meridional flow path.

The rotor blade is defined by the blade camber line of the hub and tip section, each separately defined by the blade angle β-distribution with respect to the meridional plane. The β-distribution is parameterized by a Bézier curve with three control points, one at the leading and trailing edge and one intermediate control point. This results in a total of 6 degrees of freedom.

The final blade with the pressure and suction side surfaces is created by adding a thickness distribution normal to the camber line at hub and tip. In the present optimization study, a NACA 65 thickness distribution at hub and tip has been chosen, which shape is kept constant during the optimization process.

The number of blades, which defines the full rotor, is introduced as an optimization parameter within this design study.

In total 22 parameters define the geometry of the pump and will be subject to optimization.

4.3. Flow Analysis

Every geometry in the *Iteration Loop* according to Fig. 8 has been analyzed at the design operating point using the commercial flow solver fineTurbo™. The incompressible Reynolds-Averaged Navier-Stokes (RANS) equations are solved using a Runge-Kutta scheme in conjunction with accelerating techniques such as variable-coefficient implicit residual smoothing and a multi-grid scheme. Discretization is based on finite volumes with a cell-centered scheme stabilized by artificial dissipation. For the turbulence closure the one equation model of Spalart and Allmaras [11] is used with the assumption of fully turbulent flow (inlet Reynolds number $Re_{inlet} = 6.5 \cdot 10^5$). The flow properties of lead-bismuth eutectic (LBE) according to [12] have been used for the CFD simulations.

4.4. Objectives and Constraints

The optimization of the inlet section and the rotor has two objectives:

1. Maximizing the hydraulic efficiency

$$Obj_1 = \eta_{hyd} = \frac{\Delta P_{tot}}{\rho \cdot \Delta(V_\theta U)} \tag{7}$$

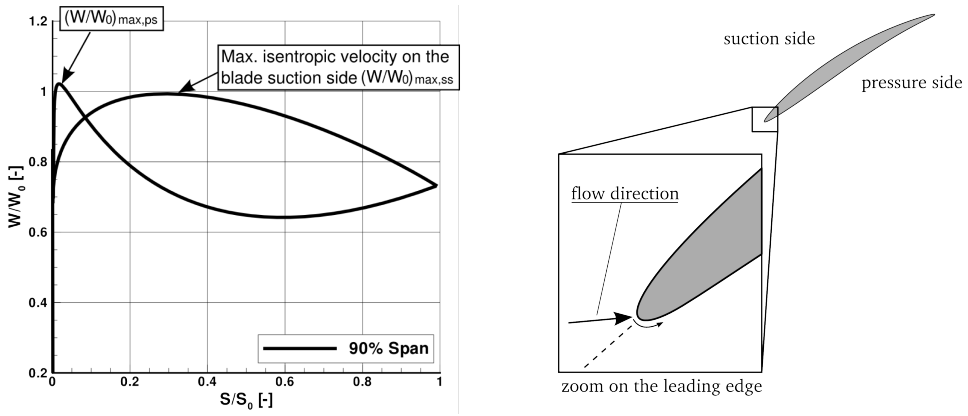

Figure 10: **Illustration of negative incidence resulting in a velocity peak on the pressure side**

where ρ is the density of LBE, ΔP_{tot} the mass-flow averaged absolute total pressure rise, and $\Delta(V_\theta U)$ the difference of the mass flow averaged angular momentum between inlet and outlet.

2. Reducing the maximum isentropic velocity $(W/W_0)_{max,SS}$ on the blade suction side at 90% span. The isentropic velocity objective aims at reducing the maximum relative velocity in the tip section (90%-span) as shown in Fig. 10 and is computed as follows:

$$\begin{aligned} Obj_2 &= (W/W_0)_{max,SS} \\ &= \sqrt{1 - C_p|_{min,SS}} \end{aligned} \tag{8}$$

with the pressure coefficient C_p:

$$C_P = \frac{P - P_{ref}}{0.5 \cdot \rho \cdot W_{ref}^2} \tag{9}$$

The two objectives are subject to two constraints:

$$\Delta H \geq \Delta H_{min} \tag{10}$$

and

$$\left[(W/W_0)_{max,ps} - (W/W_0)_{max,ss}\right] \leq 0\,. \tag{11}$$

The first constraint (Eqn. 10) ensures that the designs generated by the optimization program supply the required total head for the design flow rate. The second constraint (Eqn. 11) prevents that the isentropic velocity objective Obj_2 is not improved at the expense of a higher velocity on the pressure side at the leading edge due to negative incidence, i.e. if the flow impinges on the suction side, which results in a velocity peak on the pressure side (Fig. 10).

4.5. Results

The results of the optimization are presented in Fig. 11, showing both the total head ΔH (left) and the maximum isentropic velocity on the suction side $(W/W_0)_{max,SS}$ (right) with respect to the hydraulic efficiency η_{hyd}. Each symbol in Fig. 11 represents one design that has been analyzed by CFD. The square symbols represent the geometries analyzed for the initial database (DOE) prior to the optimization to train the metamodel. The designs generated during the optimization process are the diamond shape symbols. From the initial scattered distribution of the DOE (Fig. 11, left), the optimizer generated a large number of designs with high hydraulic efficiency η_{hyd} and minimum required total head (indicated with the horizontal line in Fig. 11). The selected design of this optimization supplies a total Head, which is above the minimum required value, with high hydraulic efficiency. The reason why this particular design has been chosen is more obvious from Fig. 11, (right) showing the two-dimensional objective space, i.e. the maximum isentropic velocity on the suction side $(W/W_0)_{max,SS}$ with respect to the hydraulic efficiency η_{hyd}.

In this plot only designs which satisfy the constraints according to Eqns. 10 and 11 are presented such that the apparent front of designs towards the lower right hand corner is the Pareto front comprising non dominated designs, i.e. no other designs outperform the Pareto optimal designs with respect to both higher efficiency and lower relative velocity. Higher hydraulic efficiency comes at the expense of higher relative velocity due to positive incidence resulting in a velocity peak on the suction side leading edge. In this optimization reducing the isentropic velocity

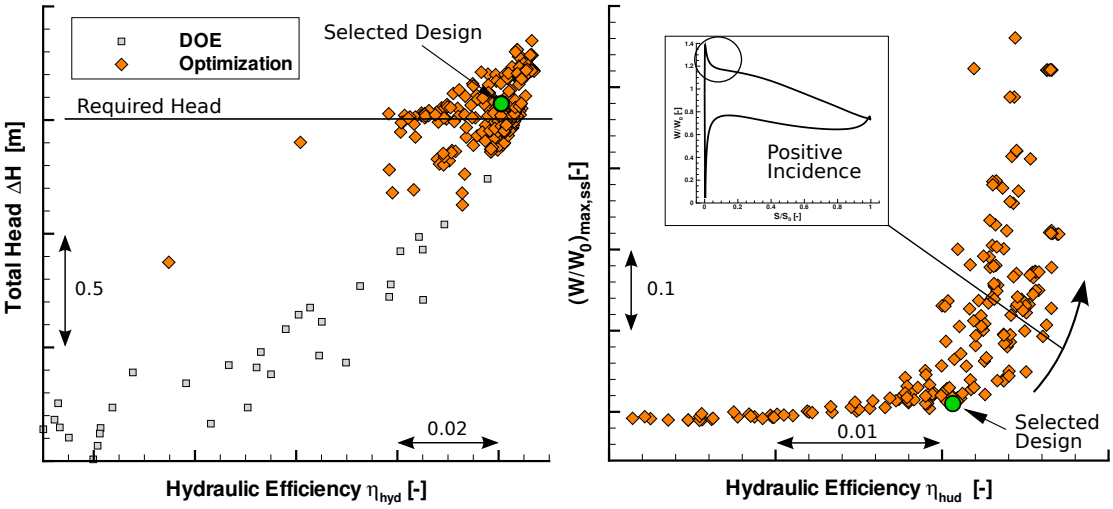

Figure 11: **Total Head vs. Hydraulic Efficiency (left), 2D Objective Space: $(W/W_0)_{max,SS}$ vs. Hydraulic Efficiency (right)**

on the suction side, i.e. the relative velocity to limit erosion had a higher priority than improving the efficiency, resulting in the selected design, which is considered as the best trade-off solution of both objectives.

The selected design, which is presented in Fig. 12, (left) is a high staggered, low aspect ratio rotor ($h/c_{tip} \approx 0.36$) with a solidity in the tip section of $(c/p)_{tip} \approx 1.26$. It is a mid-loaded blade with an equal loading in the hub and tip section and with a smooth diffusion on the suction side as illustrated in Fig. 12, (middle) showing the isentropic velocity distribution at 10% and 90% span. Additionally, as illustrated already in the 2-dimensional objective space in Fig. 11, (right), this design has a rather low velocity on the suction side which limits the erosion risk.

Figure 12, (right) illustrates the mass-flow averaged span-wise distribution of the rotor Diffusion Factor (DF) at design operating conditions. Although the Diffusion Factor introduced by Lieblein [13]

$$DF = 1 - \frac{W_2}{W_1} + \frac{\Delta W_\theta}{2\sigma W_1} \tag{12}$$

using the relative velocities up- and downstream of the rotor and the solidity σ is strictly valid for two-dimensional flows, it is a suitable parameter to estimate off-design tendencies. Except close to the side walls where the flow is overturned due to secondary flows (i.e. due to the hub and shroud passage vertices), the computed rotor Diffusion Factor is below DF ≤ 0.5, which indicates a sufficient margin towards lower flow rates.

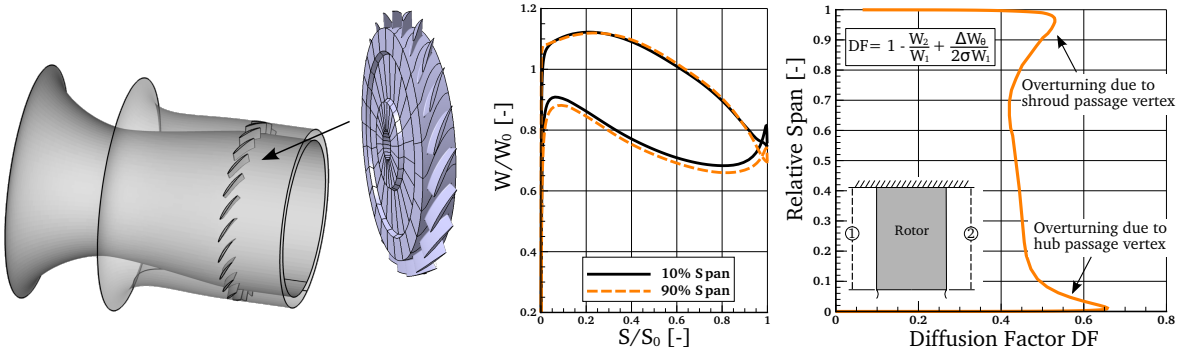

Figure 12: **Selected Design Indicated in Fig. 11 with a Close Up on the Rotor (left), Isentropic Velocity Distribution at 10% and 90% Span (middle), Span-wise Distribution of Rotor Diffusion Factor (right)**

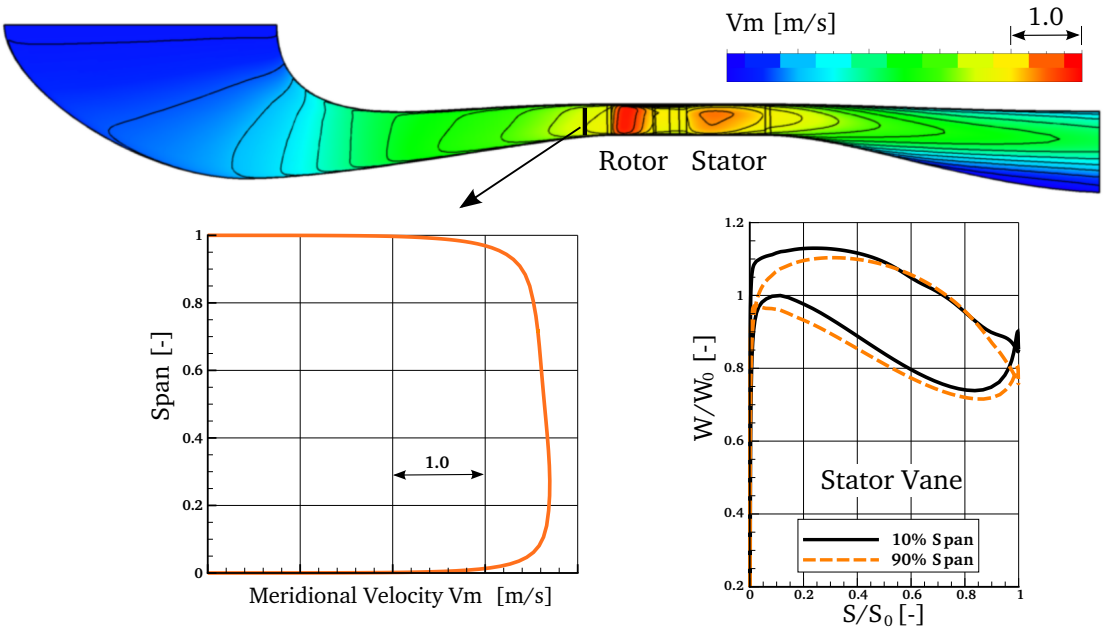

Figure 13: **Meridional Velocity in the Final Pump Design and Isentropic Velocity Distribution at 10% and 90% Span of the Stator Vane**

4.6. Stator-Diffuser Optimization

Subsequently to the inlet-rotor design optimization, the stator-diffuser has been designed and optimized. A similar parameterization as for the inlet-rotor optimization is used with 18 degrees of freedom, comprising the meridional flow path and blade shape. The design of the rotor is kept constant during this process, but the inlet and rotor are modeled in the CFD during this design effort. The objectives of the optimization are to diffuse as much as possible inside the diffuser with limited losses, while reducing as much as possible the velocity peak on the suction side of the stator vane to limit erosion. The outcome of this optimization is illustrated in Fig. 13, showing the meridional velocity with a span-wise distribution upstream of the rotor and the isentropic velocity distribution at 10% and 90% span of the stator vane.

4.7. Performance Map

The selected design (Fig. 13) has been analyzed further regarding its off-design performance. Although the pump was designed primarily for the design point, it has good off-design characteristics, which is illustrated in Fig. 14, showing the Head coefficient

$$\psi = \frac{g.\Delta H}{U_{tip}^2} \tag{13}$$

and the efficiency based on the torque

$$\eta_{Torque} = \frac{\dot{m}\Delta Hg}{\omega \cdot Torque} \tag{14}$$

with respect to the flow coefficient

$$\phi = \frac{V_x}{U_{tip}}\,. \tag{15}$$

The reason for the good off-design behavior is related to the chosen design strategy. The optimization was aiming at limiting the diffusion in the rotor and stator and reducing the incidence of both blade rows resulting in a robust design with an entirely sufficient negative slope ($\equiv \Delta\psi/\Delta\phi$) of the characteristics curve.

5. Conclusions

A hydrodynamic optimization based on evolutionary methods is used to design the primary pump of the MYRRHA nuclear reactor. The design approach is aimed at

- maximizing the hydraulic efficiency of the rotor,
- minimizing the pressure losses in the stator and diffuser, and

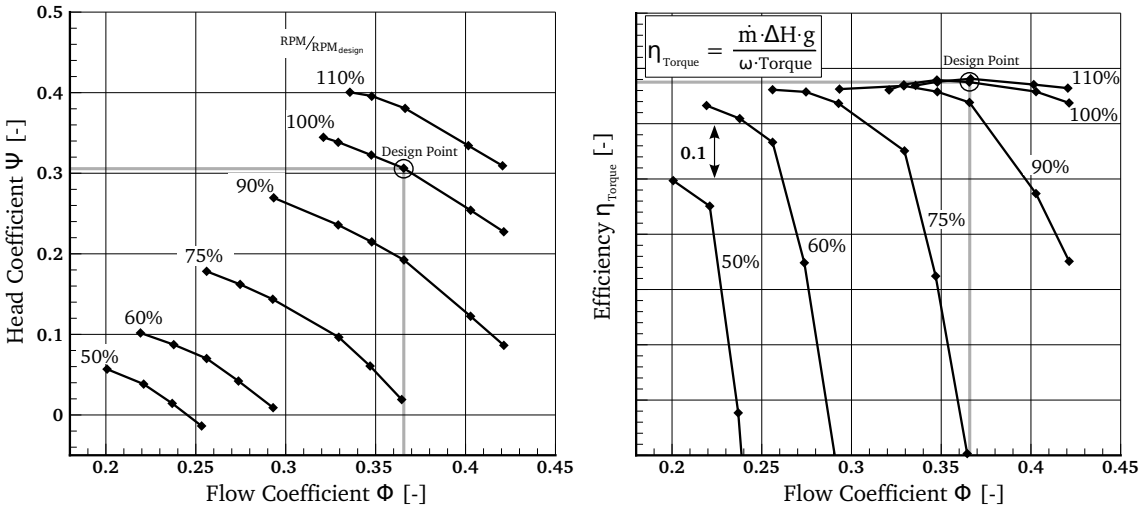

Figure 14: **Performance Map of the Pump**

- reducing the relative velocity in the rotor tip section

Based on the preliminary 1D optimization, the rotor and stator have been designed in two successive steps keeping the number of design parameters and objectives to feasible values in each optimization run. The outcome is a pump, which supplies the required Head and is respecting the design target of low relative velocity to limit erosion.

The pump has been realized as a moderate specific speed, high hub-to-tip ratio axial pump (N_s = 70, R_{hub}/R_{tip} = 0.88), although a mixed-flow pump would provide higher hydraulic efficiency according to classical specific speed charts. However, due to the additional complexity of a mixed flow configuration in the manufacturing process, an axial configuration is more attractive.

Although the pump was designed primarily for the design operating point, it has a good off-design behavior, which is the result of the chosen design strategy. The optimization was aiming at limiting the diffusion in the rotor and stator and reducing the incidence of both blade rows resulting in a robust design.

6. Publications

This work will be published under:

Mueller L., Verstraete T., Arts T., 2013, *Design Optimization of a Primary Pump*, 10th European Conference on Turbomachinery, Fluid Dynamics and Thermodynamics, 15-19 April 2013, Lappeenranta, Finland.

7. Nomenclature

Latin

c	chord
C_p	pressure coefficient
D	diameter
g	acceleration due to gravity
H	head
N_s	specific speed
p	pitch
P	pressure
Q	flow rate
R	radius
s	meridional length
U	peripheral speed
V	absolute velocity
W	relative velocity

Greek

α	absolute flow angle
β	relative flow angle, blade metal angle
Δ	delta/difference
η	efficiency
θ	circumferential component
ν	hub-to-tip ratio
ρ	density
σ	solidity
ω	angular rotational speed

Subscripts and Superscripts

$0, ref$	reference quantity
1	quantity upstream of the rotor
2	quantity downstream of the rotor

	upstream of the stator
3	quantity downstream of the stator
4	quantity at the exit of the diffuser
hub	hub section
tip	tip section
tot	total quantity
x	axial

ANN	Artificial Neural Network
CFD	Computational Fluid Dynamics
DE	Differential Evolution
DOE	Design Of Experiments
MYRRHA	Multi-purpose, HYbrid Research Reactor for High-technology Applications
Obj	Objective
PS, SS	Pressure Side, Suction Side
RPM	Revolutions Per Minute
VKI	von Karman Institute for Fluid Dynamics

References

[1] SCKCEN, Myrrha: Multi-purpose hybrid research reactor for high-tech applications, http://myrrha.sckcen.be/ (2012).
URL `http://myrrha.sckcen.be/`

[2] OKBM, Experimental Designing Bureau of Machine Building, http://www.okbm.nnov.ru/ (2012).
URL `http://www.okbm.nnov.ru/`

[3] A. Stepanoff, Centrifugal and Axial Flow Pumps, John Wiley & Sons, Inc., 1957.

[4] H. Saravanamuttoo, G. Rogers, H. Cohen, S. P.V., Gas Turbine Theory, 5th Edition, Pearson Prentice Hall., 2001.

[5] R. Storn, K. Price, Differential Evolution - A Simple and Efficient Heuristic for Global Optimization over Continuous Spaces, Journal of Global Optimization 11 (1997) 341–359.

[6] J. Crouse, D. Sondercock, Blade-Element Performance of 0.7 Hub-Tip Radius Ratio Axial-Flow Pump rotor with Tip Diffusion Factor of 0.43, Tech. Rep. NASA TN D-2481, Lewis Resarch Center, Cleveland Ohio (1964).

[7] M. Miller, J. Crouse, Design and Overall Performance of an Axial-Flow Pump Rotor with a Blade-Tip Diffusion of 0.66, Tech. Rep. NASA TN D-3024, Lewis Resarch Center, Cleveland Ohio (1965).

[8] D. Urasek, Design and Performance of a 0.9 Hub-Tip-Ratio Axial-Flow Pump Rotor with a Blade-Tip Diffusion Factor of 0.63, Tech. Rep. NASA TM X-2235, Lewis Resarch Center, Cleveland Ohio (1971).

[9] D. Montgomery, Design and Analysis of Experiments, John Wiley & Sons, Inc., 2006.

[10] T. Verstraete, Multidisciplinary Turbomachinery Component Optimization Considering Performance, Stress, and Internal Heat Transfer, Ph.D. thesis, Von Karman Institute for Fluid Dynamics - University of Gent (2008).

[11] D. Wilcox, Turbulence Modelling for CFD, DCW. Industries, Inc., 1993.

[12] NEA, Handbook on Lead-bismuth Eutectic Alloy and Lead Properties, Materials Compatibility, Thermal-hydraulics and Technologies (2008).

[13] S. Lieblein, F. C. Schwenk, R. Broderick, Diffusion Factor for Estimating Losses and Limiting Blade Loadings in Axial-Flow-Compressor Blade Elements, Tech. Rep. NACA RM E53D01, Lewis Flight Propulsion Laboratory, Cleveland Ohio (1953).

NUMERICAL MODELING OF AEROTHERMODYNAMICS DURING RE-ENTRY

Multiscale Models and Computational Methods for Aerothermodynamics

Alessandro Munafò

Aeronautics and Aerospace Department, von Karman Institute for Fluid Dynamics, Belgium, munafo@vki.ac.be

Supervisor: Thierry Magin

Associate Professor, Aeronautics and Aerospace Department, von Karman Institute for Fluid Dynamics, Belgium, magin@vki.ac.be

University Supervisor: Anne Bourdon

Directeur de recherche CNRS, Laboratoire EM2C CNRS UPR 288, École Central Paris, France, anne.bourdon@em2c.ecp.fr

Abstract

We propose to develop physical models and computational methods for an accurate description of non-equilibrium physico-chemical phenomena in aerothermodynamics flows. In this work, we focus on the development of a spectral-Lagrangian method for the Boltzmann equation for a multi-energy level gas. Internal energy levels are treated as separate species and inelastic collisions are accounted for. Computational results are compared with those obtained by means of the DSMC method in order to assess the accuracy of the proposed numerical method.

Keywords: Aerothermodynamics, Rarefied gas-dynamics, Boltzmann equation, Fourier transform, Spectral methods, Constrained optimization.

1. Introduction

Understanding non-equilibrium phenomena occurring in aerothermodynamic flows (such as the one around a spacecraft entering a planetary atmosphere) is of fundamental importance for many applications. Typical examples, taken from the aerospace domain, are the design of heat shields for space vehicles and interpretation of experiments carried out in high enthalpy wind tunnels. Non-equilibrium phenomena are also present in industrial processes making use of lasers, discharges and plasma torches. Progresses made in developing physical models and computational methods for aerospace applications, on which we focus here, could also be used in other areas (such as plasma enhanced combustion and electric propulsion) where the occurrence of non-equilibrium must be taken into account as well.

Before proceeding further, it is necessary to explain non-equilibrium. The concept can be introduced by recalling what occurs around a spacecraft entering a planetary atmosphere at hypersonic speeds. A strong bow shock is formed in front of the vehicle. The flow experiences a sudden compression. Pressure and density increase and, at the same time, most of the flow macroscopic kinetic energy is converted into thermal energy, leading to a steep temperature increase. The combined effects of pressure and temperature lead to higher values of collision frequencies between atoms and molecules and to more energetic collisions. These cause excitation of internal energy degrees of freedom and, if the collisions are energetic enough, breaking of chemical bonds can occur (molecular dissociation). If the entry speed is high enough ionization may also occur, and the gas becomes a partially ionized plasma.

The description of these flows is extremely complicated because all collisional processes need a finite time to occur. If this time is very small compared to some macroscopic characteristic time scale (such as the time needed for a fluid particle to pass across a shock wave or the boundary layer), the flow is in equilibrium as it can immediately adapt to the varying conditions of pressure and temperature without any lag. If the inverse situation occurs, the flow is said to be frozen. The intermediate situation, where a finite lag exists, is that of non-equilibrium flows. In this case, a correct description of the flow-field can be achieved only if the finite rate nature of collisional processes is taken into account in the flow governing equations.

The starting point for the description of non-equilibrium flows are the Navier-Stokes equations, where non-equilibrium effects can be taken into account by means of multi-temperature or collisional models [1]. Multi-temperature models were proposed as a simple approach to overcome all difficulties related to the modeling of non-equilibrium. They are based on Boltzmann distributions of the internal energy levels at distinct temperatures and are valid only in case of small departure from equilibrium [1]. However, they are widely used outside of their range of validity because of the lack of more accurate physical models, their easy implementation and their reasonable computational cost for 3D simulations.

State-to-state or collisional models [2; 3; 4; 5; 6; 7; 8; 9] treat each energy level as a separate pseudo-species. This approach provides more flexibility and accuracy, since effects of non-Boltzmann distributions are accounted for. However, a very large number of processes have to be considered and, for each one, rate coefficient values have to be obtained. Also, the number of equations to be solved rapidly increases with the number of internal energy levels. Applications of collisional models to 2D problems have become feasible as shown in [10; 11; 12].

A further complication in the study of non-equilibrium flows comes from the presence of rarefied gas effects [13]. These occur in flow regions (such as bow shocks and wakes) where the macroscopic spatial scales becomes of the same order of the local mean free path (average distance traveled by atoms/molecules between collisions).

Attempts to compute rarefied flows by means of a hydrodynamic description based on the Navier-Stokes equations give inaccurate results due to the failure of Newton's law for the stress tensor and Fourier's law for the heat flux vector in the rarefied regime [14]. The Boltzmann equation provides a statistical description of dilute gaseous systems valid from the rarefied to the hydrodynamic regime [14]. It describes the evolution of the species distribution function in the phase-space. Once the distribution function of each species known, it is possible to compute macroscopic observables such as density, hydrodynamic velocity and temperature by means of suitable moments. The computation of numerical solutions of the Boltzmann equation is not trivial. This is due to the integro-differential nature of the equation. A further source of difficulty is the high dimensionality of the problem (numerical solutions must be sought in the phase-space). Stochastic-like solutions of the Boltzmann equation can be obtained by means of the Direct-Simulation-Monte-Carlo (DSMC) method [15; 16]. The former is a particle-based technique and has proven to be accurate [16]. However, it shares the drawbacks of stochastic methods, the main one being the presence of noise in the numerical results [15]. The former problem affects, in particular, the accuracy of the solution for low speed and unsteady flows. Parallel to the development of the DSMC method, deterministic numerical methods for the Boltzmann equation have been proposed. These comprise, among all, discrete velocity models [17; 18] and spectral methods [19; 20; 21]. The main advantage of a deterministic method over the DSMC technique is that the numerical solution obtained is not affected by numerical noise. Deterministic methods can also be applied to flow problems in the hydrodynamic and transition regime, for which the use of the DSMC method becomes prohibitively expensive [22].

2. Motivation

Despite the research efforts performed at the present time and in the past years and the increasing available computational power and resources, the computation of non-equilibrium aerothermodynamic flows still poses problems. This is mainly due to the lack of accurate physical models (within a wide range of conditions) for collisional processes and transport phenomena in gas phase.

For the present thesis, it was decided to concentrate the research activity on the following topics:

- Development of reduced (coarse grain) collisional models for CFD applications. This activity will be performed within an innovative context at the interface between computational quantum chemistry and computational fluid dynamics.
- Development of computational methods for the numerical solution of the Boltzmann equation with chemical reactions and internal energy excitation. Applications will focus on flows out of the range of applicability of the Navier-Stokes equations (such as shock waves).

In this paper, focus is placed on the second topic of the previous list.

3. Physical Model

3.1. Assumptions and Conventions

The physical model used in the present work is based on the following assumptions and conventions

[23]:

1. The gas mixture is composed of identical particles.
2. Particles have discrete internal energy levels:
   - The indices of energy levels are stored in the set $\mathcal{I}_S = \{1, \ldots, N_s\}$, N_s being the number of species.
   - The mass of the species (energy level) $i \in \mathcal{I}_S$ is m_i.
   - The degeneracy and the energy of the energy level $i \in \mathcal{I}_S$ are g_i and E_i, respectively.
3. Only binary collisions are accounted for:

$$i + j = h + l, \quad i, j, h, l \in \mathcal{I}_S. \tag{1}$$

   - Elastic collision: $i = h$ and $j = l$.
   - Inelastic collision: $(j, h, l) \in \mathcal{I}_i^{\text{in}}$. The set $\mathcal{I}_i^{\text{in}}$ stores the ordered triplets (j, h, l) for all the possible inelastic collisions involving the species i as reactant in Eq. (1) and is defined as:

$$\mathcal{I}_i^{\text{in}} = \left\{ (j,h,l) \in \left[\mathcal{I}_S \times \mathcal{I}_S \times \mathcal{I}_S \setminus \bigcup_{s \in \mathcal{I}_S} (s,i,s) \right] \right\}, \quad i \in \mathcal{I}_S. \tag{2}$$

4. The presence of chemical reactions (such as dissociation and ionization) and external force fields is neglected.

3.2. The Boltzmann Equation

Based on the hypothesis introduced in Sect. 3.1, a Boltzmann equation [14] can be written for the velocity distribution function $f_i(\mathbf{x}, \mathbf{v}, t)$:

$$\frac{\partial f_i}{\partial t} + \mathbf{v} \cdot \frac{\partial f_i}{\partial \mathbf{x}} = \sum_{j \in \mathcal{I}_S} Q_{ij}(\mathbf{v}) + \sum_{(j,h,l) \in \mathcal{I}_i^{\text{in}}} Q_{ij}^{hl}(\mathbf{v}), \; i \in \mathcal{I}_S. \tag{3}$$

In Eq. (3) the quantities $Q_{ij}(\mathbf{v})$ and $Q_{ij}^{hl}(\mathbf{v})$ are, respectively, the elastic and inelastic collision operators [14]:

$$Q_{ij}(\mathbf{v}) = \iint_{\substack{\mathbf{w} \in \Re^3 \\ \boldsymbol{\omega}' \in S^2}} \left[f_i(\mathbf{v}')\, f_j(\mathbf{w}') - f_i(\mathbf{v})\, f_j(\mathbf{w}) \right] \sigma_{ij}\, u \, d\boldsymbol{\omega}' \, d\mathbf{w}, \quad i, j \in \mathcal{I}_S, \tag{4}$$

$$Q_{ij}^{hl}(\mathbf{v}) = \iint_{\substack{\mathbf{w} \in \Re^3 \\ \boldsymbol{\omega}' \in S^2}} \left[\frac{g_i\, g_j}{g_h\, g_l} f_h(\mathbf{v}')\, f_l(\mathbf{w}') - f_i(\mathbf{v})\, f_j(\mathbf{w}) \right] \sigma_{ij}^{hl}\, u \, d\boldsymbol{\omega}' \, d\mathbf{w}, \quad i \in \mathcal{I}_S, \; (j, h, l) \in \mathcal{I}_i^{\text{in}} \tag{5}$$

In the expressions for the elastic and inelastic collision operators (Eqs. (4) - (5), respectively), $\mathbf{v}$ and $\mathbf{w}$ are, respectively, the velocities of the species i and j, u is the relative velocity magnitude $u = |\mathbf{v} - \mathbf{w}|$, $\boldsymbol{\omega}'$ is the unit vector along the scattering direction, and σ_{ij} and σ_{ij}^{hl} are, respectively, the differential cross-sections for the elastic and inelastic collision associated to the binary interaction given in Eq. (1). As usual, primed variables in Eqs. (4) - (5) (and in what follows) refer to post-collisional values. Their values are related to pre-collisional values through the conservation of mass, momentum and energy:

$$m_i + m_j = m_h + m_l, \tag{6}$$

$$m_i\, \mathbf{v} + m_j\, \mathbf{w} = m_h\, \mathbf{v}' + m_l\, \mathbf{w}', \tag{7}$$

$$\frac{1}{2} m_i\, v^2 + \frac{1}{2} m_j\, w^2 = \frac{1}{2} m_h\, v'^2 + \frac{1}{2} m_l\, w'^2 + \Delta E_{ij}^{hl}, \quad i \in \mathcal{I}_S, \; (j, h, l) \in \mathcal{I}_i^{\text{in}}. \tag{8}$$

where the net internal energy jump ΔE_{ij}^{hl} in Eq. (8) is $\Delta E_{ij}^{hl} = E_l + E_h - E_j - E_i$. Note that for a pure gas with internal energy the mass of all the particles are identical ($m_i = m_j = m_h = m_l$).

Eq. (3) may also be used for the case of a mixture of monatomic gases without internal energy. In this situation, $m_i = m_h$ and $m_j = m_l$. Moreover only elastic collisions occur and all the terms $Q_{ij}^{hl}(\mathbf{v})$ in Eq. (3) are zero.

3.3. The Fourier Transform of the Elastic and Inelastic Collision Operators

The numerical method proposed in the present work (see Sect. 4) makes use of the Fourier transform of the elastic and inelastic collision operators [24] (Eqs. (4) - (5), respectively). The former can be computed based on their weak form:

$$\int_{\mathbf{v} \in \Re^3} \Phi_i(\mathbf{v})\, Q_{ij}(\mathbf{v})\, d\mathbf{v} = \iiint_{\substack{\mathbf{v}, \mathbf{w} \in \Re^3 \\ \boldsymbol{\omega}' \in S^2}} \left[\Phi_i(\mathbf{v}') - \Phi_i(\mathbf{v}) \right] f_i(\mathbf{v})\, f_j(\mathbf{w})\, \sigma_{ij}\, u \, d\boldsymbol{\omega}' \, d\mathbf{w} \, d\mathbf{v}, \quad i, j \in \mathcal{I}_S \tag{9}$$

$$\int_{\mathbf{v}\in\Re^3} \Phi_i(\mathbf{v})\, Q_{ij}^{hl}(\mathbf{v})\, d\mathbf{v} =$$
$$\int_{\substack{\mathbf{v}',\mathbf{w}'\in\Re^3\\ \omega\in S^2}}\int\int \Phi_i(\mathbf{v})\; f_h(\mathbf{v}')\; f_l(\mathbf{w}')\, \sigma_{hl}^{ij}\, u'\, d\omega\, d\mathbf{w}'\, d\mathbf{v}' -$$
$$\int_{\substack{\mathbf{v},\mathbf{w}\in\Re^3\\ \omega'\in S^2}}\int\int \Phi_i(\mathbf{v})\; f_i(\mathbf{v})\; f_j(\mathbf{w})\, \sigma_{ij}^{hl}\, u\, d\omega'\, d\mathbf{w}\, d\mathbf{v},$$
$$i \in \mathcal{I}_S,\ (j,\, h,\, l) \in \mathcal{I}_i^{\text{in}}, \tag{10}$$

where the quantity $\Phi_i(\mathbf{v})$ in Eqs. (9) - (10) is a smooth test function of the velocity $\mathbf{v}$. The substitution of a Fourier velocity mode $\Phi_i(\mathbf{v}) = (2\pi)^{-3/2} \exp(-\imath\, \boldsymbol{\zeta}\cdot\mathbf{v})$ in Eqs. (9) - (10) gives the Fourier transform of the elastic and inelastic collision operators and, after some algebra (similar to [19]), one obtains:

$$\hat{Q}_{ij}(\boldsymbol{\zeta}) = \int_{\boldsymbol{\xi}\in\Re^3} \hat{f}_i\,(\boldsymbol{\zeta}-\boldsymbol{\xi})\;\; \hat{f}_j(\boldsymbol{\xi})\, \hat{W}_{ij}\,(\boldsymbol{\zeta},\boldsymbol{\xi})\, d\boldsymbol{\xi}, \quad i,\, j \in \mathcal{I}_S, \tag{11}$$

$$\hat{Q}_{ij}^{hl}(\boldsymbol{\zeta}) = \int_{\boldsymbol{\xi}\in\Re^3} \Big[\, \hat{f}_h\,(\boldsymbol{\zeta}-\boldsymbol{\xi})\;\; \hat{f}_l(\boldsymbol{\xi})\, \hat{G}_{ij}^{hl}\,(\boldsymbol{\zeta},\boldsymbol{\xi}) - \hat{f}_i\,(\boldsymbol{\zeta}-\boldsymbol{\xi})\;\; \hat{f}_j(\boldsymbol{\xi})\, \hat{L}_{ij}^{hl}\,(\boldsymbol{\xi})\Big]\, d\boldsymbol{\xi}, \quad i \in \mathcal{I}_S,\ (j,\, h,\, l) \in \mathcal{I}_i^{\text{in}}. \tag{12}$$

In Eqs. (11) - (12), the quantities $\hat{f}_i$, $\hat{f}_j$, $\hat{f}_h$ and $\hat{f}_l$ are, respectively, the Fourier transform of the velocity distribution function of the species i, j, h and l, while the quantities $\hat{W}_{ij}\,(\boldsymbol{\zeta},\boldsymbol{\xi})$, $\hat{G}_{ij}^{hl}\,(\boldsymbol{\zeta},\boldsymbol{\xi})$ and $\hat{L}_{ij}^{hl}\,(\boldsymbol{\xi})$ are:

$$\hat{W}_{ij}\,(\boldsymbol{\zeta},\boldsymbol{\xi}) = \frac{1}{\left(\sqrt{2\,\pi}\right)^3} \int_{\substack{\mathbf{u}\in\Re^3,\\ \omega'\in S^2}}\int u\, \sigma_{ij} \left\{ \exp\left[-\imath\, \frac{\mu_{ij}}{m_i}\, \boldsymbol{\zeta}\cdot(\mathbf{u}'-\mathbf{u}) \right] - 1 \right\} \times \exp\left(-\imath\, \boldsymbol{\xi}\cdot\mathbf{u}\right)\, d\omega'\, d\mathbf{u}, \quad i,\, j \in \mathcal{I}_S, \tag{13}$$

$$\hat{G}_{ij}^{hl}\,(\boldsymbol{\zeta},\boldsymbol{\xi}) = \frac{1}{\left(\sqrt{2\,\pi}\right)^3} \int_{\substack{\mathbf{u}'\in\Re^3,\\ \omega\in S^2}}\int u'\, \sigma_{hl}^{ij}\, \exp\left[-\imath\, \frac{\mu_{ij}}{m_i}\, \boldsymbol{\zeta}\cdot(\mathbf{u}-\mathbf{u}') \right] \times \exp\left(-\imath\, \boldsymbol{\xi}\cdot\mathbf{u}'\right)\, d\omega\, d\mathbf{u}',\ i \in \mathcal{I}_S,\ (j,\, h,\, l) \in \mathcal{I}_i^{\text{in}}, \tag{14}$$

$$\hat{L}_{ij}^{hl}\,(\boldsymbol{\xi}) = \frac{1}{\left(\sqrt{2\,\pi}\right)^3} \int_{\substack{\mathbf{u}\in\Re^3,\\ \omega'\in S^2}}\int u\, \sigma_{ij}^{hl}\, \exp\left(-\imath\, \boldsymbol{\xi}\cdot\mathbf{u}\right)\, d\omega'\, d\mathbf{u}, \quad i \in \mathcal{I}_S,\ (j,\, h,\, l) \in \mathcal{I}_i^{\text{in}}. \tag{15}$$

In Eqs. (13) - (14) the quantity $\mu_{ij} = m_i\, m_j/(m_i + m_j)$ is the reduced mass of the species i and j. From Eqs. (11) - (15), the following observations can be made:

1. The Fourier transform of the elastic and inelastic collision operators can be written as weighted convolutions in Fourier space, the convolution weights being the functions $\hat{W}_{ij}\,(\boldsymbol{\zeta},\boldsymbol{\xi})$, $\hat{G}_{ij}^{hl}\,(\boldsymbol{\zeta},\boldsymbol{\xi})$ and $\hat{L}_{ij}^{hl}\,(\boldsymbol{\xi})$, respectively [19].
2. The convolution weights $\hat{W}_{ij}\,(\boldsymbol{\zeta},\boldsymbol{\xi})$, $\hat{G}_{ij}^{hl}\,(\boldsymbol{\zeta},\boldsymbol{\xi})$ and $\hat{L}_{ij}^{hl}\,(\boldsymbol{\xi})$ depend only on the cross-section model in use. No dependence on the value of the species distribution function occurs. This fact can be exploited by a computational method (see Sect. 4) that makes use of Eqs. (11) - (12) for the numerical evaluation of the elastic and inelastic collision operators (the weight associated to each interaction can be pre-computed [25]).
3. Since in the definition provided by Eqs. (13) - (15) no assumption is done on the differential cross-section model, anisotropic interactions can also be taken into account [26].

4. Numerical Method

Numerical solutions to Eq. (3) are sought for 1D flows. Operator splitting is used [19] (due to its ease of implementation and low memory requirements when compared with un-split implicit methods in the phase-space). Given the numerical solution at the time-level t^n, the solution at the next time-level t^{n+1} is computed as follows:

$$f_i(t^{n+1}) = C_{\Delta t}\left(\mathcal{A}_{\Delta t}\left(f_i(t^n)\right)\right), \quad i \in \mathcal{I}_S. \tag{16}$$

The operators $\mathcal{A}_{\Delta t}$ and $C_{\Delta t}$ in Eq. (16) are those of the following differential problems related to Eq. (3):

1. Collision-less Boltzmann equation (transport step - operator $\mathcal{A}_{\Delta t}$):
$$\frac{\partial f_i}{\partial t} + v_x\, \frac{\partial f_i}{\partial x} = 0, \quad i \in \mathcal{I}_S. \tag{17}$$
2. Space homogeneous Boltzmann equation (collision step - operator $C_{\Delta t}$):
$$\frac{\partial f_i}{\partial t} = \sum_{j\in\mathcal{I}_S} Q_{ij}(\mathbf{v}) + \sum_{(j,h,l)\in\mathcal{I}_i^{\text{in}}} Q_{ij}^{hl}(\mathbf{v}), \quad i \in \mathcal{I}_S. \tag{18}$$

The combination of the operators provided by Eq. (16) results in a first order time accurate scheme. This is perfectly acceptable if only steady solutions are of

interest (as it is the case for the present work). The accuracy in space is influenced by the method used for the advection step (Eq. (17)).

The advection step is performed by means of a cell centered finite volume method [27]. A uniform grid on the x-axis is assumed and Eq. (17) is then discretized on the former (for each velocity node of the velocity domain - see Sect. 4.1) by using a second order slope-limited upwind scheme [28] (with van Albada's slope limiter [27]). The integration in time is performed by means of the forward Euler method.

For the collision step, Eq. (18) is integrated in time by means of the forward Euler method. The application of the former requires the evaluation at the time-level t^n of all the collision operators on the right-hand-side of Eq. (18). This is possible only by applying:

1. A discretization of the velocity space,
2. An algorithm for the evaluation of each collision operator,

presented in more details in the Sects. 4.1 - 4.2.

4.1. Velocity Space Discretization

The discrete velocity nodes are chosen within a cube in the space $(O; v_x, v_y, v_z)$ centered at the origin and with side semi-length L_v. A uniform grid of N_v nodes along the v_x, v_y and v_z directions is assumed and, after introducing the set $\mathcal{I}_\mathcal{V} = \{0, \ldots, N_v - 1\}$ for sake of clarity, the individual velocity nodes are computed as:

$$v_{\mathrm{k_i}} = -L_v + \mathrm{k_i}\,\Delta v, \quad \mathrm{k_i} \in \mathcal{I}_\mathcal{V}, \quad \mathrm{i} \in \{x, y, z\} \quad (19)$$

where the velocity spacing Δv in Eq. (19) is $\Delta v = 2\,L_v/N_v$. A velocity grid in the Fourier velocity space $(O; \zeta_x, \zeta_y, \zeta_z)$ is also defined:

$$\zeta_{\varepsilon_\mathrm{i}} = -L_\eta + \varepsilon_\mathrm{i}\,\Delta\eta, \quad \varepsilon_\mathrm{i} \in \mathcal{I}_\mathcal{V}, \quad \mathrm{i} \in \{x, y, z\}\,. \quad (20)$$

The velocity spacing $\Delta\eta$ and the semi-length L_η of the discretized Fourier velocity domain are assumed to satisfy the relations:

$$\Delta v\,\Delta\eta = 2\,\pi/N_v, \quad L_\eta = 2\,L_v/N_v, \quad (21)$$

in order to use the Fast-Fourier-Transform (FFT) algorithm [19] in the evaluation of the Fourier and inverse Fourier transforms (see Sect. 4.2).

4.2. Algorithm for the Evaluation of the Collision Operator

The following algorithm is used for the evaluation of the collision operator associated to the interaction between the species i and j given by Eq. (1). In the case of an elastic collision ($i = h$ and $j = l$ in Eq. (1)), the following steps are performed:

1. Compute the Fourier transforms of the velocity distribution function of the species i and j:
$$\hat{f}_{i,j}(\boldsymbol{\zeta}) = \mathcal{F}(f_{i,j}(\mathbf{v})) \;\rightarrow\; O(N_v^3 \log N_v).$$
2. For N_v^3 Fourier velocity nodes compute the Fourier transform of the collision operator $Q_{ij}(\mathbf{v})$ by means of:
$$\hat{Q}_{ij}(\boldsymbol{\zeta}) = \int \hat{f}_i\,(\boldsymbol{\zeta} - \boldsymbol{\xi})\;\hat{f}_j(\boldsymbol{\xi})\,\hat{W}_{ij}\,(\boldsymbol{\zeta}, \boldsymbol{\xi})\;d\boldsymbol{\xi} \;\rightarrow\; O(N_v^3).$$
3. Compute the inverse Fourier transform:
$$\tilde{Q}_{ij}(\mathbf{v}) = \mathcal{F}^{-1}(\hat{Q}_{ij}(\boldsymbol{\zeta})) \;\rightarrow\; O(N_v^3 \log N_v).$$
4. For N_v^3 velocity nodes enforce conservation through the solution of a constrained optimization problem:
$$Q_{ij}(\mathbf{v}) = \mathrm{Opt}(\tilde{Q}_{ij}(\mathbf{v})) \;\rightarrow\; O(N_v^3).$$

The modification of the above procedure in the case of an inelastic collision between the species i and j is straightforward and can be deduced from Eq. (12). The global cost of the algorithm is $O(N_v^6)$ (per interaction) and the last step is performed in order to ensure conservation of mass, momentum and energy during collisions. This approach was originally proposed and formulated in [19] for the case of a simple gas without internal energy. In the present work, an extension of the original method to mixtures with internal energy is proposed. Elastic and inelastic collisions are treated separately and the enforcement of conservation of macroscopic moments is imposed through the following constrained optimization problems:

Elastic collisions

$$\mathcal{P}_\mathrm{el} = \left\{ \min \sum_{i,\,j \in \mathcal{I}_\mathcal{S}} \left\| \tilde{\mathbf{Q}}_{ij} - \mathbf{Q}_{ij} \right\|_2^2, \; \sum_{i,\,j \in \mathcal{I}_\mathcal{S}} \mathbf{C}_{\mathrm{el}\,i}\,\mathbf{Q}_{ij} = \mathbf{0}_{N_s+4} \right\}. \quad (22)$$

Inelastic collisions

$$\mathcal{P}_\mathrm{in} = \left\{ \min \sum_{i \in \mathcal{I}_\mathcal{S}} \sum_{(j,h,l) \in \mathcal{I}_i^\mathrm{in}} \left\| \tilde{\mathbf{Q}}_{ij}^{hl} - \mathbf{Q}_{ij}^{hl} \right\|_2^2, \right.$$
$$\left. , \sum_{i \in \mathcal{I}_\mathcal{S}} \sum_{(j,h,l) \in \mathcal{I}_i^\mathrm{in}} \mathbf{C}_{\mathrm{in}\,i}\,\mathbf{Q}_{ij}^{hl} = \mathbf{0}_5 \right\}. \quad (23)$$

In Eqs. (22) - (23), the vectors $\mathbf{Q}_{ij}$ and $\mathbf{Q}_{ij}^{hl}$ store the values of the operators $Q_{ij}(\mathbf{v})$ and $Q_{ij}^{hl}(\mathbf{v})$, respectively, on the discrete velocity nodes given by Eq. (19), while the matrices $\mathbf{C}_{\mathrm{el}\,i}$ and $\mathbf{C}_{\mathrm{in}\,i}$ are integration matrices whose k-th columns are:

$$(\mathbf{C}_{\mathrm{el}\,i})_k = \Omega_k \times \left[\begin{array}{cccc} m_i\,\delta_{ij} & m_i\,v_{\mathrm{k}_x} & m_i\,v_{\mathrm{k}_y} & m_i\,v_{\mathrm{k}_z} \end{array} \quad \frac{1}{2} m_i\,V_k^2 \right]^{\mathrm{T}}, \quad i,\, j \in \mathcal{I}_{\mathcal{S}}, \tag{24}$$

$$(\mathbf{C}_{\mathrm{in}\,i})_k = \Omega_k \times \left[\begin{array}{cccc} m_i & m_i\,v_{\mathrm{k}_x} & m_i\,v_{\mathrm{k}_y} & m_i\,v_{\mathrm{k}_z} \end{array} \quad \frac{1}{2} m_i\,V_k^2 + E_i \right]^{\mathrm{T}}, \quad i \in \mathcal{I}_{\mathcal{S}}, \tag{25}$$

where $V_k^2 = v_{\mathrm{k}_x}^2 + v_{\mathrm{k}_y}^2 + v_{\mathrm{k}_z}^2$ and Ω_k is the integration weight associated to the velocity node $k = (\mathrm{k}_x, \mathrm{k}_y, \mathrm{k}_z)$. The structure of the matrices in Eqs. (24) - (25) reflects the fact that there exists a set of N_s+4 collisional invariants for elastic collisions (the single species mass, the global momentum and energy), while, for inelastic collisions, the number of collisional invariants is equal to 5 (the global mass, momentum and energy) [14; 29].

It can be shown that the solutions to the above constrained optimization problems (Eqs. (22) - (23)) are [21; 30]:

Elastic collisions

$$\mathbf{Q}_{ij} = \tilde{\mathbf{Q}}_{ij} - \frac{1}{N_s} \mathbf{C}_{\mathrm{el}\,i}^{\mathrm{T}} \left(\sum_{p \in \mathcal{I}_{\mathcal{S}}} \mathbf{C}_{\mathrm{el}\,p}\, \mathbf{C}_{\mathrm{el}\,p}^{\mathrm{T}} \right)^{-1} \left(\sum_{p,q \in \mathcal{I}_{\mathcal{S}}} \mathbf{C}_{\mathrm{el}\,p} \tilde{\mathbf{Q}}_{pq} \right), \quad i,\, j \in \mathcal{I}_{\mathcal{S}}. \tag{26}$$

Inelastic collisions

$$\mathbf{Q}_{ij}^{hl} = \tilde{\mathbf{Q}}_{ij}^{hl} - \frac{1}{N_{\mathrm{in}}} \mathbf{C}_{\mathrm{in}\,i}^{\mathrm{T}} \left(\sum_{p \in \mathcal{I}_{\mathcal{S}}} \mathbf{C}_{\mathrm{in}\,p}\, \mathbf{C}_{\mathrm{in}\,p}^{\mathrm{T}} \right)^{-1} \left(\sum_{p \in \mathcal{I}_{\mathcal{S}}} \sum_{(q,r,s) \in \mathcal{I}_p^{\mathrm{in}}} \mathbf{C}_{\mathrm{in}\,p}\, \tilde{\mathbf{Q}}_{pq}^{rs} \right), \quad i \in \mathcal{I}_{\mathcal{S}},\ (j,h,l) \in \mathcal{I}_i^{\mathrm{in}}, \tag{27}$$

where the factor N_{in} in Eq. (27) is $N_{\mathrm{in}} = N_s(N_s^2 - 1)$.

5. Computational Results

The numerical method explained in Sect. 4 has been implemented in a parallel C code (BESS - Boltzmann Equation Spectral Solver) [21; 30]. Parallelization is performed by means of the OpenMP library [31]. The GSL [32] and FFTW3 [33] libraries are used, respectively, for vector/matrix manipulation and the implementation of the FFT and inverse FFT algorithms.

All computational results are compared with those obtained by means of the DSMC code developed by Torres [34].

5.1. Flow across a Normal Shock Wave in Ar

In order to assess the accuracy of the original numerical method [19], it was decided to compute the flow across a normal shock wave in Ar. The free-stream values for pressure and temperature are 6.25 Pa and 300 K, respectively. Three different values of the free-stream Mach number are considered. The numerical values for the former are given in Table 1 together with those for the N_v and L_v parameters. In all the cases the hard-sphere (HS) collision model [14; 15] is used. The numerical values for the Ar mass and diameter are taken from [15].

	M_∞	N_v	L_v [m/s]
1	1.5	24	2250
2	3.38	32	3700
3	6.5	44	6500

Table 1: Simulation parameters.

Figure 1 shows the kinetic temperature (T) and the parallel and transverse temperatures (T_x and T_y, respectively). In all the cases presented here, the parallel temperature experiences an overshoot, reaches a local maximum and then relaxes towards the value corresponding to the post-shock conditions. This flow-field feature (observed for the first time in DSMC simulations [15]) is more and more enhanced when increasing the free-stream Mach number and is directly related to the distortion (along the x-axis) the velocity distribution function experiences while the flow crosses the shock wave. The kinetic and transverse temperatures, on the contrary, show a monotone increase from the pre-shock till the post-shock value. For both cases shown in Fig. 1 the agreement with the DSMC results is excellent. The same conclusion can be drawn from Fig. 2 showing a comparison for the x component of the heat flux vector and the xx component of the stress tensor.

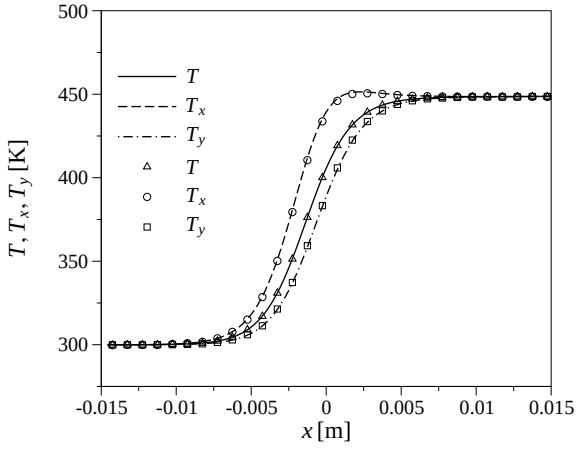

(a) $M_\infty = 1.5$.

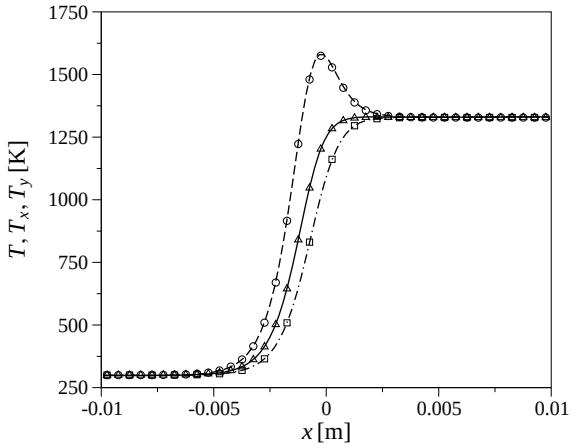

(b) $M_\infty = 3.38$.

Figure 1: Kinetic, parallel and transverse temperature (lines BESS - symbols DSMC).

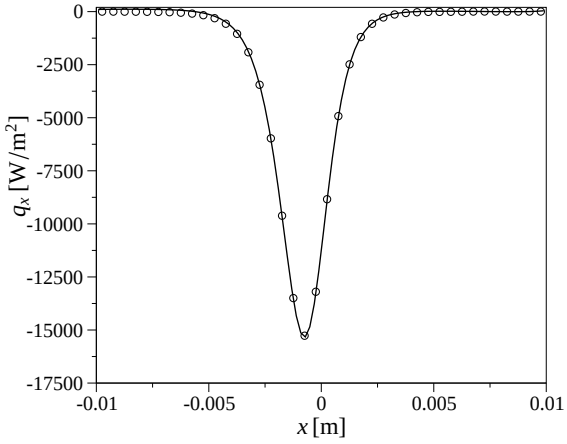

(a) Heat flux ($M_\infty = 3.38$).

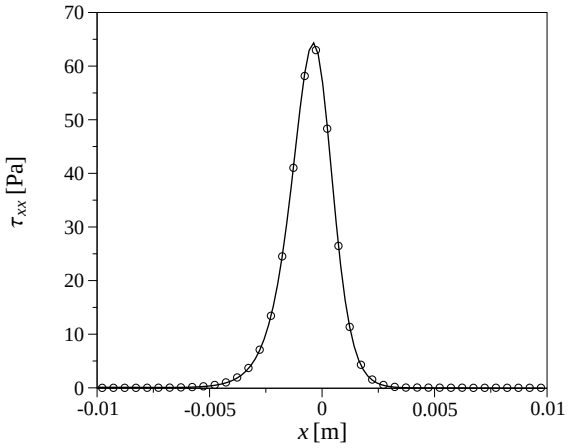

(b) Stress tensor ($M_\infty = 6.5$).

Figure 2: Heat flux and stress tensor (lines BESS - symbols DSMC).

5.2. Flow across a Normal Shock Wave in a Ne-Ar Mixture

The extension to mixtures of the the original numerical method [19] was firstly tested on the computation of the flow across a normal shock wave in a Ne-Ar mixture. A peculiar aspect of this test-case is the species separation within the shock wave. The former is due to the mass difference between the two species [15] with the lighter species experiencing the compression sooner than the heavier. The free-stream values of pressure, temperature and Mach number are 8.3 Pa, 300 K and 2, respectively. The mass fractions of Ne and Ar are 0.34 and 0.66, respectively, while for the simulation parameters N_v and L_v the values 22 and 2500 m/s, respectively, are used. The HS collision model is used. Numerical values for the species mass and diameter are taken from [15].

Figure 3 shows the species mass fractions and velocities across the shock wave. The Ne (whose mass is lower than that of Ar) experiences the compression within the shock sooner that the Ar does (as it can be appreciated from the velocity variation). This induces an accumulation of Ne atoms in the front part of the shock wave. This effect progressively disappears while the flow approaches the post-shock equilibrium state (where no species separation exists and where the chemical composition assumes the same value as that of the free-stream). The species separation can also be appreciated from Fig. 4 showing the species kinetic and parallel temperatures. For each species, the parallel temperature shows the same behavior as that of the pure gas case with the local maximum being more pronounced for the heavier species (Ar). The comparison with the DSMC results is again excellent.

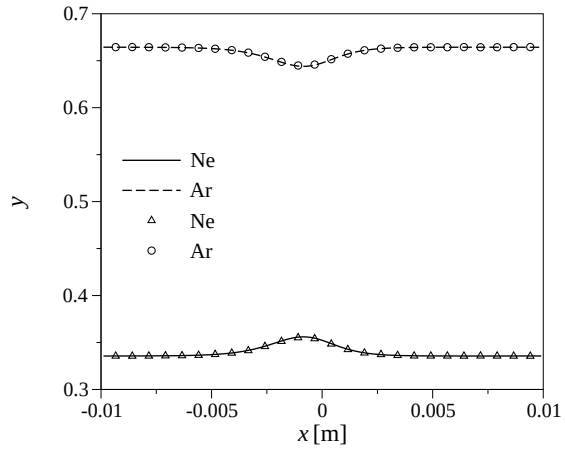

(a) Mass fraction.

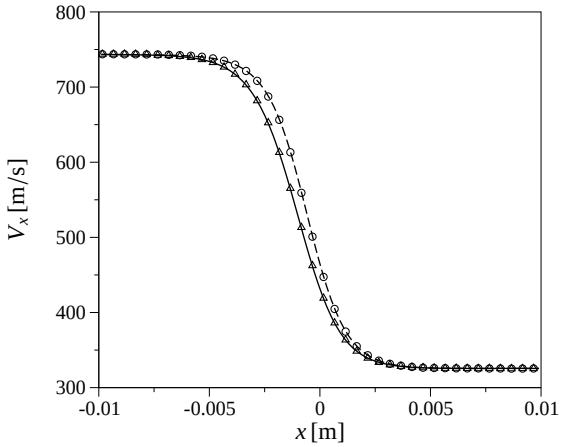

(b) Velocity.

Figure 3: Mass fraction and velocity of Ne and Ar (lines BESS - symbols DSMC).

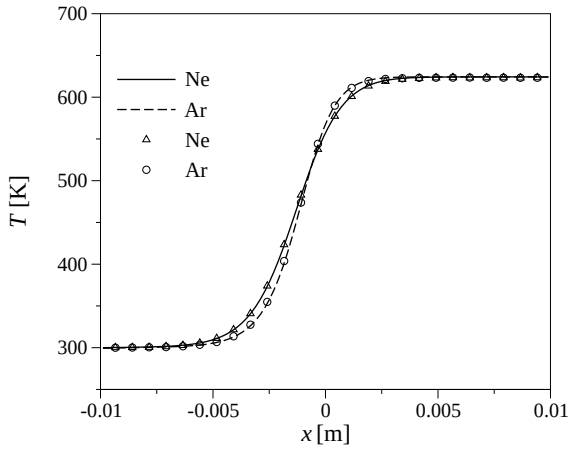

(a) Kinetic temperature.

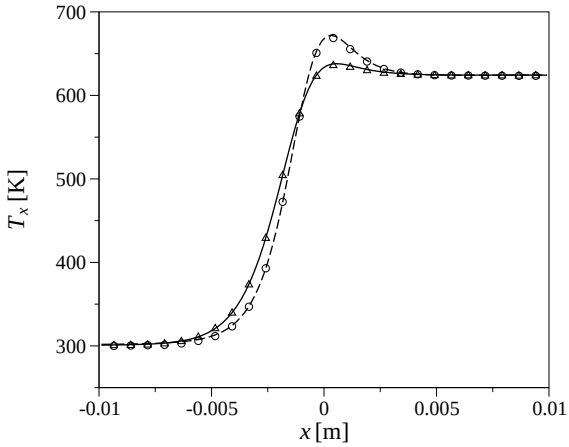

(b) Parallel temperature.

Figure 4: Kinetic and parallel temperature of Ne and Ar (lines BESS - symbols DSMC).

5.3. Isochoric Relaxation Towards Equilibrium of a Multi-Energy Level Gas

The extension of the original numerical method [19] to a multi-energy level gas was tested on a space homogeneous problem already investigated by means of the DSMC method in [34; 35]. Unlike the cases shown in Sects. 5.1 - 5.2, inelastic collisions are accounted for in the present calculations.

The system under investigation is made of Ar. The mass of the former is always taken from [15]. However, its diameter is set to 3.0×10^{-10} m (a different value than that provided in [15]). The number of internal energy levels taken into account is 5 and the related values of degeneracy and energy (taken from [34; 35]) are provided in Table 2. The Anderson model [35] has been considered for the differential elastic and inelastic cross-sections.

Level	g_i	E_i [J]
1	1.0	0.0
2	1.0	8.30×10^{-21}
3	1.0	1.66×10^{-20}
4	1.0	2.50×10^{-20}
5	1.0	3.30×10^{-20}

Table 2: Level degeneracy and energy.

The gas has a density of $1\,\mathrm{kg/m^3}$ and is set into an initial non-equilibrium state where the translational and internal degrees of freedom are in equilibrium at their own temperatures (T and T^{int}, respectively). The initial values of the translational and internal tem-

peratures are 1000 and 100 K, respectively. For the simulation parameters N_v and L_v, the values 16 and 3000 m/s, respectively, have been considered.

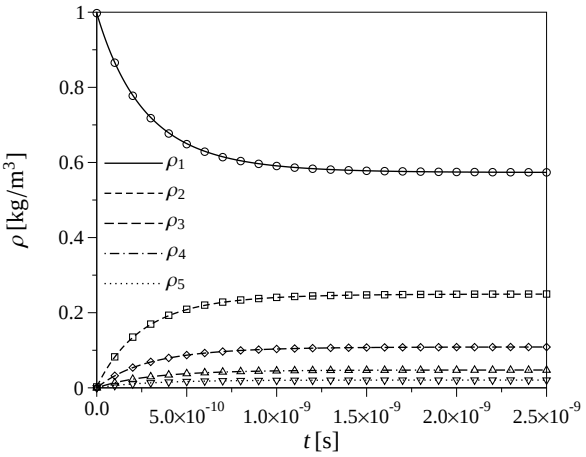

(a) Level density.

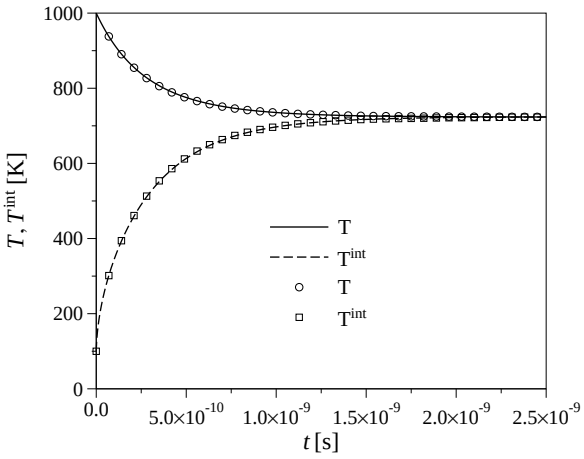

(b) Translation and internal temperature.

Figure 5: Level density and translation and internal temperature (lines BE solver - symbols DSMC).

When the simulation is started, the occurrence of collisions brings the system from its initial (non-equilibrium) state to equilibrium. The former corresponds to a temperature of 723.25 K. During the evolution, as a result of inelastic collisions, the population of the ground state (first level) decreases while that of the upper states increase. A further macroscopic effect of the translational-internal energy exchange occurring in inelastic collisions, is the decrease of the translational temperature of the system. On the contrary, the internal temperature (computed from the gas bulk internal energy as in [34]) increases till reaching the equilibrium value. The previous considerations are confirmed from Fig. 5 showing the time-evolution of the (species) level densities and temperatures (translational and internal). The comparison with the DSMC results is again excellent.

6. Conclusions

An existing spectral-Lagrangian method for solving the Boltzmann equation in the case of a pure gas without internal energy has been extended to a multi-energy level gas. The formalism developed can also be used for the particular case of an inert gas mixture made of monatomic gases without internal energy. The conservation of mass, momentum and energy during collisions is enforced through the solution of a constrained optimization problem. Elastic and inelastic collisions have been treated separately, reflecting the existence of different sets of collisional invariants associated to the elastic and inelastic collision operators. Computational results have been obtained for both inert monatomic gas mixtures and multi-energy level gases. In all the cases, the analysis of the results confirmed the effectiveness of the extended spectral-Lagrangian method in terms of conservation of mass, momentum and energy during collisions. The comparison with the DSMC method has shown to be excellent.

Future work will focus on the extension of the proposed spectral-Lagrangian method in momentum/energy space in order to account for collisions between particles having very disparate masses. Space homogeneous and inhomogeneous test-cases will be performed by considering more accurate elastic and inelastic cross-section models. The former will be based on realistic interaction potentials. A comparison with experiments is also planned for sake of validation.

Acknowledgements

The research activity presented in the paper is supported by the European Research Council Starting Grant #259354. The contents of the paper are the result of an on-going collaboration between the von Karman Institute and the University of Texas at Austin (Prof. I. M. Gamba and co-workers) for the development of deterministic numerical methods for rarefied flows. I would like to thank Prof. I. M. Gamba, at UT Austin, for the useful discussions and the support provided while developing the extended spectral-Lagrangian method and for organizing my two visits at UT Austin. I would like also to thank Dr. J. R.

Haack, at UT Austin, for the support provided while developing the spectral-Lagrangian Boltzmann solver, and Mr. E. Torres, at von Karman Institute, for the DSMC results shown in the paper.

References

[1] C. Park, Nonequilibrium hypersonic aerothermodynamics, Wiley, 1990.

[2] R. L. Jaffe, D. W. Schwenke, G. Chaban, W. Huo, Vibrational and rotational excitation and relaxation of nitrogen from accurate theoretical calculations, AIAA Paper 2008-1208, 46th AIAA Aerospace Sciences Meeting and Exhibit, Reno, Nevada (2008).

[3] D. W. Schwenke, Dissociation cross-sections and rates for nitrogen, in: Non-equilibrium Gas Dynamics: from Physical Models to Hypersonic Flights, Lecture Series, von Karman Institute for Fluid Dynamics, 2008.

[4] A. Munafò, R. L. Jaffe, M. Panesi, G. Colonna, A. Bourdon, T. E. Magin, QCT-based vibrational collisional models applied to nonequilibrium nozzle flows, Eur. Phys. J. D 66 (4).

[5] F. Esposito, M. Capitelli, Quasi-classical molecular dynamic calculations of vibrationally and rotationally state selected dissociation cross sections: $N + N_2 \rightarrow 3N$, Chem. Phys. Lett. 302 (1) (1999) 49–54.

[6] J. G. Kim, O. J. Kwon, C. Park, Master equation study and nonequilibrium chemical reactions for $H + H_2$ and $He + H_2$, J. Thermophys. Heat Transfer 23 (3) (2009) 443–453.

[7] A. Bultel, B. G. Chéron, A. Bourdon, O. Motapon, I. F. Schneider, Collisional-radiative model in air for earth re-entry problems, Phys. Plasmas 13 (4) (2006) 11.

[8] M. Panesi, T. E. Magin, A. Bourdon, A. Bultel, O. Chazot, Analysis of the fire II flight experiment by means of a collisional radiative model, J. Thermophys. Heat Transfer 23 (2) (2009) 236–248.

[9] J. L. Cambier, S. Moreau, Simulation of a molecular plasma in collisional-radiative nonequilibrium, AIAA Paper 1993-3196, 24th AIAA Plasmadynamics & Lasers Conference, Orlando, Florida (1993).

[10] E. Josyula, C. Suchyta, W. Bailey, P. Vedula, Kinetic view of the influence of internal energy states on shock structure, AIAA Paper 2011–3135, 11th AIAA/ASME Joint Thermophysics and Heat Transfer Conference, Honolulu, Hawaii (2011).

[11] M. G. Kapper, J. Cambier, Ionizing shocks in Argon. Part I: Collisional-radiative model and steady-state structure, J. Appl. Phys. 109 (11) (2011) 113308.

[12] M. G. Kapper, J. Cambier, Ionizing shocks in Argon. Part II: Transient and multi-dimensional effects, J. Appl. Phys. 109 (11) (2011) 113309.

[13] C. Cercignani, Rarefied gasdynamics, Cambridge University Press, 2000.

[14] J. H. Ferziger, H. G. Kaper, Mathematical theory of transport processes in gases, North-Holland Pub. Co., 1972.

[15] G. A. Bird, Molecular gas dynamics and the direct simulation of gas flows, Clarendon, 1994.

[16] M. K. Ivanov, A. Kashakovsky, S. Gimelshein, G. Markelov, A. Alexeenko, Y. Bondar, G. Zhukova, S. Nikiforov, P. Vashenkov, SMILE system for 2D/3D DSMC computations, in: Proc. of the 25th Int. Symposium on Rarefied Gas Dynamics, AIP, 2006.

[17] F. G. Tcheremissine, Solution of the Boltzmann equation for high-speed flows, Comput. Math. Math. Phys. 46 (2) (2006) 329–343.

[18] P. B. Clarke, P. L. Varghese, D. B. Goldstein, A novel discrete velocity method for solving the Boltzmann equation including internal energy and variable grids in velocity space, in: Proc. of the 28th Int. Symposium on Rarefied Gas Dynamics, AIP, 2012.

[19] I. M. Gamba, S. H. Tharkabhushanam, Shock and boundary structure formation by spectral-lagrangian methods for the inhomogeneous Boltzmann transport equation, J. Comput. Math. 28 (4) (2010) 430–460.

[20] F. Filbet, G. Russo, High order numerical methods for the space non-homogeneous Boltzmann equation, J. Comput. Phys. 186 (2) (2003) 457–480.

[21] A. Munafò, J. R. Haack, I. M. Gamba, T. E. Magin, Investigation of nonequilibrium internal energy excitation in shock waves by means of a spectral-Lagrangian Boltzmann solver, in: Proc. of the 28th Int. Symposium on Rarefied Gas Dynamics, AIP, 2012.

[22] V. I. Kobolov, R. R. Arlsanbekov, V. V. Aristov, A. A. Frolova, S. A. Zabelok, Unified solver for rarefied and continuum flows with adaptive mesh refinement, J. Comput. Phys. 223 (2) (2007) 589–608.

[23] T. E. Magin, M. Massot, B. Graille, Hydrodynamic model for molecular gases in thermal non-equilibrium, in: Proc. of the 28th Int. Symposium on Rarefied Gas Dynamics, AIP, 2012.

[24] A. V. Bobylev, The method of the fourier transform in the theory of the Boltzmann equation for Maxwell molecules, Dokl. Akad. Nauk SSSR 225 (6) (1975) 1041–1044, in Russian.

[25] J. R. Haack, I. M. Gamba, High-perfomance computing for conservative spectral Boltzmann solvers, in: Proc. of the 28th Int. Symposium on Rarefied Gas Dynamics, AIP, 2012.

[26] J. R. Haack, I. M. Gamba, Conservative deterministic spectral Boltzmann-Poisson solver near the Landau limit, in: Proc. of the 28th Int. Symposium on Rarefied Gas Dynamics, AIP, 2012.

[27] C. Hirsch, Numerical computation of internal and external flows, Wiley, 1988.

[28] B. van Leer, Towards the ultimate conservative difference scheme. V - A second-order sequel to Godunov's method, J. Comput. Phys. 32 (1) (1979) 101–136.

[29] V. Giovangigli, Multicomponent flow modeling, Birkhäuser, 1999.

[30] A. Munafò, E. Torres, J. R. Haack, I. M. Gamba, T. E. Magin, Investigation of nonequilibrium effects across shock-waves by means of a spectral-lagrangian boltzmann solver, AIAA Paper 2013–0305, 51st AIAA Aerospace Sciences Meeting Including the New Horizons Forum and Aerospace Exposition, Dallas, Texas (2013).

[31] B. Chapman, G. Jost, R. van der Pas, Using OpenMP, MIT press, 2008.

[32] GSL - GNU Scientific Library, `http://www.gnu.org/software/gsl/`, [Online; accessed 11-January-2013] (2012).

[33] M. Frigo, S. G. Johnson, The design and implementation of FFTW3, Proc. of the IEEE 93 (2) (2005) 216–231.

[34] E. Torres, T. E. Magin, Statistical simulation of internal energy exchange in shock waves using explicit transition probabilities, in: Proc. of the 28th Int. Symposium on Rarefied Gas Dynamics, AIP, 2012.

[35] J. B. Anderson, J. D. Foch, M. Shaw, R. Stern, B. Wu, Statistical theory of electronic energy relaxation, in: Proc. of the 15th Int. Symposium on Rarefied Gas Dynamics, AIP, 1986.

Development of a Numerical Simulation Tool for the Aerothermal Flow through an Ablative Thermal Protection System for Atmospheric Entry

Pierre Schrooyen

Aeronautics and Aerospace Department, von Karman Institute for Fluid Dynamics, Belgium, pierre.schrooyen@vki.ac.be

Supervisor: Thierry Magin

Associate Professor, Aeronautics and Aerospace Department, von Karman Institute for Fluid Dynamics, Belgium, magin@vki.ac.be

University Supervisor: Philippe Chatelain

Assistant Professor, Institute of Mechanics, Materials and Civil Engineering, Université Catholique de Louvain, philippe.chatelain@uclouvain.be

Abstract

The interaction between the mechanisms of ablation and boundary layer transition is one of the phenomena that leads to difficulties in heat-flux prediction during atmospheric entries. The objective of this work is to develop a computational tool based on a high-order discontinuous Galerkin method (DGM), that simulates and models the flow and wall phenomena in a unified approach. As a first step, a one-dimensional code has been developed for the in-depth thermal response of ablative materials. This paper demonstrates the capability of DGM for discretizing the highly-nonlinear problem equations, discusses specificities of the method to ensure stability, illustrates the subsequent validation, and reviews methods to model recession front.

Keywords: atmospheric entry, thermal protection system, ablation, laminar-turbulent flow transition, discontinuous Galerkin, moving boundary.

1. Introduction

The atmospheric entry of spacecraft presents several challenges in simulating the aerothermal flow around the heat shield. For instance, predicting an accurate heat-flux is a complex task, especially regarding the complex gas-surface interaction on the thermal protection material. These challenges are enhanced at higher entry velocities, typical of new missions to Mars or asteroids, for which ablative materials are used [1]. Requirements concerning mass efficiency for missions with very high entry velocities have led to the development of new class of light carbon composite ablator. New physico-chemical models and computational methods need to be developed to understand the material response of these new ablators in a hypersonic flow.

The components of these new ablative materials are carbon fibers and a filler matrix of phenolic resin. During atmospheric entry, a part of the heat flux is transferred inside the heat shield, leading to a gradual temperature increase of the material and to its transformation. One can separate the TPS in different zones: the virgin material, the pyrolysis zone and the char layer (see Fig. 1). The virgin material is the unaltered part of the shield. In the pyrolysis zone, the phenolic resin is progressively carbonized producing pyrolysis gases which are transported out of the material by diffusion and convection through the pores. The third zone is composed of the fibrous carbon preform and of the carbonized phenolic resin and is destroyed by ablation [2]. This char layer is contiguous with the boundary layer and interactions between the two zones exist and are not well understood.

This poor understanding of the coupled mechanisms of ablation and flow transition is one of the phenomena that lead to difficulties in heat-flux prediction. More specifically, pyrolysis and ablation

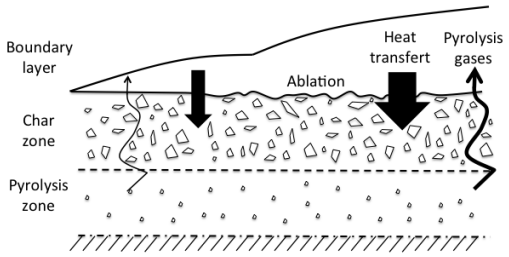

Figure 1: Schematic of the degradation zone illustrating the material response to high-enthalpy flow and the interaction with the boundary layer

generate a mass flow and a surface roughness that interact with the flow in the boundary layer [3]. Such perturbations can trigger transition of the flow from laminar to turbulent, leading to a strong increase of the convective heat-flux[4]. This interaction between the type of flow and the roughness is illustrated in Fig. 2.

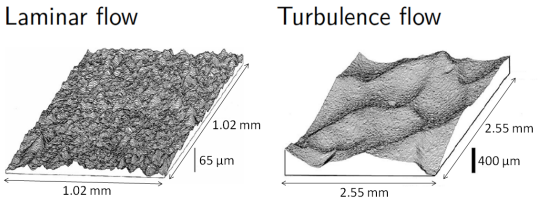

Figure 2: Surface topographies of polycrystalline graphite samples ablated under different flow regimes [3].

To simulate the phenomena in these zones, the common strategy proposed by Kendall et al [5] is to solve the flow field and the material response independently and couple them using boundary conditions on the mass flux and heat fluxes. Using this formulation, the interaction previously discussed can not be captured. For example, the effect of ablation products on the flow field are not included [6]. The objective of this project is to propose a combined simulation and modeling of the flow and wall phenomena by means of a computational approach that can go seamlessly from a compressible flow to a porous media.

In this context, this paper will review the efforts undertaken during the last year of doctoral activities. The paper deals with the development of a one dimensional material response code and the methodology proposed to simulate the two phases problem. The first part focuses on the model and simulation of the material response to high enthalpy flow. The constitutive equations used, the numerical scheme to solve the 1D in-depth thermal response and the results compared to state-of-the-art codes are described. The second part deals with a review of the different techniques to capture recession of the material hence simulate the flow field and the material in the same domain of computation.

2. In-depth-thermal Response

Most of the material response codes used for design still relies on models developed in 1960. The recent interest for higher fidelity modeling has raised numerous research studies regarding pyrolysis and ablation problem [2]. The in-depth thermal response codes can be separated in three categories following the complexity of the models used [7]. The first type of code uses simplified models inherited from the first open literature publication in 1968. For these models, three main hypotheses are assumed. Thermal equilibrium between the solid and gaseous phase is supposed, the gas velocity is supposed perpendicular and directed toward the surface and a short residence time inside the control volume is assumed [8]. Removing respectively the second and third hypothesis, it is possible to achieve type II and type III codes which implement more complex models to describe the gaseous phase inside the porous media. The second type of code models the gas motion inside the porous media with a Darcy's law. The last category includes codes with more complex models for radiation, finite rate chemistry, transport, etc.

2.1. Constitutive models

The governing equations implemented in 1D are summarized hereafter for type II and III code and the reader is referred to Lachaud et al [2] for more information regarding the development of the models.

2.1.1. Mass Conservation equation

Depending on the type of fidelity, the mass conservation equation can be evaluated for each species or an overall pyrolysis gas mass conservation equation can be derived.

$$\frac{\partial \rho_i \epsilon_i}{\partial t} + \frac{\partial (\rho_i \epsilon_i v_g)}{\partial x} + \frac{\partial (F_i)}{\partial x} = \Pi_i + \epsilon_i \omega_i \qquad (1)$$

$$\frac{\partial \rho_g \epsilon_g}{\partial t} + \frac{\partial (\rho_g \epsilon_g v_g)}{\partial x} + \frac{\partial (F_g)}{\partial x} = \Pi, \tag{2}$$

where ρ_i stands for the mass density of the gaseous species, ϵ is the volume fraction, v_g is the pore velocity, F_i is the diffusion flux through the pores, Π is the gas production rate from the decomposition of the solid and ω_i is the gas production rate due to reactions among the gaseous phase. The gas production rate is obtained using one or several Arrhenius law for the decomposition of the solid phase that are usually fitted on thermogravimetry analysis

$$\frac{\partial \rho_s}{\partial t} = -k_s \cdot exp(\frac{-E_a}{RT}) \rho_0 (\frac{\rho_s - \rho_r}{\rho_0})^{m_s}, \tag{3}$$

where ρ_0 and ρ_r are the initial and residual mass density. In this implementation, the three-component decomposition rate law from Goldstein [9] is used. In this case, the material is supposed to be composed of carbon fibers and two phenolic resin components.

2.1.2. Momentum Conservation law

The resolution of momentum equation in a porous media can often be restricted to a Darcy's law

$$v_g = -\frac{\kappa}{\mu_g \epsilon_g} \frac{\partial P}{\partial x}, \tag{4}$$

where κ is the permeability, μ_g is the viscosity and P is the pressure field.

2.1.3. Energy Conservation law

Assuming thermal equilibrium between the pyrolysis gases and the porous material, the energy conservation equation can be written as

$$\frac{\partial (\rho_a e_a)}{\partial t} + \frac{\partial (v_g \rho_g h_g)}{\partial x} = \frac{\partial}{\partial x} (k \frac{\partial T}{\partial x}), \tag{5}$$

where the total intern energy can be written as the sum of the matrix, fiber and gas phase

$$\rho_a e_a = \epsilon_g \rho_g e_g + \epsilon_m \rho_m e_m + \epsilon_f \rho_f e_f. \tag{6}$$

The properties of the solid material such as permeabilities and thermal conductivities are interpolated from the values for pure virgin and char material, as in Blondeau [10]:

$$X = \xi_v \cdot X_v + (1 - \xi_v) \cdot X_c. \tag{7}$$

For the results presented in section 2.3, type II models are implemented and gas diffusion inside the pores is neglected for simplicity.

2.2. Numerical Method

The multi-dimensional numerical tool will be implemented within the research code Argo, based on the discontinuous Galerkin Method (DGM). This method was introduced back in 1973 by Reed and Hill [11] to solve neutron transport problem. DGM cumulates the advantages of finite volume and finite element methods. The advantage lies in their accuracy on unstructured meshes, computational efficiency and parallellisability due to their compact nature [12].

A one-dimensional discontinuous Galerkin code for in-depth thermal response has been developed which possess a similar structure as Argo. It aimed to get familiar with DGM and the models to simulate material thermal response. In order to solve the problem described by the constitutive laws, the system of equations is decomposed. First the energy and mass density of the solid media are advanced in time with a Super Time Stepping (STS) scheme. Then, the pressure field is found by solving implicitly the gaseous mass conservation where the Darcy's law and the perfect gas equation have been inserted. Finally, thanks to the pressure field the velocity field is updated. The different steps and equations solved are summarized in Fig. 3 and the paragraphs hereafter describe the specificities of the method.

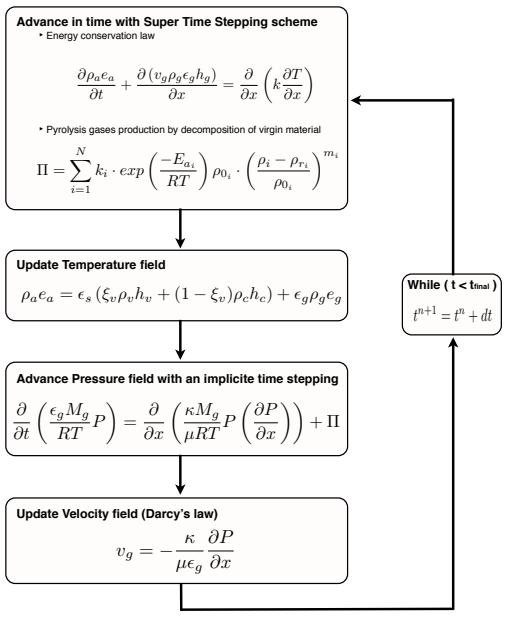

Figure 3: Numerical strategy proposed to solve in-depth-thermal response

2.2.1. Spatial discretization

The spatial discretization uses a DGM which is a particular class of Finite Elements Methods (FEM). For DGM, the residual is required to vanish locally in a Galerkin sense. The solution can therefore be approximated independently on each cell and expressed as

$$u_h = \sum_{i=0}^{p} U_i \lambda_i, \tag{8}$$

where λ_i are the shape functions that are regular on the interior of each cell but unlike other FEM, no continuity is required across the interfaces. In this case, Lagrange polynomials are used.

For a discontinuous Galerkin approach, the convective and diffusive equations are treated differently. The discretization of the convective part is always stabilized by choosing an appropriate Riemann solver or a monotone flux like classical finite volume methods [13]. In this implementation, an upwind scheme was chosen to compute the cell flux balances over the boundaries of an element. The viscous terms follow a typical finite element approach. In contrast to the discretization of the convective terms, many alternatives exist for the discretization of the diffusion terms, an overview can be found in Arnold et al. [14]. Within this work, the interior penalty method proposed in particular by Riviere [15] to solve parabolic problems in porous media has been chosen. Discontinuous Galerkin methods have also been used for ablation problem by Bathia and Roy [16] which implemented a Bassi Rebay-1 method to compute the viscous fluxes. For a general convection-diffusion problem,

$$\frac{\partial u}{\partial t} + \nabla F(u) + \nabla v(\nabla u) = 0, \tag{9}$$

the weak formulation using an interior penalty method to discretize the diffusive part can be expressed as

$$\begin{aligned} A(v,u) = &\sum_{\tau\in\Omega} \int_{\Omega_e} \nabla v \cdot F(u)\, d\Omega_e - \sum_{I_i \in I} \oint_{I_i} \mathbf{n}\cdot(vF(u))\; dS \\ &- \sum_{\tau\in\Omega} \int_{\Omega_e} (\nabla v)\cdot(v\nabla u)\, d\Omega_e + \sum_{I_i\in I} \oint_{I_i} \langle v\nabla u\rangle [v]\, dS \\ &+ \theta \sum_{I_i\in I} \oint_{I_i} \langle v\nabla v\rangle [u]\, dS + \alpha \sum_{I_i\in I} \oint_{I_i} [v][u]\, dS. \end{aligned} \tag{10}$$

The first and third terms of the right hand side are the classical Galerkin formulation on the interior of the element for the convective and diffusive part respectively. The second and fourth terms are the boundary conditions that couple the element with its neighbors. Finally, the last two terms are used to *penalize* the discontinuity of the solution between each cell. The parameter θ varies between $[-1, 0, 1]$ depending on the type of DGM e.g. symmetric, non symmetric or incomplete interior penalty method. The coefficient α is the penalty parameter that has to be chosen carefully to ensure stability [17]. The jump $[.]$ and mean $\langle . \rangle$ operators are usual notation for

$$[a] = a^- n^- + a^+ n^+, \tag{11}$$

$$\langle a \rangle = \frac{1}{2}(a^- + a^+). \tag{12}$$

In this work, a symmetric interior penalty method is used ($\theta = 1$) and the penalty coefficient depends on the mesh size and the order of the approximation chosen.

2.2.2. Temporal discretization

As shown in Fig. 3, the system of equation is splitted and two types of time integration scheme are used. The in-depth thermal response is dominated mainly by diffusion terms. The computational time associated with diffusion problems solved by explicit scheme is known to be high due to the restriction on the time step. For stability purposes, the stable time step depends on the inverse square of the spatial step. Using an implicit scheme allows to use an arbitrary time step despite the resolution of a linear system at each time step. An alternative to implicit scheme is the Super Time Stepping scheme that uses cheaper explicit procedure while relaxing the stability constraint. STS schemes were introduced to speed up explicit schemes [18]. The idea is to ensure the stability of the scheme after a time step larger than the regular stable one while trying to maximize its duration. This super time step is the sum of smaller time steps chosen to ensure stability. For example, to discretize a typical time dependent equation

$$\frac{\partial U}{\partial t} + AU = 0, \tag{13}$$

the STS explicit scheme can be written:

$$U^{n+1} = \left(\prod_{j=1}^{N} (I - \tau_j A) \right) U^n. \tag{14}$$

where the sum of the smaller time steps τ_j is called the super time step. The smaller time steps depend on the regular explicit time step defined for stability purpose

and on two parameters N and ν used to control the accuracy desired:

$$\tau_j = \Delta t_{expl}\left((-1+\nu)\cdot cos\left(\frac{2j-1}{N}\frac{\pi}{2}\right)+1+\nu\right). \quad (15)$$

The stability limit corresponds to $\nu = 0$ and it can be observed that for this the super time step tends to $N^2\Delta t_{expl}$. Since N regular explicit steps cover a $N\Delta t_{expl}$ time interval, a STS scheme is N times faster than a regular explicit scheme. The influence of the two parameters on the super time step is shown in Fig. 4.

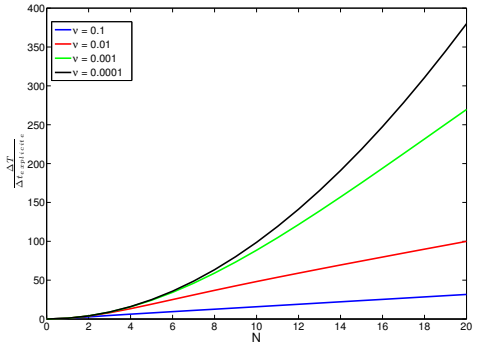

Figure 4: Comparison between Super Time Stepping scheme and regular explicit scheme.

The advantages comparing with implicit scheme are that it is rather easy to be implemented, there is no need to find the jacobian for non-linear cases and to solve the linear system associated to it. Furthermore, Alexiades [18] has shown that STS can be more advantageous than implicit scheme regarding the CPU cost-accuracy ratio. These advantages make it attractive for the first step of the time advancement strategy.

The second step solves the mass conservation law where the gas velocity is replaced by the Darcy's law. The perfect gas law is used to remove the density and to solve the equation with pressure being the only unknown:

$$\frac{\partial\left(\frac{\epsilon_g M_g P}{RT}\right)}{\partial t} = \frac{\partial}{\partial x}\left(\frac{\kappa M_g}{\mu RT}P\cdot\frac{\partial P}{\partial x}\right)+\Pi. \quad (16)$$

However, solving this equation is too expensive to be treated explicitly even using an STS scheme hence a backward Euler scheme coupled with a Newton-Raphson algorithm is used to solve the non-linear differential equation. Using an implicit scheme avoids also problems related to boundary conditions imposition as described in the next section.

2.2.3. Boundary conditions

For an interior penalty method, the boundary conditions are weakly imposed. Consider that the border of domain $\partial\Omega$ is composed in $\partial\Omega_D$ and $\partial\Omega_N$. The terms related to these interfaces in the weak formulation can be expressed as:

$$BC = -\sum_{I_i\in\partial\Omega_N}\oint_{I_i} g_N v\, dS$$
$$-\sum_{I_i\in\partial\Omega_D}\oint_{I_i} v\nabla u\cdot n v\, dS - \theta v\nabla v\cdot n(u-g_D)+\alpha(u-g_D)v\, dS. \quad (17)$$

It was observed that for an explicit time integration scheme, the boundary condition was not respected. To treat this problem, the condition was imposed strongly at the first node. However, the direct imposition for a high order method may imply a spurious overshoot which may lead to non-physical results (see Fig. 5). To treat the high gradient imposed by the boundary conditions, a generalized moment limiter for high-order methods proposed by Yang and Wang [19] was implemented. Although this method proved to match analytical results, the restriction on the time step constrained by the Darcy's law leads to long computational time. After the implementation of an implicit solver for the Darcy's law (see section 2.2.1), the problem faced before disapeared thanks to the increased time step which leads to a resolved boundary layer.

2.3. Results

2.3.1. Convergence

Because a material code is essentially a thermal conduction analysis code [20], it has been validated for a particular thermal conduction problem with variable conductivity. It is possible to find a thermal conductivity such that an analytical solution can be found [21] :

$$k = k_0\frac{Ae^{-(x*)^2}+(1-A)\frac{1}{n}e^{-(n.x^*)^2}}{Ae^{-(x^*)^2}+(1-A)ne^{-(n.x^*)^2}}. \quad (18)$$

For this particular case, the exact solution can be written as

$$\frac{T-T_0}{T_e-T_0} = A\cdot\mathrm{erfc}(x^*)+(1-A)\cdot\mathrm{erfc}(nx^*), \quad (19)$$

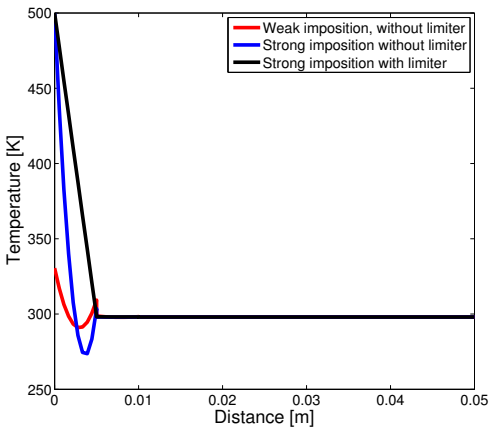

Figure 5: Boundary condition challenge implied by the weak imposition of a Dirichlet boundary condition for a thermal conduction problem. The results with and without limiter converge to the same results that match analytical solution for larger time.

where $x^* = \frac{x}{2\sqrt{\alpha_0 t}}$. The discontinuous Galerkin solution matches the analytical solution and Fig. 7 shows the convergence properties of this method.

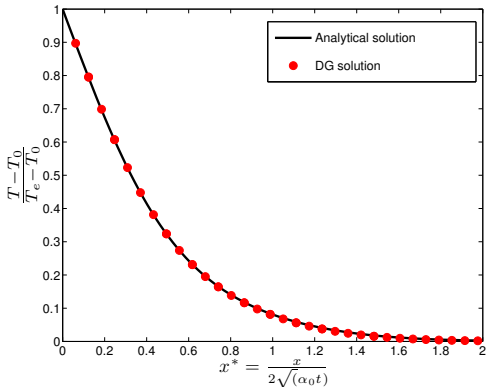

Figure 6: Semi-infinite rod with variable conductivity. The discontinuous solution of order 2 is shown for the case : $A = 0.5$, $n = 2$, $k_0 = 1e^{-2}$, $t_0 = 0$, $t_e = 1000$

2.3.2. *Verification*

In order to verify the numerical scheme implemented, the results have been compared to other codes. For the purpose of inter-code comparison, one dimensional test case has been proposed by Lachaud et al. [7]. The sample of a theoretical material with open source properties is heated on one side for 1 minute at atmospheric pressure while the back

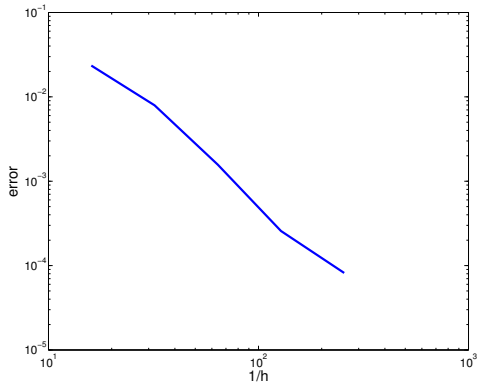

Figure 7: Semi-infinite rod with variable conductivity. The discontinuous solution of order 2 is shown for the case : $A = 0.5$, $n = 2$, $k_0 = 1e^{-2}$, $t_0 = 0$, $t_e = 1000$

wall is assumed adiabatic. The code developed was compared to the results of PATO for the second test case. PATO is the Pyrolysis and Ablation Toolbox based on OpenFOAM developed at NASA Ames by J. Lachaud. The temperature field, the mass blowing rate and the different zones positions are compared in Fig. 8 and 9 and show good agreements with PATO. A difference in temperature of less than 1% for each of the thermocouples at 60s is observed. The difference for the remaining virgin and char thickness at 60s is respectively of 1.1% and 1.3%. The mass blowing rate computed is also close from PATO's results with a difference of 2.3%. The same order of magnitude in difference can be observed for most participants of the ablation workshop.

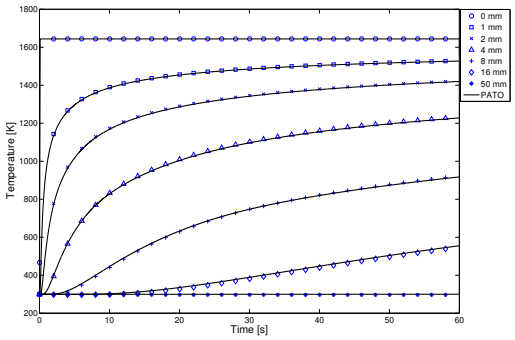

Figure 8: Temperature field for the in-depth thermal response of TACOT compared with the results of PATO.

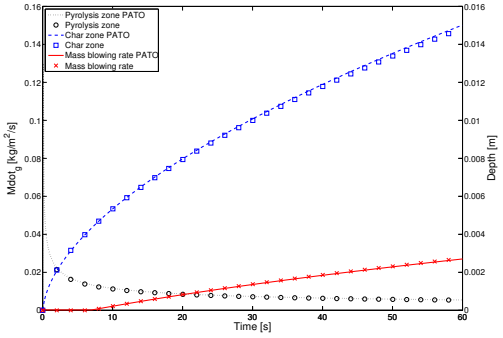

Figure 9: Mass blowing rate and char-virgin zones in the material.

It might be also interesting to look at material density profile (see Fig. 10). According to the model, the density changes are due to the decomposition of phenolic components only.

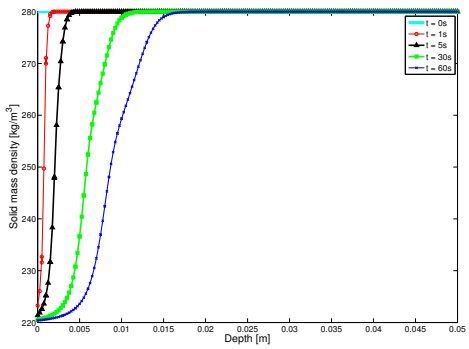

Figure 10: Solid material mass density distribution for various time.

Although results seem very close to state-of-the-art codes, some features of the code still need to be improved. The DG code developed is based on a regular mesh. However, as it can be seen in Fig. 10, the major changes occur near the wall and are steep. In order to capture these phenomena, the mesh has to be fine near the wall hence the advantages of a non-uniform mesh. Moreover, the material code implemented so far does not take into account recession. The numerical tools that can be used to model ablation are discussed in the next section. Finally, we are also currently working on upgrading the models implemented to track different species inside the porous media and achieve type III code.

3. Ablation

Since the originality of this project is to consider both the bulk phase and the material into the same domain of computation, an effort is spent to deal with a moving boundary in DGM. To account for recession, most material codes still use a moving mesh technique proposed by Rindal [8]. This *interface tracking* technique presents many limitations for multidimensional problems, since the mesh movement can seriously degrade mesh quality in case of non-uniform material recession. Remeshing can be time consuming and quite complex depending on the shape of the interface. Therefore, it is proposed to use an *interface capturing* technique, which does not require the meshes to follow the interface.

Many interface capturing methods have been developed for the finite element method. With respect to the numerical evaluation of the discretized equations, these methods can be roughly divided in *diffuse* and *sharp interface capturing* methods. Diffuse techniques, such as the *immersed boundary method* proposed by Peskin [22], smooth the discontinuity over a transition region. Due to this regularization, the method obviously is easy to implement, but on the other hand it implies the loss of accuracy near the surface. Sharp interface methods locally modify the stencil of the numerical scheme, and can thereby - in theory - keep the convergence order of the method even near the interface region. Of the several variants in this last category, both the *immersed interface* technique and the *eXtended Finite Element Method (XFEM)* are investigated. This section briefly reviews and compares those to model the fluid-structure interaction. The notation used are summarized in Fig 11.

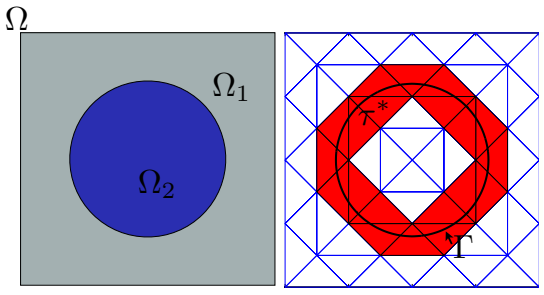

Figure 11: Domain with notations

The domain Ω is divided in two sub-domains Ω_1 and Ω_2. The mesh covers the entire domain but does

not conform with the interface Γ between each part. The elements τ^* are cut by the interface.

3.1. Immersed Interface

Immersed interface methods were first proposed by Li and Ito [23] for finite difference discretization and extended after for finite element schemes. The IFEM technique consists at modifying the shape functions associated to the elements crossed by the interface. The solution can therefore be approximated as:

$$u_h(X) = \sum_{i=0,\ \text{if}\ \tau \ni \tau^*}^{p} U_i \lambda_i(X) + \sum_{i=0,\ \text{if}\ \tau \in \tau^*}^{p} U_i \xi_i(X), \quad (20)$$

where ξ_i are the modified shape functions and p is the order of the approximation chosen. The modification of first order basis functions for a one dimensional case is shown in Fig. 12.

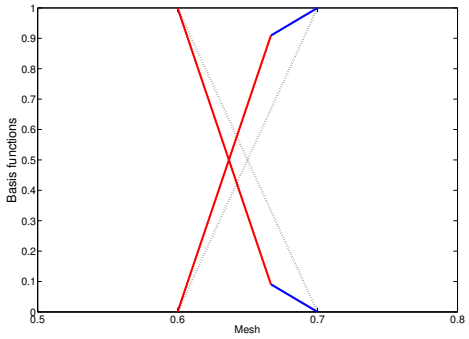

Figure 12: Modification of the basis functions for a first order, one dimensional example with a discontinuity inside one element

The IFEM has been implemented inside the one-dimensional DG tool. The code has been verified for a Stefan problem. For this test case, the boundary value problem possesses an interface which can move with time. The classical Stefan problem simulated corresponds to a conduction inside a ice/water medium and the solidification front is moving according to the boundary conditions. The results show good agreement (see Fig. 13) with analytical solution.

The major advantage of IFEM is that the modifications are only local hence leaving the regular scheme in the rest of the domain. For a first order approximation, the new basis functions can be easily computed in one or two dimensions. However,

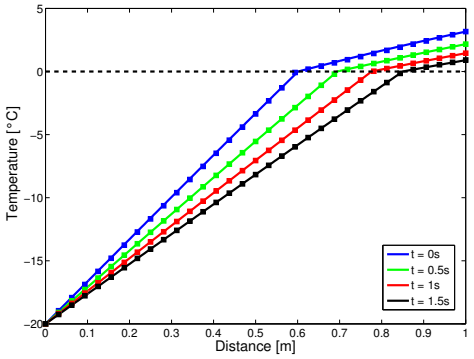

Figure 13: Stefan Problem: solidification front of an ice-water interface

despite recent efforts conducted by Adjerid et al. [24] to extend this method to high-order approximation in 1D cases, the main drawback of IFEM remains that it seems difficult to find high-order basis functions for multi-dimensional problems. Using such techniques implies also to use a different method to compute the volume integral in the variational formulation since the basis functions are no longer continuous inside an element. For a one dimensional case, the element crossed by the interface is divided in two parts where gauss-quadrature is defined. For multi-dimensional cases, the shape of the interface has to be taken into account. This problem is common for both IFEM and XFEM and several papers addressed this challenge ([25], [26], etc) but it will not be discussed here.

3.2. eXtended Finite Element Method

The XFEM developed by Belytschko [27] is based on the partition of unity principle and enriches locally the node disturbed by an interface.

$$u_h(X) = \sum_{i=0\ ,\ \forall \tau}^{p} U_i \lambda_i(X) + \sum_{i=0,\ \text{if}\ \tau \in \tau^*}^{p} A_i \Psi_i(X), \quad (21)$$

where Ψ_i are the enriched basis functions that depend on the type of discontinuity to be represented (a priori known). The A_i are the additional unknowns to be computed. This method was proposed initially to solve crack propagation problems but was applied successfully to other problems with discontinuities such as multi-phase problems, shocks, fluid-structure interaction, etc. Readers are referred to Fries and Belytschko [28] for a holistic review on XFEM. In addition to the integration problem described

previously, the main disadvantage of this method lies in the variable number of degree of freedom per node which may lead to significant problems of implementation within the existing Argo code.

Some efforts have been undertaken to build high-order basis functions for multi-dimensional IFEM without success. Although, the integration of XFEM inside Argo might be more complex, it seems that it is the best option to treat the moving boundary sharply. Several test cases are proposed to validate the approach chosen. First, the problem will be simplified and will only consider material with simple ablation models. Material like Teflon, which is mostly sublimating, is proposed to study the fluid-structure interaction. To assess the methodology, the boundary layer will be considered laminar. Then, one milestone will be to reproduce the results of Crocker and Dubief [4] which deal with a turbulent flow in a channel influenced by an eroding wall.

4. Conclusion and perspectives

The effort during this first year of doctoral activities was twofold. On one hand, the development of a one-dimensional numerical tool to solve in-depth thermal response has demonstrated the challenges and capability of a discontinuous Galerkin method to simulate such problem. The splitting of the equation, the use of super time stepping and implicit schemes has been proved to be efficient and robust. Good agreements with state-of-the art codes have been obtained. On the other hand, the literature review and the first effort conducted on moving boundary techniques has highlighted two possible techniques to account for recession. The effort in the second year will be dedicated to the implementation of such sharp interface technique into the research code Argo in 2D and 3D. Simplified case studies are proposed to verify the capability to handle a moving interface.

Acknowledgments

Fruitful discussions with J. Blondeau (Université catholique de Louvain) on the numerical strategy are gratefully acknowledged. The authors would also like to thank J. Lachaud (NASA Ames) for valuable discussions on the methodology and for providing data which were used to verify the numerical results. The author acknowledges support through a fellowship from the “Fond pour la formation à la Recherche dans l’Industrie et dans l’Agriculture ”and support of the Argo team from Cenaero.

References

[1] J. Dec, R. Braun, B. Laub, Ablative thermal response analysis using the finite element method, Journal of thermophysics and heat transfer 26(2) (2012) 201–212.

[2] J. Lachaud, T. Magin, I. Cozmuta, N. Mansour, A short review of ablative material response models and simulation tools, in: 7th European Aerothermodynamics Symposium, Brugge, 2011.

[3] G. Vignoles, J. Lachaud, Y. Aspa, J. Goyhénèche, Ablation of carbon-based materials: Multiscale roughness modelling, Composites Science and Technology 69 (2008) 1470–1477.

[4] R. Crocker, Y. Dubief, Numerical study of turbulence over a receding wall by controlled and thermal ablation, in: Proceedings of the Summer Program 2010, Center for Turbulence Research, Stanford, USA, 2010.

[5] E. P. Bartlett, R. M. Kendall, C. B. Moyer, R. A. Rindal, An analysis of the coupled chemically reacting boundary layer and charring ablator, part 1 summary report, Contractor Report CR-1060, NASA (June 1968).

[6] J. de Muelenaere, J. Lachaud, N. Mansour, T. Magin, Stagnation line approximation for ablation thermochemistry, in: 42nd AIAA Thermophysics Conference, Honolulu, Hawaii, 2011.

[7] J. Lachaud, A. Martin, I. Cozmuta, B. Laub, Ablation workshop test case, in: 4th Ablation Workshop, Albuquerque, New Mexico, 2011.

[8] C. B. Moyer, R. A. Rindal, An analysis of the coupled chemically reacting boundary layer and charring ablator. part 2 - finite difference solution for the in-depth response of charring materials considering surface chemical and energy balances, Contractor Report CR-1061, NASA (June 1968).

[9] H. Goldstein, Kinetics of nylon and phenolic pyrolysis, Contractor report, Lockheed Missiles and Space Compagny (October 1965).

[10] J. Blondeau, H. Jeanmart, Biomass pyrolysis at high temperatures: Prediction of gaseous species yields from an anisotropic particle, Biomass and Bioenergy 41 (2012) 107–121.

[11] W. Reed, T. Hill, Triangular mesh methods for the neutron transport equation, Contractor Report LA-UR-73-479, Los Alamos Scientific Laboratory (June 1973).

[12] B. Cockburn, G. Karniadakis, C.-W. Shu, The development of discontinuous Galerkin methods, in: B. Cockburn, G. E. Karniadakis, C.-W. Shu (Eds.), Discontinuous Galerkin Methods, Springer, 2000, pp. 3–50.

[13] K. Hillewaert, Development of the discontinuous Galerkin method for large scale/high-resolution CFD and acoustics in industrial geometries, Ph.D. thesis, Universite catholique de Louvain (2013).

[14] D. Arnold, F. Brezzi, B. Cockburn, M. L.D., Unified analysis of discontinuous galerkin methods for elliptic problems, SIAM Journal Numerical Analysis 39(5) (2001) 1749–1779.

[15] B. Riviere, Discontinuous Galerkin Methods for Solving Elliptic and Parabolic Equations - Theory and Implementation, Society for Industrial and Applied Mathematics, 2008.

[16] A. Bhatia, S. Roy, Pyrolysis gas flow in thermally ablating media using time-implicit discontinuous galerkin methods, in: 49th AIAA Aerospace Sciences Meeting including the New Horizons Forum and Aerospace Exposition, Orlando, Florida, 2011.

[17] K. Shahbazi, An explicit expression for the penalty parameter of the interior penalty method, Journal of Computational Physics 205 (2005) 401–407.
[18] V. Alexiades, G. Amiez, P. Gremaud, Super-time-stepping acceleration explicit schemes for parabolic problems, Communications in Numerical Methods in Engineering 12 (1996) 12–31.
[19] M. Yang, Z. Wang, A parameter-free generalized moment limiter for high-order methods on unstructured grids, in: 47th AIAA Aerospace Sciences Meeting, Orlando,Florida, 2009.
[20] N. Mansour, J. Lachaud, T. Magin, J. de Muelenaere, Y.-K. Chen, High-fidelity charring ablator thermal response model, in: 42nd AIAA Thermophysics Conference, Honolulu, Hawaii, 2011.
[21] H. Halle, Exact solution of elementary transient heat conduction problem involving temperature dependent properties, Journal of Heat Transfer 87(3) (1965) 420–421.
[22] C. Peskin, Numerical analysis of blood flow in the heart, Journal of Computational Physics 25 (1977) 220–252.
[23] Z. Li, K. Ito, The immersed interface method: Numerical Solutions of PDEs Involving Interfaces and Irregular Domains, SIAM Frontiers in Applied Mathematics, 2006.
[24] S. Adjerid, T. Lin, A p-th degree immersed finite element for boundary value problems with discontinuous coefficients, Applied Numerical Mathematics 59 (6) (2009) 1303–1321.
[25] K. W. Cheng, T. Fries, Higher-order xfem for curved strong and weak discontinuities, International Journal for Numerical Methods in Engineering 82 (2009) 564–590.
[26] G. Legrain, N. Chevaugeon, K. Dreau, High order xfem and level sets for complex microstructures: uncoupling geometry and approximation, Computer Methods in Apllied Mechanics and Engineering (paper submited).
[27] T. Belytschko, T. Black, Elastic crack growth in finite elements with minimal remeshing, International Journal for Numerical Methods in Engineering 45 (1999) 601–620.
[28] T. Fries, T. Belytschko, The extended/generalized finite element method: An overview of the method and its applications, International Journal for Numerical Methods in Engineering 00 (6) (2009) 1–53.

Development of MUTATION^{++}: MUlticomponent Thermodynamics And Transport properties for IONized gases library in C++

James B. Scoggins

Aeronautics and Aerospace Department, von Karman Institute for Fluid Dynamics, Belgium, james.scoggins@vki.ac.be

Supervisor: Thierry Magin

Associate Professor, Aeronautics and Aerospace Department, von Karman Institute for Fluid Dynamics, Belgium, magin@vki.ac.be.
Laboratoire d'Énergétique Moléculaire et Macroscopique, Combustion (EM2C), École Centrale Paris

University Supervisor: Anouar Soufiani

Research Head, Laboratoire d'Énergétique Moléculaire et Macroscopique, Combustion (EM2C), École Centrale Paris, France

Abstract

This report briefly describes the development of the MUTATION^{++}library which has been designed to compute thermodynamic and transport properties of ionized gases including equilibrium compositions and species production rates due to finite-rate elementary reactions. The gas model is currently assumed to be in thermodynamic equilibrium but chemical non equilibrium is retained in the formulation of the governing equations. Thermodynamic properties are obtained from three separate databases: the NASA 7- and 9-coefficient polynomials and a custom database which describes each atom and molecule as a rigid-rotator and harmonic oscillator. Mixture thermodynamic properties are suitably formulated from species quantities. Transport properties are derived from kinetic theory which provides relationships for macroscopic transport coefficients based on microscopic collision integrals. Finally, the chemical production rates for species based on elementary chemical reactions including third body reactions is detailed. Each set of properties are also verified against other data sources, namely the MUTATION library.

Keywords: multiphysics coupling, numerical methods, hypersonics, radiation, ablation, planetary entry

1. Introduction

Space exploration is one of the boldest and most exciting endeavors that humanity has undertaken, and it holds enormous promise for the future. After the successful manned missions to the Moon and many probe entries in the atmospheres of outer planets, our next challenges include bringing back samples to Earth by means of robotic missions and continuing manned exploration, which aims at sending human beings to Mars and returning them safely home.

Of the many design challenges associated with these goals is the difficult task of accurately predicting the heat-flux to the surface of the spacecraft thermal protection system (TPS) during planetary entry. An inaccurate prediction can be fatal for the crew or the success of robotic missions. Large safety factors are often added to vehicle TPS thicknesses to avoid such catastrophes at the expense of additional cost, weight, and reduced payload margins. The following complex phenomena that affect the surface heat-flux are considered as potential "mission killers:" 1) Radiation of the plasma in the shock layer, and 2) Complex surface chemistry on the thermal protection system material. However, current entry-vehicle design paradigms largely decouple many of these physicochemical processes due to numerical and modeling constraints, making it difficult to infer from current design tools the complex, coupled phenomena occurring for any given entry problem. Thus, our poor understanding of the coupled mechanisms of flow, radiation, and ablation leads to the difficulties in heat flux prediction.

This research focuses on addressing these issues

through the development of new multiphysics, numerical methods aimed at strongly coupling the flow, radiation, and material response fields surrounding an entry-vehicle. In the long-term, a hypersonics flow solver will be developed which makes use of an existing CFD framework such as SU^2 [1] and this solver will be implicitly coupled with a material response solver for carbon-phenolic ablators. This coupling will allow the flux of pyrolysis and ablation gases generated by the thermal degradation of the ablator to be injected into the boundary layer computed by the CFD solver. In addition, the divergence of the radiative heat flux will be computed and coupled with the flow solver in order to complete the multiphysics coupling.

As a first step however, a new library called MUlticomponent Thermodynamic And Transport properties for IONized plasmas in C++ (Mutation^{++}) has been developed in order to provide accurate modeling of the various gases which will be necessary to close the governing equations that detail the flow and material fields. The development of this library and its validation is presented in the proceeding sections.

2. Overall Design

The Mutation^{++}library is largely based on its Fortran 77 predecessor Mutation developed by Magin [2]. It has been designed with the following constraints in mind: 1) high fidelity of the physical models, ensuring the laws of thermodynamics are satisfied and results are validated against existing experimental data, 2) low computational cost, 3) modern, object oriented, extensible framework, and 4) detailed in-source and user's guide documentation in order to facilitate model improvement and collaboration. This document will focus on the physical modeling that is employed in Mutation^{++}. The properties provided by the library are necessitated by the closure of the governing equations for the systems of interest (flow field and material field).

2.1. Governing Equations

The Navier-Stokes equations describing the flow field can be readily derived from the appropriate solution of the Boltzmann equation. This derivation is performed in many standard texts (see for instance [3]). In this section, we assume thermal equilibrium of the internal energy modes and chemical non-equilibrium of the gas mixture. It is further assumed that the gas is a weakly magnetized, quasi-neutral plasma. The species continuity equations which result from conservation of the species mass is

$$\frac{\partial}{\partial t}\rho_i + \nabla\cdot(\rho_i\vec{v}) + \nabla\cdot\left(\rho_i\vec{V}_i\right) = \dot{\omega}_i \quad \forall i \in \mathcal{S}, \tag{1}$$

where ρ_i is the density of species i, $\vec{v}$ is the mass averaged bulk velocity of the gas, $\vec{V}_i$ is the species diffusion velocity for species i, and $\dot{\omega}_i$ is the mass production rate of species i due to elementary chemical reactions. For equilibrium flows, it is only necessary to enforce global continuity which is determined by summing the species conservation equations

$$\frac{\partial}{\partial t}\rho + \nabla\cdot(\rho\vec{v}) = 0, \tag{2}$$

provided that elemental remixing is not taken into account. $\rho = \sum_{i\in\mathcal{S}}\rho_i$ is the total mixture density.

Conservation of total momentum yields

$$\frac{\partial}{\partial t}(\rho\vec{v}) + \nabla\cdot(\rho_i\vec{v}\otimes\vec{v}) + \nabla\cdot\mathbf{P} = 0, \tag{3}$$

where the shear stress tensor is defined as

$$\mathbf{P} = \left[p + \frac{2}{3}\eta\nabla\cdot\vec{v}\right]\mathbf{I} - \eta\left[\nabla\vec{v} + (\nabla\vec{v})^T\right]. \tag{4}$$

p is the mixture pressure and η is the bulk viscosity.

Finally, conservation of total energy yields

$$\frac{\partial}{\partial t}(\rho E) + \nabla\cdot(\rho H\vec{v}) + \nabla\cdot\vec{q} + \nabla\cdot(\mathbf{P}\vec{v}) = 0, \tag{5}$$

where the heat flux is expressed as

$$\vec{q} = \sum_{i\in\mathcal{S}}\rho_i h_i\vec{V}_i + p\sum_{i\in\mathcal{S}}\left(k^h_{Ti} + k^e_{Ti}\right)\vec{V}_i - \lambda\nabla T. \tag{6}$$

Material response models often use simplified conservation laws and require only a subset of the closure properties that are found in the Navier-Stokes equations [4, 5]. It is therefore sufficient to provide the thermodynamic and transport properties and species production rates identified by the NS equations and the material response models will also be closed.

3. Thermodynamics

The closure of the governing equations which dictate the material response and hypersonic flow fields require several thermodynamic properties to be specified. In general, only two thermodynamic quantities are required to completely specify an equilibrium gas mixture for a give set of elemental constraints. The composition of the mixture must be added to specify a mixture out of equilibrium.

3.1. Basic Data Sources

Thermodynamic data is computed based on a pure species basis. Often, it is challenging to find thermodynamic data for all the species in a mixture (this mainly applies to ablation calculations). In addition, it is often useful in practice to compare computational results with those obtained by other methods or codes using different thermodynamic data. Mutation^{++}currently supports two commonly accepted data sources, NASA 7- and 9-coefficient polynomials, and a custom database which stores coefficients necessary to describe the various energy modes of an atom or molecule in a human-readable XML format.

The NASA polynomial databases allow the computation of species specific heats, enthalpies, and entropies through tabulated coefficients to polynomials which are fitted to highly accurate specific heat data. For the case of the 7-coefficient database, the molar specific heat at standard-state pressure for species i, $C^\circ_{p,i}$, is computed using coefficients a_1 to a_7.

$$\frac{C^\circ_{p,i}}{R} = \sum_{q=1}^{5} a_i T^{(q-1)}, \tag{7}$$

where the molar standard-state enthalpy, H°_i, and standard-state entropy, S°_i, of each species i can be determined from thermodynamic relations:

$$\frac{H^\circ_i}{RT} = \frac{\int C^\circ_{p,i} dT}{RT} + \frac{a_6}{T}, \quad \frac{S^\circ_i}{R} = \int \frac{C^\circ_{p,i}}{RT} dT + a_7. \tag{8}$$

Another common method of calculation for thermodynamic properties in CFD codes is to compute the contribution of each energy mode available to each species. Of the simplest approaches is the so called rigid-rotator harmonic-oscillator model which is described in [2] and for brevity's sake is not expanded upon here.

3.2. Derived Quantities

Mixture quantities are derived from pure species quantities. For example, the mixture enthalpy per unit mass, h, is given as

$$\rho h = \sum_{i \in \mathcal{S}} \rho_i h_i. \tag{9}$$

The mixture entropy is similarly computed from species entropies with the addition of the entropy of mixing.

$$\rho s = \sum_{i \in \mathcal{S}} \rho_i s_i - \rho R_{\text{mix}} \sum_{i \in \mathcal{S}} X_i \ln X_i, \tag{10}$$

where X_i is the mole fraction of species i and $R_{\text{mix}} = R/M_{w,\text{mix}}$ is the mixture gas constant with $M_{w,\text{mix}} = \sum_{i \in \mathcal{S}} X_i M_{w,i}$. The mixture energy is computed via

$$\rho e = \rho h - p = \sum_{i \in \mathcal{S}} \rho_i h_i - \sum_{i \in \mathcal{S}} p_i. \tag{11}$$

Specific heats are defined in terms of partial derivatives of the mixture enthalpy and energy.

$$c_p = (\partial h/\partial T)_p, \quad c_v = (\partial e/\partial T)_\rho \tag{12}$$

In equilibrium, the mixture composition is a function of temperature and pressure and this contribution must be taken into account.

$$\begin{aligned} c_{p,\text{eq}} &= \sum_{i \in \mathcal{S}} Y_i (\partial h_i/\partial T)_p + \sum_{i \in \mathcal{S}} (\partial Y_i/\partial T)_p h_i \\ c_{v,\text{eq}} &= \sum_{i \in \mathcal{S}} Y_i (\partial e_i/\partial T)_\rho + \sum_{i \in \mathcal{S}} (\partial Y_i/\partial T)_\rho e_i \end{aligned} \tag{13}$$

For frozen mixtures however, the chemical reaction contribution may be neglected.

$$\begin{aligned} c_{p,\text{fr}} &= \sum_{i \in \mathcal{S}} Y_i (\partial h_i/\partial T)_p \\ c_{v,\text{fr}} &= \sum_{i \in \mathcal{S}} Y_i (\partial e_i/\partial T)_\rho \end{aligned} \tag{14}$$

It is often necessary to know the local sound speed of the gas for CFD calculations. For a general equation of state, the sound speed is defined to be

$$a^2 \equiv \left(\frac{\partial p}{\partial \rho}\right)_s. \tag{15}$$

For an ideal gas this equates to the following for frozen and equilibrium mixtures respectively:

$$\begin{aligned} a^2_{\text{fr}} &= \gamma_{\text{fr}} \frac{p}{\rho} \\ a^2_{\text{eq}} &= \gamma_{\text{eq}} (\partial \rho/\partial p)^{-1} \end{aligned} \tag{16}$$

where $\gamma = c_p/c_v$ is the ratio of specific heats.

4. Constrained, Multiphase Equilibrium

Consider a chemical system composed of any number of ideal phases. The set of indices which denote all species in this system is $\mathcal{S} = \left\{1, \ldots, n^{\mathcal{S}}\right\} = \cup_{m \in \mathcal{P}} \mathcal{S}_m$ where $n^{\mathcal{S}}$ is the total number of species considered, $\mathcal{P} = \left\{1, \ldots, n^{\mathcal{P}}\right\}$ is the set of phase indices with $n^{\mathcal{P}}$ the number of phases, and $\mathcal{S}_m$ denotes the set of species indices belonging to phase m. Since all phases are

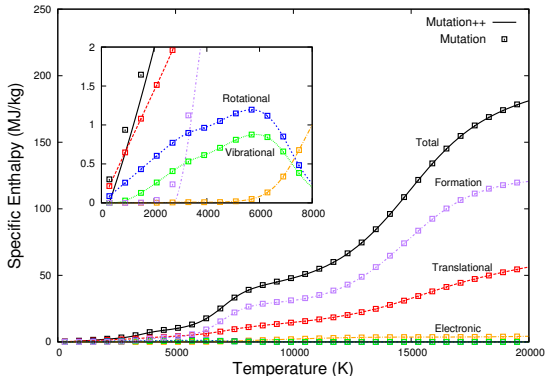

(a) Enthalpy.

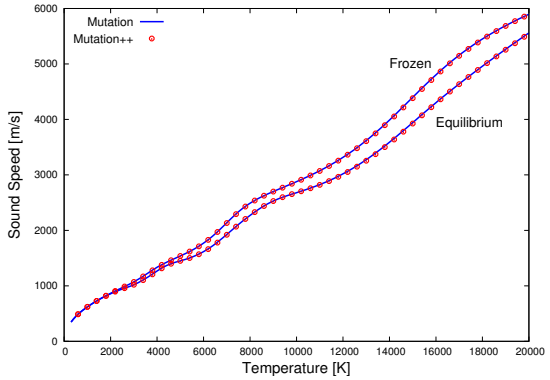

(b) Speed of sound.

Figure 1: Mixture enthalpy and speed of sound (frozen and equilibrium) for equilibrium air computed using RRHO 11 species thermodynamic model at 1 atm.

ideal, the normalized Gibbs function for this system is

$$\tilde{G} = \frac{G}{RT} = \sum_{j \in \mathcal{S}} \left(\tilde{g}_j(T,p) + \ln N_j - \ln \bar{N}_{p_j} \right) N_j, \quad (17)$$

where N_j is the number of moles of species j and $\tilde{g}_j(T,p)$ is the non-dimensional Gibbs function of pure species j at the system temperature and pressure, R is the molar universal gas constant, and $\bar{N}_{p_j}$ is the phase moles for the phase to which species j belongs.

$$\bar{N}_{p_j} = \sum_{k \in \mathcal{P}_{p_j}} N_k, \quad \forall\ j \in \mathcal{S} \quad (18)$$

The subscript $p_j \in \mathcal{P}\ \forall\ j \in \mathcal{S}$ is used to denote *the phase index to which the species index, j, belongs*. The non-dimensional Gibbs function for a pure species j is given by

$$\tilde{g}_j(T,p) = \frac{G_j^\circ(T)}{RT} + \begin{cases} \ln \frac{p}{P^\circ}, & j \in \text{gas phase} \\ 0, & \text{otherwise} \end{cases}, \quad (19)$$

where $G_j^\circ \equiv H^\circ(T) - TS^\circ(T)$ is the molar Gibbs function for pure species j evaluated at the standard state pressure P°.

The total moles of atoms of each element i in the system, c_i^{e}, can be computed from the simple elemental mass balance relation

$$\sum_{j \in \mathcal{S}} B_{ji}^{\mathrm{e}} N_j = c_i^{\mathrm{e}} \quad \forall\ i \in \mathcal{E}, \quad (20)$$

where B_{ji}^{e} is equal to the number of i atoms belonging to species j and $\mathcal{E} = \{1, \ldots, n^{\mathcal{E}}\}$ is simply the set of all element indices. It is often useful to impose other constraints on the system. Therefore, we consider any $n^{\mathcal{G}}$ general linear constraints on the number of moles of each species. Using matrix notation, the total constraints imposed on the composition are given as

$$B^T N = c, \quad (21)$$

and $n^C = n^{\mathcal{E}} + n^{\mathcal{G}}$ are total number of linear constraints. For a given B, c, and a fixed temperature and pressure, the equilibrium composition for the system is the one which minimizes $\tilde{G}$ while satisfying the linear constraints in Eq. 21.

4.1. Element Potentials

The Lagrange multiplier method is a well known technique for solving constrained minimization problems and will be used here. To begin, the Gibbs function and mass balance constraints are combined in the Lagrange function for this problem, L, which is written as

$$\begin{aligned} L &= \tilde{G} - \sum_{i \in C} \lambda_i \left(\sum_{j \in \mathcal{S}} B_{ji} N_j - c_i \right) \\ &= \sum_{j \in \mathcal{S}} N_j \left(\tilde{g}_j + \ln N_j - \ln \bar{N}_{p_j} \right) - \sum_{i \in C} \lambda_i \left(\sum_{j \in \mathcal{S}} B_{ji} N_j - c_i \right). \end{aligned} \quad (22)$$

Here, λ_i are called Lagrange multipliers or constraint potentials. Because they apply the elemental mass balance constraint, they are often referred to as the element potentials for Gibbs free energy minimization problems. The solution to the constrained minimization problem is found by differentiating the Lagrange

function and setting the result equal to zero.

$$dL = 0 = \sum_{j\in\mathcal{S}} \left(\tilde{g}_j + 1 + \ln N_j - \ln \bar{N}_{p_j} + \sum_{i\in C} \lambda_i B_{ji} \right) dN_j - \sum_{j\in\mathcal{S}} \frac{N_j}{\bar{N}_{p_j}} d\bar{N}_{p_j} - \sum_{i\in C} \left(\sum_{j\in\mathcal{S}} B_{ji} N_j - c_i \right) d\lambda_i \tag{23}$$

The term multiplying $d\lambda_i$ is simply the constraint equation which is satisfied at equilibrium and is thus zero. From Eq. 18 it also evident that

$$\sum_{j\in\mathcal{S}} dN_j - \sum_{j\in\mathcal{S}} \frac{N_j}{\bar{N}_{p_j}} d\bar{N}_{p_j} = \sum_{m\in\mathcal{P}} \left(d\bar{N}_m - \frac{1}{\bar{N}_m} \sum_{j\in\mathcal{S}_m} N_j d\bar{N}_m \right) = 0. \tag{24}$$

Furthermore, dN_j may be positive or negative and does not depend on the term multiplying it. Therefore, the differential of the Lagrange function requires that all multipliers in the first summation be zero resulting in the following $n^{\mathcal{S}}$ equations

$$N_j = \bar{N}_{p_j} \exp\left(-\tilde{g}_j + \sum_{i\in C} \lambda_i B_{ji} \right), \quad \forall\ j \in \mathcal{S}. \tag{25}$$

The equations in Eq. 25 are called the Element Potential Equations. Note that when written in terms of species mole fractions, $X_j = N_j/\bar{N}_{p_j}$, the n^C element potentials, λ_i, completely define the equilibrium composition for a fixed temperature and pressure. Physically, they represent an amount of Gibbs free energy associated with each element at equilibrium. The substitution of Eq. 25 into Eqs. (18) and (21) leads to a nonlinear system of $n^C + n^{\mathcal{P}}$ equations and as many unknowns ($\bar{N}_m, \lambda_i$).

Well known equilibrium codes such as StanJan [6] or CEA [7] use specialized forms of the Newton-Raphson iterative method to solve these equations. However, it is well documented that such procedures can fail when the nonlinear system is numerically stiff [8]. Therefore, in Mutation^{++}an alternative procedure known as the Gibbs function continuation (GFC) method developed by Pope [9, 10] for single phase mixtures is adopted here instead. While the details of this method can be quite cumbersome, it is sufficient to mention that the GFC method employes a robust continuation algorithm which guarantees convergence for all well posed equilibrium problems. In Mutation^{++}, the GFC method is extended to multiphase in a unique continuation-Krylov iterative scheme. The equilibrium composition of some common mixtures at 1 atm are shown in Fig. 2.

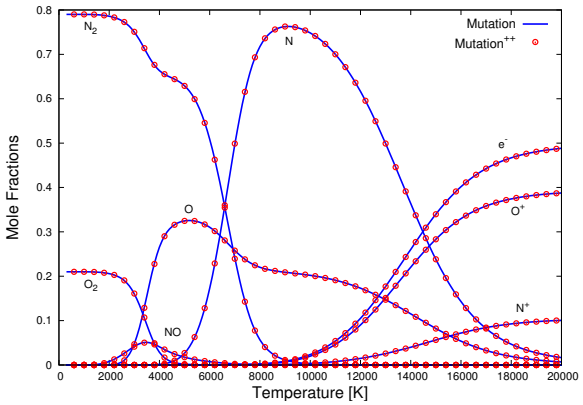

(a) 11 species air mixture.

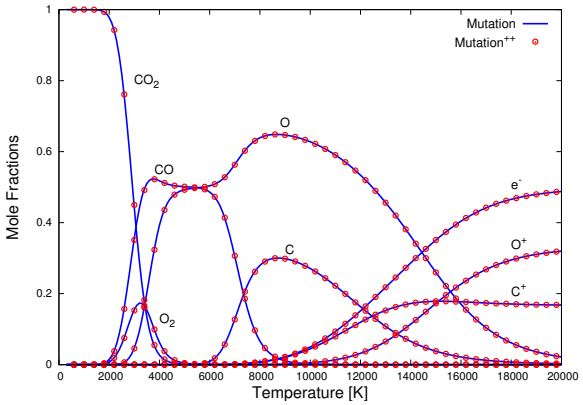

(b) 8 species CO_2 mixture.

Figure 2: Equilibrium composition of the 11 species air and 8 species carbon dioxide mixtures at 1 atm as computed by Mutation^{++}and compared to Mutation.

4.2. *Surface Mass Balance*

A common strategy for coupling a fluid solver with a material response code is to solve the surface mass balance relation at the fluid / ablator interface which computes the ablation mass blowing rate given a pyrolysis gas mass blowing rate, surface temperature and pressure, and elemental composition of the boundary layer edge and pyrolysis gases (see for instance the work of Milos and Chen [11]). If we consider a finite volume around the surface of an ablator and impose steady-state conditions, we can form the simple mass balance relation:

$$\dot{m}_g Y_{kg} + \dot{m}_c Y_{kc} = j_{kw} + (\rho v)_w Y_{kw}, \tag{26}$$

where $\dot{m}$ is a mass flux or blowing rate from the material to the surface, Y_k is an elemental mass fraction for element k, j_k is the elemental diffusion flux, $(\rho v)_w$

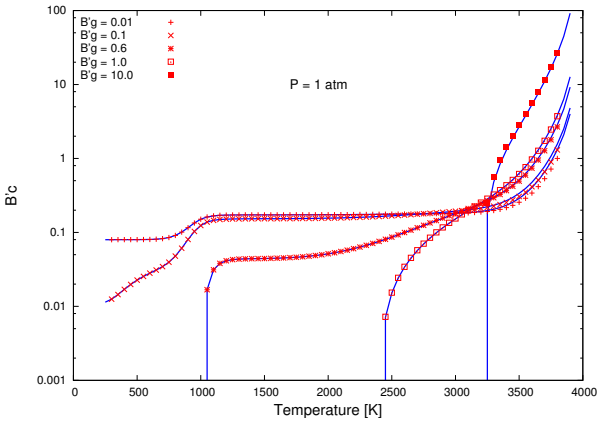

Figure 3: Comparison of $B_c^{'}$ curves computed using MUTATION^{++}(symbols) and TACOT (lines) at 1 atm.

Table 1: Elemental mole fractions for $B_c^{'}$ calculation.

Gas	X_N	X_O	X_C	X_H
Boundary Layer	0.790	0.210	-	-
Pyrolysis Gas	-	0.115	0.206	0.679
Charred Ablator	-	-	1.000	-

is the total gas flow from the wall, and the subscripts g, w, and c refer to the pyrolysis, wall, and char compositions respectively.

If we take the transfer potential methodology to determine the diffusion flux, after non-dimensionalizing, and rearranging terms, we find that the non-dimensional ablation mass blowing rate is a function of the equilibrium mass fractions of the gas at the wall,

$$B_c^{'} = \frac{Y_{ke} + B_g^{'}\left(Y_{kg} - Y_{kw}\right) - Y_{kw}}{Y_{kw} - Y_{kc}}, \tag{27}$$

where $B^{'} = \dot{m}/\rho_e u_e C_M$ is a non-dimensional flux, and the subscript e denotes a boundary layer edge gas quantity. Solving the above equation coupled with a multiphase equilibrium solver to determine the elemental mass fractions at the wall yields the mass flux due to ablation at the wall. Fig. 3 shows a comparison between a $B_c^{'}$ calculation performed by de Muelenaere et al. [12] for the Theoretical Ablative Composite for Open Testing (TACOT) test case series. Table 1 lists the elemental composition of the boundary layer edge, pyrolysis gas, and char for this calculation.

As can be seen from the figure, MUTATION^{++}is in excellent agreement with TACOT. Between 1000 K to 3000 K the carbon ablation is diffusion limited as can be seen by the plateau in the carbon blowing rate at these temperatures. In this regime, oxygen from the boundary layer diffuses against the flow of pyrolysis gases to the surface where it reacts with the carbon char, removing material from the surface. Above 3000 K, sublimation of the carbon char begins to occur effectively lifting the plateau on $B_c^{'}$ which is no longer limited by the amount of oxygen reaching the surface.

5. Transport

Closure of the transport fluxes is achieved through a multiscale Chapman-Enskog perturbative solution of the Boltzmann equation. The complete derivation of the transport coefficients is detailed in [13]. Only the resulting expressions for these coefficients which have been implemented in MUTATION^{++}will be shown here.

The shear viscosity and heavy particle translational thermal conductivity are computed via the solution of the linear systems

$$\begin{aligned} \sum_{j\in\mathcal{H}} G_{ij}^{\mu}\alpha_j^{\mu} &= X_i \quad \forall i \in \mathcal{H} \\ \mu &= \sum_{i\in\mathcal{H}} \alpha_i^{\mu} X_i, \end{aligned} \tag{28}$$

where μ represents either η or λ_h. Heavy particle thermal diffusion ratios may then be computed via

$$k_{Ti}^{h} = \frac{5}{2}\sum_{j\in\mathcal{H}} \Lambda_{ij}^{01}\alpha_j^{\lambda_h} \quad \forall i \in \mathcal{H}. \tag{29}$$

Electron thermal conductivity and thermal diffusion ratios are separately computed from

$$\lambda_e = \frac{X_e^2\Lambda_{ee}^{22}}{\Lambda_{ee}^{11}\Lambda_{ee}^{22} - \left(\Lambda_{ee}^{11}\right)^2} \tag{30}$$

and

$$k_{Ti}^{e} = \frac{5}{2}\frac{T_e}{T_h}X_e\frac{\Lambda_{ie}^{01}\Lambda_{ee}^{22} - \Lambda_{ie}^{02}\Lambda_{ee}^{12}}{\Lambda_{ee}^{11}\Lambda_{ee}^{22} - \left(\Lambda_{ee}^{11}\right)^2}. \tag{31}$$

The thermal conductivity must be corrected in order to account for the transport of internal energy. This is done via the so called Eucken corrections where thermal conductivities are supplied for the rotational, vibrational, and electronic internal energy modes.

$$\begin{aligned} \lambda_R &= \sum_{i\in\mathcal{H}_p} \frac{\rho_i c_{Ri}}{\sum_{j\in\mathcal{H}} X_j/\mathcal{D}_{ij}} \\ \lambda_V &= \sum_{i\in\mathcal{H}_p} \frac{\rho_i c_{Vi}}{\sum_{j\in\mathcal{H}} X_j/\mathcal{D}_{ij}} \\ \lambda_E &= \sum_{i\in\mathcal{H}} \frac{\rho_i c_{Ei}}{\sum_{j\in\mathcal{H}} X_j/\mathcal{D}_{ij}} \end{aligned} \tag{32}$$

Finally, the total mixture thermal conductivity is expressed as the sum of all the above thermal conductivities.

$$\lambda = \lambda_h + \lambda_e + \lambda_R + \lambda_V + \lambda_E \tag{33}$$

The electron electrical conductivity is assumed to be the only significant contributor to the total electrical conductivity. It is given by the second Laguerre-Sonine approximation which reads

$$\sigma_e = \frac{4}{25}\frac{(X_e q_e)^2}{k_b^2 T_e}\frac{1}{\Lambda_{ee}^{00} - \left(\Lambda_{ee}^{01}\right)^2 / \Lambda_{ee}^{11}} \tag{34}$$

Selected transport properties as computed by MUTATION^{++} for equilibrium air are given in Fig. 4.

5.1. Collision Integrals

The transport systems $\mathbf{\Lambda}$ and $\mathbf{G}^{\mu}$ are complex functions of collision integrals which are detailed in the work of Magin et al.[13] so they are not repeated here. Except for charge-charge collisions, collision integral data for species collision pairs are take from the work of Magin[2]. Charged collision pairs are governed by Coulomb potentials shielded by the Debye length, known as the Debye-Hückel potential. The Debye length is defined as

$$\lambda_D = \left(\frac{\epsilon_0 k_B T_e}{2 n_e q_e^2}\right)^{\frac{1}{2}} \tag{35}$$

Devoto [14] and Mason and Munn [15] have computed the necessary reduced collision integrals using the Debye-Hückel potential and provided tables for these integrals as a function of the reduced temperature

$$T^* = \frac{\lambda_D}{q_e^2 / k_B T} \tag{36}$$

For this work, these tables have been curve-fitted to 4th-order exponential polynomials of the form

$$\begin{aligned}\Omega_{ij}^{(l,s)*}(T^*) = \exp[&A + B\ln(T^*) + C\ln(T^*)^2 \\ &+ D\ln(T^*)^3 + E\ln(T^*)^4]\end{aligned} \tag{37}$$

The computed coefficients for each integral are given in Table 2 along with the corresponding residual error for each curve-fit.

5.2. Transport Algorithms

In the case of the the heavy particle thermal conductivity and shear viscosity, a linear system must be solved where the linear coefficients are functions of the collision integrals. Classical approaches [16] to solve these systems either use a determinate method whereby $\mu = \{\eta, \lambda_h\}$ is computed via

$$\mu = -\begin{bmatrix} G^{\mu} & \alpha^{\mu} \\ (\alpha^{\mu})^T & 0 \end{bmatrix} / |G^{\mu}|, \tag{38}$$

or simplified mixture rules such as those developed by Gupta and Yos [17] or Wilke[18]. Recently, state-of-the-art methods were developed by Ern and Giovangigli [19] which formulate symmetric positive definite transport systems. This allows the linear systems to be solved quickly using a direct method such as the LDL^T decomposition or with iterative methods such as the Conjugate-Gradient method. Solution via LDL^T requires a computational cost which scales with $O(n_s^3/6)$ while the CG method is $O(mn_s^2)$, where m is the number of iterations performed. It is therefore obvious that iterative methods are competitive when the number of iterations does not exceed $n/6$. In practice, it was found that only a single CG iteration is required to compute the shear viscosity of the equilibrium Air-11 mixture with an error of less than 1%.

Fig. 5 shows the performance comparison of the Wilke, Gupta-Yos, single iteration CG, and LDL^T methods. From the figure it is clear that the Gupta-Yos method can be competitive below about 9000 K, however at higher temperatures the accuracy decreases significantly. The CG method maintains excellent accuracy over the whole temperature range while costing only slightly more over the Gupta-Yos mixing rule.

6. Kinetics

For mixtures out of equilibrium, it is necessary to compute the species production rates due to elementary chemical reactions which is added as a source term in the species continuity equations. We consider elementary reactions of the form

$$\sum_{i=1}^{n_s} \nu_{ij}^{'} A_i \rightleftharpoons \sum_{i=1}^{n_s} \nu_{ij}^{''} A_i \quad \forall\ j \in \{1, \ldots, n_r\}, \tag{39}$$

where A_i represents the name of species i, and $\nu_{ij}^{'}$ and $\nu_{ij}^{''}$ are the stoichiometric coefficients of the reactants and products respectively. Note that any type of elementary reaction can be expressed in this form. The species production rate for each species s due to these elementary reaction processes is computed via

$$\dot{\omega}_s = M_{w,s} \sum_{j=1}^{n_r} \left(\nu_{sj}^{''} - \nu_{sj}^{'}\right) \tau_j \Theta_j \tag{40}$$

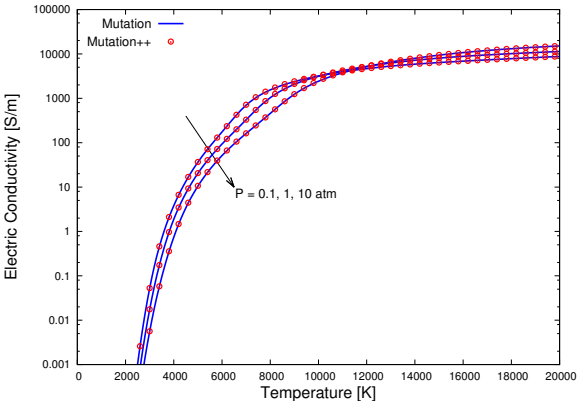

(a) Electric conductivity at 0.1, 1, and 10 atm pressure.

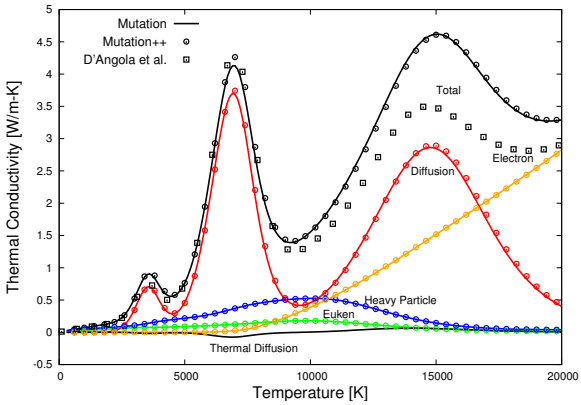

(b) Individual components of thermal conductivity at 1 atm.

Figure 4: Selected transport properties for equilibrium air versus temperature.

Table 2: Fits to collision integral functions for charge-charge collisions.

	A	B	C	D	E	R	ref
$(T^*)^2\Omega^{(1,1)*}_{att}$	-7.9270465e-01	5.8867723e-01	-8.7607125e-02	9.3018130e-03	-4.1315208e-04	0.062	[15]
$(T^*)^2\Omega^{(1,1)*}_{rep}$	-1.3980752e+00	8.0482070e-01	-9.4801647e-02	5.2812176e-03	-8.2652059e-05	0.051	[15]
$(T^*)^2\Omega^{(2,2)*}_{att}$	-8.1145738e-01	7.0419264e-01	-1.2219724e-01	1.3234707e-02	-5.6994085e-04	0.045	[15]
$(T^*)^2\Omega^{(2,2)*}_{rep}$	-1.1089170e+00	7.7460857e-01	-1.0168153e-01	6.7600878e-03	-1.5622212e-04	0.057	[15]
A^*_{att}	-1.8907314e-02	1.1539718e-01	-3.4459736e-02	3.9051788e-03	-1.5513314e-04	0.052	[15]
A^*_{rep}	2.8906871e-01	-3.0170249e-02	-6.9701558e-03	1.5032074e-03	-7.5200734e-05	0.008	[15]
B^*_{att}	2.8616335e-01	-4.8858107e-02	1.3372770e-03	5.6686310e-04	-4.4964175e-05	0.025	[15]
B^*_{rep}	3.2606973e-01	-2.3742462e-02	-9.6987749e-03	1.7799200e-03	-8.3938754e-05	0.013	[15]
C^*_{att}	-6.4672764e-01	-1.0737242e-01	1.7962157e-02	-1.8653043e-03	8.0134495e-05	0.011	[15]
C^*_{rep}	-5.0077127e-01	-1.0639836e-01	-1.1478149e-03	1.8355926e-03	-1.1830337e-04	0.013	[15]
E^*_{att}	-3.8922959e-01	-8.5334423e-02	8.7430000e-03	1.3038899e-04	-4.3583770e-05	0.047	[15]
E^*_{rep}	3.6035379e-01	-7.3192205e-02	1.3517297e-03	1.1249000e-03	-8.3717249e-05	0.016	[15]
F^*_{att}	-5.1269011e-01	-1.6184890e-04	8.4938291e-03	-2.8416333e-03	1.9700964e-04	0.093	[15]
F^*_{rep}	-1.6610568e-01	-8.4658420e-02	-5.1885768e-03	2.1711071e-03	-1.2737940e-04	0.013	[15]
G^*_{att}	-4.2962645e-01	-8.2092404e-02	1.5834420e-02	-1.5811638e-03	6.0509719e-05	0.036	[15]
G^*_{rep}	-3.3907302e-01	-7.8583290e-02	8.4227764e-04	1.3395752e-03	-9.7107273e-05	0.019	[15]
$(T^*)^2\Omega^{(1,4)*}_{att}$	-2.3064366e+00	3.9187956e-01	-5.0541034e-02	4.9996677e-03	-2.1443795e-04	0.029	[14]
$(T^*)^2\Omega^{(1,4)*}_{rep}$	-2.6061028e+00	5.7602188e-01	-8.9813364e-02	8.4176238e-03	-3.1611961e-04	0.023	[14]
$(T^*)^2\Omega^{(1,5)*}_{att}$	-2.6207402e+00	3.6889858e-01	-4.5983762e-02	4.4531740e-03	-1.8883719e-04	0.024	[14]
$(T^*)^2\Omega^{(1,5)*}_{rep}$	-2.8756074e+00	5.3793608e-01	-8.6195947e-02	8.5216824e-03	-3.3719465e-04	0.019	[14]
$(T^*)^2\Omega^{(2,4)*}_{att}$	-1.5271549e+00	5.5923597e-01	-1.0268876e-01	1.2409253e-02	-5.8149121e-04	0.081	[14]
$(T^*)^2\Omega^{(2,4)*}_{rep}$	-1.7664116e+00	6.4675076e-01	-9.8071543e-02	8.6280547e-03	-3.0256691e-04	0.035	[14]

where

$$\tau_j = k_{f,j}\prod_{i=1}^{n_s}\tilde{\rho}_i^{\nu'_{ij}} - k_{b,j}\prod_{i=1}^{n_s}\tilde{\rho}_i^{\nu''_{ij}} \tag{41}$$

is the rate of progress for reaction j and

$$\Theta_j = \begin{cases}\sum_{i=1}^{n_s}\alpha_{ij}\tilde{\rho}_i, & \text{reaction } j \text{ is third-body}\\ 1, & \text{otherwise}\end{cases} \tag{42}$$

is a third-body multiplier for reaction j. The backward rate coefficient is determined by satisfying the equilibrium relation

$$k_{b,j} = \frac{k_{f,j}}{k_{C,j}}, \tag{43}$$

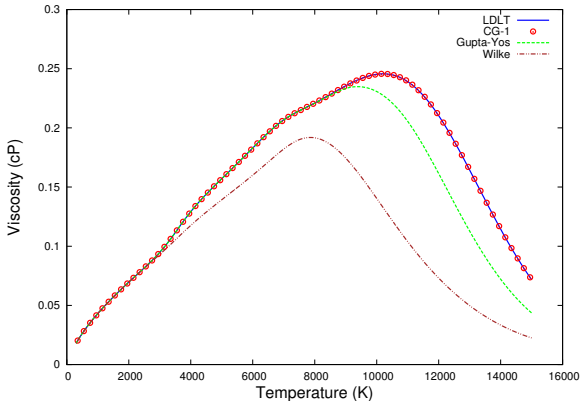

(a) Shear viscosity using different methods for equilibrium air.

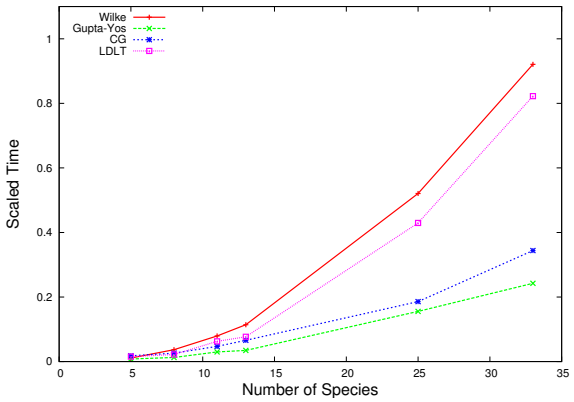

(b) CPU performance of each method as a function of mixture size.

Figure 5: Performance comparison of different solution methods for the shear viscosity.

where the equilibrium constant is defined to be

$$K_{C,j}(T) = \left(\frac{P_{\text{atm}}}{R_u T}\right)^{\Delta\nu_j} \exp\left(-\frac{\Delta G_j^\circ}{R_u T}\right). \tag{44}$$

The forward reaction rate coefficient must be specified by the user. If an Arrhenius rate law is used, $k_{f,j}$ takes the following form:

$$k_{f,j}(T) = A_j T^{\beta_j} \exp\left(-\frac{\theta_{d,j}}{T}\right), \tag{45}$$

where the rate constants A_j, β_j, and $\theta_{d,j}$ are given as input quantities by the user for each reaction considered.

Mutation^{++}was recently coupled with the SHOCKING code which solves the multi-component Euler equations behind a shock wave. The post-shock conditions are determined from the Rankine-Hugoniot shock relations which conserve mass, momentum, and energy across the shock. The temperature and chemistry relaxation behind a shock were computed to illustrate the finite-rate chemistry of Mutation^{++}. The Air-11 mixture was used withthe Park reaction mechanism to model the elementary reactions taking place. The mechanism is shown for completeness in Table 3. The results of the simulation are shown in Fig. 6 and compared to the results obtained by the SHOCK code which is the predecessor to SHOCKING and uses Mutationfor gas properties.

As can be seen in Fig. 6, the finite-rate chemistry computations agree quite well between Mutation^{++}and Mutation. Small differences are attributed to slightly different jump conditions imposed in the SHOCKING and SHOCK codes which initialize the post-shock properties, however it does not appear to make a significant difference in the resulting chemical relaxation.

Table 3: Reaction mechanism used in shock simulation for 11-species air model.

j	Reaction	A_j mol,cm,s,K	β_j	$\theta_{d,j}$ K
1.	$N_2 + M \rightleftharpoons 2N + M$	7.0e21	-1.6	113200
	$\alpha_N = \alpha_O = 4.286$, $\alpha_{e^-} = 428.6$			
2.	$O_2 + M \rightleftharpoons 2O + M$	2.0e21	-1.5	59360
	$\alpha_N = \alpha_O = 5$			
3.	$NO + M \rightleftharpoons N + O + M$	5.0e15	0.0	75500
	$\alpha_{NO} = \alpha_N = \alpha_O = \alpha_{N^+} = \alpha_{O^+} = 20$			
4.	$O + e^- \rightleftharpoons O^+ + 2e^-$	3.9e33	-3.78	158500
5.	$N + e^- \rightleftharpoons N^+ + 2e^-$	2.5e34	-3.82	168600
6.	$N + O \rightleftharpoons NO^+ + e^-$	5.3e12	0.0	31900
7.	$2O \rightleftharpoons O_2^+ + e^-$	1.1e13	0.0	80600
8.	$2N \rightleftharpoons N_2^+ + e^-$	2.0e13	0.0	67500
9.	$N_2 + O \rightleftharpoons NO + N$	5.69e12	0.42	42938
10.	$O_2 + N \rightleftharpoons NO + O$	2.49e9	1.18	4005.5
11.	$NO^+ + O \rightleftharpoons N^+ + O_2$	1.0e12	0.5	77200
12.	$O_2^+ + N \rightleftharpoons N^+ + O_2$	8.7e13	0.14	28600
13.	$NO + O^+ \rightleftharpoons N^+ + O_2$	1.4e5	1.9	15300
14.	$O_2^+ + N_2 \rightleftharpoons N_2^+ + O_2$	9.9e12	0.0	40700
15.	$NO^+ + N \rightleftharpoons O^+ + N_2$	3.4e13	-1.08	12800
16.	$NO^+ + O_2 \rightleftharpoons O_2^+ + NO$	2.4e13	0.41	32600
17.	$NO^+ + O \rightleftharpoons O_2^+ + N$	7.2e12	0.29	48600
18.	$O^+ + N_2 \rightleftharpoons N_2^+ + O$	9.0e11	0.36	22800
19.	$NO^+ + N \rightleftharpoons N_2^+ + O$	7.2e13	0.0	35500

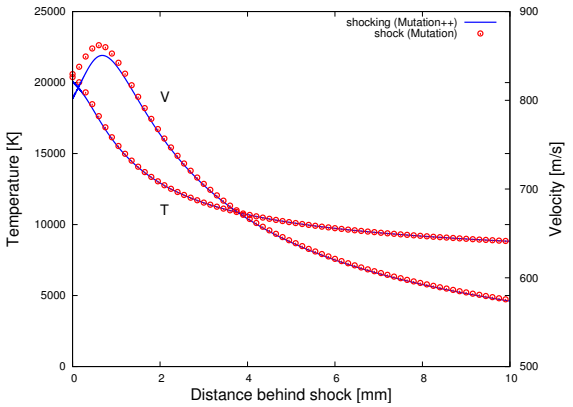

(a) Velocity and temperature profiles.

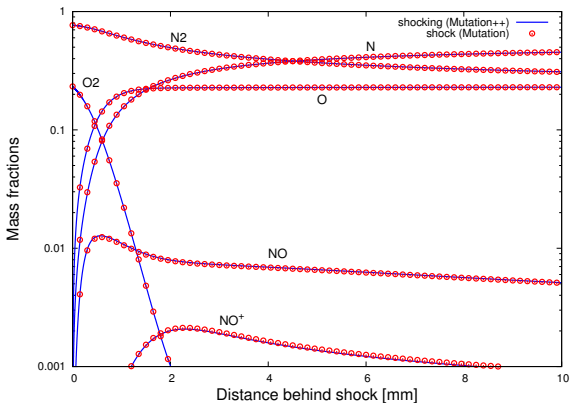

(b) Species mass fractions.

Figure 6: Comparison of 11-species air chemistry relaxation behind a shockwave using the SHOCKING code with MUTATION^{++}and SHOCK with MUTATIONand the following free-stream conditions: u_∞ = 8 km/s, P_∞ = 5 Pa, and T_∞ = 300 K.

7. Concluding Remarks

MUTATION^{++}is currently being developed to model high enthalpy gases which may or may not be ionized. Currently, the properties required to model equilibrium or single temperature multicomponent flows have been implemented and validated. In future work, a multi-temperature framework will be created which will handle energy transfer between the various energy modes available in the system. This may include a simple two temperature model or could be extended to collisional radiative processes.

Acknowledgments

This research is funded through a Fellowship provided by the European Research Council Starting Grant #259354: "*Multiphysics models and simulations for reacting and plasma flows applied to the space exploration program.*" We would also like to thank Alessandro Munafo for providing the SHOCKING code and coupling it with MUTATION^{++}.

References

[1] F. Palacios, M. R. Colonno, A. C. Aranake, A. Campos, S. R. Copeland, T. D. Economon, A. K. Lonkar, T. W. Lukaczyk, T. W. R. Taylor, J. J. Alonso, Stanford university unstructured (su2): An open-source integrated computational environment for multi-physics simulation and design, 51st AIAA Aerospace Sciences Meeting and Exhibit. Grapevine, Texas, USA (AIAA Paper 2013-0287).

[2] T. E. Magin, A model for inductive plasma wind tunnels, Ph.D. thesis, Universitè Libre de Bruxelles and von Karman Institute for Fluid Dynamics (2004).

[3] M. Mitchner, J. Charles H. Kruger, Partially Ionized Gases, John Wiley & Sons, Inc., 1973.

[4] R. M. Kendall, E. P. Bartlett, R. A. Rindal, C. B. Moyer, An analysis of the coupled chemically reacting boundary layer and charring ablator, part i: Summary report, Tech. Rep. CR-1060, NASA (1968).

[5] J. Lachaud, H. Wong, I. Cozmuta, G. Reinisch, Develpment and validation of a physics-based multi-scale model for low-density carbon/phenolic ablators, Step 2 proposal - hyp1-2. 2.1.2: High fidelity modeling of low-density carbon/phenolic ablators (edl), NASA-NRA (2011).

[6] W. C. Reynolds, The element potential method for chemical equilibrium analysis: Implementation in the interactive program stanjan, version 3, department of Mechanical Engineering, Stanford University (1986).

[7] S. Gordon, B. J. McBride, Computer program for calculation of complex chemical equilibrium compositions and applications, Tech. Rep. RP-1311, NASA (1994).

[8] P. S. Bishnu, D. Hamiroune, M. Metghalchi, J. C. Keck, Constrained-equilibrium calculations for chemical systems subject to generalized linear constraints using the nasa and stanjan equilibrium programs, Combust. Theory Modelling 1 (1997) 295–312.

[9] S. B. Pope, The computation of constrained and unconstrained equilibrium compositions of ideal gas mixtures using gibbs function continuation, Report FDA 03-02, Cornell University (2003).

[10] S. B. Pope, Gibbs function continuation for the stable computation of chemical equilibrium, Combustion and Flame 139 (2004) 222–226.

[11] F. S. Milos, Y.-K. Chen, Comprehensive model for multicomponent ablation thermochemistry, AIAA, Aerospace Sciences Meeting & and Exhibit, 35th, Reno, N.V. Jan. 6-9, 1997.

[12] J. de Muelenaere, J. Lachaud, N. N. Mansour, T. E. Magin, Stagnation line approximation for ablation thermochemistry, 42nd AIAA Thermophysics Conference, 27-30 June 2011,

Honolulu, HI.
[13] T. E. Magin, G. Degrez, Transport of partially ionized and unmagnetized plasmas, Physical Review E 70.
[14] R. S. Devoto, Transport coefficients of ionized argon, The Physics of Fluids 16 (5) (1973) 616–623.
[15] E. A. Mason, R. J. Munn, Transport coefficients of ionized gases, The Physics of Fluids 10 (8) (1967) 1827–1832.
[16] J. O. Hirschfelder, C. F. Curtiss, R. B. Bird, Molecular theory of gases and liquids, Wiley, New York, London, 1954, 1964, second printing, corrected, with notes added.
[17] R. N. Gupta, J. M. Yos, R. A. Thompson, K. P. Lee, A review of reaction rates and thermodynamic and transport properties for an 11-species air model for chemical and thermal non equilibrium calculations to 30,000 k, Technical report NASA RP-1232 (August 1990).
[18] C. R. Wilke, A viscosity equation for gas mixtures, J. Chem. Phys. 18 (1950) 517.
[19] A. Ern, V. Giovangigli, Multicomponent transport algorithms., Springer-Verlag, Berlin, 1994.

Development of Advanced Models for Transition to Turbulence in Hypersonic Flows and Prediction of Transition under Uncertainties

Gennaro Serino

Aeronautics and Aerospace Department, von Karman Institute for Fluid Dynamics, Belgium, gennaro.serino@vki.ac.be

Supervisor: Thierry E. Magin

Associate Professor, Aeronautics and Aerospace Department, von Karman Institute for Fluid Dynamics, Belgium, thierry.magin@vki.ac.be

Supervisor: Patrick Rambaud

Associate Professor, Aeronautics and Aerospace Department, von Karman Institute for Fluid Dynamics, Belgium, patrick.rambaud@vki.ac.be

University Supervisor: Vincent Terrapon

Assistant Professor, Aerospace and Mechanical Engineering Department, University of Liege, vincent.terrapon@ulg.ac.be

Abstract

A computational method is introduced to infer statistical information on boundarylayer perturbations upstream of laminar-turbulent transition in a supersonic boundary layer. The method uses the intermittency function as a basis, which specifies the amount of time a flow is turbulent at a given streamwise location. The methods yields a joint probability density function for amplitude and frequency of boundary-layer perturbations upstream of transition. It relies on linear stability theory to link the probability density function with the intermittency. In order to infer parameters governing the function, we perform a statistical inverse analysis using the Markov chain Monte Carlo method. The approach is applied to experimental data obtained in the VKI-H3 hypersonic facility.

Keywords: Laminar to turbulent transition, hypersonic flows, Uncertainty Quantification, Linear Stability Theory, Reynolds Averaged Navier-Stokes, intermittency factor, inverse problem, MCMC.

Nomenclature

Symbols

A_0	initial amplitude of the disturbances
F	dimensional frequency (kHz)
M	Mach number
N	amplification ratio
N_{crit}	critical N for transition onset
Re	Reynolds number
St	Stanton number
p_T	probability of transition
$\hat{v}(y)$	amplitude of the perturbations
x	streamwise coordinate (m)
y	normal coordinate (m)
z	spanwise coordinate (m)

Greek symbols

α	streamwise wave number
β	spanwise wave number
δ_{μ_F}	MCMC increment for the mean
δ_{σ_F}	MCMC increment for the variance
γ	intermittency factor
μ	mean
ω	non-dimensional frequency
σ	variance

Abbreviation

CFD	Computational Fluid Dynamics
DNS	Direct Numerical Simulations
$MCMC$	Markov chain Monte Carlo
QoI	Quantity of Interest
$RANS$	Reynolds Averaged Navier-Stokes
TPS	Thermal Protection System
UQ	Uncertainty Quantification
VKI	von Karman Institute for Fluid Dynamics
cdf	cumulative distribution function

pdf probability distribution function

1. Introduction

During reentry, space vehicles are subjected to an extreme thermal environment due to the deceleration at the impact with the atmosphere. They are therefore equipped with heat shields which ensure the structural integrity. It is well known that heat fluxes in turbulent flows are several times higher than in the laminar regime, thus transition to turbulence plays a key role in hypersonic reentry.
Highly conservative safety margins are currently used in the design of heat shields to take into account unexpected transition due to the variability of the physical environment. The conservative approach allows engineers to take into account variations of the free stream parameters or of the surface geometry but at the expense of a significant increase in their weight. In fact, a change of the Mach number or of the Reynolds number with respect to the design conditions, as well as the presence of roughness or misaligned tiles on the body, can promote transition causing dramatic changes in the predicted heat transfers and faster damage to the TPS.
In this research, uncertainties on free stream parameters and surface geometry are taken into account in numerical simulations. The aim is to consider the physical variability of the system to simulate and to study the effect of the uncertainties on some *Quantity of Interest* (QoI). In particular, we focus on the transition location and on the heat loads occurring during atmospheric reentry.
Since transition to turbulence is a stochastic process, deterministic simulations and a probabilistic approach are combined. The latter relies on tools of *Uncertainty Quantification* (UQ) where flight conditions, boundary conditions, or initial disturbances are treated as random and modeled by probability distribution functions (*pdf*). The objective is to define the probability distribution, and thus confidence levels, on the heat loads and the transition point. Results are then used to improve existing transitional models for a more reliable, faster and less conservative design of the heat shields. A better knowledge of the physics will allow to quantify and eventually reduce these uncertainties leading to a less conservative design to the benefit of safety and costs.
Nowadays, we can observe a renewed interest in transition driven by the design of powered hypersonic vehicles as the DARPA FALCON HTV-2 or the ESA IXV. These vehicles are designed to fly at the higher levels of the atmosphere where a laminar or turbulent flow radically affects their drag and required power. Therefore, transition is one of the most important driving factor in the design of reentry vehicles and space planes, from the thermal protection system to the engines.
Experiments and numerical simulations (CFD) are both used to investigate the transition mechanism. In experiments, the free stream parameters, as the Mach and the Reynolds number, can not represent the real flight conditions [1] due to the limitation of the facility and to the physical variability of the environment. In CFD, the real flight conditions can be simulated but models are necessary to represent the physics. These models simplify the more complex mechanisms of transition which makes its prediction less reliable [29].

2. Introduction to the deterministic and probabilistic tools

Transition prediction nowadays relies on experiments and numerical simulations. Experimental prediction is done through empirical criteria and correlations (PANT, Shuttle [33]) which have been successfully used in the past although limited to specific geometries and test conditions. Numerical simulations offer possibilities with different degrees of complexity and costs. Methods for estimating transition in CFD can be based on Linear Stability Theory (LST), Reynolds Averaged Navier-Stokes (RANS) and Direct Numerical Simulations (DNS).
Since linear stability based methods are used for the results hereafter, the fundamentals of the theory will be briefly described. An introduction to the Uncertainty Quantification approach applied to numerical simulations is also given.

2.1. Linear Stability Theory and transition prediction

Most of the current knowledge on hypersonic boundary layer transition is due to the extensive work of Mack [22] and Arnal [2] supported by the experiments carried out by Stetson [41], Kendall [17] and Schneider [36].
Mack and Arnal first focused on modeling the perturbations inside the incompressible boundary layer as wave-like disturbances according to the Linear Stability Theory. As described by Schlicthing [35], perturbations are added to the mean flow quantities

into the transport equations, which are linearized and combined into the stability equation, called the "Orr-Sommerfeld equation". The solution of this equation gives the parameters, typically the Reynolds numbers and the wave speeds (α), for which the flow becomes unstable. In general, the two-dimensional waves, called the "Tollmien-Schlichting" waves start to grow until their breakdown, which defines the "onset" of transition. This phenomenon is defined as "modal" instability since the perturbations grow exponentially in space and time until transition occurs. When the modal instability does not occur, transition may be caused by the "transient growth" phenomenon where the perturbations grow linearly and then they decay exponentially in time or space. In this case, we speak about "bypass transition" since the modal instability is bypassed in favor of the transient growth which causes transition. The transient growth mechanism is influenced by surface parameters, such as the surface roughness and the wall temperature, and by free stream conditions, such as the turbulence level.

Compressibility effects can be also taken into account in the LST by including additional parameters into the "Orr-Sommerfeld equation". The fundamentals of the LST applied to hypersonic boundary layers were given by the studies and computations of Mack [23], [24]. Mack's greatest contribution was the discovery of multiple solutions of the stability equation in the high-speed regime which were called higher modes or *Mack modes* in his honor. A *first mode* instability is physically related to the generalized inflection point in the boundary layer profiles. It has been shown that when this point exists, the profiles are intrinsically unstable. An intuitive example is the breakdown of the sea waves when they are approaching the land. When the Mach number is higher, a second type, *second mode*, of instability is physically due to the pressure disturbances which are trapped in the boundary layer between the wall and the sonic line. The acoustic waves are continuously reflected, bouncing between the surface and the sonic line until their amplification is high enough to cause transition. This second mode instability is also called "acoustic" or "radiative" instability. In high speed boundary layer, transition is generally due to the second mode instability.

Mack also carried out several studies on the effect of wall cooling on boundary layer stability. In contrast to the early stability theory [20] which considered wall cooling as a complete stabilizer of the boundary layer, Mack found that the higher modes were destabilized in presence of cold surfaces. Thus, a cold surface is characterized by a lower transitional Reynolds number than a hot surface.

Several experiments were carried out to investigate boundary layer instability in high-speed boundary layers. The existence of second mode instabilities was proved by the experiments of Kendall [17] where higher modes were found to be the dominant destabilizing source. Further investigations were carried out by the extensive work of Schneider [36] who focused on hypersonic transition on conical geometries in several wind tunnels. A detailed review, of flight data and experiments carried out in the framework of hypersonic transition can be found in [37].

Experiments are linked to LST through the e^N transition prediction method. It consists in linking the experimental transition onset to the growth of the perturbations through the N-factor [44]. This is an index measuring how much the initial perturbations are amplified along the stream-wise direction. Generally, the N-factor is around $8 \div 9$ at transition onset for low-speed flows while it is around $4 \div 5$ in hypersonic regime due to the larger free stream turbulence. It also depends on the facility where the test is carried out since it is related to free stream level of noise. In fact, the higher the noise is the lower is the threshold N-factor where transition occurs. As a consequence, transition is usually observed for N-factor around $12 \div 14$ in flight conditions, since the freestream turbulence is really low. For example, Fig. 1 shows the computed N-factor on the HIFire I reentry vehicle in flight conditions given by [11] for different frequencies of the perturbations. The onset of transition was observed at $x = 0.76$ m on the surface model corresponding to a N-factor equal to 13.5. Once the N-factor is known for certain conditions and facilities, transition prediction can be done by computing the growth rate of the perturbations by LST. Thus transition occurs where the computed N-factor is equal to the threshold value. This is known as the e^N transition prediction method, whose practical application is widespread due to its simplicity and reliability. However, its simplicity is also a limitation since it does not take into account effects such as the presence of surface roughness. Moreover, the extension to three-dimensional flows is not straightforward (i.e. cross flow instabilities). In addition, it requires to know the N-factor at the transition point in advance through calibration and wind tunnel tests. Hence the e^N approach is considered a semi-empirical method.

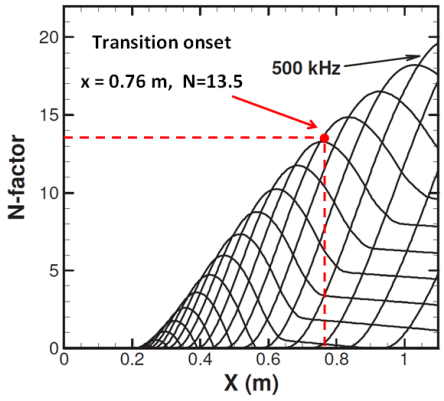

Figure 1: N factors computed on the HIFire I reentry vehicle[11] : $M_\infty = 5.28$, $H = 21$km

2.2. *Uncertainty Quantification and numerical simulations*

Iaccarino *et al.* [18] define Uncertainty Quantification (UQ) as a probabilistic approach to determine confidence levels on the results of numerical simulations. A real physical system is characterized by intrinsic uncertainties related to the input conditions. UQ aims at studying how these uncertainties affect the numerical results focusing on some *Quantities of Interest* (QoI). The typical process consists in characterizing the input uncertainties, then propagating them through the numerical simulation and, finally, defining the margins and error bars on the QoI. For example, in the context of this work, uncertainties on the free stream perturbations or free stream parameters, such as the Mach number and the Reynolds number, are investigated to quantify their effects on the transition onset and length.

UQ has been applied recently to estimate the effects of different parameters on numerical simulations. For instance Pecnik *et al.* [31] studied the effects of input uncertainties on transition prediction of transonic gas turbine compressors where numerical results were compared with experimental data obtained at the von Karman Institute for Fluid Dynamics (VKI) for several turbine guide vane test cases. A similar approach has been used by Sankaran [34] for simulations of blood flow in both healthy and diseased vascular models where the effect of hemodynamic parameters including velocities, time varying wall shear stress, pressure drops, and energy losses were investigated. Here, the input uncertainties are quantified and mapped to the stochastic space using the stochastic collocation technique. The idea of stochastic collocation methods is that the points which the model is evaluated at are chosen so that they are orthogonal with the probability distributions on the inputs as a weighting function. A detailed explanation of the method is given by Loeven [21] who also presents a modified version to obtain faster convergence on the results.

The parameters to investigate can be also part of the model used for the numerical simulations. An example can be the values of a parameter of a transition or turbulence model such as the free stream turbulence level or the eddy viscosity ratio. Studies on these type of uncertainties are performed by Gorle [14] in RANS simulations of turbulent mixing. In this study, uncertainties are identified in the Reynolds stresses and in the scalar fluxes. To correctly quantify these uncertainties, perturbations are introduced in the values obtained from the deterministic models with a range of variations based on a comparison with LES data.

Applications of the UQ strategy to high-speed flows are presented by Iaccarino [19] for two classical problems in unsteady compressible fluid dynamics: the Riemann problem and the Woodward-Colella forward step flow. These applications show the advantage of using the probabilistic approach in problems with discontinuities such as shock waves. In Fig. 2, for the Woodward and Colella forward facing step problem, the mean and the variance of the divergence velocity field are represented. It can be noticed how the position of the shock wave and its reflection radically change when uncertainties on the freestream Mach number are considered.



Figure 2: Woodward and Colella forward facing step problem. Mean velocity divergence field corresponding to an uncertain input Mach number [2.5 : 3.0]. Stochastic collocation based on $M = 3$ [19].

The propagation of uncertainties through the computational model can be achieved by either intrusive or non-intrusive techniques. A non-intrusive technique consists in several repetitions of the original deterministic models. Examples are the Monte Carlo method or the stochastic collocation approaches where the computational model is treated as a black-box and several simulations are performed. On the other hand, an intrusive technique is based

on the modification of the original deterministic model, as in the polynomial chaos approach, where a polynomial expansion simplifies the original model. Intrusive techniques suffer strongly from the *curse of dimensionality* since they are slower to converge when the number of parameters increase. In this work, a non-intrusive approach based on stochastic collocation is used.

3. Formulation of the method

This section explains how the deterministic (Sec. 2.1) and the probabilistic tools (Sec. 2.2) are used and combined in the present research.

3.1. Assumptions for the deterministic simulations

LST[35] assumes wave-like disturbances in the mean flow which can be modeled as a function of spatial coordinates x, y, z and of time t :

$$v(x,y,z,t) = \hat{v}(y)e^{i(k\alpha x + l\beta z - m\omega t)}, \quad \alpha = 2\pi/\lambda_x \quad \beta = 2\pi/\lambda_z \tag{1}$$

In Eq. 1, x is the stream wise direction, z the span wise direction and y the direction normal to the wall while α and β are the stream wise and span wise wave numbers, respectively. $\hat{v}(y)$ is the complex disturbance amplitude while k, l, m are integers representing the different wave numbers along the stream wise, span wise direction and in time, respectively. The frequency ω is related to the stream wise wave number α by the phase speed c, $c = \omega/\alpha$, at which the disturbances travel downstream. In general, α, β and ω are complex. We consider here that transition is due to *second mode* instabilities so that perturbations are amplified along the stream wise direction x. In this case, β vanishes since the direction of maximum amplification is aligned with the stream wise coordinate x. As the spatial approach is used here, ω is real while α is complex.
Transition is predicted with the $e^N - method$ which is described by Arnal [2] (see Sec. 2.1). When the spatial approach is used, the N factor is obtained by integrating the amplification rates α_i along the stream wise direction :

$$N = log\frac{A}{A_o} = \int_{x_0}^{x} -\alpha_i dx \tag{2}$$

In Eq. 2, A_0 is the initial amplitude of the disturbances at the location x_0 where they start to be amplified. According to the e^N method, transition occurs when the computed N factor equals the value determined at the experimental transition location for a specific wind tunnel. Examples of application of the method are the experiments carried out by Horvath [16] in the NASA Langley Mach 6 wind tunnel where transition onset occurs when $N = 3.8$.

3.2. Description of the method

1. Linear stability analysis: free stream conditions and geometrical parameters are defined for a test case and then boundary layer profiles are obtained from self-similar solution or CFD simulations. Then, the stability analysis is carried out by choosing a frequency for the perturbation waves in a given range of variation. For high-speed flows typical frequencies are within $400 \div 800$ kHz. The linear amplification phase is solved with the stability code VESTA developed by Pinna [32] at the VKI. It has been shown by Marxen [27] that LST is a good model for describing the linear amplification of the perturbation waves through comparison with DNS data. At the end of the stability analysis, the N-factor is computed according to Eq. 2. Therefore, the output of this first step is a series of curves describing how the perturbations with different frequencies are amplified along the stream wise direction. This output constitutes the *transfer function* which will be used in the probabilistic approach. An example is shown in Fig. 3 for one of the experimental cases carried out by Masutti [26] in the VKI-H3 facility.
2. Definition of the uncertainties: LST has been carried out by considering the variation of the dimensional frequency (F) of the free stream perturbations. The UQ approach aims at defining how the variation of this parameter affects the transition onset location. In order to do that, a probability function (pdf) with a normal distribution is assumed to describe this source of uncertainty. Generally, a normal distribution includes all the possible values of a parameters from $-\infty$ to $+\infty$. In the current work, in order to prevent non physical values, such as negative frequencies, the probability distribution has been truncated into a fixed range. Frequencies are then selected in this range that includes the typical values for *second mode* instability. An example

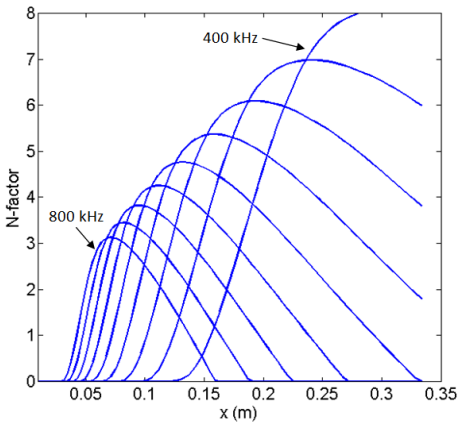

Figure 3: N factors computed on the VKI-H3 High Reynolds case [26]: $M_\infty = 6$, Frequency $\in [400 : 50 : 800]$ kHz.

of the pdf for the input uncertainties is shown in Fig. 4.

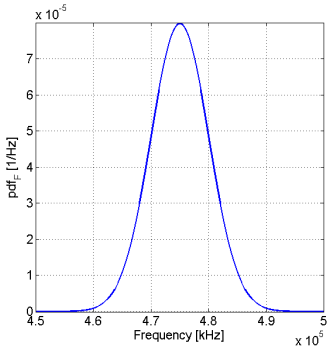

Figure 4: Example of pdf of the input parameter for the UQ analysis

3. Propagation: LST analysis defines a *transfer function* which links the input uncertainty (i.e. the frequency F) to the output (i.e. the N-factor) for the estimation of the transition onset in the simulations. Once the input pdf is assumed, the output pdf is obtained by applying the *method of transformation*. This method is valid as long as the $input - output$ relation is unique, that is when the *transfer function* is monotonic. An illustration of the method is represented in Fig. 5 for generic input, $f(x)$, and transfer function $y(x)$. In our case, the *transfer function* $N = N(F)$ is unique up to the maximum N-factor for each curve which describes the relation between the input frequency F and the output N-factor. The method consists in obtaining the output pdf by multiplying the input pdf and the *Jacobian*, $J(F,N) = dF/dN$, of the *transfer function* as reported in Eq. 3.

$$pdf(N) = J(F,N) \times pdf(F) \qquad (3)$$

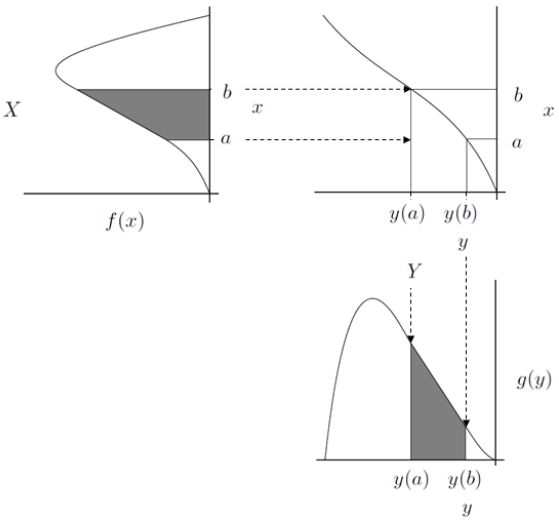

Figure 5: Example of the *method of transformation*

4. Output: the probability distribution of the $N-$factor for each station of the computational domain is the output of the analysis. Since the work aims at modeling the transition region, results are presented in terms of the probability of having transition at a fixed location. This probability is computed by integrating, at a fixed streamwise coordinate, along N up to N_{crit}, which is the N value corresponding to the transition onset experimentally observed. The integration is reported in Eq. 4.

$$p_T = 1 - \int_0^{N_{crit}} pdf(\bar{N})d\bar{N} = \gamma. \qquad (4)$$

The probability of transition starts from 0 where the flow is most likely to be laminar. Then it gradually rises to 1 where the flow is most likely to be fully turbulent. This probability can be interpreted as the *intermittency factor* γ, which has been defined by Narasihma [30] as the time ratio between turbulent and laminar flow at a fixed location. A summary of the procedure described above is reported in Fig. 6(a), while in Fig. 6(b) an example of the output probability of transition is shown.

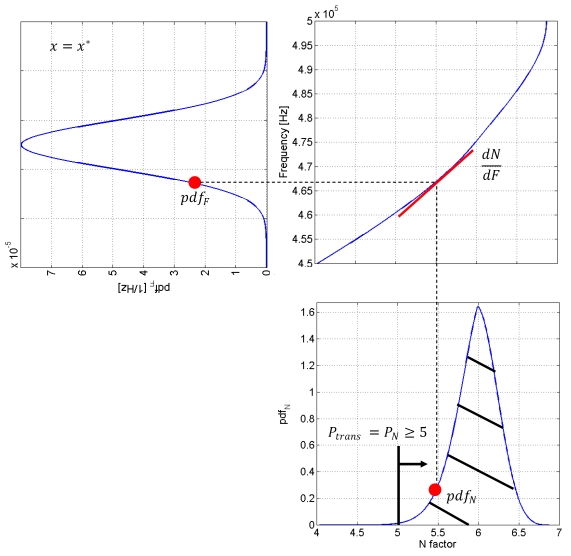

(a)

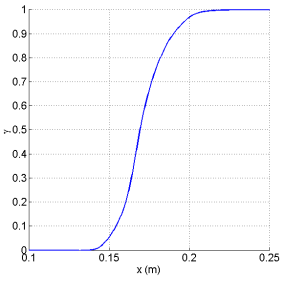

(b)

Figure 6: (a) Summary of the procedure to obtain the probability of transition, (b) Example of probability of transition.

4. The VKI-H3 test case

The assumptions described in Sec. 3.1 have been applied to different test cases with the approach described in Sec. 3.2. Here, a test case for natural transition on a 7° half cone model in the VKI-H3 facility is presented. The test conditions are summarized in Tab. 1 for different Reynolds numbers. Experiments were carried out by Masutti [26] and results are represented in Fig. 7. Transition is detected by surface measurements of the heat flux which is then expressed as the non dimensional Stanton number (St). This number quantifies the ratio of heat transferred to the wall and the heat converted through the boundary layer. From experimental data, it can be seen that the transition onset location moves upstream as the free stream Reynolds number increases.

The analysis is divided in two parts. The first is focused on studying how the uncertainties on the freestream perturbations propagate to the numerical results and on the comparison between the numerical results and the experimental data. In the second part, an inverse analysis is carried out to investigate the distribution of the free stream perturbations which are most likely to cause transition for one of the cases. The first analysis is also defined as *the forward problem* and it follows the steps described in Sec. 3.2. The second part is called the *the inverse problem* and it will be described in the following sections.

Test case	M_∞	Re_∞ [1/m]	T_w [K]
Low Reynolds	6.0	18.0×10^6	294
Medium Reynolds	6.0	22.8×10^6	294
High Reynolds	6.0	27.1×10^6	294

Table 1: Test case and free stream conditions

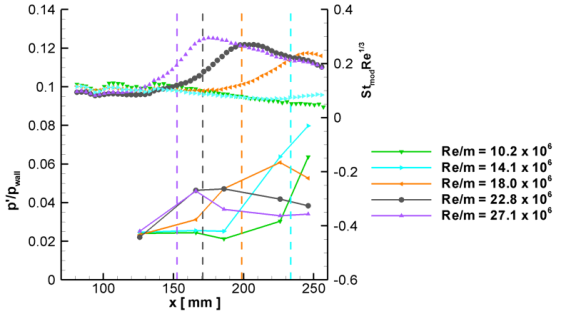

Figure 7: Experimental results obtained in VKI-H3 facility (conditions are given in Tab. 1). Modified Stanton number (top curves) and pressure variations (bottom curves) against the stream wise coordinates

4.1. The forward problem

We assume that laminar-turbulent transition is caused by perturbations in the boundary layer upstream of the transition location. The aim of *the forward problem* is to obtain the probability of transition caused by an assumed free stream perturbation spectrum.

For the conditions indicated in Tab. 1, a linear stability analysis has been carried out and the N-factor has been obtained. Then, a pdf has been assumed for the frequencies which characterize the freestream perturbations. We assume that the pdf is normally distributed around its mean μ_F with a variance σ_F in a given range of frequencies. The value of the mean

and the variance are indicated in Tab. 2 for the different Reynolds numbers. The values have been obtained by choosing the mean of frequency distribution such that the amplification ratio reaches the threshold value at the experimental transition onset. It has been found that, in the VKI-H3 facility, the limiting N-factor is equal to 5. In Fig. 8 the isolines of the N-factor are computed for the High Reynolds conditions in which transition is observed at ≈ 0.13 m (see Fig. 7). A mean frequency of 480 kHz with a variance of 25 kHz allows to have a satisfying agreement with the experimental data.

Test case	μ_f [kHz]	σ_F [kHz]	Range [kHz]
Low Reynolds	330	10	200 ÷ 800
Medium Reynolds	410	20	200 ÷ 800
High Reynolds	480	25	200 ÷ 800

Table 2: Parameters for the input pdf

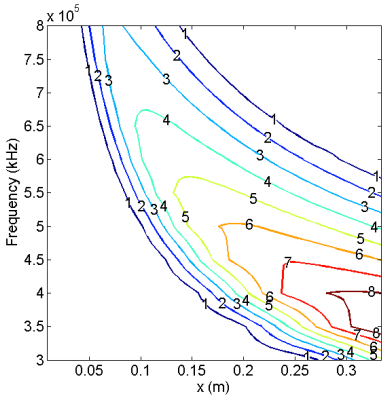

Figure 8: N-factor isolines against Frequency and streamwise coordinate for the High Reynolds condition computed with LST

Experimental data are available in term of Stanton number $St(x)$ (Fig. 7) along the cone model. In order to compare them with our results, the St has been normalized to obtain the experimental intermittency factor γ within the transition region. Since the transition onset x_{onset} and the transition offset x_{offset} are known, the experimental intermittency can be obtained through Eq. 5.

$$\gamma(x) = \frac{St(x) - St_{x=x_{onset}}}{St_{x=x_{offset}} - St_{x=x_{onset}}} \qquad (5)$$

The normal distribution with the parameters given in Tab. 2 allows to compute the probability of transition and, thus, the intermittency curves for the different test conditions. Results are represented in Fig. 9 and compared to the experimental data. The transition onset location and the shape of the intermittency factor within the transition region agree very well with the experimental data. For all cases, a characteristic shape is obtained similar to the classical error function. The good agreement with the experimental data demonstrates the validity of the approach and, in particular, confirms the validity of the e^N transition prediction for high-speed flows.

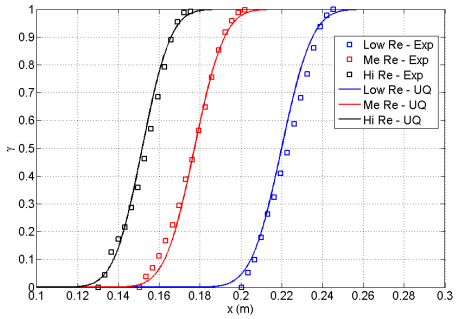

Figure 9: Intermittency as a function of the streamwise location : comparison between UQ analysis (-) and experimental results (□) for the conditions given in Tab. 1.

4.2. *The inverse problem*

The forward problem described above can be regarded as a computational model $f(s)$ that takes D input parameters $s = (s_1, ..., s_D)$ and produces a K-vector of derived outputs $m = (g_1(f(s), r), ..., g_K(f(s), r))$ with auxiliary parameters $r = (r_1, ..., r_N)$. Solving for m given s is called *the forward problem*, while inferring s given the measurements of m is denoted as *the inverse problem*.

For the test case, the two input parameters are the mean and the variance of the perturbation spectrum of the frequency, so $s_1 = \mu_F$ and $s_2 = \sigma_F$. The auxiliary parameters r correspond to the conditions indicated in Tab. 1. We consider as outputs the probability of transition γ at selected locations $x_1, ..., x_K$ and hence $m = (\gamma_1, ..., \gamma_K)$.

Due to measurement uncertainties, the input quantity s can only be characterized by its statistics, namely the probability $p(s)$. In other words, the mean and variance of the perturbation distribution are themselves probabilistic. The solution of the forward problem hence yields a probability $p(m)$. In the inverse problem, the measurements of m are noisy and the input to the statistical inverse problem is $m+\eta$, where η quantifies this noise. In the inverse problem, we start with a

given set of noisy measurements $m+\eta$ and seek the input parameters s using our computational model $f(s)$. The inverse problem is solved by applying the Bayesian inversion. Instead of calculating s, we compute a probability of s given m, $p(s|m)$, which is the so-called *posterior density*. Bayes'theorem states that the conditional probability of the parameters s given the measurements m is equal to the product of the probability of the measurements m given the parameters s, times the ratio between the probabilities of the parameters s and the measurements m:

$$p(s|m) = \frac{p(m|s) \times p(s)}{p(m)} \propto p(m|s) \times p(s) \qquad (6)$$

In Eq. 6, $p(s)$ is the *prior probability density* which is related to the information on the input parameters and $p(m|s)$ is the *likelihood probability* which relates the measurements to the input parameters. Finally, $p(m)$ is a normalizing constant that ensures that the product of the likelihood and the prior is a probability density function, which integrates to one.

Several methods are available to infer the posterior probability density. Two such methods are the Markov Chain Monte Carlo (MCMC) method or the Kalman filtering method [42]. The former includes algorithms for sampling from probability distributions based on building a Markov chain that has the desired distribution as its equilibrium distribution. The state of the chain after a large number of steps is then used as a sample of the desired distribution. The quality of the sample improves as a function of the number of steps. For the current application, this method has been implemented and used to compute the posterior probability density $p(s|m)$ with a Metropolis-Hastings algorithm [15]. For simplicity, we assume a Gaussian distribution for the prior probability density $p(s)$. The effect of this assumption will be assessed in future works.

In our specific context, the inverse problem consists in obtaining the distribution of the frequency which gives the intermittency closest to the experimental data. The parameter to be inferred are the mean μ_F and the variance σ_F of the frequency pdf at the transition onset.

This approach has been applied to the VKI-H3 experimental data for the low-Reynolds number case ($Re = 18 \times 10^6$). The inverse problem has been solved by using the Markov-Chain Monte Carlo method where the forward problem is solved several times by varying the input parameters in a given range. Starting from an initial distribution defined by μ_0 and σ_0, successive realizations are obtained with different combinations of the parameters and selected increments (δ_{μ_F}, δ_{σ_F}) for the mean and the variance, respectively. The method guarantees the convergence to the exact solution after a certain number of steps. An illustration of the sampling space is shown in Fig.10 with the starting point (μ_{F0}, σ_{F0}) and the burn in period. The converged mean and variance are evaluated on the remaining samples as represented in Fig.11 and Fig.12. The final values are reported in Tab.3 and compared to the probability distribution previously assumed for the forward problem.

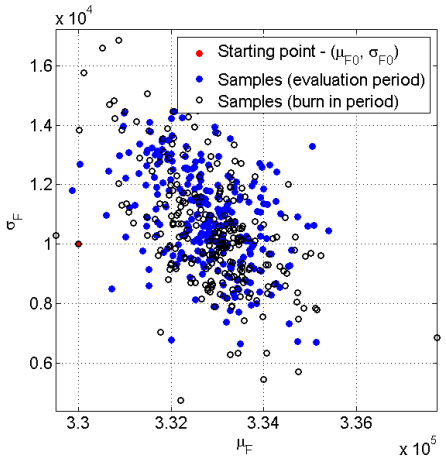

Figure 10: Sampling space : starting point (red), burn in period (black) and useful samples (blue)

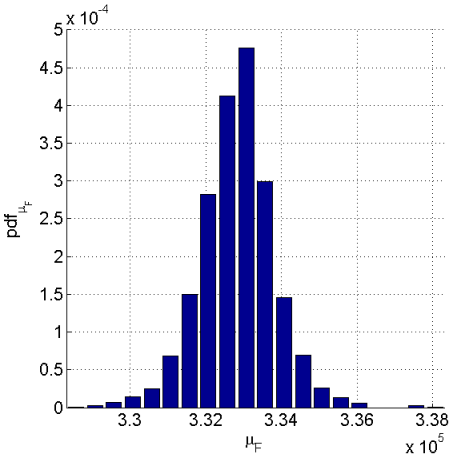

Figure 11: Probability density function for the mean of the frequency (μ_F) for the low Reynolds case

The posterior probability density is represented in

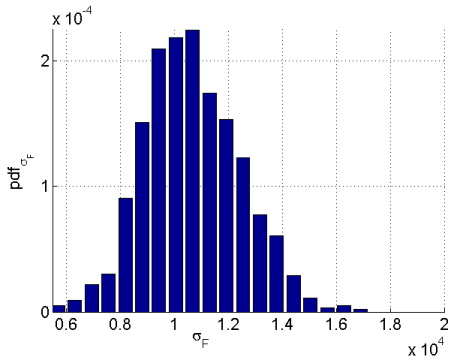

Figure 12: Probability density function for the variance of the frequency (σ_F) for the low Reynolds case

Low Reynolds	μ_f [kHz]	σ_F [kHz]	Range [kHz]
Forward problem	330	10	200 ÷ 800
Inverse problem	333	11	200 ÷ 800

Table 3: Comparison of the probability density functions for the forward and the inverse problem in the low Reynolds number case

Fig.13 where it can be seen that the computed intermittency agrees well with the experimental data in the first part of the transition region that is between $0 < P < 0.5$. On the other hand, the agreement is not as good in the second half of the transition region. This is due to the noise η which characterizes the experimental data. The error bars represent the uncertainty of the measurements, what we called the noise η, which linearly grows in the transitional zone. In fact, when the noise vanishes the agreement is almost perfect as shown for the forward problem (see Fig. 9). For the current case $n = 5000$ samples are used for the MCMC approach which is enough to guarantee the convergence. For the estimation of the steady state, the *Geweke's* [13] test has been used. This consists in splitting the samples in three parts. The first 20% of them represent the "burn-in" period which groups the number of samples necessary to assess the random walk of the MCMC method towards the exact solution. This first percentage is not considered in the final solution. The reamaining samples correspond to the 60% and the 20% of the total. The *Geweke's* test says that convergence is achieved if the mean of both distributions is approximately the same. In our case, with $n = 5000$ samples the variation on the mean μ_F is 0.1% while the variation on the variance σ_F is 3% between the last two groups of samples.

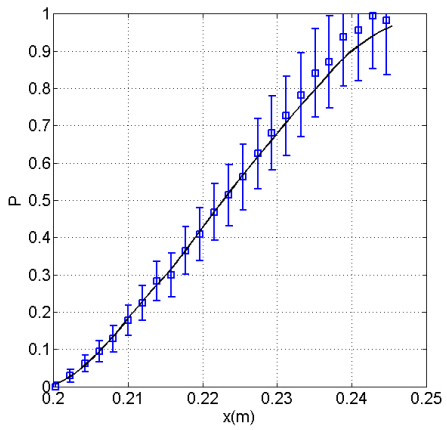

Figure 13: Intermittency as a function of the streamwise location. Comparison of the experimental data with respect to the probability of transition obtained from MCMC.

5. Conclusions

Deterministic tools and a probabilistic approach have been combined to predict laminar to turbulent transition in high speed flows. The method has been applied to experimental data available at the VKI for laminar transition studies on a cone model. Applications have been presented in terms of the *forward problem* and of the *inverse problem*.

In the *forward problem*, we assumed a distribution for the input uncertainties and, using the e^N transition prediction method, we retrieved the probability of transition or intermittency curve γ. The comparison with experimental data at different Reynolds number has demonstrated the validity of the approach for high speed flows. It should therefore be possible to use the intermittency distributions in order to improve existing transitional models. In fact, in the present case, only the Reynolds number was varied between the different cases but other parameters can vary as well, for example the Mach number. A database of intermittency distribution can be built for different conditions and used to predict transition in numerical simulations. The idea is to use the database validated through comparison with experiments to extrapolate the transition onset in different conditions. In particular, the integration of this approach into existing transitional model for RANS simulations, will be studied in future works.

On the other hand, the *inverse problem* allows to infer disturbance spectra at a location upstream of the transition onset using measured intermittency curves. In the *forward problem*, intermittency curves are computed for a given disturbance spectrum by using LST.

The inverse method applies a statistical analysis based on the MCMC method and it has been illustrated using one of the experimentally measured data in the VKI-H3 facility.
For the test case, good agreement was found between the given noisy intermittency curve and the curve resulting from inferred spectra. This suggests that the forward model is able to represent the intermittency curve sufficiently well.
These data will be processed and then used in future works for a better comparison with the results of the inverse analysis. Results could be also improved by using a higher-fidelity forward model since LST lacks in capturing the later stage of the transition process. Moreover, the present method relies on a number of assumptions, including the shape of the pdf for the frequency, as well as the kind and number of parameters that are inferred. The effect of these assumptions should carefully be assessed in future works.

6. Acknowledgement

This research has been financed by the **FRIA-FNRS 2012 fellowship**, annual fellowship of the *Fonds de la Recherche Scientifique* (F.R.S.) for doctoral students.
Results presented in the article has been obtained during the **CTR-Summer Program** 2012 at Stanford University (CA). The author would like to thank Dr. Olaf Marxen, Prof. Gianluca Iaccarino, Dr. Catherine Gorle and Dr. Paul Constantine for their fundamental contribution.

References

[1] Anderson J. D., *Hypersonic and High Temperature Gas Dynamics*, AIAA 1986.
[2] Arnal D., *Laminar Turbulent Transition Problem in Supersonic and Hypersonic Flows*, ONERA.
[3] Arnal D.,*Special Course on Progress in Transition Modeling*, AGARD report 793, 1993.
[4] Beckwith E., Creel T., Chen Fang-Jenq, Kendall J., *Free-Stream Noise and Transition Measurements on a Cone in a Mach 3.5 Pilot Low-Disturbance Tunnel*, NASA Technical Paper 2180, September 1983.
[5] Berlin S., *Oblique Waves in Boundary Layer Transition*, Doctoral Thesis, Stockholm, 1998.
[6] Bertin J., Cummings R. M., *Fifty years of hypersonic:where we've been and where we're going*, Departments of Aeronautics, United States Air Force Academy, USAF Academy, CO 80840, USA.
[7] Chang, C.L. & Malik, M. R. *Oblique-mode breakdown and secondary instability in a supersonic boundary layers using nonlinear PSE*, Instability, Transition and Turbulence, Hussaini, M. Y., Kumar, A. & Streett, C. L., editors, pp. 231-241. Springer-Verlag, 1992.
[8] Chang, C.-L. & Malik, M. R. *Oblique-mode breakdown and secondary instability in supersonic boundary layer*, J. Fluid Mech. 273, pp. 323-360, 1994.
[9] Constantine P., *Lectures on Uncertainty Quantification, ME470*, Stanford University, May 2012.
[10] Dilley A.D.,*Evaluation of CFD turbulent heating prediction techniques and comparison wit hypersonic experimental data*, NASA/CR-2001-210837.
[11] Fei Li, Choudhari M., Chang C.L., Kimmel R. and Adamczak D., *Hypersonic Transition Analysis for HIFiRE Experiments*, Hypersonic Laminar-Turbulent Transition Meeting, San Diego, California, April 16-19, 2012.
[12] Ferrier M., *Analyse de la stabilité et prévision de la transition laminaire-turbulent de l'ecoulement proche paroi sur l'avantcorps d'un véhicule hypersonique*, PhD Thesis in Fluid Mechanics, Université d' Orléans, 2008.
[13] Geweke, J., *Evaluating the Accuracy of Sampling-Based Approaches to the Calculation of Posterior Moments*, Bayesian Statistics 4, Oxford: Oxford University Press, 169-193, 1992
[14] Gorle C., Emory M. and Iaccarino G., *Epistemic uncertainty quantification of RANS modeling for an underexpanded jet in a supersonic cross flow*, Center for Turbulence Research Annual Research Briefs 2011.
[15] W.K. Hastings, *Monte Carlo sampling methods using Markov chains and their applications*, Biometrika 57, 97109, 1970.
[16] Horvath T.J., Berry S.A., Hollis B.R., Chang C.L. and Singer B.A., *Boundary layer transition on slender cones in conventional and low disturbance Mach 6 wind tunnels*, NASA Langley Research Center, AIAA 2002-2743.
[17] Kendall J.M., *An experimental investigation of leading edge shock wave-boundary layer interaction at hypersonic speeds*, PhD thesis, California Institute of Technology, 1956.
[18] Iaccarino G., Eldred M., Doostan A., Ghattas O., *Introduction to Uncertainty Quantification*,SIAM CSE Conference, Miami, FL, 2009.
[19] Iaccarino G., Pettersson P., Nordstr J. & Witteveen J., *Numerical methods for uncertainty propagation in high speed flows*,V European Conference on Computational Fluid Dynamics, ECCOMAS CFD 2011, Lisbon, Portugal, 14-17 June 2010.
[20] Lees, L., *The Stability of the Laminar Boundary Layer in a Compressible Fluid*, NACA Report No. 876, 1947.
[21] Loeven G.J.A., Witteveen J.A.S. & Bijl H., *Probabilistic Collocation: An Efficient Non-Intrusive Approach For Arbitrarily Distributed Parametric Uncertainties*, AIAA 2007-317, 45th AIAA Aerospace Sciences Meeting and Exhibit, January 2007, Reno, Nevada.
[22] Mack L. M., *Boundary layer stability theory*, 1969, JPL, Report 900-277.
[23] Mack, L. M., *Linear Stability Theory and the Problem of Supersonic Boundary-Layer Transition*, AIAA Journal., Vol. 13, No.3, pp 278-289, March 1975.
[24] Mack, L. M., *Boundary Layer Linear Stability Theory*, AGARD Report No.70g, June 1984.
[25] Malik M. R., *Instability and transition in supersonic boundary layers*, Energy Sources Technology Conference, New Orleans, LA, February 1984.
[26] Masutti D., *Natural and induced transition on a 7° half-cone at Mach 6*, Proceedings of the 2012 VKI PhD. Symposium, von Karman Institute for Fluid Dynamics, 2012.
[27] Marxen O., Iaccarino G. & Shaqfeh E., *Boundary-layer transition via spatially growing oblique waves*, under consideration for publication in Journal of Fluid Mechanics, 2011.
[28] Mayer C., Von Terzi D. & Fasel H., *Direct numerical simulation of complete transition to turbulence via oblique break-*

down at Mach 3, J. Fluid Mech., 2011.

[29] McDaniel, R.D., Nance, R.P. and Hassan, H.A, (2000), *Transition Onset Prediction for High-Speed Flow* , Journal of Spacecraft and Rockets, Vol. 37, No. 3, May-June, 2000.

[30] Narasimha R.,*On the distribution of intermittency in the transition region of a boundary layer*, Journal of Aeronautical Science, vol. 24, pp. 711-712, 1957.

[31] Pecnik R., Witteveen J. & Iaccarino G., *Uncertainty quantification for laminar-turbulent transition prediction in RANS turbomachinery applications*, 49th AIAA Aerospace Sciences Meeting including the New Horizons Forum and Aerospace Exposition, Orlando, Florida, AIAA 2011-660.

[32] Pinna F., *Numerical study of stability of flows from low to high Mach number*, PhD Thesis, von Karman Institute for Fluid Dynamics and Universitá di Roma 'La Sapienza', 2012.

[33] Reshotko E., *Transition Prediction: Supersonic and Hypersonic Flows*, RTO-EN-AVT-151.

[34] Sankaran S. & Marsden A. L., *A Stochastic Collocation Method for Uncertainty Quantification and Propagation in Cardiovascular Simulations*, Journal of Biomechanical Engineering, March 2011, Vol. 133.

[35] H. Schlichting, *Boundary Layer Theory*, Springer,1955.

[36] Schneider S.P., *Hypersonic Laminar-Turbulent Transition on Circular Cones and Scramjet Forebodies*, Progress in Aerospace Sciences, Vol. 40, pp. 1-50, 2004.

[37] Schneider S.P., *Flight Data for Boundary-Layer Transition at Hypersonic and Supersonic Speeds*, Journal of Spacecraft and Rockets, Vol. 36, No. 1, January-February 1999.

[38] Robarge T.W. and Schneider S.P., *Laminar Boundary-Layer Instabilities on Hypersonic Cones: Computations for Benchmark Experiments*, AIAA Paper 2005-5024, 35th Fluid Dynamics Conference, Toronto, June 2005.

[39] Serino G., Marxen O., Pinna F., Rambaud P. & Magin T., *Transition prediction for oblique breakdown in supersonic boundary layers with uncertain disturbance spectrum*, AIAA 20122973 pp. 111, 2012.

[40] Stetson K.F., *Hypersonic Boundary layer Transition*, Advances in hypersonic, 1992.

[41] Stetson K.F. and G. H. Rushton, *Shock tunnel investigation of boundary-layer transition at Mach 5.5*, AIAA Journal, May 1967.

[42] Tarantola A., *Inverse problem theory and methods for model parameters estimation*, Siam, 1987.

[43] Tumin A., Wang X. and Zhong X., *Direct numerical simulation and the theory of receptivity in a hypersonic boundary layer*, Physics of fluids, vol. 19, 2007.

[44] van Ingen J.L., *The eN method for transition prediction : Historical review of work at TU Delft*, 38th Fluid Dynamics Conference and Exhibit, 23 - 26 June 2008, Seattle, Washington.

Physico-Chemical Models for Rarefied Gas-Kinetic Simulations with Application to Atmospheric Entry Flows

Erik Torres

Aeronautics and Aerospace Department, von Karman Institute for Fluid Dynamics, Belgium, erik.torres@vki.ac.be

Supervisor: Thierry Magin

Associate Professor, Aeronautics and Aerospace Department, von Karman Institute for Fluid Dynamics, Belgium, thierry.magin@vki.ac.be

University Supervisor: Stefanos Fasoulas

Professor, Institute for Space Systems, University of Stuttgart, fasoulas@irs.uni-stuttgart.de

Abstract

The present research deals with physical and chemical modeling applicable to the numerical simulation of rarefied gas flows. The main application is the simulation of hypersonic flows around atmospheric entry vehicles at high altitudes by means of the direct simulation Monte Carlo (DSMC) method. Specific areas of interest include the high-fidelity modeling of internal energy exchange and chemical reaction processes occurring in the bulk gas during its compression and heating in the bow shock region in front of the vehicle.

As a first step towards a state-to-state approach, a statistical model originally developed for electronic-translational energy transfer in atoms having multiple electronic states (Anderson et al, RGD15, 1986) was applied to the study of internal energy exchange in a polyatomic gas. The model seems to be well-suited for gas kinetic simulations, because it provides an explicit expression for the transition probabilities between internal energy levels. All molecules possessing a given internal energy level are treated as a separate chemical species and all collisions involving exchange of internal energy thus become pseudo-chemical reactions. Post-collision energy levels of the two partners are determined by conserving the total energy of the collision pair and taking into account detailed balance. In the present work, DSMC simulations of relaxation in a stationary gas are performed and compared to those obtained by Anderson et al. Additionally, we apply the model to the simulation of rotational relaxation behind a normal shock wave.

Keywords: rarefied gas dynamics, RGD, reentry, hypersonics, direct simulation Monte Carlo, DSMC, non-equilibrium phenomena

1. Introduction

Modeling flow around hypersonic flight vehicles, e.g. reentry capsules, is a challenging task due to the series of complex coupled physical phenomena occurring in the gas. At high flight Mach numbers, severe compression of the flow through the bow shock causes the gas temperature to increase several thousand kelvins above its free-stream value. Molecular species become vibrationally excited and, at high enough temperatures, a fraction of the molecules dissociates. The atomic species may then recombine in the boundary layer around the vehicle releasing heat in the process. These thermochemical processes have a noticeable effect on the flow field and on the interaction with the vehicle's surface. Thus, accurate prediction of the heat flux and the chemical composition at the vehicle surface require that they all be taken into account in the fluid dynamics modeling.

The most widespread numerical method currently in use for transitional / rarefied flows is the direct simulation Monte Carlo (DSMC) method, originally developed by Bird [1]. The traditional approach to internal energy exchange in DSMC has been the phenomenological Larsen-Borgnakke (LB) [2] model. Over the years, the model has been enhanced by

adding temperature-dependent collision numbers for rotational [3] and vibrational exchange [4]. The conventional way of treating chemical reacting flows within DSMC has come to be known as the Total Collision Energy (TCE) method [5; 6; 7]. In this approach reaction probabilities for individual collisions are derived from macroscopic reaction rates. These rates are usually based on experiments performed at equilibrium. The use of the resulting reaction probabilities is therefore questionable in the case of highly nonequilibrium flows. In the early Larsen-Borgnakke model, the internal energy was considered to be continuously distributed for all internal modes. In order to take into account the quantum nature of internal energy, a discretized versions was introduced by Boyd and Bergemann for vibrational exchange [8]. Building on the quantized LB method, Bird more recently proposed the Quantum Kinetic (QK) model for chemical reactions [9; 10].

A somewhat different approach was taken by Tokumasu and Matsumoto [11] and Koura [12]. Unlike in the Larsen-Borgnakke model, where post-collision energies are sampled from an equilibrium distribution, their model uses a probability density function obtained by means of classical trajectory calculations (CTC). A key assumption in this model is that the internal energy is continuously distributed and the collision mechanics are purely classical. Thus, it disregards the quantum nature of internal energy exchange (especially important for the vibrational levels) and consequently their model is limited in applicability to rotational energy exchange at moderate temperatures.

With increasing computational power, using the state-to-state approach in DSMC has become feasible for realistic gas models (e.g. Boyd and Josyula [13] and Sohn and Levin [14]). In this framework, each internal energy level of a given component is itself considered a pseudo-species of the mixture. Transitions between levels are then treated in a manner analogous to chemical reactions. For the particular case of nitrogen (molecular + atomic) four elementary reactions are of particular interest:

$$\text{excitation/de} - \text{excitation}:$$

$$N_2{}^i + N_2{}^j \rightleftharpoons N_2{}^k + N_2{}^l, \tag{1}$$

$$N_2{}^i + N \rightleftharpoons N_2{}^k + N, \tag{2}$$

$$\text{dissociation}:$$

$$N_2{}^i + N_2{}^j \rightleftharpoons N + N + N_2{}^l, \tag{3}$$

$$N_2{}^i + N \rightleftharpoons N + N + N. \tag{4}$$

The indices $(i, j, k, l = 0, 1, \ldots, N_{\max})$ stand for the rovibrational quantum states of the nitrogen molecule. In DSMC "reaction cross sections" are required for all possible combinations of these indices. Since the nitrogen molecule possess almost 10000 rovibrational energy levels (considering only the electronic ground state), an enormous number of cross sections need to be known before applying the state-to-state approach. At present this information is not readily available for the full nitrogen system, but rigorous state-to-state calculations applied to the N_2 + N system have recently been presented by Kim and Boyd [15]. The cross sections used in their work are based on the abinitio quasi classical trajectory calculations (QCT) of Jaffe et al [16].

This paper is organized as follows. In section 2 we introduce a simplified model cross-section due to Anderson et al. [17]. We present some details on the implementation of this model and the results obtained using our DSMC code. In section 3 we show another state-specific model, which is based on rate coefficients extracted from the NASA N3 database. As this is ongoing work, we give some preliminary conclusions and suggest ways to correct failings in the current implementation.

2. Model cross section of Anderson

As a first step in our own development of a state-to-state DSMC model, we consider only molecule-molecule collisions (i.e. reactions like equation (1)). The effort to develop a QCT database for this type of collisions is ongoing [18] and for the moment we resort to a very simplified reaction cross section proposed by Anderson [17]. This model has been chosen purely for convenience, since the cross section is computed explicitly from an analytical expression. In future work, we intend to replace this model cross section with more realistic data coming from quantum

chemistry. For the current implementation of the Anderson model we will restrict ourselves to a single-species gas with discrete internal energy levels, labeled $i = 0, 1, \ldots, N_{\max}$. Each particle in a given level carries with it an amount of internal energy equal to ϵ_i. During collisions, transitions between these levels may take place, but dissociation and recombination reactions are not considered here. Thus, all collisions may be expressed generically as:

$$X_i + X_j \rightarrow X_k + X_l, \qquad i, j, k, l \in 0, \ldots, N_{\max}. \quad (5)$$

The indices i, j identify the pre-collision- and k, l the respective post-collision energy levels of both partners. Anderson et al [17] proposed a model cross section for this type of transition with the simple form:

$$\sigma_{ij}^{kl} = \sigma_0 \cdot P_{ij}^{kl}. \quad (6)$$

The factor $\sigma_0 = \pi d_0^2$ represents the hard sphere cross section, while the expression for the transition probability P_{ij}^{kl} is given by:

$$P_{ij}^{kl} = \frac{g_k\, g_l\, (\epsilon_c - \epsilon_k - \epsilon_l)}{\sum_{m,n} g_m\, g_n\, (\epsilon_c - \epsilon_m - \epsilon_n)^+}. \quad (7)$$

The collision energy ϵ_c is the sum of the pre-collision relative translational energy $\epsilon_T = \frac{m_r}{2} c_r^2$ and internal energies of the two particles, $\epsilon_i + \epsilon_j$. This quantity is conserved over the course of the collision and re-assigned between the two partners depending on the chosen post-collision internal energies ϵ_k, ϵ_l. The remainder is equal to the post-collision translational energy ϵ'_T. If the collision energy is small, the numerator of the ratio in equation (7) may become negative for certain combinations of post-collision internal energies. This would mean that the energy available is insufficient for achieving this combination of post-collision states. Such transitions are forbidden and the probability P_{ij}^{kl} is set to zero. On the other hand, the denominator is a double sum over all $N + 1$ possible levels for both collision partners. The notation $(\cdot)^+$ indicates that only positive contributions to the sum are taken into account. This ensures that the denominator does not become negative and that the transition probability can not become greater than 1.

At a given equilibrium temperature T, the macroscopic rate of transition between states $(i, j) \rightarrow (k, l)$ is given by:

$$r_{ij}^{kl}(T) = n_i\, n_j\, (\pi\, m_r)^{-1/2}\, (2/k_{\mathrm{B}}T)^{3/2} \times \times \int_0^\infty \sigma_{ij}^{kl}(\epsilon_T)\, \epsilon_T \exp\left\{-\frac{\epsilon_T}{k_{\mathrm{B}}T}\right\} d\epsilon_T. \quad (8)$$

The forward and backward equilibrium rates for each transition balance each other out, so one can set $r_{ij}^{kl} = r_{kl}^{ij}$. After substituting expressions (6) and (7) for both rates and integrating over the translational energy, one obtains the equilibrium populations of internal levels in accordance with statistical thermodynamics:

$$\frac{n_k\, n_l}{n_i\, n_j} = \frac{g_k\, g_l}{g_i\, g_j} \exp\left\{-\frac{(\epsilon_k + \epsilon_l) - \left(\epsilon_i + \epsilon_j\right)}{k_{\mathrm{B}}\, T}\right\}. \quad (9)$$

2.1. Anderson model: DSMC Implementation

We use the NTC scheme of Bird [19] for establishing the number of collisions per time step in each cell. Since we are modeling the gas as a collection of identical hard spheres, we take the total collision cross section as $\sigma_T = \sigma_0$. For each collision pair the post-collision quantum numbers k, l are determined from within the range of integers $[0, N_{\max}]$ by means of an acceptance-rejection algorithm. The post-collision states are accepted with the probability P_{ij}^{kl} of equation (7). Next, the post-collision translational energy is determined: $\epsilon'_T = \epsilon_c - \epsilon_k - \epsilon_l$. Note, that it is possible for k, l to be equal to i, j. In this case, we are dealing with an elastic collision and the translational energy remains unchanged: $\epsilon_T = \epsilon'_T$. In the final step, post-collision velocity components of the two product particles are computed as a result of a hypothetical elastic collision in which the updated translational energy ϵ'_T is conserved.

Anderson et al introduced an additional parameter, which they called the reaction probability P_r. This parameter is used to specify the fraction of collisions per time step that are treated according to their model (i.e. where the Anderson transition probability is used to determine the post-collision states k, l). The remaining collisions, i.e. the fraction $1 - P_r$, will be handled as elastic collisions without any modification to the internal quantum numbers of the particles. When $P_r = 1$, we apply the Anderson probability to all pairs (just as before), whereas if $P_r = 0$, we make no changes to the internal states of the particles and treat all collisions as elastic ones. In this manner, the rate of internal energy exchange can be manually adjusted.

2.2. Verification of Anderson's Model

In order to verify the implementation of the model cross section, one of the test cases reported in Anderson's original publication [17] was used as reference. DSMC is used to simulate the unsteady adiabatic relaxation of a spatially uniform gas. The level energies used are given in Table 1. Only 5 levels (including the ground state) are considered and a constant energy difference, equivalent to 5 kJ / mol, has been used. It should be made clear that these levels do not represent any real gas and only serve to test the implementation.

Table 1: Internal energies and degeneracies used by Anderson

level i	g_i	$\epsilon_i \times 10^{21}$ [J]
0	1	0
1	1	8.3
2	1	16.6
3	1	24.9
4	1	33.2

A single DSMC cell was used for this 0-D problem. Since there is no exchange of mass and energy with the surroundings, the particle motion step in the DSMC routines was disabled and a constant number of particles $N_p \approx 1.0 \times 10^7$ was used. The cell volume considered was $V_{\text{cell}} = 0.001\,\text{m}^{-3}$ and the total density $\rho = 1.0\,\text{kg} \cdot \text{m}^{-3}$. With a molecular mass of $m = 6.63 \times 10^{-26}\,\text{kg}$ and a hard sphere diameter of $3.00 \times 10^{-10}\,\text{m}$, the mean collision frequency at $T = 1000\,\text{K}$ is estimated to be $\nu_0 \approx 4.40 \times 10^9 \text{s}^{-1}$. Therefore, in order to remain well below the mean collision time for the duration of the simulation, the time step was kept constant at $\Delta t = 1.0 \times 10^{-11} s$. The computations were run for up to 500 steps and samples of the level populations and temperatures were taken at each time step. Based on the level populations, an energy-based internal temperature was computed for the gas.

In the first situation studied (Anderson: Case A), the initial temperature of the translational mode is $T_t = 1000\,\text{K}$, while the initial population for the levels is determined from the Boltzmann distribution at the initial internal temperature $T_{\text{int}} = 100\,\text{K}$. Since energy is conserved over all collisions in the cell, the final equilibrium temperature of the heat bath is $T = 723.5\,\text{K}$ at the corresponding Boltzmann distribution. The results for case A are shown in Figure 1. The image on the left-hand side shows the evolution of the overall translational and internal temperatures over the course of time. The cell collision number N_C used here as the abscissa is defined by Anderson as the cumulative number of collisions in the cell divided by twice the number of particles in the cell. Since the number of particles remains constant over time, N_C may be considered as an equivalent time scale. On the right-hand side we plot the level populations, which are used to determine the internal temperature at each time step. One may observe that at the early stages of the process, the overwhelming majority of particles populate the lowest energy level (i.e. the ground state). Over the course of many collisions, some of the translational energy is gradually transferred to internal energy, increasing the populations of the higher excited states. For both plots a direct comparison with Anderson's results is possible and the agreement is seen to be very good.

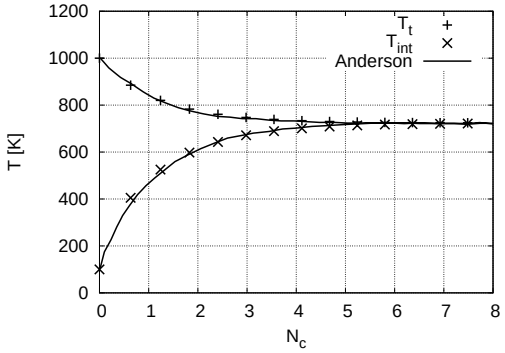

(a) Mixture translational and internal temperatures

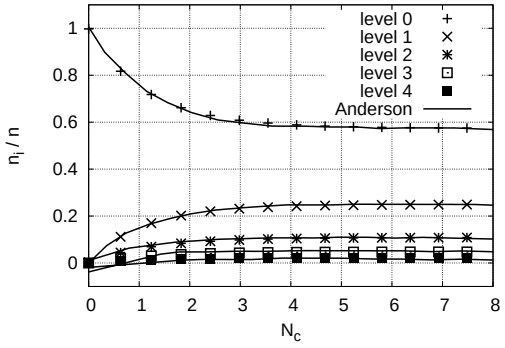

(b) Internal level populations

Figure 1: (Anderson: Case A) Solid lines: data extracted from Anderson [17], symbols: current results.

In the next case shown (originally labeled Case C by Anderson), the initial translational temperature of the heat bath is set equal to 100 K. All particles initially populate only the highest excited state (i.e. $n_4/n = 1$). This strong departure from equilibrium makes it difficult to obtain a meaningful value for the

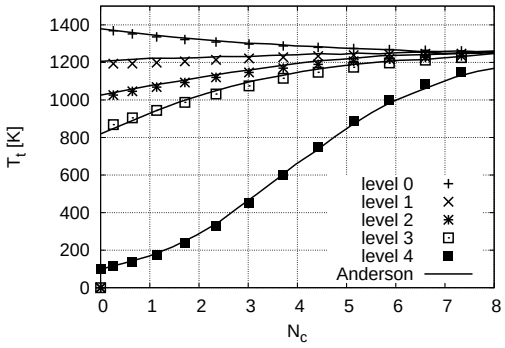

(a) Level translational temperatures

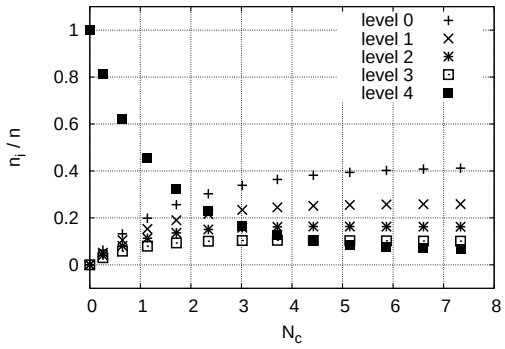

(b) Internal level populations

Figure 2: (Anderson: Case C) Solid lines: data extracted from Anderson [17], symbols: current results.

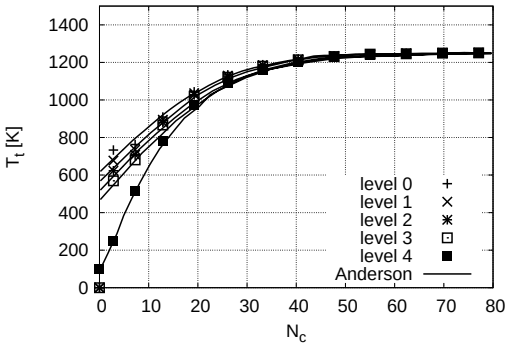

(a) Level translational temperatures

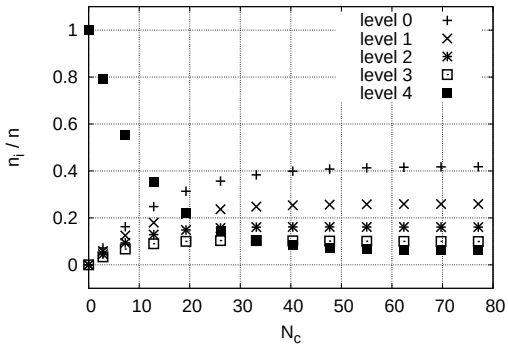

(b) Internal level populations

Figure 3: (Anderson: Case D) Solid lines: data extracted from Anderson [17], symbols: current results.

internal temperature at the early stages of the simulation. Thus, in Figure 2 (a) the translational temperature for the particles of each internal level is plotted instead. It can be seen that the translational temperatures of the sparsely populated levels 0 - 3 almost immediately jump to values above 800 K, with the initial temperature of the ground state being higher than that of the final equilibrium temperature of 1253 K.

The initial conditions for case D are identical to those of case C, therefore the final equilibrium temperature and level populations also remain the same. However, for case D the "reaction probability" (as discussed in the previous section) has been set to $P_r = 0.1$. This modification reduces the fraction of collisions computed by means of the Anderson cross section to 10 % of the total, effectively lowering the rate of energy redistribution among internal levels (i.e. relaxation) and, as can be seen in Figure 3, increasing the time needed to reach equilibrium by a factor of 10 approximately. The remaining 90 % of collisions are treated as fully elastic, bringing about no change in level populations, but instead promoting thermalization in each of the internal energy levels.

2.3. Application of Anderson's model to a Diatomic Gas

In the previous section we demonstrated the match between our results and those of Anderson et al. Now we move on to a case more closely related to our field of interest. With the current implementation of Anderson's cross section, we are restricted to excitation / de-excitation processes between particles of a single-species molecular gas (see introduction, equation (1)). Collisions between molecular and atomic nitrogen (equation (2)), as well as dissociation of molecular nitrogen (equations (3) and (4)) are neglected in this work. We limit ourselves to moderate temperatures (up to 1000 K) and will therefore remain well below the characteristic vibrational temperature of nitrogen ($\theta_v = 3392$ K). This means that practically all molecules will populate the vibrational ground state.

The rigid rotor approximation is used for the internal energy levels, the energy of level J is given by:

$$\epsilon_J = J\ (J+1)\ k_\mathrm{B}\,\theta_r, \qquad J = 0, 1, 2, \ldots \tag{10}$$

with k_B, the Boltzmann constant and $\theta_r = 2.88\,\mathrm{K}$, the characteristic rotational temperature of nitrogen. For a homonuclear molecule (i.e. consisting of two identical atoms) such as N_2, the level degeneracies are obtained by the expression:

$$g_J = (2J+1)\, g_J^\mathrm{NS},$$

$$g_J^\mathrm{NS} = \begin{cases} 6 & \text{if} \quad J \quad \text{even}, \\ 3 & \text{if} \quad J \quad \text{odd}. \end{cases} \tag{11}$$

It was decided to only take into account 51 rotational levels (i.e. $J = 0, \ldots, 50$), because at the temperatures considered here the higher lying rotational levels are not appreciably populated. We first simulate the adiabatic relaxation of molecular nitrogen in a single DSMC cell. We use the molecular mass and reference diameter for N_2 given by Bird [1]. However, since Anderson's reaction cross section has so far only been derived for hard sphere molecules, we keep the VHS parameter at $\omega = 0.5$. All particle velocities are initialized at a Maxwell distribution corresponding to a translational temperature of 800 K. The rotational levels are populated at a Boltzmann distribution with an initial rotational temperature of 300 K. The same values for time step, cell volume and overall mass density as in the previous test cases were used. However, the total number of particles in the cell was reduced to $N_p \approx 1.42 \times 10^6$.

Figure 4 (a) shows the time evolution of the translational and rotational temperatures towards the equilibrium value of 600 K. Two sets of curves are plotted. The first one, marked $P_r = 1.0$, corresponds to the case when all collisions are computed using the Anderson cross section. The other set of curves ($P_r = 0.1$) shows the case when only 10 % of all collisions are treated this way, with the remaining 90 % being fully elastic collisions. As in the test cases C and D of the previous subsection, one can see that this increases the time needed to reach equilibrium by an order of magnitude. On the right-hand side, in Figure 4 (b), we plot the rotational populations extracted from the DSMC simulation at several time steps for $P_r = 0.1$. The initial (t = 0) and final (t = 1.0×10^{-8}) populations do in fact correspond to Boltzmann distributions at 300 and 600 K respectively. For the other time steps shown, the distributions are non-Boltzmann.

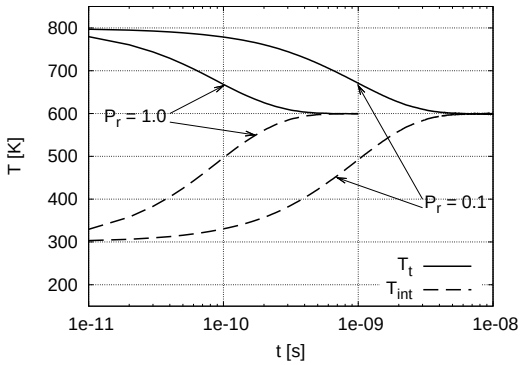

(a) Time evolution of translational and rotational temperatures for $P_r = 1$ and $P_r = 0.1$

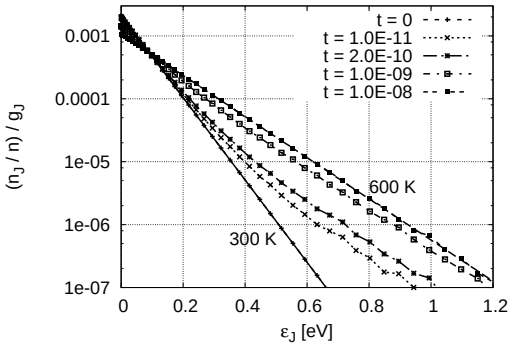

(b) Internal energy distributions for $P_r = 0.1$. The fractional populations of the rotational levels n_J/n, divided by the degeneracy of the level g_J vs. rotational level energy ϵ_J

Figure 4: Simulation of rotational relaxation of N_2 in adiabatic heat bath using the rigid rotor approximation. The rate of relaxation towards equilibrium is manually controlled by the value of the reaction probability P_r.

We now move on to simulating a normal shock wave in molecular nitrogen. The problem is treated as a one-dimensional steady flow in the frame of reference of the shock. The 1D flow domain is enclosed by a pair of stream boundaries located at $x_\mathrm{L} = -0.05\,\mathrm{m}$ and $x_\mathrm{R} = 0.05\,\mathrm{m}$ respectively. During each time step, newly created particles at the pre- and post-shock Maxwell-Boltzmann distributions are injected at the boundaries according to the macroscopic flow conditions given in Table 2.

The domain was divided into 1000 equally spaced collision cells and the time step was set to 2.0×10^{-10} s. The ratio of real to simulated particles was set to $F_N = 8.05 \times 10^{14}$, which results in an average number of particles per cell of 200 in the undisturbed super-

Table 2: Pre- and post- shock equilibrium conditions resulting from the Rankine-Hugoniot relations

	pre	post
M	1.71	0.638
T [K]	300	439.66
u [m / s]	603.86	272.74
ρ [kg / m^3]	7.486×10^{-4}	1.657×10^{-4}
λ_0 [m]	8.04×10^{-3}	3.63×10^{-4}

sonic flow and increases to approximately 440 particles per cell in the subsonic flow behind the shock. At steady state the total number of particles in the simulation stabilizes around 320000. As an initial condition, particles are generated according to the pre- and post-shock equilibrium conditions, where the discontinuity is located at $x = 0$. During a transient phase of approximately 5000 time steps the shock profile builds up around the initial discontinuity. Subsequently the macroscopic flow variables were sampled every 5 time steps and averaged over a total of 10000 samples.

The results for three different simulations are shown in Figure 5. On the left-hand side (Subfigure (a)) we plot overall density and on the right-hand side (Subfigure (b)) the corresponding temperature profiles. Just as for the heat bath simulations shown before, two different values for the reaction probability ($P_r = 1$ and $P_r = 0.1$) were considered. For comparison we also plot the result with the Larsen-Borgnakke model when using a constant rotational collision number of $Z_r^C = 10$. One can observe that for $P_r = 1$ the density profile is practically symmetric about the origin, while for $P_r = 0.1$ this is no longer the case. The density rise for $P_r = 0.1$ is not as steep as for $P_r = 1$, especially after reaching the center of the shock. The Larsen-Borgnakke profile lies in between these two curves. Differences are also noticeable in Figure 5 (b). For $P_r = 1$, the internal (i.e. rotational) temperature follows closely behind the translational temperature across the shock. The expected lag of the rotational temperature and the overshoot of the translational temperature above the post-shock equilibrium value are both absent in this case. It seems that the expression for Anderson's transition probability (i.e. equation (7)) was derived with the only purpose of fulfilling micro-reversibility. This ensures that the internal level populations obtained from a simulation will match the ones expected from statistical thermodynamics at a given equilibrium temperature. However, the expression does not provide accurate transition rates for processes away from equilibrium. The temperature profiles show a different behavior when we set $P_r = 0.1$. The translational temperature shows the expected overshoot and the rotational temperature exhibits the characteristic relaxation behavior (similar to the Larsen-Borgnakke results). Since in this case we are effectively increasing the proportion of elastic to inelastic collisions, the overall rates for internal energy exchange are reduced and the gas molecules require more collisions to reach the post-shock equilibrium.

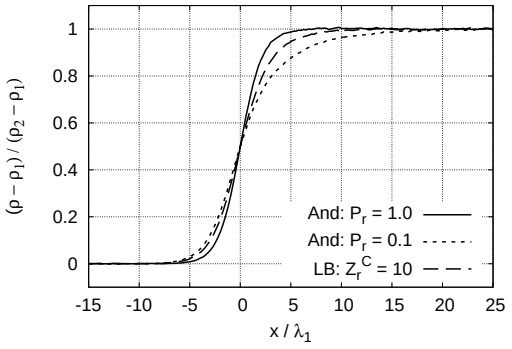

(a) Normalized density profiles. Solid line: Anderson model with reaction probability $P_r = 1$, dashed line: profile for Anderson model with $P_r = 0.1$. Long dashed line: profile for Larsen-Borgnakke model with constant $Z_r^C = 10$.

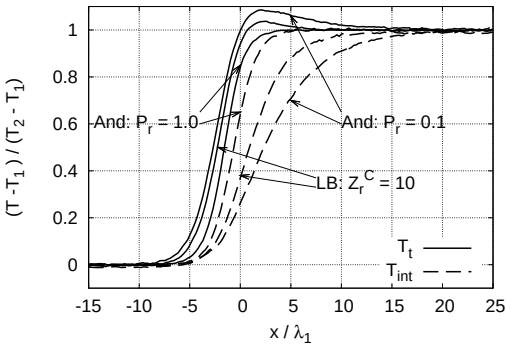

(b) Translational and rotational temperatures. Solid lines: Translational temperatures, long dashed lines: rotational temperatures, (And: Anderson model, LB: Larsen-Borgnakke model)

Figure 5: Density and temperature profiles for the Mach 1.71 shock wave. Results are shown for the state-to-state model Anderson cross section with both $P_r = 1$ and $P_r = 0.1$. The Larsen-Borgnakke result for $Z_r^C = 10$ is also shown for comparison. ($Z_r^C = \nu \tau_r$)

2.4. Anderson model, concluding remarks

A basic state-to-state model for internal energy exchange in DSMC has been applied to simulating rotational relaxation of a rigid rotor gas behind a normal shock wave. The results show that the correct pre- and post-shock equilibrium states are obtained. Josyula et al [20] have recently used the Anderson model [17] within a deterministic Boltzmann solver to study shock waves. In the future we plan to compare our calculations with their results. The Anderson cross section is based on a simple model which could be extended for the inclusion of more complex elementary processes. Some work on dissociation / recombination reactions has already been reported by Dunn and Anderson [21]. With the model cross section used in this work, the rate of internal energy exchange is affected by the value of the reaction probability P_r. This probability serves as a "tuning" parameter to increase the ratio of elastic to inelastic collisions. It was found that values of $P_r \approx 0.1$ are needed to approximately obtain the physically expected behavior (i.e. similar to Larsen-Borgnakke with $Z_r^C = 10$). The fact that the reaction probability P_r has to be set manually introduces some arbitrariness to the model. It can therefore not be expected to provide a physically accurate description of finite rate processes in a real nitrogen mixture without some ad hoc adjustments. It is no substitute to cross section data based on ab initio QCT calculations (e.g. NASA ARC [16] or CNR Bari [22]). Rate coefficients derived from this database have been used by Munafo et al [23] to study thermochemical nonequilibrium behind shocks using continuum CFD. An interesting aspect of this paper is the proposed coarse-grain model which is obtained by lumping together rovibrational energy states into so-called energy bins. Such a model would also be of interest for future implementation in DSMC due to its reduced computational cost. In the next section we show our current implementation of such a rovibrational bin model within the DSMC code. Some preliminary results are shown as well. However, this work is still at an early stage and many aspects of the implementation have not yet been resolved at this time.

3. Implementation of the QCT-based rovibrational bin model in DSMC

In this section we discuss our current implementation of the rovibrational bin model in DSMC. We limit ourselves to the study of N_2-N collisions, which at the moment are the only ones available to us from the NASA database. This means that for the moment all $N_2 - N_2$ collisions are treated as elastic collisions. The binning approach mentioned in the previous section is used in this case to reorganize the original 9390 rovibrational levels of the N_2 molecule by increasing energy and to lump these levels into a much smaller number of bins. The number of levels assigned to each bin depends on to the energy intervals considered. Each bin is assigned a base energy, equal to that of the lowest-energy level in the bin, and it is assumed that the level populations within each bin follow a Boltzmann distribution at the local translational temperature. The two types of reaction we wish to study are the excitation/de-excitation of the N_2-molecule from one bin to another due to atom impact:

$$N_2^k + N \leftrightharpoons N_2^l + N \tag{12}$$

and the dissociation of an N_2 molecule from a given bin, also due to atom impact:

$$N_2^k + N \leftrightharpoons 3\,N. \tag{13}$$

For this work we had access to a set of binned excitation rate coefficients in Arrhenius form:

$$k_{kl}^E(T) = A_{kl}^E\, T^{b_{kl}^E} \times \\ \times \exp\left(-\frac{E_{a,kl}^E}{\mathrm{k_B}\,T}\right) \qquad k < l. \tag{14}$$

And for dissociation:

$$k_k^D(T) = A_k^D\, T^{b_k^D}\, \exp\left(-\frac{E_{a,k}^D}{\mathrm{k_B}\,T}\right). \tag{15}$$

The rate coefficients for the respective backward reactions are obtained from applying detailed balance. For de-excitation:

$$k_{lk}^E(T) = k_{kl}^E(T)\,\frac{Q_k(T)}{Q_l(T)} \times \\ \times \exp\left(-\frac{E_k - E_l}{\mathrm{k_B}\,T}\right) \qquad k < l \tag{16}$$

and for recombination:

$$k_k^R(T) = k_k^D(T)\,\frac{Q_{\mathrm{N_2}}^t(T)\;Q_k(T)}{g_{\mathrm{N}}\,Q_{\mathrm{N}}^t(T)} \times \\ \times \exp\left(-\frac{E_k - 2E_{\mathrm{N}}}{\mathrm{k_B}\,T}\right) \tag{17}$$

Here, $Q_k(T)$ is the partition function including all levels of bin k:

$$Q_k(T) = \sum_i g_i \exp\left(-\frac{\Delta E_k(i)}{\mathrm{k_B}\,T}\right), \qquad (18)$$

$g_\mathrm{N} = 12$ is the degeneracy of the nitrogen atom in the electronic ground state and the translational partition functions of the N_2-molecule and the N-atom are:

$$Q^t_{\mathrm{N}_2} = \left(\frac{2\pi \mathrm{k_B} m_{\mathrm{N}_2} T}{\mathrm{h_P}^2}\right)^{3/2}, Q^t_\mathrm{N} = \left(\frac{2\pi \mathrm{k_B} m_\mathrm{N} T}{\mathrm{h_P}^2}\right)^{3/2} \qquad (19)$$

For our current work, we obtained the bin-specific reaction cross-sections from available rate coefficients. Both quantities are related to one another by expressions of the type:

$$k_{kl}(T) = (\pi m_r)^{-1/2} (2/\mathrm{k_B}T)^{3/2} \times \\ \times \int_0^\infty \sigma_{kl}(E_T)\, E_T \exp\left\{-\frac{E_T}{k_\mathrm{B}T}\right\} dE_T. \qquad (20)$$

In this case, the reaction cross-section, multiplied by the magnitude of the relative velocity of collision is multiplied with the Maxwellian velocity distribution function and integrated over the whole range of relative translational energy. Obtaining the rate coefficient from a known cross-section in this manner is a fairly straightforward operation, since the integral can always be computed numerically. The inverse operation however, is much more problematic. This is essentially an ill-posed problem, since information on the shape, i.e. the functional dependence of the cross-section on the relative translational energy can not be uniquely inferred from the value of the rate coefficient. One approach to solving this inversion problem has been to use a technique called Tikhonov regularization. Bondar er al. [24] used Tikhonov regularization to derive a dissociation cross-section from a temperature-dependent dissociation rate. Another method has been used by Minelli et al [25] to obtain dissociation cross-sections. In both cases, a reasonable cross-section can only be obtained if some prior knowledge about its shape is already available. The solutions were essentially obtained "by hand-tuning" for a small number of reactions. In the current form the methods do not seem well-suited for large-scale automatic application to extracting cross-sections for the hundreds to thousands of reactions that even a reduced bin model would require.

For the moment we have resorted to the approach outlined in chapter 6 of Bird's book [1] to obtain analytical expressions for the cross-sections. For the excitation from a bin "k" to bin "l":

$$\sigma^E_{kl} = \sigma_T \frac{\sqrt{\pi}\, A^E_{kl}}{2\,\sigma_\mathrm{ref}} \frac{\Gamma(5/2-\omega)}{\Gamma\left(5/2+b^E_{kl}\right)} \left(\frac{m_r}{2\,\mathrm{k_B}\,T_\mathrm{ref}}\right)^{1/2} \times \\ \times \frac{T_\mathrm{ref}^{1-\omega}}{\mathrm{k_B}^{b^E_{kl}+\omega-1}} \frac{\left(E_T - E^E_{a,kl}\right)^{b^E_{kl}+1/2}}{E_T^{3/2-\omega}} \qquad (k<l). \quad (21)$$

The corresponding de-excitation cross-section is computed using the Arrhenius parameters of the excitation reaction and the ratio of the bin partition functions as:

$$\sigma^E_{lk} = \sigma_T \frac{\sqrt{\pi}\, A^E_{kl}\, T^{b^E_{kl}}}{2\,\sigma_\mathrm{ref}} \left(\frac{m_r}{2\mathrm{k_B}T_\mathrm{ref}}\right)^{1/2} \times \\ \times \left(\frac{T}{T_\mathrm{ref}}\right)^{\omega-1} \frac{Q_k(T)}{Q_l(T)} \exp\left(-\frac{E^E_{a,kl}}{\mathrm{k_B}T} - \frac{E_k - E_l}{\mathrm{k_B}T}\right) \qquad (22)$$

The dissociation/recombination cross-sections are obtained in an analogous manner. In the preceding derivation, we have assumed that the total collision cross-section can be computed from the VHS potential. The main reason is mathematical convenience, because an analytical shape for the forward reaction cross-section is easily found. In the recent work of Kim [15] it has been suggested that the total collision cross-section strongly depends on the vibrational state of the colliding molecule and that it can take on values several times larger than the VHS cross-section. Therefore, the use of the VHS collision cross-section in the current work is highly questionable.

It can be seen from expression (21) that the forward reaction cross-sections are functions of the relative translational energy E_T, as would be expected. For the backward reaction however, the cross-section is independent of the relative translational energy of the collision pair and depends instead on the local translational temperature of the gas. At this moment it is not clear to us whether this apparent inconsistency in the treatment of forward and backward reactions has a detrimental effect on the implementation of the bin model.

Another issue we have so far not resolved is the inclusion of recombination reactions (see equation 13). For such a reaction to occur, a three-body collision is required, since the two recombining atoms

need a third body to remove some of the reaction energy and stabilize the newly formed molecule. In the standard DSMC routines, typically only binary collisions are considered and an extension to three-body collisions does not seem straightforward. Certainly, there have been researchers who have implemented recombination reactions in DSMC [26; 27]. However, the details of their implementations remain unclear to us and we have decided not to consider dissociation/recombination at this time.

3.1. Bin model, preliminary results

As a first step in our implementation of the DSMC bin model we have chosen to consider only excitation-de-excitation reactions. Our test case consists of a single DSMC-cell. At t = 0, about 100000 particles of N_2 and N respectively, are generated. Their initial velocities are distributed according to a Maxwellian at the initial translational temperature T. The nitrogen molecules populate a total of 10 bins according to a Boltzmann distribution at the internal temperature T_{int}:

$$\frac{n_{\text{N}_2,k}}{n_{\text{N}_2}} = \frac{Q_k(T)}{\sum_k Q_k(T) \exp\left(-\frac{E_k}{\text{k}_\text{B} T_{\text{int}}}\right)} \times \times \exp\left(-\frac{E_k}{\text{k}_\text{B} T_{\text{int}}}\right) \qquad k = 0, 1, ...9 \tag{23}$$

The total cross-section for establishing the overall collision rate is computed using the VHS model using the parameters in Table 3.

Table 3: VHS parameters for total cross-section

	$N_2 - N_2$	$N_2 - N$	$N - N$
ω_{12}	0.680	0.690	0.700
$d_{\text{ref},12}$ [m] $\times 10^{10}$	3.20	2.90	2.60
T_{ref} [K]	2880	2880	2800

In the first calculations, we have set $T = T_{\text{int}} = 30000\,\text{K}$. We consider number densities of $n_{\text{N}} = n_{\text{N}_2} = 1.43 \times 10^{25}\,\text{m}^{-3}$ at a cell volume equal to $V_{\text{cell}} = 0.001\text{m}^3$ and a constant particle weight of $w_p = 1.51 \times 10^{17}$. The time step was $\Delta t = 1.0 \times 10^{-11}$ s. Our first goal was to check whether the macroscopic rates of excitation/de-excitation, as given by the original rate coefficients, would be recovered in the DSMC calculation. To this end, we ran the simulation over a large number of time steps and recorded the time average number of excitation/de-excitation events between bins: $\overline{N_{kl}^E}$. This time average was then converted to the macroscopic rate by the expression:

$$r_{kl,\text{DSMC}}^E = \frac{w_p\,\overline{N_{kl}^E}}{V_{\text{cell}}\,\Delta t} \tag{24}$$

The theoretical excitation rate is given by:

$$r_{kl,\text{theor.}}^E = k_{kl}^E(T)\; n_{\text{N}_2,\text{k}}\, n_{\text{N}} \tag{25}$$

Figure 6(a) shows a comparison of the transition rates from the lowest bin $k = 0$ to the post-collision bins $l = 0, 1, ..9$. The solid curve represents the theoretical value as obtained directly from equation (25). The dotted line is the DSMC rate calculated from (24). The excitation/de-excitation rate coefficients provide no information on the the transition rate where $k = l = 0$ (i.e. elastic collision rate). This is why the theoretical curve drops to zero at $k = l = 0$. It can be seen from Figure 6(a) that the theoretical and simulated rates do not match for any of the transitions. In fact, the DSMC simulation predicts a somewhat lower excitation rate from bin k=0 to all post-collision bins than would be expected from theory. If we make the comparison for the rates from bin k = 4 (Figure 6(b)), we can observe that while the theoretical and DSMC de-excitation rates (i.e. $l < 4$) match, excitation rates to higher-lying bins are again underestimated by the DSMC simulation. Finally, Figure 6(c) shows the de-excitation rates from the highest bin (k = 9) to the lower-lying bins. Here, the theoretical and DSMC-rates give the same results.

At this moment we are not able to explain why the two sets of rates do not match. One possibility would be that our current selection algorithm by which a given reaction event is accepted or rejected is incorrectly implemented. An error might have been introduced by the fact that in our simulations the forward (i.e. excitation) reactions have cross-sections that are energy-dependent, whereas the backward reaction cross-sections are independent of the translational energy. Another reason might be that the total cross-section predicted with the VHS model is too small at high temperatures to predict the correct overall collision rate.

Further evidence of the problems with our current implementation can be observed in Figure 6(d). In this case we consider an isothermal heat bath with $T = 30000\,\text{K}$. The nitrogen molecules initially populate the bins according to a Boltzmann distribution at $T = 30000\,\text{K}, T_{\text{int}} = 300\,\text{K}$. Over time, one would expect excitation of N_2 into higher-lying bins and the internal temperature of the mixture to rise to 30000 K as well. However, this is not the case. The final internal temperature lies much below the expected value,

at around 19000 K. Again it seems that the rates of excitation in the DSMC simulations are too low for the mixture to reach the correct equilibrium state.

3.2. Bin model: Preliminary conclusions

In the previous section, a first step at implementing a coarse-grain model for inelastic collisions in DSMC has been presented. The discrete internal energy levels of the N_2 molecule are lumped together into a small number of energy bins and treated as individual pseudo-species. Internal energy exchange processes between these bins are treated as pseudo-chemical reactions with an associated reaction cross section.

The current DSMC implementation has shown to give incorrect results. At present the rates for the processes of excitation/de-excitation computed by means of DSMC do not match the theoretical ones. This makes it impossible to retrieve the correct equilibrium bin populations at a given temperature.

4. Future work

Two different state-to-state models have been implemented in our DSMC code. The Anderson [17] model provides a simple state-transition cross-seciton for molecule-molecule internal energy exchange. This is a convenient model cross-section for testing a state-to-state implementation, but lacks physical detail. The second approach was the use of cross-sections derived from the QCT data for Nitrogen (N3-system) of Jaffe and co-workers[16]. Our method of obtaining these cross-sections by analytically inverting binned rate coefficients has so far not been successful. Future work will concentrate on this problem using an approach proposed by Bondar and Ivanov [24] or possibly an alternative method proposed by Minelli et al. [25].

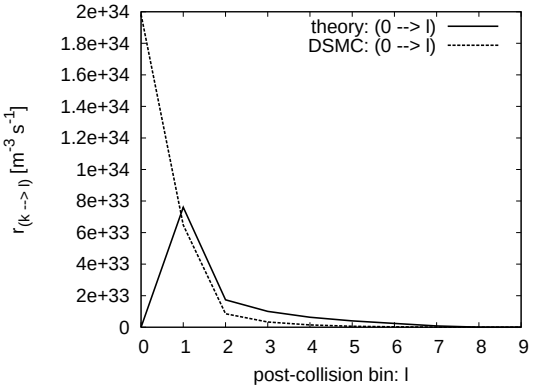

(a) Excitation/de-excitation rates from bin “0” to bin “l”

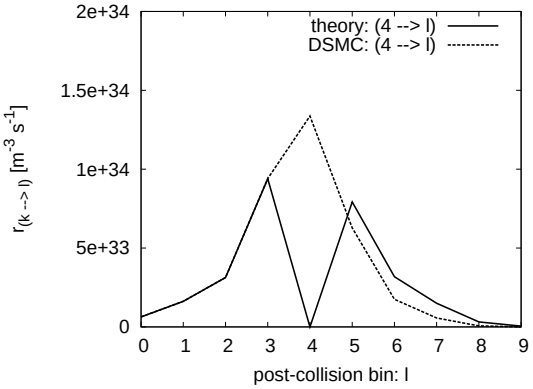

(b) Excitation/de-excitation rates from bin “4” to bin “l”

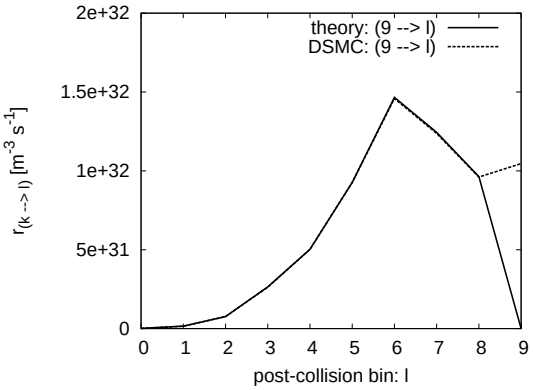

(c) Excitation/de-excitation rates from bin “9” to bin “l”

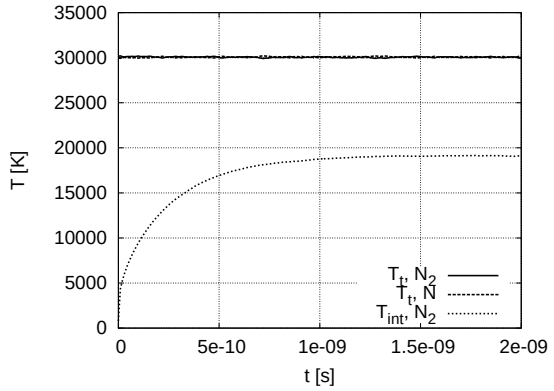

(d) Isothermal heat bath at 30000 K: Translational and internal temperatures

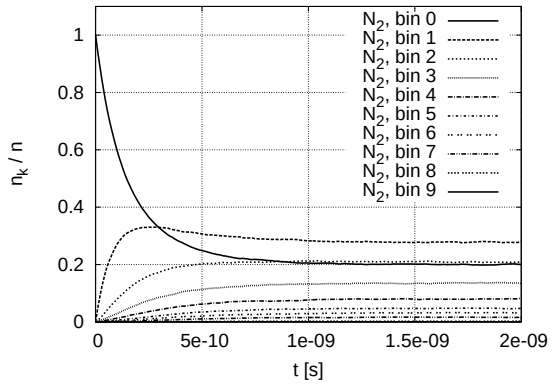

(e) Isothermal heat bath at 30000 K: Bin population fractions

References

[1] G. Bird, Molecular Gas Dynamics and the Direct Simulation of Gas Flows, Oxford University Press, 1994.

[2] C. Borgnakke, P. Larsen, Statistical collision model for monte carlo simulation of polyatomic gas mixture, Journal of Computational Physics 18 (1975) 405–420.

[3] I. Boyd, Rotational-translational energy transfer in rarefied nonequilibrium flows, Physics of Fluids A 2(3) (1990) 447–452.

[4] I. Boyd, Rotational and vibrational nonequilibrium effects in rarefied hypersonic flow, Journal of Thermophysics and Heat Transfer 4(4) (1990) 478–484.

[5] G. Bird, Simulation of multi-dimensional and chemically reacting flows, in: 11th International Symposium on Rarefied Gas Dynamics, 1978.

[6] M. Ivanov, G. Markelov, S. Gimelshein, Statistical simulation of reactive rarefied flows: numerical approach and applications, in: 7th AIAA/ASME Joint Thermophysics and Heat Transfer Conference, 1998.

[7] I. Boyd, Nonequilibrium chemistry modeling in rarefied hypersonic flows, in: 33rd Thermophysics Conference, 1999.

[8] F. Bergemann, I. Boyd, Rarefied Gas Dynamics: Experimental Techniques and Physical Systems (Progress in Aeronautics and Astronautics), American Institute of Aeronautics and Astronautics, 1994, Ch. 3. New Discrete Vibrational Energy Model for the Direct Simulation Monte Carlo Method, pp. 174–183.

[9] G. Bird, Chemical reactions in dsmc, in: 27th International Symposium on Rarefied Gas Dynamics, 2011.

[10] G. Bird, The q-k model for gas-phase chemical reaction rates, Physics of Fluids 23 (2011) 106101.

[11] T. Tokumasu, Y. Matsumoto, K. Kamijo, M. Oike, Dynamic molecular collision model for n2 - he mixture, in: 22nd International Symposium on Rarefied Gas Dynamics, 2001.

[12] K. Koura, Direct simulation monte carlo study of rotational nonequilibrium in shock wave and spherical expansion of nitrogen using classical trajectory calculations, Physics of Fluids 14(5) (2002) 1689–1695.

[13] I. Boyd, E. Josyula, State resolved vibrational relaxation modeling for strongly nonequilibrium flows, in: 49th AIAA Aerospace Sciences Meeting including the New Horizons Forum and Aerospace Exhibition, 2011.

[14] Z. Sohn, D. Levin, State specific vibrational relaxation and dissociation models for nitrogen in shock regions, in: 28th International Symposium on Rarefied Gas Dynamics, Zaragoza, 2012.

[15] J. Kim, I. Boyd, State resolved thermochemical modeling of nitrogen using dsmc, in: 43rd AIAA Thermophysics Conference, 2012.

[16] R. Jaffe, D. Schwenke, G. Chaban, W. Huo, Vibrational and rotational excitation and relaxation of nitrogen from accurate theoretical calculations, in: 46th AIAA Aerospace Sciences Meeting and Exhibit, Reno, Nevada, 2008.

[17] J. Anderson, J. Foch, M. Shaw, R. Stem, B. Wu, Statistical theory of electronic energy relaxation, in: Proceedings of the 15th International Symposium on Rarefied Gas Dynamics, 1986.

[18] R. Jaffe, D. Schwenke, M. Panesi, T. Magin, Detailed theoretical study of collisional rotation-vibration energy transfer and dissociation in n2, in: 7th European Symposium on Aerothermodynamics, Brugge, Belgium, 2011.

[19] G. Bird, Perception of numerical methods in rarefied gasdynamics, in: 16th International Symposium on rarefied gas dynamics, 1988.

[20] E. Josyula, C. Suchyta III, W. Bailey, P. Vedula, Kinetic view of the influence of internal energy states on shock structure, in: 42nd AIAA Thermophysics Conference, Honolulu, Hawaii, 2011.

[21] S. Dunn, J. Anderson, Direct monte carlo simulation of chemical reaction systems: Dissociation and recombination, Journal of Chemical Physics 102(7) (1995) 2812–2815.

[22] F. Esposito, M. Capitelli, Qct calculations for the process n2(v) + n -¿ n2(v') + n in the whole vibrational range, Chemical Physics Letters 418(4-6) (2006) 581–585.

[23] A. Munafo, T. Magin, M. Panesi, A. Bourdon, R. Jaffe, D. Schwenke, Mechanism reduction for rovibrational energy excitation and dissociation of molecular nitrogen in hypersonic flows, in: 42nd AIAA Thermophysics Conference, Honolulu, Hawaii, 2011.

[24] Y. Bondar, M. Ivanov, Dsmc dissociation model based on two-temperature chemical rate constant, in: 45th AIAA Aerospace Sciences Meeting and Exhibit, Reno, Nevada, 2007.

[25] P. Minelli, E. F., D. Bruno, M. Capitelli, S. Longo, Extracting cross sections from rate coefficients: Application to molecular gas dissociation, Journal of Thermophysics and Heat Transfer 25(3) (2011) 374–377.

[26] I. Boyd, Analysis of vibration-dissociation-recombination processes behind strong shock waves of nitrogen, Physics of Fluids A 4(1) (1992) 178–185.

[27] I. Boyd, Modeling backward chemical rate processes in the direct simulation monte carlo method, Physics of Fluids 19 (2007) 126103.

Validation of Gas-Surface Interaction Modeling for Lifting Body Re-Entry Flight Design

Alan Viladegut

Aeronautics and Aerospace Department, von Karman Institute for Fluid Dynamics, Belgium, alan.viladegut@vki.ac.be

Supervisor: Olivier Chazot

Associate Professor, Aeronautics and Aerospace Department, von Karman Institute for Fluid Dynamics, Belgium, olivier.chazot@vki.ac.be

Abstract

Re-entry space vehicles face extreme conditions when they interact with the atmosphere at hypersonic velocities. The bow shock in front of the spacecraft might increase the temperature of the gas until molecule dissociation occurs, leading to a mixture of species.

Around the spacecraft, the boundary layer is developed and its temperature gradient can promote the recombination of atoms, releasing the energy previously adsorbed at the shock towards the surrounding fluid particles or, more critically, towards the wall. These exothermic chemical reactions close to the wall are responsible of the diffusive term on the heat flux balance equation.

Depending on the TPM (Thermal Protection Material) and on the flow environment, the wall itself can enhance and accelerate the reactions. This effect is known as catalycity, and its appropriate modeling is of vital importance for an efficient spacecraft design.

The most extended approach to model catalycity is through the so-called recombination coefficient γ. It is defined as the ratio between the atoms recombining at the wall with respect to the total impinging particles. Despite TPMs are conceived as low catalytic under high enthalpy regimes, the assumption of full-catalytic wall $\gamma \rightarrow 1$ is used for TPS (Thermal Protection System) design. It is clear that this conservative hypothesis leads to a lack of efficiency on current space vehicles design. Therefore, a better modeling of the recombination parameter is required.

Other models are also used, much more detailed in terms of kinetic reaction rates, activation energy and wall processes at microscopic scale. These kinds of models, though, need a lot of parameters to be defined making its empirical determination very complex.

The purpose of this project is the validation of a catalytic model able to predict recombination effects better than the current $\gamma(T)$ model but avoiding the complexity introduced by kinetic models. Such a model would allow a suitable enough estimation of catalytic effects for spacecraft design. The first attempt will be the introduction of extra terms in the modeling of γ such as pressure and diffusion coefficients, keeping always in mind that it is of interest the global and macroscopic description of the phenomena.

IN-FLIGHT EXPERIMENTS

Radiative and Ablative Studies for In-Flight Validation on Reentry Platforms

Gilles Bailet

Aeronautics and Aerospace Department, von Karman Institute for Fluid Dynamics, Belgium, gilles.bailet@vki.ac.be

Supervisor: Thierry Magin

Associate Professor, Aeronautics and Aerospace Department, von Karman Institute for Fluid Dynamics, Belgium, magin@vki.ac.be.

University Supervisor: Christophe Laux

Professor, Laboratoire EM2C, Ecole Centrale Arts Et Manufactures, christophe.laux@ecp.fr

Abstract

The von Karman Institute for fluid dynamics is aiming to develop and launch a re-entry vehicle by 2015. Based on the CubeSat standard, with a highly constraining form factor (340x100x100mm^3), this vehicle represents an ideal low-cost approach for the study of ablation and radiation in the harsh aerothermodynamics environment. The paper exposes the interest and feasibility of an embedded spectrometer from the interesting scientific outcome expected during the mission.

Keywords: re-entry, CubeSat, spectrometer, radiation

1. Introduction

In the frame of the QB50 project led by the von Karman Institute for Fluid Dynamics (VKI) the paper exposes the preliminary results of the PhD thesis for the development of a re-entry CubeSat. The scientific objective of the QB50 project is to study the temporal and spatial variations of a number of key constituents and parameters in the lower thermosphere (50-350 km) with an international network of 50 double CubeSats (Fig. 1), miniaturized satellites weighing 2 kg in a 200x100x100 mm^3 volume. The 50 CubeSats in a circular orbit will be separated by a few hundred kilometers and will carry identical sensors that will perform in-situ, long duration (3 months) and multi- point measurements. QB50 will also study the re-entry by measuring a number of key parameters during mission with the vehicle presented in this paper.

Within this project, the VKI will develop its own nanosatellite [1] (preliminary design presented in Fig. 2) in the frame of QB50 named Qarman (QubeSat for Atmospheric Research and Measurement on AblatioN) with a size of 340x100x100mm^3 for a maximal mass of 3 kg derived from the CubeSat standard.

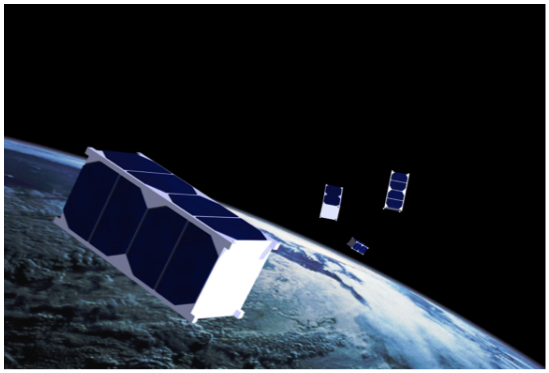

Figure 1: Artistic impression of few double-unit CubeSats of the QB50 constellation

2. Preliminary design of QARMAN

The spacecraft is composed of a standard double-unit platform with sensors for atmospheric research and a functional unit for essential satellite operations as the other CubeSats. A third unit accommodating an ablative heat shield is added to protect the vehicle against the extreme aerothermal conditions expected during the re-entry. In addition of the proposed platform, a deorbiting system based on a drag augmenta-

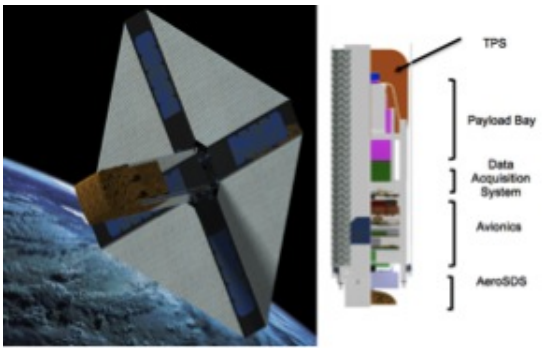

Figure 2: External and internal view of QARMAN

tion device will permit to reach a large range of trajectories (heat flux, g-load profiles) depending on its sizing. The objective of this mission is to conduct innovative in-flight experiments for re-entry study. The success of the mission is essential for VKI, allowing it to reinforce its expertise and knowledge in the field of re-entry. The comparison of the in-flight results with numerical simulations and ground test experiments will permit to assess methodologies for flight extrapolation of ground data and validation of models used for Thermal Protection System (TPS) design. The launch of the re-entry vehicle with the other nanosatellites of the QB50 project has been scheduled for 2015.

QARMAN represents an ideal cost-efficient platform for re-entry flight experiments and validation of TPS materials and other payloads. At the present date the project is within the phase B status and in-depth studies are ongoing.The measurement techniques have to be chosen carefully due to the strict platform constraints and complex physics. Some of the sensors will be developed in house based on already existing techniques. The final selection of the aerothermodynamic payloads will be made after further scientific investigation. Tab. 1 shows a possible set of sensors and their mass/power/data budgets including margins.

The proposed set of sensors permits to lay down the basis for the spectrometer selection. The present paper will focus on the emission spectrometry payload for QARMAN after having exposed the state-of-the-art through a literature survey focusing on both radiation and ablation in which it will explain the scientific outcome expected from the mission and the global needs of this scientific field. Then, the second part will focus on the expected emission during the flight. Along with it, a market survey is presented for the imbedded spectrometer.

3. Literature survey

A reentry vehicle represents a critical part in many mission designed to deliver payloads or crew to their final destination. For non-technology demonstration missions, the Thermal Protection System (TPS) is just a mean to reach the goal of the mission but its design has to be considered crucial as it is a single point failure system. A suitable TPS is essential to shield the vehicle from the harsh aerothermodynamic conditions of the reentry environment. Minimizing the weight and cost of the TPS by keeping the reliability objective of the subsystem is the continuing challenge facing the scientific community. Several phenomena affect the design of TPS [2] with ablation and radiation as the two most important and critical among others (gas-surface interaction, transition) in case of ablative TPS. Ablation consists on a removal of material from the surface by erosion and vaporization triggered by endothermic reactions hence protecting the rest of the vehicle by reducing the thermal constrain. In its side, the radiation phenomenon is an energy transfer from excited particles (mostly from the shock and the ablation products) in the form of an electromagnetic flux (i.e. radiative flux). At the opposite of ablation, the radiations will contribute to an increase of the aerothermal energy around the vehicle thus increasing the heat flux on the vehicle and constrains on the design. In addition, radiations can contribute to a diminution of the surface temperature by dissipating energy but this property is mainly used at low heat fluxes (ex.: thermal soak TPS from space shuttle). Extensive researches were mostly leant upon with pre-seventies projects (Apollo, space shuttle) where massive efforts have been made to characterize the phenomena of reentry and specifically TPS design-related issues. Several major projects can be identified such as the work done on Flight Investigation of the Reentry Environment (FIRE) 1 and 2 [3] and several programs for risk reduction on the space shuttle [4].

The efforts undergone in the following decades were sporadic but successful for some of them in the deeper understanding of the scientific background. Despite expensive budgets, missions like BSUV-1 and 2 for bow shock ultraviolet experiments [5,6,7,8] gave an excellent understanding in flight data for numerical models and ground test facilities improvement. Although the success of the mission, the data are

Table 1: Possible set of sensors

Investigated Challenge	Parameter to measure	Sensor	Total Mass [kg]	Max. Energy /Sensor [mW h]	Data Size /Meas. [bit]	Max Total Data Size [KB]
TPS Ablation	Recession	2 x Recession Sensor	0.004	1.67	10	3.0
TPS Efficiency	Temperature Distribution	8 x Thermo Couples	0.031	1.67	14	16.8
TPS and /Environment	Pressure	2 x Pressure Sensor	0.060	8.33	10	3.0
Stability	Pressure	2 x Pressure Sensor	0.060	840	10	302.4
Rarified Flow Conditions	Low Pressure / Vacuum	1 Vacuum x Sensor	0.011	756	10	151.2
Shear Force, Laminar to Turbulence Transition	Skin Friction	4 x Preston Tube	0.120	2520	10	907.2
Off-Stagnation Temperature Evolution	Temperature	10 x Thermo Couple	0.021	16.8	14	211.68
ATD Environment	Species	1 x Spectrometer	0.084	6250	28	3.5
Total			**0.391**	6250	**338**	50.3

not extrapolated for reentry speed above 5.3 km.s^{-1} where the non-equilibrium part of the chemistry became more important in the flow field. In the side of the ablation process understanding, most of the researches were done during the space reentry missions as secondary payloads [9]. This lack of risk reduction missions for research on thermal protection systems pushes to an excess of ground tests with high uncertainties (as flight conditions are not fully duplicable on ground) that have resulted on a higher program cost and higher margins on the design ending up on a smaller mass of the payload. More recently, efforts have been in regard of flight data collection for the post space shuttle era and the sample return interest for the scientific community. The Japanese spacecraft Hayabusa [10] and the American Stardust [11] are two brilliant examples of sample return missions with the characteristic hypervelocity reentry (in these cases superior to 12km.s^{-1}). In addition of their valuable asteroids sample payload, the two capsules were equipped with instrumentation. Important data have been retrieved from these missions and specifically on ablative TPS material response and on radiation from the bow shock and the vehicle itself (with spectrometer airborne for stardust). The post space shuttle era have brought programs returning to capsule shaped reentry vehicles with Orion and Dragon (Space X) capsules. The Orion capsule [12] represents an ideal testbed for all reentry related phenomenon and NASA has planned numerous test flights with a high density of instrumentation onboard. Coming papers will support the community efforts. In the coming months, the results of MSL (Mars Science Laboratory) reentry will permit to judge on the reliability and interest in the new TPS instrumentation tested during this Mars entry. In the side of Europe, few programs have been developed for the study of ablation and radiation on reentry vehicles. An ongoing program named Experimental Reentry Testbed (EXPERT) is planning to conduct several experiments during a suborbital reentry (5 km.m^{-1} at 100 km of altitude). One of the most important payload of the mission is the ReEntry SPECTrometer (RESPECT) [13] with two optical channels. This mission will permit to strengthen and actualize the data of the BSUV program and develop the technology in Europe. In addition of these missions, several challenges will have to be achieved to respond to some needs in the industry and research community

[2,3,5,7]:

Technical Engineering Development:

- Improving design and analysis tools (uncertainty quantification included), such as CFD and material response models, to verify material response and qualification test conditions.
- Developing improved testing techniques to support traceability from ground to flight aerothermal environment conditions.
- Designing tests that investigate material and system failure modes and use such data to develop improved system reliability analysis methodologies.
- Sustaining current material manufacturing capabilities and expertise to ensure that at least two proven TPS materials, for both the heat shield and back shell, are available for future Sample Return missions. Recertification or qualification of these materials needs to occur every few years.

Flight Instrumentation:

- Including TPS instrumentation in all reentry missions to generate a database of relevant flight data that will aid in the design of future entry missions as flight heritage is necessary for Technological Readiness Level ratings higher than 5.
- Multiply earth reentry TPS flight data to benefit sample return missions and ISS-orbit return.

At the difference of the above-mentioned programs, the present proposal refers to a reentry from low earth orbit (LEO) with a speed of roughly 7.5 km.s^{-1} at 120 km of altitude as a gap-filler between studies made for hypersonic/sub orbital atmospheric flight and lunar/sample return missions in the aspects of ablation and radiation studies. A mission aiming to tackle these issues named Skipper [14] was performed but unfortunately the vehicle failed in orbit before any scientific return. Equipped with two spectrometers and 20 photometers in the aim of focusing the mission on UV (ultra violet) and VUV (vacuum ultra violet) wavelength range of the emitted radiations. Even without the scientific return and without any scientific publications, we can note the scientific interest, as one can understand the need of filling the gap between FIRE and BSUV programs.

Tab. 2 exposes the summary of the in-flight experiments for radiative studies.

In the side of the numerical tools two approaches are possible. Considering the simulation of radiation and ablation as two highly complicated processes the approaches consist on a decoupled approach, which solves independently both phenomenon and coupled them back afterward and the coupled method, which solve directly the two phenomenon within the same partial differential set of equations. Advanced collisional-radiative models for thermochemical nonequilibrium and radiation modeling at the difference of coupled problems represent the-state-of-the-art in modeling capabilities for the decoupled approach [15]. To understand what an in-flight spectrometer could measure, emission spectrometry codes have to be used. Reference [16] presents an overview of the different available models and recommends the use of SPECAIR as a more reliable code than NEQAIR, the historical standard. The author mentioned the uncertainties of the present models as at low pressure (high altitudes) possible departures from a Maxwellian distribution for the free electrons are expected. This possibility is an additional strong emphasis on the necessity of the proposed study to strengthen the models. In complement of the previous list, some additional specific questions and challenges can be addressed:

- Investigating TPS materials under LEO reentry conditions for the new generation of reentry vehicles.
- Investigating the effect of ablation products (high radiative CN products) on the radiative heat flux and the chemistry of the flow.
- Investigating specific emission spectra of the LEO return (atomic oxygen, Lyman-alpha, NO, OH, and N2+ wavelengths)
- Improving the existing tools to cover the rarefied flow field and the ionized conditions.

The scientific community will have know to fill the gaps of the different numerical models (highly ionized plasma, coupled ablation/radiation) and the hardware qualification and TRL rising (high fidelity ground-to-flight extrapolation, flight experiments) to arrive to a better understanding for greater endeavors in space missions including an entry/reentry module.

Table 2: Summary of the in-flight experiments for radiative studies

Mission	Year	Entry speed [km.s^{-1}]	Altitude range [km]	Spectral range [nm]	Spectral resolution [nm]	Focus
FIRE I	1964	11.5	70-89	300-600	4	Coupled ablation /radiation
FIRE II	1965	11.5	40-83	300-600	4	Coupled ablation /radiation
BSUV I	1990	3.5	38-70	200-400	1	UV diagnostic
BSUV II (UVDE)	1991	5.1	62-110	200-400	1	UV diagnostic
Ground observations	2006	above 12		300	0.1	Global
(Stardust, ATV 1	2008	7.8	?	-	-	observation
and Hayabusa)	2010	above 12		2000	20	
EXPERT	2013?	5	?	200-850	1.5	Build a database
QARMAN	2015	7.6-7.8	50-120	225-1050?	0.8-1.5?	Payload demonstration

4. Imbedded Spectrometer

An emission spectrometer is an instrument enabling the measurement of a light source, for the present case an air plasma. The device measures the intensity of the light over a certain range of wavelengths. As observed in Fig. 3 and with the same goal as Sir Isaac Newton diffracted the light with a prism, a combination of two mirrors and one gratin screen permits the different wavelengths of the light source to be not anymore coherent and be analyzed independently according to the sensitivity of the detector.

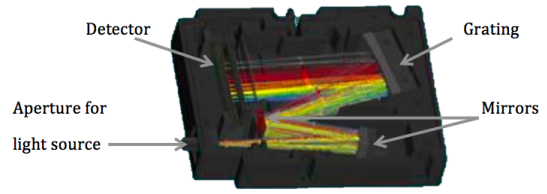

Figure 3: Components of an emission spectrometer

4.1. Spectrum on one point of the stagnation line

In order to assess the interest of radiation phenomenon, a spectrum of the most constraining situation is presented in this part. The software Mutation [17] was used to compute from the reentry conditions (Fig. 4) the temperatures of translation and vibration along with the chemical composition of the flow after the shock (Fig. 5 and Fig. 6).

The next step in the study of the spectrum is conducted using a radiation code named Specair [16].

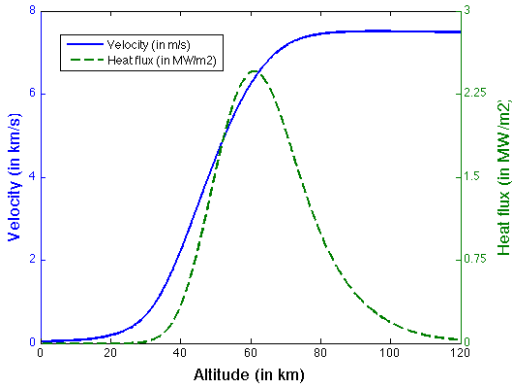

Figure 4: Velocity and heat flux profile versus altitude for the QARMAN mission

The available version (2.2) only permits to compute the spectrum at a specific point in space thus avoiding accounting for absorption and diffraction on the rest of the line of sight of a hypothetical spectrometer. A full computation of the line of sight will be made later in the project for a more accurate prediction and comparison with potential flight data. As example, the Fig. 5 and Fig. 6 presents the high intensity and the low intensity spectra for the maximal heat flux conditions of QARMAN (V=6.3 km.s^{-1}, h= 61 km) of the trajectory and a point on the stagnation line distant from 5mm to the shock (for reference, the stand of distance is around 17.5 mm).

Multiple radiation feature appears on the two previous figures. The next part will permits us, with more effort, to estimate the global radiative flux on the stagnation line.

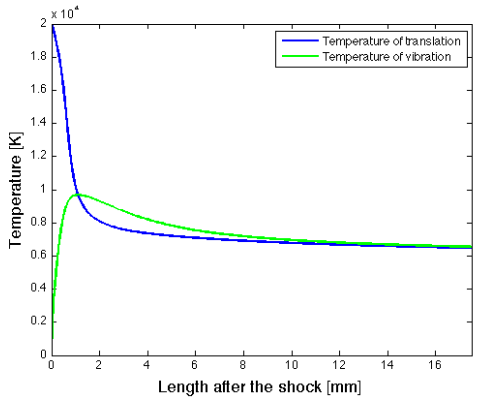

Figure 5: Profile of vibration and translation after the shock

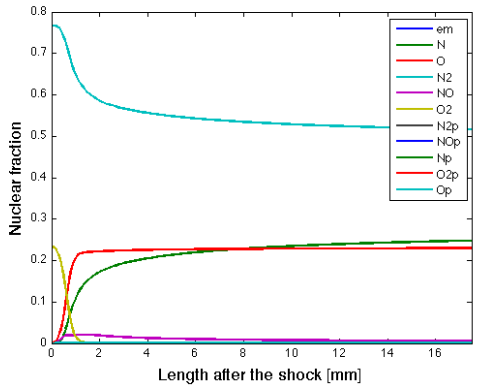

Figure 6: Chemical composition of the flow after the shock

4.2. *Spectrum on the full stagnation line*

The present set of software available for this study doesn't allow to compute the radiative transfer through the plasma in front of the vehicle. To overcome this problem, we can use the thin film plasma approximation which is a way to calculate the radiative flux without considering the absorption within the plasma in front of the vehicle. This approximation could be an issue depending on the energy of the plasma and the wavelength observed. For low energy reentry such as QARMAN mission, the error due to thin plasma approximation have been quantify [18] as quantitatively noticeable for wavelength below 200 nm and over 1000 nm. Due to QARMAN's limitations on wavelength range for the imbedded spectrometer, no potential chosen detector has a maximal wavelength sensitivity below 200 nm and above 1050 nm, the hypothesis of thin plasma can then be assumed as relevant for the present study.

The principle to apply the thin plasma approximation lies in the calculation of the radiative intensity of every wavelength over the full stagnation line. Then, by integration the result gives in first order the spectrum of the stagnation line and with second order integration the radiative flux. Next figures use the same trajectory point as used in the previous part, i.e. maximal heat flux point.

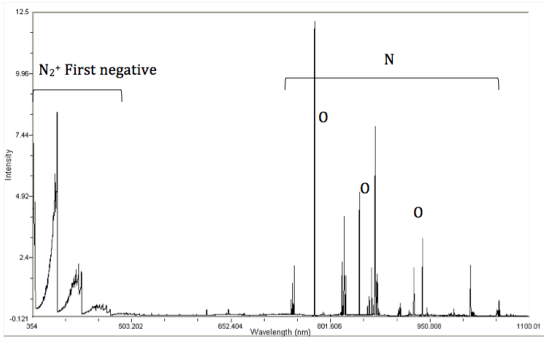

Figure 7: Spectrum at 5mm from the shock (high intensity)

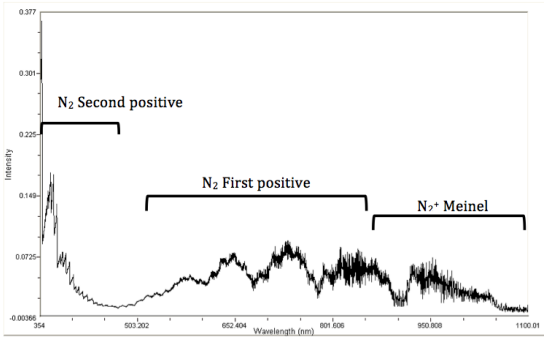

Figure 8: Spectrum at 5mm from the shock (low intensity)

Fig. 9 shows the spectrum obtained with thin film approximation for the 61 km trajectory point.

Unfortunately as one can see, a high resolution is needed to grasp the physic behind the data we can acquire. The resolution of the spectrometers whose can fit within the QARMAN vehicle (see Tab. 3) allows resolution of 14 bits per pixel which are not at all enough for this kind of spectra. Fig. 10 presents the analysis of the spectra with the actual range of sensitivity of the selected spectrometers 350-850 nm.

In this present case and with the 14 bits resolution available it is possible to capture the tiniest features of the spectrum.

Finally, Fig. 11 exposes the reconstructed radiative heat flux impinging the stagnation point and the one reaching the spectrometer in function of the altitude. Further studies will permit to quantify the exposure

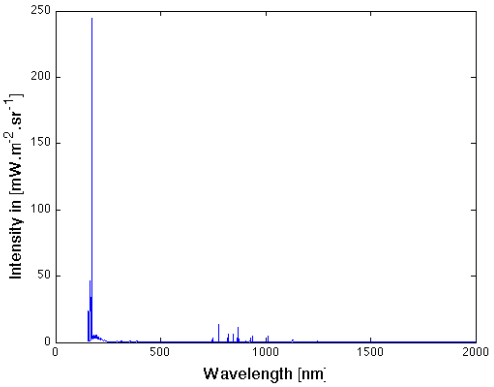

Figure 9: Spectrum at 5mm from the shock (low intensity)

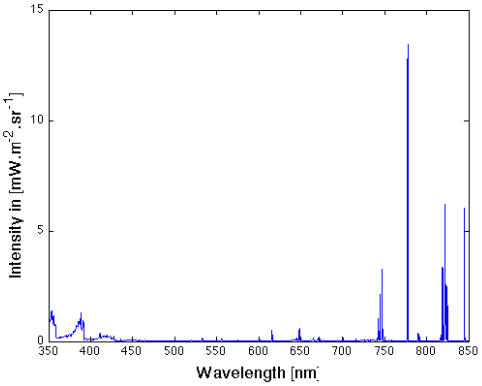

Figure 10: Spectrum at 5mm from the shock (low intensity)

time needed to acquire quality spectra in function of time. The limit of 10 seconds for the spectrum acquisition will allow to calculate the highest altitude at which we can obtain interesting data.

As one can see, the radiative flux is not strong enough to constrain the TPS sizing and further studies will have to be addressed to take in account the wall and ablation effect.

4.3. Market survey of the imbedded nano-size emission spectrometer payload

A wide range of emission spectrometer exists on the market and the chosen one should fulfill the requirements of our platform. The main requirements are the mass/volume budget. For the mass constrain, an emission spectrometer (without the board for data acquisition) is expected to weight a little less than 0.100 Kg.

The following table exposes the main characteristics of the potential candidates for the emission spectrometer payload.

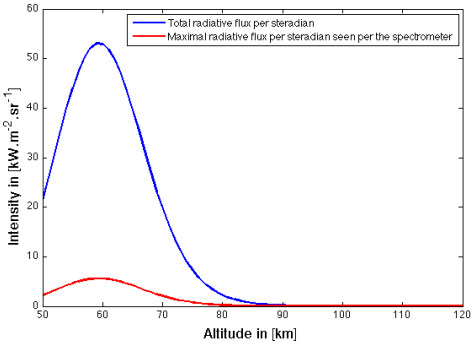

Figure 11: Spectrum at 5mm from the shock (low intensity)

Fig. 12 exposes the data of Tab. 3 overlay on the interesting spectrum features extracted from the study presented in this paper and the literature survey.

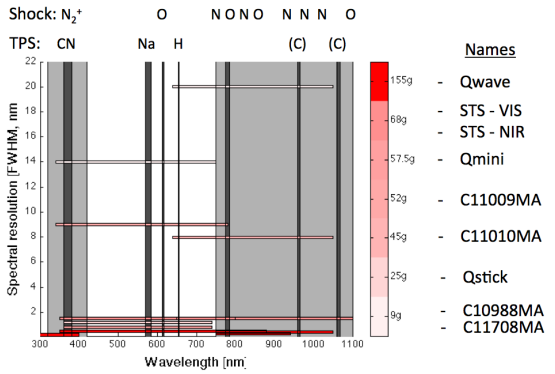

Figure 12: Summary of the market survey

Due to the high density in low FWHM, Fig. 13 presents the close up of the market survey result.

From the previous analysis and Tab. 3 and Fig. 13 it clearly appears the inability of acquiring the full spectra with an imbedded emission spectrometer. Although limited spectral ranges and resolutions, notable scientific outcomes can be expected from the mission in numerous of aspects such as non-equilibrium chemistry, ablation product contribution to the radiative heat flux. In the future the effect of ablation product with the strong radiative CN compound will be a good candidate to study in the objective to quantify the notable increase on radiative heat flux due to these ablation products.

If the interest of studying another wavelength range is maintained, an alternative could be the use of a photometer, which will only measure the intensity of a

Table 3: Characteristic of the emission spectrometer candidates

Name	Dimensions [mm^3]	Weight [g]	Maximal operating temperature [^{o}C]	Wavelength range [nm]	Spectral resolution [nm]	Reference
STS-VIS	40x42x24	68	50	350-800	1.5	[19]
STS-NIR	40x42x24	68	50	650-1100	1.5	[19]
Qmini	62x42x14.8	57.5	60	360-740	0.8	[20]
Qwave	89.5x68x19.5	155	60	350-880 220-400 750-940 750-1050	0.5 0.2 0.3 0.4	[21]
Qstick	85.7x22x10	25	60	360-740	1.2	[22]
C10988MA	27.6x13x16.8	9	40	340-750	14	[23]
C11708MA	27.6x13x16.8	9	40	640-1050	20	[23]
C11009MA	28x28x28	52	40	340-780	9	[23]
C11010MA	35x20x28	45	40	640-1050	8	[23]

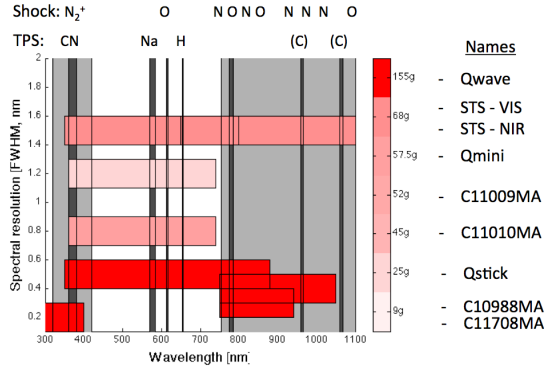

Figure 13: Summary of the market survey

specific wavelength. This device, much smaller and lighter could be useful in specific cases as identification of specific ray and specifically where the wavelength doesnt fit the imbedded spectrometer range. The future studies will have to include in addition of the full line-of-sight radiation an in-depth investigation of what is it possible to obtain from the spectrometers and the benefit we can expect from it.

5. Conclusion

Among the past years the feasibility of QARMAN has been demonstrated thus ended up with the actual preliminary design of the vehicle. Through the literature survey, the interest of such platform for the research on ablation and radiation have been observed multiple of times. The payloads for ablation are easy to integrate within the platform, as they are compatible with the QARMAN volume/mass constrains. The spectrometer in the other hand is much more of a challenge in regard of standard missions. In the project point of view, it is not conceivable to design the full device for financing constrains, as the project should remain a low cost alternative to conventional missions. The other alternative of using spectrometers already designed from previous missions is not conceivable neither as they all weight more than the full QARMAN. The only option is to use mini spectrometers out of the shelf. The preliminary study has shown that the available spectrometers available with QARMANs platform specifications permit to get an interesting scientific outcome. However, this study is in the preliminary phase and to understand the importance of this scientific outcome, further investigation will be needed.

Acknowledgments

The research leading to these results has received funding from the European Communitys Seventh Framework Programme ([FP7/2007-2013]) under grant agreement n°284427 for the QB50 Project. In addition many thanks are addressed to Mr. Jean-Marc Bouilly and EADS Astrium for their support and interest in this project. Furthermore, the author is grateful for help and collaboration of Isil Sakraker and Thorsten Scholz.

References

[1] Bailet et al., Feasability Analysis and Preliminary Design of an Atmospheric Re-Entry Cubesat Demonstrator, 7th symposium on aerothermodynamics, ESA conference, Bruges, May 2011.

[2] Venkatapathy, et al., Thermal Protection Systems Development, Testing, and Qualification for Atmospheric Probes and Sample Return Missions, JASR 9731, March 10, 2009.

[3] Cauchon, D. L., Radiative Heating Results from the FIRE II Flight Experiment at a Re-entry Velocity of 11.4 Kilometers per Second, TM X- 1402, NASA, 1967.

[4] NASA-CR-170881, SRB thermal protection system materials test results in an arc- heated nitrogen environment, Lockheed Missiles and Space Co, 1979.

[5] Levin, D., et al., Theory of Radiation from Low Velocity Heated Air, AIAA-90-0133 , 28th Aerospace Sciences Meeting, Reno , NV , January 1990.

[6] Erdman, P., et al., Measurements of Ultraviolet Radiation from a 5 Km/sec Bow Shock, AIAA Paper No. 92-2870 , Nashville , TN , July 1992.

[7] D. A. Levin, et al., Examination of ultraviolet radiation theory for bow shock rocket experiments, AIAA Paper No. 92-2871, New York, 1992.

[8] D. A. Levin, et al., Comparison of Theory with Experiment for the Bow Shock Ultraviolet Rocket Flight, Journal of Thermophysics and Heat Transfer, Vol. 7, No. 1, Jan-March 1993.

[9] E. Venkatapathy, et al., Thermal Protection System Technologies for Enabling Future Sample Return Missions, white paper to the NRC decadal primitive bodies sub-panel, 2009.

[10] Yasuhiko Takagi, Science Instruments on Hayabusa follow-on missions, JAXA, 2009

[11] M. A. Covington, Performance of a Lightweight Ablative Thermal Protection Material For the Stardust Mission Sample Return Capsule, NASA-NTRS, 2005.

[12] T. John Kowal, Orion Flight Test-1 Thermal Protection System Instrumentation, NASA-NTRS, 2012.

[13] Lein, S., et al., Optical Emission Spectroscopic Experiments For In-Flight Entry Research, 8th International Planetary Probe Workshop, Portsmouth, Virginia 6-10 June 2011.

[14] Levin, D., et al., Skipper: an innovative U.S. and Russian university space science mission, Proc. SPIE Vol. 2217, p. 292-306, 1994.

[15] T.E. Magin, et al., Review of the VKI research on nonequilibrium phenomena in hypersonics, AIAA (2012-725), 2012.

[16] C. Laux, Physico-Chemical Models for High Enthalpy and Plasma Flows, VKI-LS, 2002.

[17] J. B. Scoggings, Development of Multiphysical Numerical Methods to Study Coupled Flow, Radiation and Ablation Phenomena for Planetary Entry Vehicle, Review of the VKI doctoral research, 2012.

[18] Y. Babou,Transferts radiatifs dans les plasmas de mlanges CO2-N2 : base de donnes spectroscopiques, tude exprimentale et application aux rentres atmosphriques.

[19] Ocean Optics, [Online]. Available: *http* : *//www.oceanoptics.com/productsheets/ sts_product_sheet.pdf*.

[20] RGB Lasersystems, [Online]. Available: *http* : *//www.rgb − laser.com/data/data_pdf_datasheet/ Qmini%20data%20sheet%20for%20web.pdf*.

[21] RGB Lasersystems, [Online]. Available: *http* : *//www.rgb − laser.com/data/data_pdf_datasheet/ Qwave%20data%20sheet%20for%20web.pdf*.

[22] RGB Lasersystems, [Online]. Available: *http* : *//www.rgb − laser.com/data/data_pdf_datasheet/ Qstick%20data%20sheet%20for%20web.pdf*.

[23] Hamamatsu, [Online]. Available: *http* : *//sales.hamamatsu.com/assets/pdf/catsandguides/ mini − spectro_kacc0002e06.pdf*.

In-flight Experiment Design and Ground Testing of a Re-Entry CubeSat

Işıl Şakraker

Aeronautics and Aerospace Department, von Karman Institute for Fluid Dynamics,Belgium, isil.sakraker@vki.ac.be

Supervisor: Olivier Chazot

Professor, Aeronautics and Aerospace Department, von Karman Institute for Fluid Dynamics,Belgium, olivier.chazot@vki.ac.be

University Supervisor: Gaëtan Kerschen

Professor , Department of Aerospace and Mechanical Engineering, University of Liege, Belgium, g.kerschen@ulg.ac.be

Abstract

Real flight atmospheric entry tests are required to validate numerical/experimental tools in order to reduce the high conservative safety margins applied to the spacecraft thermal protection systems. This study covers the ground testing and ground-flight/flight-ground extrapolation methodology for QARMAN mission, that is a 3U CubeSat with an ablative thermal protection system in the front unit.

Keywords: Atmospheric Entry, Plasma Flows, In-Flight Experiments, Experimental Aerothermodynamics, CubeSats

1. Introduction

Spacecraft, returning back to Earth, experience a very harsh environment during the encounter with the particles of the atmosphere. One of the major issues of atmospheric entry is the extreme aerothermodynamic heating and the exothermic chemical reactions due to the gas-surface interaction at hypersonic free stream velocities. There is a constant effort by the space agencies to increase the understanding of the re-entry flight dynamics to optimize the spacecraft and especially its thermal protection system design. During the design process, the need of real flight tests is indispensable for ground test and numerical tool validations. However due to the high costs, such missions are rarely launched and thus there is an increasing interest in small affordable entry probes. This study discusses an aerothermodynamic instrumentation payload on a triple unit CubeSat platform that will be launched to 350 km altitude polar orbit along with the rest of the QB50 CubeSats [1]. QARMAN, QubeSat for Aerothermodynamic Research and Measurements on AblatioN, is a triple unit (3U) CubeSat respecting the CubeSat standards; a rectangular prism with dimensions $30 \times 10 \times 10$ cm. It has an ablative thermal protection material at the nose and will perform an atmospheric entry representative of real missions with 7.5 km/s at 120 km with a peak heat flux of 2.6 MW/m^2. The objectives of the in-flight experiments are to retrieve real flight data on ablator efficiency (temperature, pressure, recession) and temperature/pressure/skin friction measurements for transition on the side panels. Overall, this challenging mission targets to demonstrate the use of nano and pico satellite technology to atmospheric entry research by providing successful real flight data for highly affordable costs when compared to other missions of the space agencies that cost hundreds of million Euros.
The important research in this project is the question of "How such flight can be simulated accurately in ground facilities?".
The validation of the answer lies in the real flight data that will come from QARMAN flight. Simulating hypersonic flights where aerothermochemistry plays a major role is not as simple as lower speed flows. Special similitude laws have to be applied. Local Heat Transfer Simulation (LHTS) is the adopted methodology in VKI which states that if the enthalpy, the pressure and the velocity gradient at the boundary layer edge at the stagnation point are duplicated, the stagnation region behind the detached shock is fully sim-

ulated [2]. It should be noted that another approach has to be followed for off-stagnation regions however at the current phase of the study, this aspect will not be addressed further in this paper.

To start with, amongst the ground facilities for aerothermodynamic research, subsonic plasma windtunnels like the VKI Plasmatron are taken in to consideration. In such facilities, duplicating the pressure is currently done with high accuracy. The enthalpy on the other hand, due to the errors in the heat flux, dynamic pressure measurements and the lack of accurate knowledge of copper recombination behavior when exposed to plasma, have high uncertainties around 20%. The aim is to reduce these levels to around 5% and three independent methods are proposed, thereby verification of the measurements which will then be validated by available numerical tools at VKI.

The first one is a direct enthalpy measurement, the so called Enthalpy Probe, using a long enough heat exchanger to make sure the sucked flow inside the heat exchanger reaches equilibrium conditions to avoid the copper catalycity originated inaccuracies. The second method is to measure the same free stream with different sized probes, namely Damköhler probes. The third method to determine the enthalpy is by using optical emission spectroscopy. The two modes of this technique are the well known Boltzmann plot with oxygen and nitrogen lines and a ratio method using N_2^+ and CN Violet comparing a preloaded theoretical ratio vs. temperature and the experiments [3].

Finally, the velocity gradient depends on the probe geometry which comes from the actual vehicle geometry and flight conditions. This procedure is not so straight forward due to QARMAN geometry. The experimental and a numerical aerothermodynamic databases are currently being constructed to retrieve this information. New probes will be designed for developing the in-flight experiments for aerothermodynamic research of QARMAN. A new approach to ground-to-flight and flight-to-ground extrapolation is being developed to be used in the process from the payload design until manufacturing of such constraining platforms.

2. Ground Testing Methodology

2.1. Background and Methodology

The *Local Heat Transfer Simulation (LHTS)* approach states that for a full simulation of the stagnation region of a reactive hypersonic flow, three properties at the boundary layer edge must be identical for flight and for ground [2].

$$Enthalpy : h_e^{flight} = h_e^{ground} \quad (1)$$

$$Pressure : p_e^{flight} = p_e^{ground} \quad (2)$$

$$Velocity\ gradient : \beta_e^{flight} = \beta_e^{ground} \quad (3)$$

After a detailed analysis on flight to ground extrapolation, a ground testing methodology -suitable for VKI Plasmatron- for payload design purposes has been established. The methodology can be divided in four consecutive experimental, numerical and design campaigns.

The first campaign is related to establishing the testing conditions corresponding to the flight trajectory of QARMAN. This requires a series of tests, where the enthalpy and stagnation pressure match with flight conditions, that the outputs will be the inputs of the second campaign. The second campaign is a combination of CFD simulations for flight conditions and numerical computations for ground tests. The important output of this campaign will be the geometry of the test model which is equivalent to stagnation region of QARMAN flying at hypersonic velocities. The third campaign is a design and testing campaign where a probe with the geometry defined by the previous campaign is designed and manufactured. The probe is then tested in the plasma facility for verification and validation of the extrapolation. Once the probe concept is proven, the in-flight experiments can be tested to improve their Technology Readiness Level (TRLs) as fourth campaign. This last campaign includes the data acquisition unit testing as well which is an ambitious concept for a CubeSat platform.

2.2. Accurate Ground Tests: Enthalpy Determination Methods

As summarized in the previous section, the ground testing methodology requires accurate knowledge of what kind of flow is produced in the test chamber. For this purpose, this section is reserved for techniques proposed for improving the VKI Plasmatron free stream enthalpy determination.

2.2.1. Direct Enthalpy Measurement

The so called “enthalpy probe” is actually a heat exchanger tube, surrounded by insulating cooling jacket, connected to a vacuum pump. The heat is exchanged only inside where the plasma is flowing thanks to the pumping device. This method requires determination the correct suction rate in order not to disturb the flow.

A low suction rate leads to a too high enthalpy reading while a high suction leads to a too low enthalpy reading. Fig. 1 shows how the flow can be affected. The heat balance between the heat exchanger and the hot plasma reads:

$$H_1 = H_2 + \frac{\dot{m}_w}{\dot{m}_g} C_{p,water} \left(T_{w2} - T_{w1}\right) \tag{4}$$

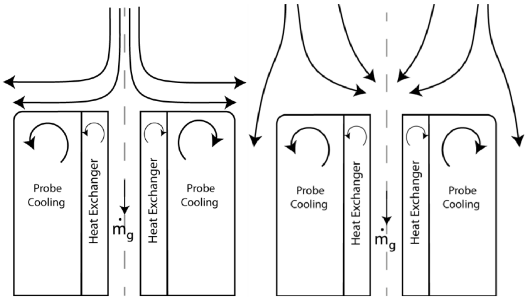

Figure 1: Effect of plasma suction on the streamlines. Left: Low Suction. Right: High Suction.

where H_1 is the enthalpy at the inlet, H_2 is the enthalpy at the back of the heat exchanger, T_{w1} and T_{w2} the water temperatures at the inlet and outlet of the cooling circuit, and $\dot{m}_w$ and $\dot{m}_g$ are the water and plasma flow rates respectively. The balanced suction rate, unique for each test condition, is found by an iterative processing method. The iterative procedure resolves two equations correlating the specific enthalpy seen by the probe and the sample plasma flow rate. An example of balanced suction rate determination is given in Fig. 2 and the correlation function is of the form:

$$H_{read} = A\frac{1}{\dot{m}_g} + B \tag{5}$$

while the plasma sampling rate reads:

$$\dot{m}_g = \rho_{@Hread} VS = \rho_{@Hread} \sqrt{\frac{2P_{dyn}}{\rho_{@Hread} k_p}} \pi R^2 \tag{6}$$

where V is the velocity in the stagnation ring (assumed constant), S is the surface of the inner ring, P_{dyn} is the dynamic pressure, R is the radius of the heat exchanger, k_p is the Barker correction coefficient and ρ is the density of the hot gas. The Eqs. 5 and 6 are solved for plasma sampling rate $\dot{m}_g$ and the enthalpy H, where the density value is taken from VKI in-house library Mutation, the thermodynamic and transport properties library for equilibrium air plasmas. As depicted in Fig. 2 the experimental suction rates are fit to the correlation and the correct specific enthalpy is iteratively calculated.

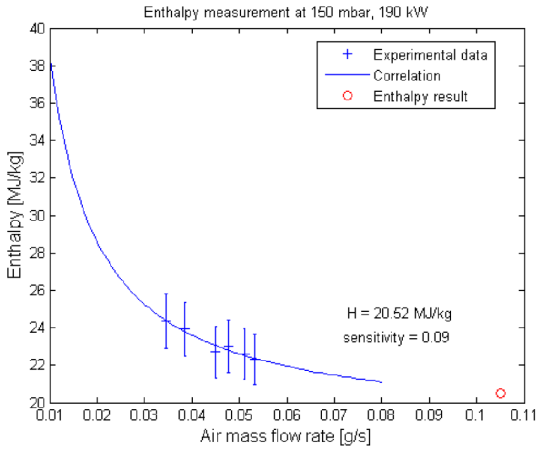

Figure 2: Determining the correct suction rate. Courtesy: Hyun Woo Krassilchikoff.

2.2.2. *Damköhler Probes*

Three water cooled copper calorimeters having different probe radii are used in the Damköhler probe campaigns. The idea behind lies on the Damköhler number definition.

$$Da = \frac{\tau_f}{\tau_c} \tag{7}$$

Where τ_f is the characteristic time of the flow and τ_c is the characteristic time of the chemistry. For given conditions, the probe radius drives the velocity gradient, then the Damköhler number in the boundary layer. One can conclude that low velocity gradient values promote chemical equilibrium while high velocity gradient values tend to 'freeze' the boundary layer. At the same free stream conditions all the probes will measure a different heat flux due to a change in the boundary layer chemistry and if the copper catalycity (γ) were known accurately enough, all the three measurements would lead to the same free stream enthalpy. Due to the lack of exact knowledge of this parameter, VKI's rebuilding code is used to compute the enthalpy for a range of catalycity values using the heat flux measurement and the radius of the calorimeter probe. . Using the $h - \gamma$ curves from three

different sized probes exposed to the same plasma, an accurate enthalpy interval can be extracted. There are several studies conducted at VKI with these probes [4; 5; 6]. However none of their campaigns included the desired test conditions of QARMAN trajectory. The results of those studies are promising considering they led to catalycity intervals of $\Delta\gamma = 4.10^{-3}$ and uncertainties down to 10% in enthalpy. Even though the previous studies did not give the desired uncertainty level of 5%, there is an improvement of about 10% and the combination with other methods will improve the numbers.

2.2.3. REDES

REDES (Real-time Enthalpy Determination with Emission Spectroscopy) uses a method adopted from Fletcher [3] for generic air plasma. This method considers the peaks and the integrated areas of N_2^+ first negative $\Delta v = 0$ and CN Violet $\Delta v = 0$ sequences. The theoretical spectrum for a given total pressure can be computed. Later the peak or the integral ratios are compared with preloaded 'theoretical ratio vs. temperature' curves and the temperature is retrieved. Using Mutation library of VKI, the temperature data is automatically converted to enthalpy assuming local thermal equilibrium. Fig. 3 shows the peak and the integral options of the method. The uncertainty of temperature is around 5%. The second mode of REDES uses a Boltzmann plot with 6 N, 4 N and 2 N spectral lines and the limitations of this method for VKI Plasmatron use are still under investigation.

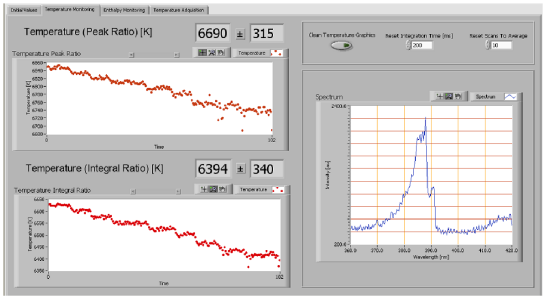

Figure 3: REDES Real-time Temperature monitoring using N_2^+ first negative and CN Violet.

2.3. Accurate Ground Tests: Velocity Gradient Determination

The velocity gradient is defined as the derivative of the radial velocity component in the radial direction along the stagnation line. The velocity gradient and the resultant velocity are depicted in Fig. 4. The generic approach of velocity gradient duplication for LHTS starts by determining the so called 'effective radius' which is a flying sphere giving the same velocity gradient at the boundary layer edge as the spacecraft. This is an extensively studied approach in the literature since the velocity gradient plays a major role in the stagnation point heating estimation by Fay and Ridell [7].

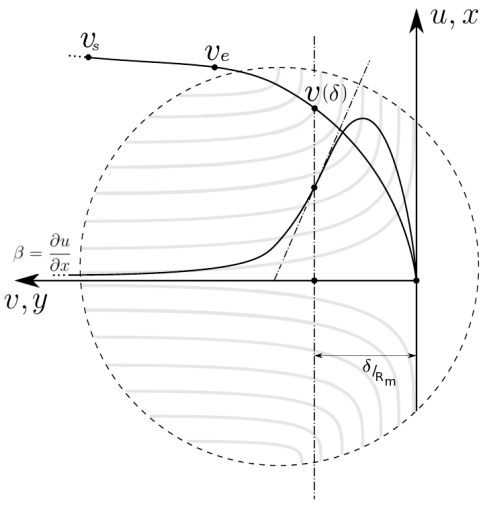

Figure 4: Velocity profile and velocity gradient in front of a wall exposed to subsonic plasma.

Due to the unconventional geometry of QARMAN, a detailed literature survey has been conducted to find out what sort of approach is suitable for determining the 'effective radius' of QARMAN-like blunt bodies. The famous study of Boison and Curtis includes experimental pressure measurements in the stagnation region of axisymmetric blunt bodies at supersonic Mach numbers [8]. They combine the Modified Newtonian Theory (MNT) and Bernoulli equations and compared to the experimental results. The most important conclusion of the paper is that for bodies blunter than $x^*/r^* = 0.25$, which means for bodies having $x^*/r^* < 0.25$, the MNT no longer applies (the geometrical parameters x^* and r^* can be found in Fig.1 of [8]). It should be noted that the bluntess of QARMAN is 0.101. For further reading on other important studies, see [9; 10; 11; 12; 13]. An interesting outcome for QARMAN is the study of Olivier [13] where mass and momentum equations are written in polar coordinates for a sphere starting from a general expression as stated in the book by Probstein and Hayes [14] where real gas effects, vorticity be-

hind the detached shock and compressibility effects are important. As a result, following velocity gradient expression is driven as a function of the shock standoff distance and density ratio across the detached shock:

$$\left.\frac{du}{dx}\right|_s \frac{D}{u_\infty} = \frac{2\left(1+\overline{\Delta}\right)}{\overline{\Delta}} \frac{P_s - P_2}{\rho_\infty^2} \frac{\rho_2}{\rho_s} \tag{8}$$

Iterative Approach for Velocity Gradient Determination

The literature survey led to a decision that the velocity gradient for such a geometry is better defined from CFD analyzes. In the case of non trivial CFD outputs, as it is the case for QARMAN geometry, the boundary layer edge cannot be directly defined to extract the velocity gradient. An iterative procedure is proposed and summarized in Fig. 5. Inviscid computations can be done in order to identify where the flow quantities deviate from the viscous computations. This solution is only theoretical however the iterative procedure will use this value as the initial condition. The results of CFD at flight conditions are compared to the numerical simulations of the ground tests (ICP) obtained from the first campaign. The comparison success criteria is defined to have the effective radius determined by CFD and ICP is to have a difference of 2% in length. The iterative procedure is repeated until it satisfies the desired value.

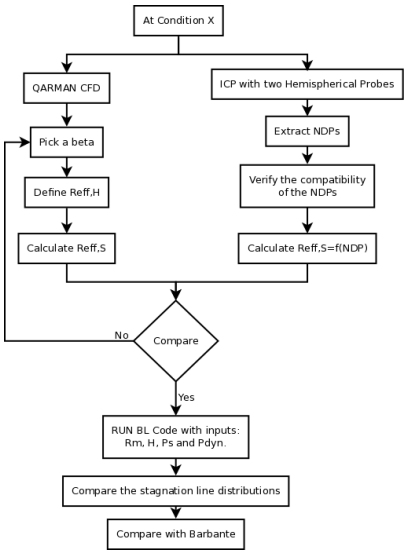

Figure 5: Iterative approach steps.

2.4. Results of Campaign 1

The first campaign as described in the methodology given in Sec. 2.1, has been recently finished. A total number of 8 points along the QARMAN trajectory are chosen to be tested in VKI Plasmatron facility. The flight conditions in terms of pressure and enthalpy are given in Table 1. To remind; the objectives of this campaign are:

- Determining which power corresponds to the desired enthalpy at a given pressure.
- Comparing and validating the freestream enthalpy measurements in Plasmatron by enthalpy probe, Damköhler probes, REDES and standard heat flux measurement.

Table 1: Campaign 1: Selected points from QARMAN trajectory v0.

Test Name	Altitude [km]	Dynamic Pressure [Pa]	Static Pressure [Pa]	Enthalpy $V^2/2$ [MJ/kg]
1	80	510.47	1.23	27.808
2	75	1104.10	1.23	27.114
3	70	2250.98	5.22	25.725
4	66.66	3443.75	8.67	24.191
5	60	6553.53	21.95	19.586
6	55	9143.54	42.52	14.948
7	53.24	10000.00	53.25	13.204
8	50	11280.50	75.95	10.025

After determining the power giving the required enthalpy for each Test from 3 to 8, two additional powers were recorded to improve the aerothermodynamic database. Keeping the pressure the same, these tests are called i.e 3a, 3b and 3c. The enthalpy measurement by spectroscopy using the integral ratio method, along with the power are given in Table 2. The integral ratio method was used since it includes the spectral line broadening information thus considered more reliable than the peak ratio method. Due to the malfunction of the inner cooling jacket of the enthalpy probe, its measurements were postponed. The Damkohler probe tests were conducted at during another test campaign due to the maximum number of probe available in the Plasmatron facility and its data are currently being processed for enthalpy.

3. QARMAN In-Flight Experiment Design

3.1. QARMAN Flight Scenario

QARMAN is a standard triple unit CubeSat with two distinctive characteristics: an ablative TPS in the

Table 2: Campaign 1: Selected points from QARMAN trajectory v0.

Test Name	Power [kW]	Integral Ratio Enthalpy [MJ/kg]	Enthalpy Error [MJ/kg]
3a	120	25.091	± 1.0317
3b	135	27.582	± 1.1681
3c	150	29.633	± 1.3543
4a	120	26.491	± 1.2038
4b	135	28.579	± 1.2920
4c	150	30.650	± 1.4563
5a	170	18.613	± 0.8681
5b	185	19.709	± 0.9497
5c	200	21.028	± 1.1081
6a	145	13.158	± 0.6509
6b	160	14.558	± 0.7025
6c	185	16.445	± 0.7899
7a	150	12.860	± 0.6408
7b	170	14.594	± 0.7051
7c	185	16.522	± 0.7923
8a	150	14.257	± 0.6963
8b	170	14.418	± 0.6984
8c	185	15.995	± 0.7654

front unit and an aerodynamic drag augmentation device. The two mission objectives are: using aerodynamic drag to control the stability and de-orbiting for atmospheric entry; and performing an Earth atmospheric entry. The vehicle will be deployed at 350 km of altitude along with the other QB50 CubeSats.
The current mission operation plan of QARMAN is sketched in Fig. 6. After the deployment from the upper stage of the launch vehicle, QARMAN will automatically enter the commissioning and detumbling phase to reach a controlled flight condition (Phase 0). The AeroSDS (Aerodynamic Stability and De-Orbiting System) will be deployed in Phase 1 for aerodynamic stabilization and to speed up the orbital decay. During this period, measurements will be performed for the evaluation of the system's performance and to get basic information on the atmospheric properties and the CubeSat trajectory. The AeroSDS will assure that QARMAN reaches 120 km of altitude with the desired entry conditions by reducing the speed down to 7.5 km/s. To guarantee fully charged batteries, the satellite will be put in a low power mode (no communication, less measurements) a short time before. During the re-entry (Phase 3), QARMAN will no longer have access to the ground station due to the telecommunications blackout because of the plasma sheet in front of the vehicle. Similar to Space Shuttle, it will send measurement results near real time via IRIDIUM transmissions to the ground. The peak heating is expected to be between 2.5-2.6 MW/m^2 at around 61km. At 50km of altitude, QARMAN will start to disintegrate.

The ablative TPS will be a new generation low density/high porosity carbon fiber preform impregnated with phenolic resin. The vehicle is being designed to withstand the high aerodynamic heating down to 50 km altitude and then has to be disintegrated for safety reasons.

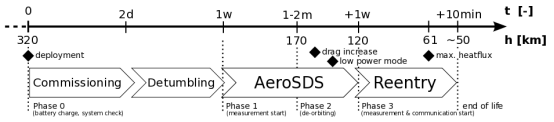

Figure 6: QARMAN flight scenario. Courtesy: Thorsten Scholz

3.2. Payload Design Methodology

There is a number of references in the literature concerning the space mission designs (i.e [15]). This paper focuses on the payload design only, rather than other subsystem designs. It should be stated that CubeSat platform has a number of significant differences when compared to the generic unmanned space missions. Therefore a methodology has to be built for a mission like QARMAN where the satellite platform meets aerothermodynamic research.

The payloads of a space mission are derived from the mission objectives and requirements. The proposed steps for a successful payload design are summarized below. One should consider that the steps are for design purposes and therefore do not include the flight model environmental tests, the deployer interface tests and the launch acceptance tests.

- *Baseline:* State the Mission Objectives and Mission Requirements.

Payload Design Steps

- Stating the Problem and Defining the Payload Objectives
- Subject Trades: Measurement Parameters/Magnitudes
- Preliminary Investigation: CFD, Experiments and Determining the 'Performance Thresholds'.

- Measurement Techniques: Mass, Volume, Power Consumption, Accuracy, Data Size, TRL, Cost and Feasibility in a CubeSat platform
- Preliminary Configuration and Operations Concept
- Ground Testing Methodology and Extrapolation to Flight
- Risk Analysis
- Success Criteria: Considering the previously defined 'performance thresholds'.
- Document and Iterate

3.3. Payloads for Aerothermodynamic Research

The measurement techniques for the chosen subjects have to be chosen carefully due to the strict platform constraints and complex physics. Some of the sensors will be developed in house based on already existing techniques. The final selection of the aerothermodynamic payloads will be made after further scientific investigation. Tables 3 and 4 show the preliminary set of sensors and their mass/power/data budgets including margins. The Phase column shows when the relevant sensor is active according to the QARMAN flight scenario [16] which leads to a power and data budget per each phase. The most critical phase in terms of power and data size is the Re-entry 'Phase 3' since the vehicle will be relying on charged batteries and the data transfer will be performed by Iridium Constellation [17]. The analysis shows that the aerothermodynamic payloads are suitable with the allowed budgets and the mission is feasible. The data acquisition unit will be developed by VKI and is currently estimated as 1 PCB with 200 g and 0.2U volume.

The conceptual design of the payload accomodation is depicted in Fig. 7. Among all, the payload "XPL01" is discussed here further in detail. XPL01 covers the measurements related to the environment, the ablation and the efficiency of the TPS. The TPS will have two thermal plugs having six type K or type R thermocouples. This approach is adopted from the MISP plugs in MEDLI project which is the pressure, temperature and recession monitoring of the Mars Science Laboratorys entry vehicle [18]. The thermal plugs will be placed on one side radially assuming an symmetric flow around the nose. Additional two thermocouples will be placed in the back of the TPS at the interface between the insulator and the subsystems for health monitoring. The four thermocouples of the thermal plugs will be located based on the brief analysis shown in Fig. 8. To catch the temperature trend at a given time, having multiple thermocouples at the first 30% of the TPS will increase the sensitivity. Therefore the thermocouples are initially proposed to be placed at 2.5, 5, 10, 20, 30 mm and one at 40 mm which can detect the constant temperature plateau together with the thermocouple at the back of the TPS. The locations will be finalized after the test campaigns explained in Section 2.

Two pressure measurements are foreseen for the TPS in the axisymmetric direction on the opposite side of the thermal plugs within another payload: XPL02.

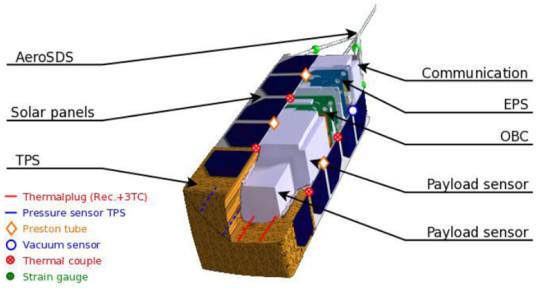

Figure 7: QARMAN Payload Accommodation

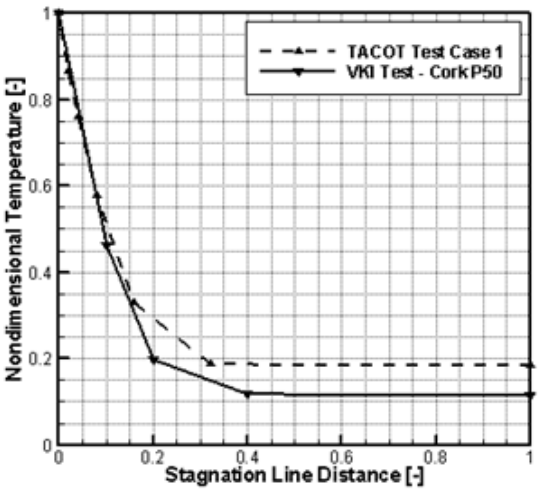

Figure 8: Temperature distribution at random time along the stagnation line for two different materials: Cork P50 tested at VKI [24] and the theoretical material TACOT [25]

Table 3: Proposed Set of Sensors.

Investigated Challenge	Parameter to measure	Sensor	Total Mass [kg]	Energy /Sensor [Wh]
TPS Efficiency	Recession	12 x TC	0.012	3
TPS & Environment	Pressure	2 x Pressure Sensor	0.050	8.33
Stability	Pressure	2 x Pressure Sensor	0.050	168
Rarefied Flow Conditions	Low Pressure / Vacuum	1 x Vacuum Sensor	0.011	75.6
				75.6
Shear Force, Laminar to Turbulence Transition	Skin Friction	4 x Preston Tube	0.050	336
				8.33
Off-Stagnation Temperature Evolution	Temperature	10 x TC	0.010	168
				3
ATD Environment	Species	1 x Spectrometer	0.084	0.208
		1 x Photodiode	0.001	8.3
Total			0.391	6250

Table 4: Proposed Set of Sensors - continued.

Investigated Challenge	Data Size /Meas. [bit]	Phase	Total Data Size [KB /Phase]	Ref.
TPS Efficiency	14	3	12.6	[19]
TPS & Environment	10	3	0.15	[20]
Stability	10	2	302.4	[21]
Rarefied Flow Conditions	10	1	151.2	[22]
		2	151.2	
Shear Force, Laminar to Turbulence Transition	10	2	60.48	[20]
		3	0.15	
Off-Stagnation Temperature Evolution	14	2	211.68	[19]
		3	1.05	
ATD Environment	28	3	3.5	[19; 23]
	10	3	0.15	
Total	338		50.3	

4. Conclusion

Hypersonic flow testing is very challenging and complex due to the high temperature effects. The numerical and experimental methods have to be validated by real flight tests, which come with very high costs. A flight-to-ground extrapolation methodology is proposed with regard to the existing ground-to-flight extrapolation methodology. The main contribution is that it includes unconventional spacecraft geometries that are not studied up to now.
In order to make a correct flight-to-ground extrapolation one has to determine accurately the flow conditions in the ground facility since the full simulation rule is to duplicate the pressure, enthalpy and the velocity gradient at the boundary layer edge. The first ground facility type under investigation is subsonic plasma windtunnels. At VKI Plasmatron, current enthalpy determination tools have significant uncertainties due to heat flux and pitot pressure uncertainties and the poor knowledge of the reference copper catalycity, changing with the flow conditions. Three methods are discussed in this paper: enthalpy probe, Damköhler probes and the spectroscopy tool REDES. The aim is to improve the free stream enthalpy determination accuracy in VKI Plasmatron.
Additionally, a velocity gradient determination procedure is proposed for the non-axisymmetric blunt shapes. The ground testing methodology is divided into four different campaigns and the results of the first campaign are presented.

The developed methodologies are to be used on QARMAN vehicle design and ground testing which is a 3U CubeSat that has an ablative TPS mounted in the first unit. The mission objective is to make a low cost real flight test to provide data for validation of numerical tools and ground testing methods. It will be launched with QB50 CubeSats. The in-flight aerother-

modynamic experiment design process is presented for the constraining CubeSat platform. The XPL01 discussed further in detail.

Acknowledgments

QARMAN project is partially supported by the European Community Framework Programme 7, Grant Agreement no. 284427 in the framework of QB50 Project.

The authors are thankful to Dr. Cem O. Asma for his sincere interest and kind guidance. The authors are grateful to Mr. Pascal Collin for his unique dedication to the operation of the VKI Plasmatron facility.

References

[1] Qb50 project, www.qb50.eu, last accessed: 10.02.2013.

[2] A. Kolesnikov, Extrapolation from high enthalpy tests to flight based on the concept of local heat transfer simulation, RTO AVT Course on "Measurement Techniques for High Enthalpy and Plasma Flows", Rhode-Saint-Genese, Belgium (October 1999).

[3] D. G. Fletcher, Nonintrusive diagnostic strategies for arcjet stream characterization, RTO AVT Course on Measurement Techniques for High Enthalpy and Plasma Flows, Rhode-Saint-Genese, Belgium (October 1999).

[4] H. W. Krassilchikoff, Procedures for the determination of the cold copper catalycity, Master's thesis, von Karman Institute for Fluid Dynamics, vKI-PR2006-18 (2006).

[5] G. de Croombrugghe, Investigation of gas surface interactions in plasma wind tunnels for catalycity characterization, Master's thesis, von Karman Institute For Fluid Dynamics, vKI PR 2012-01 (2012).

[6] M. Marotta, Investigation on the driving phenomena characterization gsis in plasmatron facility, Master's thesis, von Karman Institute for Fluid Dynamics, vKI PR 2011-17 (2011).

[7] J. A. Fay, F. R. Riddell, Theory of stagnation point heat transfer in dissociated air, in: VKI, An Introduction to Hypersonic Aerodynamics 13 p(SEE N 90-13334 05-02), 1958.

[8] J. Boison, A. Curtiss, An experimental investigation of blunt body stagnation point velocity gradient, ARS Journal (1959) 130–135.

[9] L. Lees, Recent developments in hypersonics, ARS Semi-Annual Meeting, San Francisco, California, 1957.

[10] E. V. Zoby, E. M. Sullivan, Effects of corner radius on stagnation-point velocity gradients on blunt axisymmetric bodies, Tech. Rep. NASA-TM-X-1067, NASA (1965).

[11] J. C. Ellison, Experimental stagnation point velocity gradients and heat transfer coefficients for a family of blunt bodies at mach 8 and angles of attack, Tech. Rep. TN D-5121, NASA Langley (1969).

[12] E. V. Zoby, Empirical stagnation point heat transfer relation in several gas mixtures at high enthalpy levels, Tech. Rep. TN D-4799, NASA Langley (1968).

[13] H. Olivier, Influence of the velocity gradient on the stagnation point heating in hypersonic flow, Shock Waves 5 (1995) 205–216.

[14] W. Hayes, R. Probstein, Hypersonic flow theory, Academic press, 1959.

[15] J. Wertz, W. Larson, Space Mission Analysis and Design, Microcosm Press, 1999.

[16] T. Scholz, Mission scenario, QARMAN Deliverable 2.2 (December 2012).

[17] T. Scholz, Sub-systems: Eps, obc, comm, QARMAN Deliverable 3.2.1 (December 2012).

[18] N. Cheatwood, M. Wright, M. Munk, E. Martinez, J. Herath, Medli: From instrumentation concept to flight hardware, 7th International Planetary Probe Workshop, Barcelona, Spain, 2010.

[19] Omega engineering, www.omega.com/temperature/pdf/tc_colorcodes.pdf, last accessed: 21.01.2013.

[20] M. J. Gazarik, A. Little, F. Cheatwood, M. J.Wright, J. A. Herath, E. R. Martinez, F. M. Munk, J. Novak, H. S. Wright, Overview of the medli project, IEEE Aerospace Conference, Montana, USA, 2008.

[21] Motorola, http://www.datasheetcatalog.org/datasheet/motorola/MPXS4115AC6U.pdf, last accessed: 21.01.2013.

[22] Mks instruments, http://www.mksinst.com/product/product.aspx?ProductID=644, last accessed: 21.01.2013.

[23] Rgb lasersystems, http://www.rgb-laser.com/data/data_pdf_datasheet/Qmini%20data%20sheet%20for%20web.pdf, last accessed: 21.01.2013.

[24] G. Bailet, Feasibility analysis and conceptual design of an atmospheric re-entry cubesat demonstrator, Master's thesis, PR2011-02, von Karman Institute for Fluid Dynamics, Rhode-Saint-Genese (2011).

[25] J. Lachaud, A. Martin, I. Cozmuta, B. Laub, Ablation workshop test case,, 4th Ablation Workshop, Albuquerque, New Mexico, 2011.

Mission Analysis for a Network of Atmospheric Science and In-Orbit Demonstration CubeSats

Thorsten Scholz

Aeronautics and Aerospace Department, von Karman Institute for Fluid Dynamics, Belgium, scholz@vki.ac.be

Supervisor: Patrick Rambaud

Associate Professor, Aeronautics and Aerospace Department, von Karman Institute for Fluid Dynamics, Belgium, rambaud@vki.ac.be

University Supervisor: Stefanos Fasoulas

Professor, Institut für Raumfahrtsyteme, Universität Stuttgart, fasoulas@irs.uni-stuttgart.de

Abstract

In the framework of QB50 a trajectory propagation tool is under development to simulate the orbital motion of the satellites. The highly customable software provides simple and scriptable operation overcoming the lack of flexibility in available programs when simulating multiple spacecrafts. This paper describes the assessment of several input parameters, like atmospheric models, initial orbital elements and aerodynamic coefficients, needed for the simulation of QB50 and presents the influence of them on the important parameter orbital lifetime. Since the lower thermosphere is highly undersampled resulting in large variations between different atmospheric models, a sensitivity analysis is needed to determine the envelope for the satellite motion.

Keywords: QB50, orbit simulation, trajectory simulation, atmospheric model

1. Introduction

In the framework of the QB50 project a network of 50 CubeSats will be launched to perform in-situ measurements of the spatial and temporal variation of atmospheric properties in the lower thermosphere at an altitude of 350 km to 150 km [1]. CubeSats are small nano-satellites with different form factors available. The smallest possible size is 10 x 10 x 10 cm. The CubeSats for QB50 will be 2U or 3U (units) with 20 or 30 cm length. The project will demonstrate the possibility of using the small satellites as efficient and low-cost technology demonstrators. QB50 will be the first simultaneously launched CubeSat network and helps in gaining a better understanding of such complex missions.

The choice for conducting measurements in the lower thermosphere is influenced by several factors and constraints. The atmospheric properties in this region and their relationship to Earth's climate and space-weather like sun storms are yet not well known [2]. This leads to larger uncertainties in lifetime and trajectory simulations, which the recently uncontrolled and not precise predictable re-entries of UARS, Rosat or Phobos-Grunt have shown. Another influence factor for the choice of orbit is the mitigation of space debris creation and fulfillment of the 25

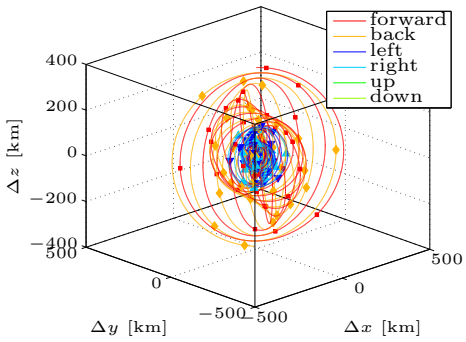

Figure 1: Influence of deployment direction on CubeSat spreading ($\Delta v = 1.5 \frac{m}{s}$, $t = 1\,d$, rotating frame)

year lifetime requirement.

The mission design of QB50 will be challenging and includes several points to be looked at. First the development of a suitable deployment strategy for the 50 CubeSats is mandatory to reduce the collision risk to a minimum. The deployment also effects the spreading and therefore the global distribution of the satellites. Figure 1 shows the distance to the deployment origin after 1 day for different directions relative to the flight direction. The deployment of the satellite and the in-orbit motion with its impact on the communication and power budget will be analyzed using a trajectory simulation tool. The necessary input like parameters, like the atmospheric environment or initial orbit (see Figure 2), have to be investigated and the associated uncertainties incorporated into the simulations. The propagation tool will be validated with other commercial available software tools like STK[1] or ASTOS[2].

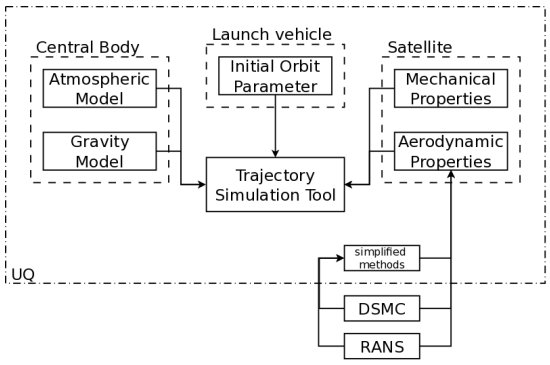

Figure 2: Schematic overview of the trajectory tool

2. Satellite motion

The motion of a satellite can be approximately expressed by solving the two-body problem in an inertial reference frame. The only force acting on the satellite in this simplified case is the gravity attraction of the central body. Using Newton's law the differential equation for the motion of a spacecraft around Earth can be described as following

$$\ddot{\mathbf{r}} = \frac{\mu}{r^2}\mathbf{e}_r = \ddot{\mathbf{r}}_g, \tag{1}$$

where r is the distance between the two objects, μ the gravitational parameter of Earth and $\mathbf{e}_r$ the unity vector pointing from the Earth to the satellite. This equation is only valid for a spherical gravity field and as already mentioned, when no other forces are acting on the satellite. The solution to this problem can be expressed analytical as a Kepler orbit using the six orbital elements to describe the orientation of the orbit plane and the position inside the plane. It is well described and can be found in text books like [5].

However in reality, additional forces are acting on the satellite in orbit beside gravity. The contribution from these forces can be incorporated by introducing additional accelerations into equation 1 leading to the perturbed equation of motion.

$$\ddot{\mathbf{r}} = \ddot{\mathbf{r}}_g + \ddot{\mathbf{r}}_{pg} + \ddot{\mathbf{r}}_{tb} + \ddot{\mathbf{r}}_t + \ddot{\mathbf{r}}_a + \ddot{\mathbf{r}}_{srp} + \ddot{\mathbf{r}}_{other} \tag{2}$$

Depending on the orbit altitude some perturbations can be neglected due to their small contribution. The magnitudes of various perturbations are shown in Figure 3 for different altitudes. For low earth orbits (LEO) the most important contributions are due to gravity (spherical gravity field $\ddot{\mathbf{r}}_g$, inhomogeneous gravity field $\ddot{\mathbf{r}}_{pg}$) of the central body and aerodynamic forces ($\ddot{\mathbf{r}}_a$) introduced by the atmosphere. With increasing distance, the third body perturbations ($\ddot{\mathbf{r}}_{tb}$) from the Moon, Sun and other planetary objects are getting more and more important. The solar radiation pressure ($\ddot{\mathbf{r}}_{srp}$) is independent of the altitude but will vary along the orbit due to the changing angle of the spacecraft towards the Sun and eclipse periods. The influence on LEOs of the later mentioned perturbations can be regarded as small [6] and are therefore currently not implemented in the trajectory tool. However the integration of these models are planned for the future. Artificial disturbances like thrusting ($\ddot{\mathbf{r}}_t$) can be also considered in the equation of motion.

It is necessary for the simulation of the satellite motion to model the perturbations and to evaluate the functions for the given position, velocity and attitude of the spacecraft, described by the state vector $\mathbf{s}$. Due to the complexity added by the perturbations, the problem is not longer analytical solvable. The ordinary differential equation can be solved using an initial state and approximate the solution using time-stepping schemes like Runge-Kutta methods [7][8].

3. Input parameters

An overview of the different input parameters and models for the trajectory simulation tool is given in

[1] Systems Tool Kit [3], Analytical Graphics, Inc.

[2] AeroSpace Trajectory Optimization Software [4], Astos Solutions GmbH

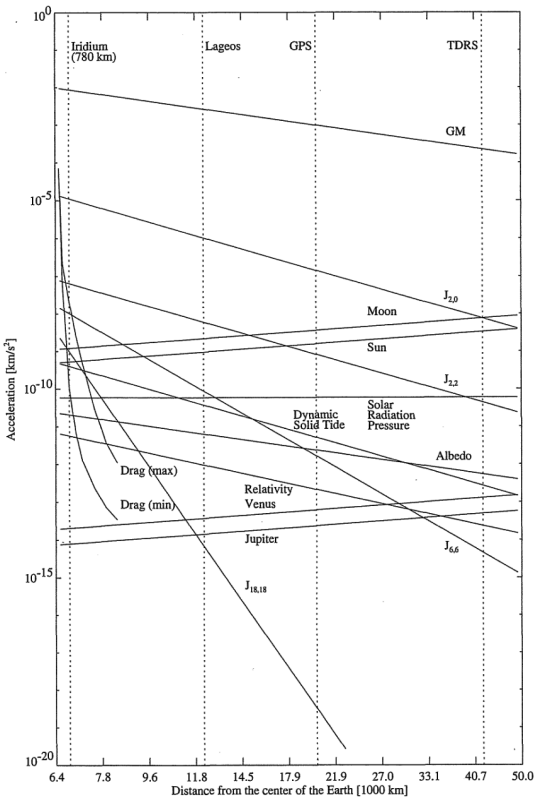

Figure 3: Order of magnitude of various perturbations of a satellite orbit [6]

Figure 2 and the preliminary results of the assessment performed so far will be presented in the following. For each simulation, the standard values for a 2U CubeSat have been used when not specified differently. The mass is 2 kg, drag coefficient $C_D = 2.3$, reference area $A_{ref} = 0.01\,m^2$ and the NRLMSISE00 atmospheric model has been used with $F_{10.7} = F_{10.7A} = 133.0\,sfu$ and $A_p = 43\,nT$ as input parameters.

The initial Kepler elements in J2000 frame are:

- semi-major axis $a = 6699\,km$
- RAAN $\Omega = 40°$
- inclination $i = 70°$
- eccentricity $e = 0$
- true anomaly $\nu = 75°$

3.1. Simulation parameters

Different numeric integration schemes have been implemented in the trajectory tool using a single or multi-step approach with fixed or variable step size. The current schemes available in the tool are going up to 8th order allowing larger time steps with

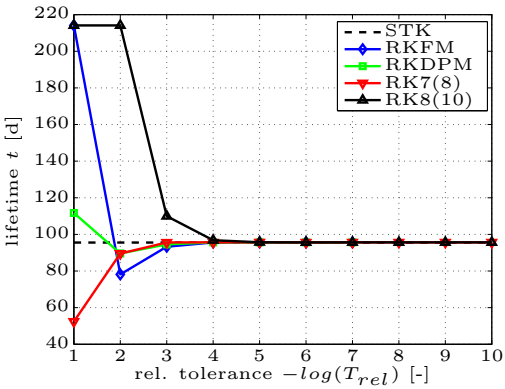

Figure 4: Influence of relative tolerance for different integration schemes ($T_{abs} = 1$, $\Delta t_{min} = 1s$)

higher accuracy by performing more intermediate steps. The performance of the schemes, RK Fehlberg 4(5) , RK Dormand Prince 4(5), RK7(8) and RK8(10) [9][10][11][12], have been compared using a typical QB50 CubeSat orbit. The two numbers inside the name represent the two orders used in the scheme to calculate the integrated state and to estimate the truncation error. The local truncation error $\mathbf{e}$ for each step is estimated by comparing the results obtained for different orders, e.g for the Runge-Kutta Fehlberg method the result with 4th (state $\mathbf{s}_{i,l}$) and 5th (state $\mathbf{s}_{i,h}$) order can be obtained. The relative tolerance is multiplied by the maximum value of last and current state and compared with the truncation error, see equation 3. Figure 4 shows the calculated lifetime for different values of the relative tolerance T_{rel} for each step. Similar an absolute tolerance T_{abs} can be specified for the integration to restrict the time step further and in cases where the state variable is equal to zero. For the convergence study, the absolute tolerance was set to 1. The time step will be adjusted automatically each integration step to fulfill the tolerance requirements [7]. An upper and lower bound for the time step can be specified to limit the adjustment process.

$$\mathbf{e} = |\,\mathbf{s}_{i,h} - \mathbf{s}_{i,l}\,| \leq |\,T_{rel} \cdot max(\mathbf{s}_{i,l}, \mathbf{s}_{i-1})\,| + T_{abs} \quad (3)$$

The required relative tolerance to obtain a *good* simulation results depends on the used methods and on the precision demands of the result. With a relative tolerance of $T_{rel} = 10^{-5}$ the orbital lifetime matches the one obtained with STK. However the higher precision necessary for the deployment and collision analysis requires a lower relative and absolute tolerance.

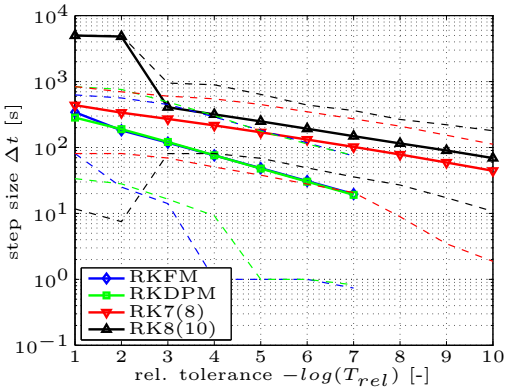

Figure 5: Minimum, average and maximum step size for different integration schemes ($T_{abs} = 1$, $\Delta t_{min} = 1s$)

The average time step distribution for the convergence study is shown in Figure 5 for the different schemes. The maximum and minimum time step for each simulation are given as dashed lines. Obeying the same relative tolerance, the possible time step for the high order schemes is approximately one magnitude larger compared to the 4th order schemes. The computation time for the high order methods is significantly shorter due to the larger time step despite the larger number of function calls to the model.

3.2. Atmospheric model

The knowledge of the neutral density along the orbit of a spacecraft is mandatory for the calculation of the aerodynamic forces and moments induced by the residual atmosphere of the Earth.

Nowadays a couple of atmospheric models based on orbital decay observations or experimental measurements exist who predict the composition, temperature and density for a given time and position. These models are based on relations between historic measurements of the atmosphere and the solar activity around the measurement time point as the main influencing parameter. With more and more data sources available the accuracy of these models advanced over time and typically an error less than 10-20% for the neutral density can be expected nowadays [13], even with the models improving over the last few years due to measurements obtained by the GRACE and CHAMP mission [14]. However due to lack of proper understanding of all processes taking place in the atmosphere, the error can not be reduced significantly any further without additional data.

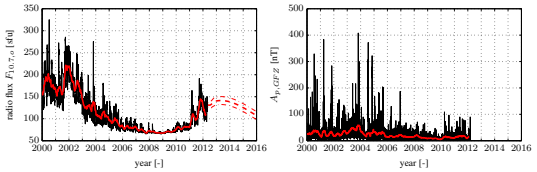

(a) solar radio flux [21][22] (b) geomagnetic index [23]

Figure 6: Historic values for solar activity indices

A second type of atmospheric models exists where the whole atmosphere is simulated to obtain the properties like composition, neutral density or temperature. These physical models are computational demanding compared to the models based on simple relations with experimental data. They are solving the mass, momentum and energy equations using a structured three dimensional grid for a large part of the atmosphere.

The performance of different models comprising both groups has been studied and the results in terms of neutral mass density compared. From the available experimental models, JB2006 [15], JB2008 [14], NRLMSISE00 [16], DTM2000 [17] and DTM2009 [18] have been choosen; from the physical models, GITM [19] and TIEGCM [20] have been selected.

The solar activity is the most important input parameter for all atmospheric models and is typically described by the solar radio flux $F_{10.7}$, which quantifies the solar radiation at an wavelength of 10.7 cm, an 81-day centered average value of the flux $F_{10.7A}$ and the geomagnetic index A_p. Recently additional parameters have been developed to include the solar radiation at different wavelength to improve further the accuracy of the models [14]. Figure 6 shows the solar activity for the last solar cycle of 11-years and, if available, predicted values for the next years. The predicted average value for the solar radio flux from [21] is given with uncertainties for different confidence levels, the 1 σ value is given as dashed lines in the figure. This uncertainty however does not represent the temporal variation of the flux itself. Therefore the distribution of both parameters for the launch year was obtained by analyzing the historic data for a representative year in the last solar cycle. Figure 7 shows the normalized results for the year 2003 including the fitted normal and log-normal distribution function.

With the distribution and prediction uncertainty, different cases can be constructed representing higher

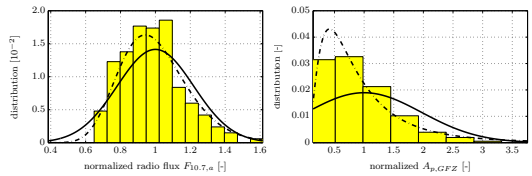

(a) solar radio flux (b) geomagnetic index

Figure 7: Distribution function for launch date equivalent year (2003)

or lower solar activity for the launch year. A typically density distribution for one altitude level obtained by the NRLMSISE00 model is shown in Figure 8. The diurnal bulge due to the increased solar radiation and the continental effects are clearly visible.

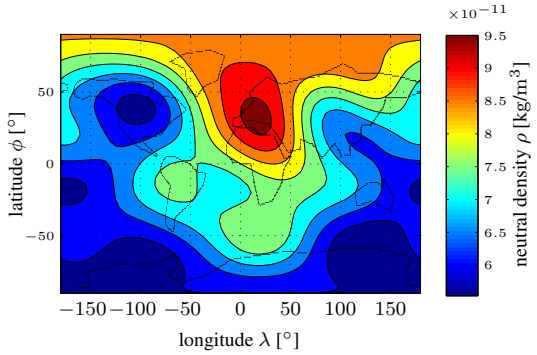

Figure 8: Neutral mass density for NRLMSISE00 at 250 *km* of altitude (1 Oct. 2014, UTC noon)

For better comparison with the US76 standard atmosphere, the average of the density was taken for each calculated altitude level. The change in density over altitude for different models is shown in Figure 9. Density values obtained by measurements of satellite drag using accelerometers on the GRACE/CHAMP mission [24] are shown in black. The error bar shows the average (black cross); maximum and minimum value of the satellite data for the period of one day are given as upper and lower bound.

With increasing altitude the difference between the various models increases which shows clearly the need of QB50 to broaden the database of atmospheric measurements in this altitude region. The detailed assessment is given in [25]. However even with the comparable output from different models, not all recent developments and changes in the atmosphere are included in the underlying database for the models.

Therefore these models can not take into account

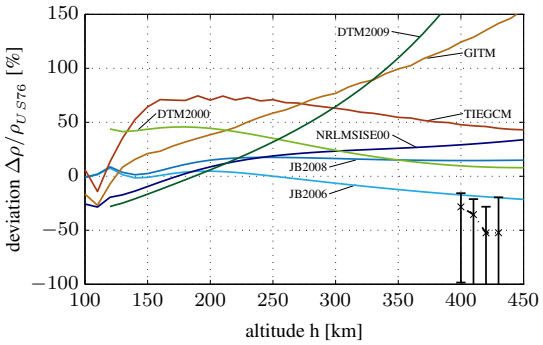

Figure 9: With US76 model normalized neutral density for different models

recent changes in the atmosphere like the observed decrease in neutral density over the past years. These changes have to be quantified and included separately in the orbital dynamics simulation. As discussed in [26] and [27], the global neutral density can be obtained with the help of the derived drag value for near-Earth satellites. Seasonal variations and other included biases in the obtained measurement have to be removed and the resulting density can be compared to the density for different atmospheric models using the measured input parameters to describe the solar activity. It can be observed that the neutral density decreases more than the model with the observed solar activity predicted due to the increase in CO_2 concentration in the lower atmosphere [27]. The trend given in the paper represents a decrease of 3.55% per decade and was obtained by a curve fit with the annual average values; the trend varies from -5% for solar minimum and -2% for solar maximum. Abnormalities like this are unpredictable and still not fully explainable today. Half of the decrease can be attributed to the lower solar radio flux and an increase of the CO_2 cooling [28] but the other half has still to be examined in more detail.

3.3. Initial orbit

The initial orbit elements have a strong impact on the propagation and the mission. The most important parameters are the semi-major axis, the longest diameter of the orbit ellipse, the inclination, the angle between the equatorial plane and orbital plane, and the true anomaly describing the position along the orbit. Only a circular orbit has been investigated for QB50 leaving the argument of periapsis undefined.

The variation in lifetime with change of semi-major axis or orbit altitude for circular orbits is shown in

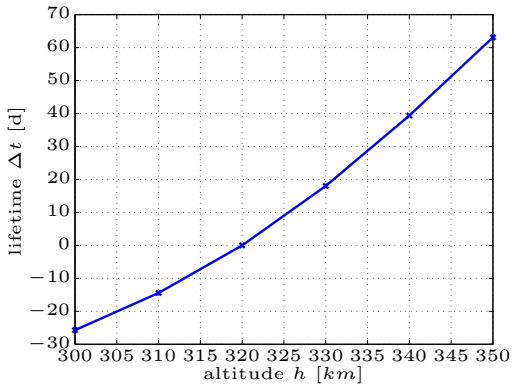

Figure 10: Influence of semi-major axis on lifetime

Figure 10 normalized with the initially planned QB50 orbit parameters (320km altitude). The exponential increase of lifetime due to decrease in density with higher altitude is already visible for the small variations. An additional lifetime of 60 days could be achieved by lifting the orbit to 350km still below ISS altitude.

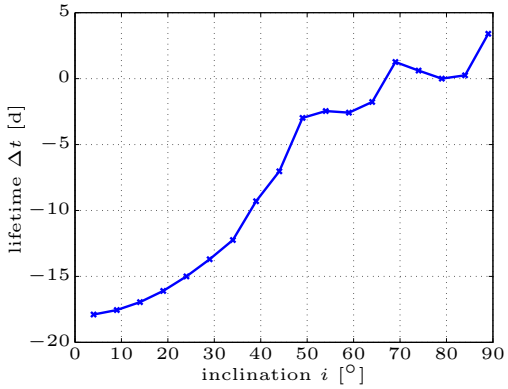

Figure 11: Influence of inclination on lifetime

The inclination has a similar effect on the lifetime which is shown in Figure 11. With increase the lifetime increases since the satellites passes more often and longer through the low density regions. Through the non-regular shape of the Earth with the flattening on the poles, the density there is smaller compared to equatorial regions.

The influence of the true anomaly on the lifetime for a circular orbit is not as intuitive as for the other parameters. By changing the initial position along a orbit, one could expect that there is no effect on the lifetime. However due to the conversion from Kepler elements to Cartesian or other coordinates used in the propagation the irregularity of the shape of the Earth is introduced again into the problem. Figure 12 shows the first orbit for two different anomalies (blue $\nu = 20°$, red $\nu = 75°$) using the developed trajectory tool and STK for comparison. The initial position is marked in both cases with a black X at the correct initial altitude. Due to the fact, that the velocity in both points are the same, the orbit shape differs and the satellite is exposed to different neutral densities during it's lifetime. The impact of the true anomaly on the lifetime is shown in Figure 13. The increase in lifetime corresponds to the higher orbit altitude with less initial drag.

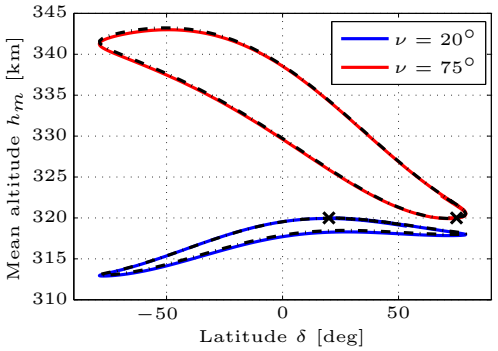

Figure 12: Altitude relative to mean Earth radius for first orbit shown for a true anomaly of 20° and 75° (STK black dashed line and trajectory simulation tool colored lines)

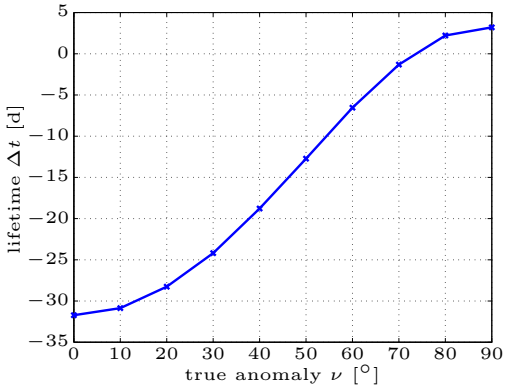

Figure 13: Influence of true anomaly on lifetime

3.4. Aerodynamic characterization

Detailed knowledge of the aerodynamic forces and moments is necessary to calculate the perturbations on the spacecraft induced by the residual atmosphere. The lift force is typically neglected when performing 3 DOF simulation to determine the satellite motion leaving the drag coefficient as the important parameter to be specified.

Different approaches can be found in the literature to estimate or calculate the drag coefficient. Oltrogge used satellite observations and motion to predict the drag coefficient using an inverse approach. He analyzed the orbits of 47 CubeSats and calculated the coefficient for each satellite from the orbit decay. Since no detailed knowledge of the attitude, mass and exposed area is available for most CubeSats, the resulting values show a large scattering, which is shown in Figure 14. However the average value for the drag coefficient is approximately around 2.3 [29].

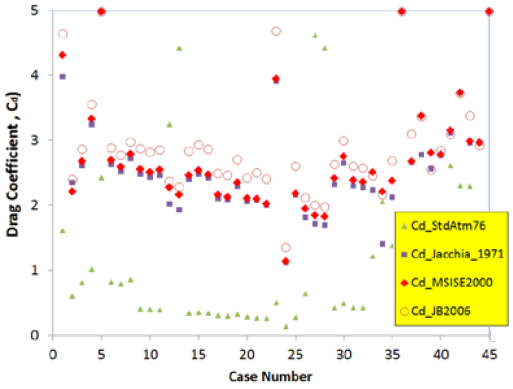

Figure 14: Best-fitting drag coefficient for different CubeSat Cases [29]

Sentman proposed already 1961 the free molecule flow theory (FMT) to calculate the exact forces and moments acting on the satellites exposed to rarefied environment [30]. The pressure distribution along the spacecraft could be obtained by calculating the angle between the free stream and each satellite surface. The drag coefficient is calculated by summarization of the forces in velocity direction. The FMT method has been implemented into the trajectory simulation tool to calculate on demand the aerodynamic coefficients beside the possibility to specify the coefficients directly.

For altitudes of 100km or above the atmosphere is so rarefied that the flow-field can not be calculated with the help of RANS solver; stochastic methods simulating each particle or a subset of them are mandatory to use. Due to the stochastic approach this method is more computational demanding than the FMT method based on the surface inclination. The computation time can be reduced by increasing the number of simulated particles resulting in higher memory consumption, however the duration is still orders of magnitudes above the simplified theory. Figure 15 shows the flow field for a 2U standard CubeSat with antennas using RGDAS. The Direct Simulation Monte Carlo (DSMC) tool RGDAS is available at VKI and has been used to generate a database with aerodynamic coefficients for the standard 2U and 3U CubeSat together with the Institute of Theoretical and Applied Mechanics (ITAM). The obtained values can be used to verify the results calculated with the FMT method.

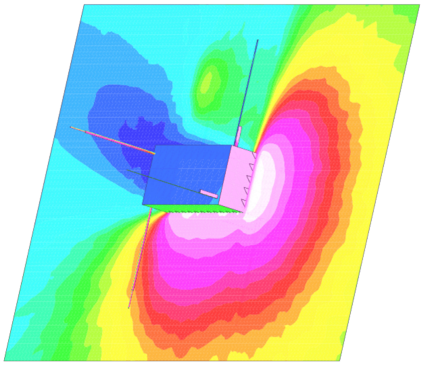

Figure 15: Visualization of the flow field around a 2U standard CubeSat with deployed antennas and Langmuir probes (ITAM)

A reduced set of obtained drag coefficients for the altitude of 350 km are given in the table 1 obtained by VKI and ITAM.

Table 1: Drag coefficient for different geometries, angle of attack and side-slip angle at $h = 350\,km$

Geometry	α [°]	β [°]	C_D [-]
2U	0	0	2.8
2U	10	10	3.6
2U	90	45	6.0
3U	0	0	3.1
3U	10	10	4.5
3U	90	45	10.3
2UwA	0	0	3.35

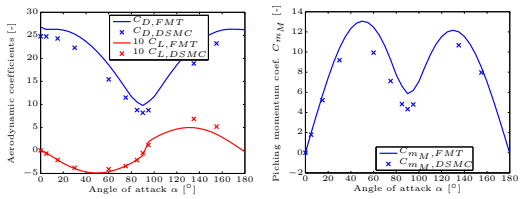

(a) drag and lift coef. (b) pitching moment coef.

Figure 16: DSMC and FMT results for QARMAN with AeroSDS at altitude $h = 320\,km$

In the current implementation in the trajectory code, the difference between the FMT method and the DSMC results are in the order of 20 % for the drag and lift coefficient which is shown in Figure 17 for QARMAN, the re-entry CubeSat of VKI with deployed AeroSDS. The drag and lift coefficient results obtained with DSMC and FMT are given in Figure 16a. The large drag coefficient results from the increased exposed area due to the deployed panels. However for easier comparison the same reference area $A_{ref} = 0.01\,m^2$ as for standard CubeSats has been used for the calculation of the aerodynamic coefficients. The pitching momentum coefficient is shown in Figure 16b. The deviation between the two methods is again in the range of 20 %.

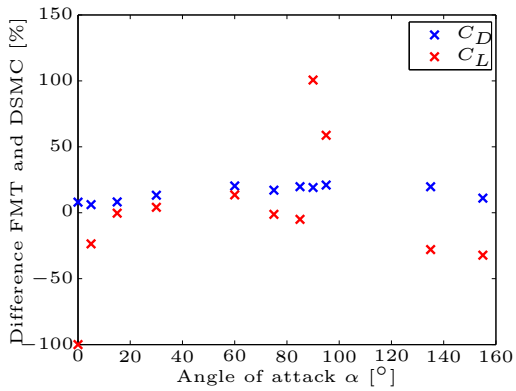

Figure 17: DSMC and FMT comparison for QARMAN with AeroSDS at altitude $h = 320\,km$

4. Conclusion

The current status of the trajectory simulation tool and the assessment of the input parameters for the simulation has been reported. The validation of the tool continues and comparisons to other high precision simulation data [31] are planned for the future. Beside these efforts, further improvements will be incorporated like 6 DOF simulation, useful for the QARMAN orbit and re-entry trajectory calculation, and detailed power and communication analysis functions.

Acknowledgments

The research leading to these results has received funding from the European Community's Seventh Framework Programme ([FP7/2007-2013]) under grant agreement n° 284427 for the QB50 Project.

References

[1] J. Muylaert, QB50: An International Network of 50 Cubesats for Multi-Point, In-Situ Measurements in the Lower Thermosphere and for Re-Entry Research, no. ESA Atmospheric Science Conference, Barcelona, Spain, 2009.

[2] R. Reinhard, C. O. Asma, J. Muylaert, The QB50 Project : A network of 50 CubeSats, System (2012) 1–5.

[3] Analytical Graphics, Inc., STK - Systems Tool Kit, `http://www.agi.com/STK`, online; accessed 11-Februar-2013 (2013).

[4] Astos Solutions GmbH, AeroSpace Trajectory Optimization Software, `http://www.astos.de/products/astos`, online; accessed 23-November-2012 (2012).

[5] D. Vallado, W. McClain, Fundamentals of Astrodynamics and Applications, Space Technology Library, Springer, 2001.

[6] O. Montenbruck, E. Gill, Satellite orbits: models, methods and applications, 2005.

[7] E. Haier, S. Norsett, G. Wanner, Solving Ordinary Differential Equations I, Nonstiff Problems, Section III.

[8] D. Griffiths, D. Higham, Numerical Methods for Ordinary Differential Equations: Initial Value Problems, 2010.

[9] E. Fehlberg, Classical fifth-, sixth-, seventh-, and eighth-order Runge-Kutta formulas with stepsize control, October (October).

[10] P. Prince, J. Dormand, High order embedded Runge-Kutta formulae, Journal of Computational and Applied ....

[11] N. Zealand, History of Runge-Kutta methods, Applied Numerical Mathematics 20 (1996) 247–260.

[12] T. Feagin, A tenth-order Runge-Kutta method with error estimate, Proceedings of the IAENG Conf. on Scientific ... (4) (2007) 4–9.

[13] D. A. Vallado, D. Finkleman, A Critical Assessment of Satellite Drag and Atmospheric Density Modeling, Specialist (2008) 1–31.

[14] B. R. Bowman, W. K. Tobiska, F. A. Marcos, C. Y. Huang, C. S. Lin, W. J. Burke, A New Empirical Thermospheric Density Model JB2008 Using New Solar and Geomagnetic Indices, Direct (August).

[15] B. R. Bowman, W. K. Tobiska, F. A. Marcos, A new empirical thermospheric density model JB2006 using new solar indices, in: AIAA, 2006.

[16] J. M. Picone, A. Hedin, D. Drob, A. Aikin, Nrlmsise-00 empirical model of the atmosphere: Statistical comparisons and scientific issues, Journal of Geophysical Research 107 (A12) (2002) 1–16.

[17] S. Bruinsma, G. Thuillier, F. Barlier, The DTM-2000 empirical thermosphere model with new data assimilation and constraints at lower boundary: accuracy and properties, Journal of atmospheric and solar-terrestrial physics 65 (2003) 1053–1070. doi:10.1016/S1364-6826(03)00137-8.

[18] S. Bruinsma, D. Tamagnan, R. Biancale, Atmospheric densities derived from CHAMP / STAR accelerometer observations, Planetary and Space Science 52 (2004) 297 – 312. doi:10.1016/j.pss.2003.11.004.

[19] A. J. Ridley, Y. Deng, G. Tóth, The global ionosphere thermosphere model, Journal of Atmospheric and Solar-Terrestrial Physics 68 (2006) 839–864. doi:10.1016/j.jastp.2006.01.008.

[20] R. G. Roble, E. C. Ridley, A. D. Richmond, R. E. Dickinson, A coupled thermosphere/ionosphere general circulation model 15 (1988) 1325–1328.

[21] National Oceanic and Atmospheric Administration - National Geophysical Data Center, Solar Radio Flux, ftp://ftp.ngdc.noaa.gov/STP/SOLAR_DATA/SOLAR_RADIO/FLUX, online; accessed 15-October-2012 (2012).

[22] National Oceanic and Atmospheric Administration - Space Weather Prediction Center, Solar Radio Flux predictions, http://www.swpc.noaa.gov/ftpdir/weekly/Predict.txt, online; accessed 15-October-2012 (2012).

[23] Deutsches GeoForschungsZentrum, Helmholtz-Zentrum Potsdam, Geomagnetic index, http://www.geomag.bgs.ac.uk/cgi-bin/apindex, online; accessed 15-October-2012 (2012).

[24] E. Doornbos, F. Matthias, B. Fritsche, T. V. Helleputte, J. V. D. Ijssel, D. Rees, P. Visser, M. Kern, L. Hermann, Air Density Models Derived from Multi-Satellite Drag Observations, Data Processing.

[25] T. Scholz, C. Asma, A. Aruliah, Recommended Set of Models and Input Parameters for the Simulations of Orbital Dynamics of the QB50 CubeSats, no. 5th ICATT 2012, International Conference on Astrodynamics Tools and Techniques, ESA, The Netherlands, 2012.

[26] J. Emmert, Thermospheric Density Trends Derived from Satellite Drag, in: 4th IAGA/ICMA/CAWSES Workshop on Long-Term Changes and Trends in the Atmosphere, no. September, 2006.

[27] J. T. Emmert, J. M. Picone, R. R. Meier, Thermospheric global average density trends, 1967–2007, derived from orbits of 5000 near-Earth objects, Geophysical Research Letters 35 (L05101). doi:10.1029/2007GL032809.

[28] J. T. Emmert, J. L. Lean, J. M. Picone, Record-low thermospheric density during the 2008 solar minimum, Geophysical Research Letters 37 (L12102). doi:10.1029/2010GL043671.

[29] D. Oltrogge, An Evaluation of CubeSat Orbital Decay, in: Conference on Small Satellite, 2011.

[30] L. Sentman, L. Missiles, S. Company, Free Molecule Flow Theory and Its Application to the Determination of Aerodynamic Forces, LMSC-448514, Lockheed Missiles & Space Company, a division of Lockheed Aircraft Corporation, 1961.

[31] D. A. Vallado, An Analysis of State Vector Propagation Using Differing Flight Dynamics Programs, Tech. Rep. 1996 (1999).

HYPERSONIC FLOWS IN GROUND FACILITY

Material Response Characterization of Low Density Carbon-Phenolic Ablators in High-Enthalpy Plasma Flows

Bernd Helber

Aeronautics and Aerospace Department, von Karman Institute for Fluid Dynamics, Belgium, helber@vki.ac.be
Department of Electrochemical and Surface Engineering, Vrije Universiteit Brussel

Supervisor: Thierry Magin

Associate Professor, Aeronautics and Aerospace Department, von Karman Institute for Fluid Dynamics, Belgium, magin@vki.ac.be.

University Supervisor: Annick Hubin

Professor, Department of Electrochemical and Surface Engineering, Vrije Universiteit Brussel, anhubin@vub.ac.be.

Abstract

An important effort in theoretical and experimental investigation is required to understand the complex material response of a new class of ablators under reentry conditions. Ablation experiments were performed in the VKI Plasmatron focusing on low density carbon-phenolic materials (AQ61, ASTERM) to investigate the pyrolysis gas chemistry, their transport phenomena in the boundary layer, as well as the char ablation zone with internal material degradation. The reactive boundary layer was investigated by means of three optical emission spectrometers, synchronized with a high-speed camera to determine the probing locations respective to the ablating surface. Emission intensities of various carbonic molecules correlated very well when reaching identical probing distances from the ablating surface. Micrographs shed a light on the subsurface char layer degradation and carbon fiber ablation, which highly varied when pure nitrogen was used for plasma generation instead of atmospheric air.

Keywords: ablation, plasma flows, gas-surface interaction, emission spectroscopy, scanning electron microscopy

Nomenclature

Roman symbols

E_i	excited energy level, cm^{-1}
f_s	sampling frequency, Hz
I	spectrally integrated intensity, $W/(m^2.sr)$
k	Boltzmann concstant, $m^2.kg/(s^2.K)$
m	mass, kg
M	number of spectral points, -
N	number of particles, m^{-3}
p	pressure, Pa
P	power, kW
$\dot{q}$	heat flux, W/m^2
t	time, s
T	temperature, K
S	normalized, calibrated spectrum intensity, -
u	flow velocity, m/s

Greek symbols

λ	wavelength, nm
ϵ	calibrated intensity, $W/(m^2.sr.nm)$

Sub- and Superscripts

$_{cw}$	cold wall
$_{exp}$	experimental
$_{s}$	static
$_{th}$	theoretical

Acronyms

HSC	High Speed Camera
ICP	Inductively-Coupled Plasma
RMSE	Root Mean Squared Error
TPS	Thermal Protection System
TPM	Thermal Protection Material

1. Introduction

Future space exploration missions, such as sample returns from Mars and asteroids at very high reentry speeds, will use ablative materials for the thermal protection system (TPS) to shield the spacecraft

against the severe heating during reentry. Ablative heat shields are able to dissipate high heat fluxes through chemical and physical decomposition, transforming the thermal energy into mass loss and recession, whilst the remaining solid material insulates the vehicle substructure [1; 2].

To achieve high performance characteristics of ablative materials, mostly composites are used, providing a pyrolyzing, ablating, and insulating material at low weight with reasonable mechanical properties due to a carbon-fiber preform. A new generation of low density carbon/resin composite ablators is currently being developed, made of a carbon fiber preform impregnated with phenolic resin. Examples are phenolic-impregnated carbon ablator (PICA) [3] and ASTERM [4], developed for high-speed entry missions.

Selection and sizing of the thermal protection material (TPM) are the two key performance parameters in TPS design and prediction inaccuracies can be fatal for the crew or the success of robotic missions. The prediction tools for ablative TPS design are still inherited from the Apollo program [5; 6] and new high fidelity material response models are proposed [7] in order to take into account the porous micro-structure of the new class materials. Our study is oriented towards the effects of material degradation through pyrolysis and ablation in various air and nitrogen plasma flow conditions in the VKI Plasmatron facility. A high speed camera coupled with three emission spectrometers was used to observe and track outgassing species, which are ejected into the boundary layer from the material. The emission spectrometer enabled a spatial and temporal resolution of various species originating from internal pyrolysis and gas-surface interaction. The high speed camera was used to determine probing distances of the adjoin spectrometers respective to the ablating surface. The materials used for this study were carbon fiber preform, AQ61, and ASTERM provided by EADS Astrium.

The materials were tested at heat fluxes of $1.0 - 3.0\,\mathrm{MW/m^2}$ at various pressure levels ranging from $1.5\,\mathrm{kPa}$ to $20\,\mathrm{kPa}$. This paper is organized according to the following objectives:

- Review of the ablation process of charring materials and existing modeling tools (section 2)
- Description of the VKI Plasmatron facility, experimental methods, test conditions and freestream characterization (section 3).
- Results on spatial radiation profiles (section 4).
- Material degradation observations from recession measurements and micrographs (section 5).
- Conclusions and perspectives (section 6).

2. Ablation of charring materials

2.1. The ablation process

The processes through which ablators are able to accommodate high heat fluxes are balanced between surface radiation, phase transitions (melting, sublimation) as well as chemical reactions (charring, oxidation) on the surface and inside the material. To achieve high performance characteristics of ablative materials, mostly composite materials are used for the ablative heat shield. When subjected to increasing temperature, the virgin material successively transforms following two mechanisms (Fig. 1):

a) During ***pyrolysis*** the phenolic resin is progressively carbonized into a low density, porous char and loses around 50% of its mass producing pyrolysis gases by vaporization. The pyrolysis gases are transported out of the material by diffusion and convection, and exhaust into the boundary layer, providing a further barrier for the heat exchange (blowing), and undergo additional chemical reactions, consuming more heat. Making use of polymers such as phenolic resins for the matrix of the composite takes advantage of their endothermic degradation nature, thereby absorbing energy, and serving as a binder for the other components [8].

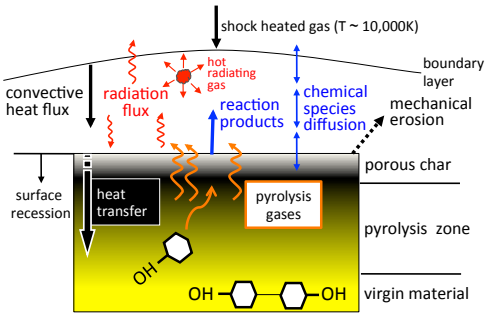

Figure 1: Ablation and pyrolysis processes of a charring material

b) ***Ablation*** of the char layer (composed of the carbonized resin and the remaining carbon fibers) is then promoted by heterogeneous chemical reactions, phase change and mechanical erosion (e.g. spallation), altogether leading to recession of the material. The rate at which an ablator recesses is a consequence of

its prevention of heat conduction and strongly coupled to the aerothermal conditions it encounters. In other words, the material will primarily respond with a higher ablation rate to increased heating whilst the heat conducted to the bondline will stay constant. This illustrates the great importance of material response models to accurately predict recession of the material. However, due to lacking good experimental data, this quantity remains as one of the largest uncertainties in material response analysis [9].

2.2. Existing modeling tools

During the Apollo program, strong efforts were invested to develop models for the prediction of complex gas surface interaction for TPMs. Those models, developed for dense ablative materials, are inspired from Kendall et al. published in 1968 [5; 10]. They rest on major assumptions and describe ablation as a surface phenomenon occurring on a homogeneous, dense material assuming equilibrium or finite-rate chemistry in a control volume close to the wall. The very complex thermochemical problem necessitates the generation of non-dimensional ablation tables, usually referred to as *B'*-tables, for pyrolysis-gas mass flux and char consumption rate (B'_g and B'_c). The coupling strategy with the flow environment is based on considering a thin control volume where the gas-surface interactions occur and where mass balance and equilibrium chemistry are satisfied. By this, the interaction of material and flow codes are approximated through the use of heat and mass transfer coefficients.

Weaknesses of this strategy are for example the model of mass transport due to diffusion into the control volume as well as negligence of blowing the pyrolysis products into the boundary layer, what will change the boundary layer condition. The efforts now focus on developing new flow solvers that can bypass the use of *B'*-tables and to couple them to in-depth, high fidelity material response solvers. For this task, innovative experiments are necessary on multiscale level for characterization of the material degradation in high enthalpy flows and subsequent model validation.

3. Experimental methods for ablation characterization

To enable a proper design of heat shields based on porous, low-density composite ablators, a complete experimental analysis with parallel modeling is necessary. The following phenomena have to be analyzed and described accurately: **finite-rate chemistry** for pyrolysis gas, **transport phenomena in porous medium** as well as in the **boundary layer**, and **volume ablation** with a possible ablation zone (microscopic description of the porous medium).

3.1. Materials of investigation

We propose a testing strategy for ablative material characterization starting with experimental characterization of the fiber preform compound, followed by fully developed ablators. The tested materials are described below:

3.1.1. Carbon fiber preform (Mersen Scotland Ltd.)

The bulk material of carbon preform was provided by Mersen Scotland Holytown Ltd. (CALCARB CBCF 18-2000) and machined in-house to hemispherical test samples of radius 25 mm and 45 mm length. The CBCF preform is a short fiber insulation originating from rayon, the short cut carbon fibers are interconnected in a fully carbonized matrix produced of phenolic resin. The carbon preform compound then consists of randomly oriented carbon fibers with a density typically ranging between $180 - 210\,\mathrm{kg/m^3}$ and a porosity of 90%. This material is very similar to the basic material used for production of cabon-phenolics such as ASTERM and PICA and was previously tested at VKI [11].

3.1.2. ASTERM (EADS Astrium ST)

The ASTERM material is manufactured by impregnating a rigid graphite felt similar to the above carbon preform with phenolic resin, which is followed by a polymerisation process and final machining [4]. This approach significantly reduces the manufacturing effort and allows a large scale production. The manufacturing approach allows a large range of final material densities, from $240 - 550\,\mathrm{kg/m^3}$.

3.1.3. AQ61 (EADS Astrium ST)

AQ61 is a basic ablative material previously developed by EADS Astrium, which represents a low density carbon-phenolic material manufactured by impregnating large pieces of carbon felts compressed to the right density during the impregnation process [4].

3.2. *Inductively-coupled Plasmatron facility*

The Plasmatron facility has been used for all the experiments carried out in this study. It is extensively utilized at the von Karman Institute for Fluid Dynamics for the reproduction of the aero-thermodynamic environment of re-entry plasma flows, creating a high-enthalpy, highly dissociated subsonic gas flow[12]. The facility is equipped with a 160 mm diameter ICP (Inductively Coupled Plasma) torch powered by a high frequency, high power, high voltage (400 kHz, 1.2 MW, 2 kV) generator (MOS technology). In order to achieve heat fluxes higher than ~5 MW/m^2, a converging nozzle can be attached to the torch of the Plasmatron (not performed for this work). As the gas is heated by induction through a coil, the advantages of ICP torches are the high purity of the plasma flows produced, due to the absence of electrodes and their associated erosion. With its 1.2MW inductively coupled plasma generator, the VKI Plasmatron facility is the most powerful of its kind in the world. An overview of the facility and the complete experimental setup for free-stream and in-situ ablation measurements can be found in Figure 2, as reviewed below.

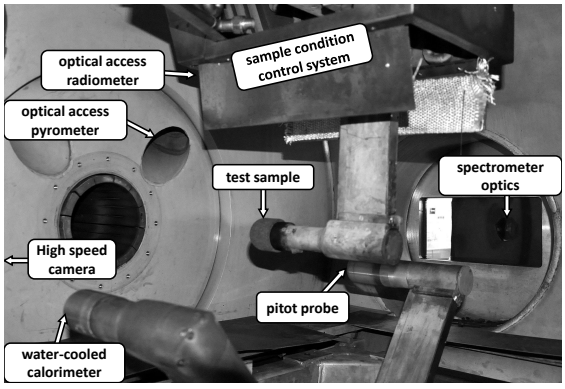

Figure 2: Experimental setup in the VKI Plasmatron facility with free-stream characterization techniques (heat flux probe, pressure probe) and measurement techniques for ablation characterization.

A 50 mm diameter copper water-cooled probe, mounting a copper calorimeter in the center of the front face, is used for the calibration of plasma flow conditions. The cold wall (~350 K) stagnation point heat flux is determined by the cooling water mass flow, controlled by a calibrated rotameter, and the inlet/outlet temperature difference, measured by two type-E thermocouples. A Teflon© insulator is inserted between the calorimeter and the probe's wall in order to have side adiabatic conditions. Both the probe and calorimeter have copper surfaces which are high catalytic to nitrogen and oxygen atoms recombination. The heat flux can be measured with ±10% accuracy. A water-cooled Pitot probe is used to perform stagnation pressure measurements. The pressure line is connected to a Validyne variable reluctance pressure transducer and a voltage demodulator amplifies the output. Beside the calorimeter and dynamic pressure probe for free-stream characterization, the measurement techniques included temperature measurements (two-color pyrometer, IR-radiation-thermometry and thermocouples), emission spectroscopy and high speed camera imaging. Validyne and amplifier are calibrated prior to the test by means of a Betz water manometer, leading to an uncertainty of ±0.2%. The Plasmatron chamber is also equipped with an absolute pressure transducer that measures the static pressure with ±2Pa accuracy. The probes are mounted inside the Plasmatron test chamber at 0.445 m distance from the ICP torch exit.

Surface temperature measurements were carried out using a two-color Raytek Marathon MR1S-C pyrometer (0.75 - 1.1 µm), with a temperature range from 1300 K to 3300 K. Measurements in two narrow wavelength bands under the assumption of a wavelength independent emissivity allow temperature estimations neglecting the emissivity. A detailed description of this technique can be found in literature [13]. An example of the surface and internal thermal response (measured by type-K and type-E thermocouples) is shown in Fig. 3. Note the destruction of the thermocouples at their limiting temperature of ~ 1500 K and ~ 1000 K, respectively. From calibration of the two-color pyrometer performed with a black body radiation source the uncertainty was found to be $\delta T_S = \pm 10$ K.

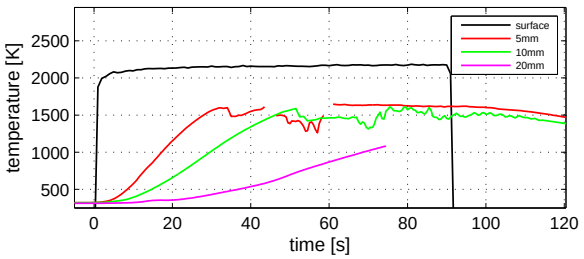

Figure 3: Surface and in-depth thermal response of an ablation test (*AQ61*, air, 1.5 kPa, 1 MW/m^2).

3.3. *Temporally & spatially resolved emission spectroscopy*

Temporally and spatially resolved emission spectroscopy enabled measurements of erosion products

and erosion rates as a function of the plasma parameters in front of the test specimen. This work used three Ocean Optics HR4000 spectrometers, which cover a wide wavelength range (200nm-1000nm) within one single acquisition and a minimum integration time of 5ms. The optical diagnostic bench consisted of a light collection system, optical fibers and the three spectrometers, synchronized with a high-speed-camera (Fig. 4).

The light emitted by the plasma was collected through a variable aperture and focused by a plano-convex, uncoated fused silica lens (LA4745, 750 mm focal length) via two mirrors on the entry of three optical fibers (Ocean Optics QP600-2-SR/BX, 600 ± 10 µm core diameter).

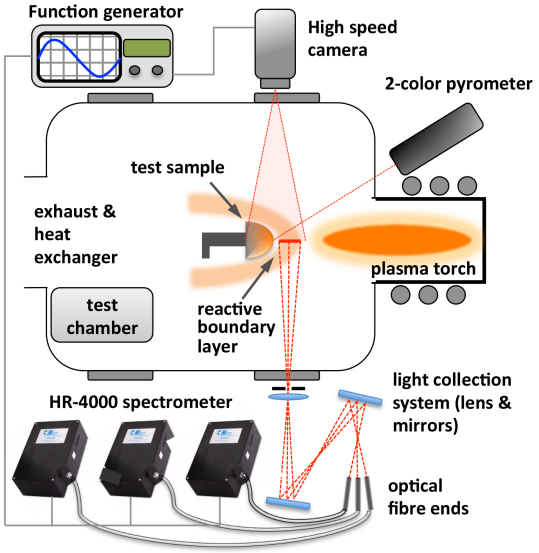

Figure 4: Schematic view of the VKI Plasmatron showing the optical paths of three adjoin spectrometeres perpendicular to the plasma flow ahead of the ablating sample (sample position: 445mm from plasma jet exit)

The optical fibers were characterized by an optimized numerical aperture to match the entrance slit of the spectrometer. The optical path was aligned perpendicular to the flow and tangential to the test sample surface. Three small probing volumes with variable distances (by the magnification and arrangement of the fibers) along the stagnation line through the boundary layer were imaged onto the three optical fibers. The magnification of the optical system was set to 3 resulting in a distance between each probing volume of $\Delta d = 2$ mm.

Each optical signal was lead to a HR4000 spectrometer, which covers a broad spectrum in the desired range (200-1100 nm), suitable to rapidly determine radiating transitions of excited atoms and main molecular bands. All optical components operated in the HR4000 spectrometer wavelength range. The fixed entrance slit width of 5µm and a 300 groove/mm grating lead to a typical resolution of approximately 0.7 nm (Full Width Half Maximum (FWHM)), as was determined by a low pressure Hg lamp (Oriel 6060).

The spectrometers were triggered with an acquisition frequency of $f_s = 4$ Hz to analyze the temporal erosion products evolution. The integration time was adjusted for each test to prevent saturation of the CCD detector, averaging the acquired spectrum during the integration period.

The optical diagnostic bench (aperture, lens, mirrors and fibers) was mounted on a movable holding system, which enabled horizontal movements to be able to adjust the line of sight. The positioning of the three probing volumes was checked and adjusted before each experiment using a laser beam, which was sent through the optics and located ahead of the stagnation point of the sample.

Calibration of the whole system consisting of the light collection mechanism and spectrometer efficiencies in [W/m^2.sr.nm] was performed between 350nm and 900nm by placing a tungsten ribbon lamp (OSRAM WI 17G) in the focus of the collection optics inside the test chamber. As the spectrometer response of the calibration lamp below 350nm is too low, calibrated spectra are only reported within the range 350-900nm. Plotted spectra below 350nm (e.g. of OH and NH emission) are shown in arbitrary units.

Calibrated emission spectra recorded by the three adjoin spectrometers in air plasma free-stream are presented in Fig 5. All three signals coincided very well for the full spectral range where the calibration was performed (350-900 nm) and suggest a sufficient intensity calibration to enable quantitative comparison of the three emission signals.

In order to determine the varying distances of the spectrometer probing volumes to the recessing surface, a high speed camera was used, synchronized with the emission spectrometer. The Vision Research Phantom 7.1 CMOS high-speed camera (HSC) provides the possibility of using short exposure times (2µs) to capture images at high sampling frequencies. Such short exposure times are required as the very bright surface during material ablation can lead to saturation of the CCD sensor of normal cameras. High-speed imaging also enables in-situ, non-intrusive determination of the surface recession. The accuracy of this method depends on the resolution of the HSC and the successive conversion of pixel into millimeters. A

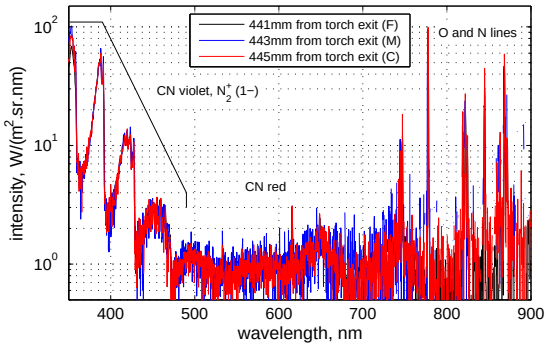

Figure 5: Calibrated free-stream emission recorded by three adjoin spectrometers along jet center line coincide well representing sufficient intensity calibration (20 kPa, 3 MW/m^2).

surface detection uncertainty of one pixel lead to a recession uncertainty of $\delta HSC = \pm 0.1$ mm.

An illustration of a surface recession measurement and spectrometer probing distance determination for the case of a preform sample is shown in Fig. 6. The linear curve fit confirms a constant recession rate and the three spectrometer positions are indicated with respect to the surface (close (C), middle (M), and far (F)).

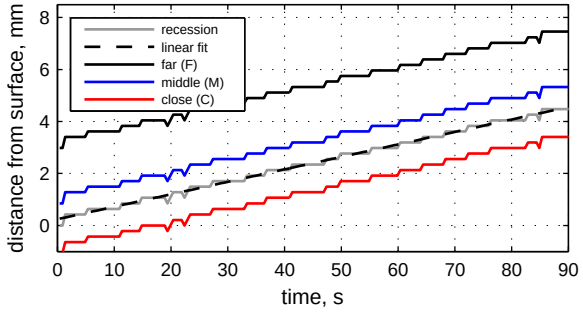

Figure 6: HSC imaging synchronized with 3 emission spectrometers for ablator recession and spectrometer probing-distance determination.

The bright surface was extracted from the original image by adjusting dark-white contrasts and applying edge detection filters.

In order to evaluate the temporal molecular emission, e.g. of CN violet, the emission signal $\epsilon(\lambda)$ of the $\Delta\nu = 0$ sequence (370-390nm) was then integrated with respect to the wavelength for each individual spectrum at time step t:

$$I_{CN}^{(t)} = \int_{370nm}^{390nm} \epsilon(\lambda) d\lambda \qquad (1)$$

An example of this integration procedure for the CN violet $\Delta\nu = 0$ sequence is shown in Fig. 7.

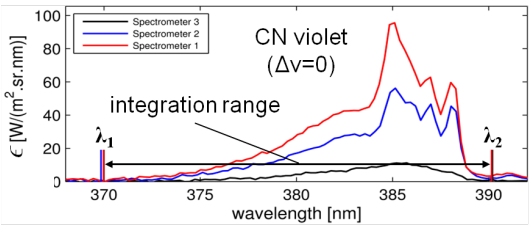

Figure 7: Integration range of emission signal $\epsilon(\lambda)$ for CN violet $\Delta\nu = 0$ sequence.

3.4. *Test procedures and conditions*

Two test gases have been used, air and nitrogen, in order to restrict the number of chemical reactions. The mass flow was kept at $\dot{m} = 16$ g/s. The duration of each test was chosen in order to maintain a similar heat load on the samples for all test cases. The actual duration of the ablation test was determined from the high-speed-camera images. For the results presented throughout this paper, the time indication $t = 0$ s corresponds to the injection of the test sample into the plasma flow. Plasmatron test conditions providing test gas, static and dynamic pressure, cold wall heat flux, test time and surface temperature are listed in Table 1.

3.5. *Scanning Electron Microscopy*

The SEM system in use for this study was a Jeol JSM-6400 type of electron microscope that images the sample surface by scanning it with a high-energy beam of electrons in a raster scan pattern. The electrons interact with the atoms that make up the sample producing signals that contain information about the sample's surface topography, composition and other properties such as electrical conductivity. Goldstein [14] provides a detailed description of the application of SEM and X-Ray Microanalysis of composite materials.

4. Results: Spatial radiation profiles of carbon-phenolic ablation in air and nitrogen plasmas

A typical example of spectrally resolved emission recorded during sample ablation in air and nitrogen plasmas is presented in Figure 8. The spectra are collected just in front of the sample stagnation point and extracted for the first seconds of the ablation test. Main radiating molecular systems and atomic lines are indicated, all of them originating either from the pyrolysis gas injection into the boundary layer, gas-surface interaction or chemical reactions in the boundary layer. We could identify atomic carbon emission,

Table 1: Plasmatron test conditions: test case reference (Carbon Preform (P), AQ61 (AQ), ASTERM (AS), followed by target heat flux in $\mathbf{MW/m^2}$ and target chamber pressure in mbar), test gas, static pressure $\boldsymbol{p_s}$, dynamic pressure $\boldsymbol{p_d}$, electrical power, mean cold wall heat flux $\boldsymbol{\dot{q}_{cw}}$, exposure time & surface temperature $\boldsymbol{T_S}$, recession rate $\boldsymbol{\dot{r}}$, and mass loss $\boldsymbol{\dot{m}}$.

test condition #	gas	p_s, kPa	p_d, Pa	P, kW	$\dot{q}_{cw}$, MW/m^2	t, s	T_S, K	$\dot{r}$, mm/s	$\dot{m}$, mg/s
P1-1-15	air	1.5	141	166	1.019	91.0	2180	0.047	48.2
P2-1-200	air	20	-	188	1.050	91.2	2020	0.041	53.2
P5-3-15	air	1.5	342	365	3.074	30.7	2848	0.049	69.8
P6-3-200	air	20	48	321	2.962	30.8	2783	0.069	74.6
P3-1-15-N	N_2	1.5	124	154	1.057	90.7	2030	0.000	3.47
P4-3-15-N	N_2	1.5	285	350	3.149	31.2	2644	0.007	8.42
AQ1-1-15	air	1.5	135	161	1.023	90.4	2167	0.047	63.6
AQ3-1-100	air	10	17.0	181	1.038	90.4	2134	0.040	54.1
AQ2-1-200	air	20	6.20	158	1.026	90.3	1890	0.035	40.2
AQ6-3-15	air	1.5	400	400	2.994	30.0	2884	0.042	132
AQ7-3-200	air	10	57.0	356	3.058	30.0	2906	0.099	124
AQ4-1-15-N	N_2	1.5	131	177	0.997	90.5	2017	0.005	26.2
AQ5-1-100-N	N_2	10	13.4	213	1.017	90.0	2051	0.006	20.2
AQ8-3-15-N	N_2	1.5	263	354	3.034	30.4	2612	0.021	74.6

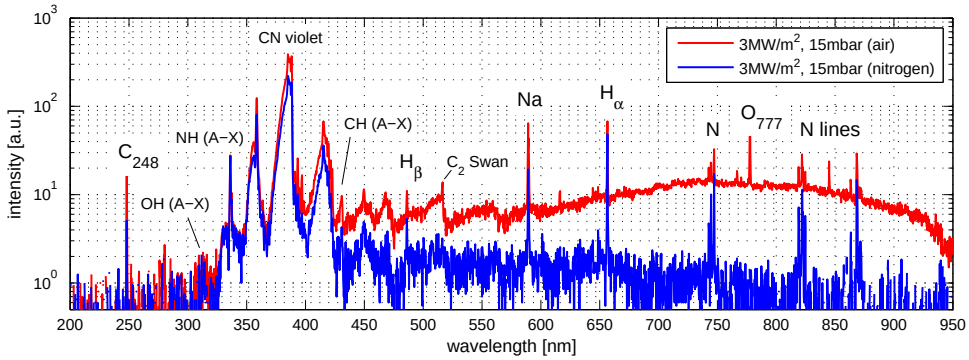

Figure 8: Emission spectra in air and nitrogen plasma of carbon-phenolic ablator (*AQ61*) at 1.5 kPa static pressure and a cold wall heat flux of 3 MW/m^2.

strong H_α and H_β lines of the Balmer series, hydromolecules such as CH(A-X), NH(A-X) and OH(A-X), purely carbonic molecules like C_2 Swan as well as carbon molecule combinations with the free-stream such as CN violet (B-X). Uhl et al.[15] performed a study of pyrolysis products ejected by the carbon-phenolic ablator PICA, also applying emission spectroscopy. The authors were able to detect CN violet and C_2 Swan emission but did not identify any hydrocarbon molecules in the boundary layer.

The resulting temporally and spatially resolved emission profiles of the three spectrometers can be found in Figure 9. Spectrometer 1 was pointing at the ablating surface for the first 15s of the test during which the CN violet bandhead emission increased until the maximum was reached just when the recessing surface passed the spectrometer's probing volume.

4.1. Air Plasma

The spatial emission of CN violet along the stagnation line in front of a Preform test sample (fully carbonized, no phenol content) in air plasma is shown in Figure 10. Good agreement of all three spectrometer responses can be observed for the test, supporting some assumptions made on the optical setup and the ablation test condition:

1. for the calibrated wavelength range of interest (>350nm) the spectrometers give reasonable emission profiles; in other words, the spectrometer close to the surface (spectrometer 1) recorded a comparable emission intensity just before test end in comparison to the farthest spectrometer (spectrometer 3) at test start (when reaching the same distance from the surface).

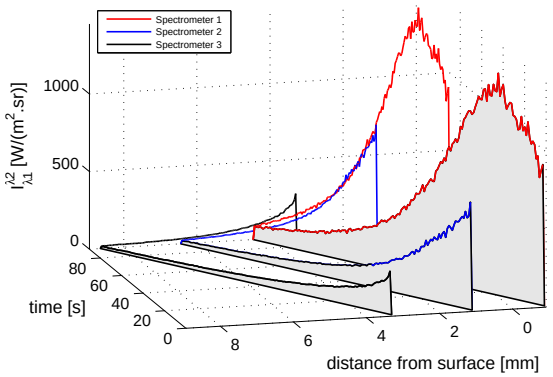

Figure 9: 3D plot illustrating CN violet bandhead ($\Delta\nu = 0$) emission over time and distance from sample surface along the stagnation line (1 MW/m^2, 1.5 kPa).

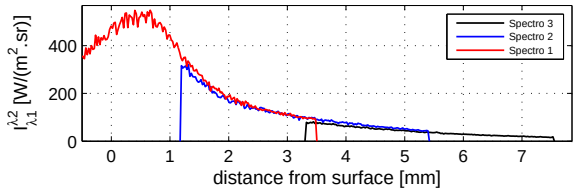

Figure 10: Spatial emission (along stagnation line) of CN violet recorded by the three spectrometers during Preform ablation in air (1 MW/m^2, 1.5 kPa).

2. if the spectrometer response is regarded to be valid (no signal truncation) the ablation process during the whole test time of 90 seconds can be regarded as very steady with a stable surface burn-off.
3. such a stable ablation process would enable to scan the boundary layer for ablation products as done for CN violet in the presented plot, where the recorded emission dropped about 90% within 4 mm away from the surface (at a low pressure condition of $p_s = 1.5$ kPa).

Interestingly, CN violet integrated emission intensities increased by a factor of two in the case of AQ61 and ASTERM ablation compared to the preform. The ablation conditions for these two cases were almost identical, with a surface temperature difference of only 50 K. A higher CN emission in the case of the charring ablator might be due to

- CN production from outgassing carbon-containing species (e.g. C_2 was identified at test start)

$$C_2 + N_2 \rightleftharpoons CN + CN \qquad (2)$$

- the highly reactive carbonized resin in the char layer, reacting with available nitrogen
- a higher content of carbon monoxide (CO) in the boundary layer due to the highly reactive carbonized resin in the char layer, decomposing to CN

$$CO + N \rightleftharpoons CN + O \qquad (3)$$

Other authors [16] found discrepancies in the radiative prediction of carbon-phenolic ablators, possibly caused by the influence of the important CN forming reaction CO + N $\rightleftharpoons$ CN + O. The strong radiative properties of CN, highly created during ablation gas-surface interaction, invoke comprehensive experimental data at various ablation conditions for the development of numerical models and their validation.

4.2. Nitrogen Plasma

Only little recession ($\sim$ 0.5 mm) was experienced by the test sample during ablation in nitrogen plasma. Resulting CN violet emission in front of the test sample is presented in Figure 11.

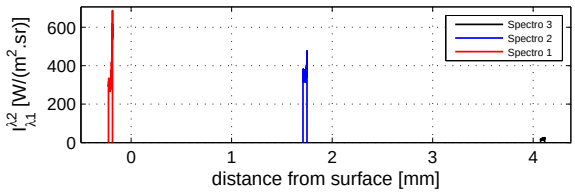

(a) Carbon Preform (no phenolic impregnation)

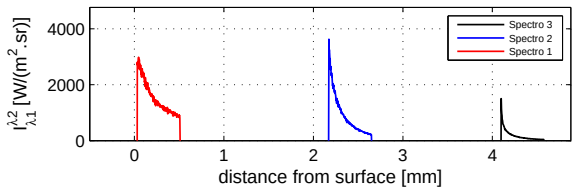

(b) Phenolic impregnated ablator

Figure 11: Spatial emission of CN violet along the stagnation line and temporal emission of CN violet for ablation in nitrogen, (1 MW/m^2, 1.5 kPa).

Although recession was almost negligible, the spatial emission profile showed a strong drop during the whole test. Such a strong CN emission drop was not recorded in the case of preform ablation and it is therefore assumed, that the phenolic content plays an important role in the production of CN. The emission drop during carbon-phenolic ablation might be explained by progressing internal heat transfer, leading to further pyrolysis inside the material (only temperature dependent), whilst the surface almost does not experience ablation (temperature and test gas dependent). This would explain a decrease of pyrolysis outgassing over time, and a possible change of the

carbonized char layer in the material sub-surface due to reactions with diffusing species from the boundary layer. Both may result in a decrease of CN production.

One may assume that CN violet is mainly generated by nitridation of the carbon fibers at the surface (especially in nitrogen plasma) or by fast reactions in the boundary layer close to the wall. However, the obtained results suggest that CN production is influenced by the outgassing products, or a change in the sub-surface microstate of the char layer.

4.3. Temperature estimation from simulated spectra

Temperature estimations within the reactive boundary layer surrounding the test sample are of high interest, as they will allow to better characterize the test condition, deviations from thermo-chemical equilibrium, and eventually help to validate numerical models by comparing experimental values to numerical predictions.

A fitting procedure was applied using the spectra simulation software SPECAIR 2.2 with the aim to estimate temperatures in the boundary layer from CN violet radiation. Cipullo et al. [17] applied this procedure to the characterization of the free-stream plasma flow in the Plasmatron facility. The spectral fitting was performed by minimizing the RMS error (RMSE) function, defined as [18] :

$$RMSE(T) = \sqrt{\frac{\sum_{i=1}^{M}(S_{ex}(i) - S_{th}(i))^2}{M}} \qquad (4)$$

with M being the total number of spectral points i, S_{ex} is the calibrated and normalized experimental spectrum and S_{th} is the normalized theoretical spectrum obtained from Specair2.2 at temperature T, convolved with a Gaussian function to reproduce the spectrometer's entrance slit.

The experimental spectra of CN violet ($\Delta\nu = 0$ and $\Delta\nu = -1$ sequences) for two different test chamber pressures (1.5 kPa and 10 kPa), as well as best fits for both experimental spectra, are compared in Fig. 12 (a) and (b). The fitted curves were produced applying a two-temperature model with a translational-rotational temperature T_{rot} and a vibrational-electronic temperature T_{vib} as available in Specair 2.2. The uncertainty of the temperature estimations was based on a 10% intensity variation of the emission measured by the spectrometer, allowing the theoretical spectrum to vary within those limits for the fitting procedure.

The best fit at 1.5 kPa test chamber static pressure (air) was obtained for $T_{rot}^{1.5kPa} = 8680K$ and $T_{vib}^{1.5kPa} = 17013K$ and at 10 kPa for $T_{rot}^{10kPa} = 6105K$

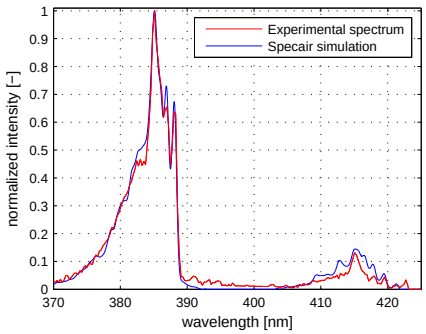

(a) 1.5 kPa:
$\boldsymbol{T_{rot} = 8680K} \pm 650K$, $\boldsymbol{T_{vib} = 17013K} \pm 1450K$

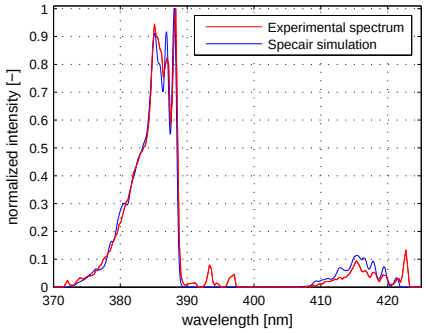

(b) 10 kPa:
$\boldsymbol{T_{rot} = 6105K} \pm 450K$, $\boldsymbol{T_{vib} = 8770K} \pm 490K$

Figure 12: Numerically fitted spectra (Specair 2.2) reveal higher deviation with respect to rotational and vibrational temperatures at low chamber pressures (AQ61, air, 1 MW/m^2, 1mm ahead of ablating surface).

and $T_{vib}^{10kPa} = 8770K$. Hence, the numerically fitted spectra revealed a higher deviation with respect to rotational and vibrational temperatures at low test chamber static pressures (1.5 kPa), suggesting a stronger deviation from thermal equilibrium.

We have to bear in mind that we obtained those results form the gas radiative signature, representing the emission spectrum of electrically excited states of the CN molecule. The particle number densities N_i of such excited molecules are only in equilibrium related to total number densities N, according to a Boltzmann distribution:

$$N_i = N \cdot \frac{g_i}{Q} \cdot exp(\frac{-E_i}{k_B T}) \qquad (5)$$

with the degeneracy g_i, the partition function Q, Boltzmann's constant k_B and the excited energy E_i. Moreover, the SPECAIR model is solely based on Boltzmann distributions of all excited states for computation of the gas radiation. Hence, SPECAIR simulations of excited populations (such as the CN vi-

olet $B^2\Sigma_u^+$ state) deviating from a Boltzmann distribution in the boundary layer (overpopulation) may yield higher values of electronic-vibrational temperatures. Further investigation is required to understand the physics of this thermal deviation at low pressures.

5. Results: Char ablation zone and carbon fiber degradation

The following section presents recession data and micrographs of ablated carbon preform, and AQ61 test samples. Recession rates of two AQ61 and carbon preform samples are plotted in Fig. 13 for increasing static pressure and surface temperature.

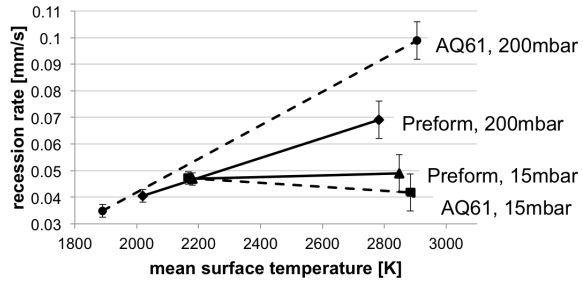

Figure 13: Influence of test chamber static pressure on recession rates of AQ61 & Preform (1 MW/m^2).

Recession rates of both samples did not change much at low static pressures (p_s = 1.5 kPa) with increasing surface temperature, being below 0.05 mm/s. Such constant recession rates, despite a surface temperature increase, can be explained by a diffusion controlled ablation regime. In this regime, oxygen is not able to diffuse fast enough through the boundary layer to react at the surface, although thermal energy would be high enough to cause a faster burn-off. At much higher surface temperatures this regimes transitions into a sublimation regime, leading to increasing surface recession.

The recession rate of AQ61 was tripled with increasing static pressure (p_s = 20 kPa) and the recession rate of carbon preform increased by a factor of 1.75 for the same pressure change. To be able to further evaluate those recession results, it is suggested to perform rebuilding of the plasma flow field and boundary layer chemistry. This will be done for future studies in order to determine free-stream enthalpy and the state of oxygen dissociation for those four test conditions.

Fig. 14 (a) depicts strong thinning of the fibers of carbon preform most probably due to oxidation from the fiber tips, resulting in an icicle shape. Such icicle shapes are reported in literature for fiber ablation of carbon-carbon composites [19; 20]. This behavior changed drastically when nitrogen was used for plasma generation, where ablated fibers show strong corrosion along the whole fiber length.



(a) air: icicle shaped fibers, oxidation from fiber tip

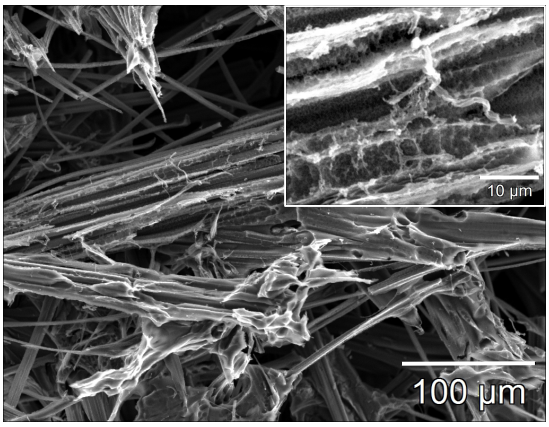

(b) N_2: strong corrosion along whole fiber length

Figure 14: Micrographs of carbon preform after ablation in air and nitrogen plasma (1.5kPa, 1 MW/m^2).

The char layer of an ablated AQ61 sample in air is shown in Figure 15. The carbon fibers were oxidized from the fiber tip, similar to carbon preform material. Charred, partially ablated resin became visible ~ 50 µm below the surface. We will refer to this zone, between fiber tips and charred resin, as ablation zone, in which all charred resin was ablated before the carbon fibers were oxidized. The porosity within this sub-surface zone and below will gradually decrease from fiber tip until the location where no charred resin is ablated anymore. The depth of this zone as well as its density gradient are subject of future investiga-

tions. They are of high interest for the development and validation of new material response models [21].

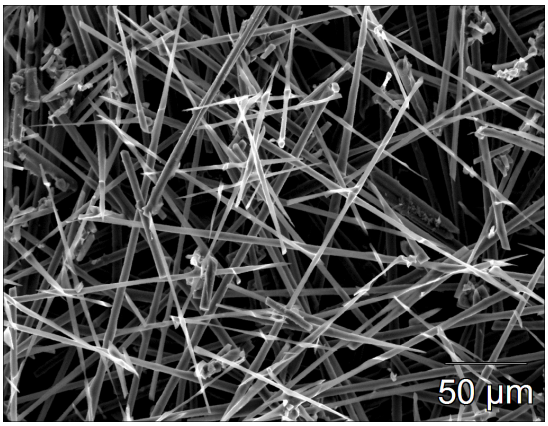

(a) air: icicle shaped fibers and high porosity (charred resin sparely identified) at surface

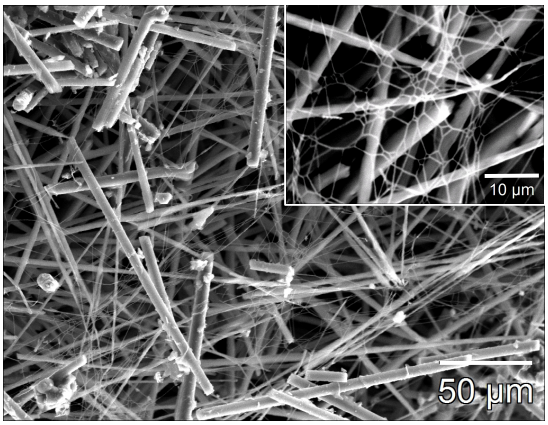

(b) N_2: "cross filaments" found on the surface

Figure 15: Post-ablation (air & nitrogen) micrographs of AQ61 (1.5kPa, 1 MW/m^2).

Ablation in nitrogen plasma lead, similar to carbon preform, to strong corrosion of the carbon fibers, Fig. 15 (b). In addition to this, a mesh of thin "cross filaments" was visible after ablation of AQ61, connecting the carbon fibers. It is well known that carbon has the ability to form very long chains of interconnecting C-C bonds, called catenation. Those bonds are strong, and stable, allowing carbon to form an almost infinite number of compounds. It seems plausible that, in a nitrogen atmosphere, available carbon in the gas phase, e.g. in form of hydrocarbons, can become solid again to form such carbon chains.

6. Concluding remarks and perspective

6.1. Summary

To enable proper design of ablative heat shields, experimental analysis with parallel modeling are mandatory. We want to investigate the pyrolysis gas chemistry, transport phenomena in the boundary layer, as well as char ablation zone and internal material degradation. This work has started an investigation of the interaction of pyrolysis gases, created in high-enthalpy air and nitrogen ablation tests of low density carbon-phenolic ablators at various pressures in the VKI Plasmatron facility. The reactive boundary layer in front of the ablative sample was investigated by means of three optical emission spectrometers synchronized with a high-speed camera in order to determine the spectrometer probing locations with respect to the ablating surface. Recorded emission signals revealed species originating from internal pyrolysis and char layer ablation such as C, H, C_2, CH, CN, NH, and OH. Post-test sample examination was performed by means of Scanning Electron Microscopy (SEM) and Energy Dispersive X-ray Spectroscopy (EDX) to analyze the material degradation and ablation subsurface char zone.

Emission intensities of various carbonic molecules recorded by the three spectrometers correlated very well for several test cases when reaching identical probing distances from the ablating surface. This enables reconstruction of the emission profile along the stagnation line and allows quantification of the steadiness of the ablation test and material burn-off. Preliminary simulations of spectra generated using the SPECAIR software yielded a higher deviation from thermal equilibrium with respect to rotational and vibrational temperatures at low chamber pressures. Micrographs shed a light on the subsurface char layer degradation and carbon fiber ablation, which highly varied when pure nitrogen was used for plasma generation instead of atmospheric air.

6.2. Future work

In addition to more experiments, especially at heat fluxes exceeding $q_{cw} = 5\,MW/m^2$, the methodology for ablative material characterization has to be extended by a ground-to-flight extrapolation strategy, combining experimental data and numerical tools. Such a flight extrapolation methodology was implemented at the VKI for experiments on reusable TPMs [22; 23], such as ceramic tiles and C-SiC compounds.

This procedure is up to now able to rebuild the free-stream properties of the plasma jet and further, to extrapolate ground tests on reusable heat shields based on the principle of surface radiation to real flight conditions in order to determine material emissivity and recombination efficiency [24]. This methodology has to be extended to the proposed work on ablative materials by coupling boundary layer solver (starting from a 1D description at the stagnation line) and material response codes.

Acknowledgements

We gratefully acknowledge EADS Astrium Space Transportation for providing the test material, in particular Jean-Marc Bouilly for scientific discussion. Mersen Scotland Holytown Ltd. is acknowledged for providing the preform material as well as informative support. The research of B. H. is supported by a fellowship of the Agency for Innovation by Science and Technology (IWT, dossier #111529) in Flanders, and research of T.M. by the European Research Council Starting Grant #259354. Pascal Collin is acknowledged for his valuable help as Plasmatron operator.

References

[1] G. Sutton, The initial development of ablation heat protection: An historical perspective, J. Spacecraft Rock. 19 (1) (1982) 3–11.

[2] B. Laub, E. Venkatapathy, Thermal protection system technology and facility needs for demanding future planetary missions, in: International Workshop on Planetary Probe Atmospheric Entry and Descent Trajectory Analysis and Science, 2003.

[3] H. Tran, Development of lightweight ceramic ablators and arc jet test results, in: NASA TM-108798, 1994.

[4] H. Ritter, P. Portela, K. Keller, J.-M. Bouilly, B. S, Development of a European Ablative Material for Heatshields of Sample Return Missions, in: 6th European Workshop on TPS and Hot structures, Stuttgart, Germany, 1-3 April 2009.

[5] R. Kendall, E. Bartlett, R. Rindal, C. Moyer, An analysis of the coupled chemically reacting boundary layer and charring ablator: Part i, NASA CR 1060, NASA (1968).

[6] F. Milos, Y.-K. Chen, Comprehensive model for multicomponent ablation thermochemistry, in: AIAA 1997-0141, Reno, NV, USA, 1997.

[7] J. Lachaud, I. Cozmuta, N. Mansour, Multiscale approach to ablation modeling of phenolic impregnated carbon ablators, J. Spacecraft Rock. 47 (6) (2010) 910–921.

[8] L. Torre, J. Kenny, A. Maffezzoli, Degradation behaviour of a composite material for thermal protection systems part i - experimental characterization, J. Mater. Sci. 33 (1998) 3137–3143.

[9] Cozmuta, I. and Wright, M. J. and Willcockson, W. H., Defining Ablative Thermal Protection System Margins for Planetary Entry Vehicles, in: AIAA 2011-3757, 2011.

[10] C. Moyer, R. Rindal, An analysis of the coupled chemically reacting boundary layer and charring ablator: Part ii, NASA CR 1061, NASA (1968).

[11] B. Helber, O. Chazot, T. Magin, A. Hubin, Ablation of carbon preform in the VKI Plasmatron, in: AIAA paper 2012-2876, 2012.

[12] B. Bottin, O. Chazot, M. Carbonaro, V. van der Haegen, S. Paris, The vki plasmatron characteristics and performance, in: RTO AVT Course on Measurement Techniques for High Enthalpy and Plasma Flows, published in RTO EN-8, Belgium, 1999.

[13] A. Gülhan, Application of pyrometry and ir-thermography to high surface temperature measurements, in: RTO AVT Course on Measurement Techniques for High Enthalpy and Plasma Flows, Belgium, 1999.

[14] Goldstein, J. and Newbury, D. and Joy, D. and Lyman, C. and Echlin, P. and Lifshin, E. and Sawyer, L. and Michael, J. R., Scanning Electron Microscopy and X-Ray Microanalysis, Kluwer Academic / Plenum Publishers, New York, 2003.

[15] J. Uhl, W. Owens, J. Meyers, D. Fletcher, Pyrolysis simulation in an icp torch facility, in: AIAA paper 2011-3618, June 2010.

[16] A. Martin, I. Boyd, I. Cozmuta, M. Wright, Chemistry model for ablating carbon-phenolic material during atmospheric reentry, in: AIAA 2010-1175, 2010.

[17] Cipullo, A., Helber, B., Panerai, F. and Chazot, O., Experimental Characterization of the Free-stream Plasma Flow Produced bythe VKI Plasmatron Facility using Optical Emission Diagnostics, in: RTO-EN-AVT-199, Paper 17, Specialists Meeting on Catalytic Gas Surface Interactions ", 2012.

[18] Cipullo, A., Savino, L., Marenna, E., and De Filippis, F., Thermodynamic State Investigation of the Hypersonic Air Plasma Flow Produced by the Arc-Jet Facility SCIROCCO, Aerospace Science and Technology 23 (1) (2012) 358–362. doi:10.1016/j.ast.2011.09.ElsevierScience.

[19] Farhan, S., Ke-zhi, L., Ling-jun, G., Quan-ming., G., and Feng-tao, L., Effect of density and fibre orientation on the ablation behavior of carbon-carbon composites, New Carbon Materials 25 (3) (2010) 161–166.

[20] Cho, D., and Yoon, B. I, Microstructural interpretation of the effect of various matrices on the ablation properties of carbon-fiber-reinforced composites, Composites Science and Technology 61 (2001) 271–280.

[21] J. Lachaud, N. Mansour, Microscopic scale simulation of the ablation of fibrous materials, in: AIAA 2010-984, Orlando, FL, USA, 2010.

[22] A. F. Kolesnikov, Conditions of simulation of stagnation point heat transfer from a high-enthalpy flow, Fluid Dyn. 28 (1) (1993) 131–137.

[23] P. Barbante, O. Chazot, Flight extrapolation of plasma wind tunnel stagnation region flowfield, J Thermophys Heat Transfer 20 (3) (2006) 493–499.

[24] F. Panerai, Aerothermochemistry testing of thermal protection systems, Ph.D. thesis, von Karman Institute for Fluid Dynamics / University of Perugia (2012).

Design of Boundary Layer Transition Experiments at Large Hypersonic Mach Numbers Focusing on the Determination of Free-Stream Conditions

Guillaume Grossir

Aeronautics and Aerospace Department, von Karman Institute for Fluid Dynamics, Belgium, grossir@vki.ac.be

Supervisor: Patrick Rambaud

Associate Professor, Aeronautics and Aerospace Department, von Karman Institute for Fluid Dynamics, Belgium, rambaud@vki.ac.be.

University Supervisor: Herman Deconinck

Professor, Université Libre de Bruxelles, Belgium, deconinck@ulb.ac.be.

Abstract

The design of hypersonic boundary layer transition experiments is presented with the characteristics of the selected model and its instrumentation. Recent advances for the flow characterization of the wind-tunnel are summarized and possibilities for flow condensation in the free-stream are assessed to explain theoretical/experimental discrepancies on free-stream static pressures. Requirements for the investigation of non-equilibrium flow expansion in the nozzle are pointed out.

Keywords: Hypersonic, boundary layer, transition, cone, static pressure, condensation, non-equilibrium.

Nomenclature

Symbols

D	probe diameter, mm
L	probe/model length, mm
M	Mach number, -
p	flow pressure, Pa
$\dot{P}$	rate of pressure decrease, s^{-1}
Re	Reynolds number, -
t	time, ms
T	flow temperature, K
x	distance along nozzle axis, mm
y	radial coordinate, mm
δ	boundary layer thickness, mm
ρ	flow density, kg/m^3

Subscripts/Superscripts

0	stagnation conditions
c	condensation
e	at the boundary layer edge
D	based on nozzle diameter
tr	transition
t_1	total conditions before a normal shock wave
t_2	total conditions after a normal shock wave
x	based on distance from leading edge
w	at the wall
∞	free-stream value
$'$	perturbation

1. Introduction

The phenomenon of hypersonic boundary layer transition from a laminar to a turbulent state is critical for all atmospheric reentries. Transition to turbulence promotes diffusion phenomena and leads, among many other effects, to heat transfer rates at the wall which can be twice larger than the ones involved with laminar boundary layers [1]. Hence, this phenomenon is particularly important for the design of thermal protection systems.

Despite the work achieved over the past 50 years and the creation of an enormous experimental database, now enriched by numerical results, the transition prediction remains a challenge due to its complexity inherent to the large number of influencing parameters (such as M_∞, Re_∞, wall temperature ra-

tio T_w/T_0, nosetip radius, pressure gradient dp/dx, chemistry... [2]).

Uncertainties relative to the prediction of transition in hypersonic environments have lead to the common design of thermal protection systems with large safety margins detrimental to the payloads. This has driven a large amount of efforts aiming at understanding better the transition mechanisms. Significant steps forward have been achieved with the discovery of the importance of the free-stream turbulence on the transition process and their acoustical origins in wind-tunnels, with the turbulent side walls boundary layers [3; 4]. Mack discovered numerically the existence of higher instability modes [5] not related to viscous instabilities which have been confirmed by measurements across boundary layers using hot-wires [6; 7]. The characterization of the boundary layer disturbances via surface measurements has been obtained more recently using fast-response pressure sensors [8; 9; 10] and heat transfer gauges [11], easing the understanding of the mechanisms responsible for transition.

The challenge is now to characterize experimentally the boundary layer perturbations and to compare their amplification rates to the ones predicted by linear stability theory (LST). The recent comparison of experiments performed in the von Karman Institute at Mach 6 in the H3 wind-tunnel with in-house stability codes [12] lead to conclusive results [13] to be extended to larger Mach numbers in the Longshot wind-tunnel (described in more details in [14]).

The model selected for the present study will first be presented with preliminary computations to approximate the transition location. In agreement with the guidelines developed in [15] for quality research on boundary layer stability and transition, it is equally important to characterize the environment in which experiments are conducted because of their large influence on transition phenomenon. Therefore, the work performed in this frame will also be developed and future working directions will be presented.

2. Design of the model

2.1. Geometry

Most of the hypersonic vehicles designed in the past were blunt to a very large extent (Apollo, ARD, MSL...) but the new generation of hypersonic vehicles might be differently designed to meet other requirements (transport over long ranges, long sustained hypersonic flights...). In these cases, sharper and slender bodies will be better suited for optimized aerodynamic performances.

From the point of view of experiments conducted in wind-tunnels, simple models such as flat plates are subject to side effects where early transition occurs, influencing measurements towards the center of the model. Larger flat plates would be required to limit this influence but they would then be limited by the nozzle exit diameter. This, in turns, constrains the length of the plate and limits the maximum Reynolds number achievable for transition studies. Moreover, the leading edge quality is critical and slight variations in thickness can significantly delay or promote transition [16]. Thus, this geometry was not considered further.

Conical models are better suited for several reasons. First, long cones can fit into the wind-tunnel test section and even partially into the axisymmetric contoured nozzle without interfering with the side wall boundary layers, nor inducing blockage, and still benefiting from long test times [14]. They also allow to reach large Reynolds numbers. Side effects are inexistent and the leading edge quality must be controlled only at a single point. From a numerical point of view, it is also easily modeled with axisymmetric computations (using RANS models) and is therefore cheaper from a CPU point of view. Finally, transition studies on conical geometries are widely reported in the literature even if they are relative to lower Mach numbers except for few cases [10; 17; 18]. Most of references focus on such conical geometries with an half-angle of 7 °, which is therefore preferred for the present work.

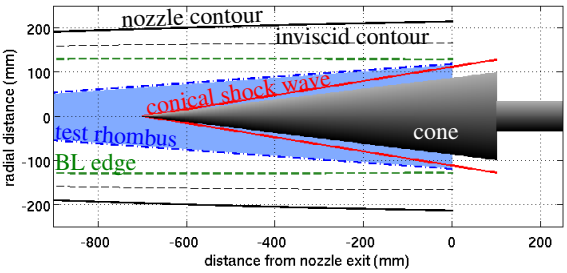

Figure 1: Maximum cone length in the VKI Longshot test section

The length of the cone was selected to be as long as possible without being too intrusive into the test section giving $L = 800$ mm. Fig. 1 shows the 7 ° cone with its attached shock wave as determined from tables [19] in the test rhombus (parallel flow domain as determined in [20]), and the edge of the nozzle wall boundary layer obtained from numerical computations [14]. Longer models would have a base diameter larger than the diameter of the uniform flow which could possibly induce wall pressure gradient and pol-

lute the measurements.

The cone will be tested at 0 ° angle of attack with different nosetips having curvature radii in the range 0.05 to 10 mm. This will allow to evaluate the influence of the bluntness effect and the associated stabilizing entropy layer.

2.2. *Instrumentation*

The purpose of the present research is to determine the transition location and to investigate the mechanisms responsible for boundary layer transition. Therefore, both the mean quantities and the fluctuations are of interest. The sensors used will be limited to wall measurements (temperature and pressure) and will mainly be located streamwise.

Coaxial thermocouples from RWTH (Aachen University), having a response time below 10 μs, will be used for the measurement of wall surface temperatures and wall heat fluxes. Since transition is typically characterized by a rise in wall heat flux, they will be useful to determine the precise transition location.

The mean wall pressure will be measured using Kulite pressure sensors equipped with screens limiting their operational bandwidth to about 20 kHz. The free-stream static pressure could be inferred from these measurements as well as the lower part of the boundary layer disturbances spectrum.

Finally, PCB sensors (132A31) will be used to measure the broadband spectrum of the pressure disturbances existing at the surface of the cone. Such sensors have resonant frequencies above 1 MHz making them suitable to track disturbances of the order of several hundreds of kHz. Several of these sensors will be located streamwise and crosswise to measure the amplification of the disturbances and to compare them with theory.

2.3. *Prediction of transition*

The accurate prediction of the onset of transition location in hypersonic flows is still a challenge even for simple configurations. More than 200 different correlations are reported in [21] with various degrees of success and with the severe drawback of being limited to specific configurations which cannot be extrapolated to other conditions. Nonetheless, there exists a correlation developed by Pate [22] for sharp cones with half-angles smaller than 10 ° based on data gathered in 16 wind-tunnels at Mach numbers between 3 and 20. Although it is still restrictive in its range of application, it includes the Longshot conditions. The main interest of this correlation is that it takes into account, indirectly, the amount of acoustical noise present in the free-stream. This correlation was in remarkable agreement with experimental data in [23; 13] among the most recent ones and should not be neglected for the only reason that it is an empirical correlation, thus lacking of physics insight.

The correlation of Pate [22] is given in Eq. 1 and is correlated with the maximum of the pitot pressure fluctuations corresponding to the end of the transition region. It requires parameters relative to the size of the wind-tunnel (circumference of the nozzle at the exit C, and a normalization parameter $\bar{C}$ accounting for a smaller nozzle than the one used in [22] as a reference) and to the free-stream noise levels (as approximated through nozzle wall boundary layer characteristics: skin friction $C_{F_{II}}$ and displacement thickness δ^*). This does not contain any physical transition mechanisms and leaves place for the current research.

$$\mathrm{Re}_{e_{tr}} = \frac{48.5\,(\mathrm{C}_{\mathrm{F_{II}}})^{-1.40}\left(\bar{\mathrm{C}}\right)}{\sqrt{\frac{\delta^*}{C}}} \qquad (1)$$

The transition Reynolds number $\mathrm{Re}_{e_{tr}}$ obtained is based on local properties determined with oblique shock relationships. This correlation was evaluated (see Fig. 2) for every operating condition of the Longshot wind-tunnel including the time dependence of the free-stream quantities.

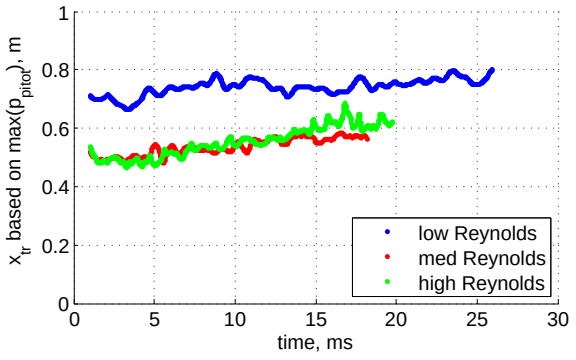

Figure 2: Prediction with Pate's correlation of the end of the transition location over a sharp cone for three different operating conditions of the Longshot wind-tunnel

The combination of the time decaying free-stream Reynolds number with the increasing free-stream noise levels gives a transition location which is relatively independent on time. With a 0.8 m long cone and the end of the transition being about 0.5 m for standard wind-tunnel operation, the phenomenon should be measurable with the characterization of the

developing instabilities in the laminar boundary layer. As for every empirical transition correlation, the uncertainties associated with this prediction are hardly quantifiable.

3. Wind-tunnel flow characterization

3.1. Flow uniformity and origin of disturbances

The determination of the flow uniformity at several axial locations along the nozzle has been reported in [14] for the "Low" Reynolds number operating condition. Relatively good agreement is obtained between numerical results (using the turbulent SST $k-\omega$ model of the CFD++ commercial software) and experimental results as shown in Fig. 3. This confirms the existence of thick turbulent boundary layers along the walls of the nozzle. Some of the disturbances measured inside the nozzle have been shown to be due to a nozzle contour discontinuity due to an incorrect implementation of the method of characteristics [20]. Similar flow non-uniformities along the nozzle center line in the nozzle exit plane may have the same origin although additional investigations would be required for definitive conclusions. The free-stream uniformity as characterized by its standard deviation in this operating condition is within 3.5%.

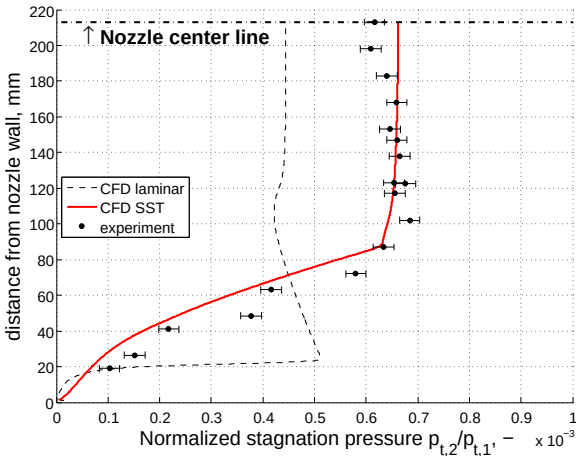

Figure 3: Normalized stagnation pressure profile at the nozzle exit for experiments at "Low" Reynolds number

3.2. Free-stream noise levels

The free-stream turbulence in hypersonic flows is often referred to as noise levels because of the dominance of acoustic radiations emitted by the side wall turbulent boundary layers. These noise levels were estimated using stagnation pitot pressure probes as reported in [14]. Comparison with similar wind-tunnels presented in Fig. 4 emphasizes the large amount of noise existing in very large Mach number facilities and are in agreement with the trends given in [24] where noise levels increase with the fourth power of the Mach number. The decay of the acoustic noise levels with the Reynolds number Re_D is in agreement with the trends presented in [25].

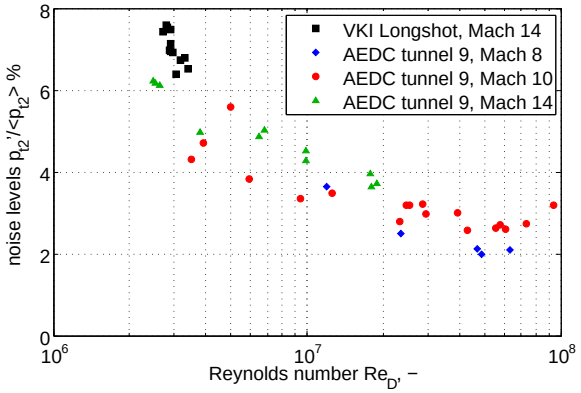

Figure 4: Free-stream noise levels in the Longshot (for experiments at "Low" Reynolds number) and similar wind-tunnels

The largest fluctuations $\frac{p'_{t_2}}{<p_{t_2}>}$ (up to 7.5%) are in a low frequency range below 20 kHz and might have been amplified by the protecting caps used in front of the sensors which have been shown to induce resonance effects in the cavities [26]. This may explain the slightly larger noise levels recorded in the Longshot facility when compared to the similar AEDC tunnel 9. Such large free-stream noise levels are clearly not representative of the low turbulence levels encountered in flight. Nevertheless, their influence on the transition process cannot be fully evaluated until a wider spectrum of the disturbances is obtained.

3.3. Measurements of free-stream static pressure

The free-stream properties of the flow are currently determined using the complex procedure presented in [27] and relying on assumptions such as the adiabatic and isentropic flow expansion through the nozzle. The direct measurement of free-stream properties, although challenging, would allow to rely only on test section measurements and would relax most of the assumptions used in the previous model. The improved accuracy would benefit to the determination of other free-stream quantities such as the Mach number.

3.3.1. Design of the probes

Two similar static pressure probes were manufactured based on previous designs presented in [28]. Four Kulite pressure sensors are located at different $\frac{L}{D}$ ratios as given in Fig. 5 to assess the influence of the viscous effects along the probes and the influence of their enlarging base.

Numerical computations have been performed to estimate the wall pressure at the measuring locations and their connection to the free-stream pressure. Results were obtained with CFD++ using pure nitrogen and a perfect gas equation of state with free-stream conditions corresponding to three different time instants as obtained with the isentropic flow expansion method described in [27]. The static pressure along the wall of the large probe is given in Fig. 6 and is closely similar to results obtained for the small probe. Viscous effects along the probe are relatively limited as from the first probing location, that is the three sensors should measure closely the same static pressure. Furthermore, when normalized by the free-stream static pressure, the influence of the time instant is relatively limited and all sensors should underestimate at any time the real static pressure by 0 to 5.3%.

The pressures of interest represent only about 5% of the full range of the sensors. Their calibration proved to be difficult because of the lack of adapted calibration equipment at these low pressures. Nevertheless, good confidence has been obtained using various methods so that accuracies of ±6.3% and ±10.3% were achieved for the small (sensor XCQ-093-5psi) and large probes (sensors XCQ-062-5psi), respectively.

3.3.2. Experimental results

A comparison of the measurements obtained during a single experiment with the two probes is shown in Fig. 7. All sensors from both probes give sensibly

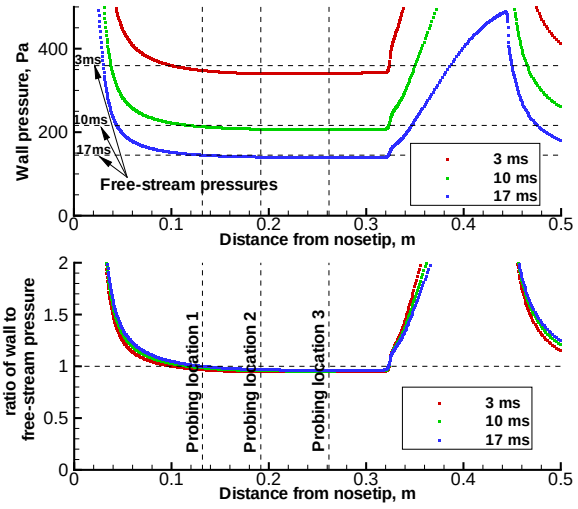

Figure 6: Static pressure along the wall of the larger probe for three different free-stream conditions

the same static pressure with a weak influence of the viscous effects in agreement with the numerical results of Fig. 6 and with differences mainly within the fluctuations of the measurements.

However, present measurements lie significantly above theoretical free-stream static pressure obtained from equations based on isentropic nozzle flow expansion through the nozzle [27]. This leads to two distinct possibilities which will be evaluated hereafter:

- the static pressure measured is biased,
- the theory used to determine the free-stream conditions is incorrect due to irrelevant assumptions.

3.3.3. Interpretation of the measurements

In order to explain the possibly biased measurements the following possibilities have been assessed:

- wrong calibration? unlikely: sensors would have to behave severely non-linearly.

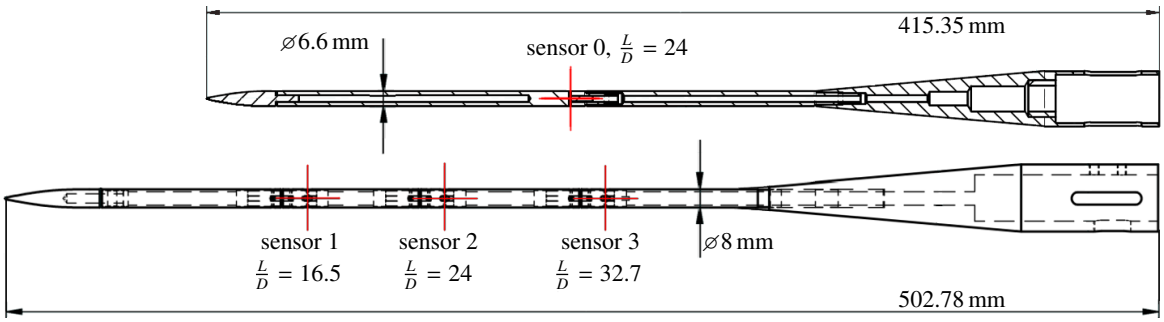

Figure 5: Comparison of the two operational static pressure probes at their respective scales

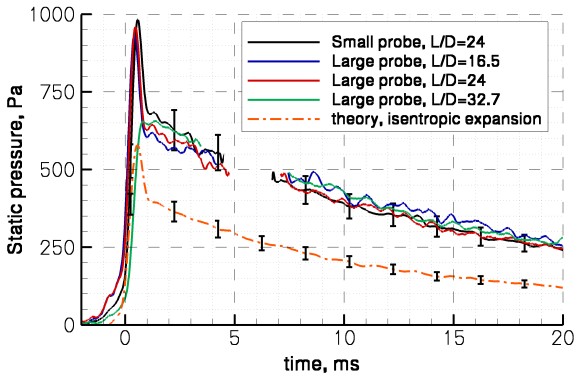

Figure 7: Comparison of the static pressure measured with the two probes and with theoretical expectations, test 1725 (noise in the signals around $t = 5$ ms has been removed for clarity)

- acceleration sensitivity? unlikely: during a test, the probes are subject to an acceleration which could influence the measurements through the inertia of the diaphragm. This should actually lead to a lower pressure measured from the mechanical design of the sensor, and large sinusoidal oscillations would be visible after some time because of the movement of the probe.

- temperature sensitivity? unlikely: the heating of the sensing element is relatively limited during the 20 ms of the experiment and this is compensated by the electronics embedded in the sensor.

- viscous effects? unlikely: the three measurements along the probe are closely the same.

- wall pressure gradient $\frac{\partial p}{\partial y} \neq 0$? unlikely: in hypersonic flows the wall pressure gradient is not necessarily zero but remains small for the Mach number considered here [29].

- recirculation bubble? unlikely: specific experiments with shock wave boundary layer interaction in the vicinity of the measurement location 3 showed very limited upstream perturbations.

- angle of attack? unlikely: a large misalignment of the probe with the flow ($\alpha = 2\,^\circ$) has lead to only 10% lower pressure.

So far, none of these considerations can explain the larger static pressure measured. Additionally, there exist other elements which are not in agreement with theoretical expectations such as the angle of the oblique shock wave and the thickness of the boundary layer along the probe. A Schlieren picture of the small probe is given in Fig. 8 and compared with numerical results. The different pictures were scaled based on the apparent diameter of the second probe visible in the field of view and with the base diameter of the probe for the numerical results. Pictures were then adjusted so that the base corners of the static pressure probe were at the same location.

The angle of the main shock wave along the small probe seen in Fig. 8 is slightly larger experimentally ($\approx 5.5\,^\circ$) than in numerical simulations ($\approx 4.5\,^\circ$). If we assume that the shock wave angle at that location has reached its asymptote and is representative of a small perturbation, this would corresponds to respective free-stream Mach numbers of ≈ 10.5 and ≈ 13. This lower experimental free-stream Mach number is in agreement with the Mach number which is determined from the pressure ratio $\frac{p_{t_2}}{p_{\infty_{measured}}}$ given by the Rayleigh equation.

Experimental boundary layer thickness appears to be thinner than in the numerical solution which would also support the possibility of a lower free-stream Mach number: hypersonic boundary layers tend to scale as $\frac{\delta}{x} \propto \frac{M_e^2}{\sqrt{Re_x}}$ leading to $M_\infty \approx 11$ instead of

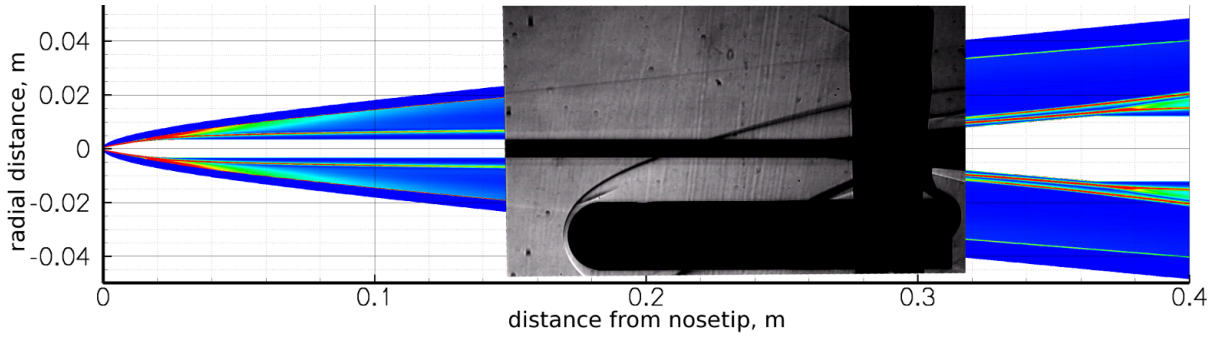

Figure 8: Schlieren picture and numerical density gradient $\frac{\partial \rho}{\partial y}$ comparing the shock position and boundary layer thickness along the small static pressure probe, test 1717

$M_\infty \approx 14$. Each of these observations was confirmed during other tests including the larger probe.

The comparison with additional numerical results performed with lower free-stream Mach numbers (in the range $10 < M_\infty < 11.2$) and static pressures in the free-stream matching the ones measured experimentally at different time instants showed a better agreement for the shock position and the thickness of the boundary layers. For these numerical cases, the viscous effects along the wall of the probes were similar to the ones presented in Fig. 6 and should not have influenced the measurements by more than 6%.

Since measurements could not be proven to be biased and since flow observation also supports the possibility of a lower free-stream Mach number due to larger free-stream temperature (and pressure in turns), the theory commonly used must be checked to ensure that none of its assumptions is violated. One possibility which would violate the isentropic flow assumption is the presence of flow condensation within the nozzle which would release heat into the free-stream, (therefore lowering the free-stream Mach number) and also increase the free-stream static pressure. Since the present measurements are similar to the effects of flow condensation, this phenomenon deserved the deeper analysis summarized hereafter.

4. Assessment of flow condensation phenomenon

4.1. Generalities

In hypersonic wind-tunnels, the flow expansion from the reservoir to the test section is so large that it lowers the static temperature of the gas to very low temperatures so that the test gas itself may condense.

Several datasets exist about the condensation of nitrogen in hypersonic nozzles [30; 31] and proved the existence of a supercooling effect, where the gas could reach temperatures below its equilibrium saturation temperature before condensing, providing the flow expansion was fast enough. The nature of the nucleation process was also seen to vary between cases: either natural (homogeneous) or promoted by the presence of other species offering seeding nuclei (heterogeneous due to residual water, CO_2 or particles). This complex phenomenon is very well described in several reviews [32; 33].

4.2. Determination of the condensation onset

The condensation onset of air and nitrogen is given in Fig. 9 from the data compiled in [34]. Temperatures significantly below the equilibrium saturation line could be achieved before reaching the experimental condensation onset. This shows the significant presence of flow supercooling, which strongly depends however on the type of nozzle used as indicated by the color code.

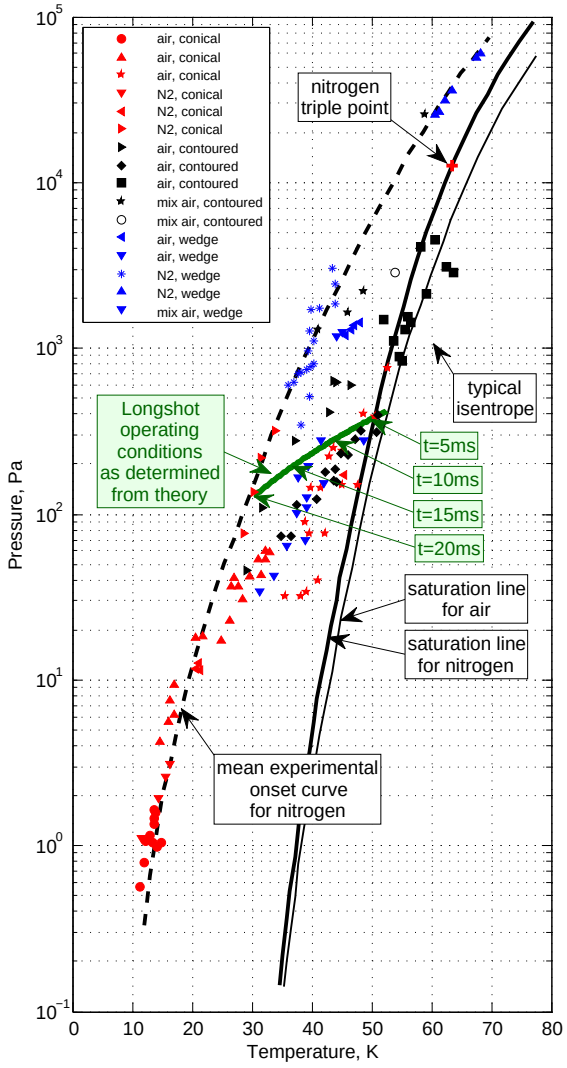

Figure 9: Comparison of air and nitrogen condensation onset behavior, replotted from [34] to emphasize the importance of the shape of the nozzle used on the amount of supercooling obtained. The evolution of the Longshot free-stream conditions (p_∞ and T_∞) obtained with a contoured nozzle have been added for comparison.

Nozzles with continuous flow expansion (conical and wedge types) allow for larger amount of supersaturation to be reached when compared to the contoured ones. The effect of the temperature gradient along the nozzle axis has been demonstrated in [32] and a long portion of flow with constant temperature

as in contoured nozzles greatly reduces the supersaturation achievable. Thus, contoured nozzles are more prone to condensation.

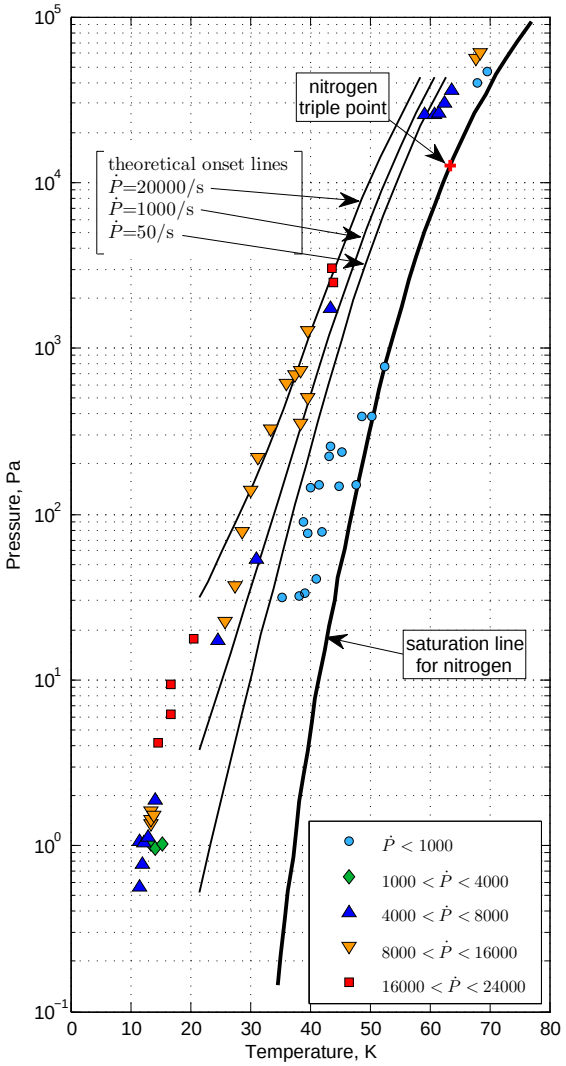

Figure 10: Expansion-rate effects, replotted from [34]

A typical range of free-stream conditions encountered during a single experiment in the Longshot wind-tunnel has been added on top of Fig. 9 as a function of time. These correspond to the ones obtained with the method detailed in [27].

It is obvious that meaningful experiments in the Longshot facility will only be possible if the onset of flow condensation is occurring at very low temperatures, that is with a large amount of supercooling. Since the wind-tunnel uses a contoured nozzle which offers a long portion of the flow without any temperature gradient, the amount of supercooling might be limited and condensation may occur quite early.

The theoretical analysis of Daum and Gyarmathy [34] shows that a nozzle expansion rate $\dot{P}$ defined as the rate of pressure decrease compared to the actual static pressure can correlate the amount of supersaturation achievable. When reconsidering Fig. 9 with this expansion rate parameter $\dot{P}$ (as shown in Fig. 10), it becomes clear that the nozzles with the largest expansion rates (as in conical nozzles) exhibit the largest amounts of supercooling. On the other hand, contoured nozzles for which the expansion rate is below 1000 have little or no flow supercooling.

The experiments with large $\dot{P}$ are in agreement with the theory developed based on the computation of the nucleation point for homogeneous condensation (Wilson lines). Nonetheless, the same theory disagrees with experiments performed in nozzles having a small $\dot{P}$. This is explained by the presence of heterogeneous nucleation mechanism due to seeding pollutants. Based on these observations, Daum and Gyarmathy developed a conservative law to be used in any wind-tunnel which allows to determine the temperature at which the gas will condense, including the amount of supercooling achievable. This takes into account the nature of the condensation phenomenon (homogeneous or seeded) and the input parameters required are the nozzle expansion rate parameter $\dot{P}$ and the static temperature and pressure of the medium.

4.3. Saturation temperature for the Longshot

The evolution of the free-stream temperature as obtained by assuming an isentropic flow expansion [27] is given in Fig. 11 for a "Medium" Reynolds experiment in the Longshot. The time decay is due to the emptying reservoir and is typical of the Longshot wind-tunnel. The free-stream pressure was obtained by the same method and will be used to determine the saturation temperature described earlier.

On the same figure, the equilibrium saturation line from the literature is given as well as the minimum temperature at which the gas is sure to condense. Condensation is however likely to occur much earlier due to the weak expansion rate and the presence of flow pollutants. This can be evaluated using the law of Daum & Gyarmathy. The expansion rate of the Longshot contoured nozzle $\dot{P} \approx 60$ proves that flow nucleation is likely to be dominated by heterogeneous phenomenon with a corresponding very limited amount of flow supersaturation [1].

[1] This is supported by previous condensation studies which were

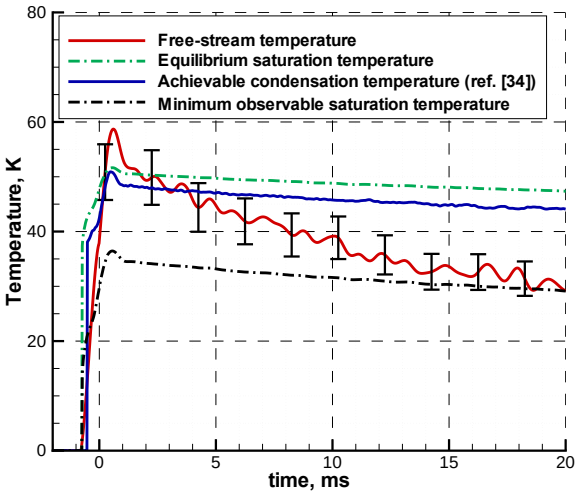

Figure 11: Longshot free-stream temperature and equilibrium/non-equilibrium saturation temperatures, test 1725

The results obtained with the correlation of Daum and Gyarmathy are plotted in Fig. 11 giving the expected condensation temperature of $\approx 44 - 48$ K depending on the time considered with a corresponding supercooling limited to 3 K. The slightly decaying trend of both equilibrium and non-equilibrium saturation temperatures with time is due to the influence of free-stream static pressure and velocity. According to theory, the flow static temperature T_∞ reaches the non-equilibrium condensation temperature after 3 ms and is then likely to condense.

4.4. Detection of flow condensation in the Longshot

4.4.1. Quantities influenced

All flow quantities are not equally influenced by the presence of flow condensation. For instance, there is limited effect on the measured test section stagnation pressure [31; 32; 36]. However, the flow condensation process releases heat into the surrounding environment thus increasing the flow static temperature T_∞. The flow temperature is rather difficult to measure but the static pressure is changed in similar proportions which makes it convenient to detect the presence of flow condensation. Therefore, the presence of flow condensation in the Longshot is assessed with the newly available static pressure probes.

performed in the Longshot and reported in [35] where the amount of supercooling achievable appeared to be limited to 5 K even while using a conical nozzle. This limited amount of supercooling was probably due to the presence of particles in the flow which promoted the nucleation phenomenon.

4.4.2. Test conditions

Experiments have been conducted in the Longshot facility with two additional conditions different from the ones used routinely and whose initial conditions are summarized in Table 1. These were successively aiming for:

- a higher reservoir temperature T_0 which should ideally reduce the risks for flow condensation by maintaining the flow static temperature above the condensation onset.
- a much lower stagnation temperature T_0 which should have instead promoted the appearance of flow condensation. If such phenomena occur, then the measurement of the static pressure should allow to detect it.

Table 1: Relevant initial conditions for nitrogen experiments in the Longshot, driver pressure is always 345 bar

Test condition	Driven pressure	Mass piston	tests number
Standard "Medium Re"	2.35 bar	3.215 kg	1725
"High T_0"	1.586 bar	2.5 kg	1726
"Low T_0"	4.333 bar	4.5 kg	1729

4.4.3. Results

Significantly higher and lower free-stream temperatures have been obtained as given in Fig.12 (determined with the isentropic flow assumption). The larger oscillations for T_∞ computed for $1 - 4.5$ ms in the case of the lower T_0 are due to an abnormal amount of particles seeding the flow, which impacted the stagnation probe used in the rebuilding procedure and biased its measurements. In the same figure, the theoretical onset of condensation as obtained from the theory of Daum and Gyarmathy (section 4.2) is given. It is closely the same for all experiments because of similar flow velocities and a weak influence of the free-stream static pressure.

The static pressure as determined from theory and measured with the small static pressure probe are given in Fig. 13. The decaying trend observed for the standard experiment and the one at larger stagnation temperature are very similar to each other. For the experiment at low T_0, the measured static pressure p_∞ lies below the two other experiments because of a lower reservoir stagnation pressure but is still significantly higher than the one predicted by theory. Note

however, that for this experiment, a significant slope change at $t = 8$ ms could indicate the presence of condensation in the flow. The influence on the corresponding theoretical static pressure is weak since the stagnation probes used for its determination are relatively insensitive to the condensation phenomenon.

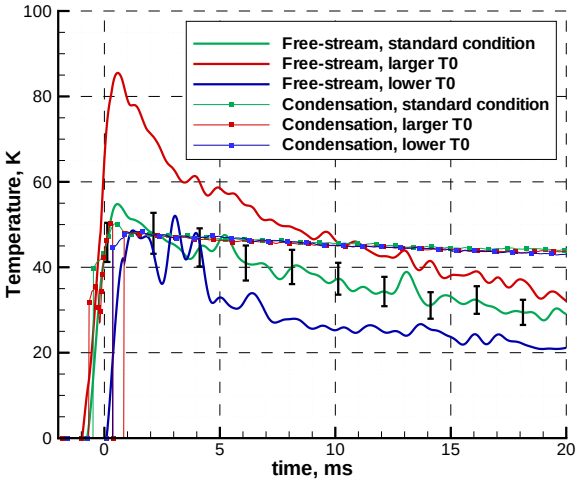

Figure 12: Free-stream static temperature T_∞ (from theory) and condensation onset temperature T_c (from [34])

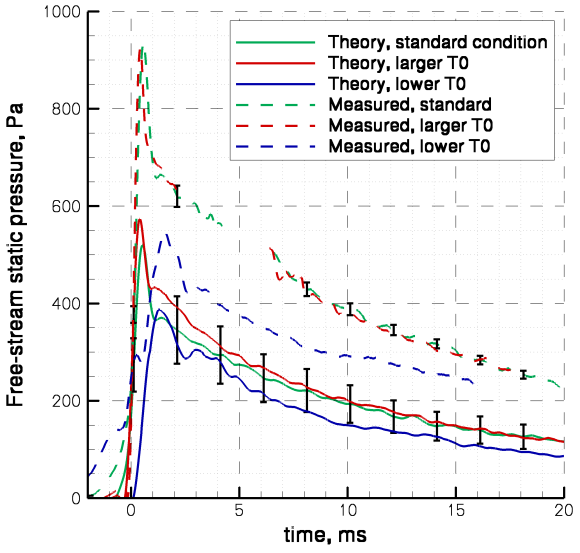

Figure 13: Measured and theoretical static pressures p_∞ (noise in the signals around $t = 5$ ms has been removed for clarity)

From the stagnation pressure p_{t_2} and the static pressure both measured in the test section, the free-stream Mach number can be determined using the Rayleigh equation [19]. Knowing then the free-stream stagnation temperature from the equation of Fay-Riddell [37], the corresponding free-stream static temperature can be determined. These have been computed and are given in Fig. 14.

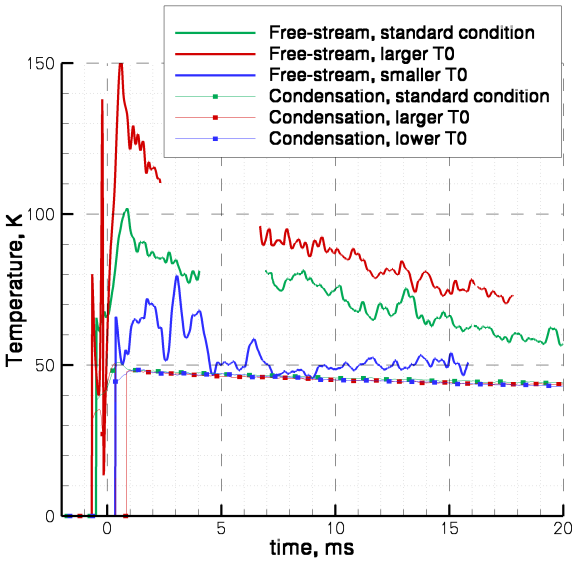

Figure 14: Free-stream static temperature T_∞ (from p_∞ measurements, noise in the signals around $t = 5$ ms has been removed for clarity) and condensation onset temperature T_c (from [34])

On such plot, the free-stream temperature (not determined from theory but experimentally using p_∞) for standard experiments is clearly above the condensation limit. The experiment performed at a lower stagnation temperature T_0 is however much closer from the condensation limit and at $t = 8$ ms, the free-stream temperature may cross the saturation line explaining the change of slope observed on $p_{\infty_{measured}}$ at that time. The equations used to determine this free-stream static temperature are no longer valid once a two-phase flow is present but are applicable before and allow to determine when the static temperature reaches the saturation limit.

Finally, the free-stream pressure is plotted versus the free-stream temperature in Fig. 15 for the three experiments considered and in a way similar to Fig. 9. For each experiment, two curves are plotted: one from isentropic theory, and the other as obtained from measurements using the static pressure probes.

Theory leads to free-stream conditions going well inside the supersaturation domain and even beyond the minimum condensation temperature for one test without noticeable changes on the slope $\frac{dp_\infty}{dT_\infty}$. This proves that theory leads to results in disagreement with literature results about condensation onset.

The same experiments reconsidered from the mea-

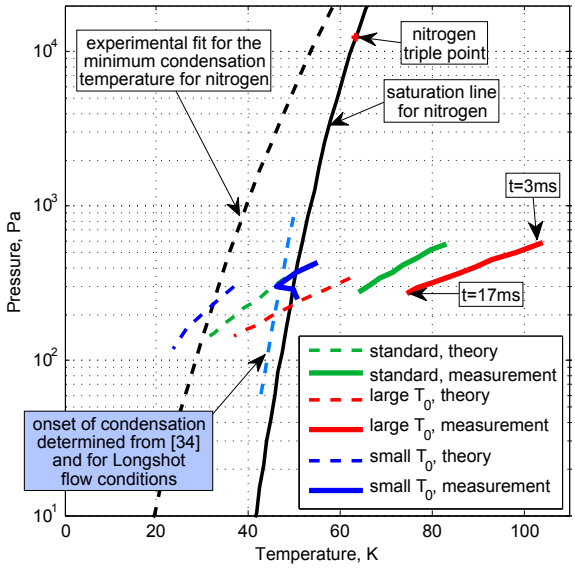

Figure 15: Comparison of free-stream conditions determined from theory and from measurements and compared to the predicted onset of condensation for the specific Longshot conditions

sured static pressure and inferred static temperature are well above the saturation limit except for the experiment at the lower T_0. In that case, the trend of the curve is sharply changing once the free-stream temperature reaches the saturation temperature determined for the specific case of the Longshot. This good agreement between the results obtained from the static pressure probe and the literature relative to flow condensation proves that the static pressure probe may measure correctly [2].

In consequence, past experiments performed in the Longshot facility with standard conditions avoided condensation but only because the free-stream temperature was larger than believed from theory. The corresponding quantities (Mach, Reynolds, Stanton numbers...) determined from T_∞, p_∞ and others are all likely to be incorrect for instance by as much as 100% for p_∞.

5. Conclusions

The design of a conical model for the studies of hypersonic boundary layer transition has been reported together with its instrumentation.

[2]Note that free-stream conditions are crossing the saturation line well below the triple point of nitrogen so that the condensate might not be liquid but rather solid nitrogen even though literature still refers to the phase change as condensation.

The most recent flow calibration at the nozzle exit has been summarized giving a uniformity of 3.5% and free-stream turbulence levels up to 7.5%.

The measurement of free-stream static pressure with dedicated probes has shown large disagreement with theory based on the assumption of an isentropic flow expansion. The different hypothesis considered to explain biased measurements could not solve the discrepancies suggesting that measurements might instead be correct (therefore corresponding to lower free-stream Mach numbers). This is supported by the observation of shock wave angles and boundary layer thicknesses which are in better agreement with $M_\infty \approx 11$ rather than with $M_\infty \approx 14$.

A non-isentropic flow phenomenon (condensation) was investigated to explain the possibly inadequate theory. The flow nucleation in standard operational conditions has been shown not to be responsible for the larger free-stream pressure. However, such standard operating conditions may actually avoid flow condensation only because the real free-stream temperature is much larger than expected from theory. Dedicated experiments promoting condensation by lowering the free-stream temperature have shown that nucleation could be detected by the static pressure probes. The pressure and temperature at which it occurred compared favorably to the saturation temperature given in the literature which is another proof to the credit of the correct static pressure measurements.

Although additional experiments are required to support the present conclusions, it seems that the theory used is based on assumptions not applicable to the Longshot facility for reasons yet to be identified. If confirmed, this would put into questions most of, if not all, experiments performed over the last decades because of a much lower free-stream Mach number than originally believed. Similar trends are expected on other non-dimensional numbers deriving from the larger free-stream temperature and pressure.

Future research activities should focus on explaining the reasons for such larger free-stream static temperature in the Longshot wind-tunnel. The analysis of non-equilibrium flows in contoured nozzles with the relaxation of vibrational energy into the free-stream might be worth to be investigated.

Acknowledgments

The author gratefully acknowledge FRIA (Fonds pour la formation à la Recherche dans l'Industrie et dans l'Agriculture) for the financial support of this project.

References

[1] S. P. Schneider, Hypersonic laminar-turbulent transition on circular cones and scramjet forebodies, Progress in Aerospace Sciences 40 (1-2) (2004) 1–50.

[2] J. D. Anderson, Hypersonic and High Temperature Gas Dynamics Second Edition, American Institute of Aeronautics and Astronautics, 2006.

[3] J. Laufer, Some statistical properties of the pressure field radiated by a turbulent boundary, Physics of Fluids 7 (8) (1964) 1191–1197.

[4] J. M. Kendall Jr., Supersonic boundary-layer transition studies, in: JPL Space Programs Summary, Vol. 3, Jet Propulsion Laboratory, 1970, pp. 43–47.

[5] L. M. Mack, Boundary layer linear stability theory, special course on stability and transition of laminar flows, Rept. 709, NATO (March 1984).

[6] K. F. Stetson, E. R. Thompson, J. C. Donaldson, L. G. Siler, Laminar boundary layer stability experiments on a cone at Mach 8, part I, sharp cone, in: 16th AIAA Fluid and plasma dynamics conference, no. AIAA paper 1983-1761, 1983.

[7] K. F. Stetson, E. R. Thompson, J. C. Donaldson, L. G. Siler, Laminar boundary layer stability experiments on a cone at Mach 8, part II: blunt cone, in: 22nd AIAA Aerospace Sciences Meeting, no. AIAA paper 1984-0006, 1984.

[8] K. Fujii, Experiment of the two dimensional roughness effect on hypersonic boundary layer transition, Journal of Spacecraft and Rockets 43 (4) (2006) 731–738.

[9] M. Estorf, R. Radespiel, S. P. Schneider, H. B. Johnson, S. Hein, Surface pressure measurements of second mode instability in quiet hypersonic flow, in: 46th AIAA Aerospace sciences meeting and exhibit, 2008.

[10] D. C. Berridge, K. M. Casper, S. J. Rufer, C. R. Alba, D. R. Lewis, S. J. Beresh, S. P. Schneider, Measurements and computations of second-mode instability waves in three hypersonic wind tunnels, in: 40th AIAA Fluid Dynamic Conference and Exhibit, no. AIAA paper 2010-5002, 2010.

[11] T. Roediger, H. Knauss, E. Kraemer, M. Estorf, S. P. Schneider, B. V. Smorodsky, Hypersonic instability waves measured using fast-response heat flux gauges, in: 46th AIAA Aerospace sciences meeting and exhibit, no. AIAA paper 2008-638, 2008.

[12] F. Pinna, Numerical study of stability of flows from low to high Mach number, Ph.D. thesis, von Karman Institute for Fluid Dynamics - Università degli studi di Roma la Sapienza (March 2012).

[13] D. Masutti, F. Pinna, E. Günaydınoğlu, T. Sopek, O. Chazot., Natural and induced transition on a 7deg. half-cone at Mach 6, in: Hypersonic laminar-turbulent transition, no. AVT-200, NATO, 2012.

[14] G. Grossir, S. Paris, K. Bensassi, P. Rambaud, Experimental characterization of hypersonic nozzle boundary layers and free-stream noise levels, in: 51st AIAA Aerospace Sciences Meeting, no. AIAA paper 2013-1130, 2013.

[15] E. Reshotko, Boundary layer stability and transition, Annual Review of Fluid Mechanics 8 (1976) 311–349.

[16] G. Simeonides, Hypersonic shock wave boundary layer interactions over compression corners, Ph. D. thesis, University of Bristol, von Karman Institute for Fluid Dynamics (April 1992).

[17] E. J. Softley, B. C. Graber, R. E. Zempel, Experimental observation of transition of the hypersonic boundary layer, AIAA Journal 7 (2) (1969) 257–263.

[18] A. A. Maslov, A. N. Shiplyuk, D. A. Bountin, A. A. Sidorenko, Mach 6 boundary layer stability experiments on sharp and blunted cones, Journal of Spacecraft and Rockets 43 (1) (2006) 71–75.

[19] Ames research staff, Equations, tables, and charts for compressible flows, Tech. Rep. NACA 1135, NACA (1953).

[20] G. Simeonides, The contoured Mach 15 Longshot nozzle: final design parameters and construction, Internal Note 87, von Karman Institute for Fluid Dynamics (September 1989).

[21] A. M. Berkowitz, C. L. Kyriss, A. Martellucci, Boundary layer transition flight test observations, in: 15th AIAA Aerospace Sciences Meeting, no. AIAA paper 1977-125, 1977.

[22] S. R. Pate, Dominance of radiated aerodynamic noise on boundary layer transition in supersonic-hypersonic wind tunnels, Technical report AEDC-TR-77-107, Arnold Engineering Development Center (March 1978).

[23] K. M. Casper, S. J. Beresh, J. F. Henfling, R. W. Spillers, B. Pruett, S. P. Schneider, Hypersonic wind tunnel measurements of boundary layer pressure fluctuations, in: 39th AIAA Fluid Dynamics Conference, no. AIAA paper 2009-4054, 2009.

[24] S. P. Schneider, Effects of high-speed tunnel noise on laminar-turbulent transition, Journal of Spacecraft and Rockets 38 (3) (2001) 323–333.

[25] A. J. Laderman, Review of wind tunnel free-stream pressure fluctuations, AIAA Journal 15 (4) (1977) 605–608.

[26] M. McGilvray, P. A. Jacobs, R. G. Morgan, R. J. Gollan, C. M. Jacobs, Helmholtz resonance of pitot pressure measurements in impulsive hypersonic test facilities, AIAA Journal 47 (10) (2009) 2430–2439.

[27] G. Simeonides, The VKI hypersonic wind tunnels and associated measurement techniques, Technical Memorandum 46, von Karman Institute for Fluid Dynamics (November 1990).

[28] H. Kindl, H. Olivier, Development of a static pressure probe (final report), Tech. rep., Shock Wave Laboratory RWTH Aachen (November 1996).

[29] M. C. Fischer, D. V. Maddalon, L. M. Weinstein, R. D. Wagner Jr., Boundary layer pitot and hot-wire surveys at Mach 20, AIAA Journal 9 (5) (1971) 826–834.

[30] P. D. Arthur, Effects of impurities on the supersaturation of nitrogen in a hypersonic wind tunnel, Ph.D. thesis, Calif. Inst. of Technol., Pasadena, California (1952).

[31] J. E. Bowman, Nitrogen condensation in the R.A.R.D.E hypersonic gas tunnel, Tech. Rep. C.P. No. 956, Aeronautical Research Council (1967).

[32] P. P. Wegener, L. M. Mack, Condensation in supersonic and hypersonic wind tunnels, in: H. L. Dryden, T. von Kármán (Eds.), Advances in applied mechanics, Vol. 5, Academic Press Inc., 1958, Ch. 7, Condensation in supersonic and hypersonic wind tunnels, pp. 307–447.

[33] H. G. Stever, Condensation phenomena in high speed flows, in: Fundamental of Gas Dynamics, Princeton University Press, 1958, Ch. F, pp. 526–573.

[34] F. L. Daum, G. Gyarmathy, Condensation of air and nitrogen in hypersonic wind tunnels, AIAA Journal 6 (3) (1968) 458–465.

[35] F. R. Bailey, B. E. Richards, Studies of flat plate heat transfer and pressure distribution including effects of condensation in the conical flow of the Longshot tunnel, in: 32nd Supersonic Tunnel Association Meeting, no. 1969-02, 1969.

[36] D. D. McBride, P. M. Sherman, Pitot pressure in hypersonic flow with condensation, AIAA Journal 9 (12) (1971) 2354–2357.

[37] J. A. Fay, F. R. Riddell, Theory of stagnation point heat transfer in dissociated air, Journal of the Aeronauticals Sciences 25 (2) (1958) 73–85.

Post-Flight Reconstruction using Conventional and Novel Instrumentation

Bart Van Hove

Aeronautics and Aerospace Department, von Karman Institute for Fluid Dynamics, Belgium, vanhove@vki.ac.be

Supervisor: Chazot Olivier (VKI)

Professor, Aeronautics and Aerospace Department, von Karman Institute for Fluid Dynamics, Belgium, chazot@vki.ac.be

University Supervisor: Lacor Chris

Professor, Dept. Mechanical Engineering, Vrije Universiteit Brussel, chris.lacor@vub.ac.be

Industry Supervisor: Karatekin Özgür (ROB)

Royal Observatory of Belgium, o.karatekin@observatory.be

Abstract

Apart from their value for planetary exploration, vehicles landing on the surface of other planets present a rare opportunity to investigate vehicle performance and atmospheric conditions. We developed trajectory and atmosphere reconstruction tools that attempt to fully exploit in-flight measurements. Both conventional and novel measurement systems have been considered. In particular, Flush Air Data Systems (FADS) are currently making their entrance on planetary exploration vehicles to Mars. We present methodology to derive flow angles and atmospheric density from such measurements, apply it to a hypersonic wind tunnel probe and consider ESA EXPERT as a case study to quantify the uncertainty on FADS reconstructed quantities during an Earth entry. We conclude that an accurate estimate of the atmospheric density is feasible and suggest attainable objectives for the VKI Longshot wind tunnel to serve as a FADS calibration facility.

Keywords: 6-DOF, reconstruction, hypersonic, atmosphere, trajectory, FADS, Flush Air Data System, IMU, Inertial Measurement Unit, EDL, entry, EXPERT, Longshot, simulation.

1. Introduction

Successfully landing vehicles on other planets is a challenging and rare achievement. Therefore in-flight measurements must be fully exploited to gain knowledge on the vehicle's behavior and the planetary environment. For this purpose, we develop tools for the reconstruction of trajectory and atmospheric profiles during Entry, Descent and Landing (EDL) of planetary entry vehicles. Entry vehicles are instrumented for real time guidance (e.g. reaction control systems and parachute deployment) and for post-flight reconstruction of trajectory parameters, aerodynamic coefficients and atmospheric conditions. These reconstructed quantities are closely coupled, for example aerodynamic coefficients are a function of angle of attack, aerodynamic forces, velocity and atmospheric density. Another example is the atmospheric pressure, which is typically derived from atmospheric density and vehicle altitude.

Entry vehicles are conventionally equipped with accelerometers and gyroscopes. By integrating those inertial measurements, an accurate 6 degree of freedom (6-DOF) trajectory can be obtained. However, because the inertial sensors are confined to the vehicle interior, deriving exterior quantities such as the atmospheric density requires modeled or estimated information. The density is most often estimated from a measured deceleration and predicted drag coefficient. This makes the drag coefficient an estimated input instead of a reconstructed output, and conflates the uncertainty on the density with that on the drag coefficient. Other exterior quantities include angle of attack and side slip angle.

In recent years, some vehicles are instrumented with an additional set of sensors directly exposed to the flow around the vehicle (e.g. Space Shuttle, EXPERT, MSL, ExoMars). This grid of pressure sensors integrated in the heat shield is commonly called a Flush Air Data System (FADS) and allows the flow angles and atmospheric density to be estimated independently of predicted aerodynamic behavior. However, FADS systems rely on surface pressure distribution and shock layer flow models. These can be developed from analytical relations, wind tunnel testing and computational fluid dynamics (CFD).

The PhD research presented here aims to accurately reconstruct atmospheric profiles during EDL exploiting any in-flight measurements available. The current focus is on hypersonic/supersonic entry up to parachute deployment on Mars and Earth. Density is a quantity of particular interest because atmospheric pressure and temperature are derived from it, and because density is used to normalize reconstructed aerodynamic forces and moments for comparison with ground predictions. The arrival of a novel in-flight measurement system (FADS) warrants a fresh look at reconstruction strategies and uncertainty quantification, as well as methods to optimally combine results from various reconstruction strategies.

This thesis project is part of the preparatory work for ESA's set of ExoMars missions in 2016-2018. The recently approved 2016 ExoMars EDM (EDL Demonstrator Module) aims to be Europe's first successful landing on the surface of Mars. Royal Observatory of Belgium PhD advisor Özgür Karatekin is co-PI of the ExoMars EDM science team (AMELIA) responsible for extracting scientifically valuable information from in-flight EDM measurements, such as atmospheric profiles. ExoMars EDM will enter the Martian atmosphere during dust season, presenting the first opportunity to study dust impact on the atmospheric conditions in-situ. The EDM heat shield is instrumented with FADS sensors from which atmospheric density can be derived more accurately than from conventional in-flight measurements.

The work presented here covers the development and validation of entry reconstruction and simulation tools for high velocity planetary entry. Both conventional inertial measurements and novel heat shield instrumentation (FADS) have been considered. Our reconstruction tools utilizing conventional inertial measurements have been applied to in-flight data from Mars Phoenix Lander (25 May 2008), and validated against independent reconstructions. Currently lacking in-flight measurements, we have applied part of our FADS methodology to a wind tunnel model at Mach 14 in the VKI Longshot wind tunnel. These tests were performed with nitrogen gas under operating conditions similar to the ESA EXPERT trajectory. Finally, we applied the complete FADS methodology to an EXPERT case study and quantified the required accuracy of the FADS modeling and wind tunnel environment for application to the EXPERT FADS instrumentation.

2. Reconstruction from conventional measurements

2.1. Approach

Conventional in-flight measurements are inertial acceleration and angular velocity measurements by accelerometers and gyroscopes contained in one or several inertial measurement units (IMU). Together, the accelerometers and gyroscopes constrain a 6-DOF (translation and rotation) trajectory that can be reconstructed by integration. In a second step, using the trajectory and some assumptions, atmospheric conditions are derived.

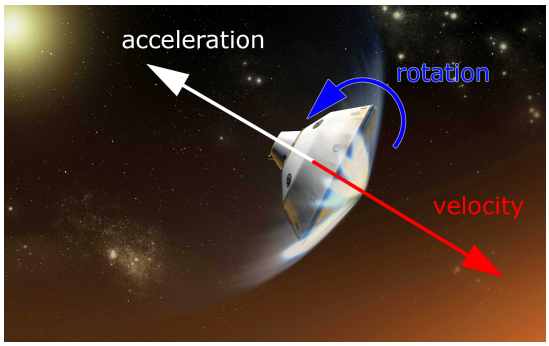

Figure 1: Hypersonic entry (adapted NASA artist concept)

The atmosphere reconstruction starts from an atmospheric density estimate ρ_∞ obtained from the axial acceleration a_{aero} measured in-flight and aerodynamic drag coefficient C_D predicted on ground:

$$\rho_\infty(h) = 2\frac{m \cdot |\vec{a}_{aero}|}{C_D \cdot S_{ref} \cdot |\vec{v}_{rel}|^2} \quad (1)$$

This method conflates the substantial uncertainty on the aerodynamic drag coefficient with that on the reconstructed density, but is the only option to derive atmospheric conditions from IMU data. FADS instrumentation would provide a density estimate independently of aerodynamic modeling. The density estimate ρ_∞ is then integrated over altitude assuming hydrostatic equilibrium, to derive atmospheric pressure

p_∞. The ideal gas law then combines density ρ_∞ and pressure p_∞ to derive atmospheric temperature T_∞.

$$p_\infty(h) = p_\infty(h_0) - \int_{h_0}^{h} g \cdot \rho_\infty \cdot dh \tag{2}$$

$$T_\infty(h) = \frac{\mu \cdot p_\infty}{R \cdot \rho_\infty} \tag{3}$$

Notice that to reconstruct atmospheric conditions, the trajectory needs to be accurately known. In the above equations, altitude h, aerodynamic acceleration $\vec{a}_{aero}$ and velocity relative to the atmosphere $\vec{v}_{rel}$ are required. Also vehicle mass and reference surface area.

2.2. *Validation with Mars Phoenix dataset*

The above reconstruction strategy has been employed for the majority of planetary exploration missions [1][2][3][4]. We applied our code to the Mars Phoenix Lander dataset and compared our reconstructed trajectory and atmosphere to reconstructions by independent authors. The Mars Phoenix dataset is representative of a conventionally instrumented entry vehicle and available on the Planetary Data System [5].

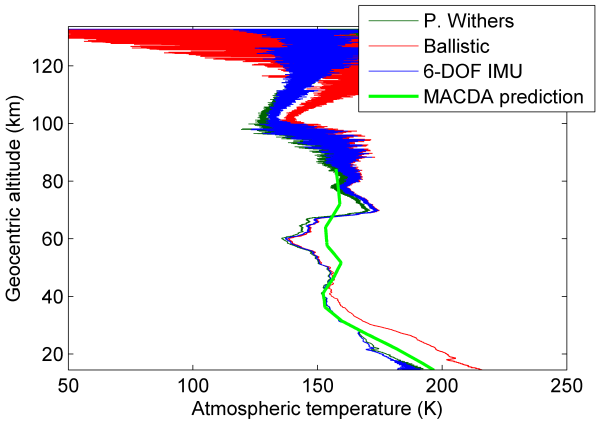

Figure 2: Phoenix reconstructed temperature profiles

Table 1: Phoenix reconstructed trajectory at parachute deployment

	units	NASA	This study
Time	(s)	227.8	228.0
Altitude	(km)	13.3	13.9
Velocity	(m/s)	387.6	387.9
α_T (°)	4.73	4.65	

We evaluate our 6-DOF reconstructed trajectory by comparing key quantities at parachute deployment in Table 1. Bias errors or discrepancies are integrated over the entire time interval from entry interface to parachute opening to yield maximal values at this final time instant. Our trajectory matches well with an independent NASA reconstruction [2]. Figure 2 shows two of our atmospheric temperature reconstructions: one assuming a 3-DOF head-on ballistic trajectory (red, accelerometer data only) and one utilizing the complete 6-DOF IMU dataset (blue, including attitude measurements by gyroscopes). The ballistic assumption has a significant impact on the reconstruction because Phoenix trimmed at a higher than expected angle of attack, which we will discuss below. Our temperature reconstruction matches great with an independent result [1] and does not deviate far from a climate model prediction assimilated with orbital observations (Mars Analysis Correction Data Assimilation or MACDA).

3. Planetary entry simulator

3.1. *Development*

Given the limited amount of in-flight measurements, especially for entries on planets other than Earth, a trajectory simulator was developed to produce our own datasets. Additionally, this will allow us to quantify the impact of atmospheric conditions (seasons, dust loading, wind velocities) and vehicle characteristics (instrumentation, geometry, aerodynamics). The simulator is a 6-DOF trajectory calculator for vehicles without reaction control mechanisms such as Phoenix and ExoMars EDM. Complete support for aerodynamics and a large number of flight mechanical and aerodynamic conventions has been implemented. Appropriate equations of motion are integrated with a 4th order Runge Kutta routine.

The simulator code was validated by comparing its outputs with those of POST II (Program to Optimize Simulated Trajectories). POST has a development history spanning many decades and has been used in the design of most NASA Mars missions. In subsequent comparisons, features of increasing fidelity and complexity were added. Figure 3 shows the Z acceleration sensed by the vehicle's accelerometers and the vertical pitch rate, both matching to machine precision with POST II results produced by the NASA Langley Research Center (LaRC). This particular test case involved complex aerodynamics including static and dynamic forces and moments, off-center center of

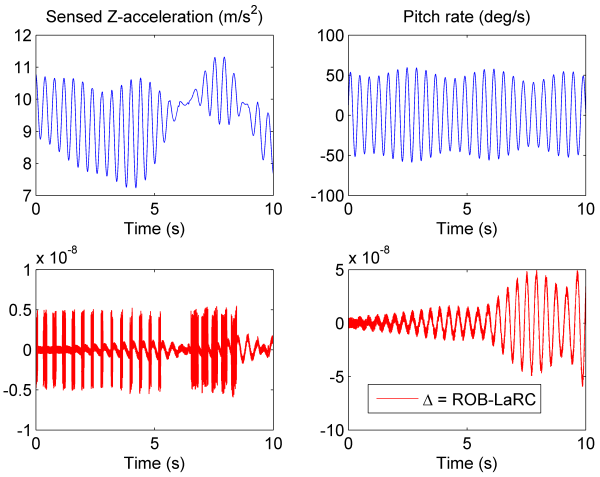

Figure 3: Simulator outputs versus LaRC POST II: nominal value (top) and absolute difference (bottom)

gravity and aerodynamic reference locations, an ellipsoid planet reference surface and numerous navigational coordinate conventions.

In Figure 2, assuming a ballistic trajectory was shown to have a significant impact on the reconstructed temperature profile. Phoenix was in fact designed as a ballistic capsule, but unexpectedly trimmed at a non-zero angle of attack. Using the simulator, probable causes for this can be identified. Specifically, an off-center center of gravity (CG) away from the vehicle symmetry axis or a bias error in the prediction of the aerodynamic moment coefficient C_m can both contribute to a trim angle change. In Figure 4, the total angle of attack reconstructed from the 6-DOF Phoenix IMU dataset (blue) is compared to various trajectory simulations.

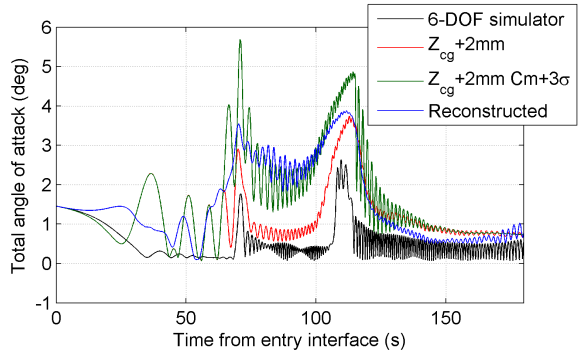

Figure 4: Phoenix total angle of attack: reconstruction and simulations

The Phoenix aerodynamic database published by NASA [6] was used to describe vehicle behavior. The resulting trajectory simulation (black) reveals two known aerodynamic instabilities at 70 and 110 seconds, but a near zero trim angle during the rest of the high velocity entry. We produced two additional simulations (red, green) in which the CG was shifted by a realistic value of 2 mm, and in one case a 3-sigma adder error imposed on the aerodynamic moment prediction. The latter simulation corresponds best to the reconstructed angle of attack and suggests that these causes likely contributed to the observed trim angle.

This analysis emphasizes the importance of accurate knowledge of vehicle characteristics and aerodynamics for correct interpretation of in-flight measurements. We have also demonstrated our capacity to assess the impact of uncertainty/error on such information by performing trajectory simulations.

4. FADS methodology

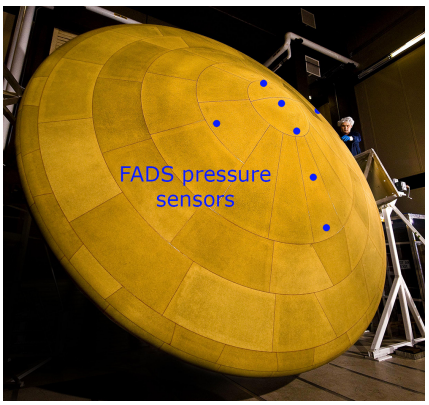

Figure 5: NASA MSL with FADS instrumented heat shield

Conventional inertial measurements (IMUs) allow for an accurate trajectory reconstruction, but are confined to the vehicle interior. Flush Air Data System (FADS) instrumentation measures the pressure distribution on the heat shield surface. It thus provides direct information on the flow field behind the bow shock (the shock layer). The recently successful NASA MSL mission (Mars Science Laboratory, 2012) is the only planetary exploration vehicle to date with an instrumented heat shield (Figure 5). The next will be ESA's ExoMars EDM demonstrator (2016).

From the measured surface pressure distribution, the direction of the oncoming flow (angle of attack α and side slip angle β), as well as the local maximum pressure or stagnation pressure p_{t2} can be de-

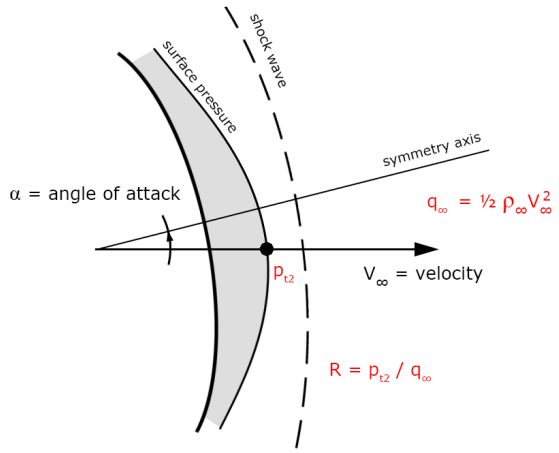

Figure 6: FADS density reconstruction method

rived. The stagnation pressure depends on the atmospheric density upstream of the shock wave, and is of interest for atmosphere reconstruction.

4.1. Approach

Our method for reconstructing atmospheric density from heat shield surface pressure measurements consists of three steps (Figure 6). The vehicle orientation relative to the oncoming flow is illustrated by the symmetry axis and velocity vector. The surface pressure distribution recorded by FADS sensors contains a local maximum equal to the stagnation pressure p_{t2}. The stagnation pressure is related to the dynamic pressure q_∞ upstream of the shock wave. The shock wave pressure ratio $R = p_{t2}/q_\infty$ allows us to derive this dynamic pressure. Finally, atmospheric density ρ_∞ is obtained by multiplying the dynamic pressure by $2/V_\infty^2$. The velocity magnitude is thus required independently, e.g. from inertial measurements.

The derivation of atmospheric density from FADS measurements requires a **surface pressure distribution** (to obtain α, β and p_{t2}) and a **shock wave pressure ratio** model (to obtain q_∞ and subsequently ρ_∞). The aerodynamic drag coefficient is not required as was the case for reconstruction from IMUs only. In fact, it could now be reconstructed for verification of pre-flight predictions. We used modified Newtonian flow theory to model the **surface pressure distribution** on hypersonic vehicles at high Mach numbers. It neglects viscous effects such as the boundary layer, but should be accurate above Mach 5. The surface pressures p_i at the FADS pressure port locations are then approximated by

$$p_i = (p_{t2} - p_\infty) \cdot cos(\theta_i)^2 + p_\infty \tag{4}$$

with θ_i the incidence angle between the flow and the heat shield surface and calculated from the pressure port location, angle of attack α and side slip angle β. The known pressure port locations are expressed by cone angles λ_i and clock angles ϕ_i.

$$\theta_i = f(\lambda_i, \phi_i, \alpha, \beta) \tag{5}$$

Atmospheric pressure p_∞ is small compared to p_{t2} and may be estimated or neglected. The solved for conditions are then stagnation pressure p_{t2} and flow angles α and β. For this the above equations must be inverted and pressure model fitted to the FADS measurements, which are usually greater in number than the three solved for variables. For this purpose an iterative non-linear least squares solver was developed, partly during a stay at NASA Langley.

A common analytical relation for the **shock wave pressure ratio** is the Rayleigh pitot tube formula:

$$R = \frac{p_{t2}}{q_\infty} = \frac{2}{\gamma M_\infty^2}\left(\frac{(\gamma+1)^2 M_\infty^2}{4\gamma M_\infty^2 - 2(\gamma-1)}\right)^{\frac{\gamma}{\gamma-1}} \left(\frac{1-\gamma+2\gamma M_\infty^2}{\gamma+1}\right) \tag{6}$$

with M_∞ the Mach number. This relation is derived for a constant heat capacity ratio $\gamma = c_p/c_v$ which is appropriate when gas temperatures are low. Such conditions are called *cold gas* or *perfect gas*. The Rayleigh pitot tube formula can be simplified in the limit of very high Mach numbers:

$$R \approx \left(\frac{(\gamma+1)^2}{4\gamma}\right)^{\frac{\gamma}{\gamma-1}} \left(\frac{4}{\gamma+1}\right) \tag{7}$$

In planetary entry scenarios, post-shock temperatures are very high and γ varies significantly through the shock wave. A more accurate model including high temperature effects was developed and consists of solving the shock wave conservation equations (mass, energy, momentum) while accurately calculating high temperature gas properties with the Mutation library developed by T. Magin [7].

Figure 7 shows our numerical predictions of the shock wave pressure ratio for air on a velocity-altitude grid designed for fast interpolation during reconstruction. The atmospheric conditions on the velocity-atltitude grid were provided by the standard US76 atmosphere. We will show later that this results in negligible errors in application to realistic non-standard

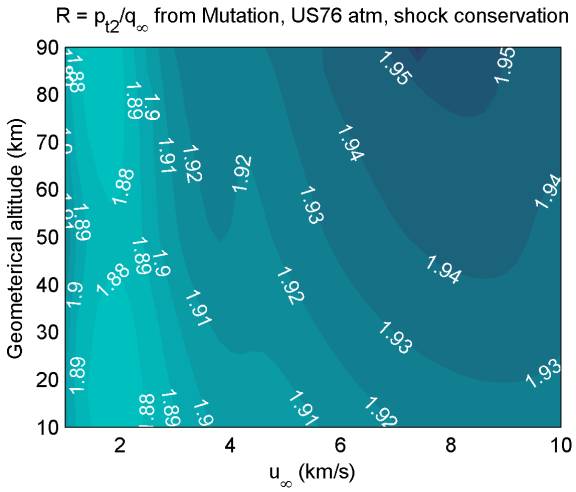

Figure 7: Shock wave pressure ratio model with high temperature effects

atmospheres. These numerical results differ significantly from the cold gas Rayleigh pitot tube solution of 1.84. A similar calculation will later be performed for CO_2 on Mars, expecting even larger deviations.

4.2. Application to wind tunnel model

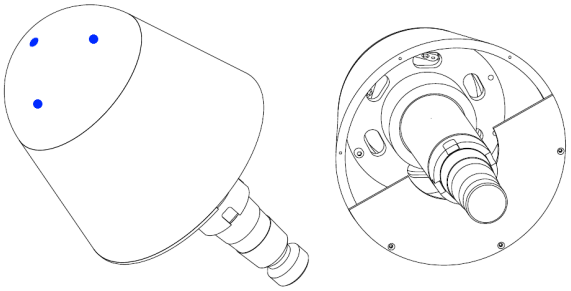

Figure 8: Hemispherical FADS probe

In the absence of in-flight measurements, we applied our FADS methodology in a wind tunnel test campaign. The VKI Longshot is a hypersonic Mach 14 wind tunnel with low to moderate gas temperatures. It is suitable to test our pressure distribution model with non-linear least squares solver to determine flow angles and stagnation pressure. The density derivation currently cannot be validated in this facility as an independent density measurement is not available. Testing was performed with a hemispherical probe equipped with five pressure sensors, three of which are indicated in blue on Figure 8. Currently only nitrogen gas (Earth) has been used. Utilizing Longshot's CO_2 (Mars) capabilities including an independent density measurement would allow us to validate the FADS density derivation. However, the derivation of flow angles and stagnation pressure does not depend significantly on the choice of gas and does not require wind tunnel density to be known.

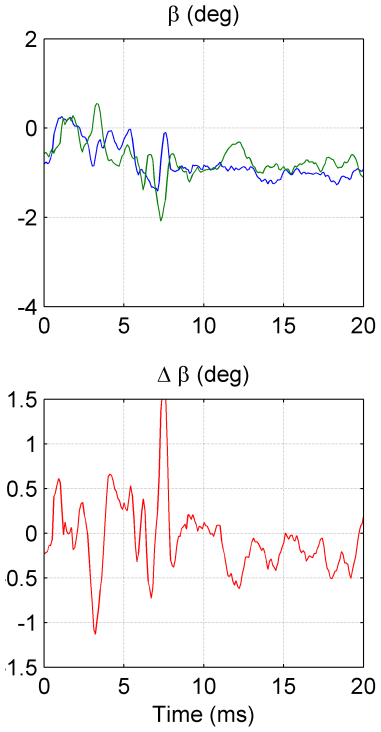

Figure 9: Repeatability test for side slip angle

The probe was positioned near the center of the uniform flow jet and recorded pressure signals. Using the least-squares inverted modified Newtonian flow equation, angle of attack α and side slip angle β were reconstructed from the FADS measurements. These can be compared with the known flow angles at which the model was set up. A range of α and β positions was tested. Figure 9 shows that wind tunnel repeatability with identically set up models is very satisfactory.

The wind tunnel stagnation pressure is routinely measured by a permanent reference probe. When the FADS probe is installed head-on into the flow, its central pressure tap should register the same stagnation pressure value. Instead, the FADS probe consistently measured a 3% lower stagnation pressure, Figure 10. The cause of this discrepancy is as yet unknown, the difference is outside the expected sensor accuracy range of ±2%. In the EXPERT case study below, we will show that a 3% accurate stagnation pressure match still permits a reasonably accurate re-

Table 2: Monte Carlo input uncertainties Longshot FADS calibration

input	3-σ	source
FADS pressures	2%	estimate of sensor accuracy
tunnel p_∞	100%	experimental mismatch
tunnel p_{t2}	3%	mismatch FADS / reference probes
FADS model α	0.006°	experimental setup
FADS model β	0.0833°	experimental setup
FADS sensors λ,ϕ	0.1°	estimated manufacturing precision

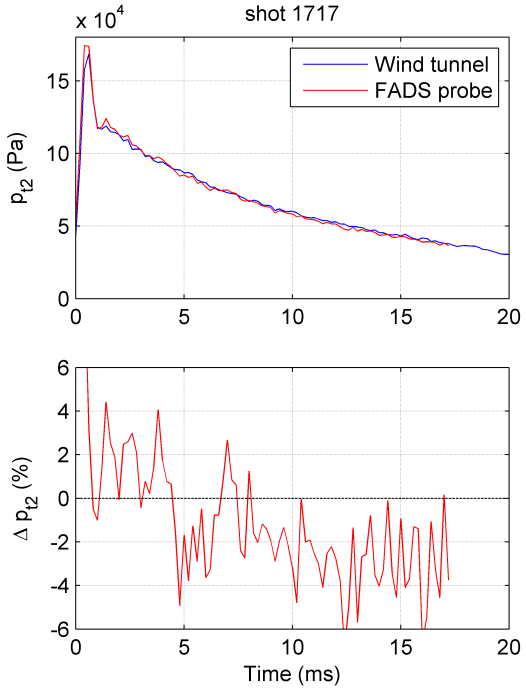

Figure 10: Stagnation pressure discrepancy

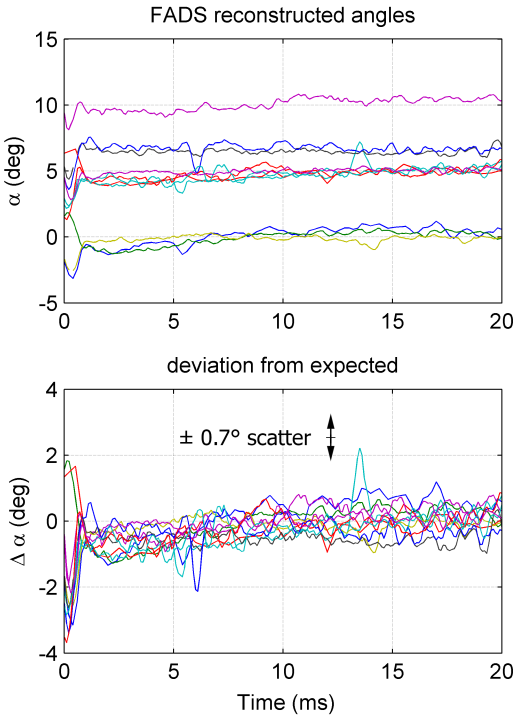

Figure 11: FADS reconstructed angle of attack

construction of density during entry.

The flow angle reconstruction contains more significant anomalies. The probe was carefully set up at various angles of attack (vertical plane) and side slip (horizontal plane). Figures 11 and 12 show the reconstructed flow angles (top) and their deviation from the expected angles at which the probe was installed (bottom). After 10 ms, the transient effects due to flow establishment and probe recoil have ceased. In the remainder of the 20 ms test time, the reconstructed angles of attack are scattered about the expected values by 0.7°, while the side slip angles have twice the scatter and a negative bias of about 1°. This is likely due to a single pressure sensor on the side of the FADS probe with unsatisfactory performance.

Equipping the probe with more sensors would reduce the impact of a single sensor and facilitate the identification of faulty sensors. To assess the benefit of increasing the number of sensors on the wind tunnel probe, a Monte Carlo analysis was run to quantify the uncertainty range within which the Longshot wind tunnel can constrain a FADS surface pressure distribution model. This correspond to the model uncertainty on α, β and p_{t2} when reconstructed by a surface pressure distribution model calibrated by or produced with the wind tunnel.

Table 2 lists the input uncertainties that went into the analysis. The angles λ and ϕ represent the pressure

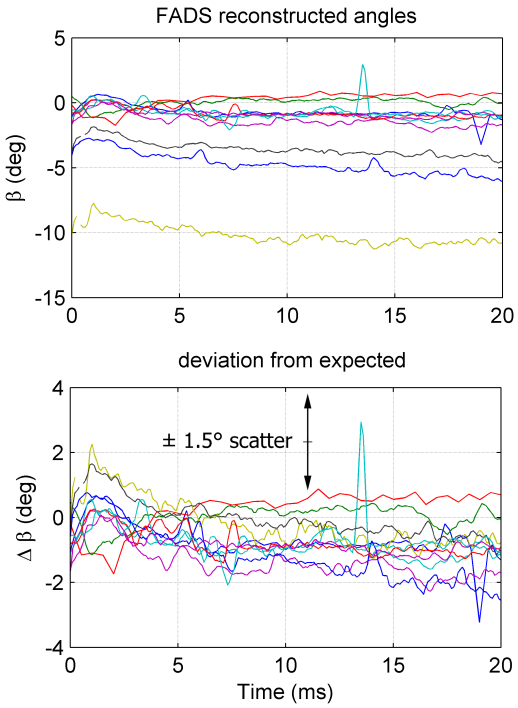

Figure 12: FADS reconstructed side slip angle

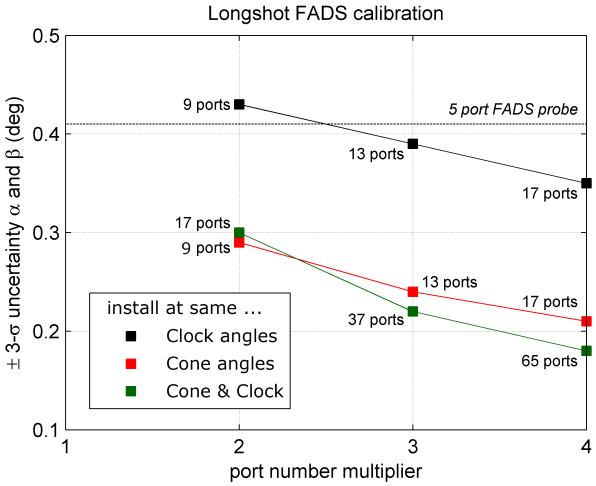

Figure 13: Flow angle uncertainty of Longshot calibrated FADS

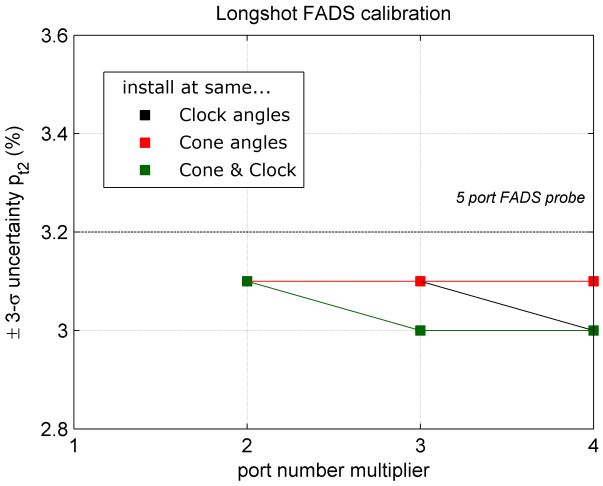

Figure 14: Stagnation pressure uncertainty of Longshot calibrated FADS

tap locations on the FADS probe and depend only on the manufacturing precision of the probe. The stagnation pressure accuracy was based on the mismatch mentioned above. The wind tunnel static pressure p_∞ has a negligible impact in the surface pressure distribution model as it is much smaller than the stagnation pressure. Its uncertainty on the other hand is very high, as an investigation is currently ongoing on a mismatch between expected and recently measured values. Uncertainty on the probe's surface pressure measurements is set to the sensor accuracy.

Figures 13 and 14 show the resulting uncertainty on the reconstructed flow angles from FADS instrumentation, given the input uncertainties in Table 2. Remember that these correspond to the accuracy with which the wind tunnel can constrain a surface pressure model. When applying the model to an actual entry reconstruction[1], these values will be conflated with other uncertainty sources, e.g. from vehicle sensor or trajectory parameter reconstruction.

The pressure port layout on the hemispherical FADS probe consisted of a central stagnation point sensor and four equally spaced off-stagnation sensors, at cone angles $\lambda = 45°$ away from the probe symmetry axis (4+1 = 5 sensors in total). Figure 13 shows the impact of multiplying the number of off-stagnation sensors along certain directions. For example doubling the number of off-stagnation sensors by installing additional sensors at the same clock angles, means placing an additional sensor between every off-stagnation sensor and the stagnation point (4+4+1 = 9 sensors). Conversely, installing at the same cone angles would imply an additional sensor between every two off-stagnation sensors, resulting in 9 sensors positioned on a circumferential circle. Conserving both cone and clock angles refers to the superposition of

[1] At appropriate free stream flow conditions, i.e. similar to those in the wind tunnel

both examples, resulting in a total of 8+8+1 = 17 sensors.

Installing more sensors could halve the reconstructed flow angle uncertainty (Figure 13). Installing them at the same cone angles is most beneficial. That is, additional sensors should all be installed at $\lambda = 45°$ to improve flow angle reconstruction. This makes sense, as the sensors farthest away from the stagnation point are most sensitive to flow angularity. The current FADS probe should be able to reconstruct the flow angles to within 0.4°, which is significantly below the scatter observed in the experimental results shown before. This supports a misbehaving sensor or may suggest flow irregularities[2] responsible for the scatter.

On the other hand, the accuracy with which a FADS surface pressure model produced in the wind tunnel would reconstruct stagnation pressure, does not benefit from additional sensors (Figure 14). It depends mainly on the accuracy with which the wind tunnel reference value is measured. This should be interpreted conversely as a good thing: the flow angle reconstruction does not suffer from a poorly known reference stagnation point measurement.

5. EXPERT case study

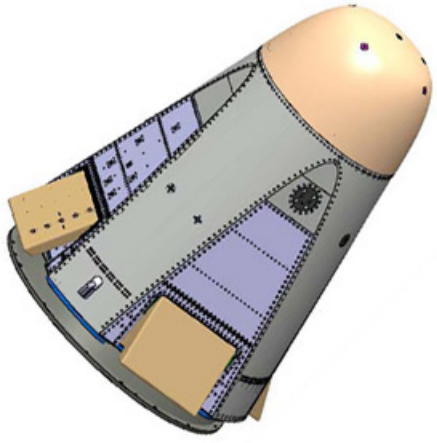

Figure 15: ESA hypersonic testbed EXPERT

Our FADS methodology requires a surface pressure distribution model, and a shock wave pressure ratio model. In the previous section we applied the surface pressure model (modified Newtonian flow) to a FADS probe in the VKI Longshot wind tunnel, and concluded we could constrain the model by no less than 0.4° on the reconstructed flow angles and 3% on the reconstructed stagnation pressure. We also lacked the facilities to validate the shock wave pressure ratio model including high temperature effects described before. We will now apply our pressure ratio model to a simulated EXPERT entry, and assess the impact of the wind tunnel uncertainties on the reconstruction of that entry.

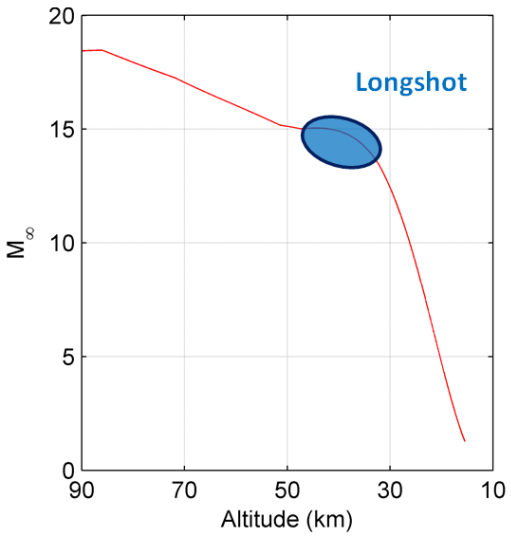

Figure 16: Mach number EXPERT trajectory

EXPERT is ESA's soon to be launched hypersonic flight testbed, and comes equipped with a similar FADS pressure tap layout as used in our wind tunnel testing (Figure 15). Also, its trajectory is planned to cross the Longshot flow conditions (Figure 16). We obtained a simulation of EXPERT's trajectory and simulated FADS pressure signals using our modified Newtonian flow model and pressure ratio model based on shock conservation equations and high temperature gas properties calculated by Mutation. Multiple pressure ratio models were then employed to reconstruct the a priori known atmospheric density back from the simulated signals. In the simulated case, the Mutation model naturally retrieves the density back exactly. This does not affect any conclusions but excludes independent validation.

To complement the previously described wind tunnel investigation, we performed a Monte Carlo analysis to predict realistic uncertainties on an EXPERT

[2]The wind tunnel stagnation pressure is known to vary slightly throughout the uniform flow jet [8]

entry reconstruction utilizing a surface pressure model constrained by Longshot wind tunnel experiments. The uncertainty on the wind tunnel derived FADS model was conflated with realistic vehicle sensor and trajectory reconstruction uncertainties.

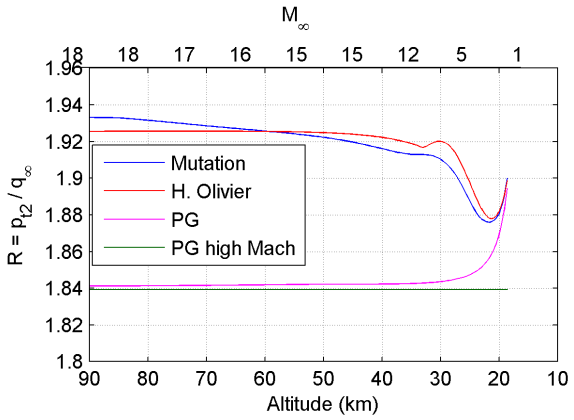

Figure 17: Various shock wave pressure ratio predictions along EXPERT trajectroy

Figure 17 shows shock wave pressure ratios predicted along the EXPERT trajectory. The perfect gas Rayleigh pitot tube formula (PG) and its high Mach number approximation (PG high Mach) vary minimally with altitude and assume cold gas conditions. By contrast, the two remaining models include high temperature effects. They are our own model using Mutation, and a polynomial expression produced independently by other authors [9]. Notice the convergence with the (Mach dependent) perfect gas prediction at about Mach 4. At Mach 12 and above, high temperature effects account for a 4% to 6% departure from cold gas predictions. Our numerical solutions don't deviate far from those of other authors.

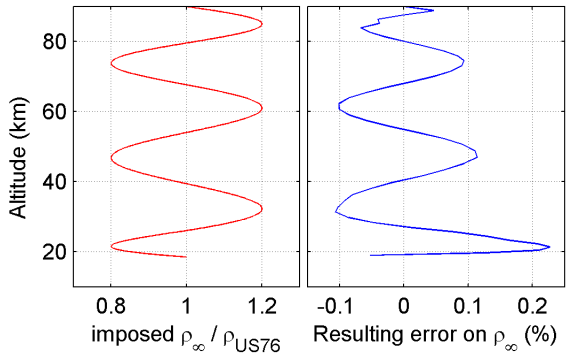

Figure 18: Impact of interpolation on standard atmosphere grid

Recall that our pressure ratio model was interpolated on an altitude-velocity grid based on the standard US76 atmosphere. We imposed a sinusiodal density disturbance on the density-altitude profiles used to simulate the FADS signals, to quantify the error inflicted by the standard atmosphere interpolation grid. Figure 18 shows this error to be negligible. The overall conclusion is that the high temperature effects are significant and fast interpolation on pre-calculated solutions is feasible.

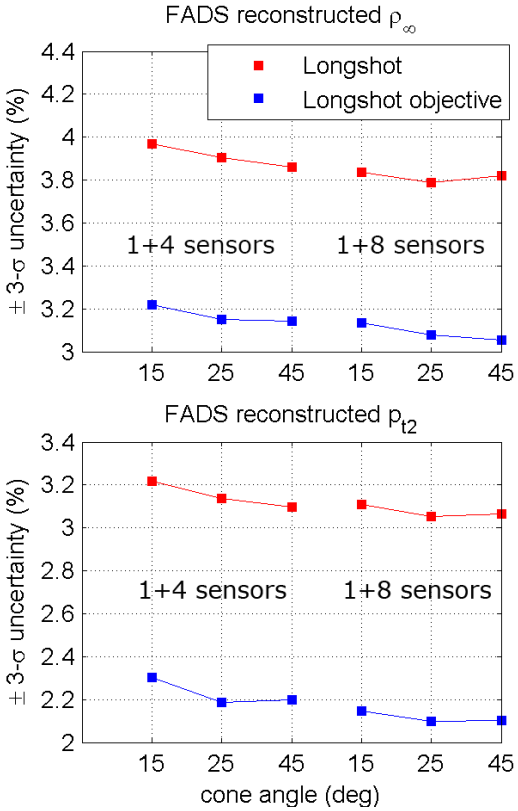

Figure 19: Monte Carlo EXPERT FADS performance

Finally, we ran a Monte Carlo analysis to estimate realistic uncertainties on reconstructed quantities from EXPERT's FADS system. The analysis is performed at the point of the EXPERT trajectory that corresponds to the Longshot operating conditions. The final uncertainty depends on the accuracy of the surface pressure distribution and shock wave pressure ratio models, that of the reconstructed trajectory (e.g. altitude and velocity) and the accuracy of EXPERT's FADS instrumentation. Table 3 describes this part of these input uncertainties. The high temperature pressure ratio model has an estimated uncertainty of 1%, about a quarter of the error made by neglecting high

Table 3: Monte Carlo input uncertainties EXPERT FADS

input	3-σ	source
FADS pressures	1.5%	EXPERT sensor accuracy
FADS sensors λ,ϕ	0.1°	estimated manufacturing precision
Pressure ratio model	1%	1/4th cold gas error
IMU V_∞	1%	typical reconstruction error
IMU p_∞	15%	typical reconstruction error
IMU altitude	600 m	typical reconstruction error

temperature effects, which is known to be the main error made by perfect gas models.

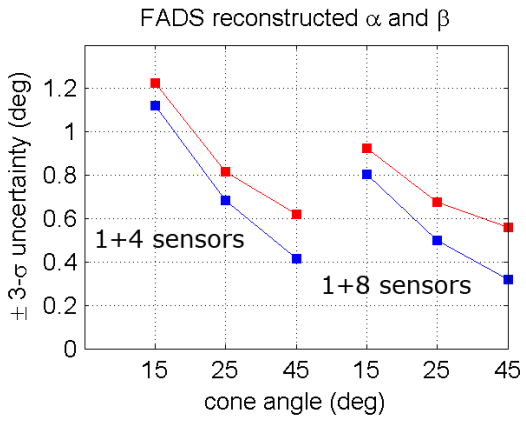

Figure 20: Monte Carlo EXPERT FADS performance

Not listed in Table 3 are the uncertainties associated with the surface pressure distribution model. For these, two alternative sets are presented in Table 4. The first corresponds to our current efforts using the VKI Longshot to constrain the surface pressure model. The other is a hypothetical set of uncertainties we suggest as an attainable obective for future wind tunnel FADS calibration. In the objectives, the stagnation pressure uncertainty is brought down to the pressure sensor accuracy, and the reconstructed flow angle uncertainty to values achievable by increasing the number of pressure sensors (Figure 13).

The predicted performance for the FADS system on EXPERT using a pressure surface model calibrated by Longshot is shown in Figures 19 and 20. Four sets of solutions were obtained: for two sets of Longshot uncertainties and two EXPERT pressure sensor layouts. The 1+4 layout is used on the real vehicle, whereas the 1+8 layout has four additional sensors equally spaced between the four existing off-stagnation point sensors[3]. In every of the four solution sets, the angular distance of the pressure taps from the stagnation point was varied around the $\lambda = 25°$ value actually used on EXPERT.

We find that the prime quantity of interest, the atmospheric density ρ_∞, can be reconstructed within 3 to 4%, depending on the accuracy of the surface pressure model. The red points at 4% correspond to our recent efforts in the VKI Longshot, the blue points at 3% to the suggested objective. Stagnation pressure reconstruction depends similarly on the quality of the surface pressure model. The 1% higher uncertainty on the density is due to the uncertainty on the shock wave pressure ratio model. Increasing the number of pressure sensors on the nose of EXPERT only benefits the flow angle reconstruction. At least as much can be gained however, by placing the sensors farther away from the stagnation point.

6. Conclusion

We reviewed our entry reconstruction and simulation tools utilizing both conventional inertial (IMU) and novel heat shield (FADS) instrumentation. The conventional reconstruction tools have been completely validated on Mars Phoenix Lander in-flight measurements. Similarly, all functionality in our six degree of freedom simulator matches exactly with NASA's well validated entry simulator.

We also presented FADS methodology to reconstruct flow angles, stagnation pressure and atmospheric density from heat shield measurements. It consists of a surface pressure distribution model (modified Newtonian flow) and numerical calculations of shock wave pressure ratios, including high temperature effects. Lacking in-flight measurements, we applied these to a hypersonic wind tunnel probe

[3] All at identical cone angles: recall that this is most beneficial.

Table 4: Remaining Monte Carlo input uncertainties EXPERT FADS

input	3-σ	source
α	0.5°	current FADS probe sensor layout
β	0.5°	current FADS probe sensor layout
p_{t2}	3%	mismatch FADS / reference probes
α	0.2°	objective FADS probe sensor layout
β	0.2°	objective FADS probe sensor layout
p_{t2}	2%	realistic objective

and in a preliminary EXPERT case study. The Mach 14 Longshot wind tunnel we used is currently incapable of validating the pressure ratio model. We obtained promising performance from the surface pressure model, but were unable to experimentally constrain it to its potential accuracy. An uncertainty analysis pointed out that installing more sensors along the circumference of the FADS probe would significantly increase accuracy. It is also of interest to utilize Longshot's CO_2 capabilities and measure the wind tunnel density independently, e.g. by tunable diode laser absorption spectroscopy (TDLAS).

Both the surface pressure and pressure ratio models were applied to a simulated EXPERT trajectory. Our high temperature pressure ratio model differs substantially from cold gas approximations and matches well with work by independent authors. Its implementation on an altitude-velocity interpolation grid is both fast and accurate. A uncertainty analysis for where EXPERT's trajectory corresponds to the wind tunnel conditions was performed, for current and desired wind tunnel performance. In both cases the final uncertainty on reconstructed atmospheric density from FADS measurements is at most 4%, a significant improvement over the typical drag coefficient method employed for conventionally instrumented vehicles.

Acknowledgments

The PhD candidate is supported by the Royal Observatory of Belgium (Uccle) to develop reconstruction tools for ESA's 2016 Entry, Descent and Landing Demonstrator Module (EDM) of the ExoMars program. He gratefully acknowledges the NASA Langley Research Center for hosting him during a very productive stay. Juan Cruz in particular has been an outstanding colleague and mentor. The von Karman Institute continues to offer sound education, expertise and test facilities. Special thanks go to Guillaume Grossir and Sebastien Paris for executing the FADS wind tunnel testing, and Bruno Dias and Thierry Magin for adapting the Mutation code to solve shock conservation equations. Paul Withers from Boston University has been very helpful in the development of the IMU reconstruction tools. Thank you Damien Le Quang for reviewing the draft.

References

[1] P. Withers et al., Analysis of entry accelerometer data: A case study of Mars Pathfinder, Journal of Planetary and Space Science 51 (1) (2003) 541–561.

[2] R. C. Blanchard and P. N. Desai, Mars Phoenix Entry, Descent, and Landing Trajectory and Atmosphere Reconstruction, Journal of Spacecraft and Rockets 48 (5) (2011) 809–821.

[3] P. Withers and M. D. Smith, Atmospheric entry profiles from the Mars Exploration Rovers, Icarus 185 (1) (2006) 133–142.

[4] B. Kazeminejad, Methodology Development for the Reconstruction of the ESA Huygens Probe Entry and Descent Trajectory, Ph.D. thesis, Karl-Franzens University Graz, Institute for Physics, Austria (2005).

[5] L. F. Huber, Atmospheric Structure Experiment (ASE) Data Archive (PHX-M-ASE-2-EDL-V1.0), `http://atmos.nmsu.edu/PDS/data/phxase_0001/`, [Online; accessed February 2012] (2008).

[6] K. T. Edquist, P. N. Desai and M. Schoenenberger, Aerodynamics for Mars Phoenix Entry Capsule, Journal of Spacecraft and Rockets 48 (5) (2011) 713–726.

[7] T. Magin et al., Nonequilibrium radiative heat flux modeling for the Huygens entry probe, Journal of Geophysical Research 111 (E07S12).

[8] G. Grossir, S. Paris, K. Bensassi and P. Rambaud, Experimental characterization of hypersonic nozzle boundary layers and free-sream noise levels, in: 51st AIAA Aerospace Sciences Meeting, no. 1130 in AIAA 2013, 2013.

[9] P. zur Nieden and H. Olivier, Determination of Atmospheric Densities from Reentry Flight Data, Journal of Spacecraft and Rockets 44 (2) (2007) 332–337.

DEVELOPMENT OF ADVANCED COMPUTATIONAL FLUID DYNAMICS

High–Order RDS and p-Multigrid Solution Algorithms for Compressible Flow

Martin Vymazal

Aeronautics and Aerospace Department, von Karman Institute for Fluid Dynamics, Belgium, martin.vymazal@vki.ac.be

Supervisor: Herman Deconinck

Professor, Aeronautics and Aerospace Department, von Karman Institute for Fluid Dynamics, Belgium, deconinck@vki.ac.be

Promotor: Chris Lacor

Professor, Department of Mechanical Engineering, Faculty of Applied Sciences, Vrije Universiteit Brussel, Belgium, Chris.Lacor@vub.ac.be

Abstract

Residual distribution schemes are discussed in the context of higher order spatial discretization for hyperbolic conservation laws. The discrete solution is approximated by a finite element space based on triangular Lagrangian P_k elements. A natural subtriangulation of these elements allows the reuse of simple distribution formula previously developed for linear P_1 triangles. Curved elements with piecewise quadratic and cubic approximation of the boundaries of the domain are considered.

In the second part, a new variant of RD scheme is proposed. This particular formulation avoids the sub–triangulation procedure.

Keywords: residual distribution, multidimensional upwind, high order, curvilinear geometry

1. Introduction

The present work follows a Residual Distribution approach [1; 2; 3], which is close to continuous finite element methods, but allows the use of a maximum principle to construct nonlinear monotonicity preserving and truely multidimensional stabilizations. In previous papers [4] we have exploited the close relation with continuous finite element discretizations to present a class of higher order residual distribution methods defined on P_k Lagrangian triangular finite elements. Here we focus on the use of curved elements to allow for a higher order representation of the boundaries of the domain, using sub- or isoparametric transformation from physical space to a Cartesian parent element.

2. Notations

We consider the steady state solution of a conservation law on a two–dimensional spatial domain Ω:

$$\frac{\partial \boldsymbol{u}}{\partial t} + \nabla \cdot \boldsymbol{\mathcal{F}} = 0 \quad \forall (x, y) \in \Omega \subset \mathbb{R}^2, \quad \forall t \geq 0, \quad (1)$$

where $\boldsymbol{u}$ is the vector of conserved variables and $\boldsymbol{\mathcal{F}}$ is the inviscid flux vector, $\boldsymbol{\mathcal{F}}(\boldsymbol{u}) = (\mathbf{f}(\boldsymbol{u}), \mathbf{g}(\boldsymbol{u}))$. We denote by $\mathcal{T}_{h,k}$ a triangulation of the domain Ω, whereby each triangular element T of the triangulation $\mathcal{T}_{h,k}$ is a Lagrangian P_k finite element equipped with $K = \frac{(k+1)(k+2)}{2}$ degrees of freedom.

In the simplest case the geometry of the P_k triangle is considered to be linear, defined by its three corner nodes. Hence, the intermediate nodes on the boundary of the element are all located on the straight edges and therefore the boundary of the domain Ω is approximated by a polygone. Such a discretization will be denoted as a P_1P_k discretization (P_1 for geometry and P_k for the solution).

We work with elements whose edges are described by second- and third- order polynomials. Elements with quadratic geometry will be denoted as P_2P_k elements (P_2 for geometry and P_k for the solution). P_2P_2 elements are called isoparametric, while P_2P_k with $k > 2$ are called subparametric elements. The notation for P_3 elements is analogous.

The geometry of the curvilinear P_2 (P_3) element is transformed to a parent element in ξ–η space. In our

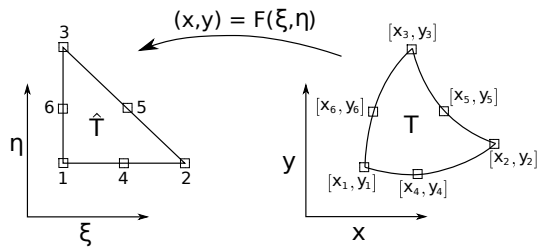

Figure 1: Transformation of triangle geometry from physical to reference space using Lagrange shape functions

case, we define $\mathbf{F}(\xi, \eta)$ from figure (1) as isoparametric mapping

$$\begin{bmatrix} x(\xi,\eta) \\ y(\xi,\eta) \end{bmatrix} = \sum_{i=1}^{N} \varphi_i^{h,k}(\xi,\eta) \cdot \begin{bmatrix} x_i \\ y_i \end{bmatrix} \tag{2}$$

where N is the number of degrees of freedom of P_2 or P_3 triangle, respectively. The number k refers to the order of shape functions φ_i and x_i, y_i denote the nodal coordinates of the triangle.

3. Residual Distribution method

For any triangulation $\mathcal{T}^{h,k}$ the cell residual for a given triangle is defined as the integral over the triangle of the spatial operator:

$$\begin{aligned} \phi^T &= \int_T \nabla \mathcal{F}(u^{h,k})\, d\Omega = \oint_{\partial T} \mathcal{F}(u^{h,k}) \cdot \vec{n}\, dl \\ &= \sum_{s=0}^{N_s} \int_{T_s} \vec{a}(u^{h,k}) \cdot \nabla u^{h,k}\, dx\, dy \\ &\qquad (N_s \ldots \text{number of sub–elements}) \end{aligned} \tag{3}$$

where we have used the expression for the Jacobian of the flux $\mathcal{F}(u)$ in (1),

$$\vec{a}(u) = \frac{\partial \mathcal{F}(u)}{\partial u} = \left(\frac{\partial f_1(u)}{\partial u}, \frac{\partial f_2(u)}{\partial u} \right) \tag{4}$$

We can also construct the residual over each P_1 sub-element of $\mathcal{T}^{h,k}$

$$\phi^{T_s} = \oint_{\partial T_s} \mathcal{F}(u^{h,k}) \cdot \vec{n}\, dl \tag{5a}$$

$$= \int_{T_s} \vec{a}(u^{h,k}) \cdot \nabla u^{h,k}\, dx\, dy \equiv \vec{a}^* \cdot \int_{T_s} \nabla u^{h,k}\, dx\, dy \tag{5b}$$

with $\vec{a}^*$ a properly defined local average of $\vec{a}(u)$ over the sub-triangle such that conservation is preserved [5]. The existence of such local average for general nonlinear conservation law is not guaranteed, but in case of the conservation law (1) applied to the Euler equations considered in this work, a conservative linearisation is possible under the assumption that the vector of Roe variables changes linearly in each cell.

The basic idea of the residual distribution (RD) method consists of distributing fractions of this cell residual to the three nodes of the element T. The fraction sent to node $i \in T$ is denoted ϕ_i and we require

$$\sum_{i \in T} \phi_i = \phi^T \tag{6}$$

This requirement can be written in terms of *distribution coefficients* β_i which for consistency sum to unity

$$\sum_{i \in T} \beta_i = 1, \qquad \beta_i = \frac{\phi_i}{\phi^T} \tag{7}$$

After assembling all contributions in the nodes, the nodal equation for node i reads, with $\mathcal{D}_i$ the set of all triangles that share node i:

$$\sum_{T \in \mathcal{D}_i} \phi_i = 0 \tag{8}$$

Since the distribution is restricted to the nodes of the triangle itself, the stencil of the scheme remains compact. This equation can be solved by embedding in a pseudo–time iteration, i.e. by finding a steady state solution of

$$|S_i| \frac{du_i}{d\tau} + \sum_{T \in \mathcal{D}_i} \phi_i^T = 0, \tag{9}$$

where $|S_i|$ is the area of median dual cell.

3.1. Residual Distribution schemes on P_1 elements

For a given P_1 (both solution and geometry) triangle we consider the set of normal vectors $\{\vec{n}_j\}_{j \in T}$, defined by the inward normals to the edges of T facing each node $j \in T$ (see figure 2 left). The norm of $\vec{n}_i$ is equal to the length of the edge. Let us define the upwind parameter

$$k_j = \frac{1}{2} \vec{a}^* \cdot \vec{n}_j \quad \text{implying} \quad \sum_{i \in T_s} k_i = 0 \tag{10}$$

In this case, using a conservative linearisation (eq. 5b, 10), we can express the cell residual as follows:

$$\phi^T = \oint_{\partial T} \mathcal{F}(u^{h,1}) \cdot \vec{n}\, dl = \int_T \nabla \mathcal{F}(u^{h,1})\, d\Omega = \sum_{i \in T} k_i u_i \tag{11}$$

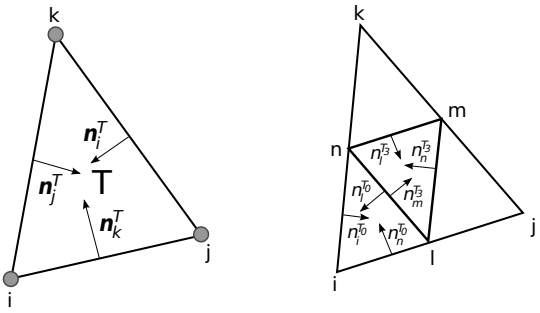

Figure 2: Definition of the normal vectors $\vec{n}_i$ in P_1 and P_2 elements

When all contributions for a given node are assembled, we end up with the following system of nodal equations, similar to equation (9), to be solved using explicit or implicit pseudo-time iterations. For example, using forward Euler method, we get:

$$|S_i|\frac{u_i^{n+1}-u_i^n}{\Delta\tau}+\sum_{T_s,\ i\in T_s}\phi_{i,n}^{T_s}=0 \tag{12}$$

Many distribution schemes (defining the split residuals ϕ_i) for P_1 elements have been developed in the past [4; 6; 7]. A particular class satisfies a multidimensional upwinding property (MU). Such distributions satisfy the requirement that a node in a triangle does not receive a contribution if its opposed face is an outflow face. The condition is easily imposed by requiring $\phi_i = 0$ whenever $k_i < 0$. Within this work, we limited ourselves to the use of the LDA (Low Diffusion A) scheme. Denoting by k_i^+ and k_i^- the positive and negative part of the upwind parameter, $k^\pm = \frac{k\pm|k|}{2}$, the distribution coefficients of the LDA scheme can be written as

$$\beta_i^{LDA}=\frac{k_i^+}{\sum_{m=1}^3 k_m^+} \tag{13}$$

This scheme is of order $O(k+1)$ (k being the order of interpolating polynomial), but not strictly monotone. We refer the reader interested in detailed description of the LDA scheme to other literature [1; 8; 4; 6; 9].

3.2. Residual distribution schemes on P_1P_k elements

Consider now the extension of multidimensional upwind (MU) schemes to high order P_1P_k elements. We will assume that the inward normals $\vec{n}_j$'s are defined on the local P_1 sub-elements $T_s \in T$, as shown on figure 2 (right) for $k = 2$. Note that if we consider a P_1P_k element (P_k element for the solution but only P_1 triangles for the geometry, defined by the 3 corner nodes), the inward normals of the sub-elements can be deduced easily from the ones of the parent element by a simple rescaling. We compute the residual on each sub-element:

$$\phi^{T_s}=\int_{T_s}\nabla\mathcal{F}(u^{h,k})\,d\Omega=\oint_{\partial T_s}\mathcal{F}(u^{h,k})\cdot\hat{n}\,dl \tag{14}$$

Then, this residual is distributed to the 3 nodes of the sub-element, using the LDA distribution scheme (13) developed for P_1 triangles:

$$\phi_i^{T_s,LDA}=\beta_i\phi^{T_s} \tag{15}$$

The linearization used to compute the parameters k_i can be based on any linearized state over the sub-triangle, without affecting accuracy nor conservation.

Remark. *This is not the only strategy to achieve residual distribution schemes on P_k elements. In particular, we refer to Lax Friedrichs distribution schemes of Abgrall and collaborators [10], [11]. In this case the residual is computed on the complete P_k element and then distributed to the N nodes of the element without making use of a sub-triangulation.*

3.3. Curvilinear P_2P_k and P_3P_k elements

We consider elements where the geometry is either piecewise quadratic or cubic. The geometry and numerical solution can be discretized independently so in general the solution can have any order k. However, we focus on isoparametric (P_2P_2 or P_3P_3) high–order elements.

To ensure conservation of fluxes, we compute the sub-element residual from equation (14) as a contour integral:

$$\phi^{T_s}=\oint_{\partial T_s}\mathcal{F}(u^{h,k})\cdot\vec{n}\,dl \tag{16}$$

The boundary ∂T_s is described by transformation (2). For every face on ∂T_s, this transformation is a function of only one parameter ζ:

$$\begin{aligned}x&=x(\zeta)\\ y&=y(\zeta)\end{aligned} \tag{17}$$

We integrate numerical the fluxes of (16) using Gauss quadrature: 3 points per face f of the sub–element for P_2 and 5 points for P_3:

$$\oint_f\mathcal{F}(u^{h,k})\cdot\vec{n}\,dl\simeq\sum_{q=1}^{N}w_q[\mathcal{F}(u_q)\cdot\vec{n}_q]J_q, \tag{18}$$

$$J_q=\sqrt{\dot{x}^2(\zeta_q)+\dot{y}^2(\zeta_q)} \tag{19}$$

where J_q is the Jacobian of transformation (17) at quadrature point q. We use the transformation also to compute the normal $\vec{n}_q$.

The integral over f in equation (18) is approximated:

- by three-point Gauss quadrature for each face of P_1P_1 triangle
- by the same quadrature for each face of each *sub–triangle* in the case of P_1P_2 and P_2P_2 elements
- by five–point Gauss quadrature on each sub–face of the P_3P_3 element

The quadrature nodes and weights on the biunit interval are given in table 1.

	Quadrature points	*Weights*
P_1P_1, $P_{1(2)}P_2$	0.0	$\frac{8}{9}$
	$\pm\sqrt{\frac{3}{5}}$	$\frac{5}{9}$
P_3P_3	0.0	0.5688888889
	±0.5384693101	0.4786286705
	±0.9061798459	0.2369268850

Table 1: Gauss quadrature used to approximate the residuals $\phi^{T,in}$.

3.4. Subsonic flow around a cylinder

We present results for a test case with stagnation point, namely the flow around a circular cylinder at $M_\infty = 0.38$. We consider four O–meshes with 16×5 (M1), 32×9 (M2), 64×17 (M3) and 128×33 (M4) points as described in [12]. The first number indicates the number of nodes in the circular direction of the mesh, the second number refers to the number of nodes in the radial direction (figure 3). The radii of the circles in each mesh follow a geometric series

$$r_j = r_0\left(1 + \frac{2\pi}{128}\sum_{k=0}^{j-1}\alpha^k\right),\ j = 1, 2, \ldots 32, \qquad (20)$$

where $\alpha = 1.1648336$ and $r_0 = 0.5$ is the radius of the cylinder. The farfield boundary is located at 20 diameters from the center. To have the same number of degrees of freedom and make a fair comparison between the P_1P_1 and P_2P_2 schemes, we create a P_1 sub-triangulation of each P_2 triangle. The P_3P_3 meshes were created independently such that the number of *elements* is equal for P_1P_2, P_2P_2 and P_3P_3 meshes. We plot the P_1 solutions on all four meshes

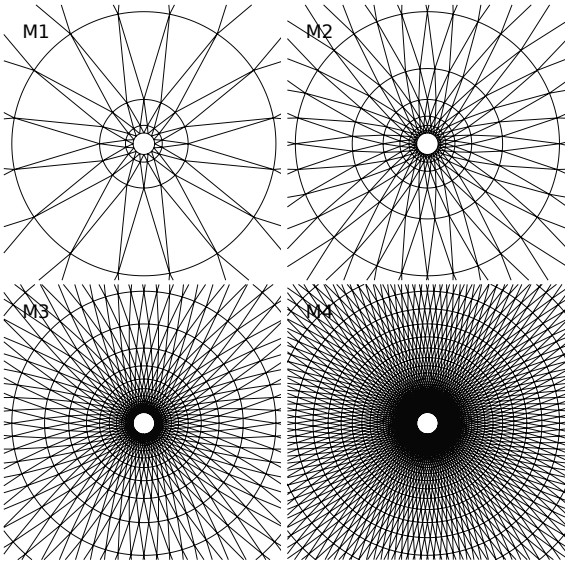

Figure 3: 16×5, 32×9, 64×17 and 128×33 meshes for subsonic cylinder test case.

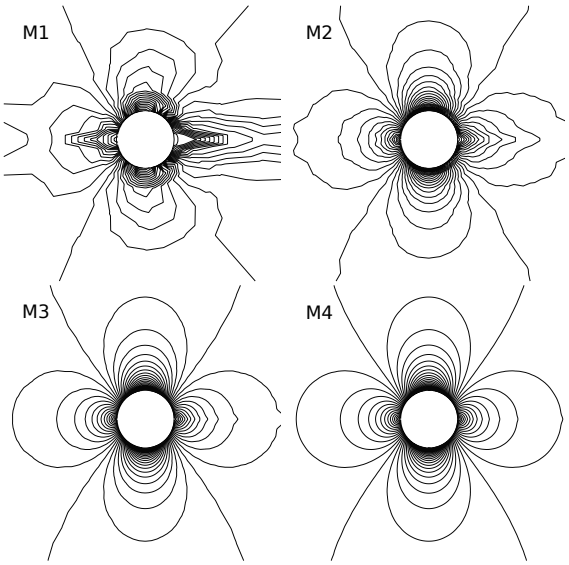

Figure 4: Mach isolines plotted for Ma $\in \langle 0, 1\rangle$, $\Delta Ma = 0.025$ on mesh with P_1P_1 elements.

(figure 4). Higher–order solution is shown in figure 5 for M2 and M3. Figure 6 presents the pressure coefficient on the cylinder wall and the entropy deviation on mesh M1. We measure the rate of convergence again by computing the relative decrease of the L_2 norm of entropy error Σ as the mesh is refined. The measured order is reported in figure 7. We did not include the entropy error on M1 in the computation of the convergence order of P_1P_2 discretization, since

this error is very large (all values are listed table 2). As a result, the convergence rate measured on all four meshes seems to be very high due to rapid decrease of the entropy error as the element size becomes small compared to the curvature of the cylinder.

		P_1P_1	P_1P_2
Mesh	NDOF	$\|\|\Sigma\|\|_{L_2}$	$\|\|\Sigma\|\|_{L_2}$
M1	288	4.87E -02	6.03E-02
M2	1088	7.64E -03	1.78E-03
M3	4224	1.13E -03	1.57E-04
M4	16640	1.78E -04	2.04E-05
Order		*1.99*	*3.05*

		P_2P_2	P_3P_3
Mesh	NDOF	$\|\|\Sigma\|\|_{L_2}$	$\|\|\Sigma\|\|_{L_2}$
M1	624	1.00E-02	1.46E-03
M2	2400	1.78E-03	5.62E-05
M3	9408	1.27E-04	5.35E-06
M4	37248	2.76E-05	5.33E-07
Order		*2.98*	*3.84*

Table 2: L_2 norm of entropy error (Σ): subsonic cylinder test case.

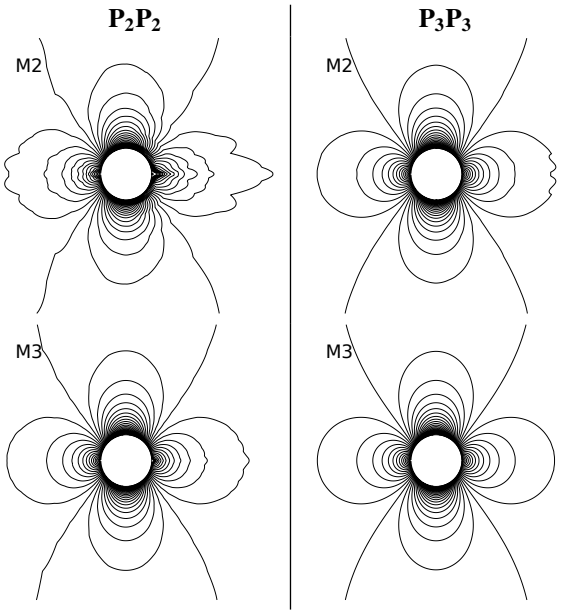

Figure 5: Mach number isolines plotted for $Ma \in \langle 0, 1\rangle$, $\Delta Ma = 0.025$ on meshes M_2 and M_3. Left: P_2 elements, right: P_3 elements.

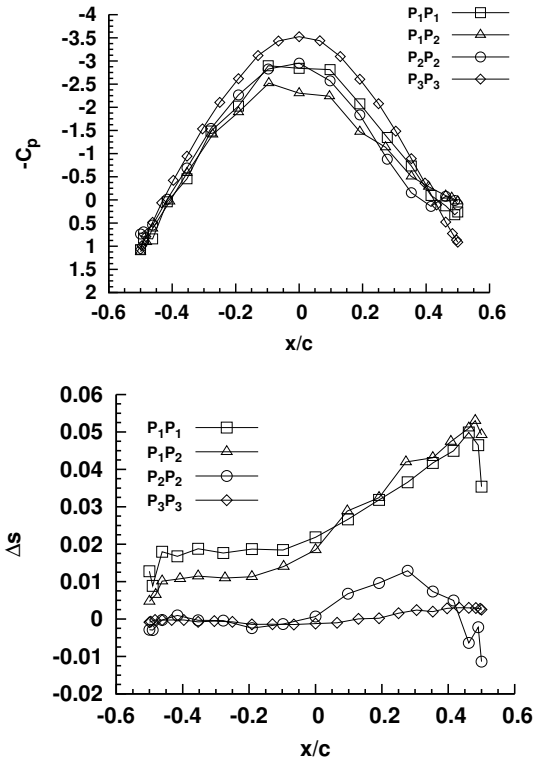

Figure 6: Pressure coefficient (left) and entropy deviation $s - s_{in}$ (right) on the cylinder wall on mesh M1

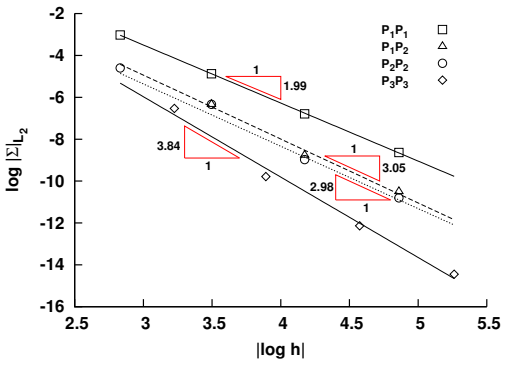

Figure 7: Subsonic cylinder test case; L_2 norm of the entropy error as a function of the mesh size h.

4. Residual distribution schemes with variable distribution coefficient

We consider a linear differential problem

$$\mathcal{L}u = f,$$

with for example $\mathcal{L} = \boldsymbol{\lambda} \cdot \nabla$ or $\mathcal{L} = \boldsymbol{\lambda} \cdot \nabla - \nu\Delta$. The numerical solution $u^{h,k}$, is a FE representation polynomial of the discrete solution:

$$u_h = \sum_{T \in \text{mesh}} \sum_{j \in T} \varphi_j u_j^{h,k}$$

When $k = 1$ ($u^{h,k}$ is a linear polynomial), RDS proceeds as follows

1. *Compute residual:*

$$\begin{aligned} \Phi^T &= \int_T \mathcal{L}u^h dX = \sum_{j \in T} \left(\int_T \mathcal{L}\varphi_j \, dX \right) u_j \qquad (21) \\ &= \sum_{j \in T} u_j \int_T k_j \, dX \end{aligned}$$

   defining k_j as

$$k_j = \mathcal{L}\varphi_j$$

2. *Distribution:* achieved eventually via the definition of coefficients $\beta_i^T = \beta_i^T(\{k_j\}_{j \in T}, u_h, \boldsymbol{\lambda}, h, \Phi^T)$
3. *Assembly/resolution:* obtain the values $\{u_j\}_{j \in \text{mesh}}$ as a solution of $\sum_{T | j \in T} \beta_j^T \Phi^T = 0$

In the linear case the derivatives of the basis functions are constants. This allows the following reinterpretation of the above scheme as a Petrov–Galerkin scheme with particular test functions.

1. Definition of the test function β:

$$k_j = \mathcal{L}\varphi_j, \quad \beta_j(x) = \beta_j^T(\{k_j\}_{j \in T}, u_h, \boldsymbol{\lambda}, h, r^T) \quad \text{with } r^T = \mathcal{L}u_h|_T$$

2. Integrate: $\Phi_i^T = \int_T \beta_i(x) r^T$
3. Assembly/resolution: get the values $\{u_j\}_{j \in \text{mesh}}$ by solving $0 = \sum_{T | j \in T} \Phi_i^T = \sum_{T | j \in T} \int_T \beta_i(x) r^K$

Since all the known definitions of β_i^T depend on the definition of k_j (i.e. on the derivatives of the shape functions), the two schemes are identical in the P^1 case. The schemes are not the same anymore for P^k interpolation, $k > 1$.

4.1. Conservation issues

In case we need apply the method to nonlinear conservation law

$$\nabla \cdot \boldsymbol{\mathcal{F}} = 0$$

a necessary condition for the scheme to converge to some weak solution is that

$$\sum_{j \in K} \varphi_j = \oint_{\partial K} \boldsymbol{\mathcal{F}}(u^{h,k}) \cdot \boldsymbol{n}$$

is satisfied for some approximation of the *physical* flux $\boldsymbol{\mathcal{F}}$ which is continuous across element edges. One possible approach to satisfy this requirement is a suitable volume integration.

Suppose that the flux is approximated by Finite Element shape functions φ^F:

$$\boldsymbol{\mathcal{F}}(u^{h,k}) = \sum_{j \in K} \boldsymbol{\mathcal{F}}_j(u^{h,k}) \varphi_j^F \qquad (22)$$

The Finite Element space which interpolates the discrete flux need not be the same as the Finite Element space used for the solution variable. However, it should be richer to account for the nonlinearity of the flux $\boldsymbol{\mathcal{F}} = \boldsymbol{\mathcal{F}}(u)$. Assuming the continuity of the flux function, the following relation is satisfied for exact integration

$$\int_K \nabla \cdot \boldsymbol{\mathcal{F}}(u^{h,k}) = \oint_K \boldsymbol{\mathcal{F}}(u^{h,k}) \cdot \boldsymbol{n}$$

Since the flux is interpolated as described in equation (22), the following identity holds

$$\begin{aligned} \int_K \nabla \cdot \boldsymbol{\mathcal{F}}(u^{h,k}) &= \sum_{j \in K} \boldsymbol{\mathcal{F}}_j(u^{h,k}) \cdot \int_K \nabla \varphi_j^F \\ &= \sum_{j \in K} \boldsymbol{\mathcal{F}}_j(u^{h,k}) \cdot \sum_{q \in K} |K| w_q \nabla \varphi_j^F(x_q) \end{aligned}$$

The quadrature points x_q and weights w_q are chosen such that the gradients of flux shape functions are integrated exactly. The nodal residual is then evaluated as

$$\int_K \beta_i(x) \nabla \cdot \boldsymbol{\mathcal{F}}(u^{h,k}) = \sum_{j \in K} \sum_{q \in K} |K| w_q \beta_i(x_q) \boldsymbol{\mathcal{F}}_j(u^{h,k}) \cdot \nabla \varphi_j^F(x_q)$$

4.2. Advantages of RD formulation with variable β

The RD schemes with variable distribution coefficient β work without any substantial modification not only on simplex elements, but also on tensor-product

elements (quadrilaterals in 2D). The construction of sub–elements used previously for the RD method becomes an important issue as the polynomial order of the underlying FE interpolation space becomes high (number of quadrature points per element quickly increases) and as we go to three dimensions (division into sub–elements becomes rather complex to implement in computer codes).

The generic formulation (21) avoids these problems and at the same time, it preserves the upwind nature of the original formulation of the RD schemes.

4.3. Examples of schemes

LDA

For the LDA scheme, we set

$$k_i = L\varphi_i = \boldsymbol{\lambda} \cdot \nabla \varphi_i, \qquad \beta_i^T = \frac{k_i^+}{\sum\limits_{j \in T} k_j^+}$$

and the nodal residual becomes

$$\Phi_i^T = \int\limits_T \frac{(L\varphi_i)^+}{\sum\limits_{j \in T} (L\varphi_j)^+} Lu_h \, dX$$

SUPG

Using the notation above, the SUPG residual can be written as

$$\Phi_i^T = \int\limits_T (\varphi_i + \tau L\varphi_i) Lu_h \, dX$$

with the upwind stabilization parameter $\tau = (\sum\limits_{i \in T} k_i^+)^{-1}$.

5. Scalar advection test case

Given a rectangular domain, we consider a steady advection equation

$$\lambda \cdot \nabla u = 0 \text{ with } \boldsymbol{\lambda} = (y, -x)$$

A cosinus profile is imposed at the inlet. The advection field is supposed to rotate this profile in the direction indicated in figure 8. The solution obtained with the LDA and SUPG schemes on a mesh consisting of P_2 triangles is depicted in figure 9.

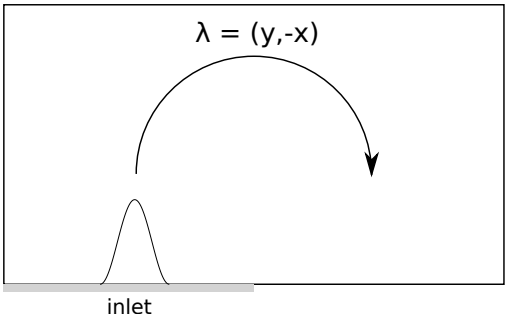

Figure 8: Setup for linear advection test case

6. Euler 2D test case

The extension of the scheme to a (nonlinear) system of equations was tested on a simple test case for Euler equations in 2D dimensions. Two supersonic states $\mathbf{u}_{L/R} = (\rho, \rho u, \rho v, E)_{L,R}$ are prescribed at the left and right half of the inlet (inlet boundary condition), and also in the left and right half of the whole domain as initial conditions (see figure 10). This test case was chosen because it does not require wall boundary condition, which are not implemented at this moment. The solution eventually forms an expansion fan (figure 11).

Acknowledgments

The presented results were obtained in collaboration with Tiago Quintino, Mario Ricchiuto and Nadège Villedieu. The construction of residual distribution schemes with variable β-coefficients as described in section 4 is due to an original idea of Mario Ricchiuto. No papers on this topic have been published so far.

References

[1] H. Deconinck, R. Abgrall, Introduction to residual distribution methods, VKI Lecture Series, Comput. Fluid Dynam., 2005.

[2] M. Ricchiuto, N. Villedieu, R. Abgrall, H. Deconinck, On uniformly high–order accurate residual distribution schemes for advection-diffusion, J. Comput. Appl. Math. 215 (2008) 547–556.

[3] H. Deconinck, K. Sermeus, R. Abgrall, Status of multidimensional upwind residual distribution schemes and applications in aeronautics, AIAA paper 2000-2328, AIAA CFD Conference, Denver (USA), June 2000.

[4] M. Ricchiuto, N. Villedieu, R. Abgrall, H. Deconinck, High–order residual distribution schemes: discontinuity capturing crosswind and extension to advection–diffusion, VKI Lecture Series, Comput. Fluid Dynam., 2005.

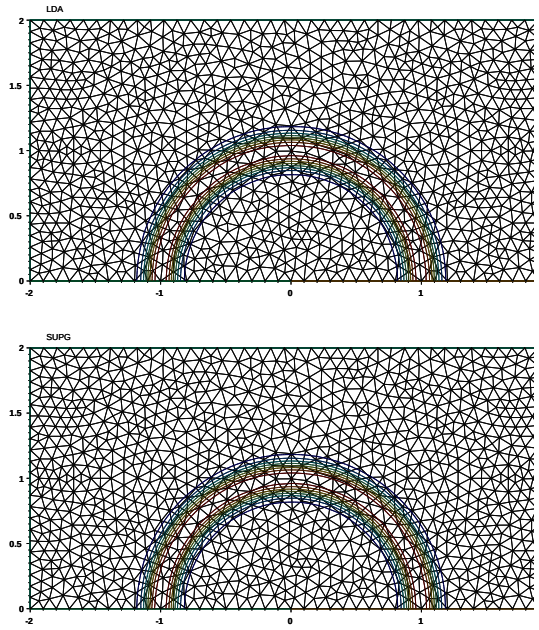

Figure 9: Linear advection test case - isolines of solution obtained with the LDA (top) and SUPG (bottom) schemes

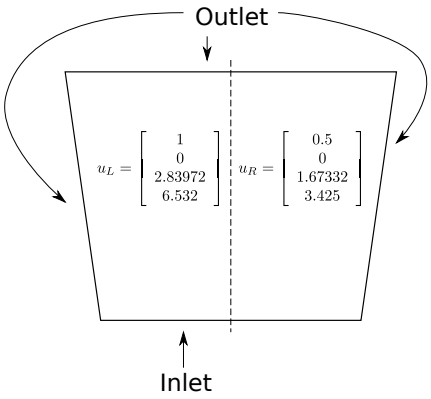

Figure 10: Initial and boundary conditions for the Euler 2D test case

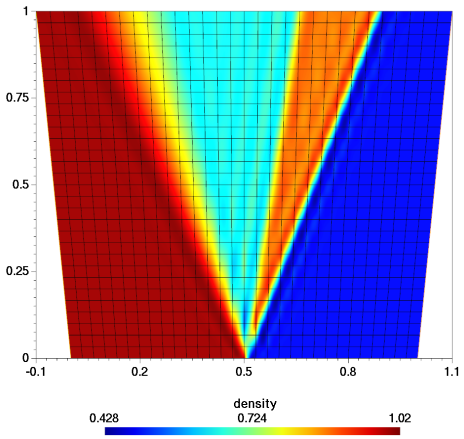

Figure 11: Solution of the Euler test case with LDA scheme on Q_2 elements

[5] H. Deconinck, P. L. Roe, R. Struijs, A multidimensional generalization of Roe's difference splitter for the Euler equations, Computers and Fluids 22(2/3) (1993) 215–222.

[6] H. Paillere, Multidimensional upwind residual distribution schemes for the Euler and Navier–Stokes equations on unstructured grids, Ph.D. thesis, Von Karman Institute for Fluid Dynamics and Université Libre de Bruxelles, Faculté des Sciences Appliquées (1995).

[7] E. van der Weide, H. Deconinck, Positive matrix distribution schemes for hyperbolic systems, with application to the Euler equations, Computational Fluid Dynamics (1996) 747–753.

[8] E. van der Weide, Compressible flow simulation on unstructured grids using multi–dimensional upwind schemes, Ph.D. thesis, Von Karman Institute for Fluid Dynamics and TU Delft (1998).

[9] N. Villedieu, T. Quintino, M. Vymazal, H. Deconinck, High-order residual distribution schemes: Unsteady and viscous terms, 35th Computational Fluid Dynamics Lecture Series, VKI/ADIGMA Course on High order Discretization Methods, Von Karman Institute for Fluid Dynamics, 2008.

[10] R. Abgrall, A. Lerat, M. Ricchiuto, C. Tavé, A simple construction of very high order non-oscillatory compact schemes on unstructured meshes, Computers and Fluids 38(7) (2009) 1314–1323.

[11] R. Abgrall, Residual distribution schemes: Current status and future trends, Computers and Fluids 35(7) (2006) 641–669.

[12] F. Bassi, S. Rebay, High–order accurate discontinuous finite element solution of the 2D Euler equations, J. Comput. Phys. 138 (1997) 251–285.

WHO'S WHO?

Who's who


Gilles
Bailet


Francesco
Baldani


Filip
Ballien


Christopher
Chahine


Leandro
Dantas De Santana


Cis
De Maesschalck


Fabrizio
Fontaneto


Clara
García Sánchez


Guillaume
Grossir


Bernd
Helber


Imre
Horváth


Bart
Janssens



Michaël
Joly



Ugur
Karban



Lasse
Müller



Alessandro
Munafo



Jorge
Pinho



Işil
Şakraker



Jérôme
Sans



Sebastian
Scholl



Thorsten
Scholz



Pierre-Louis
Schrooyen



James B.
Scoggins



Gennaro
Serino



Alessia
Simonini



Chiara
Spaccapaniccia



Erik
Torres



Stefano
Vagnoli



Bart
Van Hove



Alan
Viladegut



Martin
Vymazal

PhD candidates who have not presented a paper at the symposium



Jayson
Babajee



Evangelos
Bacharoudis



Georgios
Bellas Chatzigeorgios



Khalil
Bensassi



Henny
Bottini



Alessio
Cipullo



Boris
Conan



Stefano
D'Angelo



Giulia
Dell'Era



Anthony
Delmas



Balazs
Farkas



Jorge
Fernandes Lopes de Sousa



Victor
Fernández Villace



Jesus
Garicano Mena



Gabriele
Grasso



István
Horváth



Mohamed Hassanine
Aissa



Damien
Le Quang



Silvania
Lopes



Delphine
Laboureur



Sergio
Lavagnoli



Marcos
Lema Rodriguez



Davide
Masutti



Mehmet
Mersinligil



Domingo
Muñoz Esparza



Fatma
Ceyhun Şahin



Roberto
Tomasssini



Peter
Tóth



Nicolas
Van de Wyer



Laura
Villafañe